KAPPA

Cased Hole Logging

v5.40

The theory and practise of cased hole log acquisition and analysis and their application to well integrity, production profiling and reservoir monitoring.

Nicolas Kotlar, Olivier Allain et al.

Main authors

Nicolas Kotlar (NK)
Engineer degree from UNMDP, Argentina (2009), MSc in Reservoir Engineering from YPF (2011). Joined KAPPA in 2013. Currently Emeraude Product Champion, consultant and instructor.

Olivier Allain (OA)
Ecole Nationale des Ponts et Chaussées (1987); MSc and Engineer degrees in Petroleum Engineering from Stanford University (1987, 1988); Technical Director of KAPPA since 1991.

Contributing authors

Losamo Benano (LB)
ENSEIRB-MATMECA, Msc degrees in Applied Mathemathics and in Fluid Mechanics, University of Bordeaux (1991-1994); PL and FT Development Team Lead, at KAPPA since 1999.

Vincent Artus (VA)
PhD in Reservoir Engineering from IFP (2003); Post-doc at Stanford University (2004) and Research engineer at IFP; joined KAPPA in 2005; currently in charge of all numerical developments.

Credits to

Reviewers: **Yusak Barnabas, Erin Summers, Kevin Siggery**

Technical author: **Véronique Chassignol**

Past Project contributor: **David Wynne, Olivier Houzé**

Artworks: **Claire Turner**

About this book

Following the spirit of the KAPPA Dynamic Data Analysis book, in 2021 the first edition of the KAPPA Cased Hole Logging book was released. The objective is to provide a solid technical reference on sensor physics, operational aspects and the interpretation methodologies of the various Cased Hole Logging (CHL) techniques supported by Emeraude.

This book also constitutes a set of notes for various Emeraude courses offered by KAPPA, on Production Logging, Well Integrity, Thermal interpretation, and in-house courses with flexible content.

This book is NOT about software functionality. Tutorials, online videos and online Help exist for that purpose.

This book is a living document, which will be regularly updated with new methodologies added to the software. The version (starting with v5.40) is the same as the current major Emeraude release. It covers techniques that are supported by Emeraude at the time of writing. For example, Emeraude v5.40 does not handle magnetic thickness tools, and consequently this relevant topic is not covered in the v5.40 version of the book.

The book refers to, and shows, pictures and data of various commercial CHL tools. KAPPA would like to thank the companies for allowing the use of these. However, the book does not promote the use of any specific tool. The tools or data shown do not represent author's preference or recommendations for a specific job.

Most of the chapters of this book are independent, and can be read without following a specific order. The only exception are those related to Production Logging (3 to 6); following them in the given order will be easier for the reader with no previous knowledge of the topic.

The KAPPA Dynamic Data Analysis v5.40 book presents a number of overlaps with this CHL book. Chapter 17 of the DDA on Production Logging will be removed in future versions, as this is now covered in more detail here. Also, Chapter 18 of the DDA, on Thermal Analysis and Simulation, is now Chapter 7 of this book.

Foreword

The KAPPA journey in Cased Hole Logging started more than twenty years ago with Emeraude v1.0, at a time when PL interpretation was essentially the realm of service companies, and operators were not doing much analysis themselves. The situation was the result of a lack of a tool agnostic common software platform and the misconception that a Production Log was measuring rates, whilst in fact an inflow profile relies on the skilled interpretation of the acquired data by an experienced analyst.

‘**Production Logging is not rate measurement…**’ became our mantra. With Emeraude as a vendor-neutral, easy-to-use (are we allowed to say fun?) interpretation package, KAPPA embarked on an Evangelical campaign to educate which, in turn, developed the software’s market, to eventually become the industry standard.

Starting with conventional PL, the software kept pace with the industry as it developed increasingly sophisticated tools including Array, PNL, DTS, and MFC to arrive where it is today as a fully integrated Cased-Hole analysis platform.

This book gathers the knowledge we have acquired and developed along the way. We gratefully acknowledge the past and ongoing insight and interaction with our clients and tool manufacturers. The various chapters combine general knowledge with detailed explanations of how we believe interpretations should be done along with details of the workflows we have implemented.

Cased Hole Analysis draws engineers and scientists from many different disciplines, from Reservoir to Completions, Production to Petrophysics. It is science geek heaven combining as it does electronics, sensor technology, fluid mechanics, optics, acoustics, signal processing, thermodynamics, rock mechanics, material science, geology, etc, etc.

Our idea was not only to provide a useful and readable technical reference of depth and breadth but also inspire the reader to learn more about the fascinating way we measure and interpret cased hole data.

We have all come a long way from a simple spinner on the end of a cable.

We hope you enjoy reading this book.

OA

Book content

1 – Why CHL?: Applications of CHL throughout the life cycle of the well. Introduces key concepts on well integrity, production optimization and plug and abandonment. Summarizes CHL applications in CCS and geothermal wells.

2 – Acquisition and Operations: Covers the conveyance techniques, data transmission and storage, depth control and auxiliary measurements. These topics are common to the various CHL applications.

3 – Flowmeters and Single-phase Profiling: This is the first chapter on Production Logging. Presents the main flowmeter type: the spinners. Provides an introduction to Doppler flowmeter. The process to go from raw flowmeter data to fluid velocity, and a single phase flow profile is detailed.

4 – Fluid Identification Tools: Density, capacitance and gas hold-up used in conventional PL. Also presents the electrical, optical and capacitance tools used in Multiple Probe tools.

5 – Multiphase Flow and Profiling: Revision of key multiphase flow concepts, including flow maps and correlations. Applications in Production Logging. Interpretation methodologies.

6 – High Deviation and Horizontal PL: Flow regimes encountered in high deviation wells. The main Multiple Probe Tools (MPT) and specifics of the operations are presented. Rate computation from MPT.

7 – Thermal Analysis and Simulation: This chapter explores the different applications of temperature data, followed by a summary of the key theoretical concepts on thermodynamics. The different thermal methods offered by Emeraude and Rubis are described.

8 – Multifinger Caliper Interpretation and Applications: Description of Multifinger Caliper tools, and the processing steps to go from raw to process data. Applications on corrosion, pipe deformation and mechanical properties. Introduction to ultrasonic internal pipe radius measurements.

9 – Passive Acoustic Logging: Noise logging tools, acquisition and processing steps. Review of noise propagation and its interpretation. Introduction to DAS and sand detection probes.

10 – Cement Evaluation: Introduction to Sonic and Ultrasonic cement evaluation tools. Annular cement evaluation and common cases are presented.

11 – Pulsed Neutron Logging: Introduction to logging tools, sources and detectors. Neutron interactions. Focus on PNL Capture mode, and brief presentation of Carbon/Oxygen and Oxygen activation logs.

12 – Appendices: Selective Inflow Performance. APERM

13 – References

NOTE: This book does not include a Chapter on PVT. Although the necessary concepts are presented in the context of the CHL interpretation throughout this book, the reader is referred to Chapter 9 of the KAPPA Dynamic Data Analysis book, for a detailed introduction to black oil models and EOS.

1 – Why Cased Hole Logging?

1.A Introduction

Cased Hole Logging (CHL) started in the 1930s, with the initial objective of determining cement tops during well construction. The need for monitoring the well integrity and to identify the source of the different fluids led to the introduction of early mechanical multifinger calipers, noise logs and basic production logging tools in the 1950s. The following decade (1960s) witnessed the development of early prototypes of cement bond logs and thermal decay (pulsed neutron) tools. As horizontal wells became more common, specific tool configurations using distributed probes were introduced in the 1980s. Currently, cased hole logging is a multi-physics discipline, applying amongst other techniques, the latest knowledge of nuclear interactions, sonic propagation, optical measurements and fluid mechanics.

Cased hole logs are run with the objective of evaluating the integrity of different well barriers, such as tubing, casing, cement and packers. This may be required by local regulatory bodies at various stages in the life of a well. This includes well end of life, where barriers are installed to keep the fluids in the reservoir effectively forever.

Cased hole logs are also run to get a better understanding of the reservoir, finding the source of the different fluids (oil, gas, water), evaluating the layers' pressures and productivity, measuring the saturations behind casing and finding remaining reserves. CHL applications for reservoir monitoring or production optimization are rarely mandatory, and some wells may never experience one of these logs. In some locations, Production Logs (PL) are only run if something goes wrong, typically excess water production. Also, Pulsed Neutron Logs (PNL) may be run if the original set of open hole logs was incomplete. This chapter aims to stress the benefits of cased hole monitoring in the ultimate well production and profitability of the well.

Section 1.B presents an introduction to the applications of CHL throughout the life of the well. This includes well construction, reservoir monitoring, production optimization and finally plug and abandonment. Section 1.C demonstrates how some of the techniques and skills from CHL in oil and gas wells can be used in geothermal and carbon capture applications. The reader is referred to Chapters 2 to 11 to learn more about the specific CHL techniques and their interpretation.

1.B CHL through the well life cycle

All producing wells follow a life cycle, with a number of phases as summarized in Figure 1.B.1.

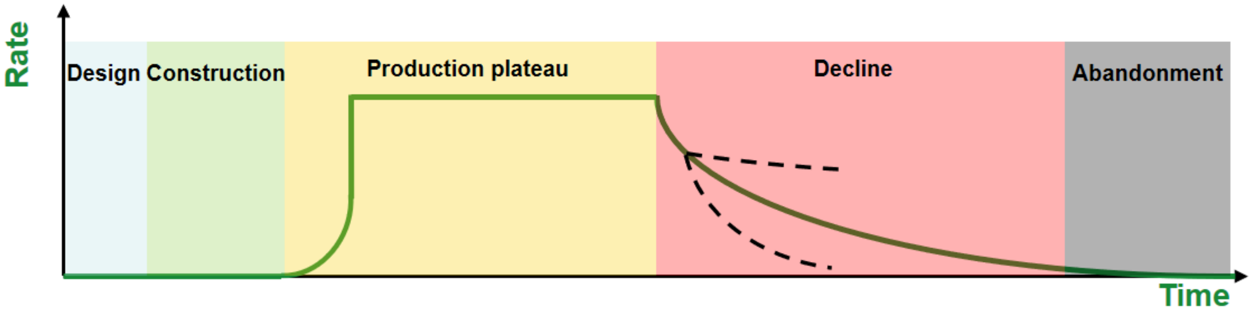

Fig. 1.B.1 – Well life cycle

The **Design** phase can be divided into two stages:

- Geological and reservoir design basis: the location, target depth and subsurface architecture (vertical, deviated or horizontal) are determined based on all the available geological and reservoir information. For prospect wells to be drilled in producing fields, the cased hole logs recorded in neighboring wells can provide dynamic data on the fluid saturations, contacts, layer productivity, reservoir pressure and pay zone thickness. These are key inputs in the reservoir model which can help target new wells more accurately. Applications of reservoir characterization are introduced in Section 1.C.3
- Well design: The drilling and completion program is defined. This includes well design, material selection, the open hole acquisition program, any required stimulation and the possible need for artificial lift. Similar to the above, dynamic well data helps in determining the optimal well architecture for production under the operational plan. Integrity logs run in existing wells of the field provide information about corrosion mechanisms that in turn lead to the selection of adequate tubulars and associated inhibitors and chemicals.

The **Construction** phase consists of drilling and completing the well, following the design study. Each part of the well is designed to control any pressure or flow that the well will see during further drilling, completion, production, intervention, stimulation or abandonment. The long term capability of the different barriers to contain the pressure and prevent fluids from moving depends on the presence and integrity of tubulars, cement barriers and seals. Cased hole logs are run at this stage to verify the presence and evaluate the annular cement, identify and quantify casing wear and assess the well deformation or tortuosity. The concept of well barriers and examples of cased hole logs run during this phase are presented in Section 1.C.1.

Once the well is operational, the **Production plateau** will be reached. The objective is to maximize this period of maximum production, which may be limited by the size of the reservoir. The onset of the decline can be postponed by delaying the water production, keeping the gas in the reservoir whilst its expansion works as a drive mechanism and understanding the layer's depletion. These points fall under the Production optimization domain and are treated in Section 1.C.2.

The last part of the operational life of the well is the **Decline** period, and this may last for decades. Late life symptoms include well barrier failures, leaks, sustained annular pressure and other well integrity issues, summarized in Section 1.C.4. Reducing the rate of decline to maximize the recovery, while producing the well in a safe way is one of the main endeavors of mature field management programs. Well re-entry for plug setting, wireline operations or workovers are typical options. However, the condition of the well at intervention are not the same as they were when the well was originally completed. A number of well intervention scenarios are summarized in Section 1.C.5.

Plug and Abandonment is the final phase in the well life cycle. A number of barriers are set across the wellbore cross-section to essentially re-establish the natural cap rock barrier capability which was penetrated during the well construction phase. P&A strategy depends on the conditions under which the well is received as the existing barriers i.e., the casing and cement, may or may not be used for this final intervention. Cement, noise and integrity logs are typical methods to assess the condition. This is treated in Section 1.C.7.

1.B.1 Well construction

From the drilling operation to the abandonment phase, wells are controlled by setting a number of well barriers. Since no barrier is perfect, to minimize the risk of an uncontrolled release of fluids, the industry has adopted a two barrier philosophy. NORSOK D-010 (2004) states that there must be *'at least two well barriers available during all well activities and operations, including suspended or abandoned wells…'.* During drilling, the primary barrier is the drilling fluid column, while the secondary barrier is provided by the casing cement, last casing set, wellhead and drilling BOP.

Figure 1.B.2 shows a schematic of the well barrier envelopes for a flowing well, as described by NORSOK D-010. Each well barrier is formed by one or several 'Well Barrier Elements' (WBE), which individually cannot prevent flow across itself. The primary well barrier is shown in blue, including the production packer, completion string (tubing) and SCSSV. The secondary well barrier elements include the casing cement, casing, wellhead, tubing hanger, and production tree. A single barrier envelope failure will not result in a pathway for fluid to flow in or out of the well, provided that the other barrier remains intact.

Setting, verifying, maintaining and monitoring the barrier elements are key points of the well integrity management system. During drilling, pressure testing is used to verify the sealing capability of the different casing sections, before continuing with the next drilling stage.

At this point, the first cased hole logs may be run, mainly to verify the presence and quality of the cement, and asses the integrity of the casing, as some drilling and completion operations may lead to different types of damage or deformation.

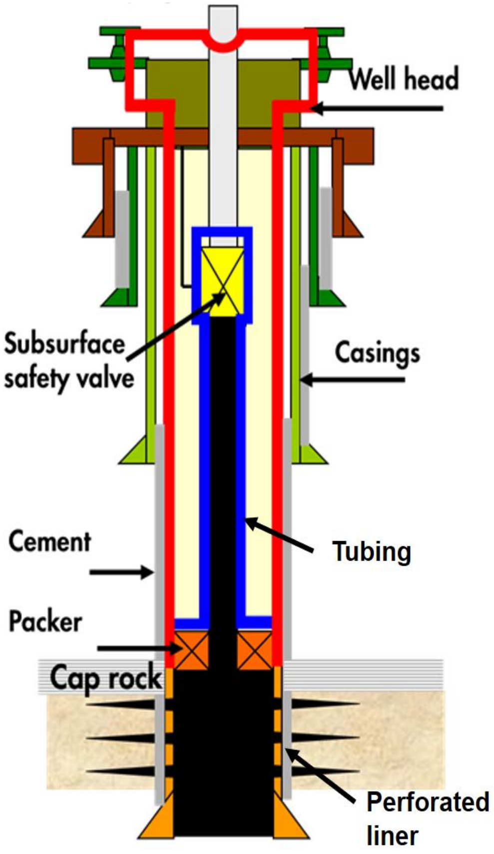

Fig. 1.B.2 – Primary (blue) and Secondary (red) well barriers (Courtesy: Altus Intervention)

1.B.1.a Cement evaluation

The theory and application of cement logs is presented in Chapter 10. All available tools are designed to measure through a single casing string, making the drilling phase the ideal period to evaluate the annular isolation behind the different casings (production, intermediate, surface, etc.).

One of the main objectives of cement logs is to evaluate zonal isolation as absence of cement may result in fluid movement behind casing, leading to undesirable fluid production. Moreover, annular cement is one of the well barrier elements which needs to be verified. But the absence of cement can also be detrimental for other barrier elements. For example, the direct contact of formation fluids with the external casing wall can lead to an accelerated corrosion rate. The loss of metal thickness can compromise the mechanical properties of the pipe, and ultimately lead to failure.

Cement logs are used to assess production packer setting depth, which acts as one of the primary barriers. Packer setting depth and establishing the top of cement (TOC) were the objectives of the cement logging job shown in Figure 1.B.3.

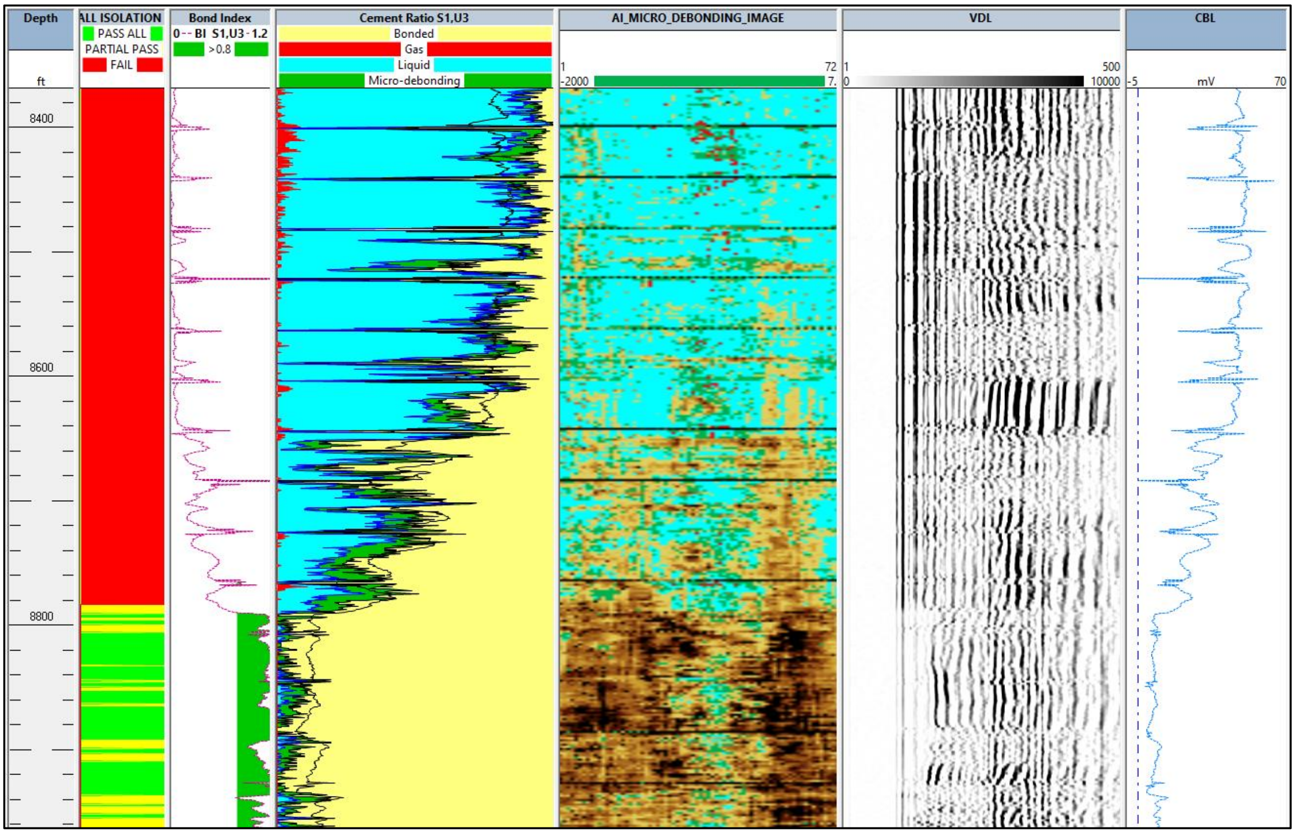

Fig. 1.B.3 – Ultrasonic cement log (Courtesy: Equinor)

Cement evaluation during well construction is key, not just for the annular sealing capability, but also for the long term sealing integrity of other well barriers.

1.B.1.b Casing wear

Once a casing string is set, a drill string may need to be run through it in order to continue with further drilling, rotate cement, or possibly drill a side-track. The constant impact of the rotating drill pipe on the casing wall may lead to a wear groove, also known as key seat. The force applied by the string is referred as side force, and its estimation for wearing prediction purposes, is one of the main objectives of Torque and Drag simulations made during the well design phase. Casing wear tends to be highest in the regions of maximum dog leg severity (DLS).

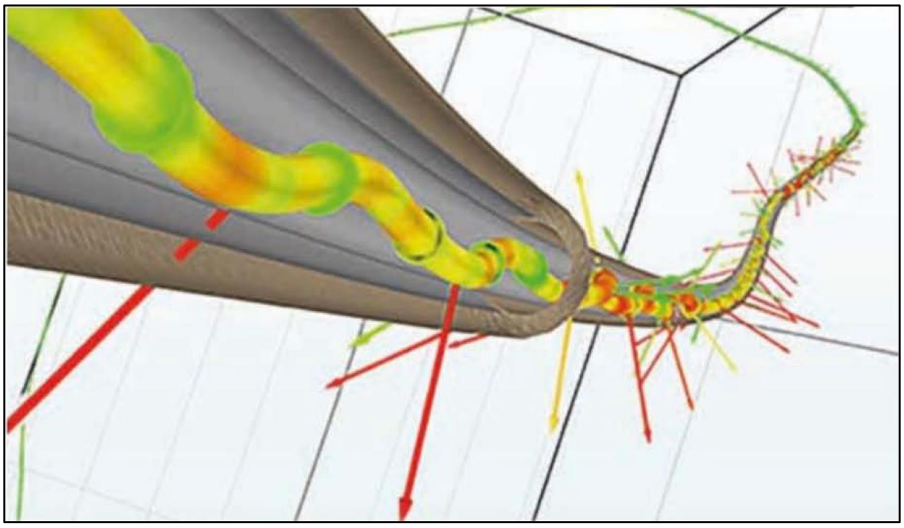

Fig. 1.B.4 – Buckled drill pipe inside a casing. SPE-183386-MS

Whilst the drilling engineers try to predict and minimize casing wear, varying drilling conditions may induce its occurrence, and the groove will affect the burst and collapse ratings of the pipes. This can lead to the first pipe integrity log that the well will receive during its life cycle, and in general it is a multifinger caliper (MFC) or an ultrasonic pulse-echo tool, detailed in Chapter 8.

The groove appears like a band of increased internal radius, typically continuous even across connections. Its severity can be quantified by the penetration percentage and the number of fingers that 'feel' the groove. This information is feedback to the well planning software, where the pipe pressure rating is re-calculated accordingly.

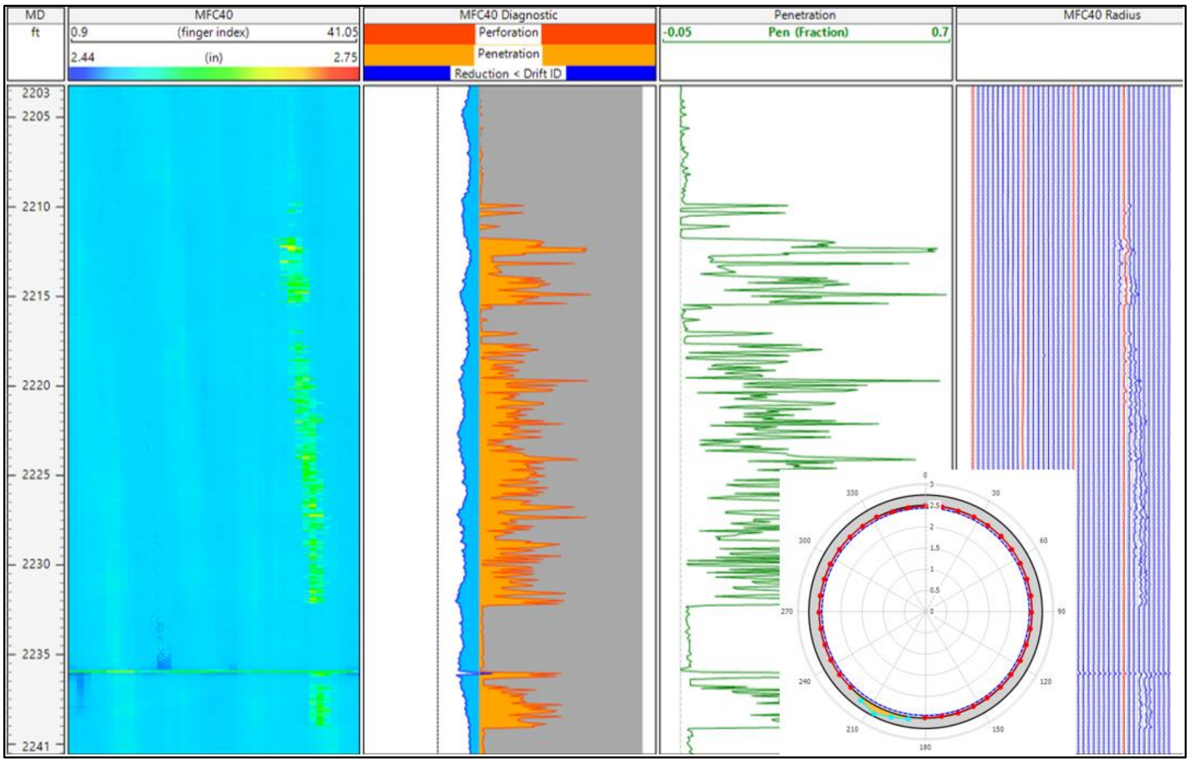

Fig. 1.B.5 – Casing wear evaluation through MFC

1.B.1.c Well trajectory and deformation

During drilling, a deviation survey is measured typically over an average span of two or three drill pipes. Therefore, parameters such as the dog leg severity or DLS, the angular difference between two points at a certain distance, are also reported as an average every 20 or 30 meters. Wellbore surveying, using gyro or logging while drilling, usually reveals that directional wells do not follow exactly the planned trajectory. Trajectory variation occurring over less than one pipe joint length is a common occurrence. Additionally, once the casing is run, there may be induced deformation mechanisms, such as buckling, shown in Figure 1.B.6

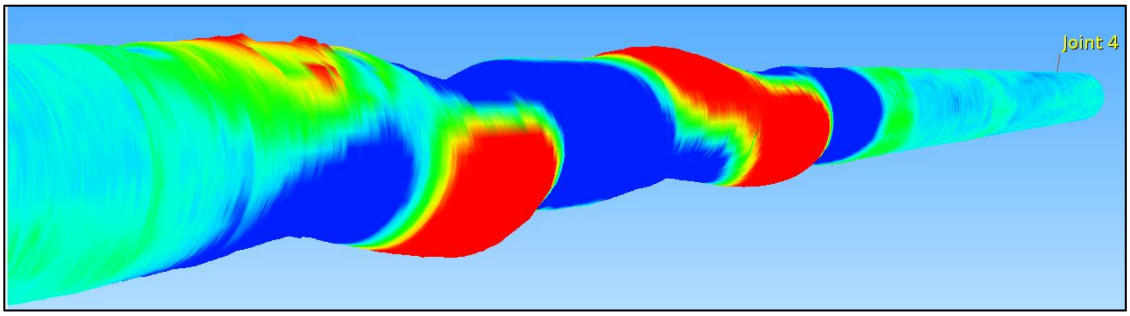

Fig. 1.B.6 – Casing deformation

These scenarios are not accounted for by the DLS calculation, and are also referred as micro-DLS, or pipe tortuosity (T):

$$T = \frac{S}{L} - 1$$

Where S is the distance between two points along the well (following the trajectory) and L is the straight line distance between the same two points.

As the tortuosity increases, running completion elements or any bottom hole assembly (BHA) through a deformed section, gets more complex, and at some point it may be impossible to proceed forward. Figure 1.B.6 is a 3D representation of a casing interval showing buckling, obtained through multifinger caliper (Chapter 8). Going through this section may be possible for a small OD tool, but the situation may not be the same for a large OD tool (i.e. a plug or packer).

1.B.2 Production Optimization

Once the well is completed, the objective is to maximize production whilst operating safely both during the production plateau and decline phases of the well life cycle. To optimize any engineering parameter, it is necessary to measure its current performance and analyze what parameters can be improved. In the case of production optimization, the objective is to measure the current well performance, decoupling the reservoir and well components, and finally establishing what variables can be maximized.

Consider a fully-penetrating vertical well producing from a homogenous reservoir. The production rate (q) can be calculated from the pseudo-steady state Darcy equation in cylindrical coordinates. In oilfield units:

$$q = \frac{k\,h}{141.2\,B\,\mu}\;\frac{(\bar{p} - p_{wf})}{(\ln\frac{r_e}{r_w} + S)}$$

Where k is the permeability, h is the thickness, B is the formation volume factor, μ is the viscosity, r_e is the reservoir radius, r_w is the wellbore radius, S is the skin, $\bar{p}$ is the average reservoir pressure and p_{wf} is the bottomhole flowing pressure.

Lumping all the variables separately from the pressure gives the Productivity Index (PI), which includes reservoir and completion characteristics. This leads to the well-known expression of the straight-line Darcy Inflow Performance Relationship (IPR), which relates the rate to the productivity index and pressure drawdown:

$$q = PI * (\bar{p} - p_{wf})$$

This equation shows that, to maximize the rate, either the reservoir and completion properties are improved, or the drawdown is increased. Practically, the productivity index can be increased by performing such interventions as acid treatments, hydraulic fracturing, increasing the net pay and re-perforating underperforming intervals.

The bottom hole flowing pressure (P_{wf}) is controlled by the wellhead pressure (P_{wh}) and the sum of the hydrostatic, frictional and acceleration losses (Chapter 5).

$$P_{wf} = P_{wh} + \rho_m \Delta z\, g + \frac{2\, f_f \rho_m u^2\, L}{D}$$

Increasing the drawdown is practically achieved by reducing the P_{wf}. Although the wellhead pressure is one of the parameters that can be varied, its value is constrained by the separator pressure and surface network configuration. Optimizing the P_{wf} typically involves reducing the hydrostatic column by performing water shut-offs, implementing artificial lift, reducing frictional pressure drops and removing downhole restrictions.

Calculating the P_{wf} at several rates leads to the Vertical Lift Performance curve, or VLP (Section 5.C.1). This reflects the capacity of the well to produce the reservoir fluids.

IPR and VLP analysis is the basis of production optimization. A number of cases are now presented.

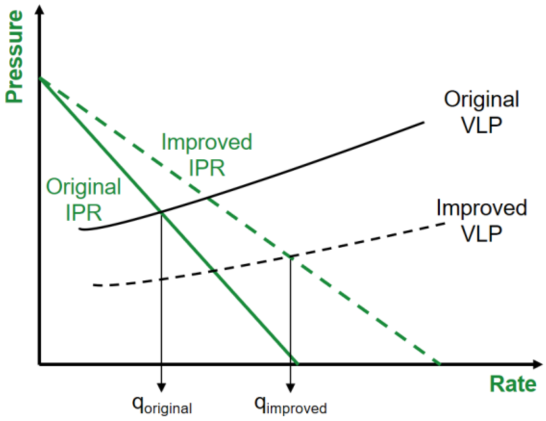

Fig. 1.B.7 – IPR-VLP analysis

1.B.2.a Increasing producing thickness

The productivity index is proportional to the permeability-thickness product. Doubling this would lead to doubling the barrels produced for the same drawdown value.

The suite of open hole logs run in old wells was often incomplete. As a result, by-passed reserves may still be in place, and the only way to produce them is to perforate these layers. One of the applications of Pulsed neutron logs, described in Chapter 11, is to quantifying the formation saturations behind casing. Figure 1.B.8 shows the results of a sigma log interpretation, where several feet of by-passed oil was detected between the two perforations.

Before opening these intervals, it is necessary to perform a complete petrophysical analysis to evaluate their porosity and permeability, as a stimulation treatment may be required. Newly opened layers may be at different reservoir pressure, which can lead to cross-flow. A PL may be run, post-perforation, in order to evaluate their dynamic behavior.

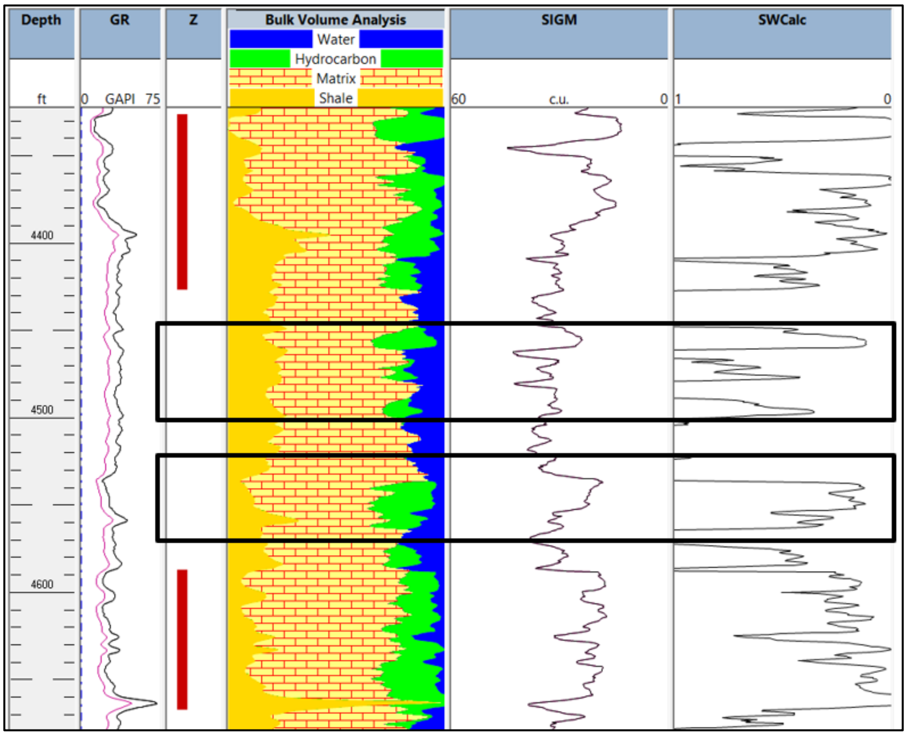

Fig. 1.B.8 – PNL (sigma) interpretation showing by-passed oil

1.B.2.b Reducing well damage

Decreasing skin improves the productivity index. In Chapter 3 it is shown how a multirate PL can provide an estimate of a layered productivity index in an analysis called Selective Inflow Performance. However, to differentiate between high damage or low permeability, pressure transient analysis is needed. PL toolstrings are equipped with a pressure gauge of sufficient resolution and accuracy to record a build-up or fall-off.

Figure 1.B.9 shows two cases of well damage. On the left, the green curves show the original condition of the well, characterized by a large skin (high delta P). The red curves show the well after a hydraulic fracture, leading to a much smaller delta P.

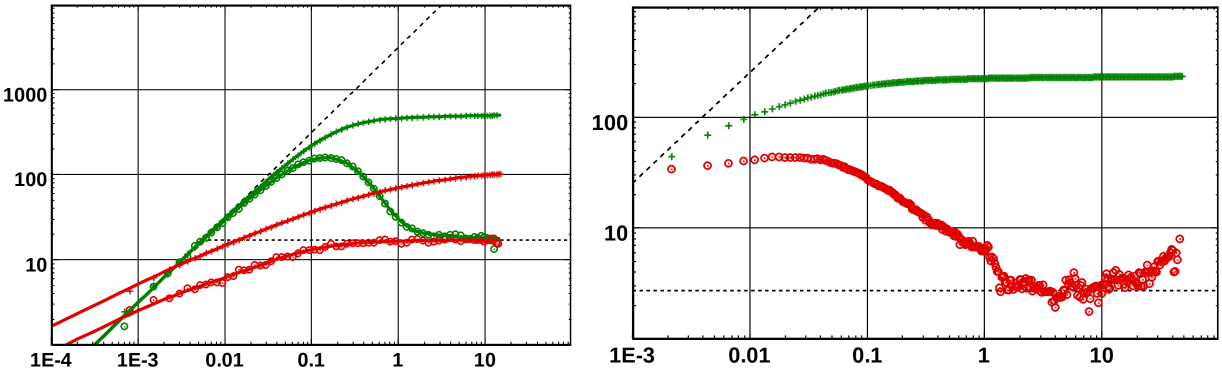

Fig. 1.B.9 – Damaged (green) and fractured (red) well PTA (left)
Partially penetrating well (right)

Figure 1.B.9 right shows that the same recipe is not applicable to all wells. In this case there is also large damage, but the derivative signature shows a -1/2 slope, characteristic of partial penetration. In this case, re-perforation (increase thickness) can be a more suitable solution.

1.B.2.c Water Shut-off

Whilst the previous two examples were related to the productivity index, the following two examples affect the vertical lift performance.

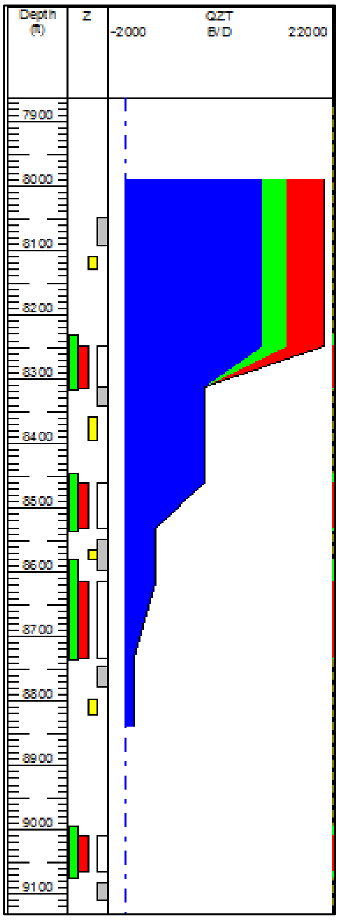

The main component of pressure drop in the pipe is the hydrostatic head. As this is a function of the mixture density, the presence of water leads to an increased weight of the column, hence increasing the bottomhole flowing pressure. Excess water is the main reason production logs are run.

Fluid identification tools and multiphase flow are presented in Chapters 4 and 5 respectively. The techniques and sensors described in these chapters are used to quantify the multiphase flow profile, as shown in Figure 1.B.10. Luckily, this well shows that 92% of the produced water comes from the bottom 3 perforations. The decision to perform a water shut-off seems obvious. Apart from decreasing the P_{wf} and potentially increasing the hydrocarbon production, the lifting costs and corrosion rates would also be reduced.

Not all the water identification PL jobs are as clear as this one. A layer may produce thousands of barrels of water, but still contribute with hundreds of barrels of oil. The decision to shut off a layer or continue producing it is down to the operator, and includes economic, integrity and surface capacity considerations.

Fig. 1.B.10 – PL profile and water inflow identification

1.B.2.d Removing scale

Scale deposition on the inner pipe wall increases the frictional pressure drop due to the combined effect of restricted ID and increased roughness. Chapter 2 (Section 2.D.3) presents an image of a scaled-up pipe (Fig 2.D.4), and explains the use of Gamma Ray sensors to identify its presence.

Figure 1.B.11 is a multifinger caliper cross-sectional image, showing that the internal diameter decreased by 20%, with a direct influence on the frictional drop:

$$\Delta P_{fr} = \frac{2\, f_f \rho_m u^2\, L}{D}$$

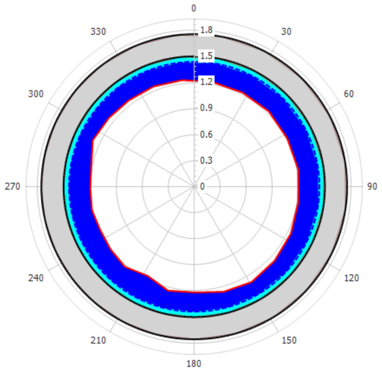

Scale minerals like calcium carbonate present an absolute roughness two orders of magnitude higher than steel, which has an impact on the friction factor (f_f) in the above equation. Chemical and mechanical scale removal operations are available, depending on the mineralogy. After the treatment, a second MFC survey might be run, as the pipe condition may have been affected, and this was previously unknown due to the deposition.

Fig. 1.B.11 – Scale deposition and reduced ID

1.B.3 Reservoir Characterization and monitoring

Different cased hole logs help in characterizing and monitoring the evolution with time of the building block variables of any reservoir model, such as the permeability, layer pressures and saturations. These are vital for multilayered reservoirs were the different properties can vary dramatically with depth.

Figure 1.B.12 shows an early production log in the largest oil field in the world, Ghawar, Saudi Arabia. This log shows a 4 ft interval with a productivity index of 5843 B/D/ft!! However, most of the interval is a tight dolomite, with not particularly high values of porosity and permeability, shown at the right of the log. This super permeability streak detected in the Arab D formation had a large impact on the field development. Apart from contributing large amounts of oil, this super-k streak leads to early water breakthrough.

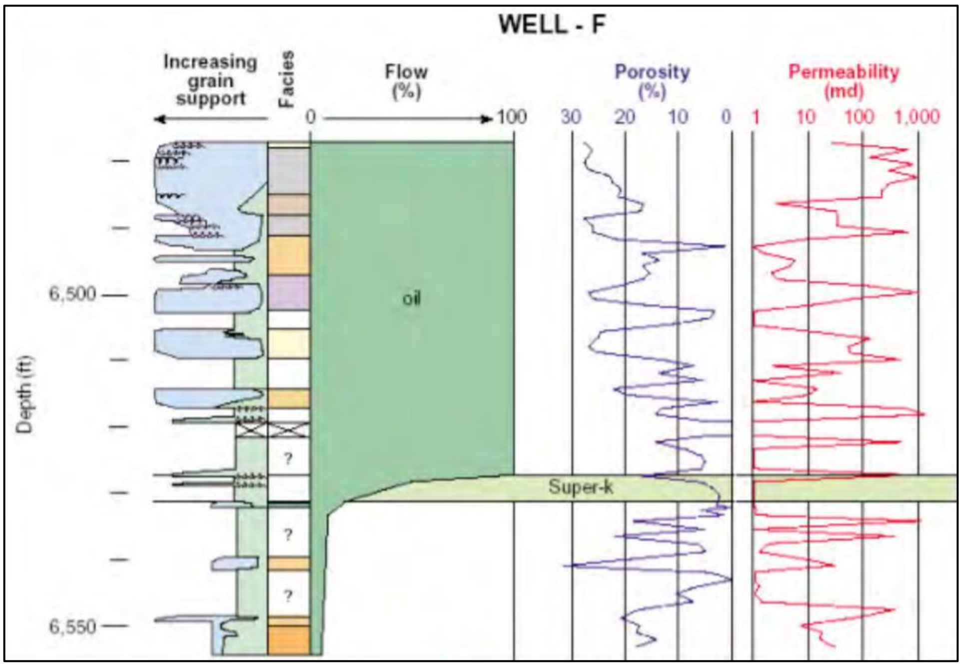

Fig. 1.B.12 – "Stratigraphic and Petrophysical Characteristics of Cored Arab-D Super-k Intervals, Hawiyah Area, Ghawar Field, Saudi Arabia", GeoArabia, v.5. no.3, 2000, p.355

Dynamic estimations of permeability are very useful, especially in fractured carbonates, vuggy or dual porosity reservoirs, where the core permeability is low, leading to a low permeability transform (phi-k). However, when the well is producing, the reservoir response is given by the combined effect of the low permeability matrix and the high permeability fissures.

As a result of the PL analysis, the layer rates are computed. At the same depth, the bottomhole flowing pressure is measured, and the fluid PVT properties are (hopefully) known. With an estimate of the average layer pressure, which may come from a SIP analysis, it is possible to estimate the permeability by solving the Darcy pseudo-steady state equation presented previously (straight-line IPR). This method is called Apparent Permeability, and also requires the knowledge of the layer skin, for which a PTA is required.

Figure 1.B.13 shows the conventionally obtained and the PL-derived permeability maps for the massive Tengiz field, in Kazakhstan. The authors reported that the history matching and interwell connectivity test accuracy improved significantly when using dynamic permeability estimations.

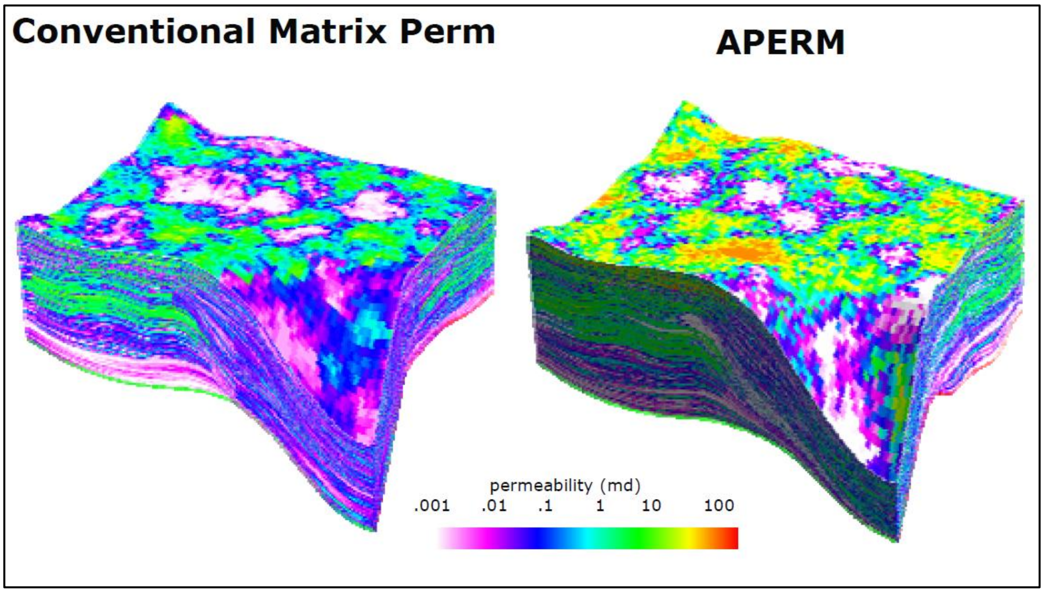

Fig. 1.B.13 – Conventional reservoir model (left) and model constructed using APERM (right) – SPE-102894-MS

Tracking and predicting the formation saturations is also crucial for current and future wells. The advance of the water front in fields under secondary recovery is a function of the phase mobilities, and involves relative permeabilities, capillarity, and other variables which may be difficult to predict.

Figure 1.B.14 shows a pore volume analysis with a number of water saturations calculated from pulse neutron logs run in four different years. Feeding this information into a reservoir simulator helps to increase the accuracy of multiphase production forecasts.

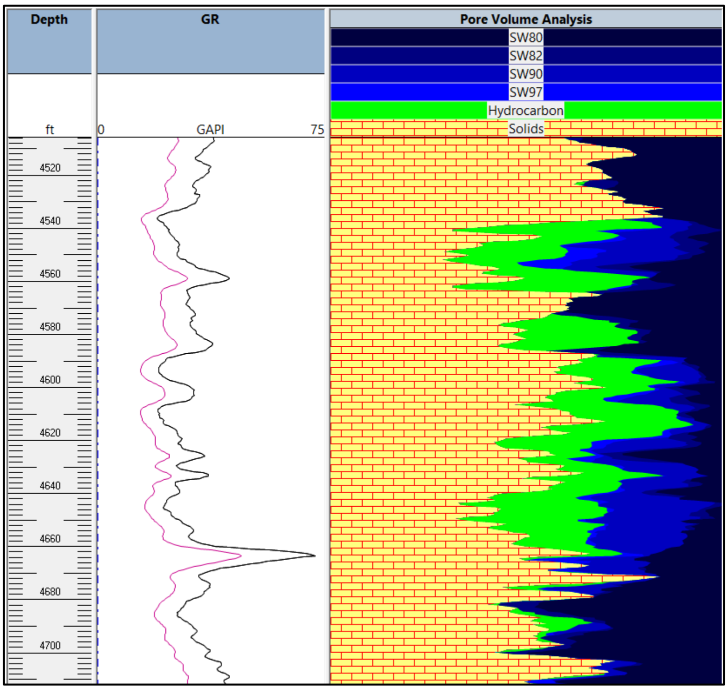

Fig. 1.B.14 – Time-lapse pulsed neutron logging

Passive acoustic, or simply 'Noise' logs (Chapter 9) also provide valuable information on reservoir flow. The acoustic signature is characterized by the amplitude and frequency. As noise is generated in response to turbulence, the frequency is related to the characteristic length of the turbulence. The narrower the flow path, the higher the frequency due to the smaller size of the eddies.

Figure 1.B.15 shows an integrated PL-Noise interpretation. The oil and water production come from a single perforation; however, the spectral noise logs suggest that the reservoir fluid movement occurs below the perforation, in a region where carbonate macroporosity is expected based on the NMR modeling. The noise frequency shows a peak below 8 kHz, indicating macropore flow, and correlating with the NMR. Noise logging applications for reservoir characterization are presented in Chapter 9.

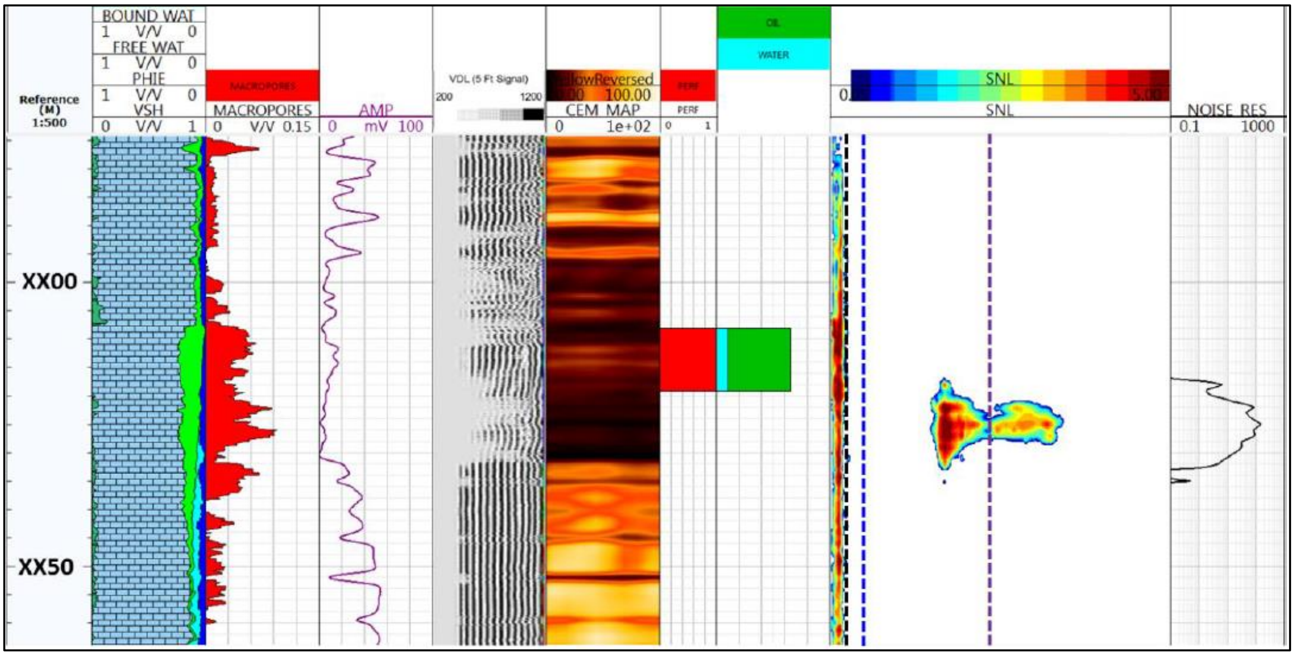

Fig. 1.B.15 – Image from 'Quantitative Spectral Analysis of Noise Log Measurements for Enhanced Dynamic Characterization of Complex Reservoirs' – Cicione, Galli, Pirrone and Raimondi – ENI S.p.A (presented at OMC-2017)

1.B.4 Well Integrity

Having talked about well integrity previously, a proper definition is pertinent. NORSOK D-010 (2004) standard defines well integrity as the '*application of technical, operational and organizational solutions to reduce the risk of uncontrolled release of formation fluids throughout the life cycle of the well*'.

Well integrity starts before drilling the well, during the design phase where the materials are selected, and barriers are designed. As time passes, however, the wells start to exhibit late life symptoms, which lead to mechanical issues.

The UK Continental Shelf is an example of a maturing basin, where the average life of the 2148 operational wells in 2017 was 27 years. The Oil and Gas Authority reported (Wells Insight Report, 2018) that around 600 of the operational wells are shut-in, with well integrity and water production issues accounting for 62% of these. It is also estimated that an additional 22.5 MMBOE could be recovered by improving underperforming wells and reactivating shut-in wells.

In a study by the Norwegian Petroleum Safety Authority (PSA) of 406 wells, 18% had reported well integrity barriers failures, and 7% had to shut-in due to loss of barriers. The study included a breakdown of the well integrity issues found in this well population. Tubing issues accounted for 39% of the failures, while casing problems was around 11%. Even though this study was conducted 15 years ago, it is believed that the failure distribution remains similar. And this is one of the reasons why Multifinger Caliper is still a key service throughout the life of the well.

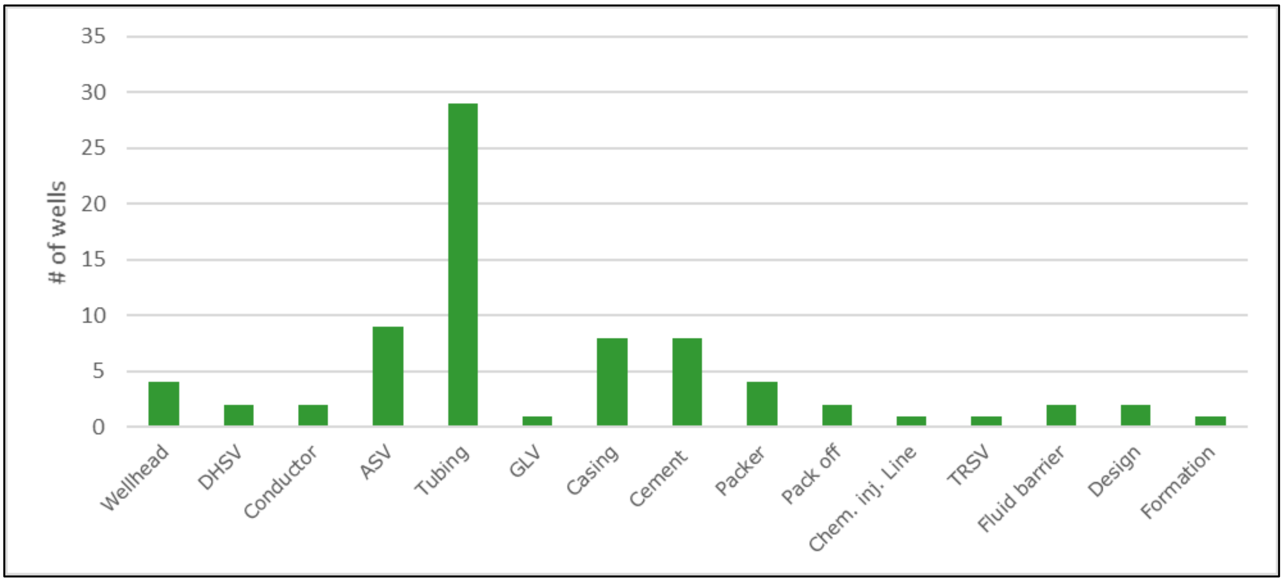

Fig. 1.B.16 – Number of wells with integrity problems (out of 406 studied) - PSA 2006

Another typical well integrity problem is Sustained Casing Pressure (SCP). This is a pressure in any well annulus that is measurable at the wellhead and rebuilds when bled down, not caused solely by temperature fluctuations nor imposed by operators.

The origins of sustained casing pressure can be tubing and casing leaks, poor primary cement and damage to primary cement.

In a study conducted by Louisiana State University on request of the Mineral Management Service (An agency of the US Department of Interior), it was found that in the Gulf of Mexico, 11498 casing strings in 8122 wells exhibit sustained casing pressure or, on average, more than one annular per well. Fortunately, most SCP cases were found in the A-annulus, between tubing and production casing. This is in-line with the observations made by the PSA, as A-annulus pressure is usually related to tubing and packer leaks.

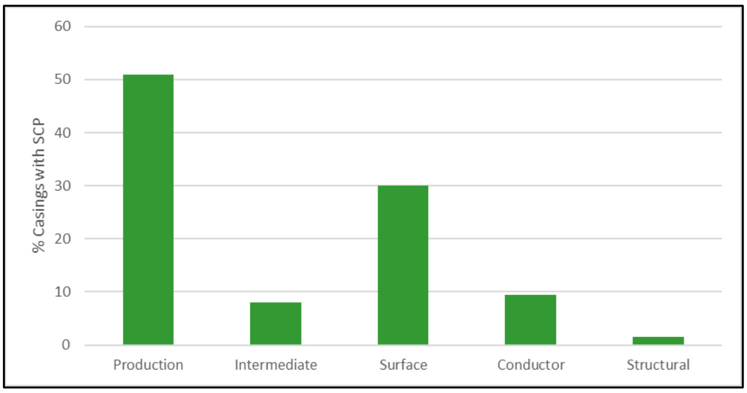

Fig. 1.B.17 – SCP by string – GOM, 2000

Chapters 7 to 10 present the typical tools used to identify and evaluate well integrity problems. Also, a number of common issues and their causes are introduced. As summarized in this section, tubing leaks are a big industry problem, but fortunately these are easier to find and solve than an external casing or cement failure. The sensors included in the leak detection toolstring may include multifinger calipers, temperature, spinners, and noise logs. Figure 1.B.18 shows the combination of all of these to pinpoint a leak in a 5.5-inch tubing, while pumping water through the tubing and producing through the annulus.

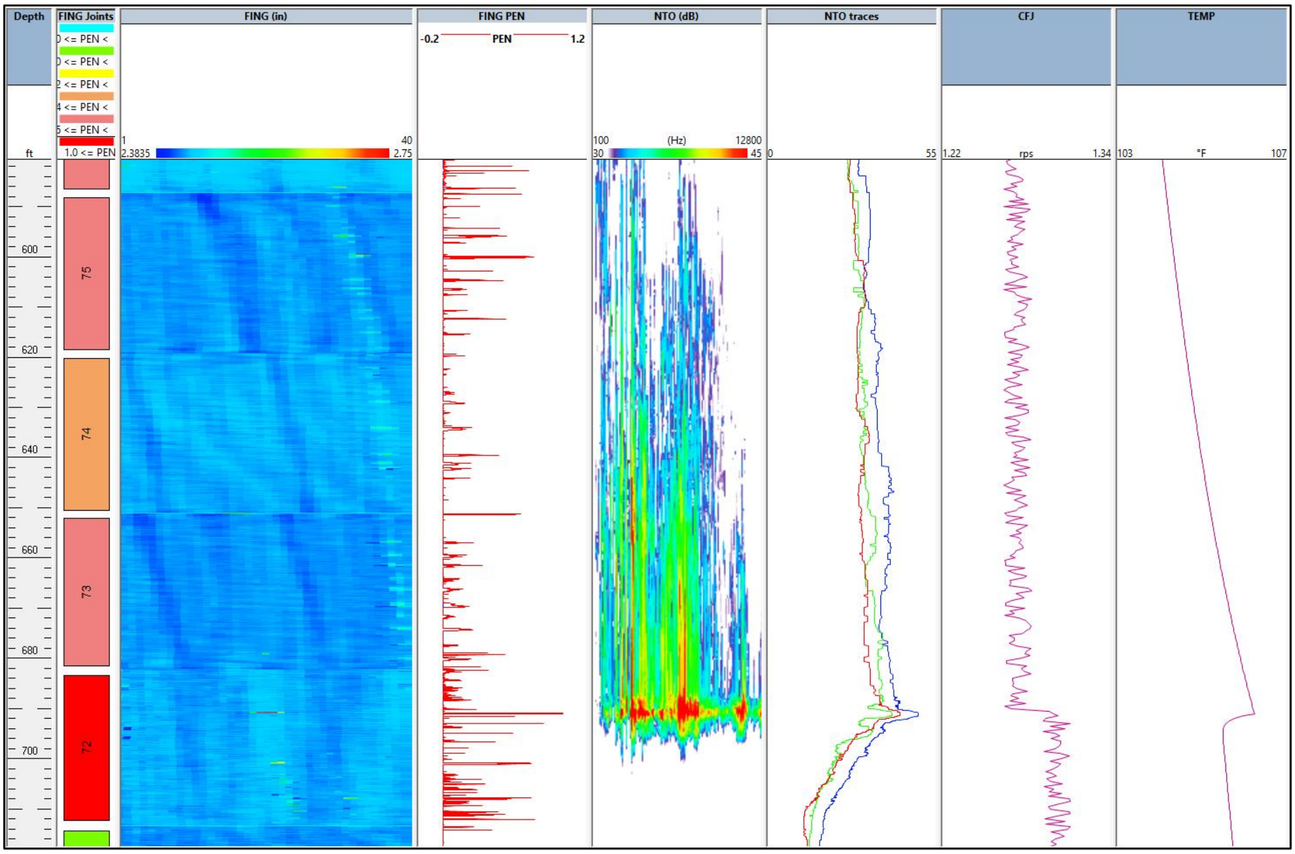

Fig. 1.B.18 – Tubing leak detection through MFC, noise, spinner and temperature

1.B.5 Well Intervention

Throughout the well life cycle it may be necessary to perform interventions to monitor the reservoir or well integrity, modifying the completion or perform, for example, a pressure pumping operation. These operations can be live well operations as in slickline or wireline, or may require killing the well in the case of a workover. Regardless of the objective, to safely and successfully run these operations, the well condition must be such that the bottomhole assembly reaches the target depth and the different barriers withstand the applied pressures and stresses. This is particularly important for mature wells, as the mechanical properties of the tubulars are not the same as they were originally, due to the loss of metal thickness.

To illustrate the well integrity implications in the context of a well intervention, consider the operations performed during a hydraulic fracture. In an ideal plug and perf operation, a plug is set below the interval of interest, then the pipe is perforated (in the same run), the wireline is retrieved and then finally the fracture treatment is pumped.

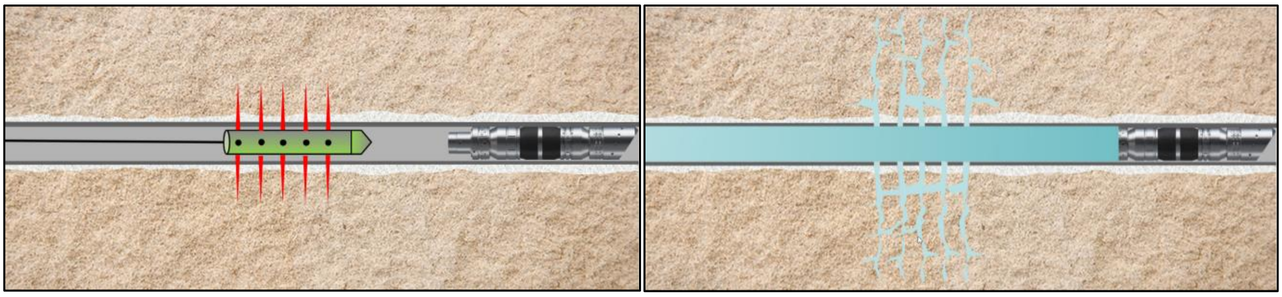

Fig. 1.B.19 – Plug setting and perforating (left) – Fracture pumping (right)

This applies to both, conventional and unconventional fractures, in new or old wells. Regardless, the successful completion of the operation requires:

1. The plug and perforating guns must reach the depth of interest
2. The fracture treatment must be directed to the target perforations
3. The fracture treatment must not compromise the mechanical integrity of the pipe
4. The fracture treatment must not propagate laterally without control due to lack annular isolation

Reaching the depth of interest may not be possible if the pipe is severely deformed or scaled up. While the latter is possible remove, the former is not and will constrain the maximum depth of intervention. Figure 1.B.6 shows a buckled pipe, and other deformation mechanisms are presented below.

The localized tortuosity limits the maximum rigid body length that can pass through it. Figure 1.B.20 (left) shows a 3D MFC image recorded along a bent casing joint.

The image on the right shows an ovalized cross-section. As the ovalization increases, the minimum diameter decreases, and may reach the situation where the plug or packer cannot pass.

Also, the plug setting depth cannot exceed certain ovalization percentage (i.e. 3 to 5%) as the sealing capability of the packing elements decrease.

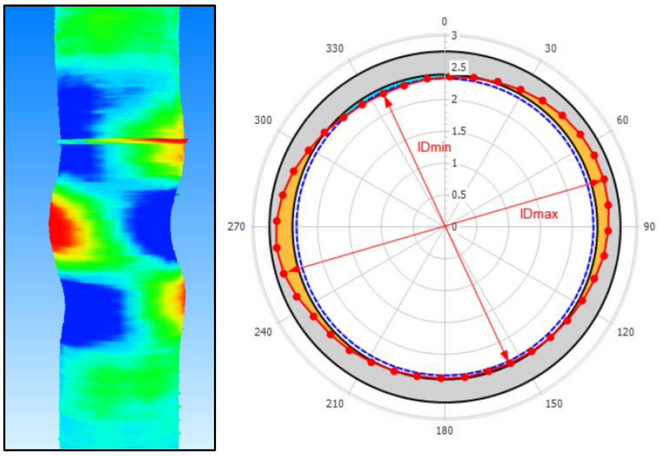

Fig. 1.B.20 – Bend (left) and Ovalization (right)

Making sure that the fracture, acid or any pumping operation reaches the target depth is also critical for bullheading operations, or when pressure testing is required before conducting certain treatments.

Leaks detected with MFC or ultrasonic pulsed echo tools were shown in the previous section, and a picture of a retrieved corroded tubing is shown in Figure 1.B.21 (left). Needless to say, that the treatment will also leak and go elsewhere. Another point is the capacity of the pipe to sustain the pressures exerted during the pumping operation. Figure 1.B.21 right shows a casing burst, where the hoop stresses exceeded the strength of the pipe. The pipe mechanical properties calculations are described in Chapter 8, and demonstrate that the maximum pressure that the pipe can sustain is proportional to its thickness. After months or years of exposure to corrosive fluids, the pipes lose metal thickness, reducing the burst and collapse pressures. Evaluating the integrity of the well before conducting a hydraulic fracture is critical for avoiding catastrophic failure.

Fig. 1.B.21 – Corroded tubing (left) and casing burst (right). (Courtesy: Altus Intervention)

Finally, if, when the treatment reaches the target depth, the annular seal has failed, the fluids will not necessarily propagate to the formation at the depth of the perforations. If it is allowed to propagate laterally, the fracturing pressure and propagation rate will be affected, and the proppant may not reach the open channels created by the fluid. As a consequence, the effectiveness of the hydraulic fracture decreases, and it may lead to communication with other perforated intervals or production of the proppant during the flowback. Cement evaluation is the subject of Chapter 10.

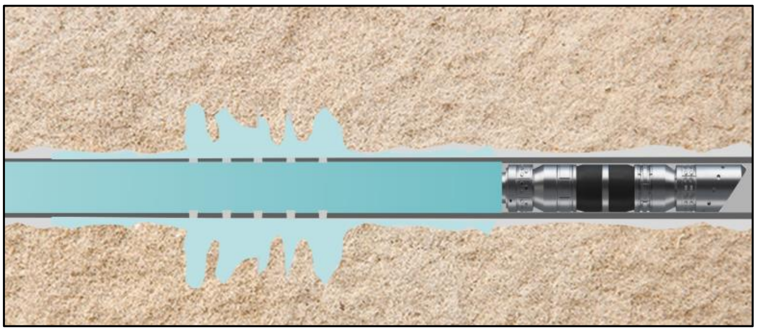

Fig. 1.B.22 – Lack of annular sealing during a hydraulic fracture

This example used a hydraulic fracture treatment to demonstrate the importance of well integrity in the context of interventions, as this operation is particularly 'aggressive' and involves multiple runs, pumping and wireline. However, all the points presented previously are applicable for any other intervention which requires reaching a target depth and pumping a certain treatment.

1.B.6 Well Operational Envelope

Optimizing well production whilst ensuring well integrity and maximizing the expected reservoir recovery is a multidisciplinary endeavor where cased hole logging plays a key role.

The Inflow Performance Relationship for each layer can be estimated through the SIP method. This defines the range of bottomhole flowing pressure to produce the well in order to obtain the target production, without experiencing crossflow. Other reservoir factors can limit the P_{wf} range, including critical drawdown for coning, or for solid production in unconsolidated formations.

However, this safe region from the reservoir point of view may not be ideal when considering flow assurance as, for example, liquid loading may occur in gas wells when the rates are low, or the other extreme where the erosional velocity is reached when the rate is too high. These are now two boundaries in the safe region for production.

Finally, it is necessary to incorporate the well integrity and pressure, or differential pressure, ratings of the different barriers. The current mechanical properties of the pipes are not necessarily the same as when the well was completed due to corrosion. The updated burst and collapse pressure and maximum differential pressure across packers, are all the boundaries from the well integrity point of view.

It is possible to include all these factors in a single plot, which uses the same axes as the IPR (pressure and rates), and is called 'Well Operational Envelope'. A schematic example is shown in Figure 1.B.23 for a producing well. In most producing wells with relatively good casing and tubing condition, the burst and collapse pressure should not be limiting factors. However, for high pressure reservoirs with accelerated corrosion, or water injectors these factors become very important.

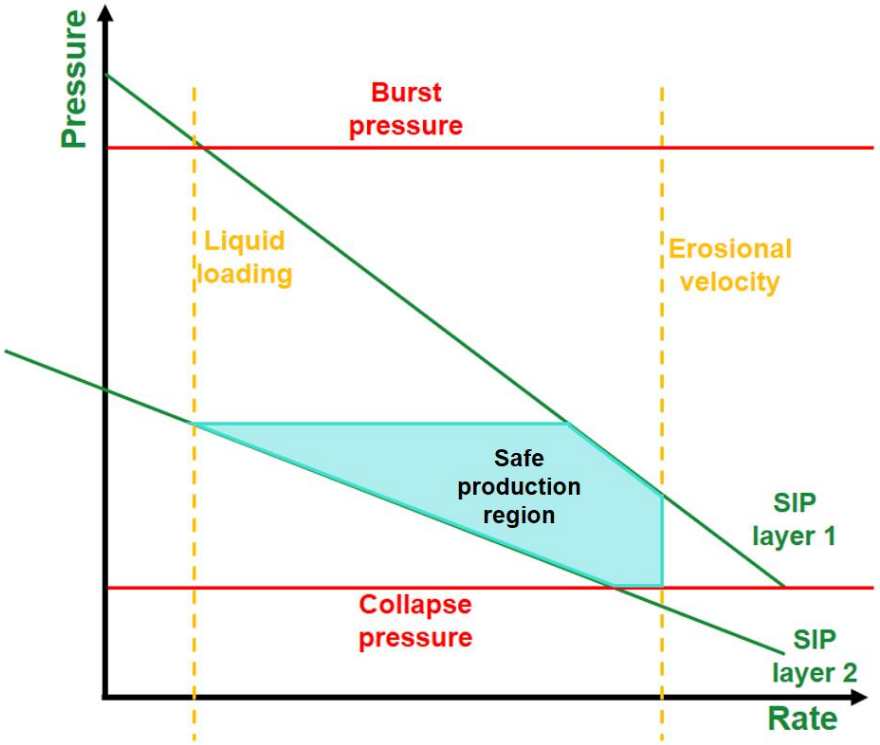

Fig. 1.B.23 – The well operational envelope

This plot is a snapshot at a particular time in the life of the well. As the reservoir pressure drops, layers' PI vary, flow regimes change, corrosion continues to reduce the pipes' metal thickness and this analysis becomes 3D. Many of these factors can be forecasted with reasonable accuracy, such as the reservoir pressures and corrosion rates. However, keeping track of these variations is vital for predicting and hopefully extending the life of the well, thus maximizing the hydrocarbon recovery and the profitability of the well.

1.B.7 Plug and Abandonment

The last phase of the well life cycle consists of safely and permanently abandoning the well. The reasons for abandoning the well may be because the well has reached its economic limit and is simply no longer profitable to operate. But it can also be due to severe well integrity failures, depleted reserves (maximum recovery), etc. The Plug and Abandonment (P&A) operation is the beginning of the end of the life of the well.

At the time of writing (2021) there is a P&A 'wave' in the North Sea. Oil and Gas UK (Well Insight Report 2018) shows that more wells are being P&A than drilled. P&A accounts for 45% of the total decommissioning cost, and in 2016 alone £402 million was spent on abandonments. Over 150 wells per year are expected to be abandoned.

During the well construction phase, a number of formations that act as geological barriers are penetrated for the hydrocarbons to flow to surface. The objective of P&A is to restore the cap rock functionality, by setting a number of effective barriers across the wellbore cross-section. These barriers '*…shall be designed such that they take into account well integrity for the longest period of time the well is expected to be abandoned'* (Norwegian Petroleum Safety Authority). To achieve this objective, the barriers must be impermeable, ensure long term integrity, non-shrinking, etc. The most typical material is cement with multiple additives.

P&A is a highly regulated activity, and follows government acts, regulations, standards and company requirements. But most regulations use the principle of the two-barrier philosophy previously presented. Each of these has to extend over the cross-section of the wellbore, that is, rock to rock. The presence, or absence, of good annular cement over a certain length will change completely the P&A strategy.

Figure 1.B.24 shows the schematic of an abandoned well which produced from a single reservoir. The plugs in blue and red represent the primary and secondary barriers towards the reservoir respectively and a low pressure environmental barrier is shown in green. The length of each barrier depends on the local regulations. NORSOK D-010 suggests a minimum plug length of 100 meters for the primary and secondary barrier. This must also be pressure-tested independently. Note that the barrier requirements change depending on the completion style and number of reservoirs.

To reach the cross-sectional barrier, the tubing and probably a number of casing sections must be cut and retrieved, as shown in the figure on the left.

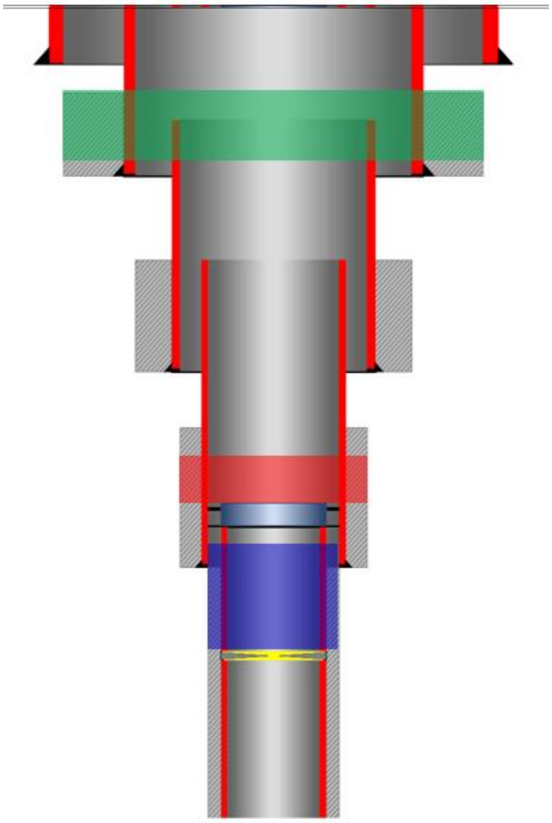

Fig. 1.B.24 – P&A well with primary (blue), secondary (red) and environmental (green) barriers

Figure 1.B.25 shows a balanced plug and the potential leak paths. The cement plug itself may leak due to microcracks, permeability or an internal micro annulus. This should be detected by the barrier pressure testing. Ensuring a good internal casing barrier is not enough, as the fluids may flow through the casing-formation annulus due to a lack of cement, channeling, or lack of formation-to-cement bond. If it is not possible to prove that the annular cement is of good quality and of sufficient length (i.e., 100 meters by NORSOK), then it cannot be considered a useful well barrier element. As a consequence, to establish the cross-sectional barrier it is necessary to either perform a section milling of the casing or to perforate, wash and cement, to get the rock-to-rock barrier.

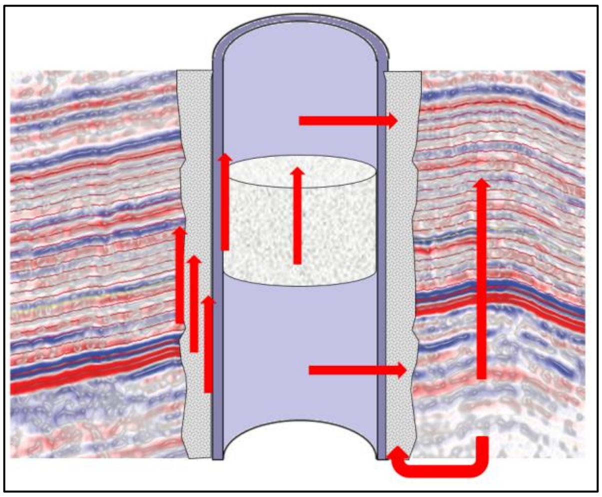

Fig. 1.B.25 – Leak paths around a plug

Pipe integrity is an issue as well, not only because it may act as a leak path, but also because the well may not pass the required pressure test to prove the effectiveness of the different barriers.

Finally, the formation itself may be a flow path, and for this a geological and reservoir study is necessary to define the plug setting depth. Low permeability formations are candidates, but the assessment also includes geomechanical modeling, to ensure the formation will not fracture in case the reservoir fluids recharge the rock.

The integrity of the well and its various barriers completely determines the P&A strategy. During the planning phase, the subsurface basis for abandonment is defined, and for this a clear understanding of the well condition is necessary. This is one of the reasons why it is not possible to accurately predict the final cost to P&A a well. Imagine that the cement log reveals no annular isolation at the target plug setting depth. A section milling job will be necessary requiring the mobilization of an expensive rig. This is critical in offshore P&A, and a proper understanding of the well condition helps to delay or negate the need for rigs, whilst conducting as many operations as possible, such as wireline or coiled tubing, from the platform.

Similar to a generic well intervention described in the previous section, completing a P&A requires:

- Access to the target depth: the well may be affected by deformation, ovalization, and deposition and these will change the plug setting depth. Multifinger calipers and ultrasonic tools are used.
- Assessing the tubing and casing condition: for a certain pipe string to pass the pressure test and avoid leak paths, the mechanical condition has to be good. Otherwise, tubing/casing cut and pull is possible, at a much higher cost. For tubing and production casing, MFC is the typical log run to evaluate this. However, for external casing string, multibarrier electromagnetic tools and noise logs are used.
- Annular seal evaluation: the requirement of rock-to-rock barrier includes the evaluation of the annular cement behind casing. Sonic and ultrasonic cement logs are used.

When pressure testing the plugs, a noise log can also be recorded as a station just above the barrier. In case of failure of the pressure test, the noise log helps to identify the leak path.

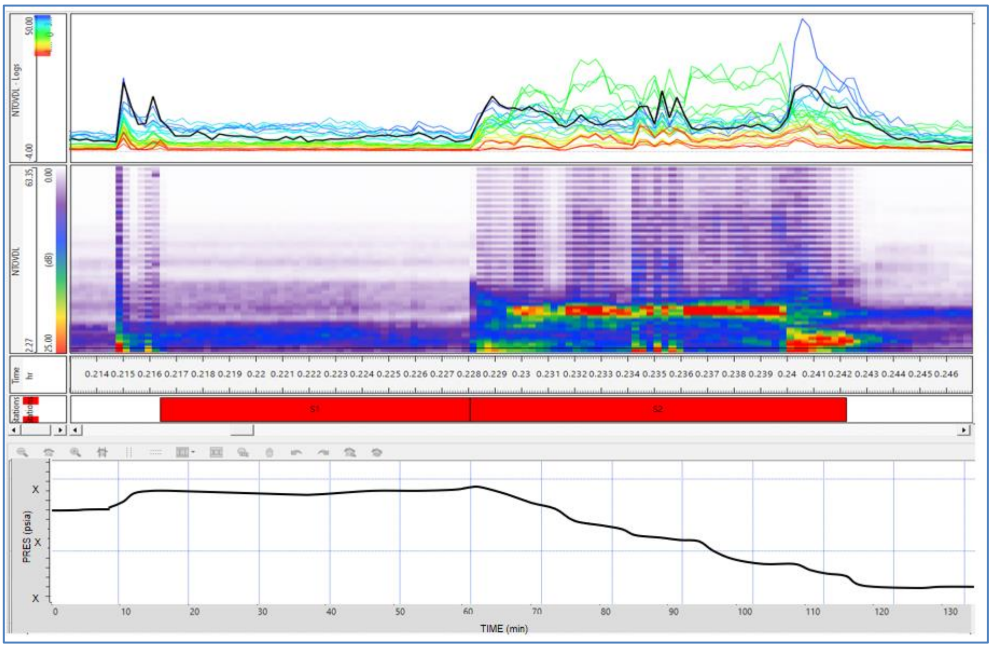

Fig. 1.B.26 – Noise log during plug pressure test

In summary, P&A planning relies on multiple cased hole logs used during other periods of the well life cycle. The well integrity conditions the P&A strategy and the costs, and this has to be determined through the various techniques presented in this book.

1.C Beyond Oil and Gas

Many cased hole logging tools and interpretation techniques used in the oil and gas industry are applicable to geothermal energy and Carbon Capture and Storage (CCS) wells. A brief summary of these areas, with focus on the need of CHL measurements, is presented below.

1.C.1 Geothermal Energy

Chapter 7 reviews the fundamental concepts of heat transfer in the earth. The decay of radioactive particles in the earth's core produces a constant source of energy, reaching temperatures higher than 5000 °C. The temperature decreases as the radius increases, following a geothermal temperature gradient given by the rocks' properties (Fourier's law). A temperature delta results in a heat flux, and this can be used to generate energy. As shown in Figure 7.D.4, the maximum heat flux occurs at the edges of tectonic plates.

Geothermal energy has been used for centuries, and the first examples were hot springs used for public baths, spas and heating. In Reykjavik, Iceland, a large percentage of the buildings are still heated by natural hot water springs. By 2017 the geothermal installed power generation capacity was led by the United States, followed by Philippines and Indonesia.

The current concept of Geothermal energy consists of the use of hydrothermal resources for power generation. A simplified schematic showing the main components of the generation system is presented in Figure 1.C.1. It requires a water injection well, pumping large volumes of cold water. As it flows through the hot porous media, heat exchange leads to water warm-up and boiling. The steam is produced by a nearby production well. As it reaches the surface, it is used to turn generator turbines, located near the wells to minimize the heat losses. The schematic corresponds to a 'Dry' steam power plant, but when liquid water is produced by the well, other types of plants are used, like the binary cycle power plant, using heat exchangers to heat a different fluid that turns into steam. This allows power generation from much lower temperature sources, that do not lead to dry steam.

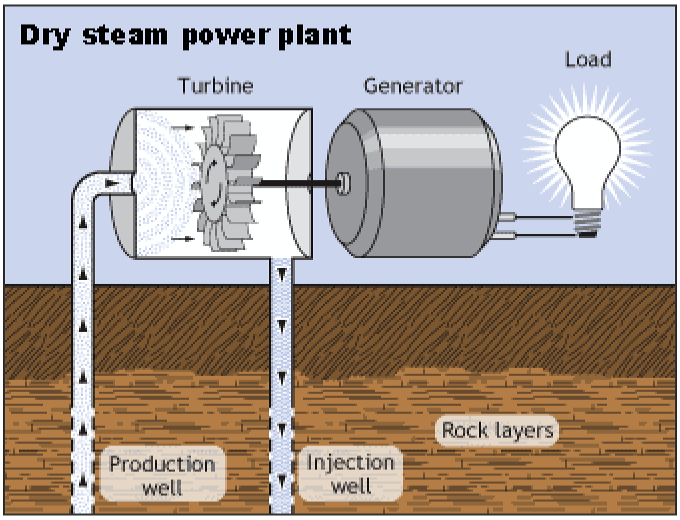

Fig. 1.C.1 – Dry steam plant – US Dept. of Energy

Geothermal wells have many similarities with oil and gas wells, and in some countries there are initiatives to re-use old producing wells for geothermal purposes. The overburden sections of the well include multiple barriers, with steel casing and annular cement. However, in geothermal applications the objective is to maximize the exposure to the permeable formation, and therefore a typical well completion consists of a slotted liner below the production casing. Open sections between 1000 and 2000 meters are not uncommon in this type of well.

After completing the geothermal well, a number of tests are conducted to evaluate the injection capacity and distribution, which helps to estimate the expected mass flow rate that the well will handle, in order to design the surface facilities. It also provides information on the reservoir properties, key for optimizing future development plans. Fall-off Pressure Transient

Analysis is used to determine reservoir permeability, skin, and reservoir pressure. Injectivity tests are also conducted throughout its life cycle.

As explained in Chapter 3, quantifying a single-phase injection profile using production logging requires mainly a spinner flowmeter and a number of auxiliary tools. If the well is logged at multiple injection rates, apart from getting the 'snapshots' of the injected water distribution, it is possible to perform a Selective Inflow Performance analysis (SIP) to obtain the layered injectivity index (B/D/psi) and the layer pressure.

Figure 1.C.2. shows the layered IPR for 3 layers. The one in green presents an injectivity two orders of magnitude greater than the other two layers.

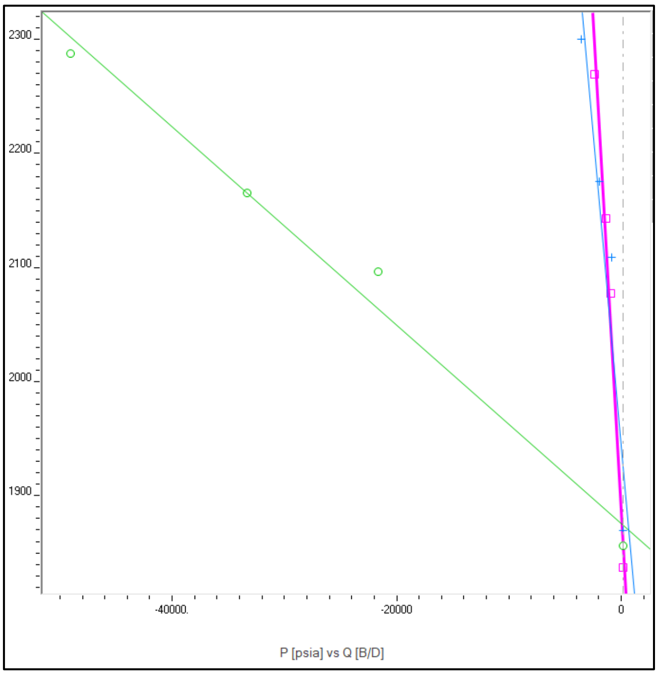

Fig. 1.C.2 – SIP analysis in geothermal injection well

The injectivity of the different layers is, in general, lower than expected by logs or modeling. The causes for this lower performance include insufficient cleanout and consequent near wellbore damage, reaction of the injected water with other fluids (drilling, chemicals), reaction with the formation (i.e., clay swelling), precipitation of carbonates and other minerals and fines movement. Quantifying the layers' injectivity and understanding their variability is a necessary step to optimize the production of steam or warm water. Many of these problems presented here are common to oil and gas wells.

The well performance changes with time, and therefore monitoring is required. A technique frequently employed in geothermal injectors is to record temperature passes with the well shut-in and measure the warm-back as the cold injection water reverts back to the geothermal temperature. This technique is detailed in Chapter 7 (Section 7.F)

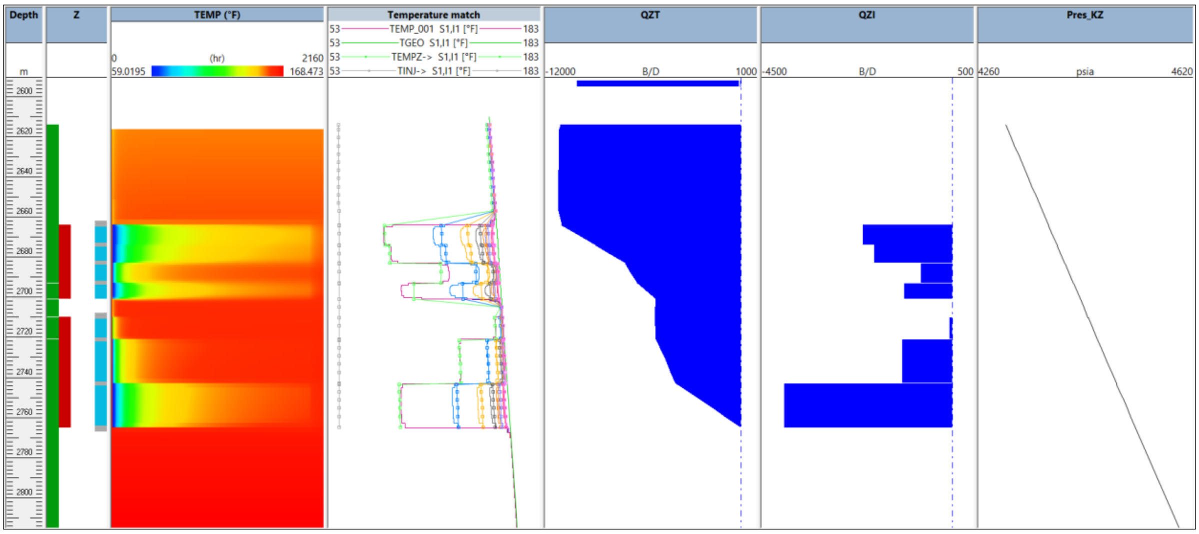

Fig. 1.C.3 – Temperature-based injection profiling using WIFO method

The integrity of the various well barriers is key for the geothermal operations. Apart from the metal and cement degradation discussed for oil and gas wells, high temperature (150°C to 300°C) water wells present a number of extra challenges:

- Formation water chemistry may include oxidizing elements such as dissolved CO_2, H_2S and O_2. Due to different geological circumstances, the formation water chemistry may vary drastically in short distances, and since the wells have a large reservoir contact, it is difficult to restrict the inflow of corrosive fluids
- There is a positive correlation between temperature and corrosion rate, and these well are necessarily hot.
- Various minerals are dissolvable in water, which may precipitate as scale.
- Thermal expansion may lead to casing deformation (buckling, bending, etc.), decoupled casing joints due to thermal stress and also result in failure of the cement to exert a tight bond on the pipe. Thermal cycling, caused by warming and cooling, exacerbates the negative effects of the thermal expansion and contraction of the different barriers.
- Lack of, or poor annular cement does not provide tension support to the casing, which results in larger stresses and can produce further deformation.
- Most geothermal reservoirs are associated with local or regional faulting, leading to lost circulation zones, which affect the drilling operation and the cementing.

Special considerations regarding material selection and cement formulation are applied for design of geothermal wells. However, downhole integrity monitoring through Multifinger Caliper (Chapter 8), Noise logs (Chapter 9) and Cement Evaluation logs (Chapter 10) are key for well integrity management of the well, from drilling to abandonment. High Pressure/High Temperature (HPHT) tools are required in these wells, as most conventional CHL tools are only rated up to 150-177°C.

1.C.2 Carbon Capture and Storage

Carbon Capture and Storage (CCS) refers to a variety of processes which capture and store CO2 emissions, generally from industrial processes. The CO2 is transported to the wellhead using pipelines or tankers, and injected into geological formations, typically depleted oil and gas reservoirs. This long-term underground storage is known as 'geological sequestration'.

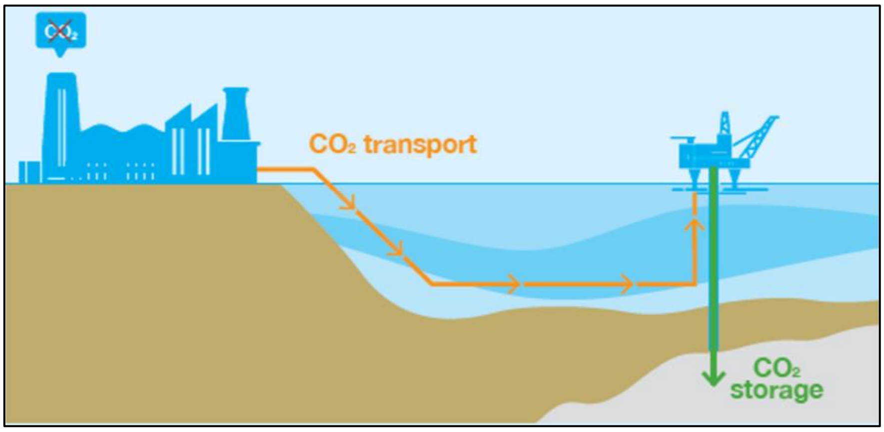

Fig. 1.C.4 – Schematic of CCS process – Oil & Gas Authority UK

Selecting candidate reservoirs for geological sequestration requires a complete and stringent sub-surface study, as the injected CO_2 must remain in place effectively forever. Whilst in oil and gas exploration the hydrocarbons in place is one of the key parameters, in geological sequestration the pore volume determines the amount of CO_2 that the reservoir can hold. Large reservoirs of good porosity are preferred, as the surface installed capacity will be used for longer.

As the CO_2 reservoir pressure increases, its containment becomes critical. The cap rock and geological traps must be adequate for this fluid, and the maximum reservoir pressure, given by the volume of the injected CO_2 must not fracture the rock and create leak paths to shallower formations or surface. New CCS wells are equipped with downhole pressure and temperature gauges.

Another reservoir characteristic is the injectivity. The formation must accept CO_2 at the required rate. For this reason, high permeability formations are preferred.

Verifying the injection distribution and monitoring the CO_2 front are key for understanding if the different physical barriers are performing as expected, and also to assess if the injection is homogenous or a particular layer is quickly becoming overpressured. Figure 1.C.5 provides an example of these in the CCS Carinfield project, where PLT injection profile and Pulsed neutron are used as monitoring tools. All the tracks show time-lapse views, with the logs in black from 2009, before starting the injection, and in red are from 2010, after one year of CO_2 sequestration. Compared to the injection profile (2010), the CO2 saturation front is located at shallower depths, as expected for this buoyant fluid of lower density than the reservoir water. The image also shows the large pressure increase (1000 psi) and 36°C temperature drop. All this information is vital for updating the reservoir and geomechanical models, to maximize the storage capacity while ensuring the safe and long term containment.

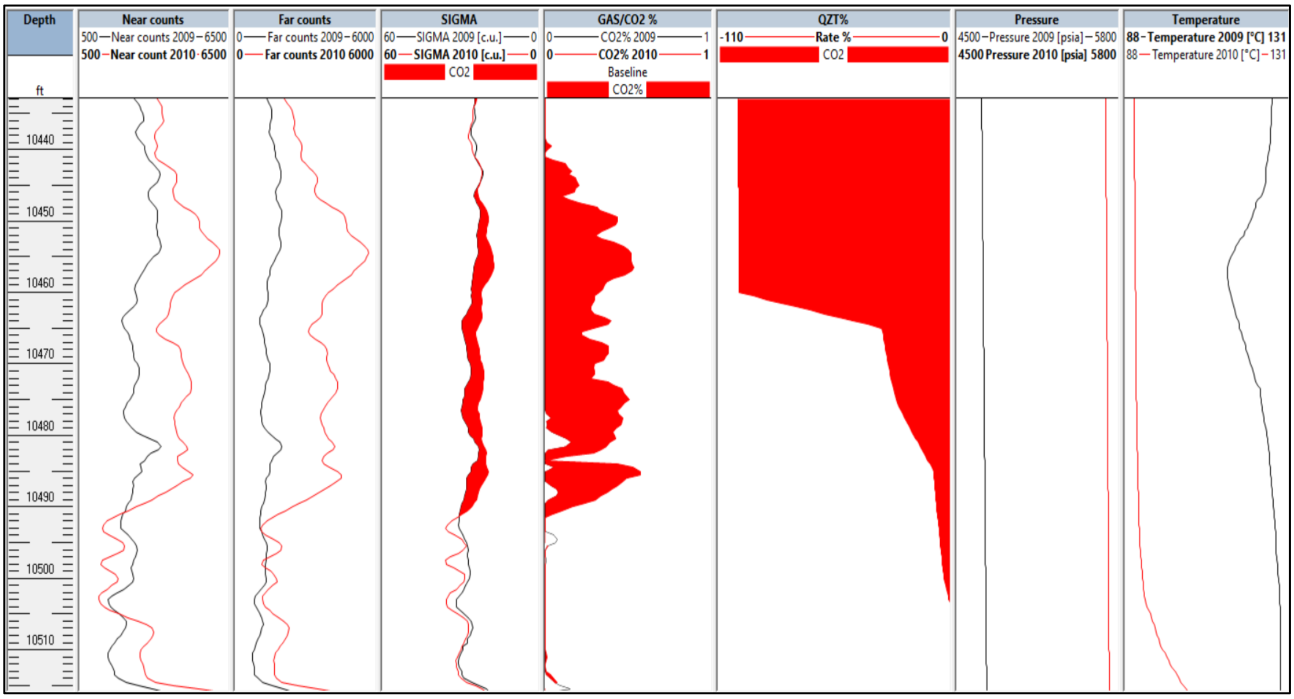

Fig. 1.C.5 – Time-lapse pulse neutron for CO2 monitoring – Cairnfield project

The cap rock is the natural barrier for CO_2 sequestration, however, failure of the well barriers would provide a leak path for the gas to reach the surface or shallow drinking-water layers. This is especially important as conventional oil and gas wells are being converted to CO_2 injectors, and therefore a well integrity evaluation is required to ensure the long term condition of the multiple barriers. For this, all the techniques and described in Section 1.B are important, including P&A, as it is expected that carbon sequestration projects will be located in reservoirs with abandoned wells.

Dry CO_2 (gas or supercritical fluid) is not corrosive to metals and alloys. However, when CO_2 gets in contact with formation water, it generates carbonic acid:

$$H_2O + CO_2 \rightarrow H_2CO_3$$

This acid is highly corrosive for conventional carbon steel pipes. Newly drilled carbon sequestration wells are expected to be completed with special materials, including ‘critical service’ steels, more resistant to CO_2 or ‘sweet’ corrosion. However, for old wells that are in general more economical for CCS projects (as they already exist), a complete well integrity analysis and periodic monitoring is necessary.

In short, from the well integrity point of view, the objective of long term CO_2 containment requires the multiple well barriers to maintain their mechanical properties and remain impermeable throughout the well injection life and afterwards, as similar to P&A, the fluids should remain in place for eternity. The cased hole logging techniques described in this book are equally applicable to CCS.

2 – Acquisition and Operations

2.A Introduction

Regardless of the main objective of cased hole log (i.e., measure the formation saturation, identify a leak, etc.), all jobs share a number of common principles: run the toolstring in a live well, record or transmit the data to surface, know the depth of the toolstring, and determine the number of auxiliary modules needed to facilitate its deployment. This chapter covers these fundamental building blocks applicable to any CHL acquisition.

Section 2.B summarizes the main conveyance techniques: Wireline, slickline, tractoring, coiled tubing, and carbon rods. This section is an introduction to pressure control equipment and lift and tension analysis. Section 2.C deals with how the data is transmitted to surface: real-time operations (SRO), memory, digital slickline, and fiber optics. It also summarizes the main file formats that reach the analyst’s computer.

As cased hole logging measurement results are versus depth, it is necessary to accurately measure from surface and verify them downhole. The various tools used for this purpose are detailed in Section 2.D. Auxiliary measurements and ancillary components used to deploy the tool in the well are described in Section 2.E.

This chapter is kept generic in the sense that specific tool modules or logging programs are not discussed. These will be covered in the next chapters, as the type of tools and number of passes required for flow profiling is very different from the ones necessary to verify the pipe integrity.

2.B Conveyance

This section presents different ways to get the tools downhole. Without focus on a specific toolstring or measurement type, one should start by understanding the main deployment techniques to reach the depth of interest of the well. Compared to open hole logging, cased hole logs are typically acquired in live wells. The exception is cement evaluation logs, which may also be run during the well construction phase, when the well is 'killed'.

2.B.1 Wireline

Wireline, also known as E-line, is used for logging, perforating, plug setting, etc. This type of deployment allows for real time surface-toolstring communication and power transmission. The building blocks of a wireline system can be broken down into the following:

- **Toolstring:** The tool modules included in the toolstring depend on the objectives of the operation and will be presented in upcoming chapters. Common auxiliary modules are presented in Section 2.E.
- **Cable:** This has two main functions: mechanical (safely deploying the tool to the depth of interest) and electrical (transmitting power and signal). The latter is described in Section 2.C.1.
- **Pressure control equipment:** Used to contain well fluids whilst running the tool and cable in and out of wells under pressure. More on Section 2.B.3
- **Rig-up equipment:** Sheaves, shackles, chains, goosenecks, and other elements needed to direct the cable to the well.
- **Surface system:** This may be a wireline truck or a portable cabin. It contains the wireline drum, depth measure head, hoist control, logging systems, etc.

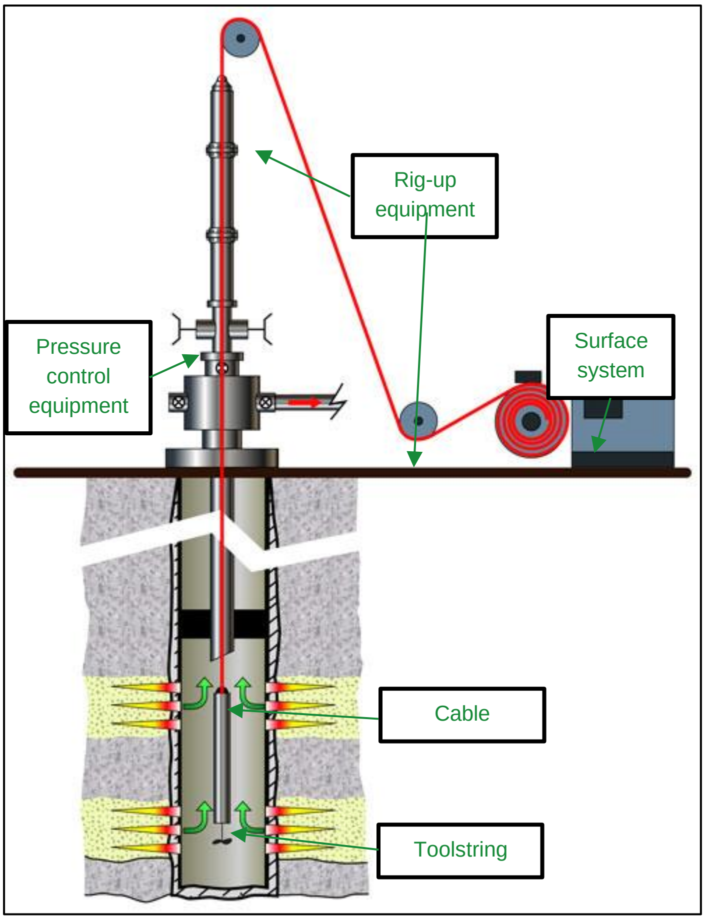

Fig. 2.B.1 – Wireline components

A schematic of the wireline cable is presented in Figure 2.B.2. The core of the cable is the copper conductor strand. Cased hole logging usually uses a single electrical conductor cable, known as 'Monoconductor'. Open hole cables are typically 'Heptacables' (7 conductors). Surrounding the conductor is polymeric insulation (represented in blue) that avoids electrical leakage. The mechanical support is provided by several inner and outer armor wires. The number of wires and the alloy type will determine the maximum loads they can hold, and their capacity to resist corrosive environments.

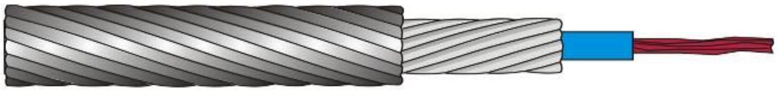

Fig. 2.B.2 – Wireline cable

A wide range of cable properties exists in the market. The manufacturers provide the cable specs, including the diameter, breaking strength, weight per 1000 ft, electrical resistance, etc. Typical diameters range from 7/32'' to 15/32''.

The wireline cable is spooled in a drum, which spins using a hydraulic or mechanical transmission system. The wireline operator controls the speed and direction of the drum spinning, aided by a 'spooling arm'. At the exit of the drum, there is a surface depth measurement head, detailed in Section 2.D.1.

The toolstring runs in hole due to a combination of its weight and the cable's weight. When the deviation increases, there are larger friction forces opposing the tool movement (Section 2.B.4). Therefore, wireline is limited to well deviations between 60 and 70 degrees.

2.B.2 Slickline

Conventional slickline operations provide a way to run the tools in hole, but do not transfer data or power. Recently different service providers started offering real time slickline, which allows for data transmission (see Section 2.C.3). The layout of the operation and building blocks of a slickline operation are similar to the ones shown in Figure 2.B.1, but there are a number of differences:

- **Toolstring:** As there is no communication with surface, the data is stored in a memory (see Section 2.C.2). The power is provided by lithium batteries, which output a voltage that matches the toolstring requirement (~18V). The duration of the battery can be calculated as the battery capacity (measured in Ampere-Hour) divided by the current (in Ampere) consumed by the toolstring. The more tool modules and the higher their consumption (i.e., motorized sections), the shorter the battery life. This is also affected by high temperature and aging.
- **Cable:** Slick and braided lines are used. These do not contain electrical conductors, so do purely mechanical work. Normal slickline is a single 'piano wire' made of alloy or stainless steel, and is typically 2/16'' diameter. Braided lines are multi-strand (typically 3/16 to 5/16''), and withstand larger loads.

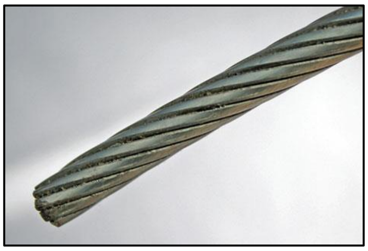

Fig. 2.B.3 – Braided line

- **Pressure control equipment:** Simpler set-up than wireline (Section 2.B.3).
- **Surface unit:** Contains the cable drum, hoist control, depth measurement system, etc. It does not contain a surface acquisition system and display, present in the wireline units, as there is no real time communication with the tool.

This deployment method is also limited to wells with deviation lower than 70 degrees. As the tools are battery powered, there are some limitations in the type of tools that may be run. Other memory-related issues are reviewed in Section 2.C.2.

2.B.3 Pressure control

When the intervention is performed in a live well, the toolstring and cable are run against the wellhead pressure. The tool will not run in hole if the force exerted by the fluid is larger than the toolstring weight. Moreover, a number of barriers need to be set to contain the well fluids. This is handled by the pressure control equipment (PCE). International standards (API 6a, NORSOK D-SR-008) regulate the surface equipment, materials, and operations. A typical PCE set-up is shown in Figure 2.B.4.

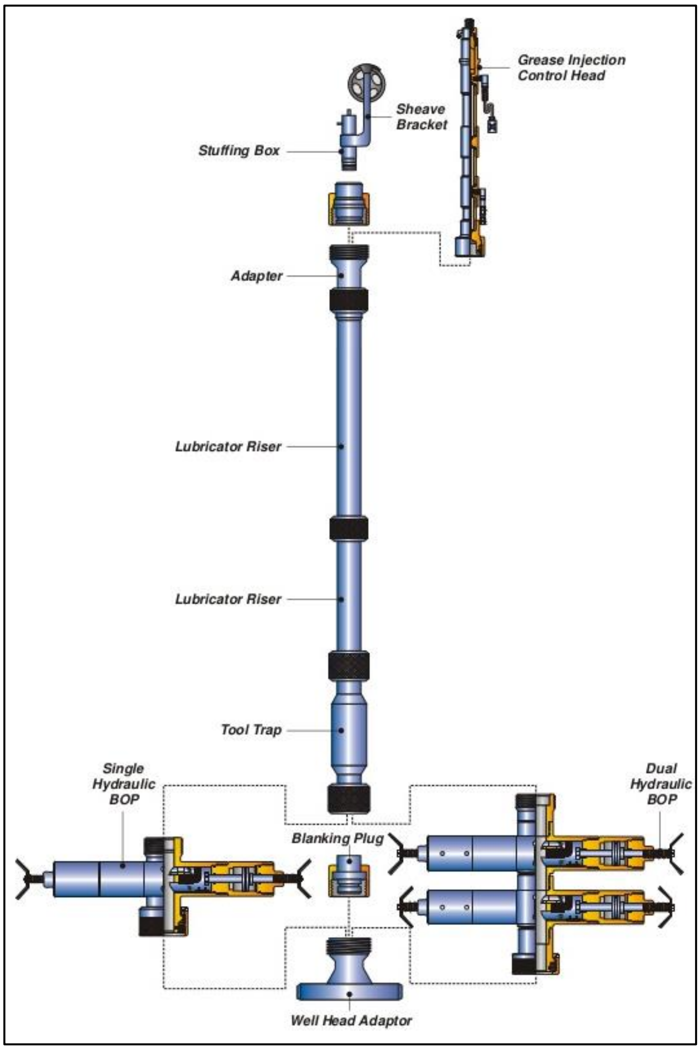

Fig. 2.B.4 – PCE (Courtesy: Parveen Industries Ltd.)

The cable enters the well through the uppermost end of the PCE. This can be:

- **Stuffing Box**: Provides a seal around the cable by means of packing elements.
- **Line wiper at the top of the grease injection head:** In wireline or braided line operations, grease injection is required at a pressure higher than the wellhead. This exerts a tight dynamic seal around the line while the grease fills the interstitial grooves between the line strands.

When grease injection is required, a hydraulic injection system is used to pump the grease at the desired pressure. These pumps contain tanks with extra grease reserves in case of a leak and are rated based on the pressure they can handle. The need for grease injection increases the complexity of the logistics of a wireline operation compared to slickline.

Below these elements, the lubricator is located. This works as an intermediary between the well and the surface and is composed of a number of steel connections. The length of the lubricator depends on the toolstring being run. Sometimes, crane availability or rig up capacity in offshore platforms limits the maximum lubricator, and therefore toolstring length.

Between the lubricator and the top of the wellhead, a wireline BOP is placed. This contains one or more rams capable of closing over the wireline in case of an emergency. The pressure control philosophy establishes that no single barrier failure should lead to unacceptable consequences. And, since no barrier is perfect, there has to be more than one barrier to reduce the risk.

1. The primary well control system typically depends on the size of the line. For slickline operations, a stuffing box is used, while for wireline cables, it is necessary to inject grease.
2. The secondary well control system is located in the wireline BOP, and consists of one (for slickline) or two (for wireline) rams. These are hydraulically operated and should be able to close against full working pressure. These are minimum requirements as per NORSOK D-SR-008, but there are BOPs with higher numbers of rams.
3. The tertiary well control system consists of an independent shear/seal BOP, located as close as possible to the wellhead.

Other relevant elements are installed along the PCE rig-up, including tool trap (flapper valve in case the cable breaks at surface), ball check valve, etc. PCE equipment is rated based on the maximum working pressure: 3, 5, 10, 15, 20 ksi.

2.B.4 Forces in the tool and cable

When planning a logging job, the service provider needs to perform ‘well entry’ or ‘lift’ calculations to understand if the tool will go down against the well’s pressure and rate, to estimate the maximum depth that will be reached due to the tool’s own weight, and what will happen if the tool gets stuck. These calculations are performed by specialized software and require accurate well, toolstring, and cable properties.

2.B.4.a Running in hole

Starting with a shut-in well scenario, the toolstring and cable do not suffer lift forces due to fluid movement. The main pressure differential is felt by the cable in the interface between the top of the lubricator (stuffing box/wiper) and the environment. A cross section of the cable will feel an upwards force calculated as:

$$F_{WH} = WHP * \pi \frac{ID_{Cable}^2}{4}$$

From this equation, it is concluded that the smaller the cable diameter, the smaller the lifting force acting on it. Wireline and braided line suffer larger forces than slickline.

Running in hole with the well flowing brings friction and drag into the problem. The wall shear stress will act on the toolstring and cable and will generate a force (F_f) opposing the fluid movement that is calculated as a function of the fluid velocity (u), fluid density, and Moody friction factor (*f*) as:

$$F_f = 0.5\, f\, S\, \rho\, u^2$$

This equation shows that the higher the fluid velocity and the larger the surface area (S) of the tool and cable, the larger the friction force will be in a producer well. The sign of the force is opposite for an injector, this means, acting in the direction of the weight.

There will also be a drag force. The equation is similar to the friction but instead of *f, it* uses a drag coefficient, which is a function of the shape of the submerged object. For simple objects, analytical expressions exist. Otherwise, they are obtained experimentally.

The surface-measured cable tension responds to a force equilibrium, considering the total 'buoyed' weight, drag, and friction components. For a producer:

$$T = Weight - Buoyancy - Friction - Drag$$

The tension profile will vary with depth as more cable is added, increasing the weight, and at the same time, the friction force increases with the surface area. The logging engineer looks at the tension drop with respect to the shut-in situation. Service companies typically base their criteria on a percentage tension drop (i.e., 30%), above which it is no longer safe to continue with the job in current well status, as the tool may be lifted by the flow.

If the calculations suggest that the wellhead pressure or the tension loss represents a risk to the operation, or simply it is not possible to run in hole, it is necessary to add weight to the toolstring. Tungsten weight bars are added to counterbalance the force. These are wired through, so they can be used for wireline operations.

2.B.4.b Reaching TD

In a vertical well, once the tool can safely run in hole, the target depth (TD) will be reached due to the tool's own weight. When the deviation of the well increases, the kinetic friction between the cable/toolstring and the pipe adds another force component to the tension equation presented earlier.

The friction force is calculated as the coefficient of kinetic friction (μ_k) multiplied by the normal force, which acts perpendicular to the surface. This force can be calculated from the tool (m_{tool}) and cable (m_{cable}) mass as:

$$F_k = (m_{tool} + m_{cable})\mu_k \, g \, sin\theta$$

When the tension becomes zero (or very small), it implies that the tool will not continue falling due to its own weight. Therefore, it is possible to calculate the 'Free fall limit' depth, and in order to go below it, coiled tubing or tractor assistance is required.

2.B.4.c Tool stuck

Another undesired event to consider is the tool getting stuck. After a number of attempts to release the tool, the service company and operator may decide that it is necessary to leave the tool in the well. This is achieved by pulling the cable, and hopefully breaking the link between the toolstring and the wireline, known as 'weakpoint'. During the pre-job planning, the service company must ensure that the weakpoint will break before the cable.

As previously mentioned, the cables have a breaking strength (BS) that is a function of the material, number of strands, etc. The cable is never subject to BS since its mechanical properties will degrade with the use, fatigue, corrosion, etc. The maximum safe working limit is normally set to 50% of BS.

The topmost element of the toolstring is called the 'Cablehead'. It provides the mechanical and electrical connection between the wireline and tools. Its shape is designed to facilitate the tool fishing; hence the top is called 'fishing neck'.

The weakpoint is built inside the cablehead using the cable inner and outer armors, and its rating is a function of the cable strength and number of strands used. The weakpoint is determined based on calculations, including depth of the operation, tool weight, cable BS, etc.

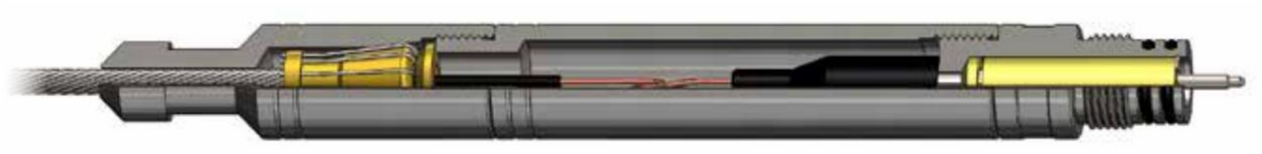

Fig. 2.B.5 –Electrical Cable Head (Courtesy: Hunting)

When the tool gets stuck, it is assumed that the tool weight is supported by whatever is holding the tool. To pull the weakpoint, it is necessary to put tension above the cable weight and not the toolstring, which is a function of the depth where the tool is stuck. For this, proper tension modeling is required.

Let's assume the following situation, as shown schematically in Figure 2.B.6: due to local availability, the job is constrained to use a low BS cable (i.e., 6000 lbs.), for which a safety factor of 50% (red line) is applied. A weakpoint rating is selected, and when plotting the tension to pull the weakpoint, it increases with depth as there is more cable in the well (blue line). Should the toolstring get stuck at the bottom of the well, with the current cable-weakpoint selection, the cable would break first, possibly leaving thousands of meters of cable in the well, complicating the fishing operation. This analysis suggests the need to change either the weakpoint (which cannot be too small, as it can break during normal pulling) or the cable.

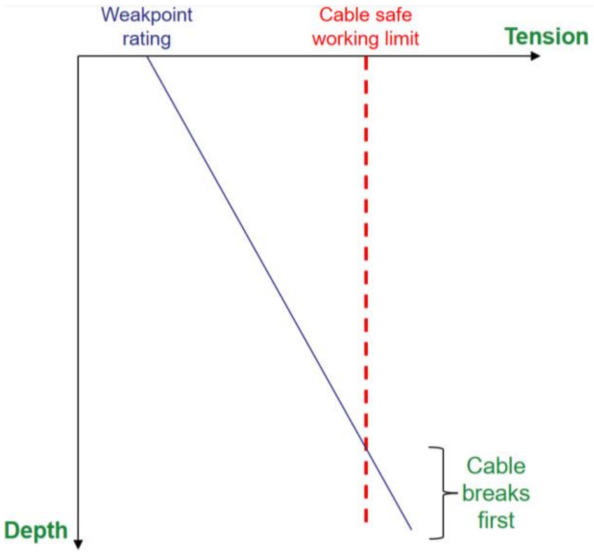

Fig. 2.B.6 – Tension calculation schematic

An alternative to mechanical weakpoint is an electrical release device. If the tool gets stuck, instead of pulling from the cable, a surface panel sends a signal downhole to unlatch the toolstring, leaving a fishing neck at the top. This is used frequently with the deployment techniques to be discussed next, as in horizontal wells, the tension modeling can be more complex due to the undulations.

2.B.5 Tractors

When the tool does not descend using its own weight (Section 2.B.4.b), it is possible to add a tractor powered by an E-line. Tractors are modular tools formed by a number of wheel sections, electronics, and hydraulic modules. A single wheel section is shown in Figure 2.B.7. In this particular model, each section includes 4 wheels oriented in the same plane. This varies for different tool providers, and in other models, there are more wheels, with 90 degrees offset, etc. Depending on the toolstring weight and well deviation, it may be necessary to add more than one wheel sections.

The tool is run in hole with the wheel's arms closed until the free fall depth limit is reached. At this stage, the tractor is powered, the wheels are deployed, and it begins spinning through a hydraulic or electric system. Tractors are wired through, and most of them allow logging while tractoring. In the past, tractors with high energy consumption did not enable the toolstring to be energized and record data while the wheels were turning.

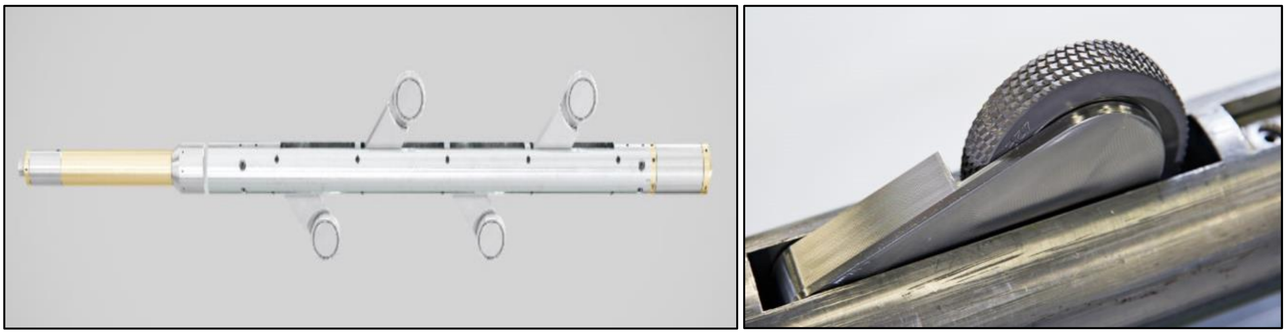

Fig. 2.B.7 – Hydraulically-driven wheel section (left) –
Tractor wheel (right) (Courtesy: Welltec)

The tractoring speed depends on the hole size and type (cased/open), number of wheel sections, toolstring weight, fluid velocity. Typically, maximum tractoring speeds are 15 m/min. Once TD is reached, to run the up pass instead of 'reverse gear', the wheels are closed, and the toolstring moves using only the cable.

2.B.6 Coiled tubing

Coiled tubing (CT) uses its rigidity to convey tools in wells of any deviation. Continuous tubing with outer diameters from 1 to 3½ in. is spooled on a portable reel, with typical lengths of 20,000 ft (although lengths of 32,000 ft can be achieved). At the well site, the tubing is unspooled from the reel and fed around a gooseneck, then through an injector, stripper and BOPs into the well's tubing string. The injector moves the tubing in and out of the well at speeds comparable to those achieved with wireline while supporting all the tensile loads of CT in the well. The stripper maintains a pressure seal around the tubing. The elements involved in a CT operation are shown in Figure 2.B.8.

Once deployed, fluids can be circulated through the CT typically to start the well before or after the logging. Due to the plastic deformation of the CT, it will adopt a helical shape that in turn increases the contact points with the casing. At some depth, the friction between the CT and the casing will be large enough to prevent further movement of the string in hole. This is called 'Lock-up depth', and is shallower for smaller CT OD and larger pipe ID

The CT operations can be real time or run on memory (see Section 2.C). The connection between the CT and the toolstring consists on a logging head, which provides a mechanical and electrical connection, and allows for fluid circulation. Coiled tubing logging operations require more personnel and equipment than tractor deployment.

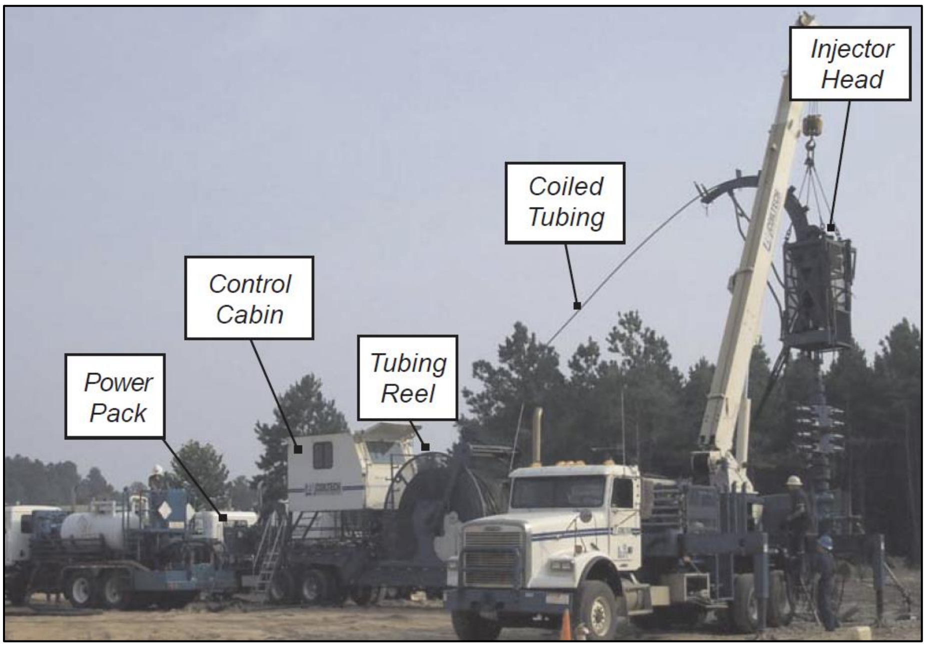

Fig. 2.B.8 – Coiled tubing intervention (Courtesy: ICOTA)

2.B.7 Carbon rod

A relatively new deployment technique consists of a carbon rod around 0.6’’. The rod is made of composite material, using carbon fibers in a polymer matrix, manufactured in a continuous process, with lengths of more than 20000 ft. The material is corrosion resistant, and can be exposed to H_2S and CO_2. A conductor cable is installed in the center of the rod to power the tool. As shown in Chapter 7, some carbon rod providers include fiber optics for DTS and DAS measurements. The rod is spooled in a drum, similar to the one shown in figure 2.B.8.

The carbon rod conveys the toolstring along the horizontal due to its own rigidity, and similar to CT, the maximum depth is determined by the friction forces between the rod and the pipe. The carbon is rigid enough to perform mechanical interventions such as jarring and plug retrieval.

2.C Data recording and transmission

So far the intervention side of the operation has been presented. This is common for logging acquisition, mechanical interventions, pipe cutting, etc. The next section focuses on how the data goes from the tool to the analyst's desk.

2.C.1 Surface readout (SRO)

Cased hole logging operations with real time data control require a telemetry system that transmits the data continuously to the logging unit. This system is used not just in wireline operations but also with tractors. Coiled tubing logging may include a wireline inserted inside for SRO operations or could be memory jobs.

In surface read-out jobs, the surface-measured depth (Section 2.D) is attached to the downhole measurements in real time. The logging unit displays logs versus depth while acquiring the data, allowing for real time data quality, operational analysis, and making decisions while logging. For example, it may be decided to run a repeat pass over a zone of interest, wait more time for pressure stabilization, increase the rate, bleed the annular, etc. This is very important when rig time is expensive or in offshore operations that are run from vessels.

The components of a surface read-out system are:

1. **Surface acquisition system:** Located in the logging unit, this can be a portable system (panel + laptop) or a rack-mounted system. Through this system, the depth and tool data are merged in real time, and can be viewed while logging. This system generally includes a printer used to produce the typical API log field prints.
2. **Mono-conductor telemetry:** This provides the link between the tool and the surface panel. It works as a digital bi-directional telemetry system with data rates >50 kbps. Apart from transmitting the data to surface, the cable is used to send commands to the tool via downlink to configure the tool, control motorized modules (i.e., multifinger calipers), modify the acquisition mode, etc. Another function of the cable is to energize the tool. A voltage around 200V DC is applied to the line.
3. **Tool telemetry**, **which at the same time can be sub-divided in:**
    - **Inter-tool communications bus:** Single wire bi-directional system that operates at higher data rates than the uplink to surface (typically >500 kbps).
    - **Telemetry controller:** This unit or cartridge is located at the top of the toolstring. It controls the data collected by the tools below and packages them for transmission to the surface system. It receives the commands from surface and responds back if necessary. This controller accommodates multiple sensors (known as 'tool addresses'). Another function of this module is to convert the high voltage from the line (~200V) to the lower working voltage required for the different sensors, usually lower than 20V.

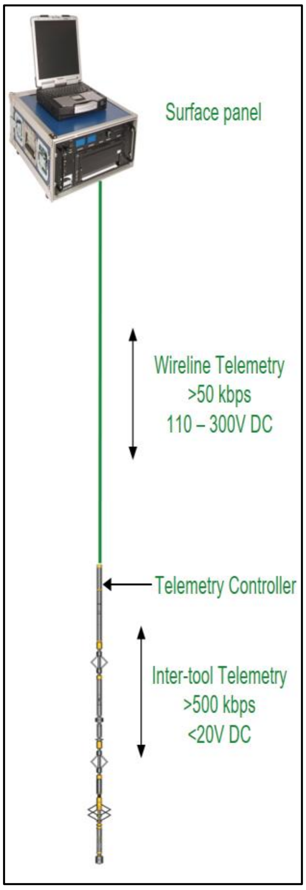

Fig. 2.C.1 – SRO Schematic

The telemetry is based on a communication protocol established by the tool manufacturers. Tools from different providers cannot always be combined, and in some cases data from part of the tools is transmitted to surface, while tools with incompatible telemetry are recorded in memory.

2.C.2 Memory

Memory jobs are typically conveyed with slickline or coiled tubing. As there is no communication with the logging unit, it cannot be verified if the tools are working. A proper maintenance schedule of the sensors is required and the well conditions and access should be verified through a dummy run.

For this type of job, the tool is equipped with a memory section consisting of a small (typically between 128 MB and 1 GB) flash memory and a processor board, which incorporates the firmware to communicate with the sensors. The inter-tool communication bus is the same as described for SRO.

Before running a job, the memory has to be programmed for logging. The logging engineer instructs what the different sensors will do during the job. Each sensor can be programmed independently and with different commands versus time. For example, to save memory and battery, during certain periods, the tool may be set to ‘sleep’, and after to ‘log’. Motorized tools may accept commands like ‘open’ or ‘close’.

Once programmed for logging, the memory is connected to the toolstring. A bi-directional communication will be established, with the memory sampling the different tools many times per second (i.e., 50 Hz) while sending commands to the different modules.

At the end of the job, the toolstring is disassembled, and the data from the memory is downloaded to a computer. At this stage the data is time-driven, and it is only after the logging engineer merges the memory and cable data that the final versus depth data presentation is achieved.

2.C.3 Real time slickline

An intermediate solution to wireline SRO and memory jobs is called ‘Digital slickline’ or E-slickline. This technology leverages the advantages of the slickline interventions (smaller PCE), and at the same time, establishes bi-directional communication with the downhole tool. This allows the analyst to perform a downhole depth correlation in real time, check tool status, assess log quality, etc.

The real time slickline uses a standard slickline cable core coated by an insulator polymer, which uses the telemetry over the wire. The toolstring is equipped with a slickline telemetry cartridge. However, compared to wireline, in these operations, a battery is required to energize the tool, as the slickline does not transmit power. Moreover, a memory is connected to record the measurements from different sensors. The data transferred to surface in real time varies depending on the service provider and includes depth control measurements (GR, CCL), cable tension, deviation, pressure, and temperature. The data from the other sensors are stored in memory, and can be downloaded when the tools are back at surface.

By sending commands from surface to the tool, this technology includes a controlled electric release (should the tool get stuck), jarring control for mechanical operations and perforations.

2.C.4 Fiber optics telemetry

Similar to the previous point, coiled tubing operations may include a fiber optic cable for real time data transmission. Fibre optic cable is a lighter alternative than coiled tubing equipped with wireline as it facilitates the intervention and reduces the crew, as the wireline unit is not needed. Fiber optics are acid resistant, therefore it is possible to perform a stimulation treatment while measuring downhole.

The fiber optics cable may be used as a continuous Distributed Temperature Sensing measurement (Chapter 7), which is used to monitor injection operations, and detect increases in temperature while the rock is being dissolved in an acid stimulation operation (exothermic reaction), etc.

The downhole telemetry sub is responsible for converting the electrical signal measured by the tool to optical pulses that will be transmitted to surface. This telemetry system is compatible with a large variety of production logging and well integrity tools. It is limited for certain tools which require a large bandwidth of data transfer. As fiber optics do not provide power, the toolstring requires a battery.

2.C.5 Data formats

The logging data is stored in a database, with a proprietary format defined by the acquisition system provider. The database includes a number of internal tool measurements that are of no interest to the final user. The data may be present with a very high sampling rate, which may be unnecessary for the analysis. Also, the database format is rarely supported by petrophysical software.

Well log data is distributed using standardized file formats, and the most typical are summarized below.

LAS files

The *Log ASCII Standard* (LAS) was created by the Canadian Well Logging Society in the 1980s. This format is an ASCII text file and can be opened by any text editor, which allows looking through the file and understanding the present logs. However, being a text file it requires a lot more storage space than an equivalent DLIS or LIS file.

The structure of the LAS format is standardized, and different versions exist (1.2, 2.0, and 3.0). All LAS versions are divided into logical sections, which begin with a tilde ~. These include: Version, Well, Parameter, Curve, and ASCII. The *Curve* section contains the mnemonic and unit of each of the measurements in the file. The log data contained under the *ASCII* section can be time or depth indexed.

DLIS files

This is a file format developed by Schlumberger and published by the American Petroleum Institute in 1991. The data is stored in a binary representation and cannot be opened and read as a LAS file.

The log data is organized in objects called Frames, which can be considered as tables of data, and each column is a channel. These can be time or depth indexed. There may be multiple frames in one file, and each frame represents one run. The files contain metadata related to the acquisition of a log.

Multiple array datasets are stored in one pass of a DLIS file making this format the default option for data that includes cement maps, borehole images, waveforms, etc.

LIS files

Log Interchange Standard (LIS) is the predecessor of the DLIS file, also developed by Schlumberger in the 1970s.

This is a binary format, and similar to DLIS, it may contain data from multiple passes. However, it cannot store array data. This format has been largely replaced by DLIS, but there are still many historical logs in this format.

WITSML

Wellsite Information Transfer Standard Markup Language (WITSML) is a standard maintained by Energistics. It is an XML-based specification used to transmit, in real time, well data acquired during drilling, completion, and logging of a well.

With the advent of fiber optics measurements, an extension of the WITSML standard, called PRODML, was developed to focus on production data. This is used for DTS and DAS data, among other applications.

2.D Depth control

Depth is a critical measurement as it is used as a reference for geological markers (layer's top/bottom). When considering multiple wells, accurate depth determination is key for correlating between wells to map the reservoir and ultimately determine the reserves in place. Well construction is also referenced to depth measurements, and clearly we want to perforate the reservoir section. The implications of getting the depth wrong can impact the reserves estimate, completion design, perforation and stimulation program, etc.

This section explains how depth is measured at surface, which basically measures the amount of cable put in hole. Regardless of the deployment technique, the elastic properties of the cable or pipe will require corrections based on downhole sensors. For cased hole logging applications, the industry uses Gamma ray, Casing Collar Locator (CCL), and Magnetic Markers Locator (MML).

2.D.1 Surface depth measurement

The primary way to measure the cable depth is by integrating the line movement in and out of the well. For wireline operations, this is performed at the logging unit by measure wheels in contact with the moving cable as it exits the drum. Provided that a good grip exists, the length of cable per revolution of the rotating wheels can be estimated as $2\pi R$. The wheel rotation is quantified by optical encoders, consisting of a rotating glass disk with offset markings, interrupting the light path between a LED and a phototransistor. The encoder will generate multiple pulses per revolution, which, combined with the knowledge of the measure wheel diameter (length per revolution), enables the estimate of pulses per length of cable. This will determine the resolution of the depth measurement.

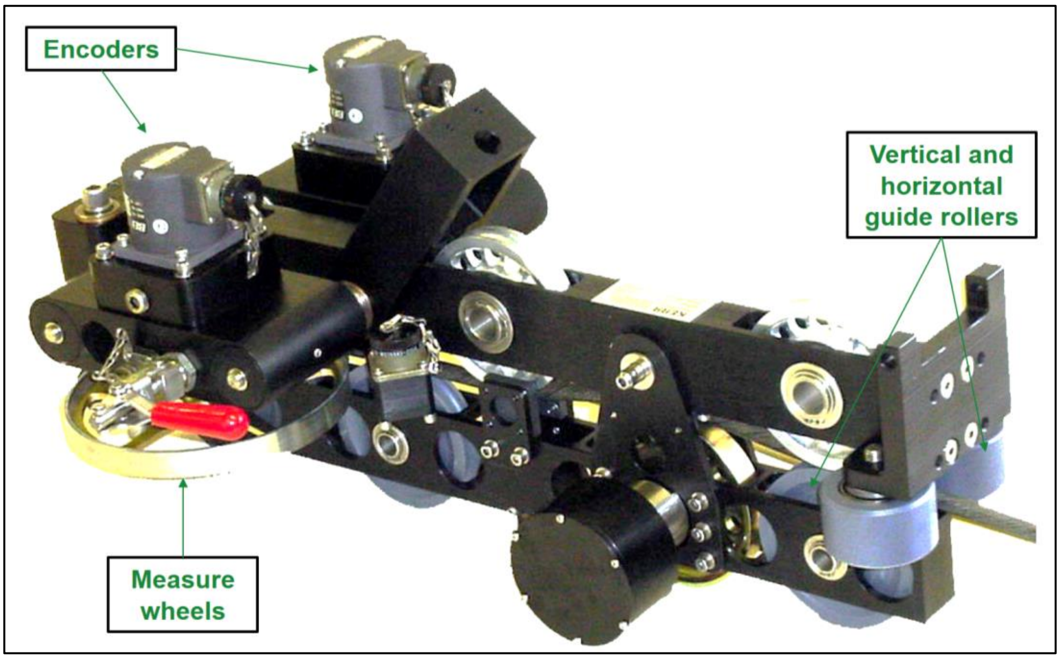

Fig. 2.D.1 – Dual tangential measure wheel (Courtesy: NOV ELMAR)

A number of factors can affect the relationship between cable length through the wheels and encoder pulses:

- Wheels are subject to wear, which alter their reference diameter. During a single run, wear does not typically lead to significant errors. Periodic maintenance and replacement are needed.
- Slippage may exist. The cable passes through the wheels, but these do not turn (no grip). Dual wheels with independent encoders are used in open hole to overcome this situation. However, in cased hole, it is more common to have a single encoder.
- Surface temperature variations. Wheels are manufactured with low thermal expansion materials (hardened steel, Inconel) to minimize this effect.

As a back-up mechanism, magnetic marks are placed at a calibrated length (25 m, 50 m, or 100 ft) along the electric line. The surface measurement is equipped with a magnetic detector, typically based on Hall Effect. Note that, similar to the dual encoders, this back-up mechanism is more typical for open hole operations, as there are less known downhole features that can be used as a reference.

The depth measurement output is called ‘Measured Depth’ (MD), relative to a known reference, usually Kelly Bushing (KB) or Drill Floor (DF). The depth measurement is ‘zero’ by positioning the bottom of the toolstring (known as ‘Zero point’) at the same depth as the chosen reference. The surface system depth and backups are set to zero, and positive depths will be measured as the tool runs in hole.

So far, this section has focused on wireline depth control. This also applies to tractor operations, considering that the cable spooling speed may be slightly different from the tractoring speed, which may lead to slack. For coiled tubing operations, the depth is usually measured at two positions: the injection head and the exit of the reel (see Section 2.B.6).

The true depth (distance along the actual course of the well) will be different from the measured depth. The cable can be affected by stretch, thermal expansion, slack due to deviation or restrictions, or any change of cable length between the unit and the reference depth (for instance, moving sheaves). It will be necessary to tie or correlate the measured logs to a previous log, considered as a reference log, or known well completion items, using at least one of the measurements described in Sections 2.D.2 to 2.D.4.

2.D.2 Sensors depth

When the tool is at 1000 mKB, it means that the bottom of the tool is at that depth even though all the sensors are not physically at that depth. Figure 2.D.2 shows a toolstring diagram, where the first column displays the name (or mnemonic) of the sensor, and the second column shows the offset relative to the tool zero (UTCTIM in this case).

For versus depth data, the depth correction for offset is handled by the acquisition system. However, stations are reported at a single depth (again relative to tool zero), but all the sensors are not at that depth. A 'Tool shift' may be applied individually to each sensor to display the measurement at the actual depth. This is important in cases where the station is recorded close to an inflow or a leak, and some sensors may be above, while others may remain below the depth of interest.

The field engineer must ensure that the tool order is the same as displayed by the toolstring diagram, including ancillary equipment (i.e., centralizers).

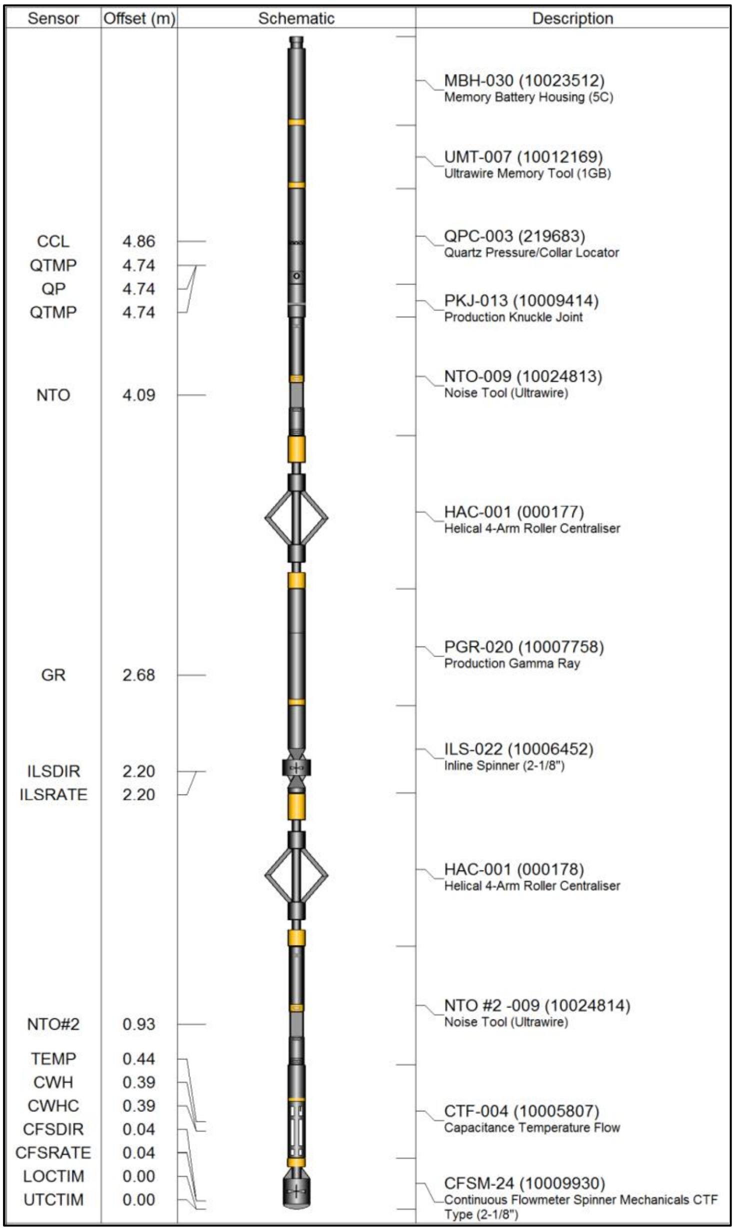

Fig. 2.D.2 – Toolstring diagram and offsets (Courtesy: READ Cased Hole)

2.D.3 Gamma Ray

A large percentage of the cased hole logging jobs incorporate a Gamma ray (GR) sensor to correlate against an open hole, reference, GR. As described in this section, this measurement allows the engineer, to perform a basic lithology analysis and assess the presence of scale.

Three naturally occurring isotopes are responsible for the gamma radiation detected by these devices. These are Potassium, Thorium, and Uranium, which tend to be present in clay minerals. GR measurements are used to detect shaly intervals and quantify the shale volumes (V_{shale}). When these isotopes decay, they emit gamma rays of characteristic energies. The GR devices used in cased hole logging measure the total gamma flux, but there are spectral GR tools that may be used to quantify the relative proportion of the different elements.

GR detectors consist of NaI scintillation crystals. When hit by ionizing radiation, the atoms become excited, and these will produce low energy photons as they return to their stable energy. The quantity of photons is directly proportional to the energy of the GR. To measure the number of photons, these are transformed into charged particles (electrons) through a photomultiplier tube. When the photons hit a photocathode, an electron will be emitted due to the photoelectric effect. The photomultiplier tube is subject to a large voltage (~1600 V), which in turn accelerates the electrons. As these impact a number of dynodes, more electrons are released, and this generates a measurable pulse that can be quantified by the tool's electronics.

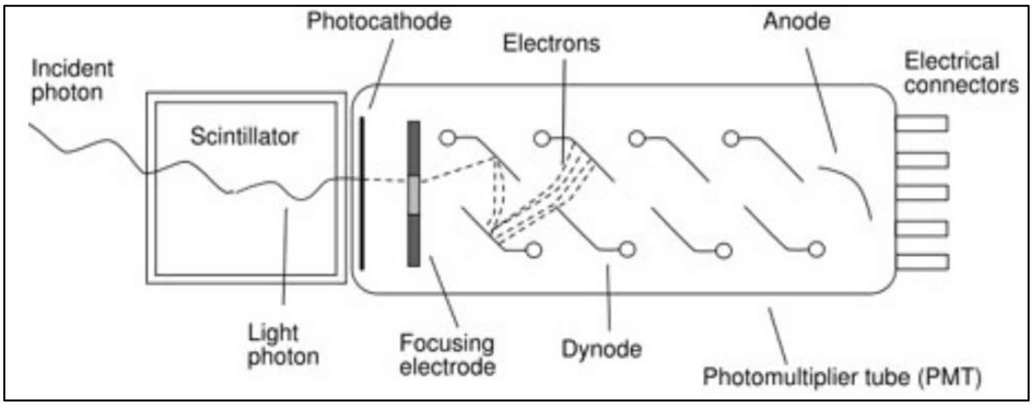

Fig. 2.D.3 – GR detection and quantification
(Courtesy: Stanford Scintillator Materials group)

The sensor output is the number of pulses per unit time (or counts per second). In oilfield applications, the API unit of radioactivity is used. This is based on an artificially created radioactive formation located at the University of Houston. This formation contains 4% K, 12 ppm U and 24 ppm Th, and was defined to have 200 API.

Note that GR measurements are statistical. If two passes are run at different speeds, there will be less detail in the faster pass due to the reduced number of Gamma ray impacts over a period of time.

When overlaying the open hole to the cased hole GR, lower API values for the measurements in cased wells are expected. Gamma ray attenuation is a function of two contributions: Compton scattering and photoelectric absorption. The first one is a function of the material's bulk density (this is the principle used for GR density devices), while the second one has a larger probability of occurrence for low energy GR. However, there may be a number of situations that lead to a cased hole GR larger than an open hole. A summary of the main causes is presented below:

1. **Naturally occurring radioactive minerals (NORM):** Different ions present in sedimentary minerals are soluble in water, including potassium, calcium, magnesium, barium, etc. These may emit different types of radiation, including Alfa, Beta, and Gamma. During production, NORM is transported by water and it is possible to detect its ingress due to high GR in front of a perforation. Figure 2.B.4 (left) shows the cased hole GR (red) exceeds the open hole measurement at the two bottom perforations, which are likely to produce water.

2. **Scale deposition:** The solubility of the ions mentioned in the previous point is reduced with decreasing pressure and temperature. Also, mixing incompatible waters (seawater and formation water) produces fluid mixtures with ion concentrations above the solubility limit. Clusters of minerals will start to precipitate on different surfaces. As the thickness of the deposition increases, more heterogeneous sites for nucleation will be

created, which catalyzes the deposition process. Scale may be deposited inside the pipe (Figure 2.D.4, right), decreasing the internal diameter and increasing the roughness, leading to increased frictional pressure drops. Needless to say that this will complicate the interventions that need to go through the affected interval. Scale may also be deposited in the formation, causing damage (skin). Mechanical calipers are run to determine where the scale is deposited, as this results in different types of scale removal treatments (chemical/mechanical pipe wash, matrix stimulation, etc.).

Scale may contain radioactive radium (Ra^{226}), leading to a similar GR response as seen in Figure 2.D.4.

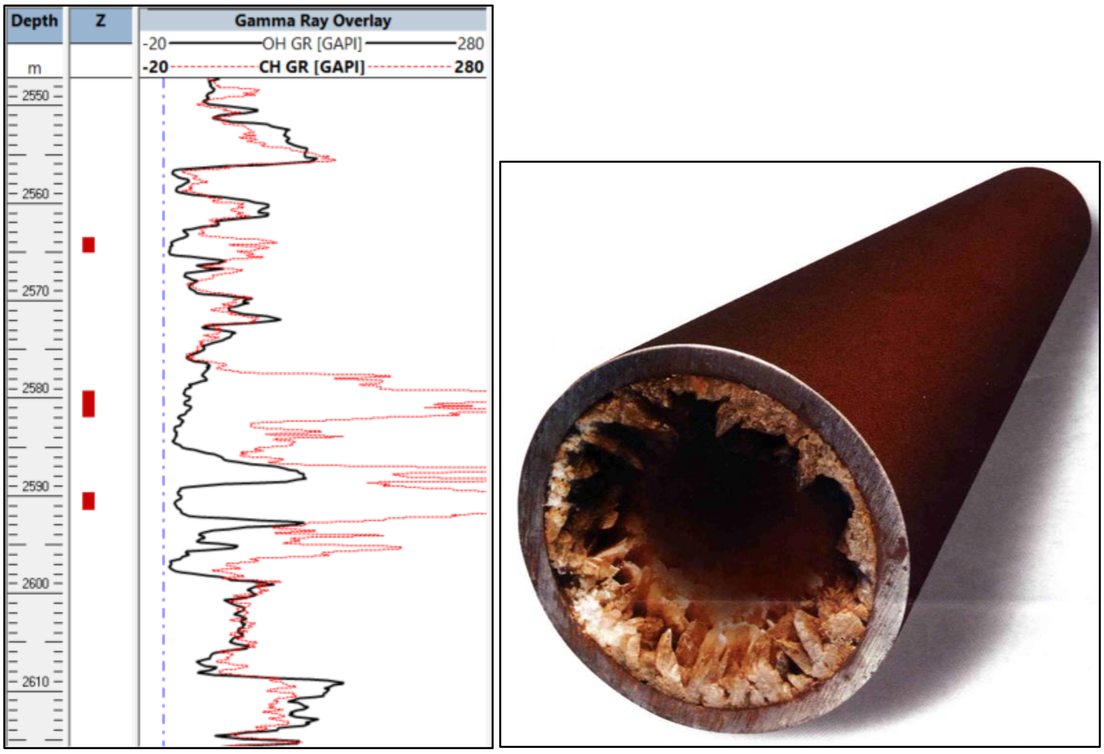

Fig. 2.D.4 – NORM detection through CH GR (left) – Internal scale deposition (right)

3. **Proppant:** Comparing GR logs before and after a hydraulic stimulation with tagged proppant, it may be possible to infer the vertical fracture propagation. Figure 2.B.5 shows the overlay of a GR acquired during a cement evaluation log (black) and a PLT GR recorded afterward. The temperature derivative is displayed, indicating that the fluid inflows are localized at the perforated level. The GR logs are in agreeance away from the perforation (discarding the possibility of issues with tool calibration). At the perforation level, the PLT Gamma ray shows a larger vertical extension than the inflow.

4. **Pip tags**: Radioactive markers located in the casing threads. These are used in situations where it is difficult to correlate, for example, horizontal carbonates.

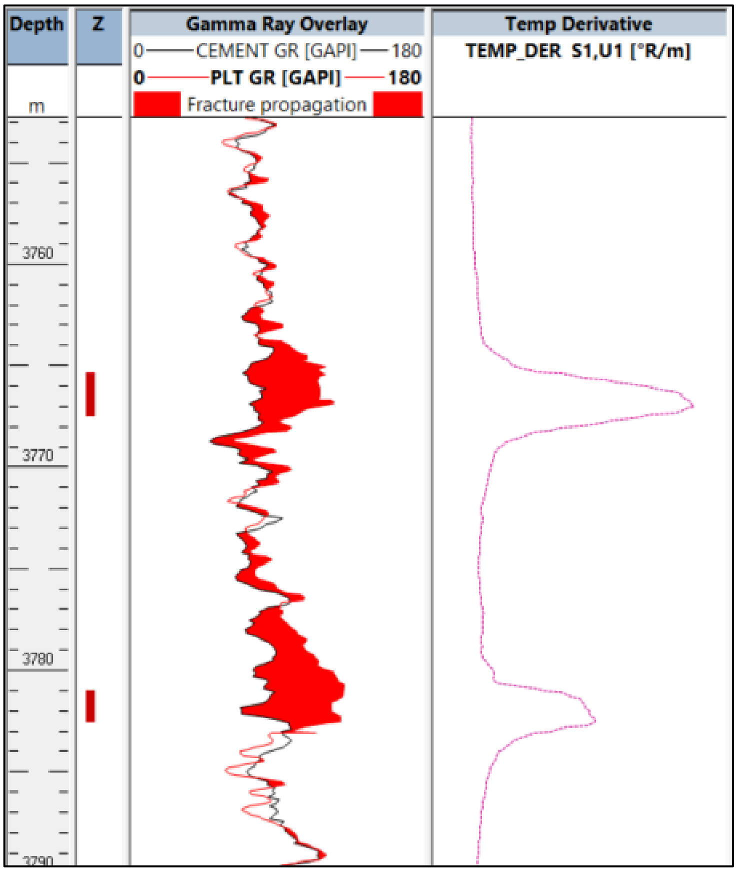

Fig. 2.D.5 – Fracture extension

2.D.4 Casing Collar Locator (CCL)

The casing collar locators indicate changes in metal thickness along the completion. The physical principle of the CCL is Faraday's law of induction. This is, a change in magnetic flux (φ_B) will induce an electromotive force (ε) on a coil, which is sensed as a voltage.

$$\varepsilon = -\frac{d\varphi_B}{dt}$$

In the CCL, the magnetic flux is generated by two opposing permanent magnets. A coil is placed between the magnets, which is connected with the electronic section of the tool. The tool output is a frequency or a voltage, depending on the tool provider.

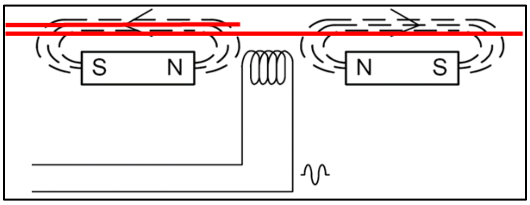

Fig. 2.D.6 – CCL Measurement (Courtesy: Sondex)

Although the name suggests that this tool detects the position of collars, metal thickness variations occur due to a number of features: connections, valves, packers, casing centralizers (behind casing), SSDs, perforations, leaks, etc. As shown in Figure 2.D.7, the analyst should identify the signature of the different features, as it helps to perform a proper correlation and identifies unexpected elements at certain depths, which may end up being integrity issues.

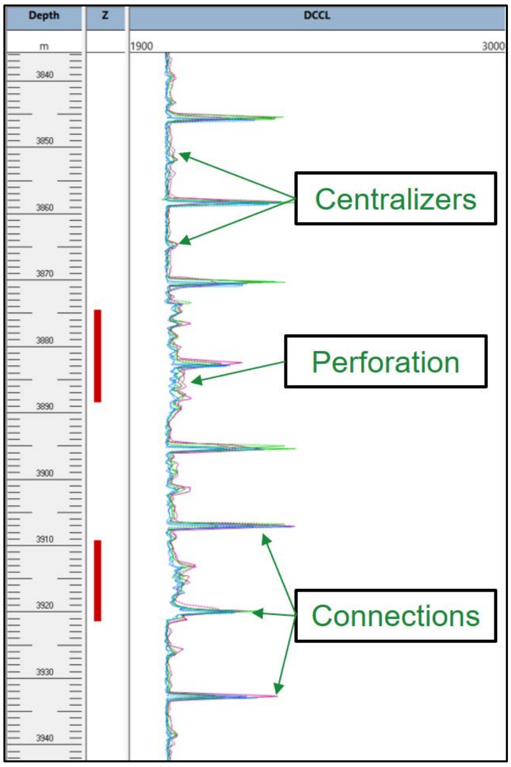

Fig. 2.D.7 – CCL log and completion

The baseline response of the CCL does not have a specific meaning. In Figure 2.D.7, the measurements are around 2000 cps, and it reads higher values in response to the different metal thickness variations. Other tools output larger values (i.e., 16000 to 20000 cps), but some also output positive and negative (i.e., -5 to 5). The value of the CCL is not used for any calculation, and in general, only the spikes are noted, as these indicate the depths with metal thickness variations.

CCL data recorded at a high sampling rate is used to assess the status (open/closed) of SSDs. The measured log is compared with a footprint, recorded at surface (yard logging).

2.D.5 Magnetic Markers Locator (MML)

The Magnetic Marker Locator (MML) is a magnetic field measurement. The presence of the different completion elements will lead to anomalies on the measured earth magnetic field. Similar to the CCL, the MML can detect the presence of different completion elements, even though the signature of these two measurements is not necessarily similar. Figure 2.D.8 shows the response of an MML, CCL, and Caliper across an interval completed with SSDs.

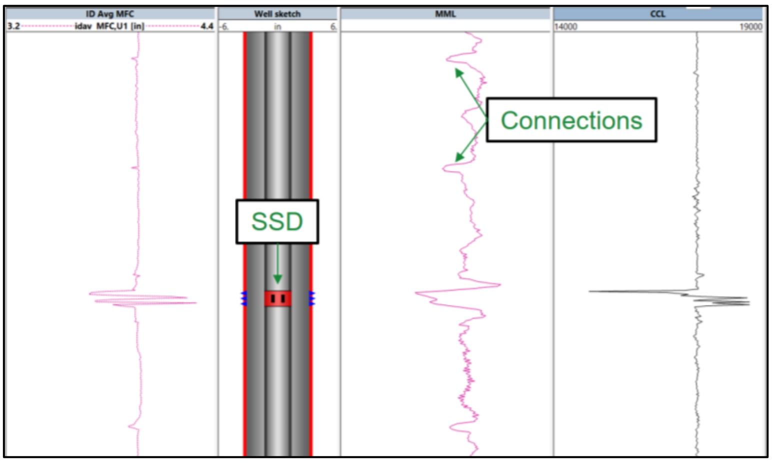

Fig. 2.D.8 – MML, CCL, and Caliper

2.D.6 Log correlation operations

One of the first quality checks performed after loading the data is to verify that the cased hole logs are at depth with the reference logs and or with a completion diagram. The main open hole log used for correlation is the Gamma ray, but in pulsed neutron operations, open hole resistivity logs are also used. It is common to have a reference CCL from a previous operation, which was correlated using a GR.

It is a standard practice to start from the top of the logged interval. The analyst looks at distinctive features in the open hole GR, and assesses the correlation with the cased hole GR. In Figure 2.D.9 (left) the peaks in the CH GR are deeper than the OH GR. It is possible to apply a bulk depth shift to the whole pass, as shown on the right. As mentioned previously, GR measurements are statistical, and therefore the shape of the OH and CH logs may not be identical. Also, as the CH GR is more attenuated, it may be necessary to apply a multiplier or adjust the horizontal scales to correlate the different features.

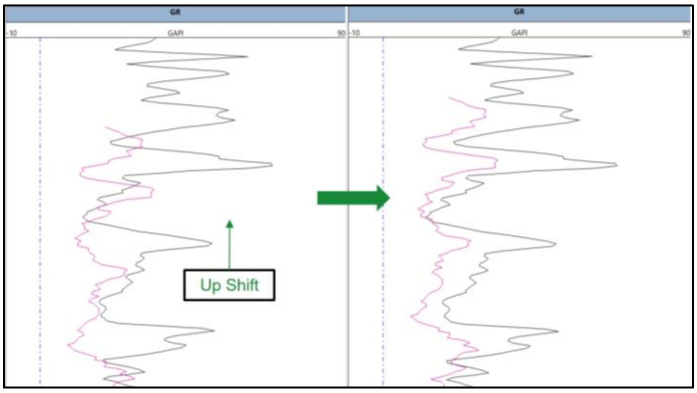

Fig. 2.D.9 – Log shift

Matching a GR or completion feature at the top of the logged interval does not guarantee a good depth correlation deeper in the log. As previously mentioned, due to cable stretch and coiled tubing buckling, the length of the line in the well does not necessarily correspond to the true depth of the toolstring. Different stretch/compression operations are available in interpretation software. The simplest is to apply a constant (or *Full log*) multiplier, which will homogeneously stretch or compress the whole log. Alternatively, it is possible to apply zonal or multi-point stretch operations, as the multiplier is likely to vary, especially with changes of deviation, variations in friction, etc.

Figure 2.D.10 shows a case where the CCL was on depth with the top SSD, but the packers and bottom SSD did not match the CCL signature. The top SSD is used as an anchor, and a multipoint stretch operation was applied (the final result is shown on the right).

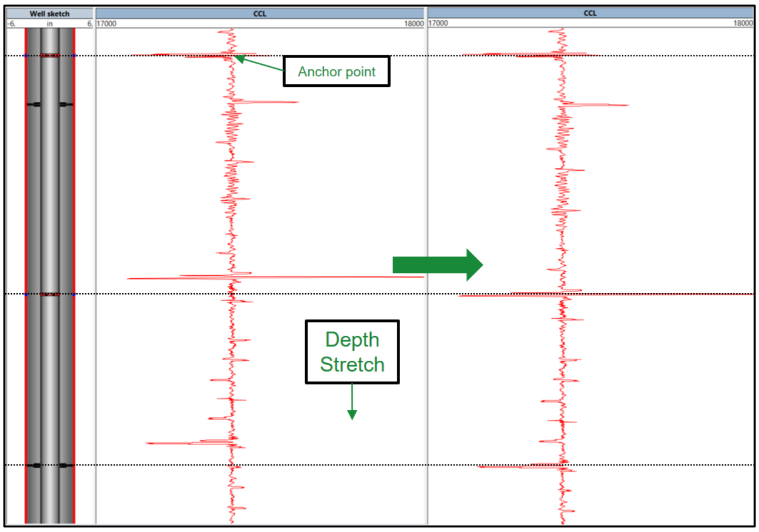

Fig. 2.D.10 – Depth stretch

2.E Ancillary components

Multiple ancillary components can be added to the toolstring to improve the data quality and facilitate the deployment. The main ones are summarized next.

2.E.1 Mechanical centralizers

Proper tool centralization is necessary to ensure good data quality for multifinger calipers, sonic/ultrasonic pulse-echo tools, and horizontal PL tools that are not self-opening.

Centralizers are tools with spring-loaded arms, which exert a radial force through the full operating diameter. Centralizers are characterized by an opening force (i.e., 25, 50, 100 lb), and the selection is based on the weight of the toolstring to centralize and the well deviation. As shown in Figure 2.E.1 (right), centralizers are available as springbows, used for openhole completions, with 3, 4, or 6 arms. The latter may contain rollers to decrease the friction as the tool moves through the pipe. As centralizers are wired through, they can be connected anywhere in the toolstring.

Centralizers have moving parts, which increases the risk of getting stuck and makes it harder going to ID changes (i.e., re-entering to the tubing). Therefore, when designing the toolstring diagram, it is necessary to evaluate what tools require centralization to minimize the number of moving parts in the toolstring, but at the same time preserve the data quality.

Fig. 2.E.1 – Bowspring and 4-arm roller centralizers (Courtesy: Sondex)

2.E.2 Knuckle and swivel joints

All the modules stacked in a toolstring form a rigid body, even though they experience bending due to their own weight. At a certain position in the toolstring, it may be beneficial to add knuckle joints, which provide a limited angular movement. This element helps to remove excess weight from centralizers and decouple the weight from the cable or coiled tubing. By running these in pairs, close to centralizers, it will allow for centralized and de-centralized tools.

The swivel joints decouple the torque of the cable or CT, so the toolstring does not rotate excessively. This is usually placed under the cablehead.

2.E.3 X-Y Calipers

Calipers are mechanical devices that measure the pipes' internal diameter across two orthogonal directions, referred as X-Y or C1-C2. The tool output includes an average ID, calculated as $\sqrt{(X^2+Y^2)}$. These tools help to identify integrity issues, such as deposition, collapsed casing ovalization, etc. Unfortunately, the vertical sampling rate used for this tool is too large, and the angular coverage is too small to detect small leaks. The knowledge of the pipe ID is critical in Production Logging applications since the cross-section must be known to convert velocities to flowrates.

The arms of the caliper are connected to the central shaft of the tool through metal sleeves. When the arms open and close, the sleeves move up and down, and this is detected by induction through a coil array inside the shaft. To convert the electric tool output to diameters, the tool requires calibration. This is done through a number of calibrated rings of known diameter. As the calibration is non-linear, it is recommended to calibrate in more than two rings, encompassing the IDs to be measured in the job.

Calipers can be integrated into the spinner flowmeter or included as a separate module. The arms of the calipers may include rollers or skids. Like the centralizers, calipers are prone to sticking and may get stuck in parted tubing or other severe integrity problems.

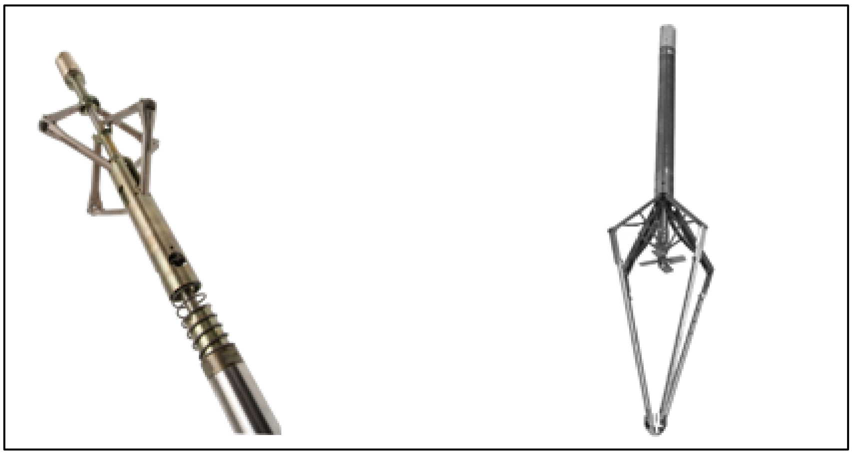

Fig. 2.E.2 – Independent X-Y caliper; X-Y caliper combined with fullbore spinner (Courtesy: Sondex and Schlumberger)

2.E.4 Inclination measurements

The well deviation survey is reported every 12 to 36 meters (1 to 3 drill pipe lengths). Important well parameters, such as the Dog Leg Severity (DLS), are calculated based on this measurement. However, the resolution of the deviation survey is not enough to characterize the well tortuosity, micro DLS events, etc. A higher level of detail is required in horizontal PL, where the sudden changes of deviation around 90 degrees may act as fluid traps. With the multifinger caliper, sudden changes of deviation may be used to evaluate deformation.

Figure 2.E.3 shows a cased hole deviation measurement from two different passes (green and yellow), overlapped with the 'drillers' deviation survey in black. In this case, since the well trajectory fluctuates around 90°, there will be sudden fluid slippage velocity variations that will affect the holdup distribution, even in the absence of fluid entries.

Traditional inclination measurements are based on capacitance variations, as one plate of the capacitor is free to move, and the other is held centralized in the tool. This type of tool requires calibration, with the sensor in the vertical position pointing upwards and downwards.

A different technology consists of Micro Electro Mechanical Systems (MEMS), which are very small sensing structures available for a number of measurements in mobile phones and smart watches. The MEMS accelerometers may be capacitive or piezoresistive.

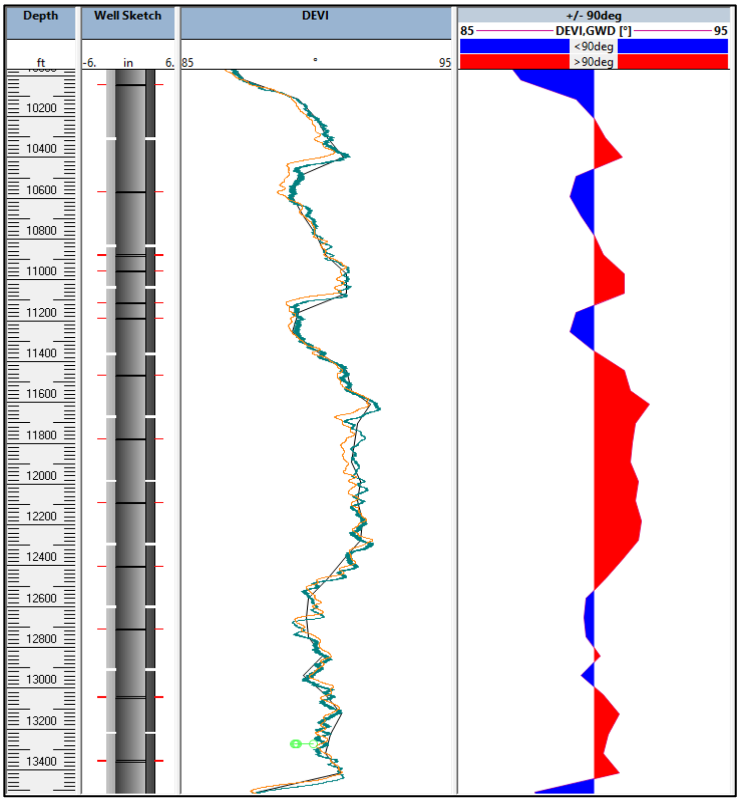

Fig. 2.E.3 – Inclination measurements in a horizontal well

3 – Flowmeters and Single-phase Profiling

3.A Introduction

When a multilayered well is put on production, an informed guess on how much the different layers are producing based on the formations' petrophysical properties can be made. With these inputs and assuming the completion behaves as expected, the deliverability equations for each layer can be estimated. In many cases, the complex reservoir structure, or the limited open hole logs available, may lead to uncertain estimations. Quite often, which layer is the most prolific is unknown, or whether all the layers contribute to production. This picture also changes with time, as depletion and damage influence and modify the deliverability.

Understanding the inflow profile of the well is vital for reservoir management, as discussed in Chapter 1. And we need to perform downhole measurements to quantify this. This is the field of Production Logging (PL).

The questions needing answers through a PL include: Where is the production coming from? What is the percentage contribution from each layer? Are all the perforations active? Are the SSDs open? Is there cross-flow? Are the fluids coming from the perforated intervals or from a place they are not supposed to, like a leak?

This chapter is the first of 4 on Production Logging and begins with the most important sensor of a PL tool string: the flowmeter. Section 3.B focuses on the main flowmeter type, the spinners. The principles of these tools, the operations, calibration, and computation of the fluid velocity are covered. Section 3.C introduces Doppler flowmeters, a relatively new technology for downhole applications.

With the knowledge of the spinner principles and the workflow to compute the fluid velocities, we are equipped to obtain a single-phase, production, or injection profile. This is the subject of Section 3.D. Many of the concepts covered in this section are applicable to multiphase profiling, but the specifics of this topic will be covered in Chapter 5.

3.B Spinner Flowmeters

These are THE tools naturally associated with Production Logging. Despite numerous attempts to use other technologies, the spinner-based tools remain the primary way to assess fluid velocities. Even the latest multiple probe tools use micro-spinners placed at strategic points in the wellbore cross-section.

Imagine a propeller located inside a pipe filled with a static (not moving) fluid of certain viscosity (μ) and density (ρ). In this condition, the blades of the spinner are in force equilibrium and will not rotate. To provide angular acceleration (α), a torque (T) must be applied:

$$T = I\,\alpha$$

The torque is given by a force, applied at a certain distance from the center of rotation. The conversion to angular acceleration is a function of the rotational inertia (I).

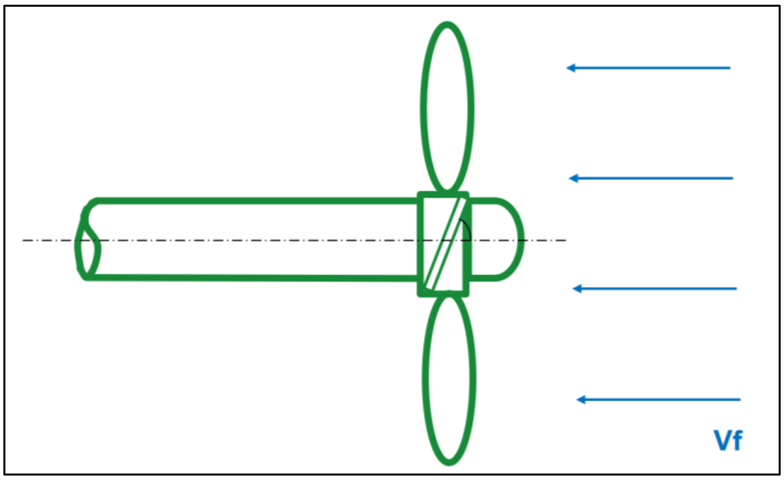

Fig. 3.B.1 – Spinner schematic

The forces that generate the fluid-driving torque are the lift and drag forces in the blades. The lift occurs perpendicular to the stream, while the drag is parallel, and their relative magnitudes are given primarily by the shape of the rotating object. To maximize the spinner rotation for certain stream velocity, which determines the flowmeter resolution, the lift to drag ratio must be as high as possible. For blade turbines, as shown in Figure 3.B.1, there is an angle between the direction of the flow stream and the pitch of the blade, called the 'angle of attack'. The lift will improve as the angle increases. The limit is for the blades to be parallel to the flow, which does not generate lift, or perpendicular, which will maximize the surface area and the drag. Twisting the blades increases the turbine's efficiency to extract energy from the flow by reducing drag and increasing the speed.

The actual spinners used in production logging flowmeters are shown in Figure 3.B.2. The spinner on the left is known as 'Blade' type, and its lift to drag ratio is not great. However, it contains many advantages that make it very useful in real applications. First, the blades can collapse or close (like a flower) when the tool is in reduced diameters. Secondly, when it opens, the blade diameter will typically be considerably larger than the other types of spinners.

The spinners in the middle and right of Figure 3.B.2 are called 'helical' and 'turbine', respectively. These designs are much more efficient than the blades. However, in practice, these are much smaller than blade spinners, which reduce the torque applied by the fluid on them.

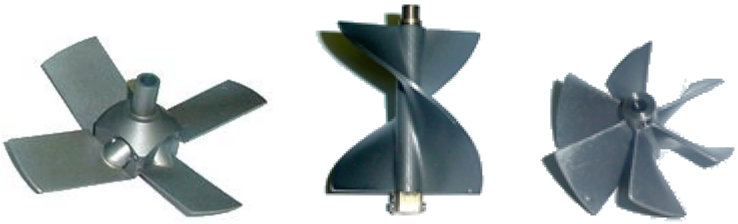

Fig. 3.B.2 – Various types of spinners (Courtesy: Sondex)

Spinners are made of materials including titanium, corrosion resistant alloys, and polymers. Typically, blade and turbine spinners are mounted at the end of a shaft, which includes ball bearings to reduce friction. The other end of the shaft contains two magnets used to compute the revolutions per second. Hall effect switches generate a pulse several times per revolution. For example, in Figure 3.B.3, there are 2 magnets (in red) and 5 switches (in green). Therefore, for every revolution, the spinner will pulse 10 times. Also, the operational sequence of the switches is used to determine the rotation direction.

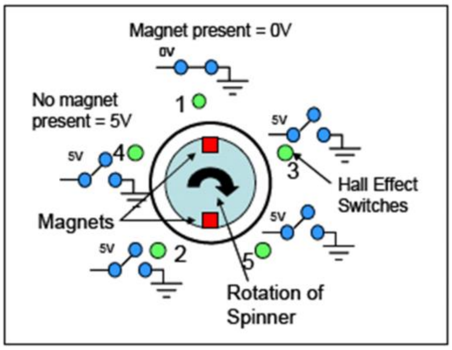

Fig. 3.B.3 – Schematic of the Hall effect (Courtesy: Sondex)

Helical spinners, which are found as conventional flowmeters or minispinners in MPT tools, can also have 'jeweled' bearings. In this case, both ends of the spinners are sitting in pivots, with an optimized shape to decrease the friction. Certain minispinners use optical encoders to measure the spinner revolution instead of Hall effect switches.

The spinner's output is an angular frequency, typically in units of revolutions per second, or RPS. Ultimately, the interest is in relating this value to the volumetric flow rate. However, it will be demonstrated that this relationship is not linear due to the different flow regimes, so it is best to work in terms of the fluid mixture velocity as:

$$Q = V_m \pi \frac{ID^2}{4}$$

If the spinner in Figure 3.B.1 is placed in a pipe where it can accurately measure the flow rate, fluid velocity, and spinner RPS, a calibration plot can be constructed as shown below:

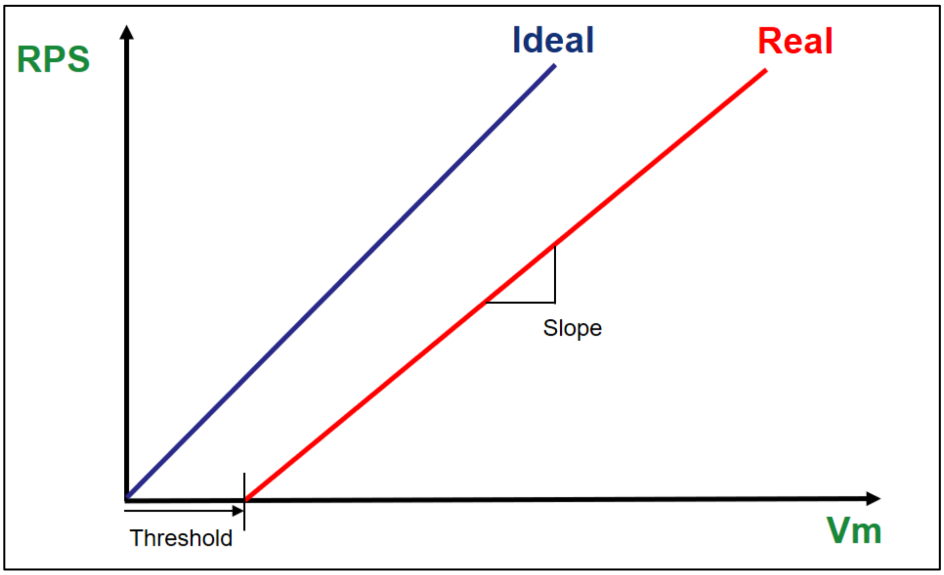

Fig. 3.B.4 – Ideal and Real spinner response

In an **ideal** scenario, it would require an infinitesimal flow velocity to generate the torque that creates the angular acceleration for the spinner to start to rotate. Once it is moving, the RPS value would be a linear function of the velocity. This is a function of the 'pitch', which relates the distance in the axial direction the spinner would traverse in one revolution if it acted like a screw thread on the fluid. Spinners' datasheets typically include the 'pitch' that depends on the geometry only.

In **real** spinners, retarding torques due to fluid drag on the blades and friction in the bearings will generate a region of small fluid velocities that will not be enough for the spinner to rotate. The minimum fluid velocity for the spinner to start to rotate is called 'threshold' and has units of velocity. Due to the same retarding torques, the spinner angular velocity will be lower than the ideal case. The proportionality between RPS and fluid velocity will be a function of the geometry and will incorporate factors as the fluid properties and bearing friction. Instead of using the pitch, use the 'slope' to associate the measurement to a fluid velocity.

The impact of the type of fluid on the slope and threshold are shown in the following image. The main properties affecting the response are:

- Density: The lift on the spinner can be calculated as:

  $$L = \frac{1}{2} \rho \, v^2 \, A \, C_L$$

  Where ρ is the density, v is the fluid velocity, A is the surface area, and C_L is the lift coefficient. The larger the density, the larger the lift on the spinner, the more RPS.
- Viscosity: This affects the lift and is included in the C_L parameter of the previous equation. The viscous sub-layer is a function of viscosity, and the larger this is, the more energy is dissipated in friction and less used for actual lift creation.

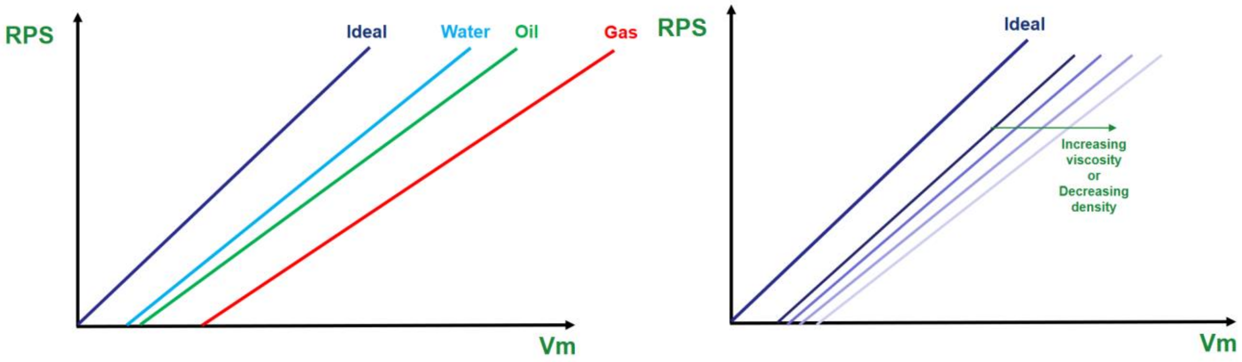

Fig. 3.B.5 – Influence of the fluid properties in the spinner response

The spinner output in RPS needs to be converted into velocity to conduct a quantitative interpretation. As explained in this section, the relation between RPS and velocity depends on the spinner itself and the fluid properties. There may be multiple zones with different viscosity and density along a logged interval, and a surface or 'flowloop' calibration will not be enough for accurately obtaining the velocity. For this reason, an in-situ calibration is required in the fluids of interest.

3.B.1 Types

The spinners are packaged in several types of tools. There are four main types of flowmeters: Inline, Continuous, Fullbore, and Petal Basket. Other types are not described here.

Fig. 3.B.6 – Inline, Continuous, Fullbore, and Petal Basket flowmeters (Courtesy: Sondex)

Inline flowmeters use helical or turbine spinners, which have small diameters and can be used to log in completions with restricted diameters (tubing, scaled up wells, etc.), as the tool OD is 1 11/16′′. Due to the small spinner diameter, they have lower sensitivity (slope) and higher threshold and may not be ideal for low velocity wells. Because of the small spinner size, good centralization of the tool is required. These flowmeters have two connections and can be located anywhere in the toolstring. For this reason, these are typically considered as a back-up of the main (larger diameter) spinner located at the bottom of the toolstring.

Continuous flowmeters are located at the bottom of the toolstring. Similar to the inline flowmeters, these use turbine, and helical spinners. As the spinner diameter can be larger than the tool OD, the sensitivity is improved, and the threshold is reduced. The spinner is considerably protected from deformation.

Fullbore flowmeters have larger blades that are exposed to a greater part of the flow cross-section. When the blades collapse, the tool OD becomes 1 11/16′′ to pass through the tubing and other restrictions. They expand and start turning when the cross-section becomes sufficiently larger. Fullbore flowmeters have good sensitivity and can be run for a wide range of flow rates and velocities. There may be issues with injectors where the blades may collapse when the flow coming from above is too great. As the blades can easily bend under strain, these tools are caged with bowsprings or arms with rollers. In some cases, the cage of the fullbore spinner acts as an X-Y caliper. Different blade sizes are available, depending on the size of the casing to log: 2.6′′, 3.5′′, 4.5′′, etc.

Fig. 3.B.7 – PFCS Fullbore flowmeter with built-in X-Y caliper (Courtesy: Schlumberger)

Petal Basket flowmeters concentrate the flow towards a relatively small spinner. While they are highly efficient at low flowrates, they are not sufficiently rugged to withstand logging passes and are primarily designed for stationary measurements. The tool shape often affects the flow regime.

As previously mentioned, spinner-based flowmeters do not measure rates. The output of a spinner is a rotation in RPS (or CPS for some tools). The process of converting RPS to apparent velocity, then average velocity, and ultimately rates is the essence of Production Logging Interpretation and requires additional measurements and assumptions. This is described next.

3.B.2 Operations

3.B.2.a The logging program

The basic assumption in Production Logging is that the well is in steady state. As a snapshot of the well’s production or injection profile is taken at a specific time, the well must reach stabilization before running the tools.

A text book job sequence is depicted in Figure 3.B.8. In red are the highlighted periods where the PL measurements are recorded as continuous passes or stations. The sequence includes an initial shut-in survey, a stabilization and flowing survey recording, and a final shut-in. Typically, the most important survey is with the well flowing (producing or injecting). This will allow the analyst to generate the profile and describe the contributions from the different layers. It may also provide information about leaks.

Shut-in surveys are also recorded with the goal of calibrating the tools in an environment with segregated phases. Shut-ins can also reveal cross-flow due to differential depletions, providing a reference gradient in shut-ins, and a baseline for measurements in flowing conditions, e.g., temperature. During the pressure build-up of the second shut-in, the transient behavior will cause an evolution of the measurements. This is quite useful in water injectors, as the warmback provides information about the injected water distribution (See Chapter 7).

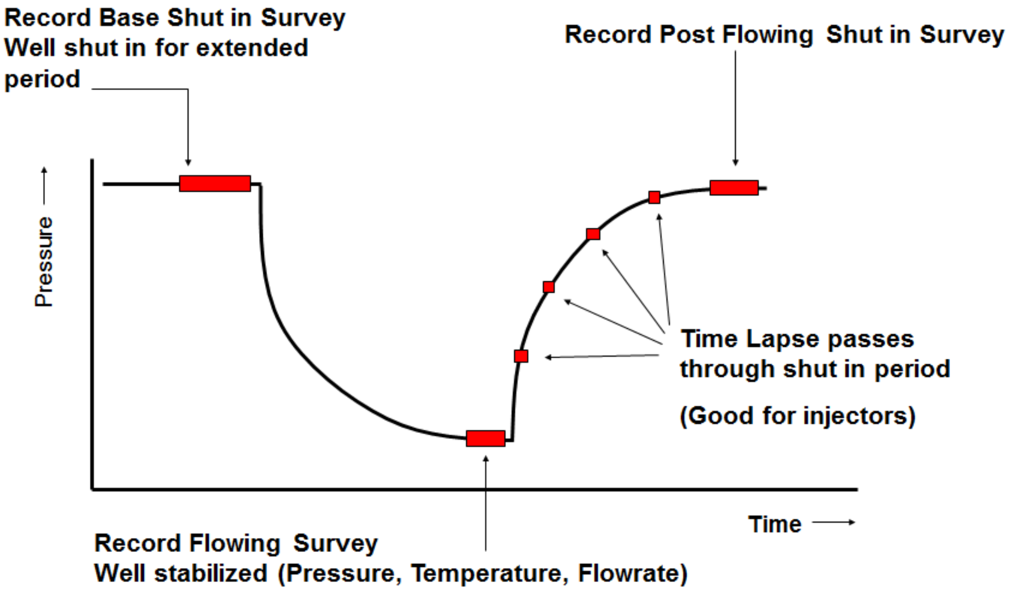

Fig. 3.B.8 – A typical PL job sequence

Part of the job planning is accounting for how long it takes for the well to stabilize. The notion of stability is defined as a pressure variation over time since it is known from welltest that the flowing pressure will usually not be strictly constant. In SRO jobs, the stabilization can be monitored in real time, using stationary measurements typically at the top of the upper perforation or inflow zone. As shown in Figure 3.B.9, the pressure continues to draw down, while the spinner RPS increases 50%, which is practically proportional to the rate variation. A PL recording during this period would not be a steady state snapshot.

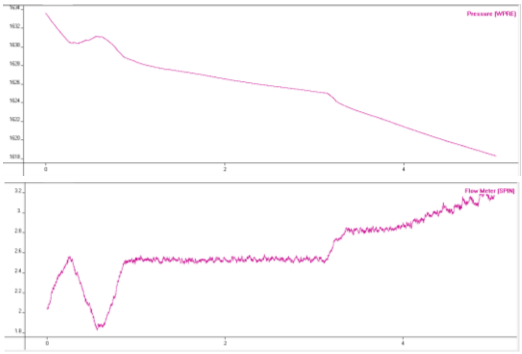

Fig. 3.B.9 – Pressure and Flowmeter stations

As in memory jobs, it is not possible to monitor stability in real time. It is necessary to establish with reasonable accuracy what would be a sufficient stabilization time when writing the logging program.

The job sequence is also determined by operational constraints. For example, some liquid-loaded gas wells cannot be shut-in as the well would be immediately killed. On the other hand, in some locations, it is mandatory to shut-in the well before rigging up the tool and lubricator.

3.B.2.b Multirate PL and SIP

Production logging recorded at multiple surface rates is called 'Multirate PL'. This allows the analyst to compute one production/injection profile for each flowing and shut-in period. The contributions from each layer are coupled with the bottomhole pressure recording to perform a Selective Inflow Performance (or SIP) analysis. The SIP methodology is presented in the Appendix.

The number of flowing surveys is a function of the expected IPR behavior. If Darcy flow is anticipated, then the IPR of each layer will be a straight line and can be generated with two points. Therefore, two surveys at different BHP's are enough (one can be shut-in). Adding more points increases the accuracy of the IPR, as it is obtained via regression. If a non-linear IPR behavior is likely, for example, due to turbulence, more than two surveys are required. The sequence shown below includes 3 flowing surveys and is typically used in gas wells. Needless to say that the quality of the IPR is a function of the pressure stability.

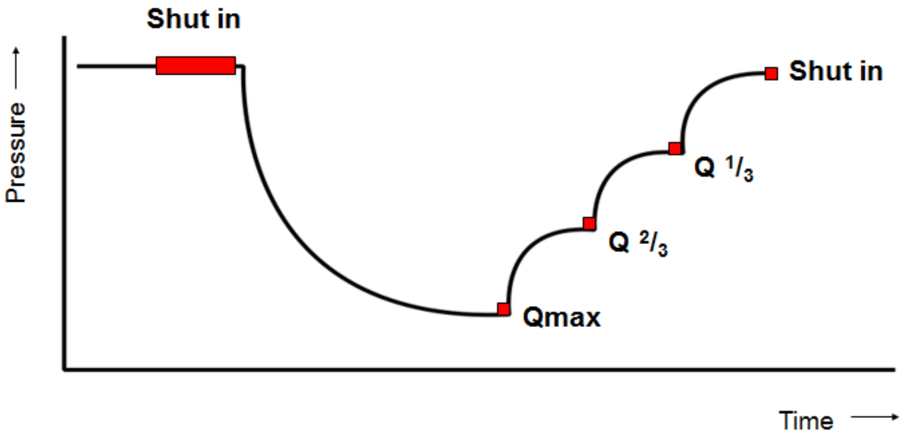

Fig. 3.B.10 – Multirate PL sequence

3.B.2.c Data recording: Passes and stations

In a single-phase situation, a typical tool string will comprise temperature, pressure, spinner, and the auxiliary tools reviewed in Chapter 2 (CCL, GR, Caliper). No further information is required, assuming of course that the flow conditions are indeed single-phase. It is not uncommon to encounter fluids downhole that are not produced at surface. If in doubt, it is always better to add a fluid identification tool in the string, such as density or holdup, before running the job.

In a multiphase situation, there are n-1 additional unknowns, n being the number of phases. In two-phase flow, a density or holdup is required, and in 3-phase, two such independent measurements are required. This will be the subject of Chapter 4.

For all tools, except the spinner, one pass would be sufficient for calculation. However, comparing several passes for other tools is a way of judging the wells' stability. Having multiple passes also provides a better likelihood of having a representative measurement if the data is bad in some sections of passes.

The spinner calibration, explained next, requires several passes at various logging speeds. A typical job will comprise 3-4 down and 3-4 up passes, as illustrated below. The cable velocity is typically 10, 20, 30, and 40 m/min. For decompressed gas (low density), the exerted lift is smaller, and it may be better to avoid slow cable speeds (10 m/min) and possibly add a faster speed (50 m/min). Passes are normally run by increasing speed, and the slow passes are recorded first. This means that Down 1 is normally the first and slowest pass in the well.

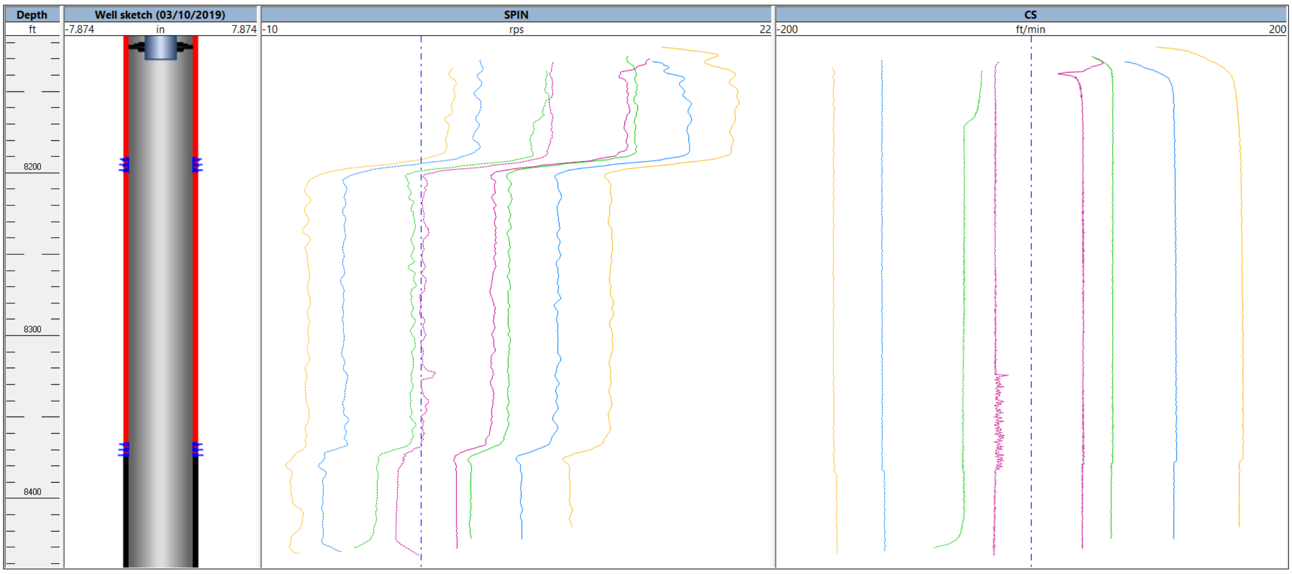

Fig. 3.B.11 – Spinner and cable speed for an 8-passes job

The passes should survey the whole producing interval if there are no well access issues. Before running the PL, a dummy run is performed to verify that a tool of the same OD as the PL will make it to the target depth. As shown in Figure 3.B.11, it is necessary to survey an interval above the uppermost inflow and preferentially below the deepest one. This is because the layer contributions calculation scheme uses the rates above and below each inflow zone. Accessing the interval below the bottom perforation, typically referred to as the 'sump', is not always possible. It may contain fluids that are not representative of the produced hydrocarbons and water. However, getting into the sump will prove valuable for computing the spinner calibration parameters.

Apart from the passes, stations may be recorded for certain tools that require it. Stationary spinner measurements can be used for calibration purposes, as will be explained next. In addition, the ability to display the measurement of a station versus time is a further indication of well stability or instability. Figure 3.B.12 shows a stationary spinner recording over a 5-minute station. The RPS fluctuates between 0.2 and 2 RPS, revealing interesting aspects of the flow regime of the well (slug or plug flow).

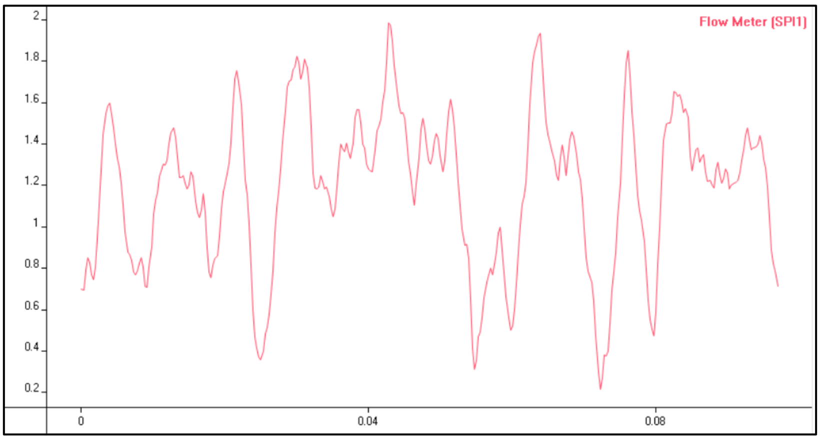

Fig. 3.B.12 – Stationary spinner recording

3.B.3 Calibration

As mentioned earlier in this section, going from Spinner RPS to fluid velocity requires the knowledge of two parameters: Slope and Threshold. As these are a function of the fluid properties, which are different for every well and vary with depth, it is necessary to obtain these calibration parameters in-situ in the fluid of interest. This process is referred to as Spinner Calibration.

Generating a plot as shown in Figure 3.B.4 in a producer or injector well would not be practically possible. It would imply measuring several surface rates with high accuracy and then converting these to downhole conditions in order to plot them versus RPS. The total rate would reflect the rates above the topmost inflow, and the fluid mixture here may not necessarily represent the fluids below. Therefore, varying surface rates and measured RPS is not a feasible option.

Fortunately, the flowmeter relies on the principle of Relative Velocity:

$$V_{Rel} = V_{fluid} - V_{tool}$$

When multiple runs at different tool velocities (controlled by the cable speed) in an interval of stationary fluid are performed, a calibration cross-plot can be obtained. In practice, Cable velocity is plotted in the horizontal axis of the calibration plot.

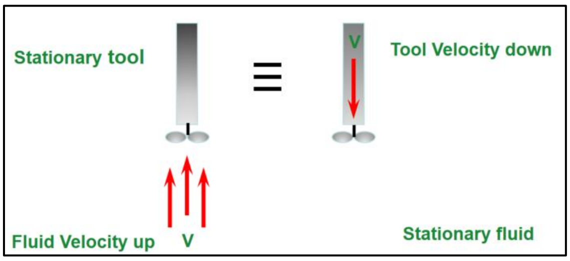

Fig. 3.B.13 – Relative velocity principle

The usual sign conventions consider that the tool velocity is positive going down and negative coming up. Similarly, the spinner rotation is considered positive when the fluid is seen by the spinner as coming from below and negative when it is seen as coming from above. With these conventions, the spinner rotation is relative to the sum: Cable Speed + Fluid Velocity.

A schematic of the calibration crossplot is presented below. The blue line represents the ideal response (no friction), while the red lines represent the real response. There are 2 distinct response lines for Up passes (negative CS) and Down passes (positive CS). Note that both the slope and the threshold can be different between up and down passes, as the tool body acts as a shield. This should not be the case with a symmetrical tool like an in-line spinner.

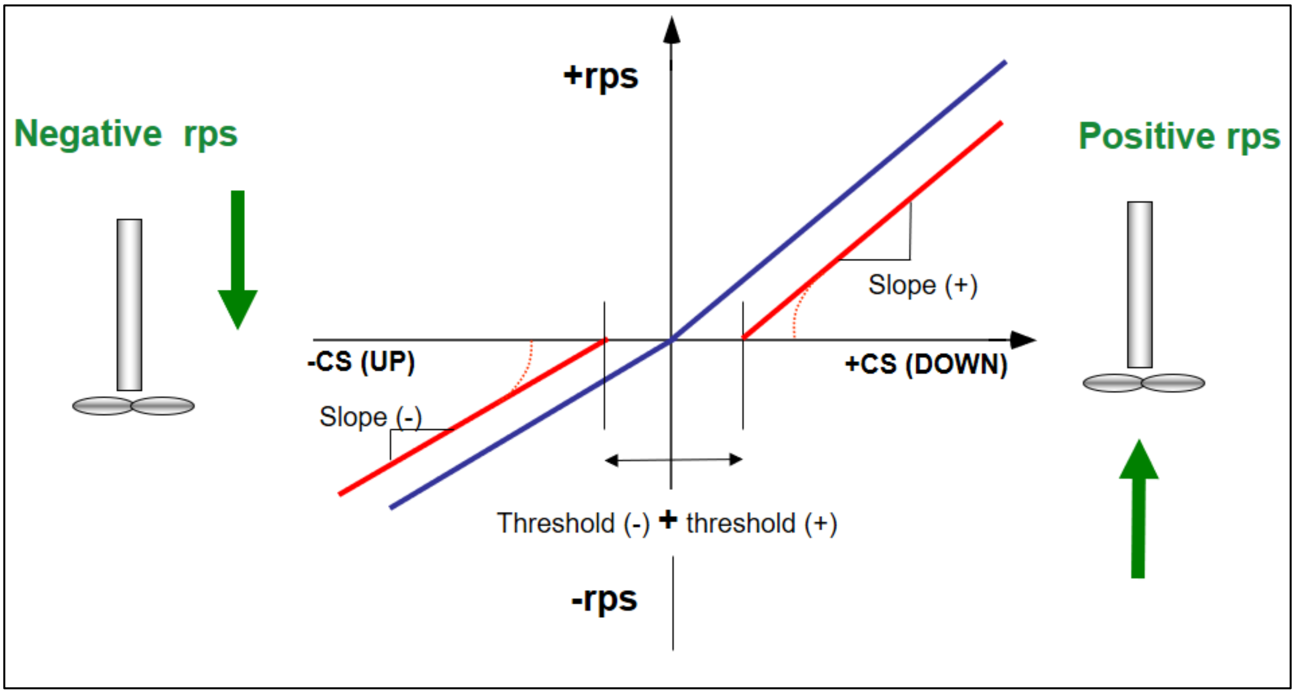

Fig. 3.B.14 – Calibration Cross-plot

The real spinner response shows that at a low RPS, the calibration becomes non-linear due to friction and viscous effects. The equation below is a possible representation (SPE Monograph Vol. 14; Hill A.D.):

$$rps = aV_{fs} - \frac{b}{\rho V_{fs}} - c\sqrt{\frac{\mu}{\rho V_{fs}}}$$

Where *a* is the pitch coefficient (geometrical), *b* is the bearing friction coefficient, *c* is the fluid friction coefficient, *ρ* is the fluid density, and *μ* is the fluid viscosity.

For PL interpretation, it is considered that the calibration is still a straight line. For calibration and velocity calculations, disregard the low spinner rotations, which are not represented by a straight line.

The plot above represents the spinner response in a no-flow zone as a function of the cable speed. The analyst will be able to calibrate in this condition, in shut-in conditions with no cross-flow, below the bottom perforation (or above if it does not contribute), etc. If the fluid is moving at some velocity V_{fluid}, the tool response will be the same but shifted to the left by V_{fluid} as shown below. The reason behind the shift is that since the spinner reacts to the sum of (V_{fluid} + Cable Speed), the RPS value for a CS value 'X' in V_{fluid} is the response to a CS value of (X+ V_{fluid}) in the no-flow zone.

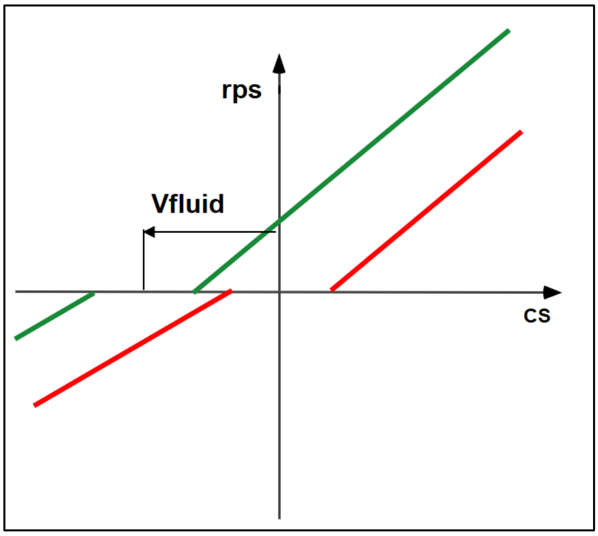

Fig. 3.B.15 – Real spinner response in a no-flow zone, and a zone with production

The threshold can only be obtained in a no-flow zone, represented by the red lines. For calibration performed in intervals with moving fluid (green line), the positive and negative RPS lines also show intercepts, separated by certain cable speed magnitude. The sum of the positive and negative threshold should be equal to this distance. Sometimes this distance is split in half, or a fixed ratio is considered (see Section 3.B.3.a) as a way to estimate the positive and negative thresholds.

In practice, the objective is to build the calibration response in-situ to account for the changing fluid properties and their effect on the spinner calibration. Figure 3.B.16 shows the spinner RPS, cable speed, and density. Three different fluids can be identified, and therefore it is necessary to obtain three sets of calibration parameters since the spinner will respond differently to the changing fluid properties. Zones in yellow represent the spinner calibration zones, whilst zones in red represent the perforations.

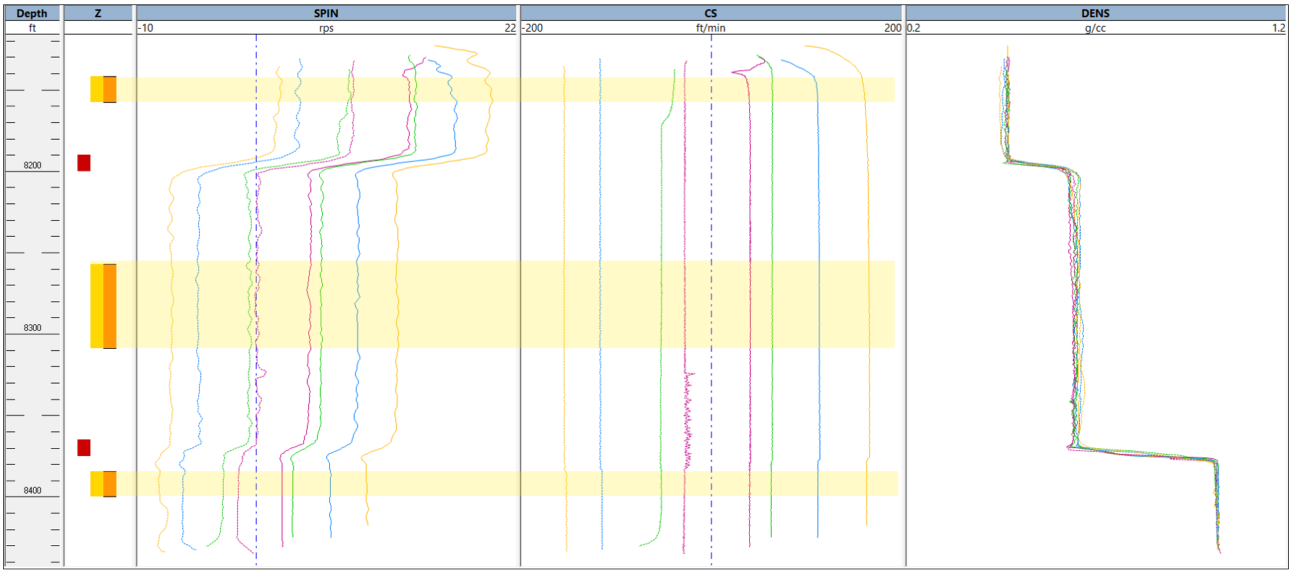

Fig. 3.B.16 – Spinner calibration zones

For each spinner calibration zone, the average spinner RPS and cable speed are plotted in the calibration cross plot. The lines are drawn by linear regression:

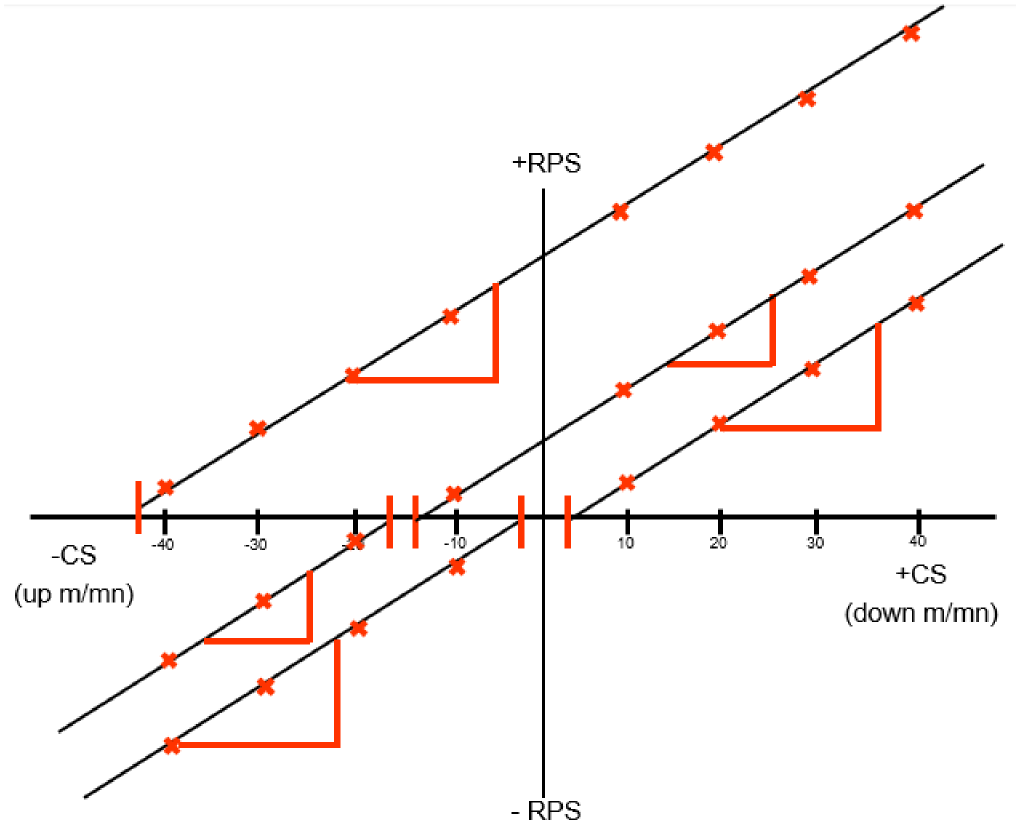

Fig. 3.B.17 – In-situ calibration for the case above

The need for in-situ calibration leads to the requirement of multiple up and down passes at different cable speeds. While two passes would be enough to form a line, as explained before, it is common to run 3 or 4 passes in both directions. This will help reduce the error, as the lines are computed using linear regression. These passes must be recorded under a constant downhole rate, meaning the well must be stable throughout the duration of the job.

Historically when doing calculations by hand, the usual method was to consider a spinner calibration zone in stable regions in-between every perforation, as above. The velocity was then calculated directly from the cross-plot for every zone. Today's idea is that you only put in spinner calibration zones because you think there has been a change of slope or threshold (usually due to a change of fluid type). In theory, a single phase well only needs one spinner calibration zone. In reality, having multiple zones, as long as they are stable, ensures that any change is properly captured.

The calibration does not give the fluid velocity directly, and some calculations or assumptions remain to be done. Suppose the response of the various sections were strictly parallel. In that case, we know from the previous discussion that the fluid velocity could be obtained by estimating the horizontal translation between, say, the positive line of a given zone and the positive line of the no-flow zone. This method is fine for manual analysis, but it is quite limited. A general approach needs a systematic way of handling slope and threshold variations.

Tool manufacturers typically provide nominal calibration parameters that can be used if it is not possible to perform an in-situ calibration. The analyst should refer to the specific datasheet for the tool to get accurate values. For example, the reported fullbore spinner slope for Sondex CFB is around 0.05 RPS/ft/min. This depends on the blade diameter. The threshold for this spinner is 1.8-2.5 ft/min for water, 2.3-3 ft/min for oil, and 7-12.5 ft/min for gas. As a rule of thumb, the threshold of gas is 3 times larger than the one in water.

3.B.3.a Threshold options

Below are the options in Emeraude to handle the thresholds when multiple spinner calibration zones are required.

3.B.3.b Unique value of (+) and (-) thresholds for all zones

The apparent velocity for a point on a positive line is calculated based on the slope of that line and the common positive threshold. The apparent velocity for a point on a negative line is calculated based on the slope of that line and the common negative threshold. This mode is suitable incase of single-phase fluid.

3.B.3.c Distinct thresholds, unique ratio threshold(-)/[Intercept(-) – Intercept(+)]

This ratio is equal by default to **7/12** = **0.583** but can be set from the value of a no-flow zone. Obviously, this can be used only on zones with both positive and negative intercepts.

3.B.3.d Independent Thresholds

This mode allows different thresholds for each calibration zone and is the most general. Note that the only problem with this mode is that on a zone where there is fluid movement, at best it provides the sum of the thresholds. Deciding the positive and the negative can be done bluntly (i.e., halving the sum) or based on the split on the no-flow zone.

3.B.4 Apparent Fluid velocity

After the calibration is complete, the goal is to obtain a continuous apparent velocity curve representing the velocity at every depth. This can be calculated based on the following equation:

$$Vapp = \frac{RPS}{slope} - CS + Th$$

Where RPS and CS are taken from the logs, and the slope and threshold are calculated from the spinner calibration for each zone.

This can be done graphically for each depth by plotting the pairs RPS-CS, extrapolating to zero RPS using the slope, and correcting by thresholds.

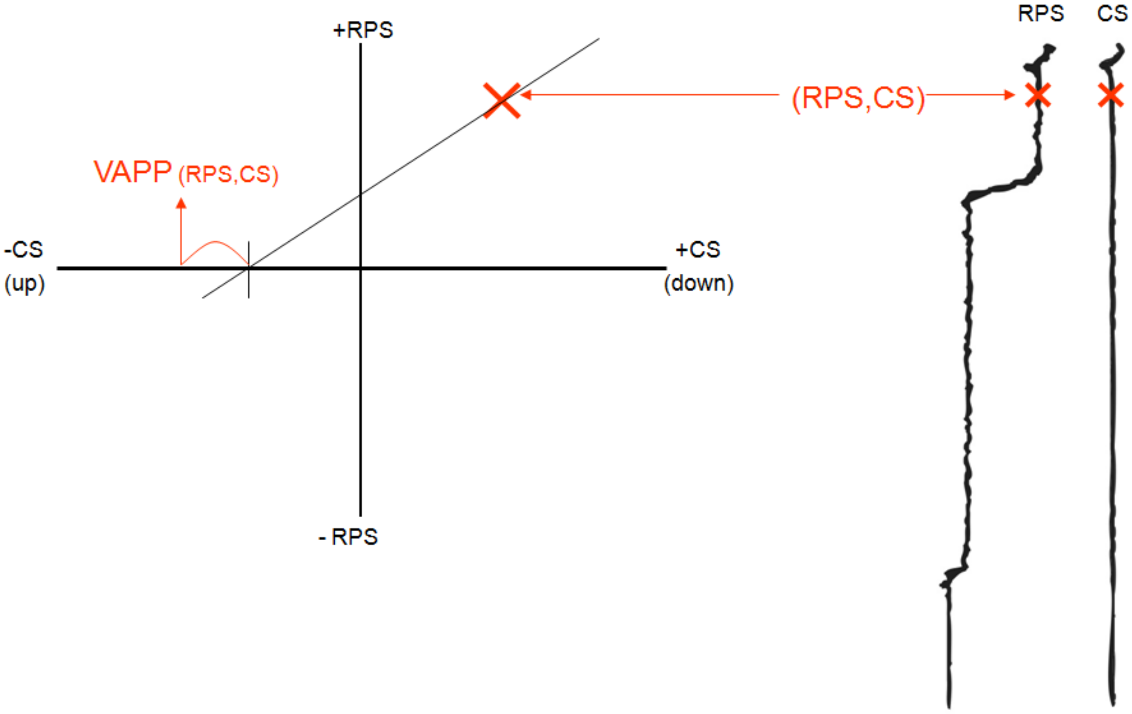

Fig. 3.B.18 – In-situ calibration for the case above

Once the calibration parameters are defined, a single pass would suffice to obtain the apparent velocity. However, producing one apparent velocity channel per pass allows an overlay and is a further check of the well stability and the calibration adequacy, as shown in the middle track of the image below (VASPIN). When this check has been made, the multiple apparent velocity curves are typically replaced with a single average value (median stack or lateral average). This single apparent velocity curve is the sole information required for quantitative analysis (track on the right).

Regardless of themethod used, the measurement of velocity representing the fluid velocity will be seen by the spinner. This value is the average velocity in the cross-section covered by the spinner and is different from the actual fluid average velocity. For this reason, it is referred to as apparent velocity, noted Vapparent or VAPP.

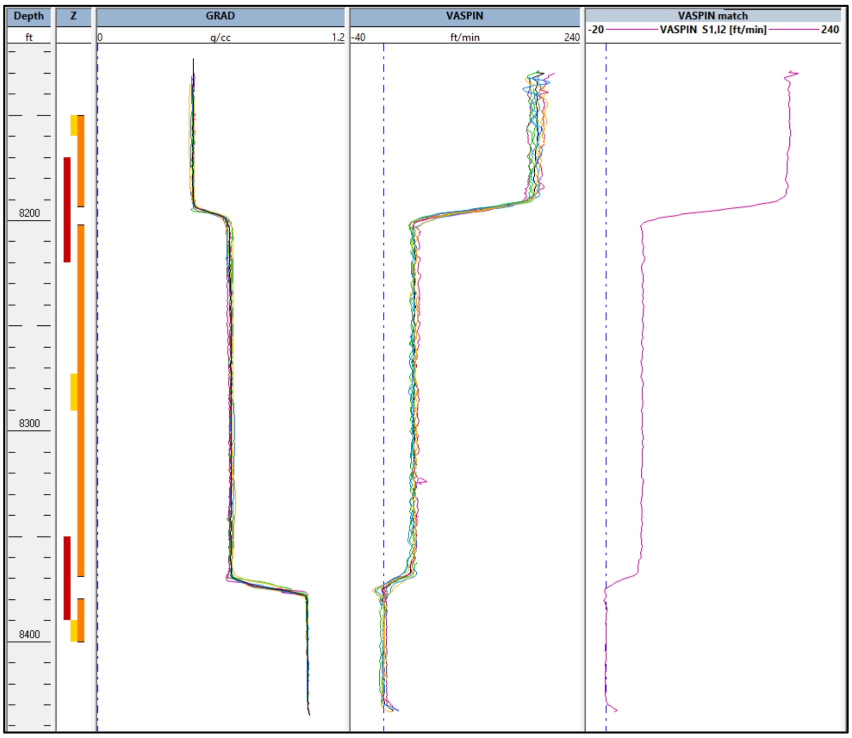

Fig. 3.B.19 – Apparent fluid velocity

3.B.4.a Spinner Calibration Application Zones

In situations such as in Figure 3.B.18, where more than one set of calibration parameters are calculated, it is necessary to establish which parameters are used where. The Z track shows three orange zones called Spinner calibration application zones. By default, these are the same size as the spinner calibration zones, originally shown in Figure 3.B.16. Emeraude offers three options to control the transitions:

- Interpolation: Between the spinner calibration zones, the slopes and thresholds are interpolated using a distance-weighted approach. This is the default transition method. Figure 3.B.16.
- Sharp: The spinner calibration application zones are in contact, and therefore a single transition depth is defined between two zones.
- Free: The length of the zones is typically adjusted to encompass one fluid. In the gaps between two zones, a linear interpolation of the calibration parameters will be applied. Figure 3.B.19.

As a general rule, where a spinner calibration application zone (orange) is present, it will use the calibration parameters obtained in the spinner calibration zone (yellow) in contact with it. If there is a gap between orange zones, distance-weighted interpolation will be applied.

3.B.5 Velocity profile correction factor

Rate calculations may be performed on each depth frame or averaged on calculation zones of interest. Such calculation zones could be the calibration zones or the top of each perforation zone. In most cases, the engineer will define where the rate calculations are most relevant.

The spinner calibration allows us to get the apparent velocity, V_{APP}, everywhere there is a measurement.

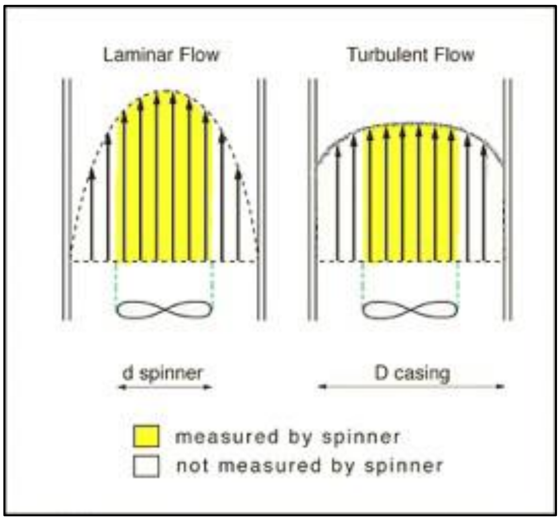

Fig. 3.B.20 – Velocity profiles and spinner sampling section

The previous image shows that in single phase, a well-centered spinner is in the region of maximum fluid velocity. To get a single phase rate, the total average flow velocity is required, which can be expressed from V_{APP} with some correction factor usually noted VPCF:

$$V_M = V_{APP}\,VPCF$$

Historically, and at least for any manual interpretation, VPCF is taken as 0.83. However, as shown in Figure 3.B.20, this factor should be different for laminar and turbulent, and therefore it is a function of the Reynolds number:

$$N_{Re} = 7.742\ 10^3\ \frac{\rho\ D\ v_m}{\mu}$$

The Reynolds number is expressed above for fluid density ρ in g/cc, diameter D in inches, velocity in ft/sec, and viscosity in cp.

Under a value of 2000 for the Reynolds number, the flow is laminar, and the analytical expression of the velocity profile can be derived from the Navier-Stokes equation:

$$v(r) = v_{max}\left[1 - (\frac{r}{R})^2\right]$$

Due to the no-slip condition at the pipe wall, the minimum velocity is zero, and the average velocity is simply 0.5 v_{max}.

Above N_{Re} of 4000, the flow is turbulent, and the velocity profile cannot be obtained directly from Navier-Stokes. A well-known expression of the turbulent velocity profile is the power low solution:

$$v(r) = v_{max}\left[1 - \frac{r}{R}\right]^{1/n}$$

Compared to the laminar flow profile, turbulent is flatter due to the existence of the viscous sub-layer, and therefore the average velocity is above 0.7 v_{max}.

Note that v_{max} would only be measured if the spinner was a single-point measurement located in the center of the pipe. In reality, the spinner sweeps a certain percentage of the pipe, indicating the VPCF is also a function of the ratio of blade diameter to pipe diameter. This is illustrated in the figure below:

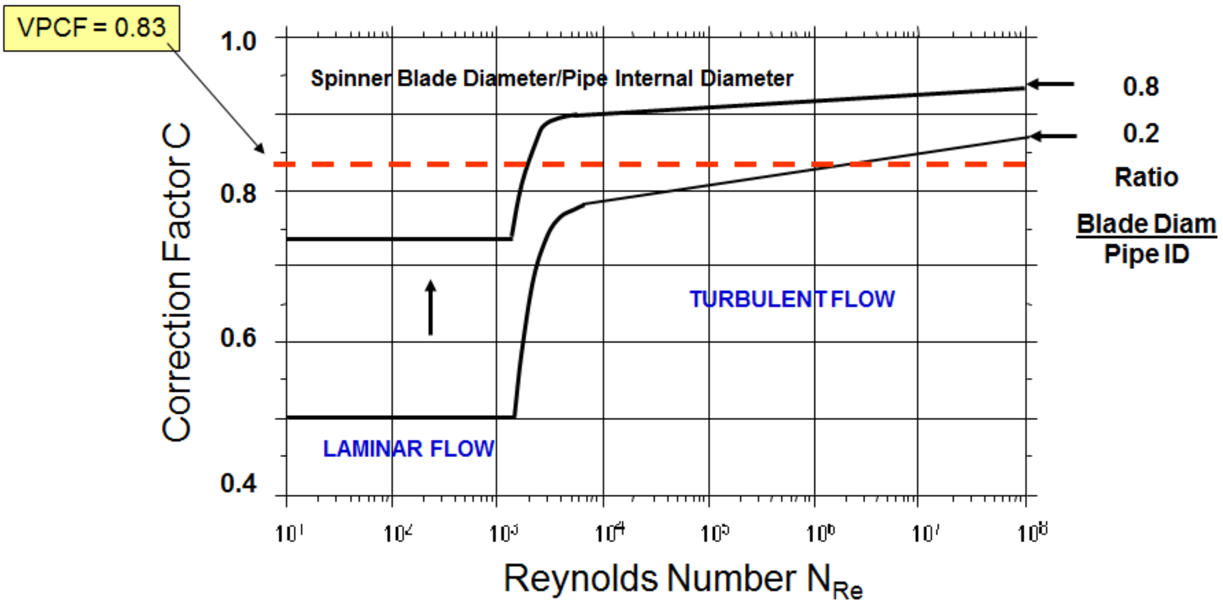

Fig. 3.B.21 – VPCF vs. Reynolds number for different ID ratios

When the Reynolds number increases, the correction factor increases from 0.5, and its value tends asymptotically to 1. Also, as the blade diameter tends to the pipe ID, the correction factor moves towards 1.

Remember the goal is to estimate the VPCF to calculate the fluid velocity, v_m. The fluid velocity value is part of the Reynolds Number equation, meaning that an iterative solution is required. The classical solution is to assume a value of velocity, typically based on a VPCF of 0.83, then calculate the Reynolds number. A new value of VPCF would be calculated, providing a corrected estimation of the flow velocity.

The process would go on until the solution eventually converges.

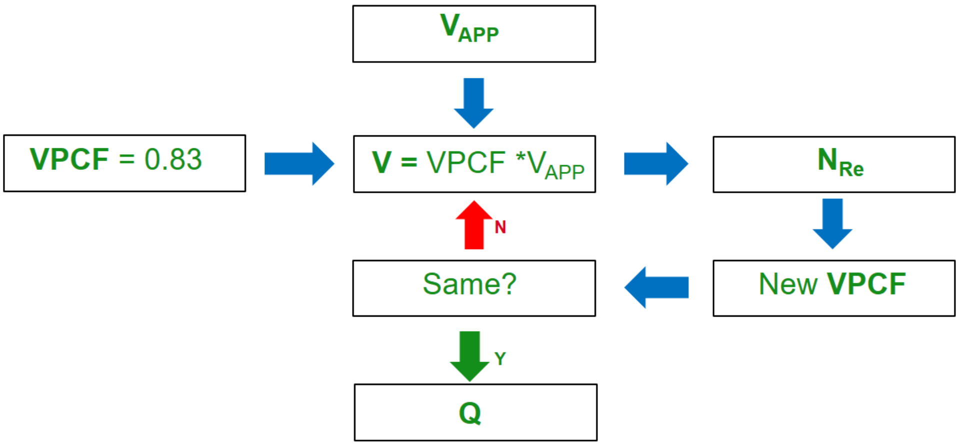

Fig. 3.B.22 – Single phase interpretation workflow

Note that for computing the fluid velocity, v_m, it is necessary to provide the density and viscosity of the fluid mixture. This is done by defining a black-oil PVT model, that is initialized based on the pressure and temperature measurements included in the PL toolstring.

FAQ 1: What is the minimum rate a spinner can detect?

When designing a PL acquisition, we need to have an idea of the minimum detectable rates to set the expectation bar. This is critical for low rate wells or when we want to detect a very small inflow (or leak).

Rate (in B/D) can be calculated based on the apparent velocity (in ft/min), VPCF, and pipe ID (in inches) using the following formula:

$$Q = 1.4 * V_{app} * VPCF * ID^2$$

Tables of fluid velocity (v_m) for different rates and pipes sizes are available. Some values for the 7 in casing are presented below:

Nominal OD (in)	**Weight (lb/ft)**	**v_m (ft/min) for 1000 B/D**	**v_m (ft/min) for 100 m/D**
7″	17	16.7	10.5
	23	17.6	11.1
	29	18.7	11.8
	35	19.8	12.4

For spinner data recorded in passes, as long as the relative velocity is above the threshold, then this velocity does not affect the resolution of the spinner. The logging program typically includes cable speeds larger than the threshold, which will lead to acceptable relative velocities.

If we record a pass in a 7'' 35 lb/ft casing, a 1000 B/D localized fluid entry will increase the velocity of the stream by 19.8 ft/min. Whatever the velocity below the inflow, the total velocity above will be 19.8 ft/min larger (assuming no recirculation). Therefore, the RPS of all the passes, regardless of the cable speed, will be shifted to larger values. The delta RPS will be based on the sensitivity of the spinner, which is characterized by its slope. Using the nominal slope of the fullbore spinner in liquid, the delta RPS for 1000 B/D is:

$$\Delta RPS = 0.05\ RPS/ft/\min * 19.8\ ft/\min \approx 1\ RPS$$

All the passes will be shifted by 1 RPS to the right (more positive values). Most of the factors that we find in practical applications tend to decrease the sensitivity (bearing friction, 'real' downhole fluids, recirculation). So this calculation is conservative.

The spinner RPS resolution informed by various manufacturers is around 0.1 RPS. This allows us to conclude that for the 7 in casing, 100 B/D is the rate resolution, as any entry smaller than this would lead to a lower delta RPS than the resolution. In practice, one should also look at the fluctuations or noise to signal ratio of the spinner measurement. Effects like a yo-yo or severe stick and slip can easily generate RPS variations larger than 0.1 RPS.

The previous analysis applies to data recorded in passes. For stationary data, the relative velocity is entirely given by the fluid velocity. Therefore, if this is lower than the threshold velocity of the spinner, there will be no rotation.

3.B.6 Special spinner behaviors

This section presents a number of 'common anomalies'.

3.B.6.a Yo-yo effect

When starting up passes, especially for fast cable speeds, yo-yo effects may be seen along the log. The cable, which is an elastic material with certain Young modulus (E), does not get in tension instantaneously from top to bottom. The toolstring will start to bounce, following an oscillating movement, which tends to be larger at the bottom of the log (beginning of the up passes). This can be seen in the spinners and other tools, like density measurements. The yo-yo effect is reduced when the well is flowing.

The average filter may be applied to reduce the amplitude of the oscillations. It is a good practice to log a section of the sump to avoid the worst part of the yo-yo effect right in front of the deepest perforation. However, accessing the sump is not always feasible.

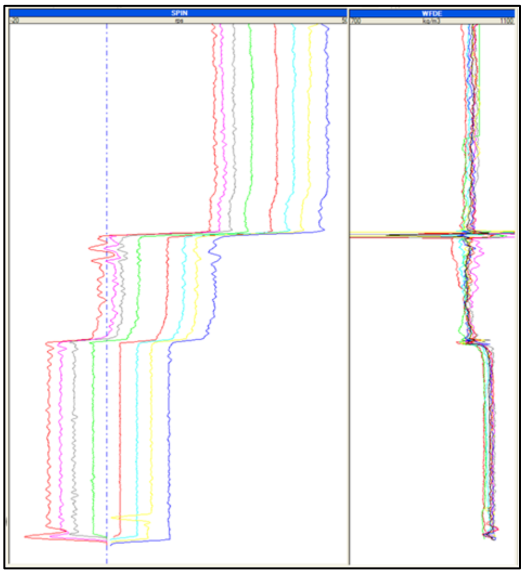

Fig. 3.B.23 – Yo-yo effect

3.B.6.b Stick and slip effect

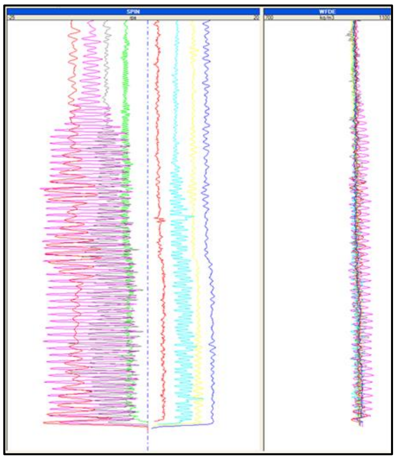

Similarly, oscillations may appear on the flowmeter due to the cable sticking/slipping along the length of the completion. Even though at surface there is a continuous cable speed spooling/unspooling speed, downhole the cable and toolstring may be moving only after enough tension builts-in to overcome the friction. The oscillation effect is more common in deviated wells, where the friction forces are larger.

These oscillations can be edited out with sliding window averaging.

Fig. 3.B.24 – Stick and slip effect

3.B.6.c Unsigned spinner

In the past, spinners from different providers were unsigned, meaning that the RPS was only positive. In most modern tools, this problem has been solved, however, the analyst may face some legacy PL datasets with this issue.

As shown in Figure 3.B.25 for an injector, the spinner on the left is signed, while the one on the right only shows positive RPS. Emeraude includes a 'Spinner reversal' option, which will change the sign of the RPS at specific depths, indicated by the analyst.

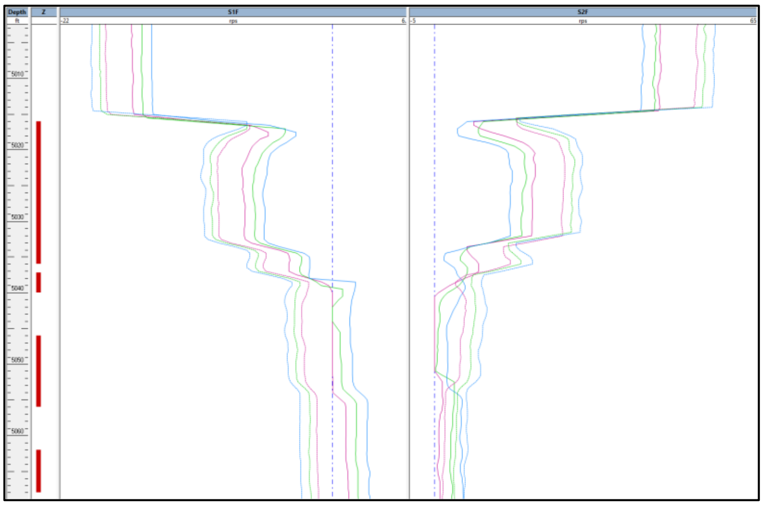

Fig. 3.B.25 – Signed (left) and unsigned (right) spinner RPS

3.B.6.d Overlapping intercepts

Overlapping intercepts can often be found in deviated wells with multiphase flow, where the light phase is flowing faster on the high side of the hole. During logging, the spinner trajectory can be in the oil when logging down, and the slower water when logging up.

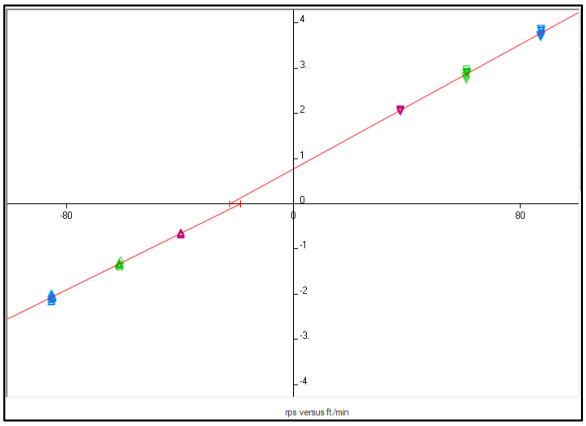

Fig. 3.B.26 – Overlapping intercepts

As will be explained in Chapter 6, if this behavior is present, it may be implying that distributed spinner measurements (MPT tools) are required. In this case, a reasonable solution would be to average the positive and negative slopes to compute the apparent velocity.

3.C Doppler flowmeters

The Doppler effect has been widely used for surface flowmetering for, at least, a couple of decades. However, only recently have the Doppler transducers have been used for downhole applications as a potential replacement of conventional flowmeters. The Doppler effect is the change in frequency of a wave in relation to an observer, moving with respect to the wave source. The observed frequency (f) will be shifted compared to the emitted frequency (f_0), based on the relative velocities of sound in the medium (c), the source (v_s), and receiver (v_r):

$$f = \left(\frac{c \pm v_r}{c \pm v_s}\right) f_0$$

The plus and minus signs depend on whether the source and receiver are moving together or apart. For the latter, the observed frequency decreases, as perceived when an ambulance moves further away, or the redshift effect, which helped to conclude that the universe is expanding.

For flowmetering applications, an ultrasonic wave is used. OpenField's FAST tool incorporates ultrasonic transducers for Doppler effect-based flow metering. The miniature transducers can be integrated into the tool body or within the tip of a 1/16'' Inconel tube. These two configurations are shown in Figure 3.C.1. The measurements are oriented through relative bearing measurements:

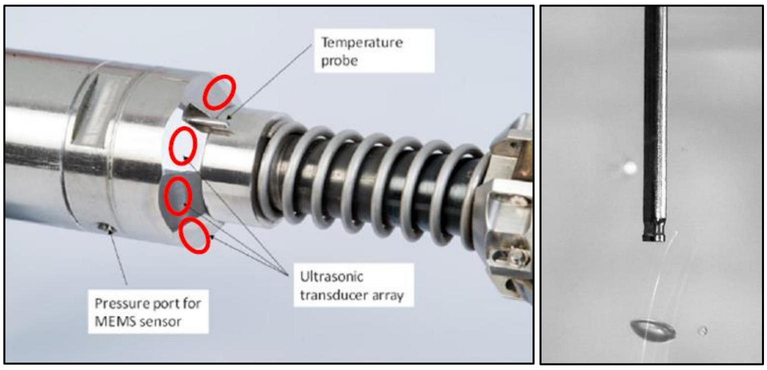

Fig. 3.C.1 – FAST Doppler in tool body (left) and as a probe (right) (Courtesy: OpenField)

A 10-MHz ultrasonic wave is emitted through the fluid and scattered back from heterogeneities such as bubbles, droplets, or solid particles carried by the flow. The Doppler sensor performs real-time FFT computations, first to convert time-domain signals into frequency-domain spectra, then to analyze these spectra. The spectrum of reflected energy as a function of Doppler shift provides qualitative information on the flow pattern and quantitative information on flow velocity. At a certain depth, the spectrum looks like Figure 3.C.2. Versus depth, this becomes a 3D array.

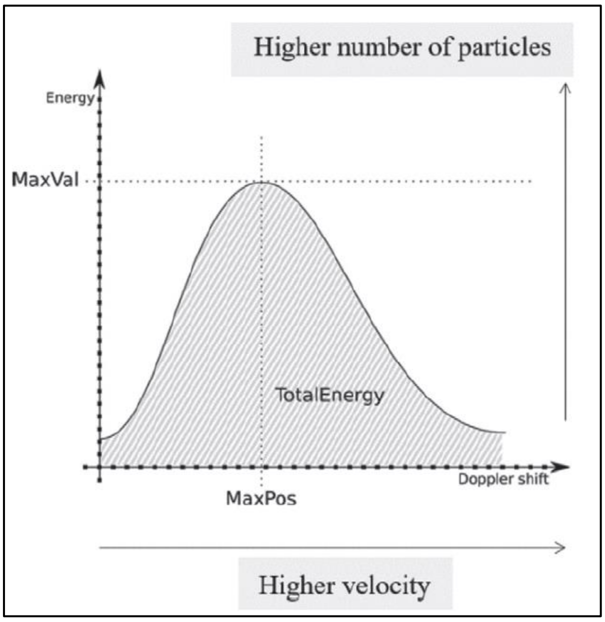

Fig. 3.C.2 – Doppler Spectrum. (Courtesy: OpenField)

Primarily, the frequency shift increases with the speed of the moving structure. In addition, a majority of structures in the flow will have speeds close to the flow velocity, involving a higher reflected energy. A flow-speed distribution presents a typical Gaussian-shaped spectrum, as shown in the figure, centred on the main velocity, or the speed the highest number of moving targets have in common.

Apart from including part of the spectrum array, a number of extractions are made. This data includes the total spectrum energy (CE), maximum value of the peak energy (MaxVal), and Doppler shift of the maximum peak (MaxPos). From these three data points, the overall spectrum shape can be reconstructed.

The image below shows the CE and MaxVal in the first track, the MaxPos in the second, a mini spinner and bubble count (more on this in Chapter 4):

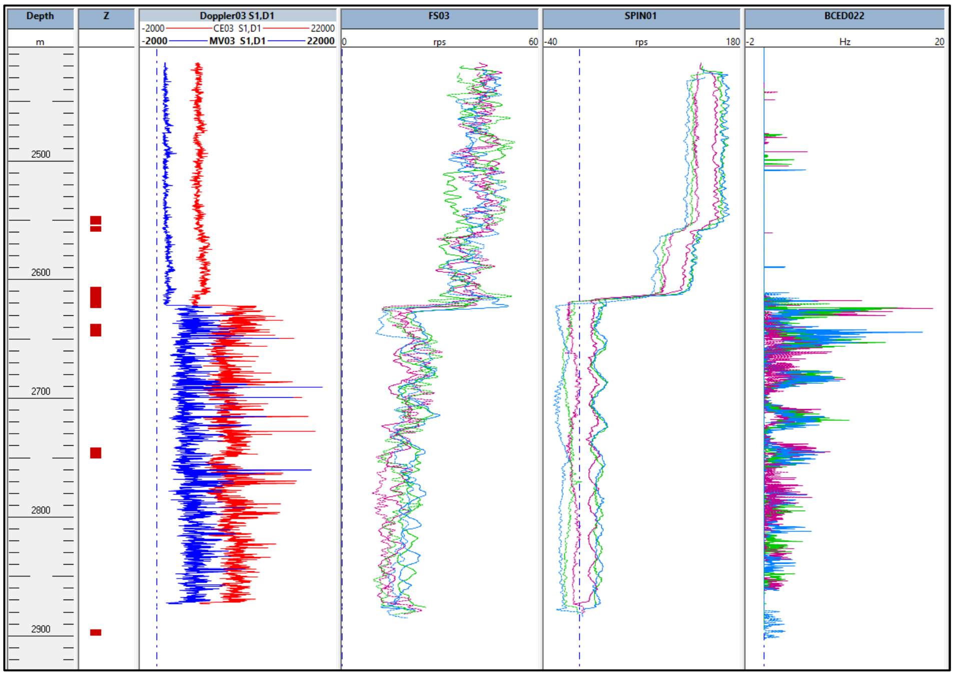

Fig. 3.C.3 – Doppler energy extractions

The MaxPos resembles the flowmeter, indicating the depths of fluid inflow. Looking at the total energy and the bubble count, it is possible to cross-plot these as shown in Figure 3.C.4. at the bottom of the log (purple points), the energy and the bubble counts are larger. On the other side, at the top of the log (red points), even though the total rate is higher as given by the spinner, both the energy and bubble counts are low. This occurs because, in the upper part of the log, the flow is much more homogenous, there are fewer interfaces, and therefore the total energy of the Doppler is smaller.

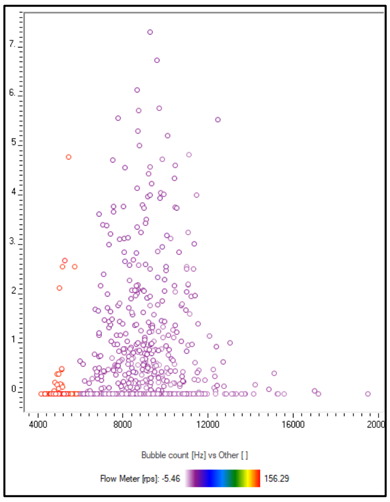

Fig. 3.C.4 – CE vs Bubble count

At the time of writing (2021), the methodology to go from the different frequency extractions to fluid velocity is still under development since these are a function of the flow direction, flow regime, cable speed, etc. Doppler flowmeters are currently used qualitatively.

3.D Single Phase Flow Profiling

A typical toolstring that can quantify a single-phase flow profile is shown below. As discussed previously, the main component is the flowmeter spinner, and a back-up (in-line) is typically added should the main spinner fail. In this case, the main spinner is a continuous one, but it could be a fullbore. Pressure and temperature are required to compute the PVT properties, and like any other cased hole logging operation, GR/CCL are added for depth control. Centralizers are included, and as shown in this chapter, these are not only for facilitating tool deployment but also because it is assumed the spinners are centered when computing the VPCF.

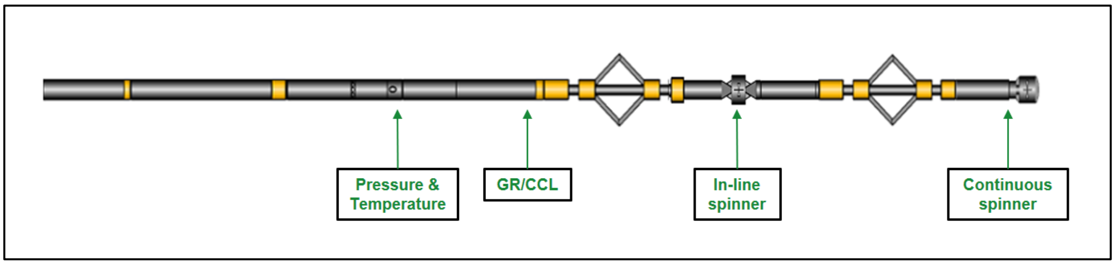

Fig. 3.D.1 – Typical toolstring for single-phase flow

After calibrating the spinner and obtaining the apparent fluid velocity, the single-phase interpretation process in nearly completed. The flow profile is a continuous rate (Q) log that can be obtained as:

$$Q = v_m * A = v_{app} * VPCF * A$$

As shown in Figure 3.B.22, the VPCF is calculated as part of an iterative loop. In modern software, this has been replaced by a regression algorithm. The single-phase calculation is only a specific case of what is calculated for more complicated processes such as multiphase rate calculations and processing multiple probe tools.

The principle of the non-linear regression process is to take as unknowns the results we wish to get, in this case, the single-phase downhole rate Q. The target will generally be the observed tool measurement. In the case of a single-phase calculation, the target is the apparent velocity calculated after the spinner calibration.

From any value of Q in the regression process, the velocity is calculated, hence the Reynolds number, hence the VPCF, hence a simulated apparent velocity.

This allows the creation of a function VAPP = f(Q). Next solve for Q by minimizing the standard deviation between the simulated apparent velocity and the measured apparent velocity.

$$Q \rightarrow v \rightarrow N_{\mathrm{Re}} \rightarrow VPCF \rightarrow V_{APP}$$

$$Simulated\ Apparent\ Velocity: \quad V_{APP} = f(Q)$$

$$Measured\ Apparent\ Velocity: \quad V_{APP}^{*}$$

$$Minimize\ Error\ Function: \quad Err = \left(V_{APP} - V_{APP}^{*}\right)^2$$

Rate calculations may be performed on each depth frame or averaged in calculation zones of interest. Such calculation zones could be the calibration zones, or the top of each perforation zone. But in most cases the engineer will define where the rate calculations are most relevant.

3.D.1 Producing Wells

Figure 3.D.2 shows a gas production profile based on continuous spinner flowmeter (CFSR track) data. The toolstring contained an in-line spinner (ILSR track). It is clear that the continuous spinner shows more repeatable data between passes, and the sensitivity is higher than the ILSR, as can be seen by the maximum RPS reached. When more than one spinner is present, in general we will calibrate and obtain the apparent velocity using only the one with the best data quality. However, nothing impedes the analyst to use both spinners.

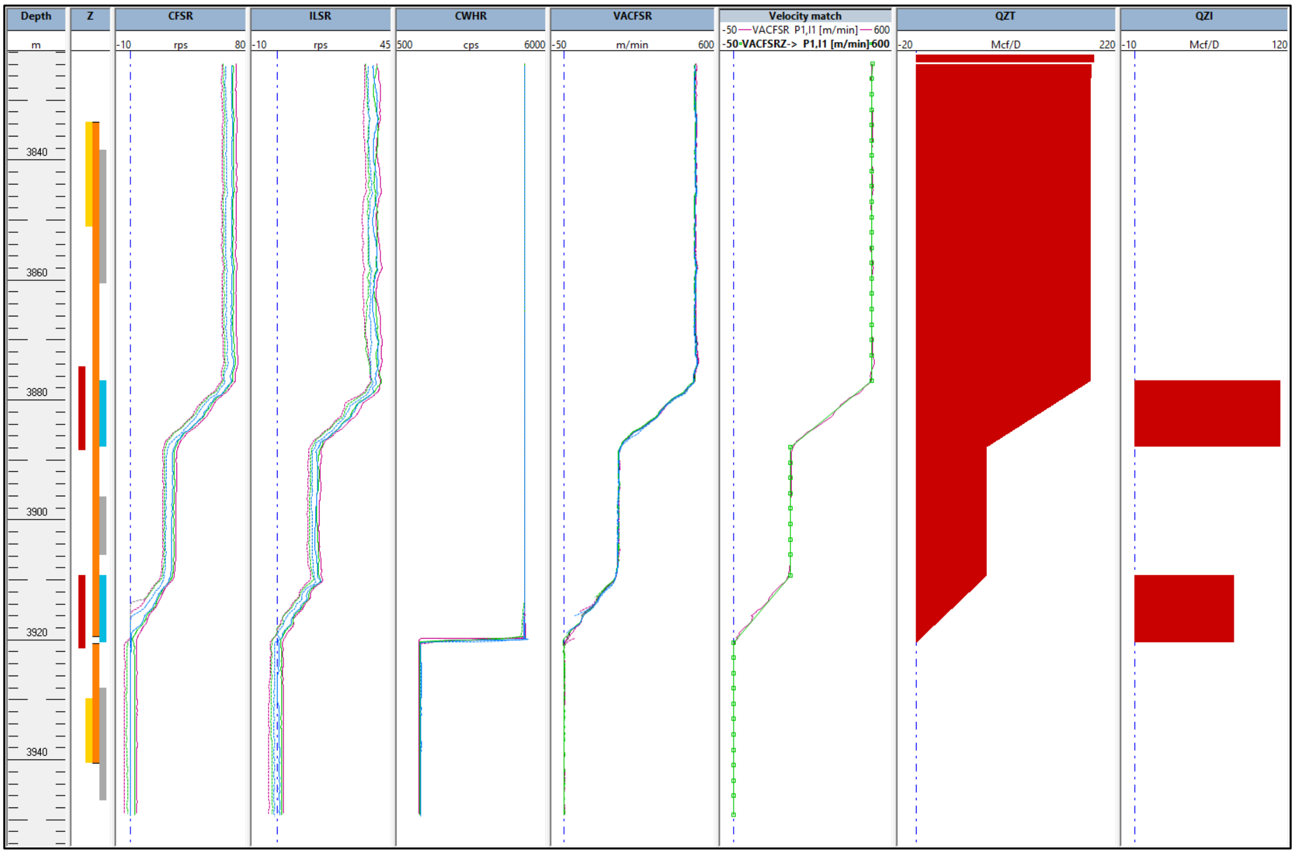

Fig. 3.D.2 – Typical toolstring for single-phase flow

The capacitance tool (Chapter 4) shown in the CWHR track, suggests water in the sump (the interval below the bottom perforation). Above this, single-phase gas is present. The capacitance measurement was used as a guide to set the spinner calibration application zones. As previously mentioned, capacitance or other fluid identification tools are not mandatory in single-phase wells, but they are useful to understand fluid distribution. The next chapter will show how the pressure measurement can be used for similar purposes.

After calibrating the continuous spinner, the apparent velocity for each pass was generated and displayed in track VACFSR. The fact that all 6 apparent velocities (one for each pass) are overlapping is an indication of good spinner calibration and stable well conditions.

3.D.1.a Zones

Apart from the calibration (yellow) and application (orange) zones, the Z track shows two more important zones:

- Rate calculation zones (gray): These are set by the analyst, above and below each inflow/outflow (perforation/SSD/ICD, etc.) interval. The non-linear regression described previously was executed on all intervals to get the zonal rate.

- Inflow zones (blue): Between two rate calculation zones, Emeraude will create an inflow zone. If this interval contains a perforation, by default, the length of the inflow zone will be set equal to the perforation. However, inflow zones can be distinct from the perforations (red) to capture the fact that not all perforation intervals may be producing or taking fluid.

3.D.1.b Results

After running the nonlinear regression in each rate calculation zone, the resulting rates are extended up to the inflow zone above and down to the inflow zone below. The results are summarized by the QZT track. The only place where the rates can change is in the inflow zones (not the perforations). It is assumed that the inflow zone produces in a homogenous way, as the rates at the top and bottom of the inflow zone are connected by a straight line.

The QZI track represents contributions or injections which are obtained by the difference of the rate above and below an inflow. The simplest way to calculate the contributions per layer would be by direct subtraction of the rates calculated in the rate calculation zones above and below the inflow. However, and especially in gas wells with large distances between zones, the rate change is in part given by the fluid expansion with changes in pressure and temperature. Therefore, a material balance is applied to obtain the contributions:

$$q_i = \left(q_{top} - q_{bot}\right) * \frac{\rho_{bot}}{\rho_{top}}$$

The nonlinear regression is computed in each rate calculation zone independent of the zones above or below. As a result, these rates may entail contributions of a sign or amplitude that is not physically justified. This is particularly problematic in multiphase scenarios, where there may be an inflow zone producing one phase and injecting another, which is not physically possible. Potential inconsistencies in a global regression process will be addressed in Chapter 5.

The Velocity match track shows the target V_{APP} (red) and the simulated equivalent (green). When these two overlap, it indicates the error of the simulation is low everywhere, even though the regression is only in the calculation zones (using the zoned method). This is generally the case in single-phase, provided that the inflow zones reflect the intervals where the rates vary. Note that in Emeraude it was arbitrarily decided to take the apparent velocity as the target function, rather than the real tool response in RPS. The alternative was to integrate the spinner calibration in the regression process and match the RPS measurements for the different selected passes.

The simulated (green) apparent velocity and the QZT logs are referred to as schematics in Emeraude.

3.D.1.c Matching surface conditions

As PL measurements are recorded at bottomhole pressure and temperature, the QZT and QZI are obtained at these conditions. However, it is common to compare the PL total cumulative rate (above the upper perforation) with the reported surface rates.

Converting downhole rates to surface conditions requires the knowledge of the fluids' PVT. As the fluid travels up in the pipe, it will:

- Expand/shrink as given by the formation volume factor (B_i):

  $$q_{surf} = \frac{q_{surf}}{B_i}$$

  The formation volume factor of gas is smaller than 1 (typically 0.003 to 0.01 rcf/scf), and expands towards the surface. For water, it is around 1, as there is little change in volume. Oil, on the contrary, shrinks as it travels up the pipe, with typical formation volume factors of 1 to 2.4 RB/STB
- Change phase: Part of the downhole oil volume is occupied by gas in solution, which will come out as it is produced. This is given by the Solution gas-oil ratio, R_s. Even the water can have gas in solution, so it has an associated R_{sw}. In the case of wet gas or retrograde gas condensate, part of the downhole gas will turn into oil.

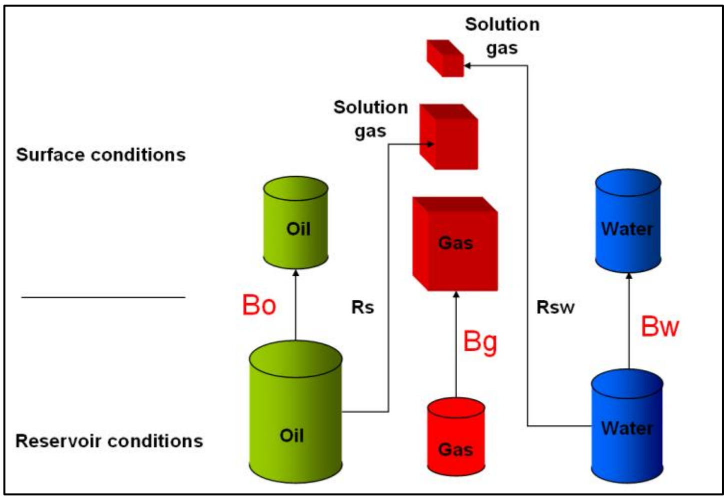

Fig. 3.D.3 – Downhole to surface rates conversion

An inaccurate PVT description will result in discrepancies with the surface rates. Note that the surface test separator uses formation volume factors, as its pressure and temperature are not standard conditions, but the rates are reported as standard.

The quality of the surface rate measurements will affect the agreement, as the various techniques (multiphase meters, separators, etc.) also have certain assumptions and limitations. Which surface rates are used is important, as it is not equivalent to use a daily average or the rates recorded exactly during the PLT acquisitions.

The analyst is free to force a match between the PL interpretation and the surface rates. In single-phase, a multiplier on the VPCF is applied. In multiphase, a multiplier on the slippage velocities is applied to modify the proportions of the different fluids.

Before forcing a surface match, it is worth reviewing the quality of all the different factors that may lead to a discrepancy between the surface and PL rates: quality of the surface measurements, selection of the multiphase correlations, PVT description, spinner calibration, etc. Blindly forcing a surface match does not improve the validity of the interpretation.

3.D.1.d Cross-flow

The profile presented in the image below shows the upper layer is producing gas, and the bottom layer is injecting, acting as a thief zone. This is called cross-flow and occurs due to layer pressure unbalance. Although it is more common to detect cross-flow with the well shut-in, it can also be observed when the well is flowing, especially for large layer pressure differences.

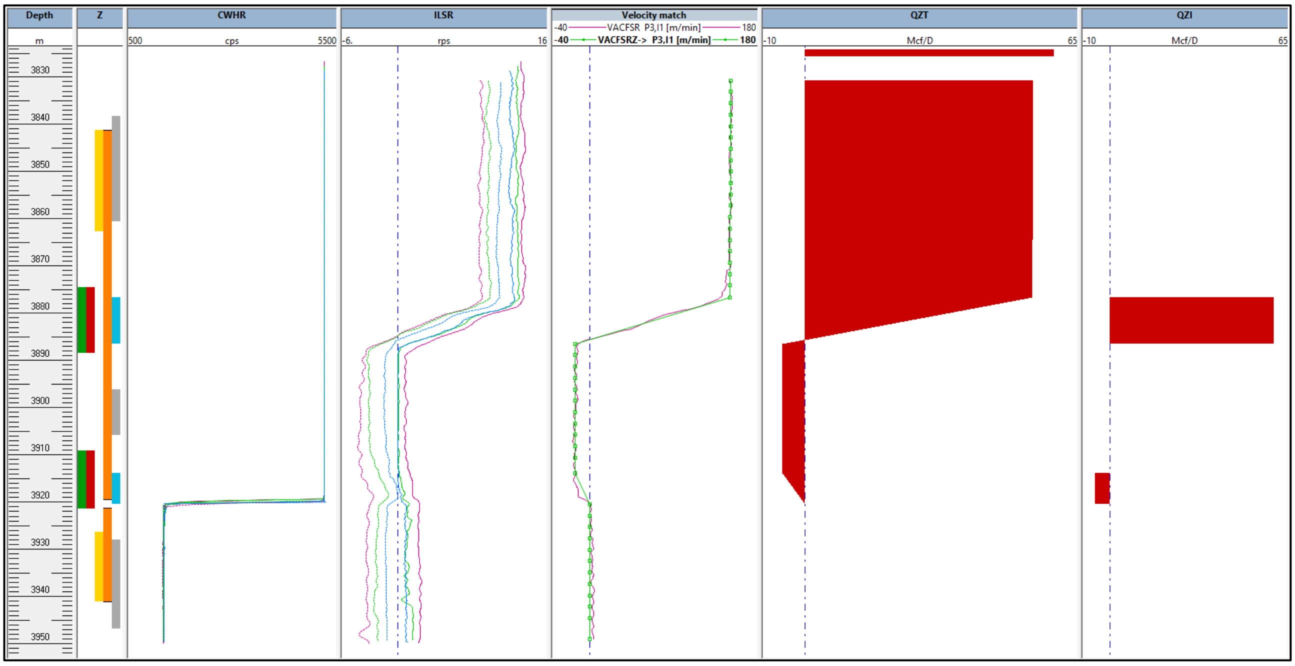

Fig. 3.D.4 – Cross-flow during production

3.D.2 Injecting Wells

All the points explained previously for producers apply to injectors. In terms of spinner calibration, in general, one zone would be enough since there should not be variations in fluid properties, and the parameters should remain constant. The typical place to calibrate is in the sump, where both thresholds and slopes can be obtained. However, as the sump may be filled with a different fluid than the injected water, it is a good idea to set another calibration zone to verify if the calibration properties remain unchanged.

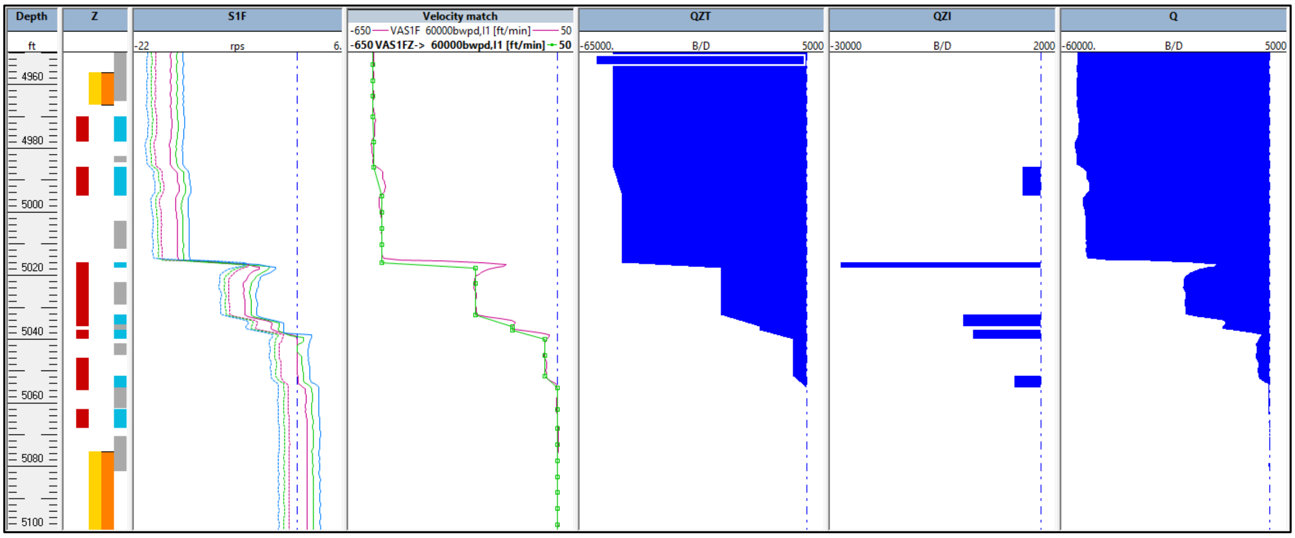

Fig. 3.D.5 – Typical log presentation for a water injector

PL in injectors is also known as 'ILT'. The toolstring, is similar to the one shown in 3.D.1, and fluid identification tools are not required. Fullbore spinners are not used, as the blades can close by the water pressure from above. By convention, the injection profile is expressed as negative rates. During shut-in, there can be cross-flow, with one or more layers producing water. Multi-rate injection PL is helpful to evaluate the injectivity and layer pressures of the different intervals.

Note that in Figure 3.D.5, the third perforation from the top does not inject homogenously. Setting the inflow zone size the same as the perforation would result in a bad match between the simulated and measured data. It is necessary to realize and quantify that only a small percentage of the perforation is working.

A common approach is to discretize the perforation using multiple inflow zones. In this case, two inflow zones are set at the top and bottom of the perforation, and the rates are only allowed to change in those intervals.

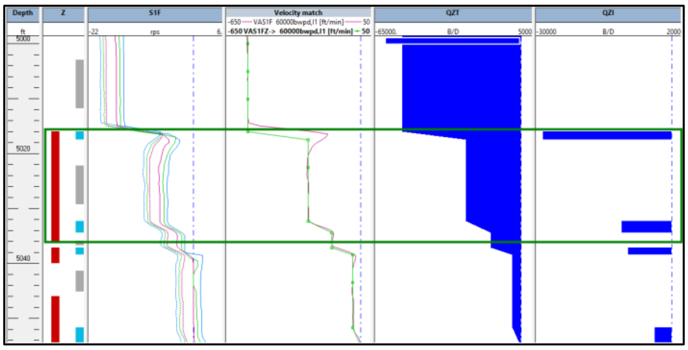

Fig. 3.D.6 – Perforations discretization

The last rate track of Figure 3.D.5, noted Q, represents the application of the nonlinear regression at every depth, with the goal to obtain a continuous log everywhere faithful to the log data. Having this log provides a guide to refining the position of calculation and inflow zones.

4 – Fluid Identification Tools

4.A Introduction

Chapter 3 covered flowmeters and how to obtain a single-phase production profile. The total rate can be calculated from the mixture velocity as:

$$q_t = v_m A$$

In single-phase environments, spinner measurements may deliver flow rates. However, when several phases flow simultaneously, the problem becomes under-defined, and additional measurements are needed to differentiate possible solutions. For generic two-phase flow, the light and heavy phase rates at any depth are given by:

$$q_l = v_l A Y_l$$

$$q_h = v_h A Y_h$$

Where v_l and v_h are the light and heavy phase velocities, which are not directly measured by the spinner. This will be the subject of Chapter 5. Y_l and Y_h are the light and heavy phase holdups, and their measurements will be covered in this Chapter.

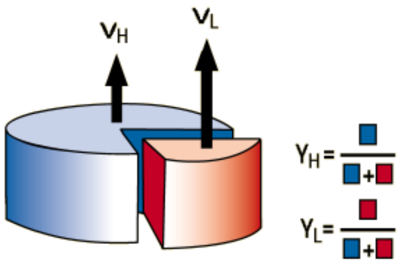

Fig. 4.A.1 – Definition of holdup

The holdup of a phase at any given depth is the volume fraction occupied by that phase. Figure 4.A.1 shows a heavy (blue) and light (red) phase and indicates the corresponding holdups.

By definition, holdups add up to 1.

The holdups can be measured in two ways:

- Derived from density measurements, presented in Section 4.B.
- Direct measurements based on a physical property of the fluids (resistivity, refractive index, dielectric constant), presented in Sections 4C to 4F.

For a two-phase interpretation, at least one fluid identification tool is required to divide the total rate into light and heavy phases. For three-phase flow, an additional independent fluid identification tool is needed. If there are more tools than necessary, all measurements can not be matched exactly at the same time due to the nature of the calculations. More on this later.

Fluid identification tools are run as part of the PL toolstring for multiphase flow profiling. They prove helpful in leak detection jobs, especially if the leaking fluid is different from the one coming from the perforations.

4.B Density tools

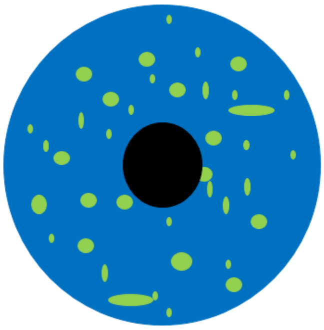

Fig. 4.B.1 – Centerline tool in well mixed fluid

Under certain assumptions, holdups will be derived from density tools. For example, for a two-phase flow, the cross-sectional mixture density at any depth is given by:

$$\rho_m = Y_l\,\rho_l + Y_h\,\rho_h$$

From this, the heavy phase holdup can be calculated as:

$$Y_h = \frac{\rho_m - \rho_l}{\rho_h - \rho_l}$$

The main assumption is that the flow is well mixed, and a single point measurement provides a good average mixture density, regardless of the tool centralization. The validity of the measurements is largely dictated by the flow regime. Moreover, the accuracy of the holdup estimation depends on the knowledge of the in-situ light and heavy phase densities. Therefore, a strong understanding of the PVT system is required. These factors will be analyzed in Section 4.B.5.

There are four main tools that may give a fluid density: gradiomanometers, nuclear density tools, tuning fork density tools (TFD), and pressure gauges after differentiation.

4.B.1 Gradiomanometers

The tools measure the pressure difference between either side of a strain gauge differential pressure transducer (P_2-P_1). This diaphragm is connected with the well fluids through silicon oil-filled tubes. Since the distance between the pressure transducer and the tube ports in contact with the well fluid is known, the total pressure drop between ports (P_B-P_A) can be calculated. This is composed of the hydrostatic (containing the well fluid density) and friction and acceleration pressure drops. The measurement has to be corrected for deviation, as the true vertical distance between the ports is equal to *h* only for 0° deviation. The generic equation to calculate the well fluid density is:

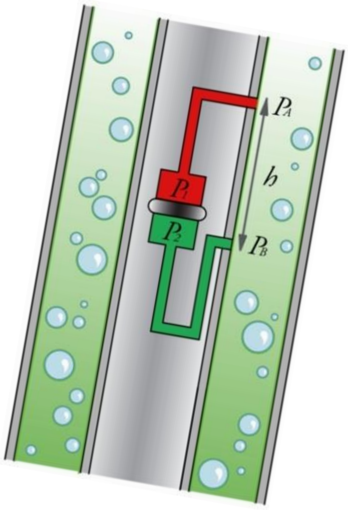

Fig. 4.B.2 – Gradiomanometer

$$\rho_{fluid} = \frac{[P_2 - P_1] - \Delta p_{fric} - \Delta p_{acc}}{gh\cos(\theta)} + \rho_{so}$$

The density of the silicon oil is a polynomial function of the pressure and temperature, and this is generally accounted for by the acquisition system.

One of the limitations of the gradiomanometer density tool is the maximum well deviation. At 90° deviation, the hydrostatic pressure drop is zero, and therefore the tool cannot be used in horizontal wells. However, due to accuracy and resolution (0.02 g/cm^3 and 0.002 g/cm^{3,} respectively, for the Schlumberger tool), the maximum deviation is around 65°. As the deviation increases, the contrast between maximum and minimum measured density decreases, and at a certain point, the delta is in the order of the tool resolution.

Note that different service providers output the mixture density corrected and uncorrected for deviation. If the analyst decides to use the uncorrected density as an input for the interpretation, a well deviation survey or an accelerometer is required for correcting the measurement.

For a given surface, the friction gradient is a function of the friction factor (*f*) the density, the relative velocity, the friction surface, and the flow area, related by:

$$\left[\frac{dP}{dZ}\right]_{friction} = \frac{f\rho V^2}{8} \times \frac{S}{A}$$

The friction factor is estimated from the Moody diagram as a function of the Reynolds Number and the pipe roughness. In general, the absolute roughness of steel (0.0018 in) is used as a first approximation. However, if the pipe has scale deposition, it will be necessary to increase the roughness to predict a more accurate density. This may be an unknown, and the analyst may use the surface rate split as a reference.

Generally, the friction is split into tool friction and pipe friction:

$$\left[\frac{dP}{dZ}\right]_{friction} = \left[\frac{dP}{dZ}\right]_{pipe} + \left[\frac{dP}{dZ}\right]_{tool} = \frac{f_p \rho V^2}{2} \times \frac{D}{(D^2 - d^2)} + \frac{f_t \rho V_t^2}{2} \times \frac{d}{(D^2 - d^2)}$$

Although the tool outputs a mixture density measurement, this is not the final corrected density used in multiphase calculations. As the friction correction is a function of the fluid velocity and mixture density itself, which are unknown, the corrected density is calculated as part of an error minimization process and only available at the end of the interpretation.

The second limitation is due to the frictional pressure drop. If it is in the order of the hydrostatic pressure drop, then the density calculation will be severely influenced by the roughness input. Some authors suggest a maximum fluid velocity of 4 m/s, above which the gradiomanometer density does not provide usable data due to friction.

The acceleration term is typically ignored, apart from single-phase gas or mist flow, which are calculated through multiphase flow correlations.

A final limitation that affects the operation is that the differential pressure transducer may burst when exposed to ΔP larger than 100 psi which should be considered when running in hole and passing through the wing valve.

4.B.2 Nuclear density tools

The tool principle is the transmission of Gamma rays through matter. The main interaction types are photoelectric absorption and Compton scattering, associated with the electron density (ρe). This is related to the bulk density (ρb) by:

$$\rho_e = 2\,\frac{Z}{A}\,\rho_b$$

For most elements, Z/A is about 0.5, but for hydrogen, this ratio is 1.

The Gamma rays are generated by a chemical source, typically Americium 241, due to its high count rate and low penetration. This is located on one side of the chamber with well fluid access shown in Figure 4.B.3. On the other side, there is a Gamma ray detector, including photomultiplier and electronics (see Section 2.D.2). The Gamma rays reaching the detectors are attenuated as a function of the electronic density of the fluid, which is in turn related to the volumetric density through a calibration chart.

Fig. 4.B.3 – Nuclear density tool (Courtesy: Sondex)

The measurements in the sump may lead to confusing readings, as the fluid may be the completion mud with an altered electron density. This should be considered when looking at the density end point for constraining the PVT.

The tool does not require deviation or friction corrections. However, for segregated or stratified flows, typical of high deviations, the fluid filling the chamber may not be representative of the cross-sectional fluid mixture at that depth. The existence of a radioactive source is a limitation for some companies, who prefer not to run this type of tool due to the risk of losing it during the job.

4.B.3 Tuning Forks

A steel tuning fork vibrates at its natural (or resonant) frequency, driven by the tool electronic section. The mixture fluid inside the chamber and its temperature affect the vibration frequency. The frequency output of the tool is converted to a mixture fluid density through a master calibration chart, which is a function of the temperature and has a weaker dependency on the pressure. This output is converted into the acquisition system.

As for nuclear density tools, there is no need to correct for friction and deviation.

Fig. 4.B.4 – Fluid Density Inertial (Courtesy: Sondex)

4.B.4 Pressure Gauges and Pseudo-density

Even though pressure gauges are presented in this Chapter dedicated to fluid identification, this measurement type is also used for other applications, especially in PL operations:

- Pressure is required for PVT calculations: Together with temperature, they are used to calculate the PVT properties at downhole conditions
- It can be used as an indication of the production stability: A constant or slow varying pressure during a stationary recording or overlapping pressure readings across multiple passes are indications of a stable well
- Pressure gradient: Both through gradient stops or continuous passes, pressure measurements are used to calibrate Vertical Lift Performance (VLP) curves
- Selective Inflow Performance: Provides the pressure for the layered IPR technique
- Pressure Tests: A Build-up or Fall-off may be recorded with the PL toolsting in the well
- Pseudo-density: When differentiated, it provides a differential pressure measurement

Pressure gauges are divided into Strain or Quartz gauges. With Strain gauges, the mechanical distortion caused by the applied pressure is the primary measuring principle. There are several sensor types based on Bourdon tubes, thin-film resistors, sapphire crystals, etc.

In Quartz gauges, the fluid enters through the 'Pressure inlet' shown in Figure 4.B.5. The fluid acts on the bellows filled with silicon oil, avoiding corrosive fluids access to the main measurement section. A quartz sensor oscillates at its resonate frequency, which is a function of the pressure and temperature. A 'Temperature crystal' is isolated from the well pressure, but as it is thermally coupled, it is used to compensate. The Quartz gauge requires calibration (pressure as a function of the frequency and temperature), which is typically provided by the quartz manufacturer, and accounted for by the acquisition system. This may need recalibration over time.

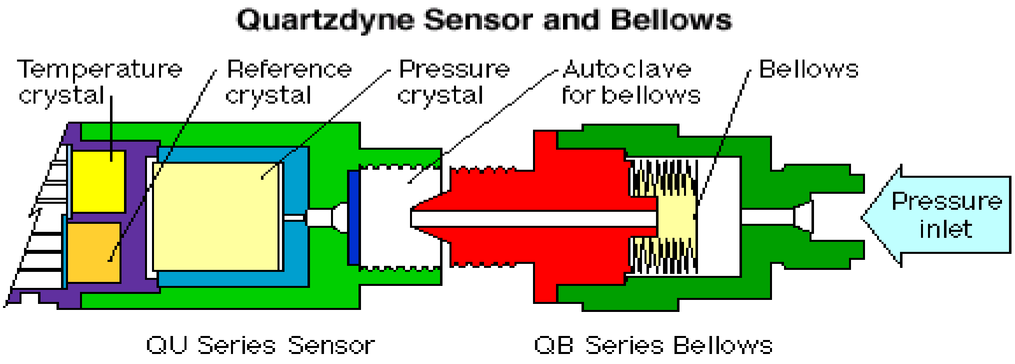

Fig. 4.B.5 – Quartz sensor example (Courtesy: Quartzdyne)

The pressure derivative, also called 'pseudo-density', gives an instantaneous picture of the fluid density. The pressure gradient in a flowing well is a function of the hydrostatic, frictional, and acceleration components, as discussed in Section 4.B.1. Therefore, the pseudo-density needs to be corrected for these components as part of the error minimization process. As the derivative is created with respect to measured depth in deviated wells, it is necessary to enter the deviation survey to account for real vertical depth variations.

The first track of Figure 4.B.6 shows the pressure for 8 passes. The first up and down passes are in red, and the last in yellow. Pressure drops during the acquisition, meaning that the well is not fully stable. Depending on the deliverability of each layer, the rates may be varying significantly. The second track shows the pressure derivative (DPDZ), which clearly shows the presence of three distinctive fluid types, but compared to the gradiomanometer measurement shown in track 3, the pseudo-density has a larger error.

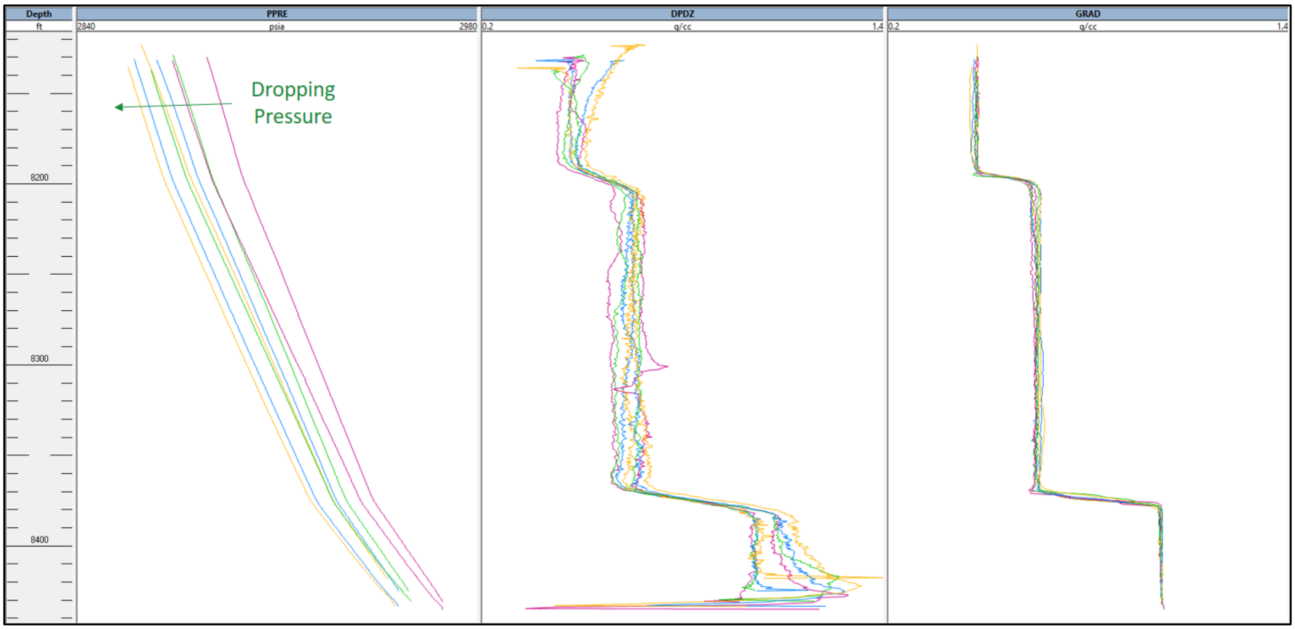

Fig. 4.B.6 – Pressure, Pseudo-density, and Gradiomanometer Density

If the well is unstable, the pressure derivative will exacerbate the pressure variations, and it will not have sufficient quality for quantitative purposes. In general, a density tool will show better quality than a pressure derivative. However, if the main fluid identification tool fails, it will be necessary to use the pseudo-density after filtering and averaging the passes.

4.B.5 Limitations and errors

The main objective of running a density tool is to obtain a representative estimate of the fluids holdup in the logged interval. Apart from the tool's metrology characteristics (mainly accuracy and resolution), the holdup will only be accurate if the proper inputs are provided to the following equation:

$$Y_h = \frac{\rho_m - \rho_l}{\rho_h - \rho_l}$$

This means:

- The light and heavy phase densities at downhole conditions are known through the PVT description
- The density tool actually provides a mixture density, ρ_m

These factors are analyzed next.

4.B.5.a Influence of PVT parameters

Figure 4.B.7 shows the sensitivity of the oil holdup calculation (second track) to the end point gas density. Mixture and oil density are kept constant, and it is assumed that no water is present above 8370 ft.

Increasing the end point gas density will be translated as a higher amount of gas and a lower oil holdup.

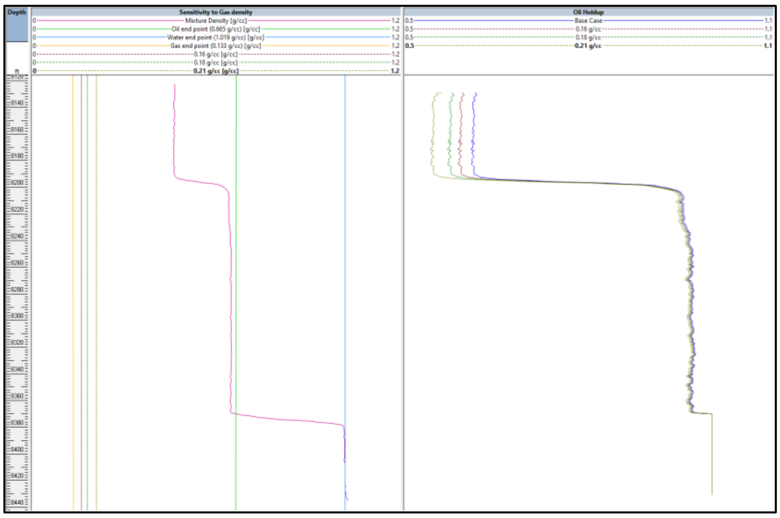

Fig. 4.B.7 – Influence of the gas density on the oil holdup

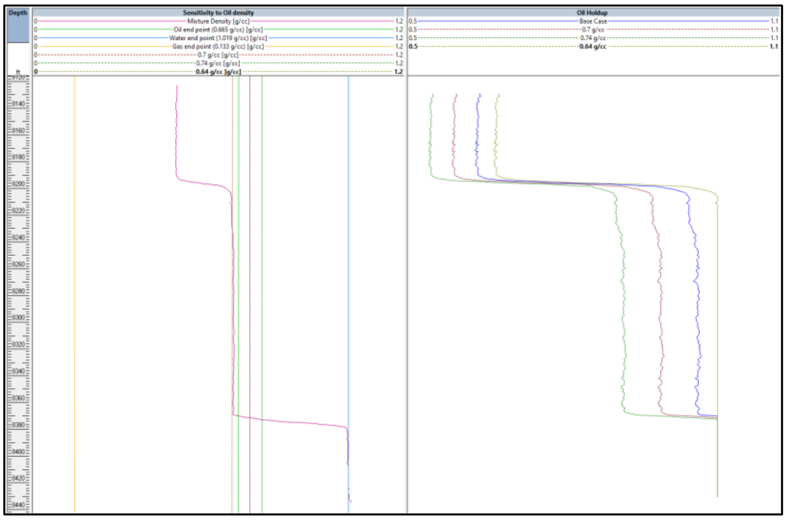

A similar analysis is shown in Figure 4.B.8, where the only variable is the oil end point density. Large variations in oil holdups are seen when the end point oil density varies from 0.64 to 0.74 g/cc. Note that, since the fluids are moving, a multiphase correlation is used to compute the holdups. The relation between the correlations and holdups will be discussed in Chapter 5.

Fig. 4.B.8 – Influence of the oil density on the oil holdup

When a shut-in survey is available, it is common practice to look for areas of segregated oil, gas, and water. The analyst can take a direct downhole density measurement, and using the pressure and temperature, constrain the black-oil PVT definition.

This analysis also shows that, as the density of both phases is similar, the dynamic range to calculate the holdup decreases. Consider the case of heavy oil at 0.95 g/cc and 1 g/cc water. The denominator of the holdup calculation will be 0.05 g/cc, in the order of the tool accuracy.

4.B.5.b Influence of the flow regime

Although some density tools, like the nuclear or tuning fork, work in horizontal wells and do not require a correction for deviation, it does not mean that they provide a representative cross-sectional fluid density. These two density tools and the Capacitance (Section 4.3) measure the fluid that enters a chamber or window in the tool housing. Only when the flow is well mixed will the density measured in a particular point of the cross-section be valid to compute the holdups.

As the deviation increases, the light phase will tend to be on the high side of the pipe cross-section due to gravity. At lower deviations and higher fluid velocities, the light phase may still be distributed (i.e., bubble flow), but as deviation increases or fluid velocity decreases, stratification will occur.

Figure 4.B.9 shows a holdup image measured by an MPT tool (Chapter 6) in track 1 and the density (nuclear) measured in an up and down pass. Without going into details on the MPT tools, a number of cross-sections are displayed on the right, showing that the flow is stratified with intermittent gas, oil, and water. In the center of the cross-section there is a circle representing the position of the density tool in the hypothetical case of a perfectly centralized tool.

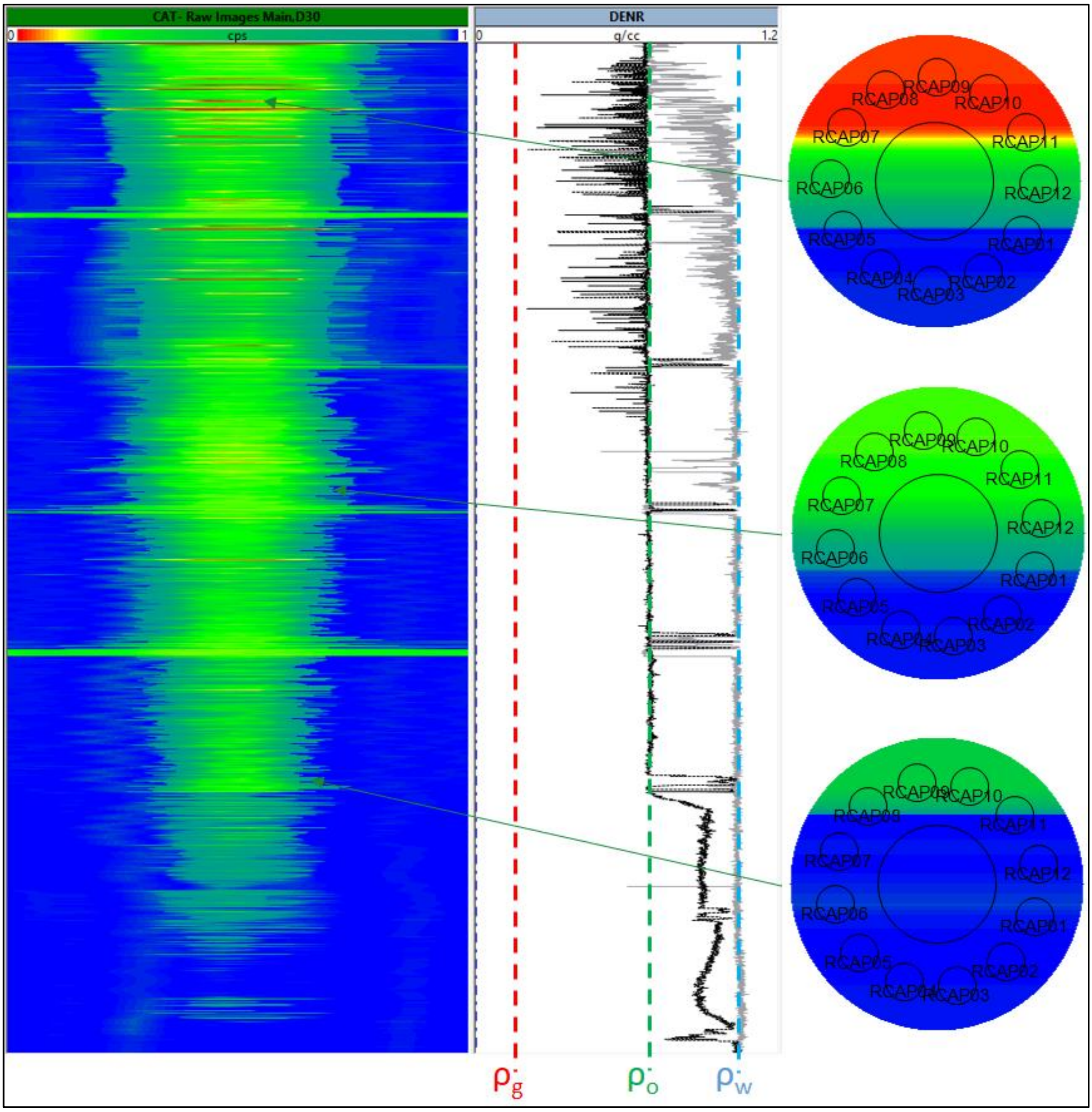

Fig. 4.B.9 – Influence of the gas density on the oil holdup

The density data shows that across the log, the tools are immersed either in oil (black pass) or water (gray pass), indicating a holdup computation using this data would result in Yo=1 or Yo=0, depending on what pass is used. However, the cross-sections reveal that in reality, there is a distribution of holdups, and discrete measurements are required. This is why MPT tools exist.

4.C Capacitance

The water holdup can be determined by measuring the electrical response of the fluid mixture. Two main properties differentiate water from hydrocarbons:

- The dielectric constant of the water is around 78 times the vacuum permittivity, while for hydrocarbons, it is between 2 and 4 (gas and oil, respectively). This is the principle of the capacitance holdup tools
- Due to the dissolved salt, water is conductive, while hydrocarbons are insulators. This is the principle of conductivity/resistivity probes.

Capacitance is a water holdup tool. The way to find the dielectric constant of a substance is to put it between the plates of a capacitor. One of the plates is the tool housing, while the other is a central rod. A resistor-capacitor (RC) circuit is created, which leads to a total impedance comprised of these two factors. The way to estimate the capacitance (imaginary part of the impedance) is to find the resonant frequency of the circuit. As a consequence, the output of the tool is a frequency measured by a free-running oscillator.

Fig. 4.C.1 – Capacitance tool (Courtesy: Weatherford)

Each tool includes a calibration chart, which relates the capacitance measurements (typically a frequency) to the water holdup, as shown in Figure 4.C.2. It can be seen that for a water holdup of around 40 to 55% (depending on the tool), the frequency spans over a large range. However, for water holdups higher than this value, the dynamic range decreases considerably. Therefore, Capacitance tools are recommended for 40-55% water holdup since above this value, the conductive water becomes the continuous phase, and the capacitor is short-circuited.

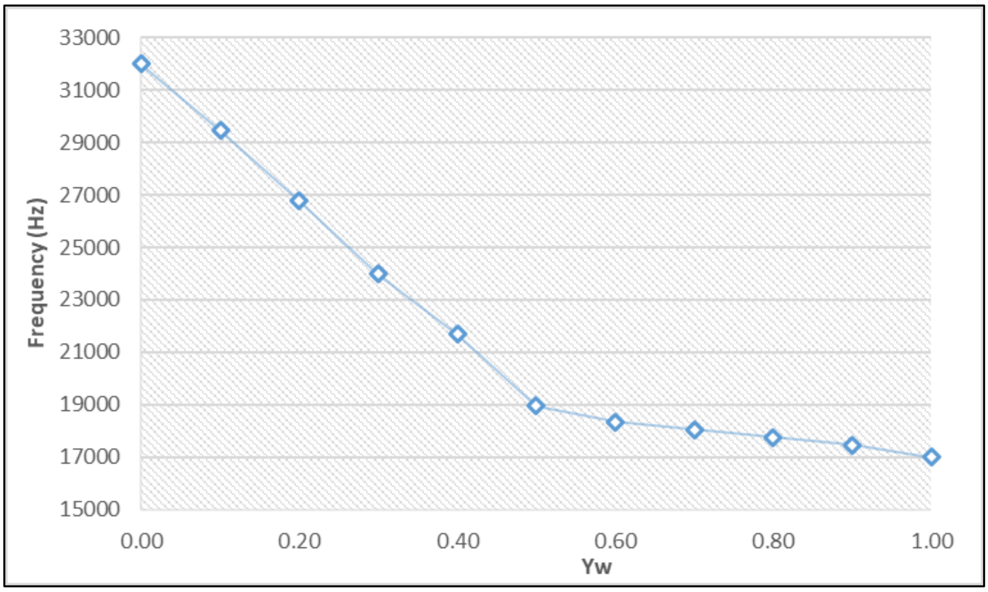

Fig. 4.C.2 – Capacitance calibration chart

The Capacitance tool is also subject to delays in the response by filming (down passes) and wetting effects (up passes), hence the risk of misinterpretation of the fluid contact.

Apart from selecting the tool calibration chart, the analyst has to pick the end point frequency values in water and hydrocarbon. As shown in Figure 4.C.3, the end points can be easily selected during a shut-in survey, where fluid segregation occurs. A density tool can be used as a reference.

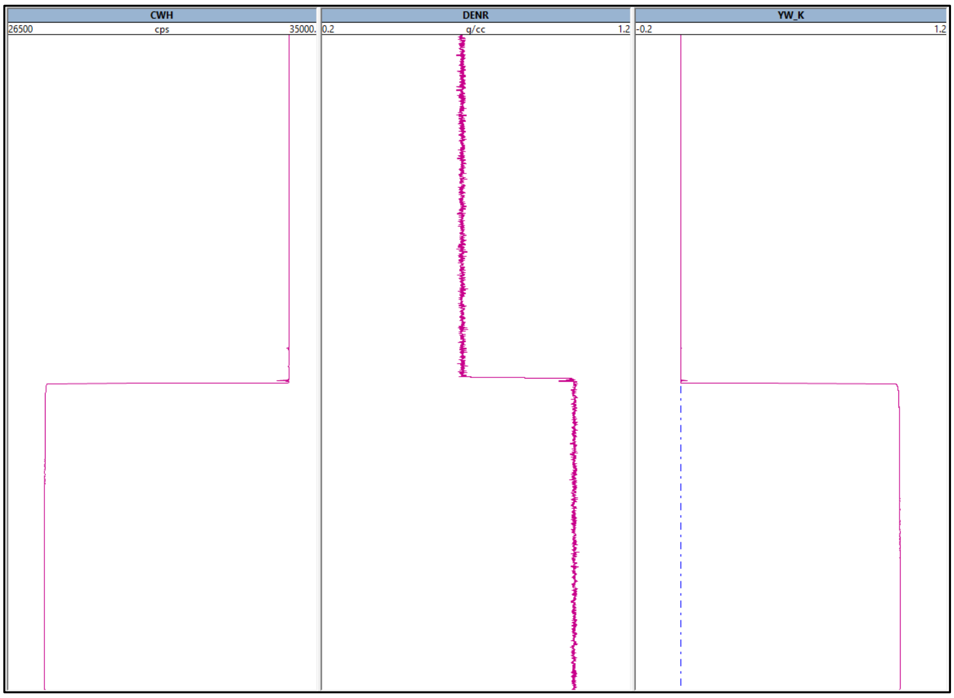

Fig. 4.C.3 – Capacitance, Density and Capacitance-based Water Holdup

By default, when using a Capacitance tool for multiphase flow interpretation, Emeraude works directly with the frequency value as part of the error minimization process. As displayed in the last track of Figure 4.C.3, once the calibration chart and end points are defined, compute the water holdup and use this curve as a reference of the interpretation scheme.

4.D Gas Holdup - Nuclear

Similar to the nuclear density tool, the gas holdup nuclear tool uses a radioactive source and responds primarily to the electron density of the fluid mixture. However, the produced Gamma rays are not collimated to a chamber in the tool housing but are emitted to the annular between the tool and the pipe. A tungsten disc shield blocks the direct passage of the Gamma ray from the source to the receiver through the tool.

Fig. 4.D.1 – Gas holdup tool (Courtesy: Sondex)

This tool is designed to calculate the gas volume fraction in the fluid. A transmitter emits Gamma rays; the measurement distinguishes the gas based on the amount of backscatter, recognizing that the gas has a low electron density and a low backscatter.

The tool gives a measurement across the wellbore with no influence from the formation behind the casing. It is not sensitive to deviation and requires no friction correction.

The downside is that it uses a short half-life radioactive source and must be run centralized. Raw counts have to be corrected by the pipe ID. Prior knowledge of certain PVT properties and results may be affected by scale.

4.E Electrical Hold-up probes

The next three sections cover different types of probe holdup measurements. These, together with the minispinners constitute the building blocks of the Multiple Probe Tools (MPT) used for high deviations and horizontal wells, covered in Chapter 6.

This family of sensors is based on the principle that salty water conducts electricity, and hydrocarbons are insulators. Ohm's Law defines a relationship between three fundamental electrical properties: Voltage (V), Current (I), and Resistance (R):

$$V = I * R$$

The inverse of the resistivity is known as Conductance (C), and Ohm's Law is expressed as:

$$V = I * \frac{1}{C}$$

To measure the conductivity or resistivity of a substance, one option is to apply a voltage (for example, through a battery) and measure the current in the circuit. Alternatively, a constant current is applied, and the voltage is measured. Both approaches are used in downhole applications. The other necessary elements of the sensor are two electrodes, where the voltage difference is applied. The three sensors described next are slightly different in architecture and electronic processing, as they all depend on the same principles described here.

Note that, as water and hydrocarbons are immiscible (do not form a homogeneous mixture), they will form bubbles, slugs, and separated streams in the case of stratified flow, etc. For this reason, an instantaneous sample of resistance or conductance can only be one of these options: water (low resistance/high conductance) or hydrocarbon (high resistance/low conductance). The sensors are sampled thousands of times per second. To go from a binary electrical measurement to the water holdup, a time average is applied.

In short, electrical holdup probes, also known as conductivity or resistivity probes, are discrete water holdup sensors. Each probe provides an independent 'water holdup' measurement that is calculated as the time the probe is immersed in water. This is a different definition from the one provided in Section 4.1. Obtaining a cross-sectional average from multiple discrete measurements will be the subject of Chapter 6.

4.E.1 Schlumberger FloView Probes

FloView is the commercial name of the Schlumberger water holdup probes. These can be mounted in the arms of a fullbore spinner (PFCS, shown in Figure 3.B.6), in the arms of a spring bow centralizer called DEFT (Figure 4.E.1), and in the FSI tool (Chapter 6). FloView uses the electrical conductivity of water to distinguish between the presence of water and hydrocarbons. The sensor uses two separate electrodes (Figure 4.E.2), one active at the probe tip and one return or 'earth wire'.

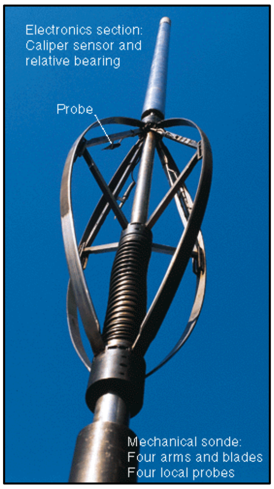

Fig. 4.E.1 – DEFT

(Courtesy: Schlumberger

In a continuous water phase, the current is emitted from the probe tip and returns to the tool body. A droplet of oil or gas has only to land on the probe tip to break the circuit and be registered.

In a continuous oil phase, a droplet of water touching the probe tip will not provide an electrical circuit. Instead, the water droplet must connect the electrical probe to the earth wire. This phase requires a larger droplet than is needed for gas or oil detection in a continuous water phase.

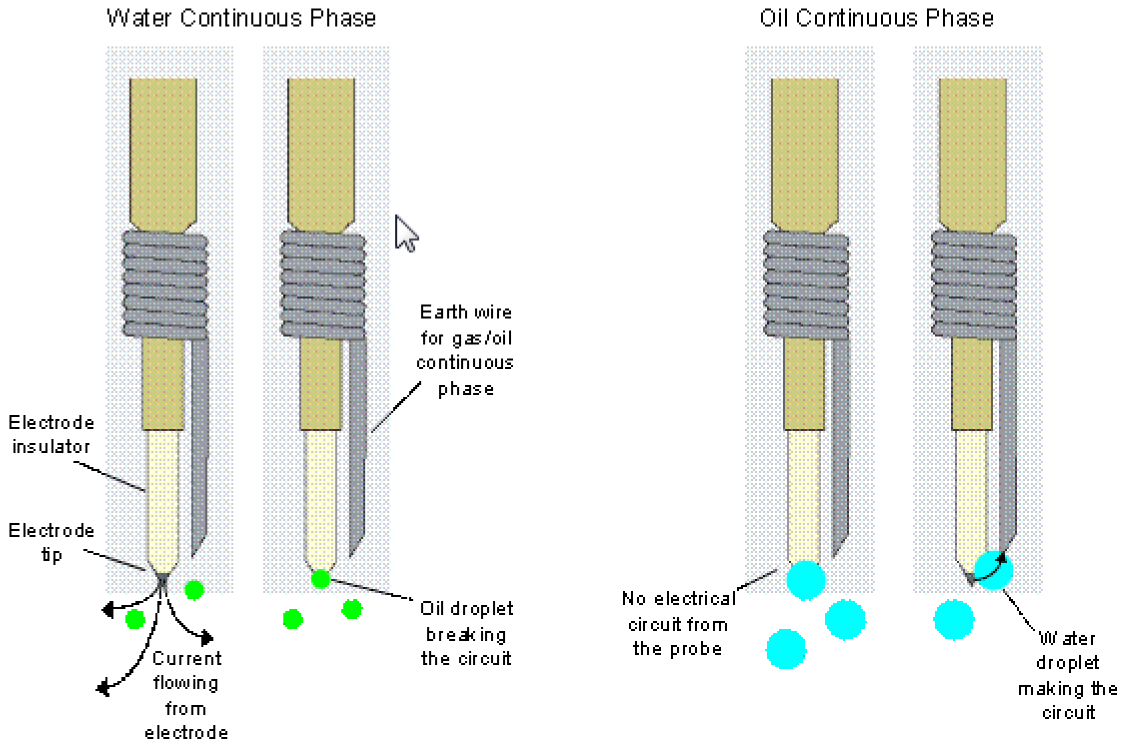

Fig. 4.E.2 – Theory of FloView Probe Operation (Courtesy: Schlumberger)

One of the sensor's limitations is the minimum droplet size to bridge the gap between electrodes. As shown in Figure 4.E.2, if the water droplet is in contact with only one of the electrodes, then the reading will indicate hydrocarbon. The bubble diameter decreases as the mixture velocity increases ($d \propto \frac{1}{V_m}$), and therefore the tool provider establishes maximum recommended fluid velocities.

The second limitation is due to water salinity. Water conductivity increases with salinity and temperature. It is not possible to estimate the water holdup if the produced water is fresh. The tool provider establishes a minimum recommended salinity of 1000 ppm.

The signal from the FloView probe lies between two baselines, the continuous water-phase response and the continuous hydrocarbon-phase response. When capturing small transient bubble readings, a dynamic threshold is adjusted close to the continuous phase and then compared with the probe waveform. A binary water holdup signal results, which, when averaged over time, become the probe holdup. The number of times the waveform crosses the threshold is counted and divided by 2 to deliver a probe bubble count.

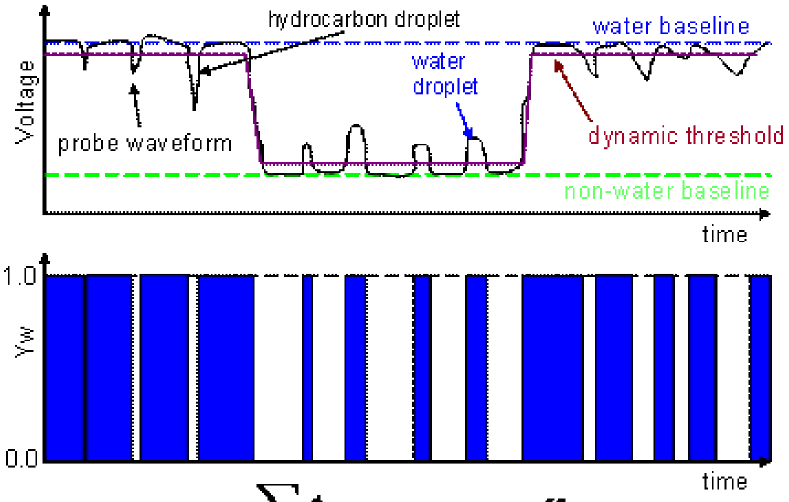

$$Y_w = \frac{\sum t_w}{t} \qquad bc = \frac{n_b}{t}$$

Fig. 4.E.3 – FloView Probe Waveform Processing (Courtesy: Schlumberger)

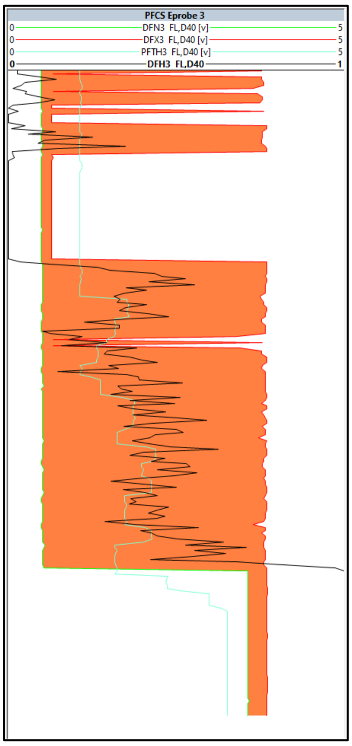

Apart from the water holdup and the bubble count, each sensor records the waveform minimum, maximum, and dynamic threshold. This record is used as a quality check to assess if the thresholding algorithm worked correctly. Figure 4.E.4 shows these parameters. When the minimum and maximum are lower than the threshold (blue curve), then the water holdup is zero (black curve). Contrary, when the minimum and maximum are above the threshold, it implies that the conductivity of the fluid is always high, 100% water. When the threshold is between minimum and maximum, there is a fluid mixture.

Electrical probes, and in general most holdup probes, provide the most accurate readings during down passes. In up passes, especially in low velocity wells, the tool may be moving at a similar velocity to the flow, lifting the bubbles or immersed in a slug, providing a non-representative estimate.

Fig. 4.E.4 – FloView LQC view

4.E.2 Sondex Resistance Probes

These probes are part of the Sondex RAT and Baker Hughes PAI. The sensor mechanics comprise: (1) a probe tip that ultimately connects to the sensor electronics input and (2) a reference contact, typically at earth potential.

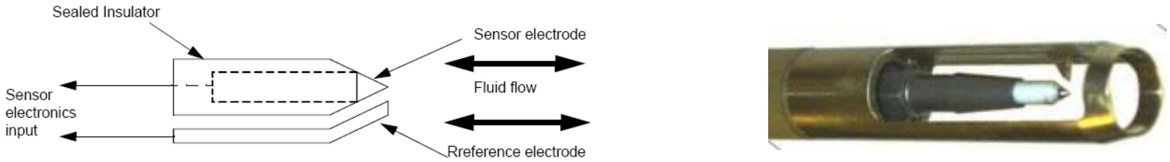

Fig. 4.E.5 – RAT, and RAT probes (Courtesy: Sondex)

Resistance measurements are made between the probe tips at sampling rates up to 10 kHz and result in a number that is proportional to the logarithm of the resistance detected between the electrodes and the fluid resistivity. The data is stored or transmitted as statistics, typically mean normalized resistivity and a standard deviation over a small time window (i.e., 1/6 sec), as well as histograms. The standard processing is based on the mean resistivity, R, considered a linear function of the conductive water resistivity Rc and the insulating hydrocarbon resistivity Ri.

The water holdup is obtained directly as: $Y_w = \frac{R - R_i}{R_c - R_i}$

Figure 4.E.6 shows the normalized mean resistance (RATMN) and the computed water holdup (RATHU). To go from RATMN to RATHU, the user has to select the water and hydrocarbon end points, represented by the blue and green vertical dashed lines in the RATMN track. Unless there are large salinity or HC PVT changes, these end points should be constant throughout the log.

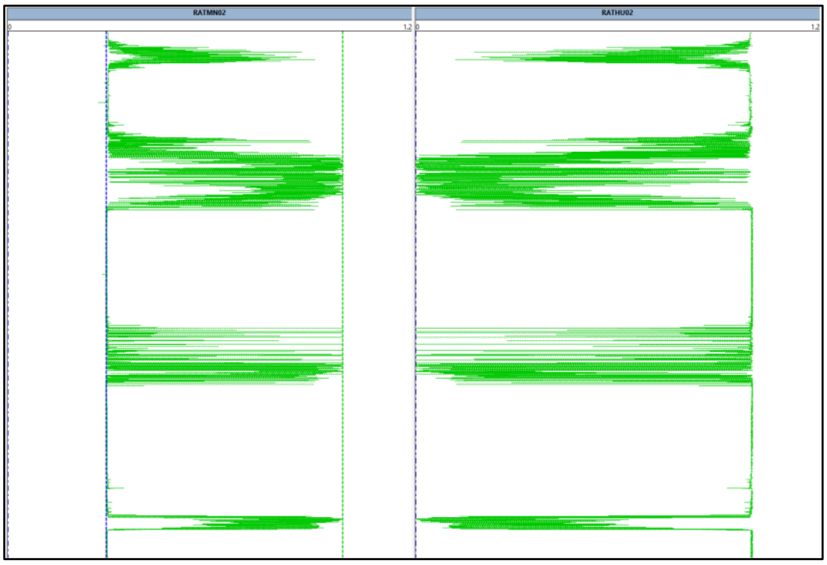

Fig. 4.E.6 – RAT mean and RAT Holdup

As mentioned for FlowView probes, this sensor cannot detect small bubbles that do not bridge the electrodes.

4.E.3 OpenField Conductivity Probes

The Electrical probes for water holdup determination works on the principle of a digital switch between the conductive water and insulating hydrocarbon. Compared to the previously presented water holdup sensors, both electrodes are contained on the tip of the probe, which reduces the distance to bridge by a bubble

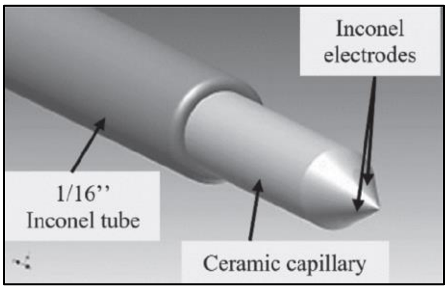

Fig. 4.E.7 – OpenField’s Conductivity Probe (Courtesy: OpenField Technology)

The waveform is analyzed downhole by the tool electronics, and the following statistics are extracted for every probe (displayed in Figure 4.E.8):

- Average conductivity, Majority (most frequent value), Maximum and Minimum. These are displayed in track 1.
- From the dynamic thresholds, the number of measurements above/below the up/down dynamic threshold divided by the total number of measurements. These two values (HUE and HDE), together with the computed water holdup (WHE) are displayed in Track 2.

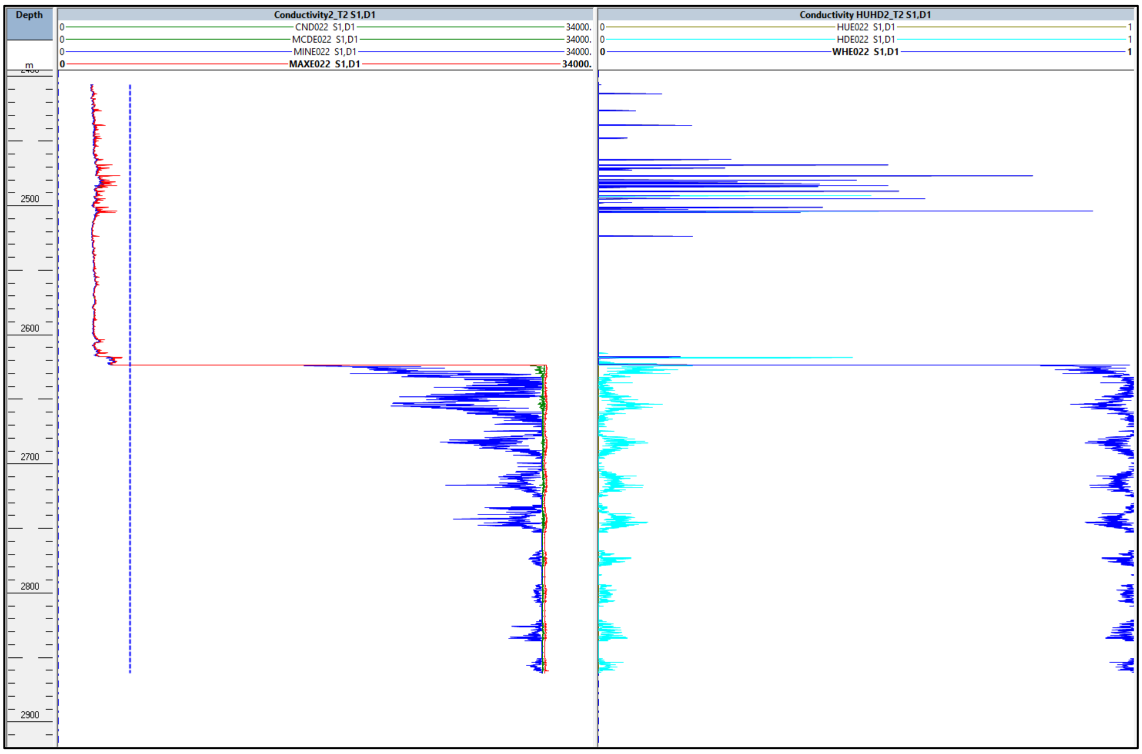

Fig. 4.E.8 – Output curves for one conductivity probe

The presence of these outputs allows the analyst to recompute the holdups. A water transition level (blue dashed line in track 1) is used to identify the intervals with water or hydrocarbon as a continuous medium. Then, based on the measurements above/below the dynamic thresholds, the holdups can be recomputed.

4.F Optical Hold-up probes

This family of sensors is based on the difference in the refractive index of fluids found in a producing well. Refractive index is the ratio of the speed of light in vacuum (c) and the velocity of light in the medium (v):

$$n = \frac{c}{v}$$

When the light reaches an interface between two media of different n (i.e., probe and fluid), the intensity of the reflected light is determined by the reflectance, as predicted by the Fresnel equation (for normal incidence):

$$R = (\frac{n_1 - n_2}{n_1 + n_2})^2$$

Figure 4.F.1 shows that if a line is shined on air or gas, most of the light will be reflected. On the other hand, for crude oil, most of the light will be transmitted.

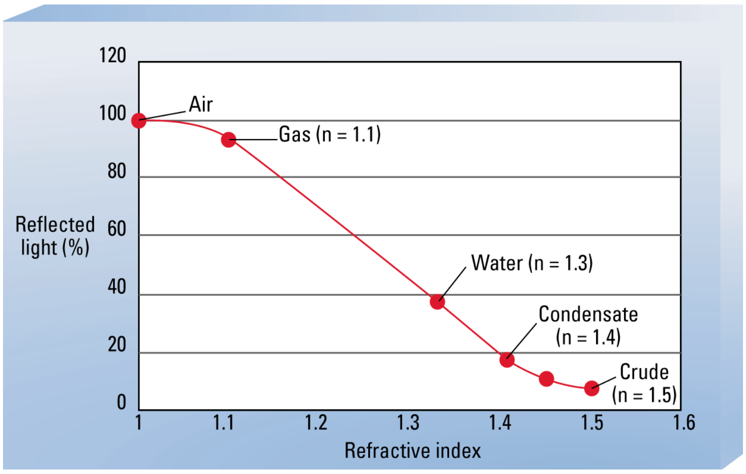

Fig. 4.F.1 – Reflected Light versus Refractive (Courtesy: Schlumberger)

This is the physical principle of the optical probes. The sensor requires a light source, a way to measure the intensity of the reflected light, and probe material that allows the light exiting its tip. The probes from two different tool manufacturers will be described next. Schlumberger GHOST is a gas holdup probe, while OpenField's probe provides three-phase holdups.

4.F.1 Schlumberger Gas Holdup probes

The probes are present in the 4 arms of a spring bow centralizer (GHOST) and in the FSI tool (Chapter 6). The probes use the refractive indices of gas, oil, and water to distinguish between the presence of gas and liquid.

Light emitted at a suitable frequency is fed down an optical fiber through a Y-coupler and finally to an optical probe made from synthetic sapphire crystal. The light that does not escape is returned via the Y-coupler to a photodiode and is converted to a voltage (Figure 4.F.3).

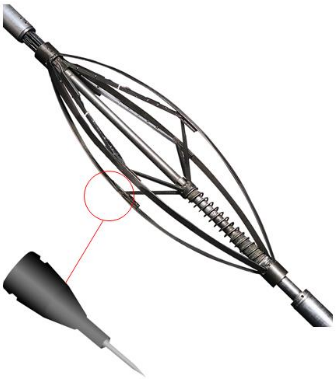

Fig. 4.F.2 – GHOST tool (Courtesy: Schlumberger)

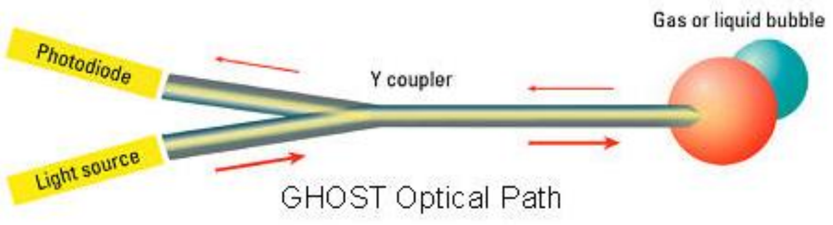

Fig. 4.F.3 – Sensor Optical Path (Courtesy: Schlumberger)

The signal from the optical probe is at or below the gas baseline and at or above the oil baseline. To capture small transient bubble readings, a dynamic threshold is adjusted close to the continuous gas phase and close to the continuous liquid phase. The threshold is then compared with the probe waveform to deliver a binary gas holdup signal, which is averaged over time. The number of times the waveform crosses the threshold is counted and divided by 2 to deliver a probe bubble count.

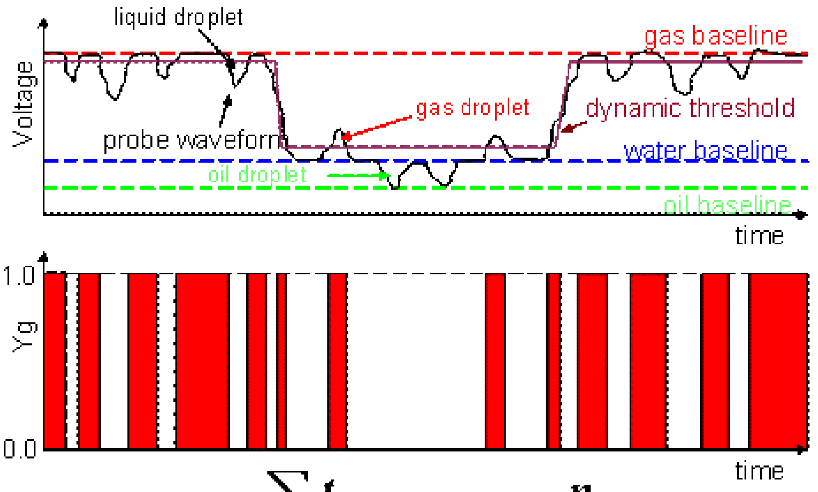

$$Y_g = \frac{\sum t_g}{t} \qquad bc = \frac{n_b}{t}$$

Fig. 4.F.4 – Optical Probe Waveform Processing (Courtesy: Schlumberger)

Similar to the SLB electrical probes, it is possible to plot the minimum, maximum, and dynamic threshold for each probe, in order to assess the validity of the automatic thresholding and, consequently, the calculated gas holdups.

4.F.2 OpenField Optical Probes

The OpenField optical probes are based on a sapphire biconical design and measure the refractive index ranging from 1 to 1.6 (see Figure 4.F.5). These probes can discriminate and quantify oil, gas, and water. Like the Electrical probes, the Optical probes are sampled at a high frequency (>16 kHz). Therefore, the waveform is represented by its Average, Majority, Minimum, and Maximum values. The normalized counts above and below the dynamic thresholds are also stored. The analyst can compute the three-phase holdups, setting the oil and gas transition levels, which allows them to determine what is the continuous media at every depth.

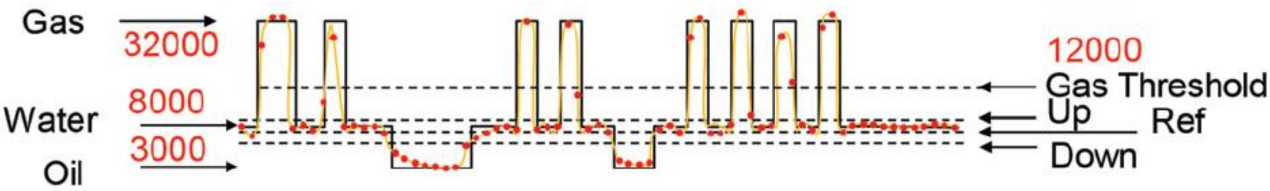

Fig. 4.F.5 – FAST 3-phase optical probe (Courtesy: OpenField Technology)

Figure 4.F.6 shows the various outputs of the tools. The first track shows the waveform statistics (average, majority, maximum, and minimum refractive index). From this track, it is possible to identify the dominant or continuous phase versus depth and set the transition levels. The second track shows the normalized counts above and below the dynamic threshold. These are used to compute the three-phase holdup, shown in tracks 3 to 5.

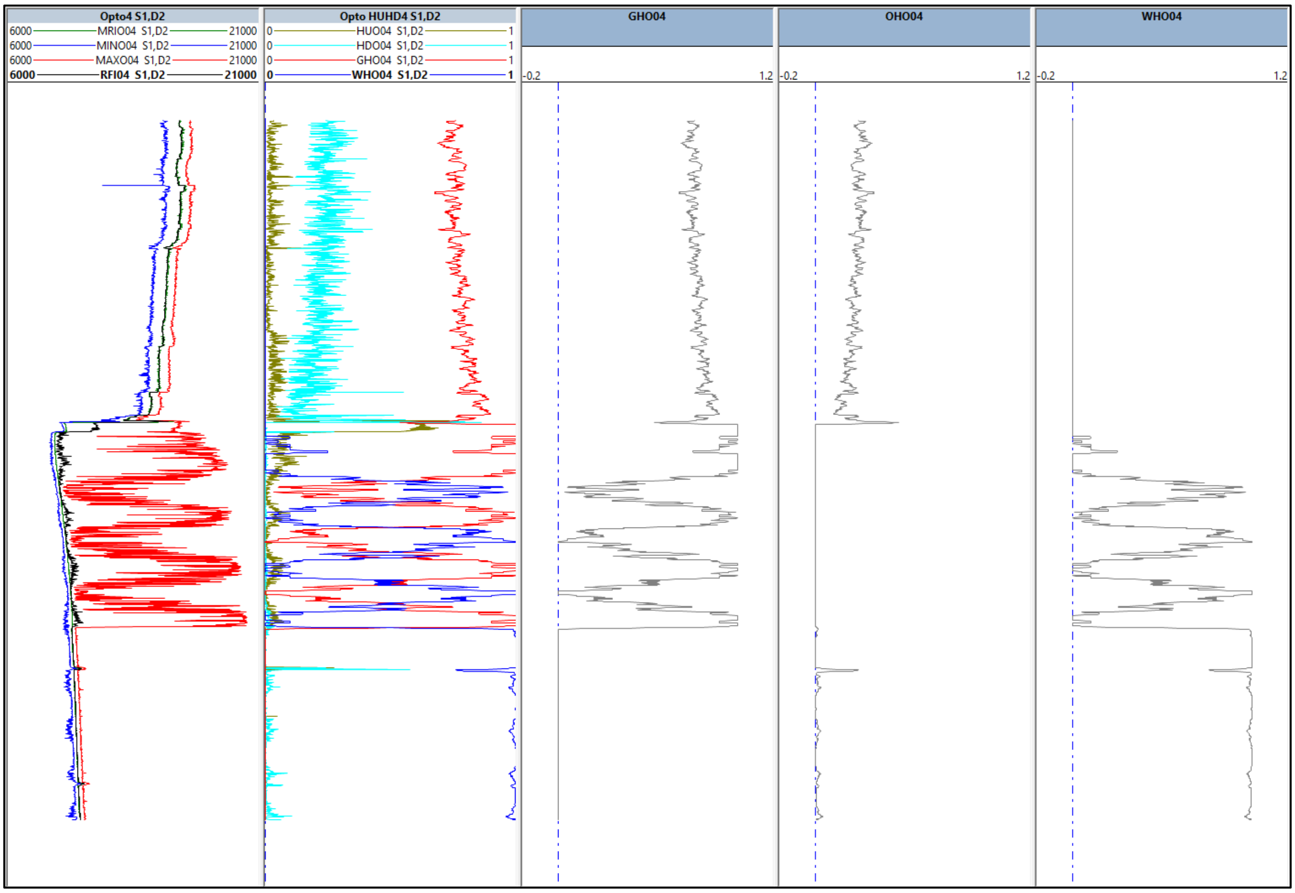

Fig. 4.F.6 – FAST optical probe outputs

4.G Capacitance Hold-up probes

Conventional Capacitance measurements were presented in Section 4.C. The principle of the Capacitance probes is similar, however, in this case, the circuit is established between the sensor and the tip of the sensor.

Also, compared to the conventional (bulk) capacitance, which is a water holdup tool, these probes can distinguish oil, gas, and water.

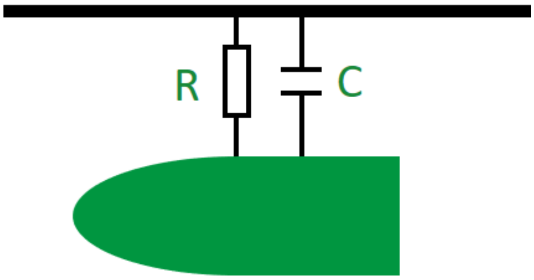

Fig. 4.G.1 – Capacitance probes

4.G.1 Sondex Capacitance Probes

Sondex Capacitance Probes are mounted in the springbows of the Sondex Capacitance Array Tool (Chapter 6). As with any capacitance sensor, the CAT probes discriminate primarily between water and hydrocarbons. The contrast in dielectric values for oil and gas may be used to differentiate the two fluids.

The output from each probe includes a raw frequency value and a normalized value. In a stratified environment, the probe response can be used to get holdup values using 2 two-phase calibrations as represented in Figure 4.G.2. When the normalized probe response is between 0 and 0.2 a gas-oil system is considered, and from 0.2 to 1, an oil-water system. To solve in three-phase without any assumption about the local holdups, a three-phase response can be used as shown below. This response is an extension of the previous graph representing the intersection of the surface with the side walls.

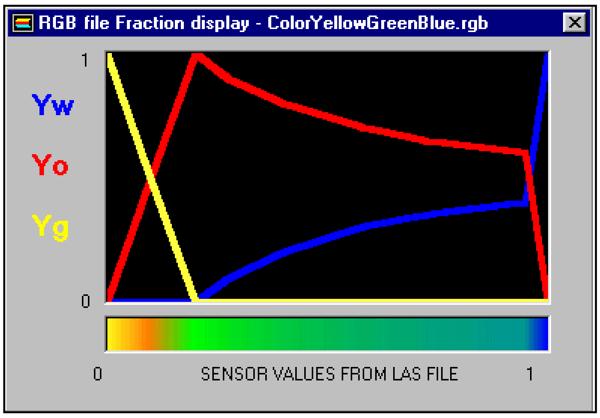

Fig. 4.G.2 – Normalized CAT response

In the case of three-phase mixed flow, it is not possible to determine the oil, gas, and water holdups, based on a single capacitance value. Note that, as shown in Figure 4.G.2, for high water holdup values, the response becomes non-linear. Similar to the conventional capacitance, the conductive water shorts-out the capacitor by bridging the gap between the sensor and the spring bow.

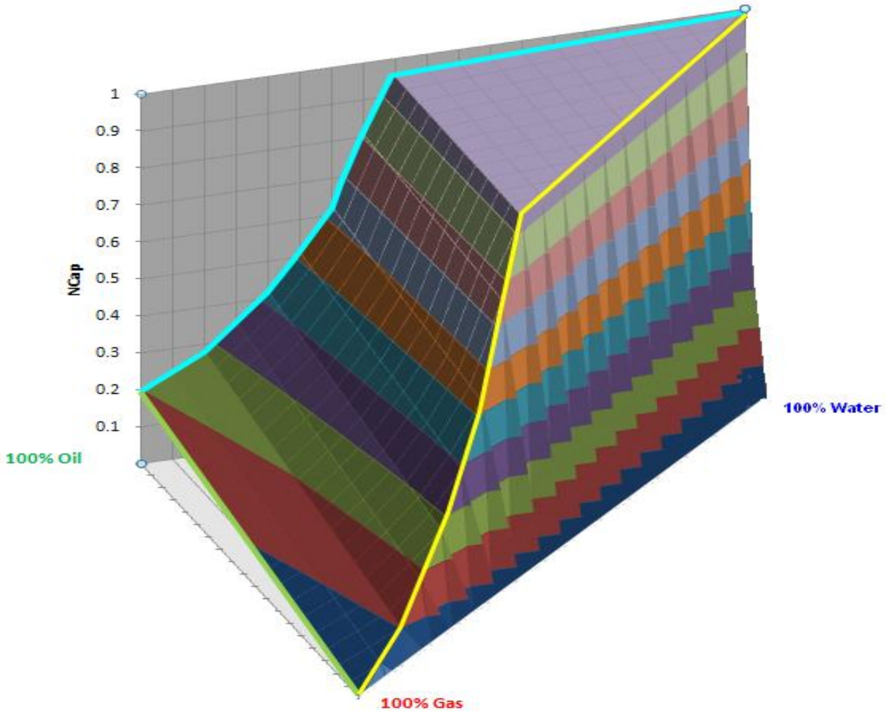

Fig. 4.G.3 – 3-Phase CAT response - Note the 2-phase segments:
Oil-Gas Oil-Water Gas-Water

The two outputs of the CAT sensor are shown in the first two tracks of Figure 4.G.4. These correspond to the raw frequency (RCAP) and normalized response (NCAP). Going from these to the computed holdups shown next (water, oil, and gas holdup), it is necessary to select the end points for water, oil, and gas, as shown in the first track as dashed blue, green, and red lines.

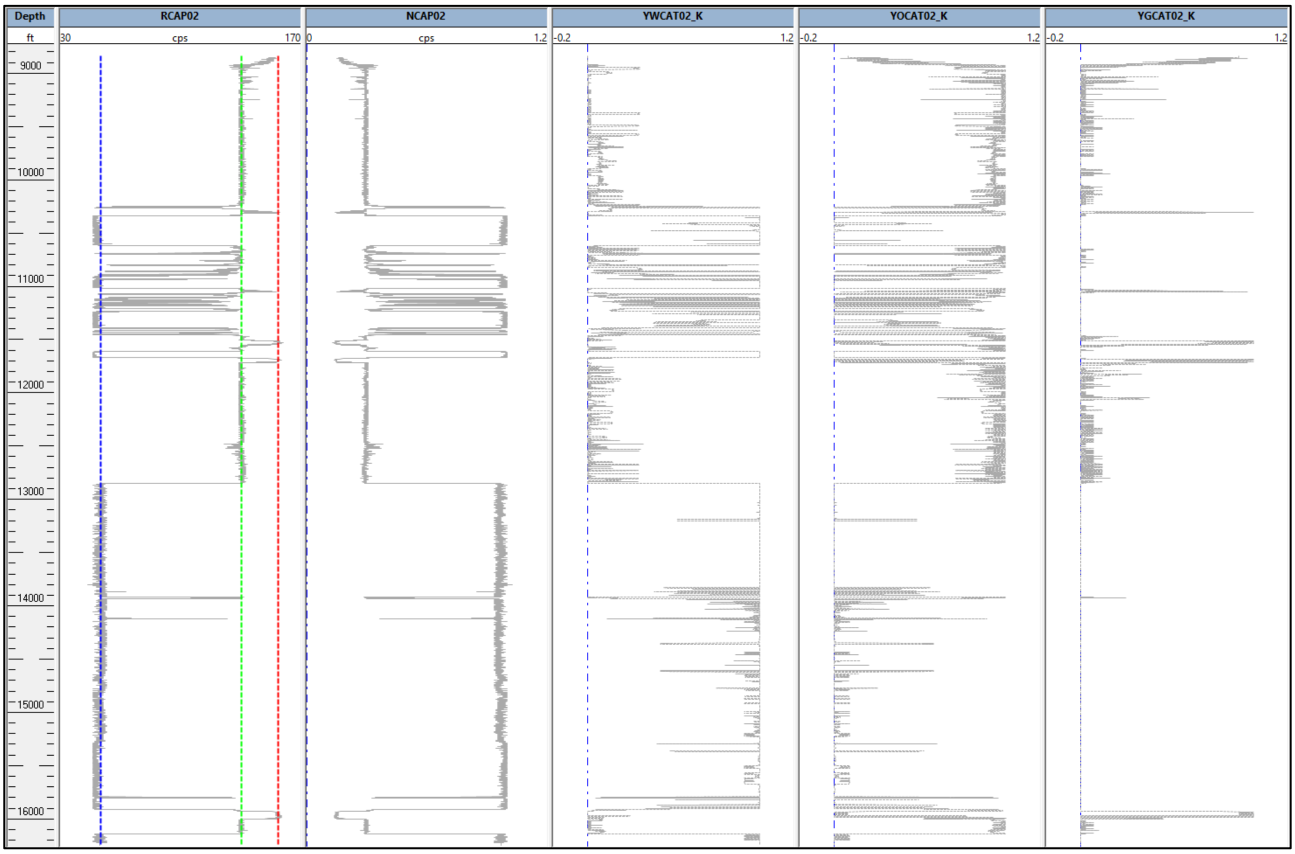

Fig. 4.G.4 – 3-Phase CAT response

5 – Multiphase Flow and Profiling

5.A Introduction

As the field matures, the wells are likely to start producing water with the associated increase of lifting cost, accelerated corrosion rates, sub-optimal recovery, etc. A large percentage of Production Logs run worldwide are due to water problems. Depending on the completion style and source of the water inflow, it may be possible to perform a water shut-off, shift sliding sleeves, or take other measures to minimize the water production. Accurately pinpointing water entry and establishing water cut from different inflows is key. If the main water source is from an interval producing a 30% water cut, it might not be economical to perform a water shut-off.

Excess gas production may also be undesired. The pipelines' take out capacity for fields developed years ago may not be sized for the current gas production once the reservoir pressure drops below the bubble point. For a gas expansion reservoir drive, it may be convenient to leave the gas in the reservoir to continue producing oil and maximizing recovery.

In general, to quantify a 2-phase rate (*l* for light and *h* for heavy), the following equations should be solved at any depth:

$$q_l = v_l \, A \, Y_l$$

$$q_h = v_h \, A \, Y_h$$

Fluid identification tools to measure or estimate the holdups were presented Chapter 4. The mixture velocity (Vapp*VPCF) can be computed from the flowmeter, as demonstrated in Chapter 3. The mixture velocity is neither the v_l nor v_h, and an extra input is required to solve for the 2-phase rates. This comes from the existence of slippage velocity, a difference between the velocity of distinct phases flowing together. When light and heavy phases are considered, the slippage velocity is defined as the difference between the light phase velocity and the heavy phase velocity, namely:

$$v_s = v_l - v_h$$

Slippage velocity is a function of the flow regime. Section 5.B introduces multiphase flow and flow regime maps. The slippage velocity is not measured directly by a downhole tool, rather it is estimated from correlations. A summary on the main multiphase flow correlation applied to PL interpretation is presented in Section 5.C. Section 5.D shows how the velocity, holdups, and correlations are put together to obtain a multiphase profile.

5.A.1 Definitions

Key definitions that will be used along this chapter are presented next.

5.A.1.a Holdup

This definition was given before, but it is repeated for clarity. The holdup of a phase is the volume fraction occupied by that phase. Figure 5.A.1 shows a heavy (blue) and light (red) phase and indicates the corresponding holdups.

The holdups are usually noted 'Y'; they add up to 1 by definition.

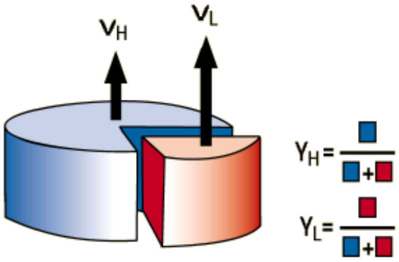

Fig. 5.A.1 – Holdup definition

In 2-phases with a heavy ('H') and a light phase ('L'): $Y_h + Y_l = 1$

In 3-phases with water ('w') oil ('o') and gas ('g'): $Y_w + Y_o + Y_g = 1$

Correlations developed for the chemical industry or dealing with boiling/condensation processes, also referred as 'Void' fraction, to the holdup of the light phase (i.e., vapour).

5.A.1.b Average phase velocities

The average velocity of a particular phase is obtained from the rate, holdup, and cross sectional area by: $v_P = \frac{Q_P}{A\,Y_P}$

5.A.1.c Superficial velocities

The superficial velocities assume that a given phase occupies the whole pipe cross sectional area: $v_{sp} = \frac{Q_P}{A}$

Several correlations use this definition to identify the flow regimes. It is convenient, as the sum of the superficial velocities is equal to the mixture velocity:

$$v_m = \frac{q_h + q_l}{A} = v_{sh} + v_{sl}$$

5.A.1.d Water cut

Defined as the ratio of water rate compared to the total liquid rate:

$$W_{cut} = \frac{q_w}{q_w + q_o}$$

Holdup and water cut are often confused, but in most cases, they are not the same. Water cut is a ratio of rates, so the definition considers the phase velocity. Water cut and water holdup are only equal when the phases move at the same velocity, that is, if the slippage velocity is zero. Increasing the slippage velocity results in a disproportionate amount of the heavy phase being present at a certain depth.

5.A.1.e Relationship between holdups and slippage velocity

Holdup and slippage velocity are two manifestations of the same phenomenon. The heavy phase is ‘held-up’ at the bottom as the lighter phase travels faster. The higher the slippage velocity, the larger the heavy phase holdup at a certain depth. These two variables are related as:

$$v_s = v_l - v_h = \frac{q_l}{A\,(1 - Y_h)} - \frac{q_l}{A\,Y_h} = \frac{v_{sl}}{(1 - Y_h)} - \frac{v_{sh}}{Y_h}$$

This can also be expressed as:

$$Y_h = \frac{v_s - v_m + \sqrt{(v_m - v_s)^2 + 4 * v_s * v_{sl}}}{2\,v_s}$$

5.A.1.f Putting all together

Attempting a quick multiphase split from total rates may go wrong due to the slippage effect, holdups, and fluid density may be deceiving. Using the PL data fieldprint to estimate contributions from different phases may be misleading. For example, at the top of the upper perforation in Figure 5.A.2, the mixture density is 0.96 g/cc. It may not sound like much oil, but incorporating the PVT information leads to a water holdup of 0.73 (27% oil). This does not mean that the water cut is 73%, as oil flows faster than water. The selected correlation (Choquette) predicts a slippage velocity of 38.4 ft/min. The downhole water cut above the upper perforation is 65%. When reporting the results at surface, the oil rate decreases due to the formation volume factor, while the water volume has little change. The water cut at surface conditions is 67%.

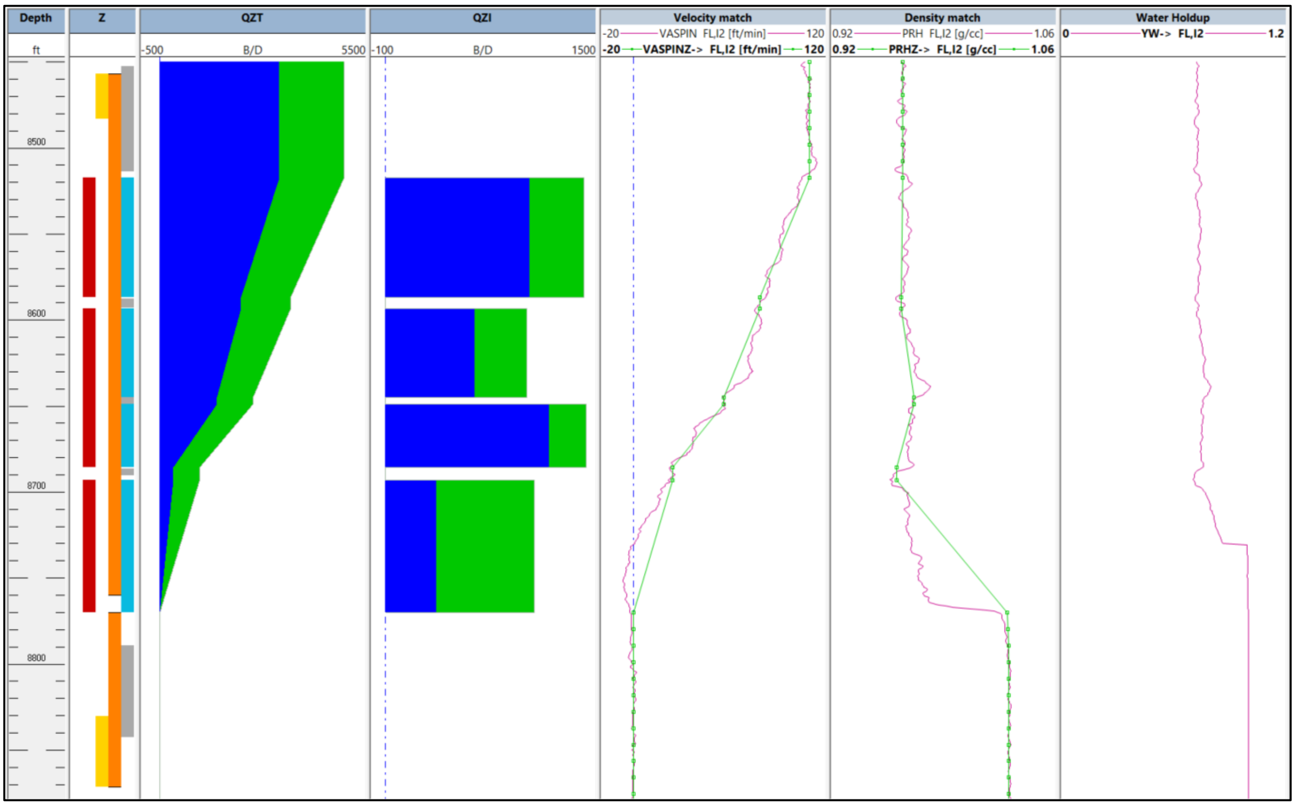

Fig. 5.A.2 – Holdup, slippage, and water cut in PL interpretation

5.B Multiphase Flow

The term multiphase flow refers to any fluid flow composed of more than one phase or component. This field encompasses numerous engineering and technological applications and may include solids, suspensions, aerosols, cavitating flows, slurries, etc. This chapter focuses on liquid-liquid and liquid-gas systems.

It is important early on to differentiate between two different topologies, which in the context of PL interpretation, implies different sensors and interpretation methodology:

- **Dispersed flows:** One of the phases is distributed (as bubbles, slugs, etc.) in a continuous phase. As will be evident in Section 5.D, this is the scope of the 'conventional multiphase' workflow, using centralized measurements and correlations.
- **Separated flow:** Two or three continuous streams separated by interfaces, with the most emblematic one called Stratified flow. These cannot be measured by conventional tools or modeled by the techniques presented here; they will be presented in Chapter 6 (High Deviation and horizontal PL).

Oil, gas, and water flow in pipes are immiscible. They adopt geometrical distributions, or flow patterns, which depend on fluid properties, holdups, velocities, well deviation, pipe size, etc. The geometrical distribution affects the interfacial area between phases, impacting the friction, lift, drag, and energy exchange between phases. The slippage velocity is a function of the flow regime, and if this velocity is estimated, the flow regime at that depth needs to be known. Usually, the flow patterns are recognized by visual inspection, with names that are now standard. Images of liquid-gas mixtures flowing up through a vertical pipe are presented in Figure 5.B.1, with the gas velocity increasing from left to right:

Fig. 5.B.1 – Experimental determination of flow regimes for water-air upwards flow (T. Okawa, Osaka University)

Typical flow patterns encountered in vertical gas/liquid systems are briefly described below. Note that different authors have identified other flow regimes not presented below.

Bubble flow: Uniformly distributed gas phase in a continuous liquid phase. The gas bubbles move faster than the liquid, mostly due to buoyancy (density difference). Bubbles may start to coalesce (Figure 5.B.1) and create bigger bubbles, reducing the surface energy. This is a function of the fluid velocity (Weber number), as when this is very high, there is little time for the bubbles to interact.

Slug flow: Formed by bullet-shaped gas pockets, separated by liquid slugs. The gas adopts a geometry known as Taylor bubbles, and its dimensions are comparable to the pipe diameter. These gas pockets are surrounded by liquid films with a negative (downwards) relative velocity. When this flow regime is observed near surface, the well produces intermittently, resulting in technical challenges (i.e., use of slug catchers).

Churn/Froth: As the gas volume increases, the liquid-gas flow becomes chaotic. It is difficult to distinguish the continuous phase, and an alternating direction of motion may be present.

Annular flow: Characterized by a central gas core and liquid film flowing upwards on the pipe wall.

Mist flow: Instead of annular flow, the liquid phase may become very small droplets homogeneously distributed by the gas. Due to the small droplet size, the liquid is carried by the gas, and no relative velocity (slippage) is observed between phases.

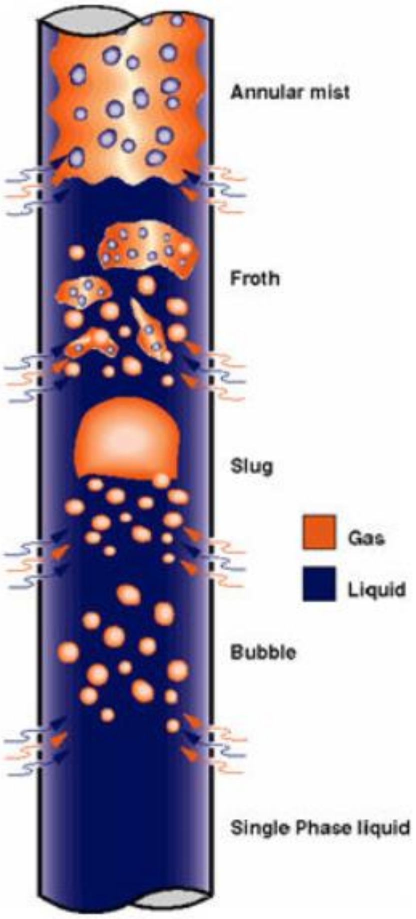

Fig. 5.B.2 – Liquid-gas flow patterns

Droplets are held together by the liquid surface tension, while fast gas flows and tries to shatter the droplets. This process is seen in the transition to mist flow. The Weber number represents the ratio of the velocity forces to surface tension:

$$N_{We} = \frac{v^2 \rho_g d}{\sigma g}$$

Some authors identify transitions between fluid patterns based on the Weber number. For example, for free falling droplets, Hinze shows that a critical value between 20 and 30 is required to shatter the bubbles.

The two ways of predicting and modeling multiphase flows are:

- Mechanistically: Through computational models and theoretical derivations
- Experimentally: Laboratory flow loops, equipped with high precision pumps and accurate holdup/fluid velocity instrumentation

Modern studies tend to combine both since the experimental results are typically conducted in models of much smaller scale and lower pressures than the conditions found downhole. Therefore, the computational model helps to extrapolate from laboratory scale to the actual application.

Several studies have focused on vertical pipes for liquid-gas flow and the dependence of the volumetric rates of both phases and fluid properties (density, viscosity, surface tension). The results are typically displayed in a flow regime map that identifies the flow patterns occurring in various parts of a parameter space defined by the component flow rate.

The boundaries between flow regimes are usually poorly defined, as the instabilities that cause one flow to transition to another depend on variables like pipe roughness, entrance effects, etc. It is important to remember that, even in single phase flow, a distance between 30 and 50 pipe diameters from the entrance is necessary to establish a fully developed turbulent flow. This means that some of the flow patterns described by the literature may actually be transitional flow.

Emeraude offers 9 liquid-gas, 6 oil-water, and 2-phase and 3-phase correlations. It is not the purpose of this document to describe the flow maps and equations of each correlation but to provide a clear and conceptual understanding of how they work in the context of multiphase profiling. Therefore, only one flow map will be presented next.

Figure 5.B.3 shows the flow map developed by Duns and Ros. This experimental work consisted of approximately 4000 tests in a 185 ft vertical test loop, with pipe sizes from 1.26 to 5.60 in. The flow regimes were identified through a transparent pipe section, and holdup was measured through radioactive tracers. The flow map axes are Liquid (N_{lv}) and Gas (N_{gv}) velocity number, which is a function of the liquid and gas superficial velocities (v_{sl} and v_{sg}), liquid density (ρ_l), gravity (g), and surface energy (σ_l):

$$N_{lv} = v_{sl}\sqrt[4]{\frac{\rho_l}{g\,\sigma_l}} \qquad N_{gv} = v_{sg}\sqrt[4]{\frac{\rho_l}{g\,\sigma_l}}$$

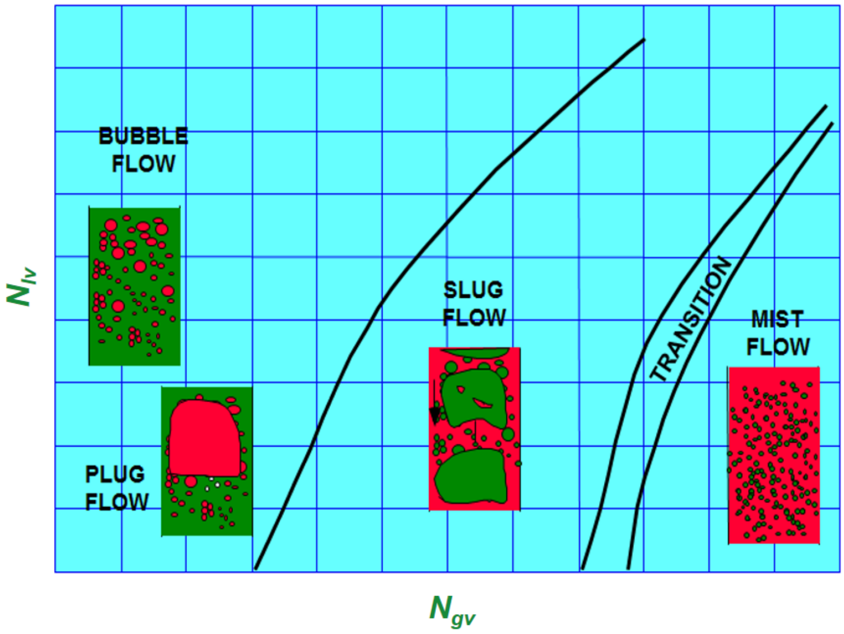

Fig. 5.B.3 – Duns and Ros flow map

As shown in the above figure, the transitions between flow regimes are functions of the liquid and gas velocity numbers, for example:

- Bubble to slug boundary: Given by the following equation, where L_1 and L_2 are functions of the pipe diameter, and the liquid density and surface tension:

$$N_{gv_{B/S}} = L_1 + L_2\,N_{lv}$$

- Slug to transition boundary: Occurs when ${N_{gv}}_{S/Tr} = 50 + 36\, N_{lv}$
- Transition to mist boundary: Given by ${N_{gv}}_{Tr/M} = 75 + 84\, {N_{lv}}^{0.75}$

For each flow pattern, the energy, mass, and momentum transfer will be different. Multiphase studies may focus on different aspects of the flow. For example, for chemical engineering and reactor processes, the mass transfer and reaction rate is the main point of the study. In petroleum engineering applications, the slippage and holdups prediction for the different flow regimes are the key elements of the multiphase flow correlations. This is the subject of the next section.

Some of these maps are dimensional, which means that they apply to the specific conditions (pipe diameters, fluid types) used by researchers to develop correlations. There is no universal dimensionless flow map that incorporates all possible variables to estimate the flow regime and its characteristics.

5.C Multiphase Correlations

Summarizing the chapter so far, to compute a multiphase profile, the spinner-derived fluid velocity is not enough. An extra velocity is required, which comes from the concept of the slippage between phases. This is a function of the flow regime, and flow pattern maps are used to know the topology of the flow. This section presents the way slippage and holdups are estimated from multiphase correlations.

5.C.1 Where correlations come from?

Most (if not all) multiphase correlations were not developed with the objective of computing a PL profile, with many of them coming from other industries. The main applications of the multiphase correlations in Petroleum Engineering are to calculate pressure drops along pipes. This is used for: designing surface networks (i.e., from the wellhead to the separator/battery/processing plant), converting surface pressure to downhole conditions, estimating the Vertical Lift Performance of a well, etc.

The mechanical energy balance in the pipe is composed of the potential energy, frictional, and kinetic pressure components. The pressure gradient can be expressed as:

$$\frac{dp}{dz} = (\frac{dp}{dz})_{PE} + (\frac{dp}{dz})_{Fr} + (\frac{dp}{dz})_{KE}$$

This equation can be further expanded and expressed as a function of pressure drops, as:

$$\Delta p = g\,\bar{\rho}\,\Delta z + \frac{2\,f\bar{\rho}\,u^2 L}{D} + 0.5\,\bar{\rho}\,\Delta u^2$$

The slippage holdup dependency comes into play in the in-situ average density, present in the three terms (and implicitly in the Friction factor, *f*). For a generic 2-phase flow:

$$\bar{\rho} = \rho_L * (1 - Y_L) + \rho_L * Y_H$$

These equations show how to calculate the pressure at a certain depth of the well, based on the following inputs: pipe diameter, deviation and roughness, PVT properties, total rates (to compute the velocity, *u)*, and the selection of a multiphase correlation to estimate the holdups. As shown for the Duns and Ros map, the superficial light and heavy phase velocities are needed to predict the flow regime at any depth, from where the appropriate slippage velocity expression will be selected.

For a typical pressure traverse calculation, all the inputs mentioned above can be provided or estimated with a considerable degree of accuracy. Computing the downhole pressure (P_{wf}) can be calculated by integrating the pressure gradient:

$$P_{wf} = P_{wh} + \int_0^L \frac{dp}{dz}\,dl$$

In nodal analysis, the well is discretized in nodes. The rates can be calculated in each node by taking the surface rates and applying the formation volume factors and other PVT properties. As the fluid properties are a function of the pressure and temperature, and these are not known, an error minimization process is applied in each node in a stepped way, from surface to downhole.

If the pressure traverses are calculated for a range of surface rates (with all other variables being constant), a VLP curve is obtained. Figure 5.C.1 shows this schematically for 6 rates (increasing from left to right) for constant wellhead pressure and GLR:

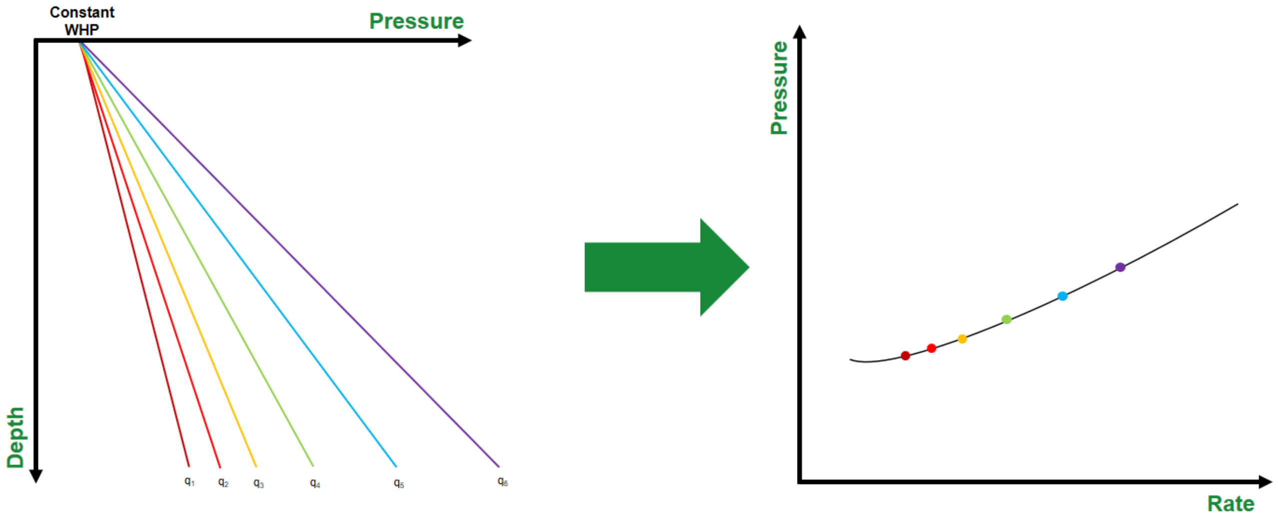

Fig. 5.C.1 – From pressure traverse to VLP

The Vertical Lift Performance curve is one of the building blocks of nodal analysis. Combined with an Inflow Performance Relationship (IPR), the analyst can diagnose and (hopefully) improve the well production. Figure 5.C.2 shows the Original VLP and Potential VLP, after considering water shut-off, smaller tubing ID, artificial lift, lower separator pressure, etc.

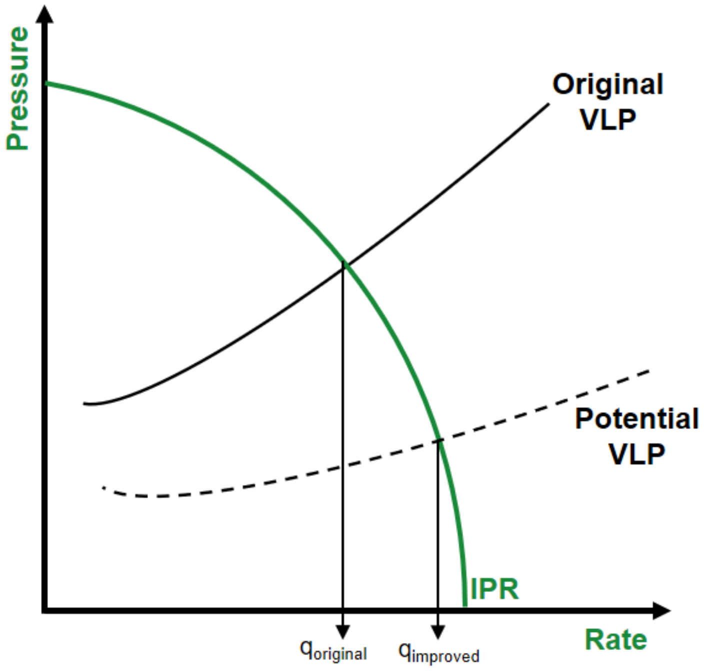

Fig. 5.C.2 – IPR/VLP analysis

Again, multiphase flow correlations were not created for PL analysis, but these are needed to achieve the interpretation’s objectives. A brief review of the different models is presented next.

5.C.2 Liquid-Liquid correlations

In water, continuous phase for vertical and slightly deviated pipes, bubble flow is the most likely flow pattern. The slippage velocity is determined mainly by the density difference and holdups. Three well-known correlations are briefly described next:

5.C.2.a Choquette

An experimental study in a vertical test loop facility. The study considered only bubble flow, without regard of flow pattern maps. The slippage velocity can be calculated as:

$$v_s = 39.414\,(\rho_w - \rho_o)^{1/4} e^{\left(-0.788\cdot(1-Y_w)\cdot\log\left(\frac{1.85}{\rho_w-\rho_o}\right)\right)}$$

Graphically it is clear that the slippage increases with increasing density contrast between the oil and gas. Slippage decreases with decreasing water holdup, with the maximum reached when a single droplet of oil is flowing up in nearly 100% water. As the water holdup decreases, the faster-moving oil starts to lift the water, reducing the relative velocity.

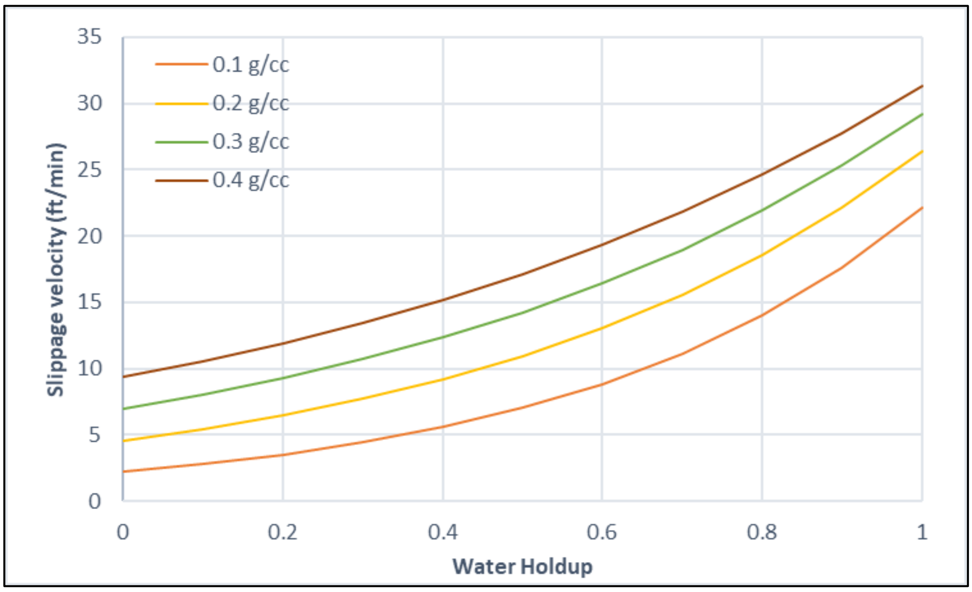

Fig. 5.C.3 – Choquette slippage velocity prediction for different Δρ

This correlation has an important limitation. When the water holdup decreases below a certain point, oil becomes the continuous phase, and water droplets are entrained in the oil. The average fluid velocity is given by the continuous oil, and the discontinuous water cannot travel slower or faster than this. Therefore, zero slippage velocity is expected for low water holdups, and this is not predicted by this or other correlations based on the bubble rise experiment.

5.C.2.b Nicolas

An experimental correlation that considers bubble flow only (no flow map). The slippage velocity is a function of the water holdup and limit (or terminal) velocity:

$$v_s = {Y_w}^n * V_{lim}$$

The limit velocity is calculated from the density difference and the surface tension. It represents the velocity of a single oil bubble rising in a water column (again, bubble rise experiment).

$$V_{lim} = C\,(\frac{g \cdot \sigma \cdot \Delta\rho}{\rho_{liq}})^{\frac{1}{4}}$$

Even though the assumptions are similar to Choquette, as the water holdup decreases, the slippage velocity tends to zero, as expected for continuous oil.

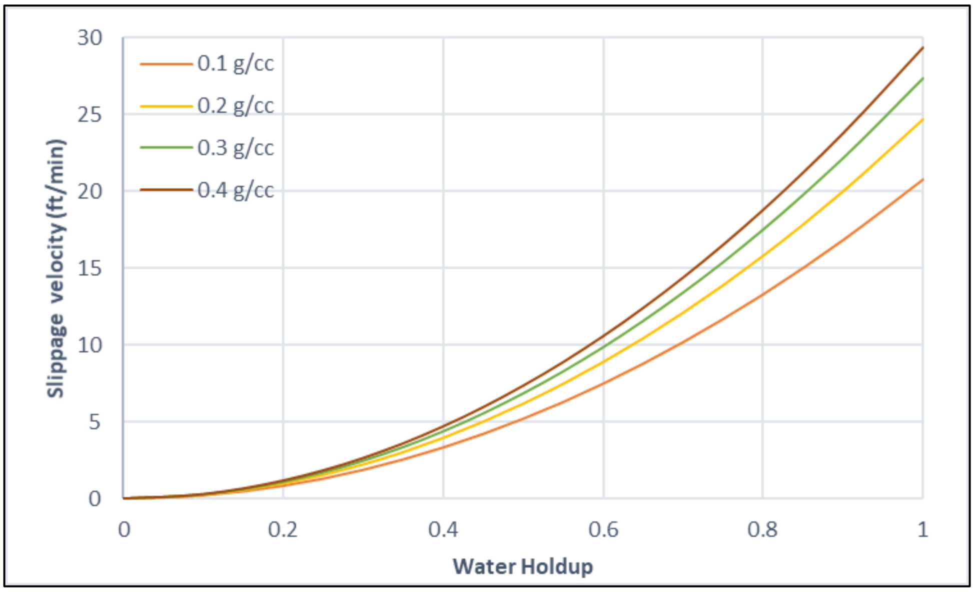

Fig. 5.C.4 – Nicolas slippage velocity prediction for different Δρ

5.C.2.c Hasan and Kabir

This work includes a flow regime map with three patterns: bubble, pseudo-slug, and churn flow. Compared to the Choquette and Nicolas, the Hasan and Kabir correlation predict an inversion point where oil becomes the dominant phase. This is achieved for an in-situ oil fraction (f_o) of 0.7, and above this point, the slip velocity becomes negligible.

The correlation uses the terminal velocity concept, and the relationship between f_o, superficial oil velocity, mixture velocity, and terminal velocity is given by:

$$f_o = \frac{v_{so}}{1.2\,v_m + v_{lim\theta}(1 - f_0)^2}$$

5.C.3 Liquid-Gas correlations

This is by far the largest population with many empirical correlations (Duns and Ros, Hagedorn and Brown, Orkiszewksi, etc.) and mechanistic models (Dukler, Kaya, Hasan and Kabir, Petalas and Aziz, etc.). Most of these correlations have been primarily designed for representing wellbore pressure drops in the context of well performance analysis. These correlations typically consider multiple flow patterns, apart from Hagedorn and Brown and Artep, which do not include a flow map.

Liquid-gas correlations use very different calculation approaches, and as previously mentioned, only a couple of correlations will be described next, to describe their use conceptually.

5.C.3.a Duns and Ros

As the Duns and Ros flow map was described in Section 5.B.3, it is convenient to proceed with this correlation.

For each flow pattern, there is a different empirical correlation for a dimensionless slippage velocity number, *S*:

$$S = v_s \sqrt[4]{\frac{\rho_l}{g\ \sigma_l}}$$

For **bubble flow**, the empirical slippage velocity number correlation is a function of gas and liquid velocity numbers, and three parameters (F_1, F_2, F_3) described in the original work, also a function of the liquid velocity number:

$$S = F_1 + F_2\ N_{lv} + F_3\ (\frac{N_{gv}}{1 + N_{lv}})^2$$

If the flow map indicates **slug flow**, a different equation is used, also a function of various experimental parameters (F_5, F_6, F_7) indicated in the original paper:

$$S = (1 + F_5)\ \frac{{N_{gv}}^{0.982} + F_6}{(1 + F_6\ N_{lv}\ )^2}$$

For **mist flow**, the slippage velocity drops to zero, as the liquid is transported as small droplets by the continuous gas phase.

5.C.3.b Dukler

The correlation by Taitel, Barnea, and Dukler includes a flow pattern map and distinguishes between fine bubble, bubble, slug, froth, and mist. It was developed for vertical wells.

The proposed slippage velocity equation for bubble flow is only a function of the gas holdup and is shown in Figure 5.C.5. At low gas holdup values, the slippage is around 60 ft/min. This value can be found in former interpretation manuals, where the analyst would use a single slippage velocity value to compute the flow profile.

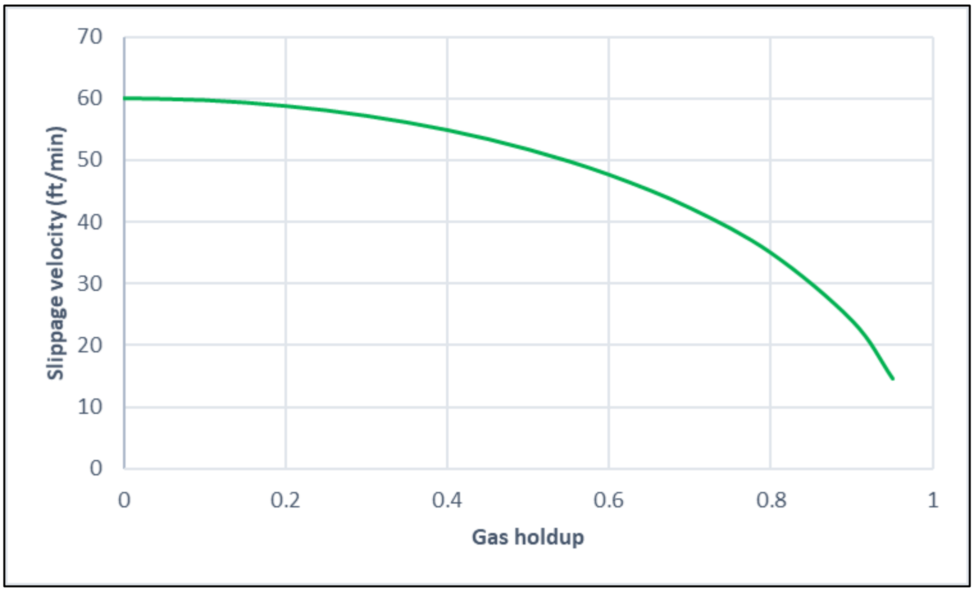

Fig. 5.C.5 – Dukler bubble flow slippage velocity

5.C.4 Pipe deviation

Choquette, Nicolas, Duns and Ros, and Dukler correlations discussed previously were developed for vertical flow which is also the case for Hagedorn and Brown, Aziz and Govier, etc. As deviation increases, the light phase moves to the high side of the pipe cross section due to buoyancy. As it faces less resistance by the heavy phase, the light phase moves faster, and an increased slippage velocity compared to the correlation prediction will be expected.

For correlations that do not account for pipe deviation corrections, the Ding correction is available. As shown in Figure 5.C.6, this correction consists of a multiplier on the correlation's slippage velocity (v_s), which is a linear function of the angle. For example, for a 10° deviation, the multiplier to v_s is 1.4, meaning that the light phase moves 40% faster relative to the heavy phase, compared to the correlation prediction.

This correction is applicable until 45°, as above this value, the slippage will decrease.

Note that as deviation varies from the correlation experimental setup, the flow regime may change. A correlation predicts bubble flow for vertical flow, which may not be true for a 40° deviation, and a different set of equations should be used. This is not accounted for when using the Ding correction. High deviation flow regimes are covered in Chapter 6.

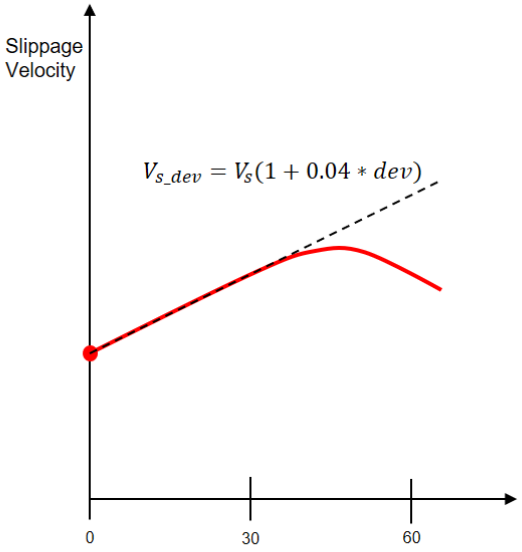

Fig. 5.C.6 – Ding Correction

Other experimental and mechanistic correlations were developed for a range of pipe deviations, with some including horizontal wells (90°). These include Petalas and Aziz, Kaya, Artep, Stanford Drift Flux, Beggs and Brill, etc.

Figure 5.C.7 shows the flow regime map proposed by Beggs and Brill for liquid-gas horizontal flow. The axes are defined by the Froude number (N_{Fr}) and the Input Liquid content (λ_l):

$$N_{Fr} = \frac{{v_m}^2}{g\,d} \qquad \lambda_l = \frac{q_l}{q_l+q_g}$$

In the case of the Beggs and Brill correlation, a single holdup equation is used for all the flow regimes. This assumes the pipe is horizontal. However, the empirical coefficients (a, b, and c) depend on the flow pattern:

$$H_{l(0)} = \frac{a\,{\lambda_l}^b}{{N_{Fr}}^c}$$

The holdup is corrected for the pipe deviation using a factor Ψ (function of the deviation and other empirical factors):

$$H_{l(\theta)} = H_{l(0)}\,\Psi$$

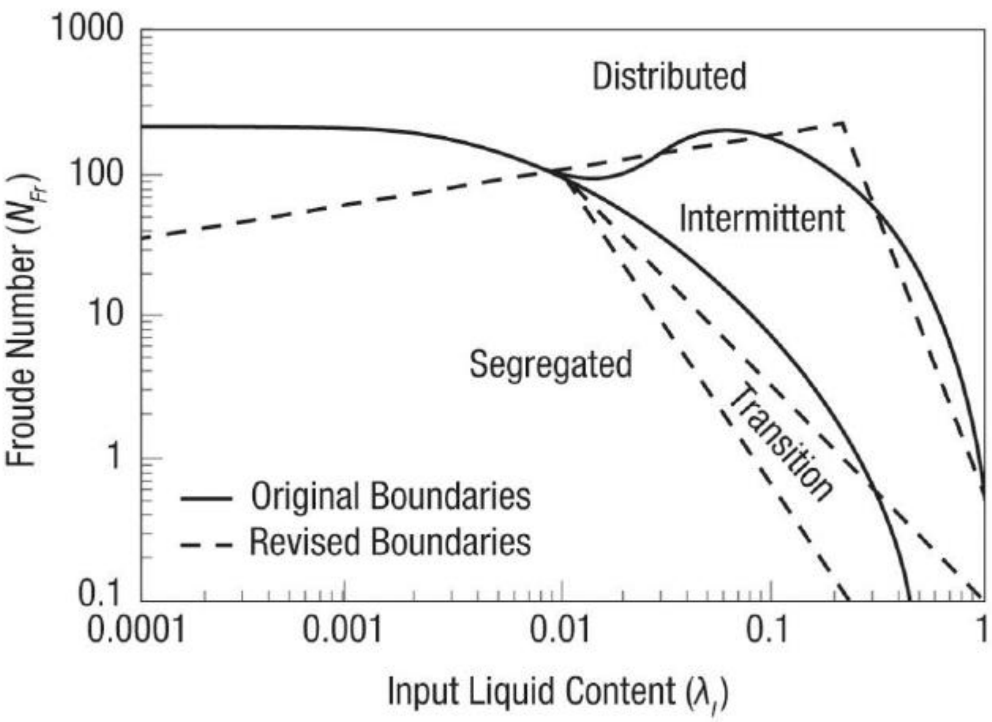

Fig. 5.C.7 – Beggs and Brill flow map – JPT (May 1973), 607-617

The Beggs and Brill correlation was specifically developed for deviations between 45° and 90°.

This section showed two different ways to handle deviation. As mentioned earlier in this chapter, for separated flow regimes (i.e., segregated, stratified), a completely different approach is used, as explained in Chapter 6.

5.C.5 Three-phase correlations

There are very few 3-phase correlations, and when they exist, they are for a very specific situation, e.g., stratified 3-phase flow (Zhang). In practice, 3-phase slippage/holdup prediction from rates is done using two 2-phase models, known as '3-Phase L-G'. The 2-phase flow equations are applied twice, first for the liquid phase (between oil and water) and second between the liquid and gas.

The analyst must evaluate whether the downhole condition is truly 3-phase, or if it can be considered as a 2-phase system. For example, the gas may evolve from the solution above the perforated interval, and therefore the PL calculations should not consider the slippage between the liquid and gas.

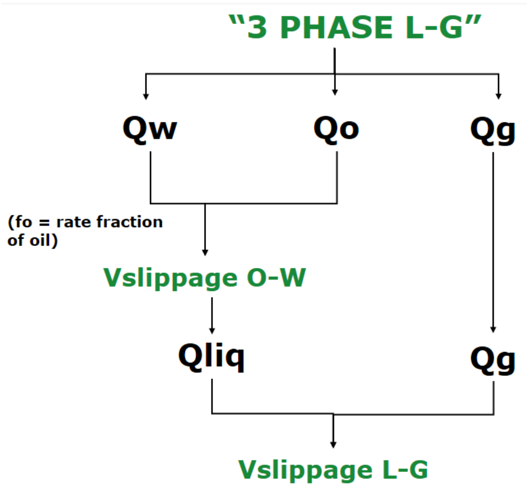

Fig. 5.C.8 – 3-Phase Liquid-Gas model

5.C.6 Liquid loading

A common but serious multiphase problem is when gas wells start to produce water. As the mixture density increases, so does the bottomhole flowing pressure. This reduces the well's drawdown, and at a certain point the gas may not have enough energy to lift the water, which will ultimately kill the well.

From Newton's Second Law, a particle in force equilibrium is not accelerating. In this case, the particle is a droplet of water, which is subject to its weight force and the drag from moving gas. If these two forces are balanced, the water droplet will fall at a certain 'terminal' velocity.

Turner proposed that if the gas velocity is equal to the terminal velocity, then the gas would just lift the water and prevent liquid accumulation.

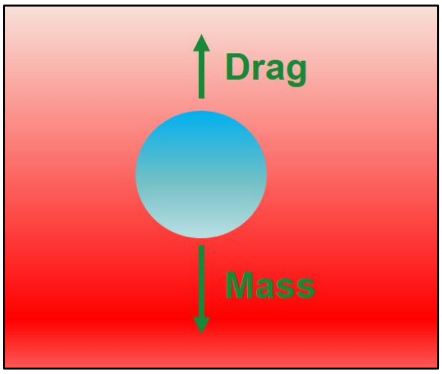

Fig. 5.C.9 – Force balance in a water droplet

A simple force balance shows that the terminal velocity, also known as Turner velocity, can be calculated as:

$$V_t = \frac{1.3 * C * \sigma^{0.25} \, (\rho_L - \rho_g)^{0.25}}{{C_d}^{0.25} * {\rho_g}^{0.5}}$$

This equation is a function of the liquid and gas density difference ($\rho_L - \rho_g$), interfacial tension (σ), and drag coefficient (C_d) taken as 0.44. *C* is an adjustment factor, which Turner set to 1.2, while Coleman used 1.0. Other studies (i.e., Whitson et al.) have focused on Condensate accumulation, and similar expressions as the one above have been developed, incorporating the condensate density and different empirical factors.

In production logging interpretation, comparing the measured velocity by the flowmeter with the Turner velocity (other correlations exist) indicates the capacity of the flow to lift the water. This may be recirculating, resulting in a complex spinner behavior that may be misleading and confused with crossflow.

5.D Multiphase Profiling

In this section, the slippage velocity predictions are at the service of the analyst for computing a multiphase profile.

5.D.1 Simplified rate calculation

The rate calculation for a generic 2-phase flow (water-oil, water-gas, or oil-gas) follows. This is **not** the approach used in the software calculation engine, where non-linear regression is used. However, the deterministic approach is described here, whose value is to explain the concepts in a simple situation and introduce the basic notions / presentations used in the general case. Recalling the definitions from Section 5.A and using the subscript 'h' for heavy and 'l' for light, the following equations can be written as:

$$Y_h + Y_l = 1 \qquad\qquad Q_h + Q_l = Q_t$$

$$v_s = v_l - v_h = \frac{Q_l}{A\,Y_l} - \frac{Q_h}{A\,Y_h} = \frac{Q_t - Q_h}{A\,(1 - Y_h)} - \frac{Q_h}{A\,Y_h}\,.$$

Solving for the heavy phase rate (Q_h) gives: $Q_h = Y_h\,[Q_t - (1 - Y_h)\,V_s\,A]$

This equation shows that the Q_H can be obtained from measured values, like the water holdup (Y_H) and total rate (Vm*A). The only other variable is the slippage velocity, which is obtained using a multiphase correlation. Assuming a flow regime, then the slippage is calculated analytically using a simple equation like shown for Choquette or Nicolas.

The light phase rate can be obtained as: $Q_l = Q_t - Q_h$

As explained in Chapter 4, holdup is a quantity that can be measured directly or inferred from density. If a mixture density is measured and the individual phase densities downhole are known, holdup can be obtained as shown below:

$$\rho = \rho_h\,Y_h + \rho_l\,Y_l \qquad \Rightarrow \qquad Y_H = \frac{\rho - \rho_l}{\rho_h - \rho_l}$$

Note that when density is measured with a gradiomanometer, the reading needs to be corrected for friction. This correction requires knowledge of velocity and the fluid properties, as in a single phase case, such calculations will necessitate an iterative solution scheme.

With an estimate of the slippage, spinner-based fluid velocity, and density measurement, the steps of a manual deterministic approach are straightforward. The rate at any depth is determined as:

(1) Estimate Q_T from V_{APP} and VPCF = 0.83

(2) Estimate Y_H from ρ and ρ_h and ρ_h. Iterate for frictions and VPCF as desired

(3) Get Vs from a multiphase correlation

(4) Estimate Q_H and thus Q_L

This deterministic approach has multiple limitations for modern, real-life interpretations, including:

- The flow regime is, in general, not known, and its determination through flow regime maps is based on the rates (or velocities) of both phases, which is the unknown.

- If two fluid identification tools are present in the toolstring, they are likely to provide different results as they are based on different physical principles. With the deterministic approach, the problem would be over-specified.
- The apparent fluid velocity is transformed to mixture velocity using the VPCF, which is the function of the Reynolds number, thus the mixture velocity itself (unknown).
- Tools like the gradiomanometer or the pseudo-density require friction corrections, which are a function of the density itself and the fluid velocity
- It is not possible to add measurements like temperature, which require an integral (or global) computation

For these reasons, an error minimization approach is used to compute the rates.

5.D.2 General (actual) solution

At any depth in the well, the PL measurements (i.e., fluid velocity, density, capacitance, etc.) can be simulated if the rates and holdups are known. For the generic 3-phase flow problem, this is: Q_w, Q_o, Q_g, Y_w, Y_o, Y_g. Since the sum of the three holdups is equal to 1, one holdup can be dropped.

Fortunately, an extra source of input is available: multiphase correlations. These provide the holdups directly, or are computed from the slippage as shown in Section 5.A. With this input, the PL measurements at any depth can be simulated if the three rates are known: Q_w, Q_o, Q_g. Quantifying these rates is the reason why a PL is run in the first place, so these are unknown when starting the interpretation. Therefore, an error minimization scheme is applied, as the rates that serve as inputs of the models are unknown.

Consider the case of nodal analysis. When calculating a pressure traverse, at any depth, the rates are known by taking the surface rates to downhole conditions using the formation volume factor and considering possible phase changes (gas coming out of solution, condensate dropout). Still, a loop is needed since the PVT properties are functions of pressure and temperature, which are not known before calculating the variables at the specific node. As the rates are known, the multiphase correlation calculates the holdups for the specific flow regime, and from these, the phase velocities and densities can be computed. This can be considered as a forward approach.

In PL interpretation, the rates at any depth are unknown, but the density and fluid velocity are measured. These are matching variables and called ‘Velocity match’ and ‘Density match’ as shown in Figure 5.D.1. As in single phase, the suggested workflow relies on using non-linear regression to find the rates that minimize an objective function defined by the error between the target measurements (match variables) and the simulated equivalent. In this figure, for instance, all that is required is a forward model that from an assumption of the rates Q_H and Q_L calculates the simulated V_{APP} and density. The measured pressure and temperature, in this case, are interpretation inputs needed to compute the PVT properties but are not matching variables. These, together with the density, are shown in the track on the right.

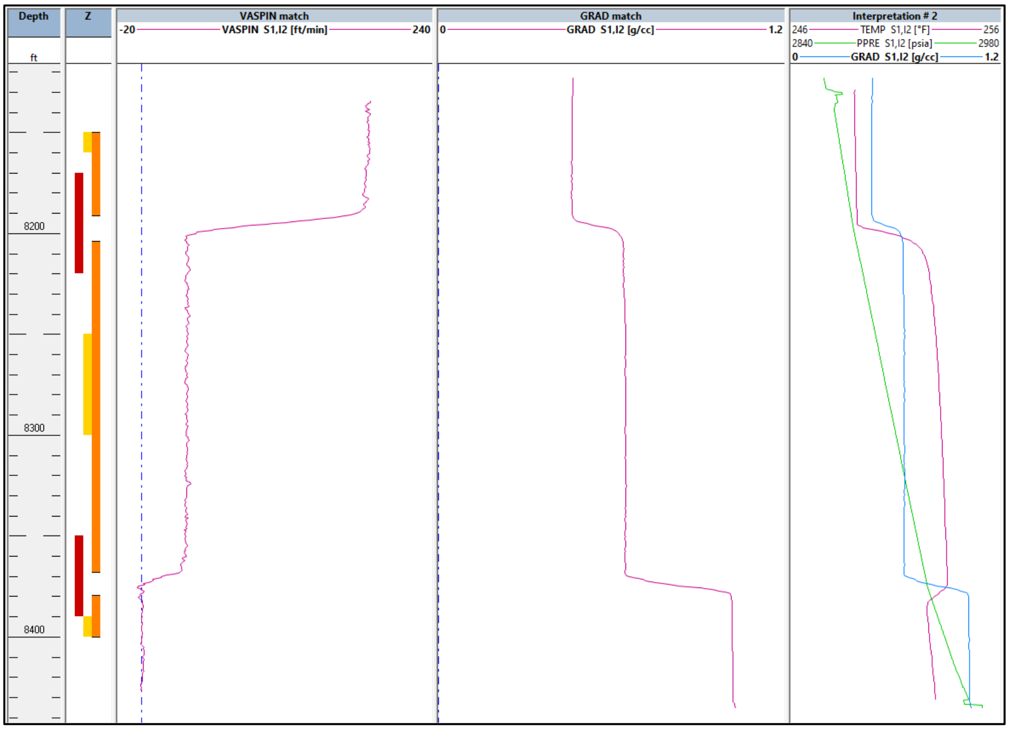

Fig. 5.D.1 – Target measurements for rates computation

In a general situation, the steps are as follows:

(1) From the rates, the fluid, and the local geometry, get the slip velocities

(2) From the slip velocities and the rates get the holdups

(3) From the holdups calculate the fluid mixture properties

(4) Calculate the simulated tool response using the relevant model (i.e., VPCF, friction equations, capacitance charts, etc.).

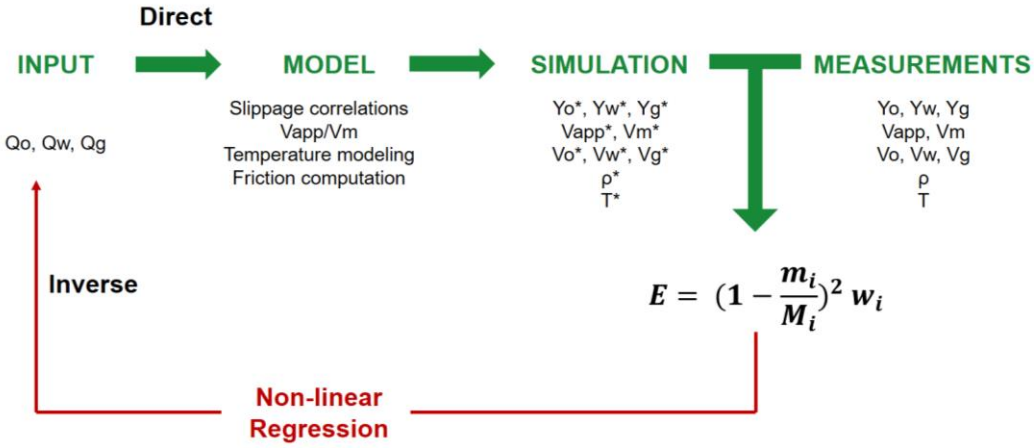

Fig. 5.D.2 – Methodology using non-linear regression

The interest of this approach is that any number and type of measurements can be identified as targets, providing they are sufficient, and the problem is not undetermined (insufficient measurements for the number of unknowns). Redundant measurements occur when the regression tries to find a compromise based on the confidence assigned by the user to the different measurements.

Below is the typical presentation of results after defining the fluid properties and the input variables shown in Figure 5.D.1. The velocity and density match views compare the target (red) and simulated (green) measurements. The simulated curves are obtained by feeding the known rates at every depth into the forward model, including, in particular, the slip correlation. The simulated curves and the QZT logs are referred to as schematics in Emeraude.

The QZI track represents contributions or injections which are obtained by the difference in rates above and below an inflow and applying a mass balance (Section 3.D.1.b). The Q track represents the application of the non-linear regression at every depth frame.

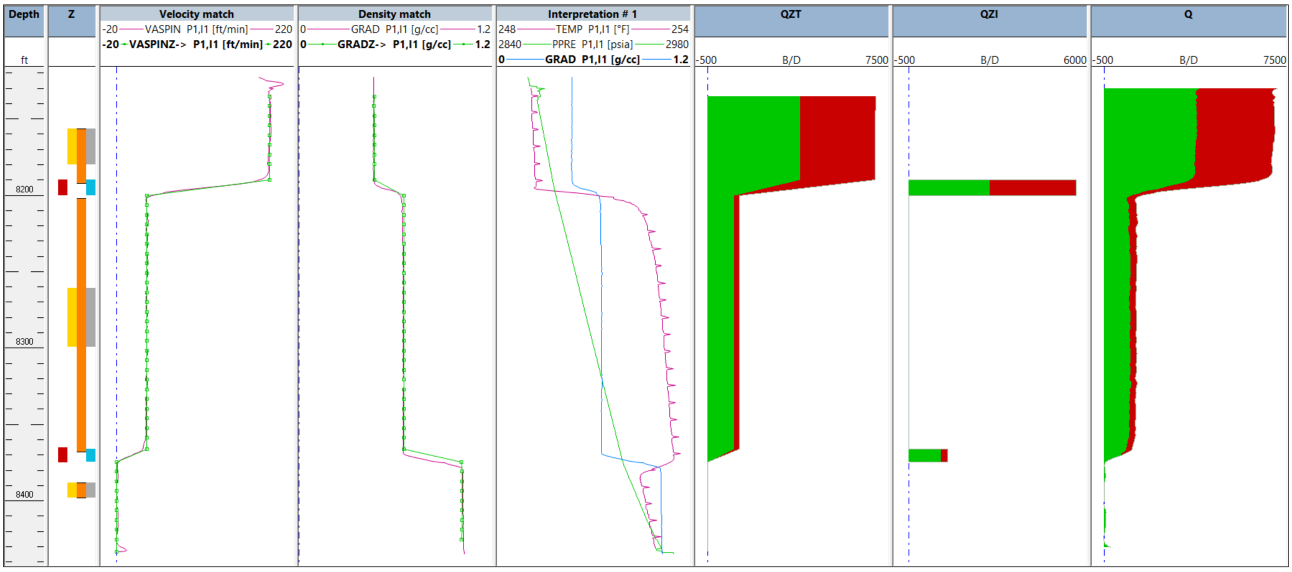

Fig. 5.D.3 – Typical multiphase result; Zoned approach

It is important to realize in the above procedure that slippage correlations are a necessary evil to relate the rates to holdups because holdups are the best measured quantities. When PL can measure phase rates or phase velocities directly, the Holy Grail of Production Logging, the procedure can do away with slippage correlations.

Multiphase PL interpretation by means of an error minimization scheme can take a few different branches, defined by the data used for matching, and how Emeraude treats the slippage estimate. The analyst may define zones of stable data above and below the inflow intervals, which is known as the Zoned approach. In this context, the error minimization may be local (inside calculation zones) or global (all inflows). The Zoned approach is described in Sections 5.D.4 and 5.D.5. The other option is to apply the regression everywhere, using the Continuous approach. This is explained in Section 5.D.6.

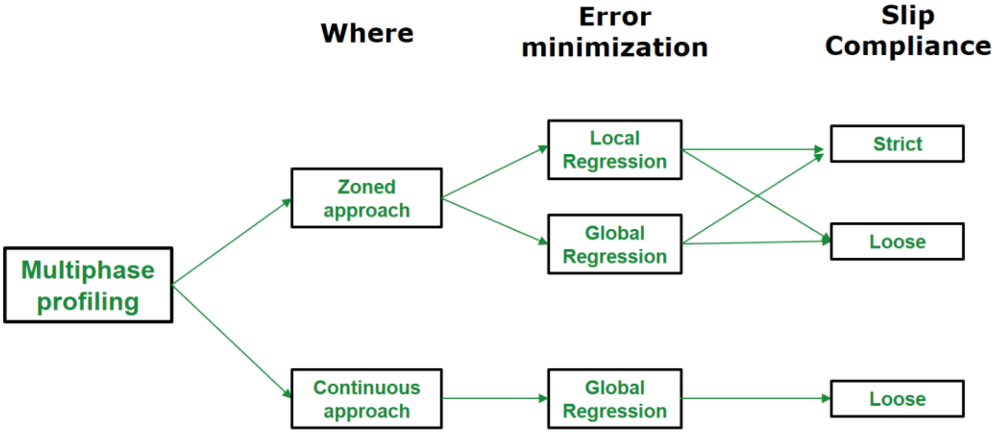

Fig. 5.D.4 – Multiphase PL approaches

5.D.3 Graphical presentation

A graphical presentation, albeit based on a 2-phase analogy, can help illustrate some of the previous concepts and compare different correlations.

For a given mixture rate Q, consider the possible mixture and plot the corresponding mixture density. The X axis value range from 0 (100% Light phase) to Q (100 % Heavy phase). The density at the end points is the relevant single phase density. The equation derived previously for Q_H is now used to express Y_H:

$$Y_h = \frac{Q_h}{[Q_t - (1 - Y_h)\, v_s\, A]}$$

This equation shows that without slippage, the heavy phase holdup would be equal to the heavy phase cut. This situation is represented by the red line in Figure 5.D.5. With slippage velocity, Vs is positive uphill; hence the equation above shows that Y_H should be higher than the cut. The curve representing the case with slippage is above the no-slip line. An opposite situation would be expected downhill.

Another way of considering the plot below is to realize that for a given cut, the higher the slippage, the heavier the mixture. This is because the light phase is going faster and occupies less volume in the pipe. The light phase is 'holding up' the heavy phase, leading to a heavier phase present at any depth than there would be with no slippage. For a given solution with slippage, the density will read heavier than if there is no slip.

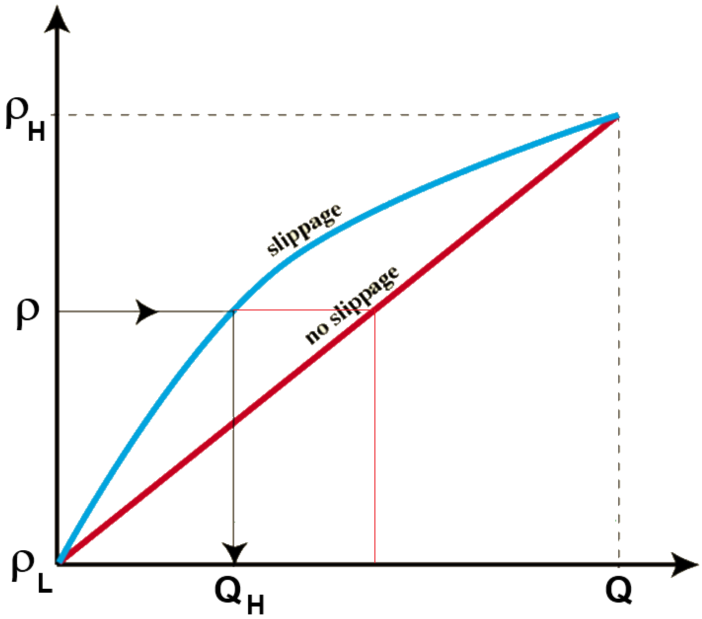

Fig. 5.D.5 – Density vs. heavy phase rate with and without slippage

Another point of view to understand this plot: with a density measurement, the solution (determined by the non-linear regression) is seen graphically by interpolating the relevant curve for this density value.

5.D.4 Emeraude Zoned approach and the Zone Rates plot

The simplest interpretation method in Emeraude, the Zoned approach, amounts to using the regression described previously on a set of user-defined calculation zones. As in single phase, the zones are selected in the stable intervals above and below the inflow zones.

The flow profile shown in Figure 5.D.3 was obtained through the Zoned approach. In this vertical oil-gas producer, three different calculation zones (grey) were selected to isolate the contributions of the two perforations (red). The non-linear regression described previously was executed on all three calculation zones to get Qo, and Qg. In the bottom zone, the rate was set to 0 and water holdup to 1. In the other zones there are only two measurements (spinner, and density) and Qw=0 is imposed, so the regression is only solved for Qo and Qg. The results are summarized by the QZT track, where the value of a given calculation zone is extended up to the inflow zone above and down to the inflow below.

For each zone, an error function is defined, consisting of the difference between the measurement (red curves in Figure 5.D.3) and the simulation (green curves). In this case, the two measurements are the spinner apparent fluid velocity and density. Thus:

$$Error = W_1 * (Dens_{sim} - Dens_{mes})^2 + W_2 * (Vapp_{sim} - Vapp_{mes})^2$$

Each term of the error function is called a 'residual,' and a weighting factor can be applied.

From an initial guess of the rates, density and apparent velocity are simulated, and the error is computed. The error function is minimized using a gradient technique (i.e., Newton-Raphson, Levenberg-Marquardt), working with the partial derivatives of the error with respect to the measurements ($\frac{\partial E}{\partial l_k}$). The rates shown for each rate calculation zone are the ones that minimize the Error function.

For each rate calculation zone, Emeraude shows the regression results as in Figure 5.D.6. For the gas-oil case presented in Figure 5.D.3, the average along the zone of the measured and simulated apparent velocity and density are reported, together with their residual. Also, on the top of the image, the rates at downhole and surface conditions are shown, along with the holdup, flow regime, and slippage velocity estimation by the selected multiphase flow correlation:

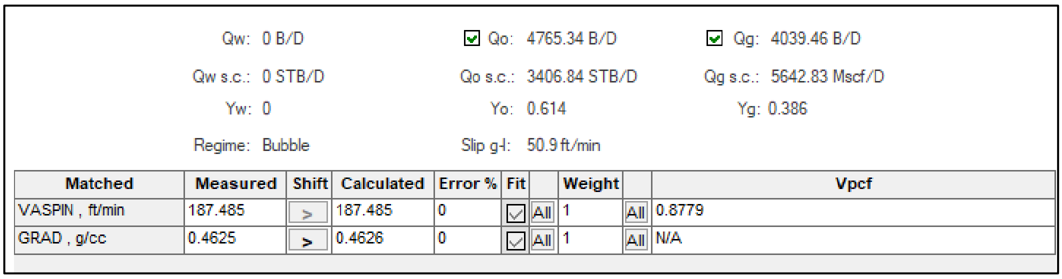

Qw: 0 B/D
☑ Qo: 4765.34 B/D
☑ Qg: 4039.46 B/D
Qw s.c.: 0 STB/D
Qo s.c.: 3406.84 STB/D
Qg s.c.: 5642.83 Mscf/D
Yw: 0
Yo: 0.614
Yg: 0.386
Regime: Bubble
Slip g-l: 50.9 ft/min

Matched	Measured	Shift	Calculated	Error %	Fit		Weight		Vpcf
VASPIN , ft/min	187.485	>	187.485	0	☑	All	1	All	0.8779
GRAD , g/cc	0.4625	>	0.4626	0	☑	All	1	All	N/A

Fig. 5.D.6 – Results of the error minimization for a rate calculation zone

Another way to view the results is graphically in the Zone Rates plot schematically explained in Figure 5.D.5. The Y-scale displays density or holdups as relevant. Below is an illustration of a 2-phase oil-gas situation with spinner and density. The dashed line represents the measured density. The current solution is such that for the selected correlation (Duns and Ros) the predicted density value (horizontal dotted line) is similar to the measured one (horizontal dashed line).

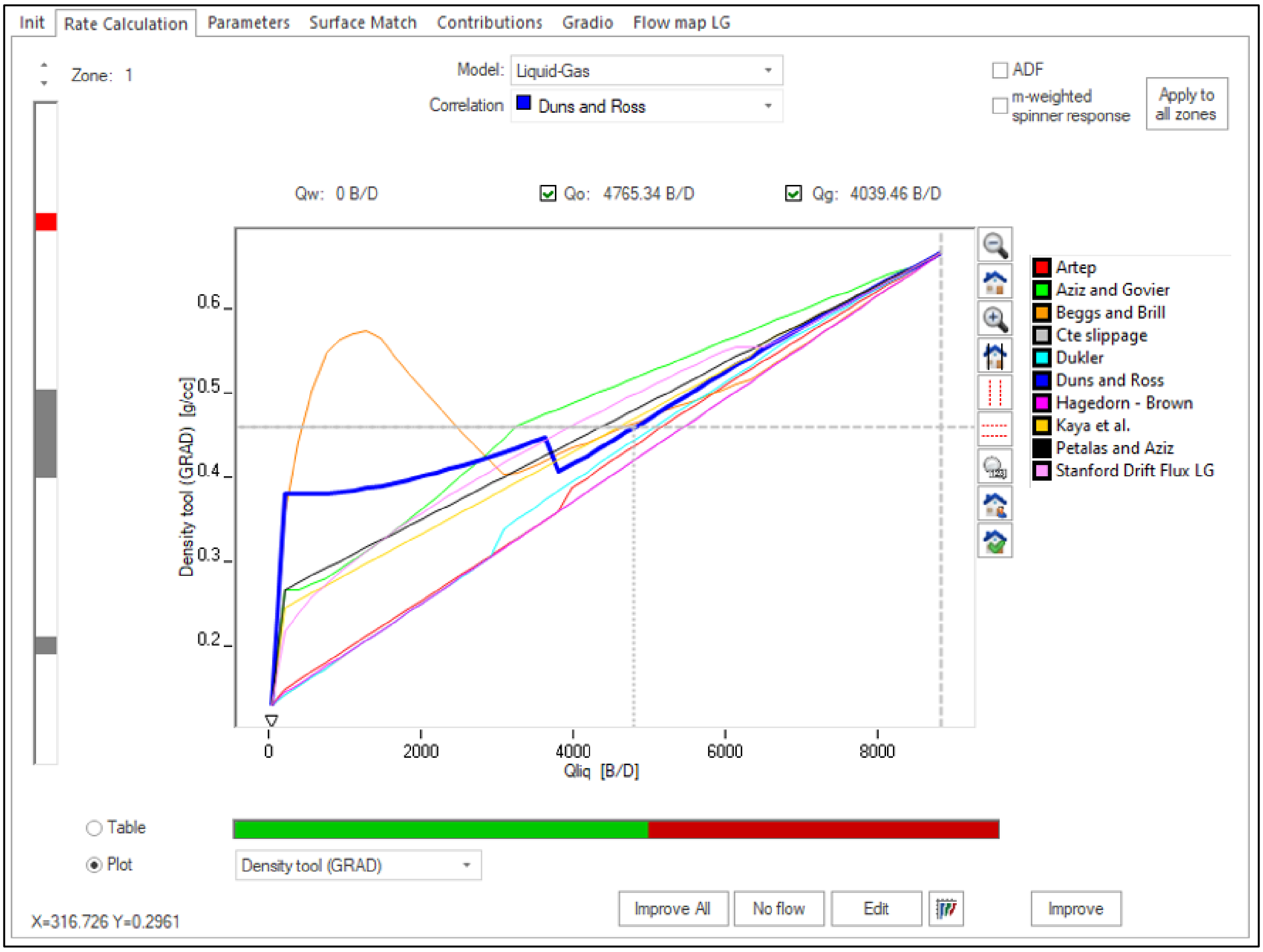

Zone: 1

Model: Liquid-Gas

Correlation: Duns and Ross

Qw: 0 B/D ☑ Qo: 4765.34 B/D ☑ Qg: 4039.46 B/D

Plot: Density tool (GRAD)

X=316.726 Y=0.2961

Fig. 5.D.7 – Emeraude Zone Rates plot

Each colored line represents a different correlation. Instead of the smooth curve shown in Figure 5.D.5, most correlations show discontinuities, changes of slope, shapes, etc. This is due to the different flow regimes predicted for the plotted density range. Note that the correlation shown in yellow (Beggs and Brill) is cut by the density three times. By using an error minimization approach, there is a risk of falling in a local minimum instead of the global minimum.

For each rate calculation zone, the flow regime map predicted by the different correlations is displayed, with the superficial velocities in the axes. A gray line shows the points that satisfy the spinner-based mixture velocity: $V_{SH} + V_{SL} = V_M$.

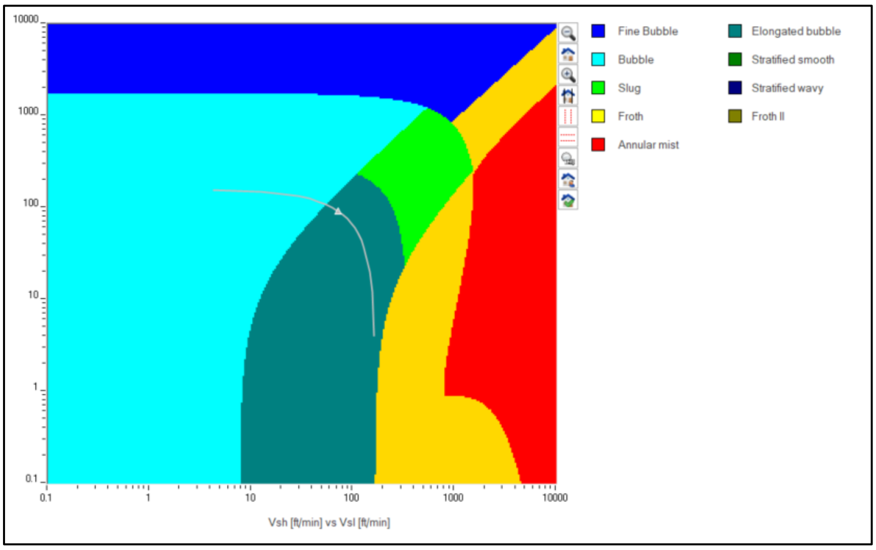

Fig. 5.D.8 – Petalas & Aziz Flow Map for a rate calculation zone

As done previously, one way to look at the Zone Rates plot is to consider how different the rate solution will be depending on the selected correlation. The rationale behind a proper selection is to start by ruling out the correlations developed for situations not applicable to the particular test. Beyond this first elimination, check which correlation is the most consistent with additional information, surface rates in particular. This selection is a very important step of the analysis and should be noted and justified. Software defaults will not be a sufficient excuse.

Computing the oil rate with the extreme case correlations of Figure 5.D.8 (maximum: Aziz and Govier, minimum: Stanford Drift Flux LG) would result in an oil rate difference of 1500 B/D. This is partly explained by the fact that the available correlations identified different flow regimes for the same flow condition. For oil-water wells, especially in low deviations, these differences are negligible, as the correlations consider mainly bubble flow. The image below is for the upper rate calculation zone of Figure 5.A.2, where, excluding the constant slippage line, the maximum water rate difference is 70 B/D, for a total rate of 4900 B/D of liquid. Most of the displayed correlations are smooth as in Figure 5.D.5, due to the lack of flow regime transitions.

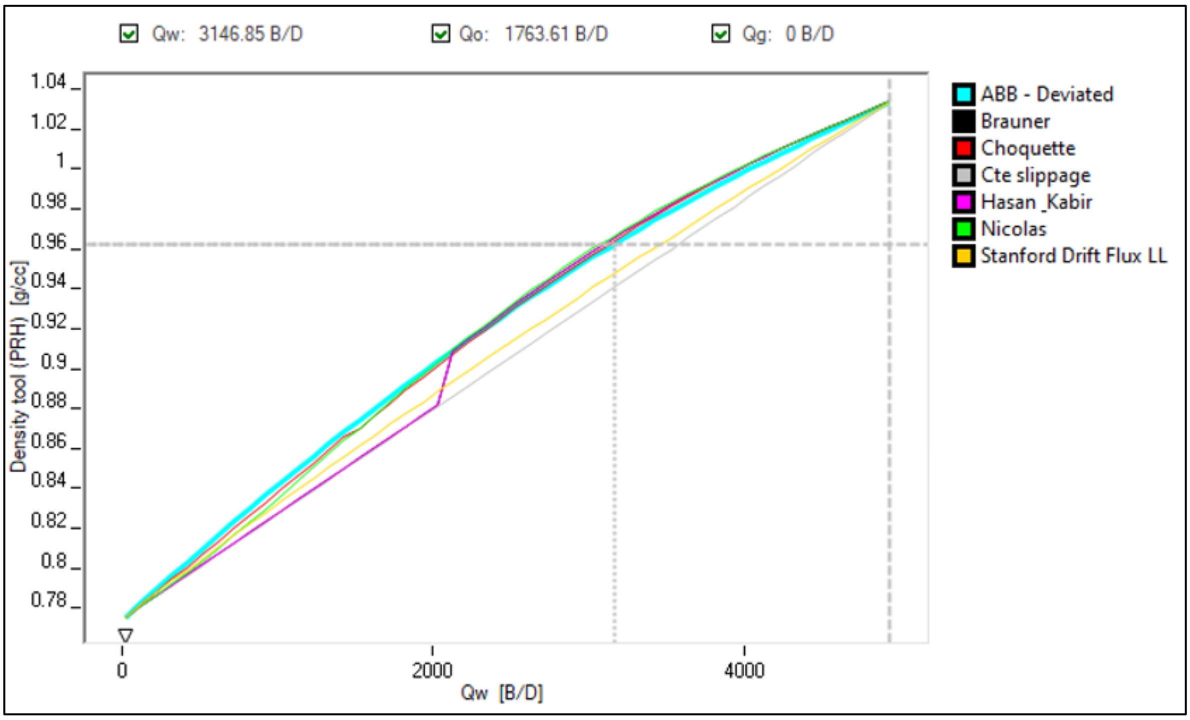

Fig. 5.D.9 – Water-Oil solutions.

5.D.5 Zoned Approach and Global Regression

As a summary of the Zoned approach, for each rate calculation zone, a non-linear regression is executed, and the rates are calculated only in these intervals. The contributions per inflow zone are obtained by the difference of rates above and below each zone. As explained for single phase flow in Chapter 3, a mass balance is applied by default to account for volume changes between zones (expansion or compression). By proceeding this way, there is no guarantee that in the end, the contributions of a given zone will be of the same sign. For example, the image below shows the contributions for multiple inflow zones obtained by the Zoned approach. For the top perforation, water is injected while oil and gas are produced. These ‘downhole separators’ are not physically possible and are a result of the calculation method:

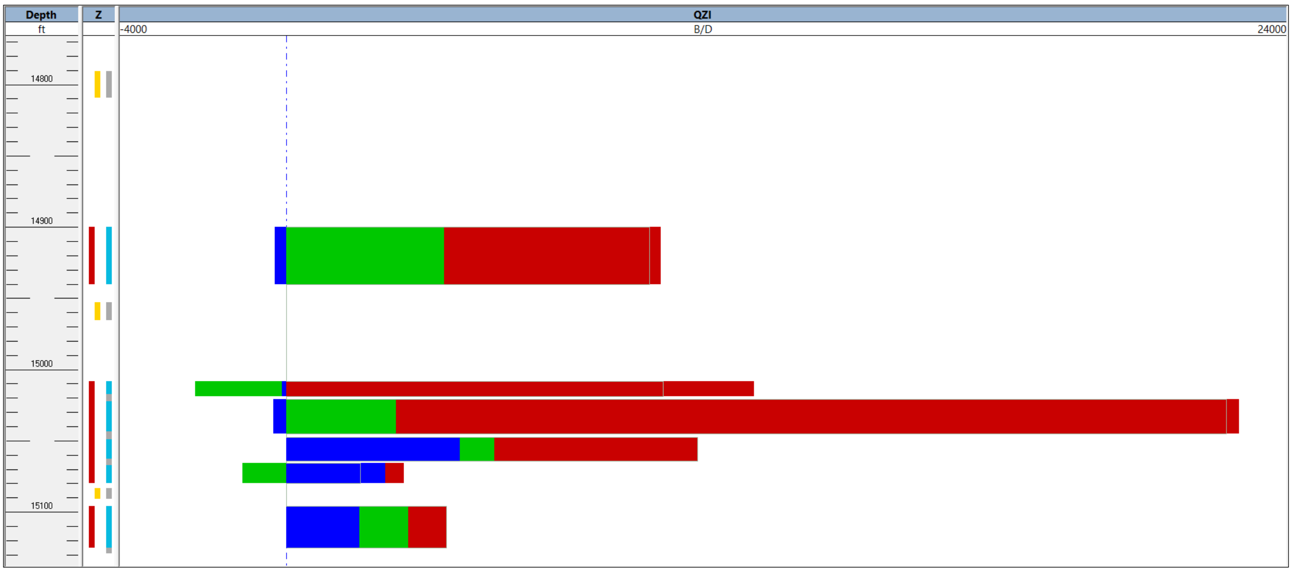

Fig. 5.D.10 – Typical multiphase result; Zoned approach

To avoid this, solve for the entire well with a single global regression, where the unknowns are the zone contributions, dQ's. Since the contributions are the direct unknowns, a sign constraint can be imposed upfront. For each iteration, the assumption of the dQ's translates into a series of Q's on the calculation zones, which can be injected into the forward model to calculate the objective function. Here again, the objective function is evaluated on the calculation zones only; and to this error, other components might be added, such as a constraint using the surface rates.

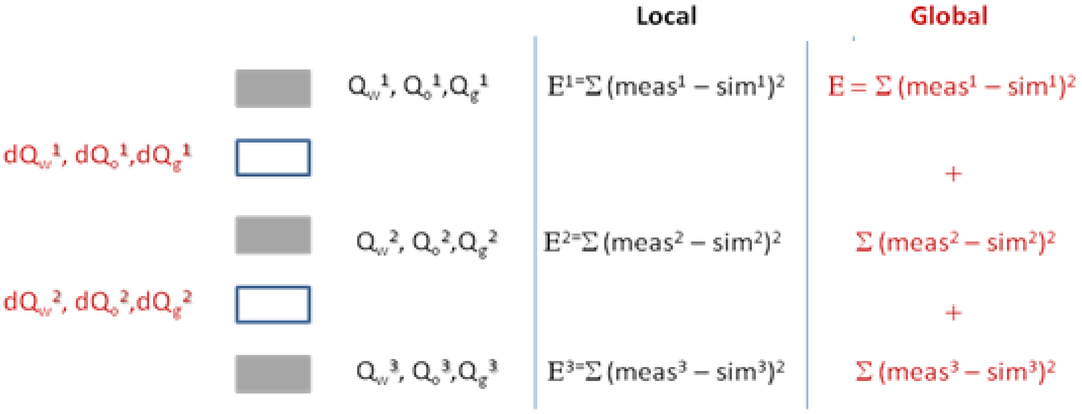

Fig. 5.D.11 – Local vs. global regression

Note that whether the regression is local or global, the end result is influenced by the solution on the few user-defined calculation zones. This is why the approach is called the 'Zoned' approach.

5.D.5.a Slippage compliance and Zoned method

In multiphase calculations using the Zoned approach, the simulated holdups are derived from the local rates and the selected slippage correlations. Two different treatments are offered in Emeraude when using the Zoned method:

- Strict compliance: The error is minimized between the simulation and measurements. The simulated holdups come directly from the slippage correlations.
- Loose compliance: The holdups can depart from the slippage correlation prediction to be closer to the measurements. This is done by including the slippage velocity as an extra term in the error minimization process (more on this in the next section).

It is up to the user to select the slip compliance approach to be applied in a particular interpretation. The decision will be based, among other reasons, on the confidence in a given correlation to predict the expected holdups in a particular flow regime.

5.D.6 The Continuous approach

The clear advantage of the Zoned approach is speed since only a few points are required to get an answer, even if the Global regression is run. Its main drawback is that the choice of calculation zones drives the results. A way to remove this dependency is to run a Global regression with the errors evaluated *everywhere* on the logs, and not only at a few points. This can be done, for instance, by minimizing the difference between the data and the simulated measurement logs (the schematics) everywhere. However, the match views show that the schematics are square in shape. This is because between inflow zones, the mass rate does not change and, if using strict slippage compliance, there are little variations in holdups and deduced properties.

The only way to account for changes seen in the data is to let the holdups differ from the model prediction, as described previously for the loose slip compliance. With the Continuous approach, the Global regression can be modified as follows:

- The **main regression loop** is still **on the contributions,** but the objective function considers an error on the log points.
- At each depth, the simulated log values are evaluated by running a second **regression on the holdups** to minimize an error made on the difference between simulated and measured values and, at the same time, a new constraint using the slip model holdup predictions. In cases where one can do without the slip model, this new constraint is not included.

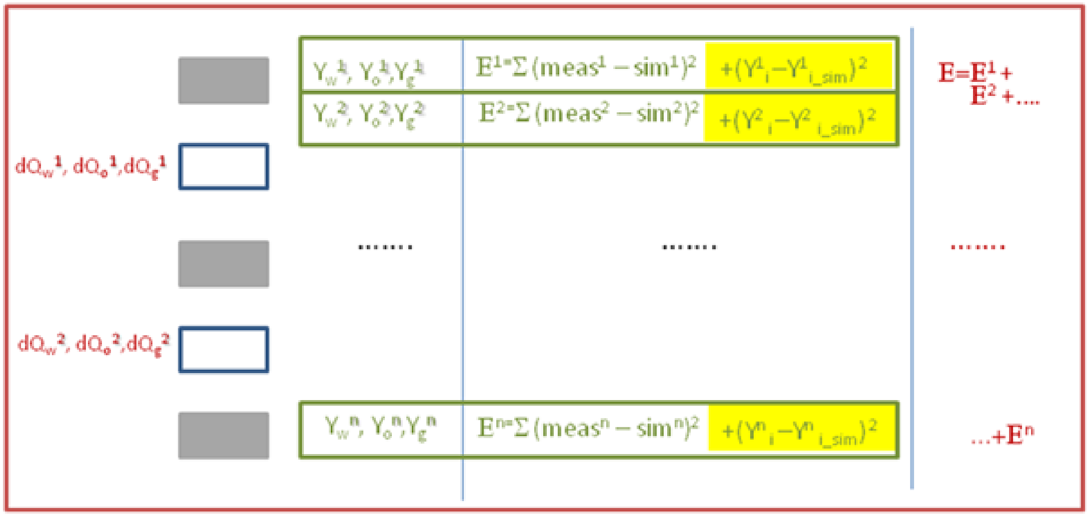

Fig. 5.D.12 – Global regression in Continuous mode

5.D.6.a Illustration with a 3-Phase example

The Fig. below shows the result of the Zoned approach on a 3-phase example. The calculation zones (grey) are defined. Observe how the second perforation has been split. Local regressions have been run, followed by a Global regression with the constraint that all contributions are ≥ 0. Without running the Global regression, the contributions would look like Figure 5.D.9.

Along the bottom two perforations, the match on the density and gas holdup is not perfect. With 3 independent holdup measurements, the problem is overspecified. Unless all three are perfectly consistent and indicate the same holdup distribution, the final solution will find a compromise on the errors (residuals) of each measurement.

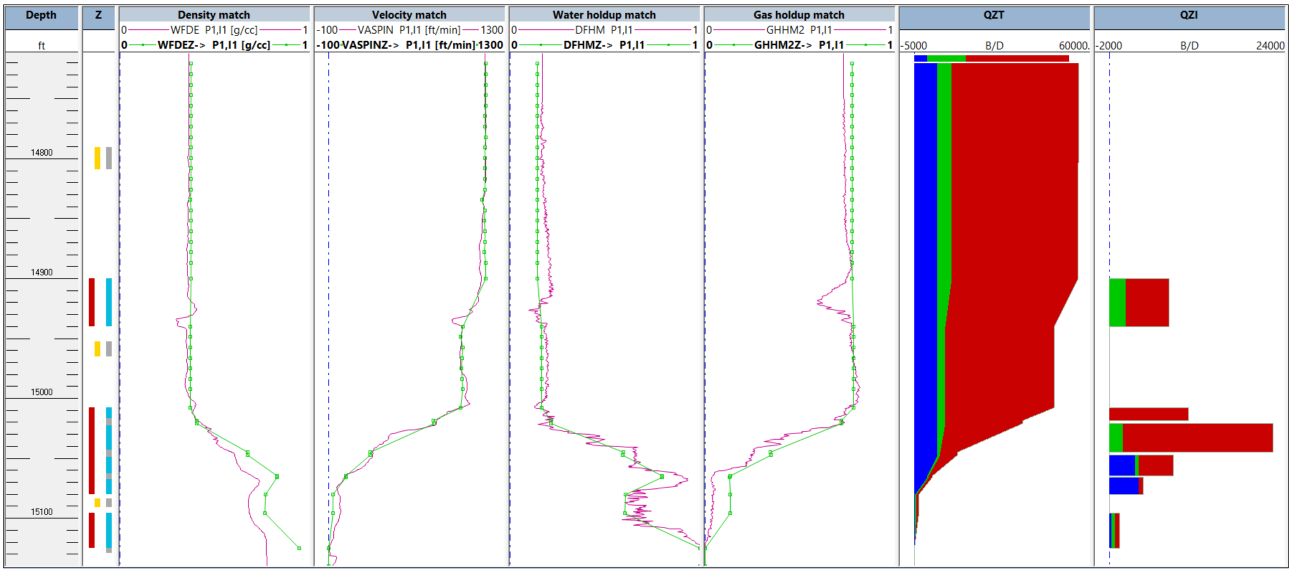

Fig. 5.D.13 – Example of Zoned approach results in Emeraude

This example is now interpreted with the continuous approach and the Global regression rerun. In the end, there are certain differences. The match looks better overall, but at the expense of not honoring the slip models. The deviation from the slip models is indicated in the rightmost track (line=model, markers=solution). *Note that the number of depth samples on the logs is user-defined.*

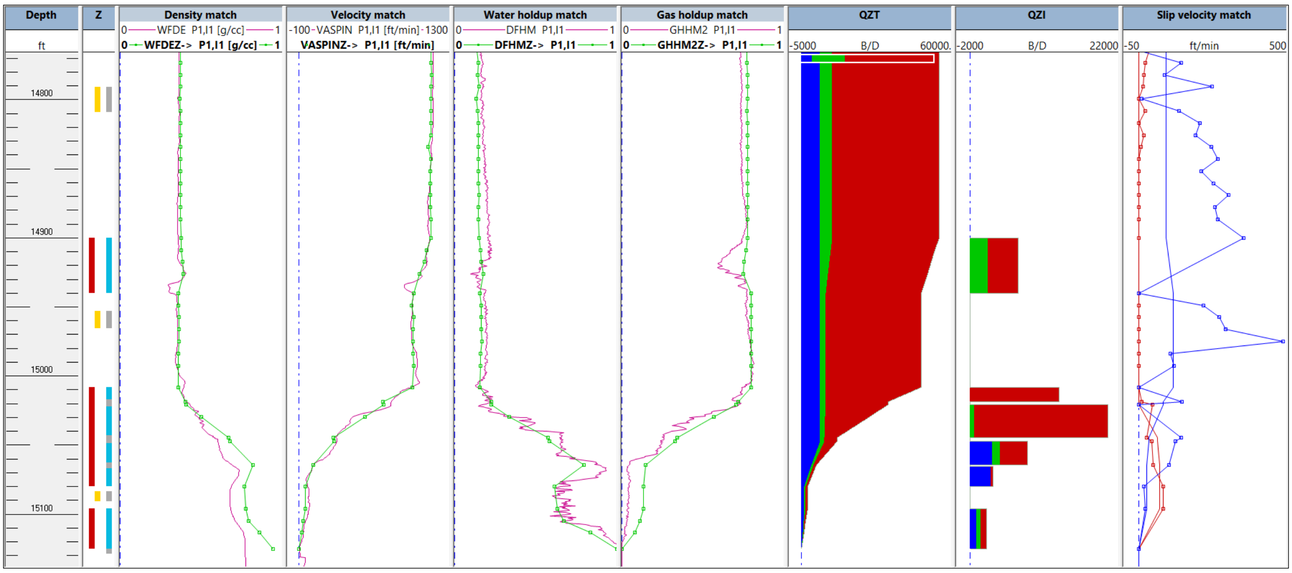

Fig. 5.D.14 – Example of continuous approach result in Emeraude

In the above example, there is no drastic benefit to use the Continuous method. But there are cases where the reverse will apply.

- When the data is unstable between contribution intervals, the location of the calculation zones may dangerously impact the Zoned method results. Note that the continuous method is also influenced by the location of the calculation zones *inside the inflows,* since the way the inflows are split has a direct influence on the shape of the simulated logs over the inflows.
- Another situation where the Continuous method is a better answer is when the temperature is incorporated into the rate calculation, as this measurement is essentially an integral response. Temperature calculation is only available with the Continuous method. In Emeraude, the two methods, Zoned and Continuous, are offered in parallel, and can be switched from one to the other at any stage.

It is important to stress that a nice-looking match does not necessarily mean a right answer. It all comes down to the interpreter’s judgment. All regressions are biased by the weights assigned to the various components of the objective function. Different weights, lead to different answers. The starting point is critical as a complex objective function admit local minima.

The Continuous approach is not a magical answer, and more complexity does not mean better. The Continuous approach is more computing-intensive and a bit of a black box.

5.D.7 Mass-weighted spinner response

Consider a spinner measuring in distributed 2-phase flow. From the mixture velocity, the total rate is obtained, which is the sum of the light and heavy phase rates:

$$Q_T = Q_H + Q_L$$

In terms of fluid velocities, the above equation can be expressed as:

$$V_M = Y_H * V_H + Y_L * V_L$$

This shows that the spinner response is a holdup-weighted function of the phase velocities. Whittaker et al. proposed using a mass-weighted response:

$$V_M = \frac{Y_H * \rho_H * V_H + Y_L * \rho_L * V_L}{Y_H * \rho_H + Y_L * \rho_L}$$

This model is applicable to bubble flow only and is relevant when a large density contrast exists between phases. As this model penalizes the lighter phase, which in bubble flow is always faster than the heavy phase, the calculated average velocity is smaller with the mass-weighted than the holdup-weighted model.

5.D.8 Limits of the conventional PL interpretation – Weighting

In every iteration of the non-linear regression, the measurements are modeled considering distributed flow. This is reflected, for example, in the holdup-weighted expressions of the mixture density and mixture velocity.

The log displayed in Figure 5.D.16 is from a 73° deviated well. A distributed water holdup tool is displayed as an image view and cross section view (detailed in Chapter 7). These images indicate stratification from the bottom of the log to the upper perforation. A cross section in the stratified region is shown on the right, with the inner circle representing the position of a centralized tool (density, spinner, etc.).

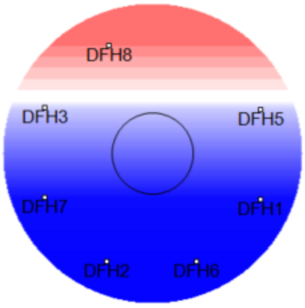

Fig. 5.D.15 – Example of continuous

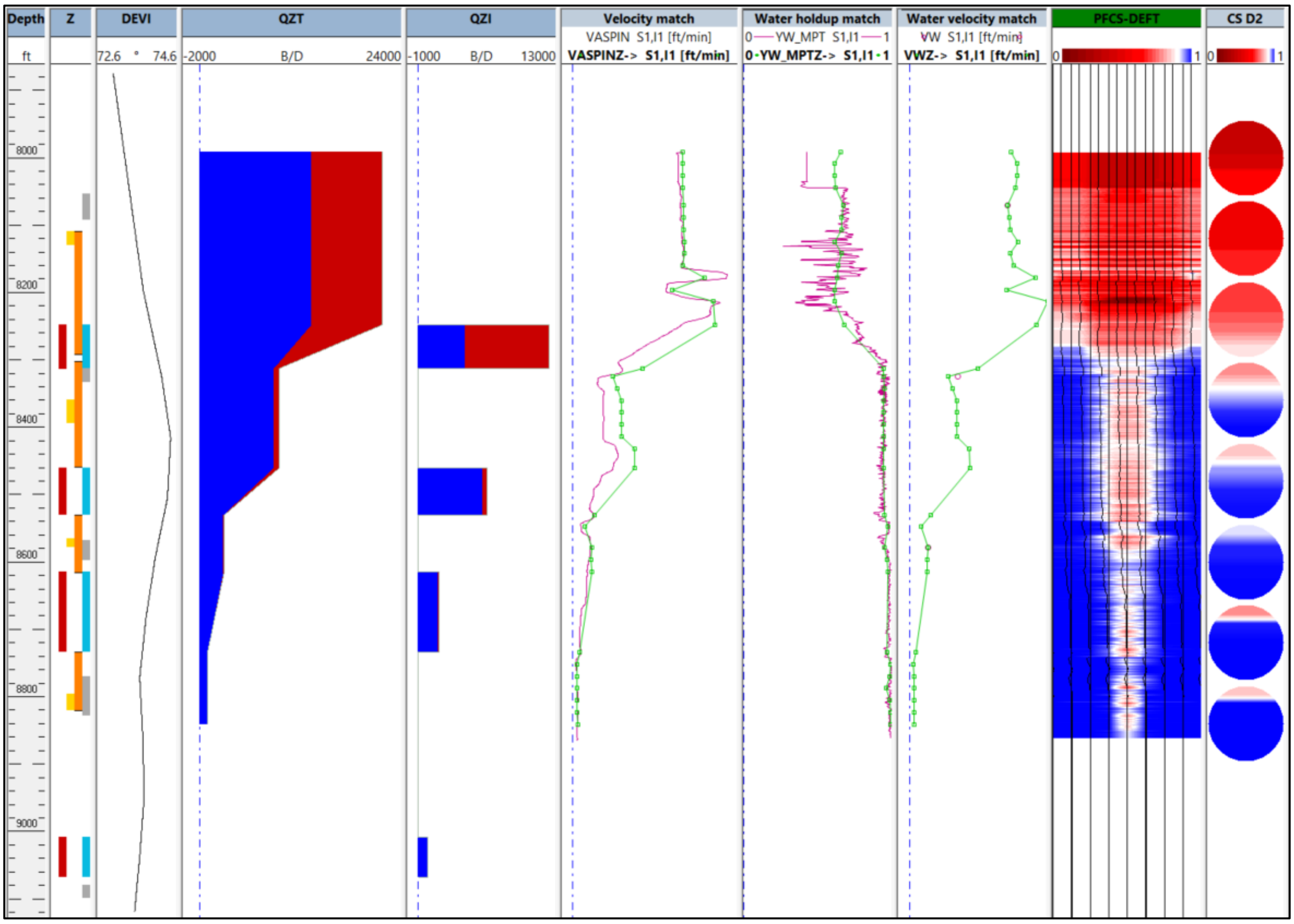

Fig. 5.D.16 – Example of continuous approach

It would be incorrect to assign the spinner-based apparent velocity as a mixture velocity (holdup or mass-weighted), knowing that the sensor is immersed in water. The same applies for other conventional centerline measurements.

The analyst must remember that even though correlations can predict stratified or segregated flows, the measurements will be modeled assuming the centralized tools measure average properties. In the error minimization process, a measurement immersed in water is compared with a simulated value assuming mixed flow. The resulting rate is not likely to be accurate. The actual procedure and tools for these types of flow regimes is the topic of the next chapter.

The interpretation displayed in Figure 5.D.16 incorporates stationary water velocity measurements obtained by the pulsed neutron, oxygen activation technique (Chapter 11). The analyst must ensure that the rate calculation zones encompass these measurements. The match between the measured water velocity stations (red points) and the model (green curve) is very good. However, the match on the apparent velocity is not. This is intended and controlled by the weighting of the different measurements. As the spinner velocity is considered not representative in the stratified region, but the water velocity measured through pulsed neutron is, the analyst decides to reduce the weight of the residuals for the apparent velocity in the rate calculations where stratified flow is seen.

Applying weights on different measurements is a mechanism followed by the analyst to demonstrate trust and reflect the limitations of the different sensors. The weighting is independent of the various zones. For example, deeper in the well, the water holdup may be higher than the capacitance limitation, so it may be liable to remove it from the regression and to put trust in the density. However, at a shallower depth, there may be no reason to disregard the capacitance, and this may receive the same weight as the density.

5.D.9 Non-uniqueness

A solution is reached when the errors (local or global) between the measurements and the model are minimized. There may be multiple models that can be adjusted to the data, which would result in different flow profiles.

As with any other cased hole log, the first step of the interpretation is data validation. This includes to check the quality of the various measurements, calibrate or normalize them accordingly, define the necessary well information and provide an accurate PVT description. If one of these steps is not done properly, the error will not propagate until the final results.

Even when all the necessary QC steps have been properly followed, as multiphase interpretations use correlations, and there is not a universal work that incorporates all pipe deviations, fluid and flow regime variables, the analyst selection will impact the final result. As an analogy with Pressure Transient Analysis, multiple models can be used to match the derivative, but the production forecast from the different models may considerably differ.

Figures 5.D.17 and 5.D.18 show two flow profiles obtained for the same input data (density, capacitance, and fluid velocity) but using two sets of correlations. Profile 1 was obtained using Dukler + Hasan and Kabir, while Profile 2 used Duns and Ros + Choquette. In both cases, the measurements are well matched by the model. However, there are some differences in the oil and gas rates from the upper two perforations. Fortunately, both interpretations indicate that the water comes from the mid perforation, as it is quite clear from the capacitance change. Note that the correlation selection does not affect the total downhole rates nor the percentage contribution of total rate (oil, gas, water) coming from the various intervals. However, the split of the total rate into the individual phase is affected.

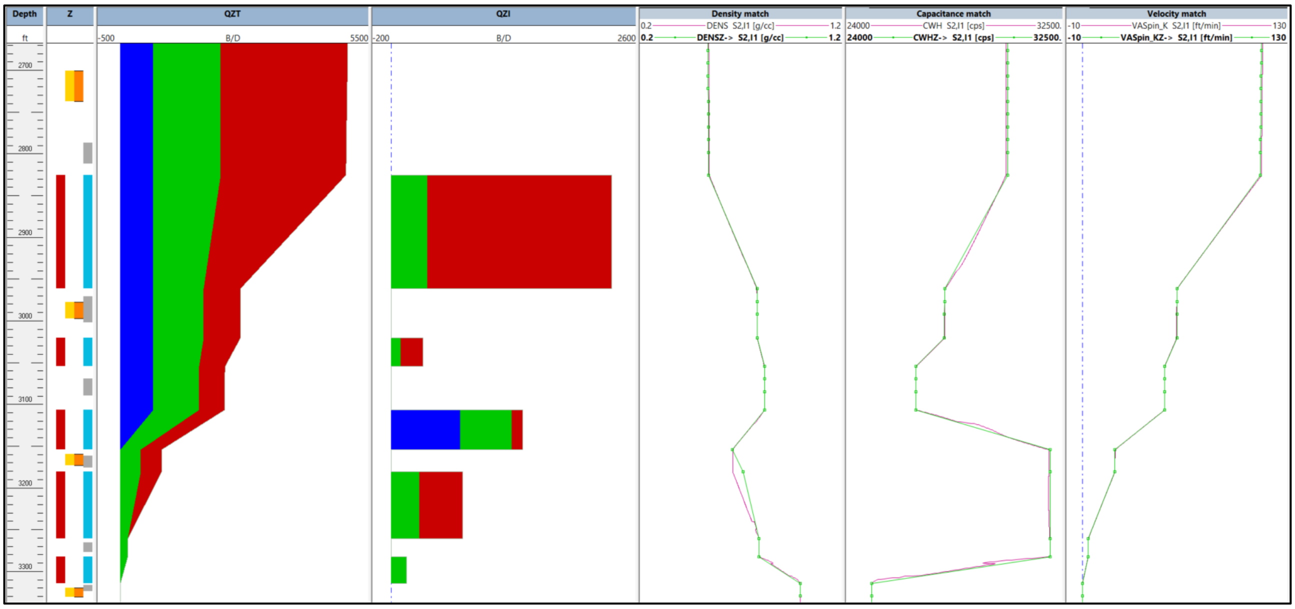

Fig. 5.D.17 – 3-phase interpretation – Profile 1

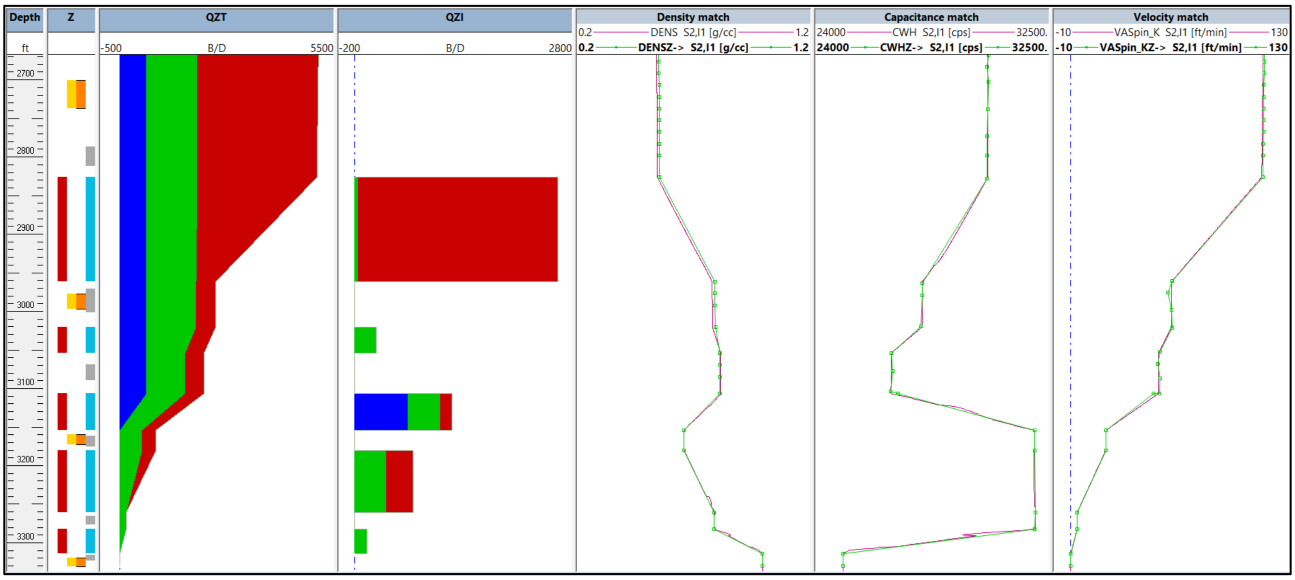

Fig. 5.D.18 – 3-phase interpretation – Profile 2

In this case, the combination of high gas rates and low water holdup has a significant impact on the correlation selection. Some liquid-gas studies predict mist flow (zero gas-liquid slippage), while others predict slug or bubble. Due to the small water content, it is more appropriate to use a correlation that predicts an inversion point (Hasan and Kabir) instead of the typical assumption of water continuous phase.

The choice of the correlation is driven by several factors. As mentioned previously, the correlations were developed for specific conditions, including deviation, fluid types, holdup ranges, etc. The PL analyst should have these assumptions in mind and use this to rule out certain correlations which are not applicable for the well to be interpreted. The flow regime can be identified from the tools response, for example, by looking at density variations during high sampling rate stationary measurements or stratified flow with MPT tools. These observations can be contrasted with the flow pattern prediction by the correlation.

As these correlations are the same as the ones used for nodal analysis, the analyst may choose the same correlations used to estimate the VLP to interpret a PL in the same well. Needless to say, correlations for nodal analysis are non-unique.

As correlations affect the split of the total flowrate, the surface rates (i.e., separator) may be used to base the selection. Bear in mind that formation volume factors are used to convert results to surface, which may add extra uncertainty if the PVT definition is inaccurate.

6 – High Deviation and Horizontal PL

6.A Introduction

In vertical or slightly deviated multiphase wells fluids move as immiscible phases. Depending on properties such as velocity, hold-up, and deviation, the fluids will assume a characteristic flow regime with bubbles, slugs, plugs and annular flow amongst others. Single point (centreline) measurements and multiphase flow correlations provide flow quantification as the measured mixture velocity, density or hold-up distribution is independent of the measurement location in the cross-section of the pipe. However, as the deviation increases, light fluid bubbles migrate to the high side of the pipe due to buoyancy, where they travel faster than the heavy phase (slippage). Increasing the well deviation to near horizontal results in the separation of the heavy and light phase fluids; a situation known as 'stratified flow' (Figure 1). It is clear that centreline sensors will not be representative of the cross-sectional hold-up and velocity distribution, as the tools will be immersed in only one of the phases or in the interface between them.

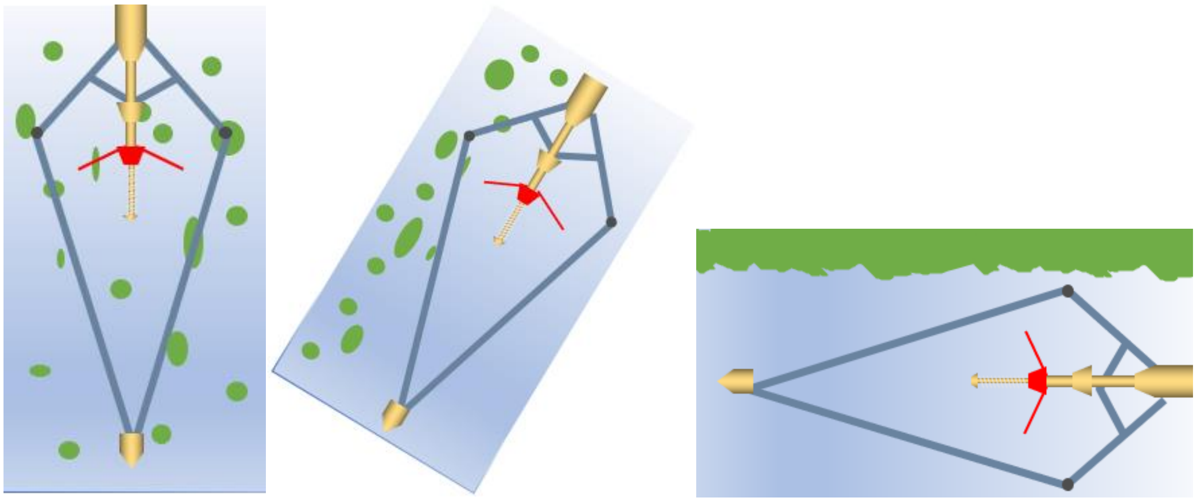

Fig. 6.A.1 – Centreline tools and pipe deviation

The assumptions and equations presented in Chapter 5 no longer hold when the tools do not provide the necessary inputs for the multiphase flow correlations. Specific flow regimes encountered in high deviation and horizontal wells are presented in Section 6.B.

Distributed measurements, known as Array or Multi Probe Tools (MPT), record distributed velocity and hold-up measurements across the pipe. The sensors can be radially or vertically distributed across the pipe cross-section. The main tools available in the market are presented in Section 6.C. Operational aspects of horizontal well PL are covered in Section 6.D. The interpolation of the velocity and holdup measurements and later integration of these, leads to the computation of the downhole rates of each phase, waiving the need for multiphase flow correlations. This is the subject of Section 6.E.

6.B Flow regimes in high deviation wells

In the following, three characteristic flow regimes typically present in deviated and horizontal wells are detailed.

6.B.1 Recirculation

Consider an oil-water producing well. If the well is perfectly vertical (0° deviation), the oil will travel faster than the water, as predicted by the slippage velocity (V_s) correlations. For example, the Nicolas correlation established a relationship between the slippage, water holdup (Y_w) and limit velocity (V_{lim}) as:

$$V_s = {Y_w}^n * V_{lim}$$

Where the limit velocity is a function of the interfacial tension and density difference between oil and water:

$$V_{lim} = C\,(\frac{g \cdot \sigma \cdot \Delta\rho}{\rho_{liq}})^{\frac{1}{4}}$$

The slippage velocity increases with the water holdup, and the maximum is achieved when a single droplet of oil travels up in continuous water. As the amount of oil increases, and the water holdup decreases, the oil lifts the water and this reduces the relative velocity between the two phases.

As the well deviation increases, due to gravity the oil migrates to the high side of the pipe cross-section. The oil bubbles experience less water resistance, which is reflected in a higher slippage velocity, as predicted by the Ding correction.

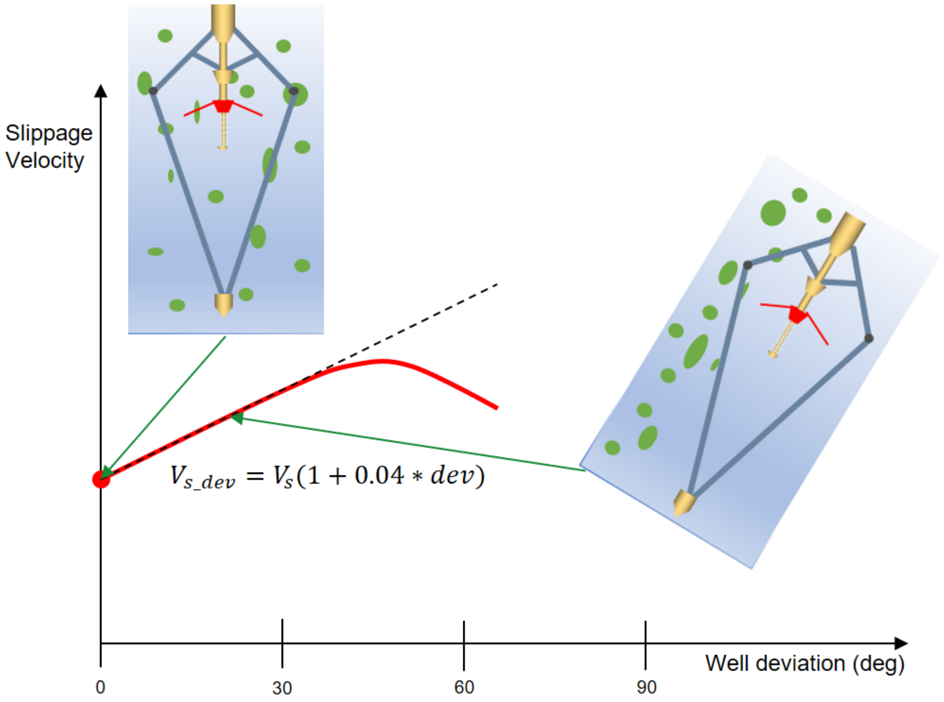

Fig. 6.B.1 – Slippage versus deviation

Under these conditions, and for zero or very small water rates, the oil bubbles flowing on the high side of the pipe will lift the water. In order to compensate the total zero rate, there must be a negative water velocity vector, which occurs on the low side of the pipe. This phenomenon is called water recirculation. In most situations, the conventional spinner and fluid identification tools are centralized or more towards the low side of the pipe, in the region occupied by water. The spinner measures a net negative RPS caused by the recirculating water, as a consequence of the light phase moving on the high side of the pipe. In production logging interpretation, this is known as 'Apparent down flow' (ADF), and occurs in deviated, multiphase wells, especially in the low velocity regions, and when fluid contacts exist.

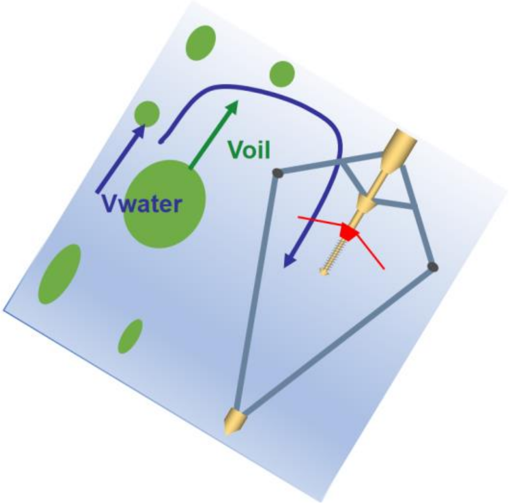

Fig. 6.B.2 – Apparent down flow

This phenomenon is often confused with crossflow, but the analyst should be aware of the different nature of both. Cross-flow is caused by reservoir pressure unbalance, while ADF is a flow behavior. Figure 6.B.3 shows a well producing through casing perforations and SSDs. Below the horizontal dashed line, the capacitance indicates 100% water (capacitance match track), and the spinners (FLOW track) shows negative RPS deflection. When the apparent velocity is calculated, negative velocities are seen in the water region. The results of the unconstrained multiphase interpretation are shown in the QZT and QZI tracks.

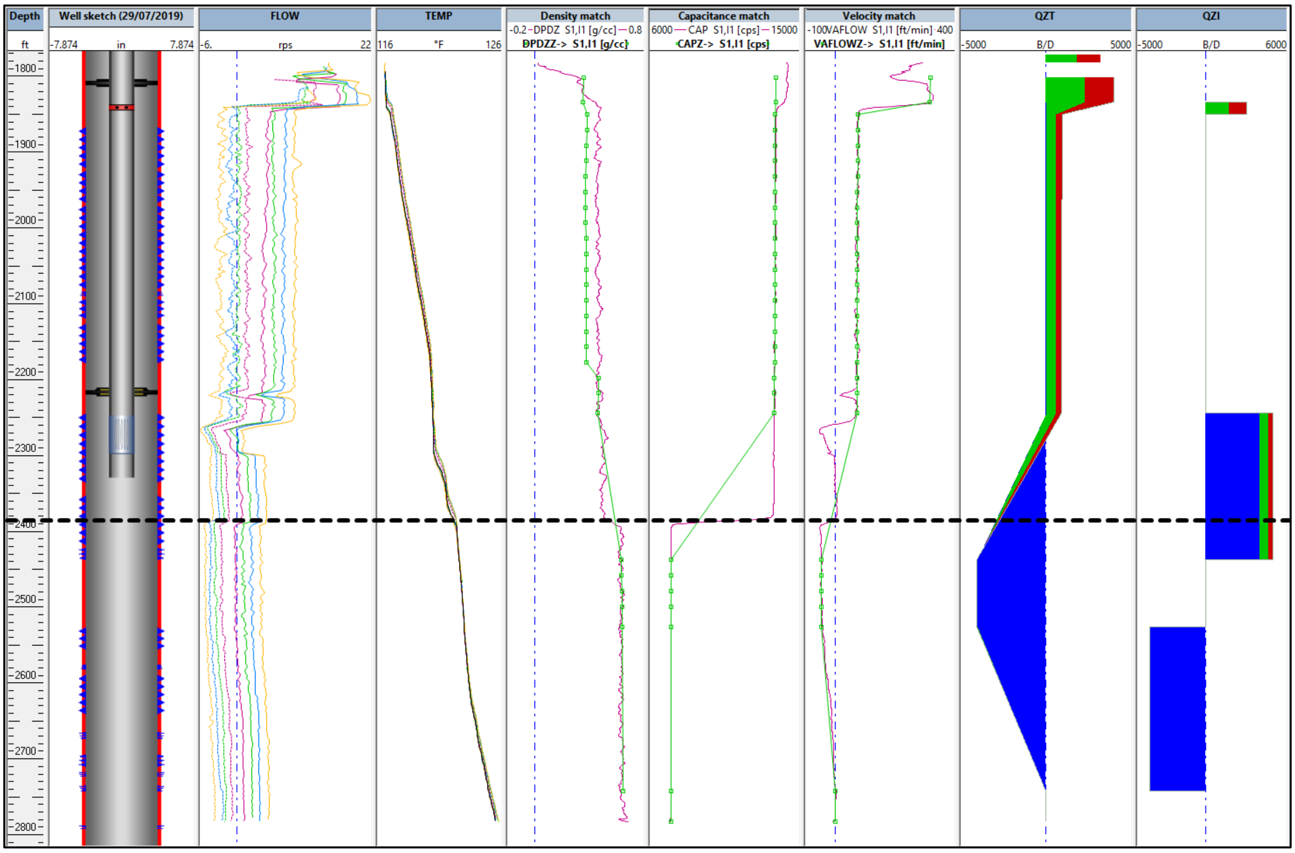

Fig. 6.B.3 – Apparent down flow

These results indicate that the middle inflow zone produces oil, water and gas. The hydrocarbons go up, while the water cross-flows to the bottom perforation, which supposedly acts as a thief zone. This 'selective cross-flow' behavior should be an early warning sign that this interpretation may not be correct, together with the fact that this occurs at a fluid interface. The analyst should evaluate whether cross-flow is possible in the well (single/multiple reservoirs) as well as if water is produced at surface. If it is real crossflow, the rate should increase during shut-in conditions, so it is also necessary to evaluate multiple rates and IPR behavior. Temperature is often one of the most valuable sensors to help understand if there is crossflow or production.

If it is decided that the negative RPS is caused by Apparent Down Flow, a method to estimate the production for the inflows in the ADF interval is available. There are a number of assumptions:

- Spinner velocity is ignored: As a negative velocity cannot be used where a positive rate is expected.
- Water velocity is set to zero: This is an important assumption as ADF can also occur in low water velocities.
- The light hydrocarbon phase velocity is estimated from a multiphase flow correlation.

Under these conditions, the light phase velocity is calculated, in terms of superficial velocities, as follows:

$$V_{SL} = C * V_S\,(1 - Y_h)$$

Where C is a constant that can be edited by the analyst, and the slippage (V_s) comes from the correlation selection. Note that a valid cross-sectional holdup is required. Tools such as nuclear density, tuning fork and capacitance, where the fluid needs to enter the chamber, may not provide a representative value in segregated conditions. The Interpretation shown in Figure 6.B.4 demonstrates the use of the ADF option. In the region of recirculation, the capacitance is not matched, as this reads 100% water holdup. The pseudo-density is used as primary holdup source. Note that in this region, the spinner-based fluid velocity is also not matched.

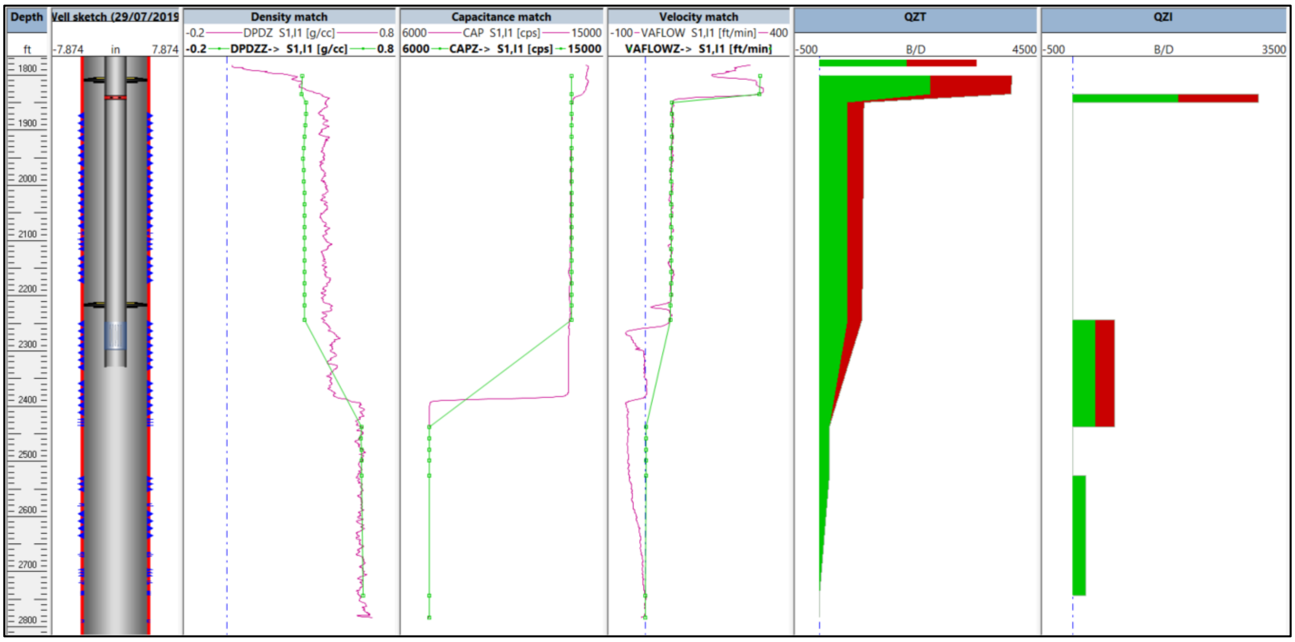

Fig. 6.B.4 – Profile obtained using the ADF option.

Another possible way of dealing with this situation is to use the temperature quantitatively as one of the target measurements. This obviously requires a forward temperature model representing the necessary thermal exchanges between the fluid, the reservoir and the well. This will be covered in Chapter 7.

6.B.2 Stratified Flow

As the well deviation increases, and typically above 70°, complete fluid segregation may occur. For two-phase flow, the flow morphology will consist of two separate streams, with the lighter phase on top of the heavy, and a well-defined interface between fluids. This is called stratified flow. The following simplified theoretical description uses Cartesian coordinates, assuming steady-state flow, no variations in the X and Z directions (infinite plates) and focuses on the fully developed region away from inflow zones to avoid entry effects:

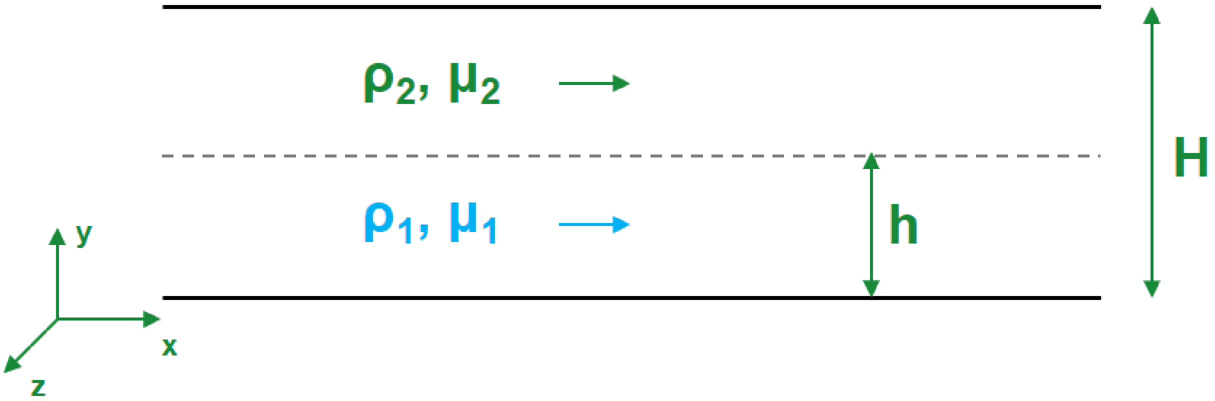

Fig. 6.B.5 – Stratified flow schematic.

The continuity equation for each fluid (1 and 2) is:

$$\nabla(\rho_i \, \overrightarrow{u_i}) = 0$$

Considering incompressible flow, the density can be removed:

$$\frac{\partial u_1}{\partial x} + \frac{\partial v_1}{\partial y} + \frac{\partial w_1}{\partial z} = 0$$

As the flow is fully developed, there are no variations in X. The same is assumed for Z due to infinite plates. The continuity equation reduces to:

$$\frac{\partial v_1}{\partial y} = 0$$

The same can be obtained for fluid 2. This equation shows that the velocity does not change with y (pipe height in our case). As the pipe walls are impermeable, V1 and V2 have to be zero everywhere inside the fluids, including at the interface. This means, a flat and well defined interface is present between the fluids. This will have important consequences in the next derivations.

The Navier-Stokes (NS) equation in the x direction for one of the fluids is:

$$\rho\left(\frac{\partial u}{\partial t} + u\frac{\partial u}{\partial x} + v\frac{\partial u}{\partial y} + w\,\frac{\partial u}{\partial z}\right) = -\frac{\partial P}{\partial x} + \mu\left(\frac{\partial^2 u}{\partial x^2} + \frac{\partial^2 u}{\partial y^2} + \frac{\partial^2 u}{\partial z^2}\right)$$

This can be simplified based on the previously-mentioned assumptions (fully developed flow, no variations in x, steady-state flow, zero velocity in y and z). The equation reduces to:

$$0 = -\frac{\partial P}{\partial x} + \mu \frac{\partial^2 u}{\partial y^2}$$

The terms on the left of the NS equation represent inertial terms. On the right, there are pressure and viscous forces. The left-hand side disappears, which intrinsically means that this is applicable for low Reynolds number (laminar flow). This final expression shows that the viscous forces are balanced by the pressure forces.

The Navier-Stokes equation in the y direction is simplified to:

$$0 = -\frac{\partial P}{\partial y}$$

The pressure does not change in the y direction, including at the interface. The interface does not deform and there is no discontinuity.

Coming back to the NS equation in the X direction, the well is considered to be horizontal (90°), with no gravity effects. The fluids only move due to the pressure gradient, which is the same for both fluids:

$$\frac{\partial P}{\partial x} = \mu \frac{\partial^2 u}{\partial y^2}$$

The derivatives on both sides are functions of different variables. The only way these can be equal is if they are equal to a constant. Integrating twice, the velocity profile in the Y direction for both fluids is:

$$u_1 = \frac{1}{\mu_1}\frac{\partial P}{\partial x}\frac{y^2}{2} + c_1\, y + c_2$$

$$u_2 = \frac{1}{\mu_2}\frac{\partial P}{\partial x}\frac{y^2}{2} + c_3\, y + c_4$$

The fluid velocity for both streams is parabolic, and in the case of perfectly horizontal well, the shape is characterised by the viscosity and holdups (represented by *h* in this derivation): The reader can obtain the constants by applying the boundary conditions:

- No slip boundary:
  - $u_1(0) = u_2(H) = 0$
- At the interface (y=h):
  - Continuity of velocities: u_1=u_2
  - Continuity of shear stress: $\tau_{yx1} = \tau_{yx2}$. Assuming Newtonian fluids, $\mu_1 \frac{du_1}{dy} = \mu_2 \frac{du_2}{dy}$

Figure 6.B.6 shows schematically the results of the velocity equations. Starting from the left:

- Two phase flow, with both fluids of same viscosity. This is equivalent to single phase, Hagen-Poiseuille flow. Single peak at the centre of the pipe. As the velocity derivatives at the interphase must be of the same sign due to continuity of shear stresses, there can only be one maximum.
- Blue fluid of greater viscosity than the green fluid and same holdup. A single peak occurs in the faster moving green fluid of lower viscosity.

- Green fluid of greater viscosity than the blue fluid and same holdup. The maximum velocity is now in the blue fluid.
- Green fluid of larger viscosity than the blue fluid, but now there is a large green holdup. If the green holdup keeps increasing, it will eventually go back to single phase, and the peak has to go to the large holdup fluid.

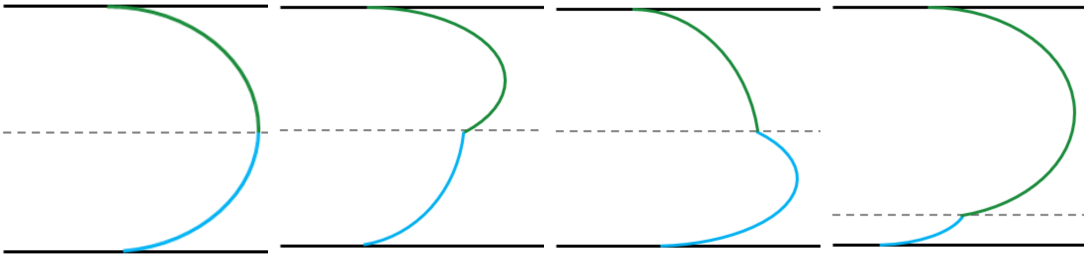

Fig. 6.B.6 – From left to right: $\mu 1 = \mu 2$ equal holdup. $\mu 1 > \mu 2$ equal holdup. $\mu 1 < \mu 2$ equal holdup. $\mu 1 > \mu 2$ large green holdup

The previous analysis applies for 90° deviations where the fluids move only as a consequence of the pressure gradient ($\frac{\partial P}{\partial x}$). However, horizontal wells are rarely strictly horizontal, and the fluid velocities and holdups are very sensitive to slight changes of deviation from the horizontal. Adding gravity ($\rho_i \, g_x$) to the Navier-Stokes equation incorporates the deviation dependency. Compared to the perfectly horizontal case, where $\frac{\partial P}{\partial x}$ was equal for both fluids, in deviated wells the gravity effect is density-dependent. Therefore, for deviations greater than 90°, gravity causes the heavy phase to move faster, which leads to a decrease in holdup (if there are no changes in rate). On the other hand, for deviations less than 90° the light phase will move faster, leading to a reduced holdup.

Figure 6.B.7 schematically shows the holdup dependency for a 50% water cut, equal viscosity mix. At exactly 90°, gravity does not favour either phase, so both move at the same velocity and therefore occupy the same percentage of the pipe (50% water holdup). The water holdup dramatically changes around 90°, increasing for uphill trajectories and decreasing for downhill. This schematic is a function of the total rate. As will be explained in the next section, as the velocity increases the flow can transition from stratified to mixed flow. In perfectly distributed flow, the deviation dependency is not as severe as in stratified flow, and this curve will be flatter.

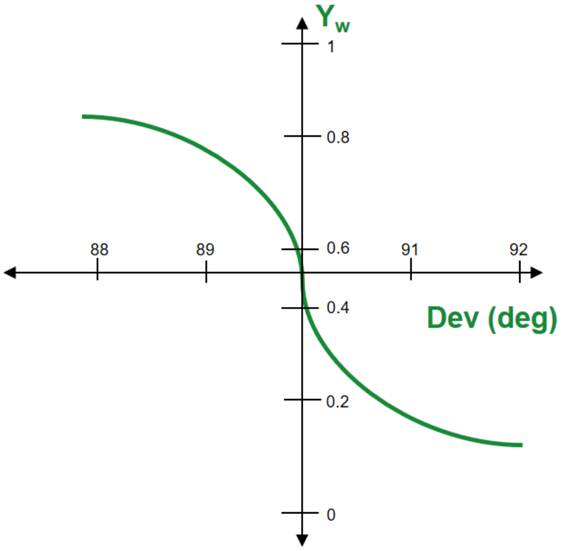

Fig. 6.B.7 – Holdup vs. deviation for 50% Water cut

The pictures below, taken in the Schlumberger Cambridge Research flow loop, show this dependence. A 50-50 mixture water and oil is flowed. Simultaneously a blue dye is injected into the water and a red dye into the oil. At 90° both phases move at the same speed and the holdups are each 50%. At 88° i.e. going uphill by only 2 degrees, the oil flows much faster and its holdup decreases significantly. Conversely, going downhill by 2° at 92°, the situation is reversed with the water going faster.

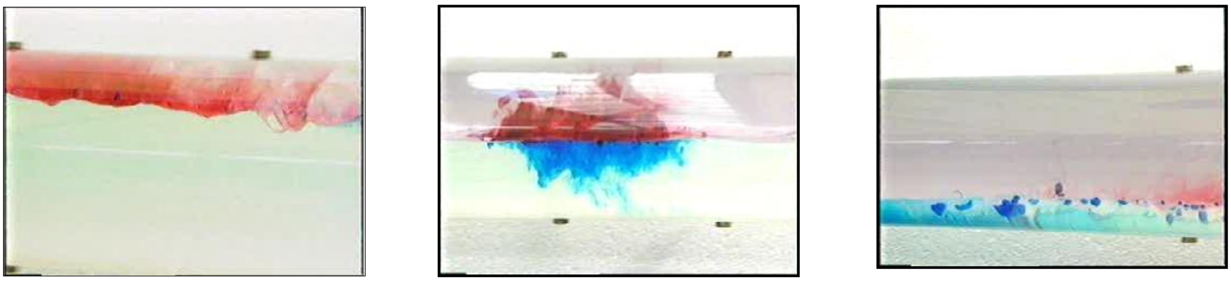

88° 90° 92°

Fig. 6.B.8 – Slippage dependence around the horizontal (Courtesy: Schlumberger)

The deviation dependency on the holdups and velocities is shown for an actual well in Figure 6.B.9. While the flow seems to be stratified, the repeated variations in deviation can give rise to transitional flow regimes, such as waves or slugs. The undulation of the wellbore will also create natural traps for heavy fluids in the lows and light fluid in the highs. Those trapped fluids will act as blocks and impact the tool responses when they occur.

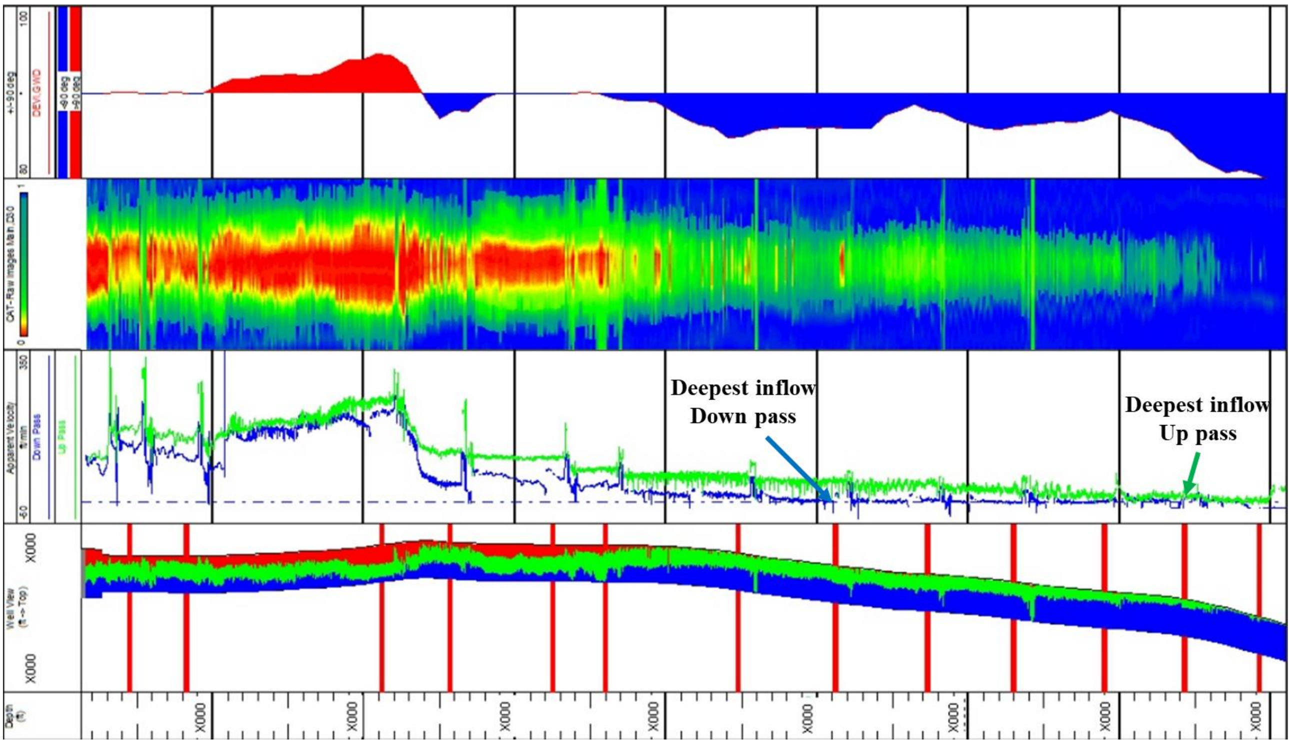

Fig. 6.B.9 – Deviation and holdup

From the tool selection point of view, this analysis shows that, apart from distributed holdup measurements (Chapter 6), distributed velocity measurements are also required when the expected flow regime is stratified.

6.B.3 Mixed flow

The previous section proved that stratified flow is a possible flow morphology, characterized by a flat surface, with zero vertical velocity and pressure continuity at the interface. Essentially a well-defined interface that does not deform. This is not always the case, as changes in deviation, fluid inflows, etc., will lead to velocities in the vertical (Y) direction.

Separated flow regimes may become unstable when waves form at the interface between fluids. Buoyancy and surface tension act as stabilizing forces, in the sense they try to maintain the fluid stratification. However, when waves occur, there will be a Bernoulli effect on the flow, that implies a change in the pressure acting on the interface, generated by a velocity change as a consequence of the vertical displacement induced by the wave. For example, as shown in the Figure below, Fluid 2 velocity increases along the wave, while Fluid 1 velocity decreases. Applying Bernoulli, a localized pressure discontinuity occurs, acting as a destabilizing force. This can result on a transition to a distributed flow, and the phenomena is known as Kelvin-Helmholtz instability. The destabilizing force increases with the velocity difference between two phases:

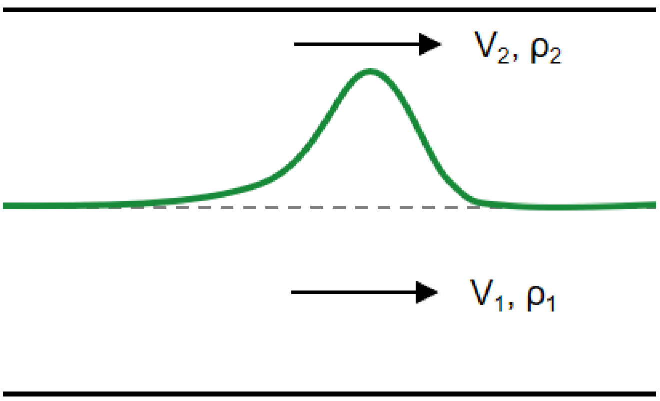

Fig. 6.B.10 – Kelvin-Helmholtz instability

From stratified flow, the flow regime transitions to an intermittent behavior, such as slug or plug flow. As the wavelength decreases and the amplitude of the waves increase, the flow regime becomes more distributed. Wavy interfaces tend to entrain drops in one or both sides, and this increases with flow rate. Eventually, for sufficiently high rates, one entire phase becomes discontinuous. Different authors have proposed a number of flow regimes which may be detected via visual observation, measurements or pressure drop behavior. For example, Beggs and Brill presented the following flow regimes for horizontal pipes:

Fig. 6.B.11 – Wavy interphase (Courtesy: Baker Hughes)

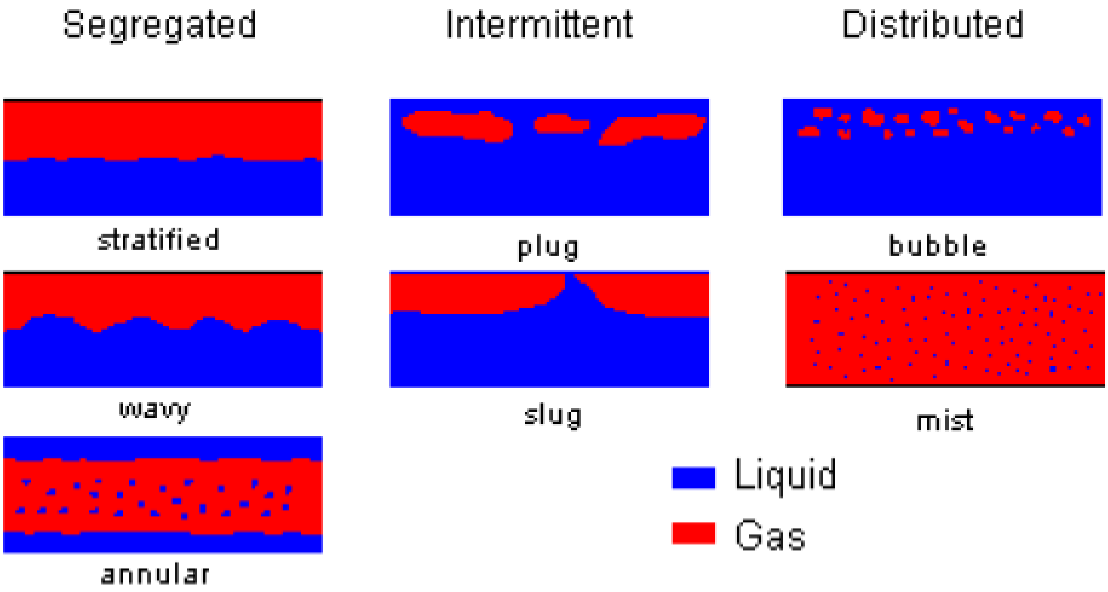

Fig. 6.B.12 – Proposed flow regimes for horizontal pipes - Beggs and Brill

For distributed or intermittent flows, the deviation dependency of the holdup is not as strong as with stratified flow (shown in Figure 6.B.7) as there is more interaction (shear at the interface, entrained bubbles, etc.) between fluids.

Compared to conventional PL, this chapter does not go into the details of multiphase flow correlations, mostly because the use of distributed holdup and fluid velocity measurements will inherently take care of the slippage between phases.

Figure 6.B.13 shows an image view and two cross-sections of a Resistance Array Tool (RAT) in a water-oil well. In the bottom half, the flow is stratified, with two separate streams of water and oil. However, in the upper half the flow is mixed. The transition between flow regimes occurred due to a large water inflow, which led the oil stream to break and form distributed bubbles in the continuous water.

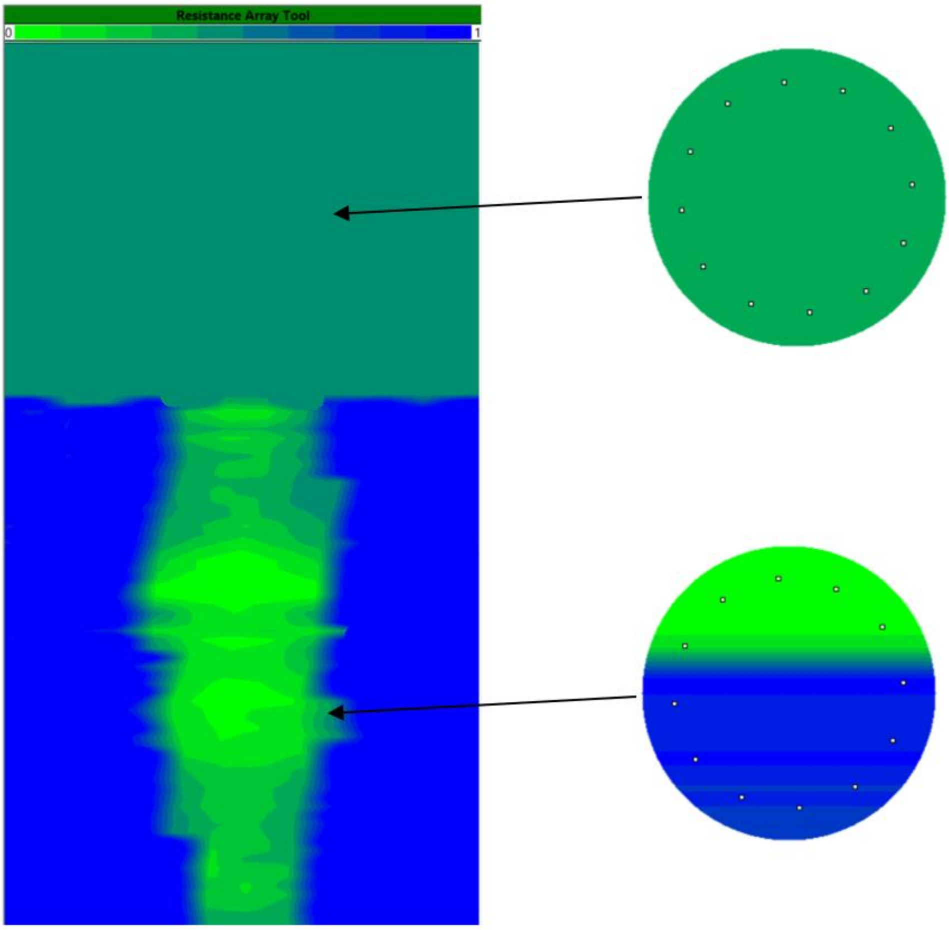

Fig. 6.B.13 – Transition from stratified to mixed flow

Note that in the case of horizontal wells with mixed flow, conventional centralized tools would suffice for profiling purposes. However, given the cost of the interventions and the limitations in the ability to predict the expected flow regimes, it is common practice to run MPT tools in most multiphase horizontal wells.

6.C Multiple Probe Tools

The methodology for multiphase profiling using correlations and conventional tools was presented in Chapter 5. Average fluid velocities and holdups, or density, are required, which can be obtained by centreline tools for well-mixed flow as in vertical, slightly deviated, bubble, mist, etc. As the deviation increases, and depending on the fluid velocities, segregation will occur, and the centreline measurements will no longer provide the necessary inputs of mixture holdups and velocity. For a horizontal well, the response of conventional tools will be, most of the time, useless. Even if they were reliable, slippage models that capture the physical behaviours in this situation are few.

For all the above reasons, specific tools were developed, called Array or Multiple Probe Tools (MPT). The goal with these tools is to replace a single value response with a series of discrete points in order to better characterize the flow behavior and ultimately to remove the need for slippage models.

Multiple Probe Tools are arrays of holdup and fluid velocity sensors, radially or vertically distributed. The minispinners and probes were presented in Chapter 3 and 4, and this section will show how these sensors are arranged on the main commercial tools available in the market.

As explained in Section 6.E, it is necessary to know the spatial location of the sensors inside the pipe. Using cylindrical coordinates, at any depth of the well, the following geometrical parameters are needed:

- The distance of the probe from the centre of the pipe. This is given by the tool geometry and the assumption that the tool is properly centralized: arms opened to the maximum, standoff, etc.
- The angular location: For this, all tools are equipped with a relative bearing device, which measures the deviation from the vertical axis.

6.C.1 Schlumberger FloScanner (FSI) *(Courtesy: Schlumberger)*

The FSI combines five micro-spinners (MS) with six FloView probes (Electrical - Ep) and six GHOST probes (Optical - Op). The tool is designed to sit on the low side of the pipe by gravity, hence providing water holdup, gas holdup, and velocity profiles on the vertical axis.

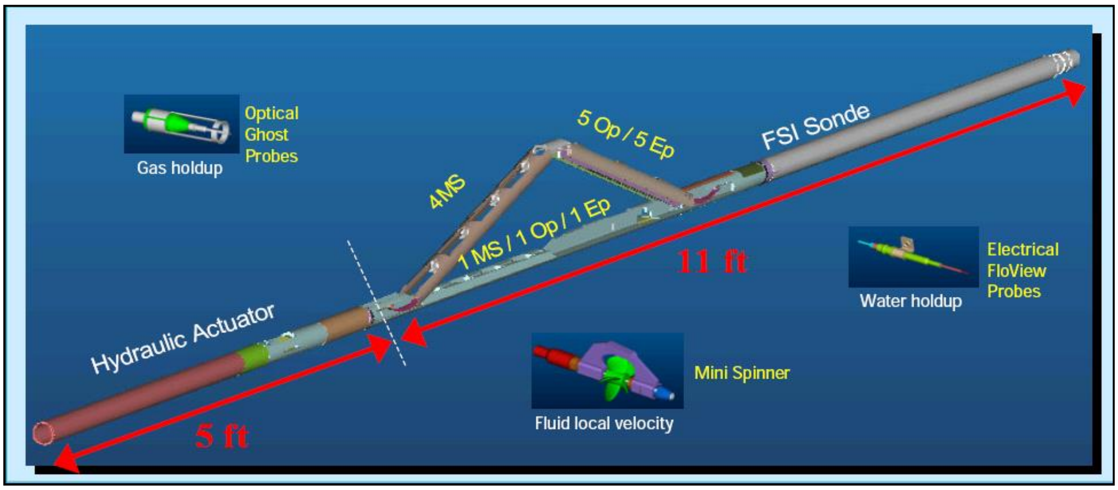

Fig. 6.C.1 – FSI tool geometry (Courtesy: Schlumberger)

The arm of the FSI is hydraulically actuated; the tool may be RIH closed to go through tubing and restrictions, with an OD of 1 11/16in. Once at the target depth, the arm opens up to 9 in. The minimum recommended pipe ID is 2 7/8in. The tool length is 3.54 m, but it is necessary to add pressure, temperature, gamma ray, CCL and ancillary equipment such head tension and swivel joints.

Figure 6.C.2 shows a number of common FSI images and logs. From left to right:

- Holdup image: Comprises six vertical bands, each showing the holdup distribution of oil, gas and water in green, red and blue respectively, as measured by the electrical and optical probes. The bottom band, on the left, shows the holdups measured by the probes on the bottom of the tool.
- Velocity Image: Shows the velocity vectors for each of the 5 minispinners. At the top of the cross-section, on the right-hand side, the velocity is higher, as would be expected for deviated oil-water stratified flow.
- Relative bearing: This is necessary to orient the probes, and act as a quality check. If this reaches 90°, all the sensors would be on the same horizontal line, thus no vertical coverage. As the relative bearing moves from zero, there is a chance of missing the light phase flowing on the high side of the pipe.
- Caliper: Also used to orient the probes, and as quality check to make sure the FSI is fully opened.
- Minispinners (0 to 4): These will be converted to velocity to calculate the flow profile at downhole conditions.

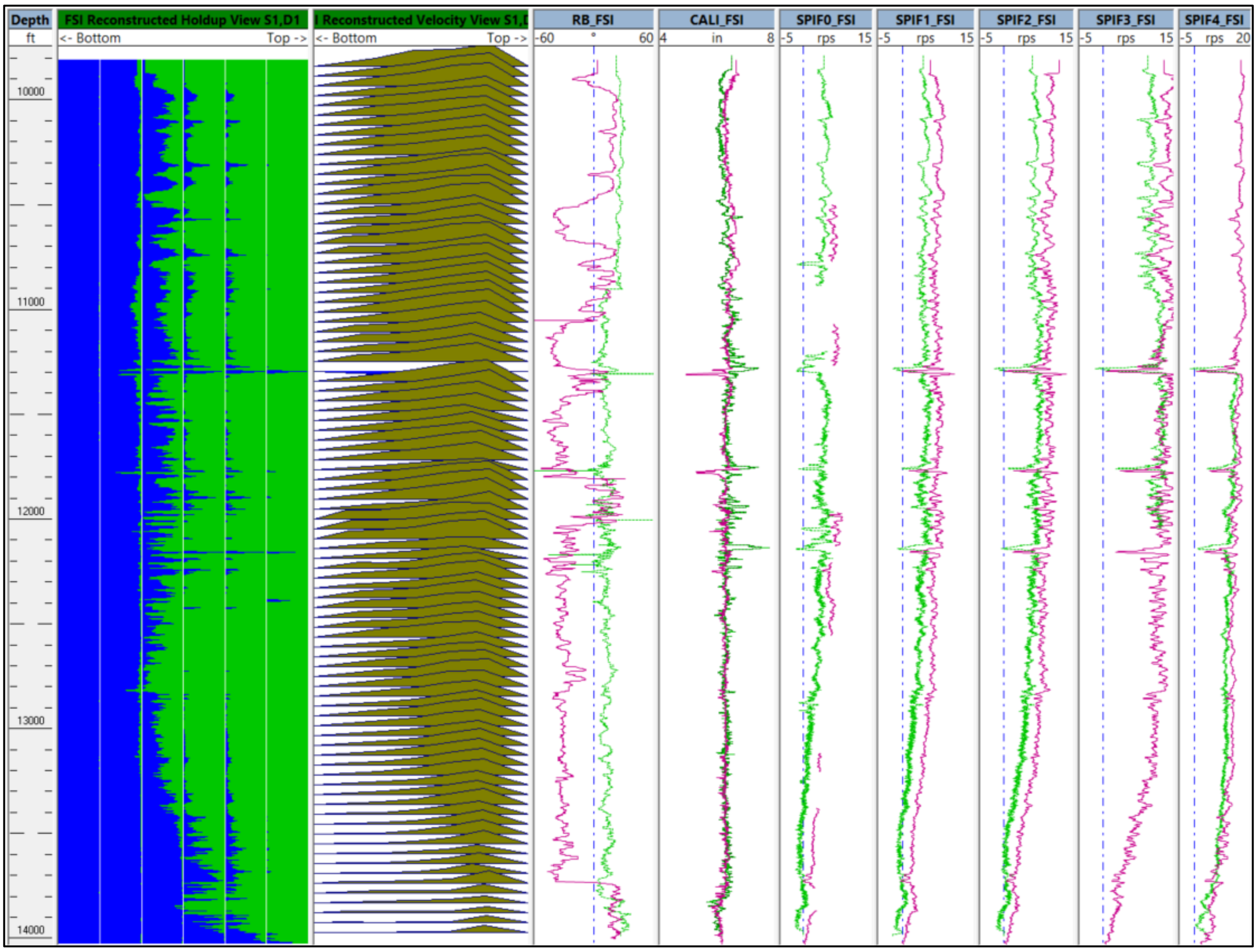

Fig. 6.C.2 – FSI data

The holdup and velocity distribution can be displayed at any depth of the well as cross-sections. As shown in the figure on the right, the holdups are presented in blue and green (no gas), whilst the velocity vectors are represented by the yellow points. The well deviation is also included. This image shows a case where the tool relative bearing is 41°. Note that the four working spinners only sweep around 40% of the pipe cross-section, missing the bottom and top, which may jeopardize the detection of low holdup phases.

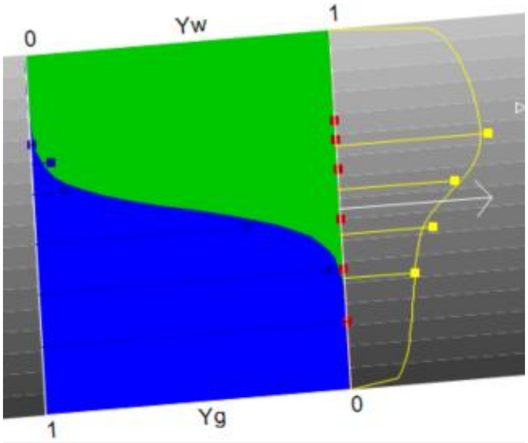

Fig. 6.C.3 – FSI Cross-section

6.C.2 Baker Hughes-Sondex MAPS

MAPS tools were originally developed by Sondex, and in Emeraude they are still referred to as Sondex tools, even though they are now part of Baker Hughes.

The Multiple Array Production Suite (MAPS) comprises three independent modules with sensors distributed around the circumference, mounted on springbows. These are not self-opening, and the arms resting on a surface would close. Therefore, mechanical centralizers are required before and after each tool. Relative bearing and deviation measurements are included. Maximum arm opening is 7 in, setting the maximum recommended pipe ID. From left to right:

- Spinner Array tool (SAT): six plastic or titanium (depending on the tool module) minispinners. A small magnet is mounted in each spinner, and the revolutions are quantified by means of a GMR sensor.
- Capacitance Array Tool (CAT): twelve capacitance sensors for 3-phase holdup in stratified flow conditions (Chapter 4).
- Resistance Array Tool (RAT): twelve resistance sensors for water holdup measurement (Chapter 4).

Fig. 6.C.4 – MAPS Suit: SAT, CAT and RAT (Courtesy: Sondex)

The RAT and CAT are 1.3 meters long, whilst the SAT is 1.15 meters. Additionally, it is necessary to include GR/CCL, pressure, temperature, centralizers, and it is also common practice to add a continuous or inline spinner. A full toolstring, including memory and battery, is shown below. The total length is 10.7 meters, which in certain cases may be above the rig-up capability due to crane availability or platform constraints. Note, it may not be necessary to include both CAT and RAT, and this will decrease the length of the toolstring.

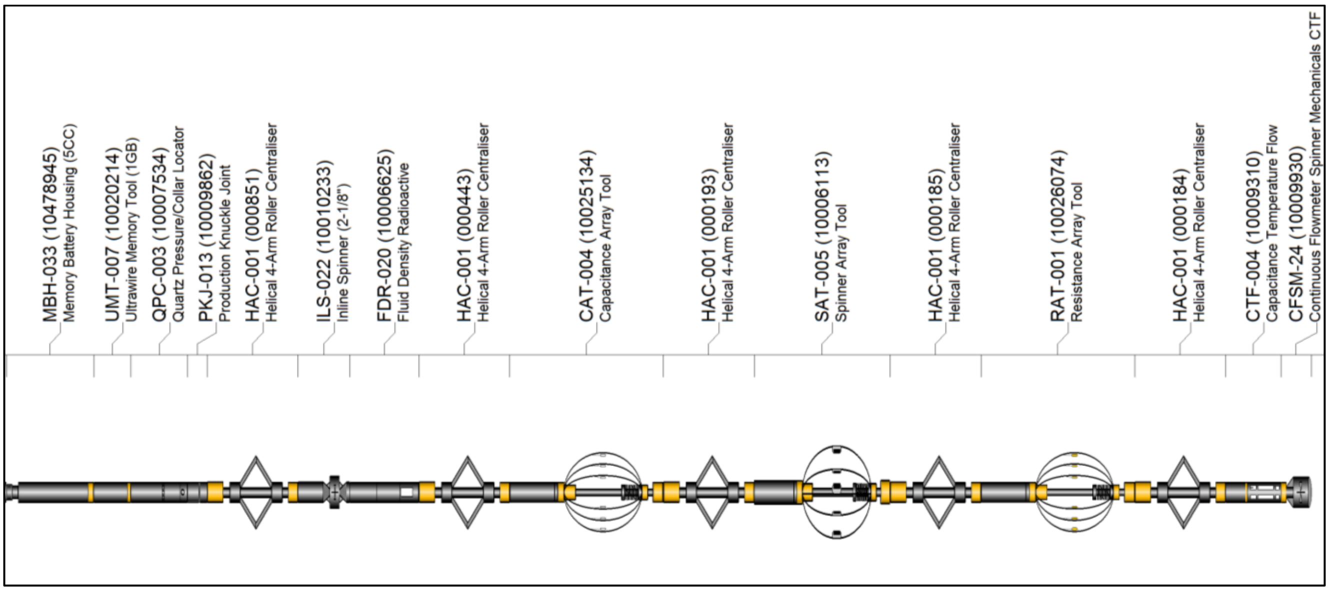

Fig. 6.C.5 – Full MAPS toolstring

Typical image and cross-sectional views are shown below for the RAT, CAT and SAT. The unwrapped holdup and velocity/spinner RPS images are also shown, with the centre displaying the high side of the cross-section by default, and this is reflected in the cross-sectional views.

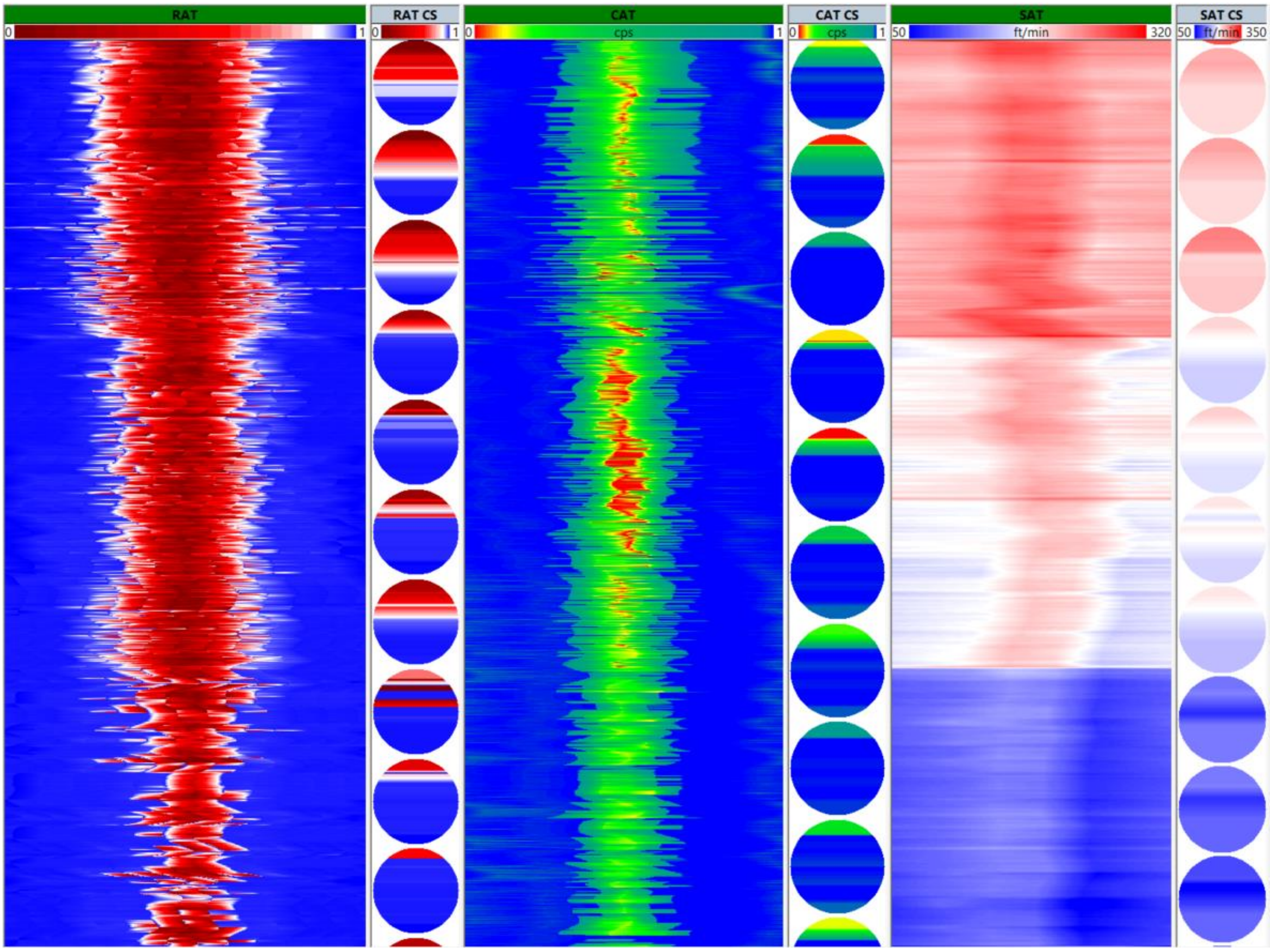

Fig. 6.C.6 – RAT, CAT and SAT images and cross-sections

Compared to MPT tools with sensors on the same axis, circumferentially distributed measurements are immune to relative bearing variations. As will be demonstrated next, multiple passes may be stacked for MPT processing, and if these passes have different relative bearing, a better vertical resolution may be achieved. On the other hand, spinner calibration can get more complex, as the minispinners will be immersed in different fluids along the measured interval.

6.C.3 Baker Hughes PAI

The Production Array Imager (PAI) is a six-arm tool, which includes in each arm a SAT spinner, RAT (water holdup) and an optical gas hold-up sensor (GAT). The tool is 2.07 m long, and it is possible to combine two tools with a 30° angular offset to increase the vertical resolution. When closed, the tool OD is 2.125 in, with a maximum open OD of 9 in. The tool body incorporates a relative bearing measurement and deviation. As shown in Figure 6.C.7, each arm can be collapsed independent of the others.

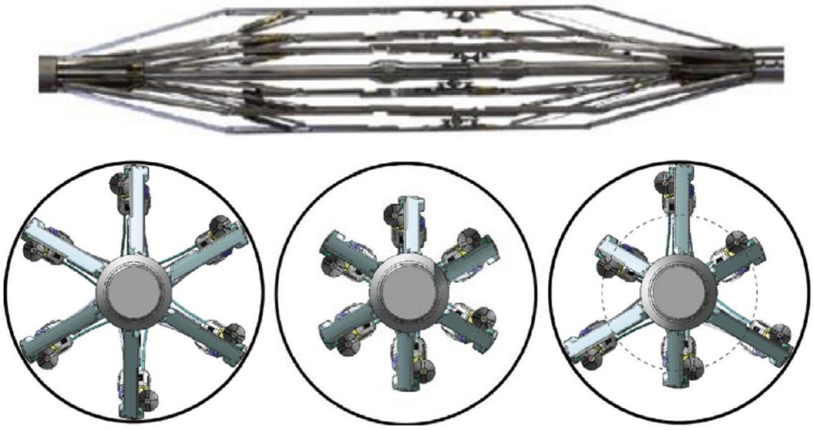

Fig. 6.C.7 – PAI tool (Courtesy: Baker Hughes)

PAI is relatively light at 18.6 kg. It is typically run with centralizers above and below, and is combined with centered measurements such as GR, spinner, and CCL.

6.C.4 OpenField FAST

The Flow Array Sensing Tool (FAST) is three feet long with four arms. Each arm includes two sensor positions, and the type and number of probes can be adapted to the specifics of the job. The sensors, presented in Chapters 3 and 4, can be 3-phase optical, electrical, minispinners, Doppler flowmeters, sand detection (Chapter 9), etc. As shown in the image below, a number of measurements are included in the tool body, such as temperature, pressure, relative bearing, MML and ultrasonic Doppler transducers.

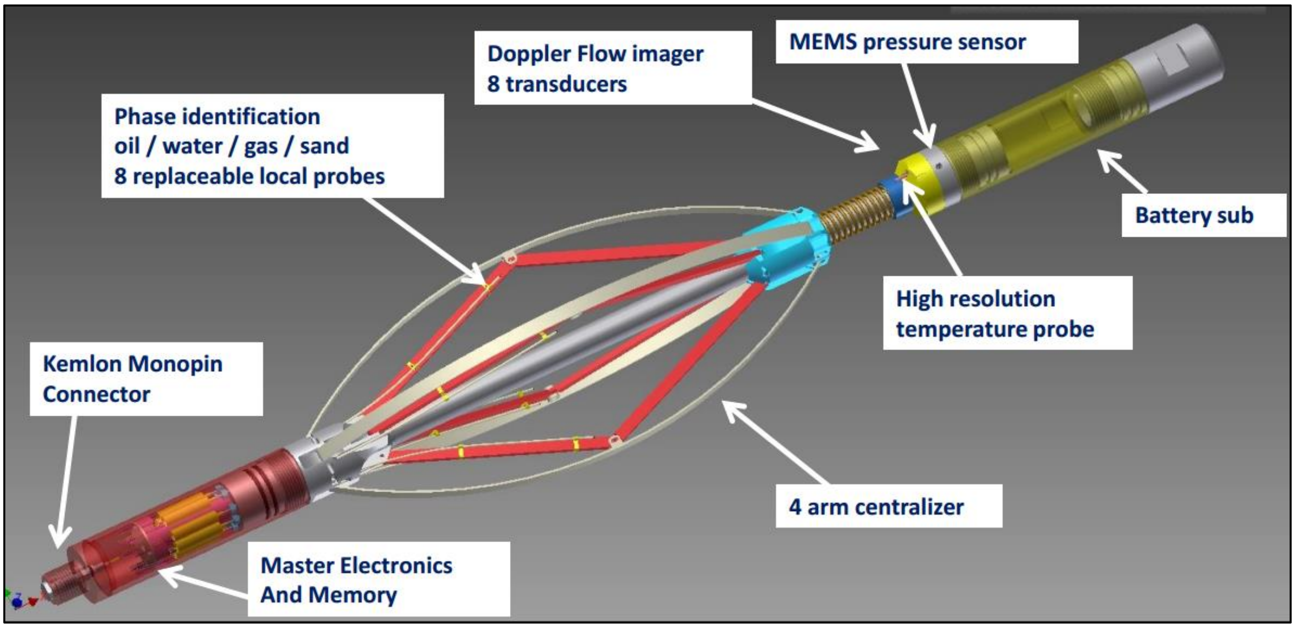

Fig. 6.C.8 – FAST v2 tool (Courtesy: OpenField)

When several MPT tools are run together, combining the sensors from different modules improves the cross-sectional resolution of the holdups and velocities. This is seen in Figure 6.C.9 and 6.C.10. SPIN01, 05 and 07 are from Tool 1, while the rest are from Tool 2. The angular offset went from 90° for a single tool, to 45° for the tool combination. Even though, SPIN 3 of Tool 1 is absent, there is still good cross-sectional coverage due to the combined tool configuration.

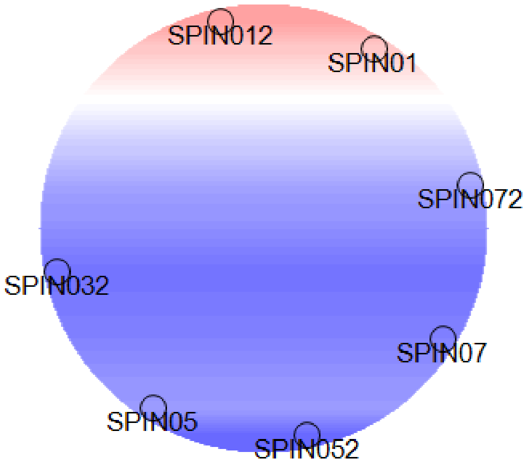

Fig. 6.C.9 – Dual FAST spinner

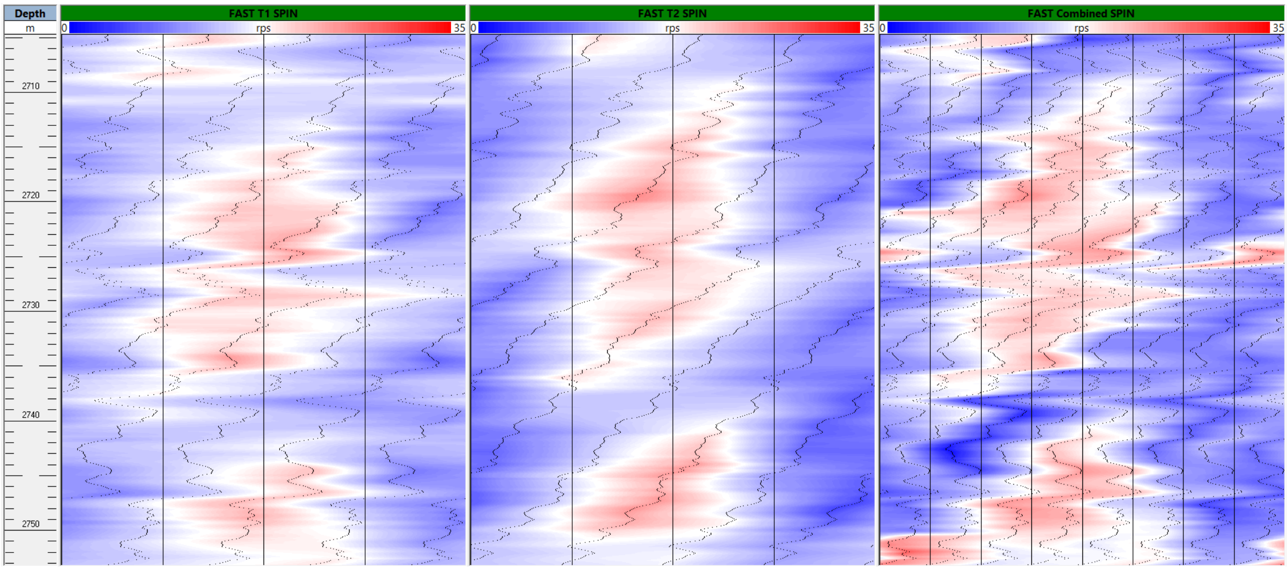

Fig. 6.C.10 – Combined FAST Spinners

6.D Horizontal PL operations

The first problem in horizontal well logging is that the tools do not descend by gravity alone. Dedicated conveyance systems are required, primarily coiled tubing, tractors and carbon rods. These conveyance methods were presented in Chapter 2. It is not uncommon that the regional availability, contracts and logistics condition what conveyance methods is used in certain well. For example, if there is a coiled tubing unit at a platform at the time a PL is planned, the company may decide to go for CT conveyance, even if it is not the ideal choice. If a pumping treatment is required after the PL, then CT is a convenient logistic solution.

Other constraints are imposed by the toolstring length and the rig up height. Adding multiple MPT tools, plus the ancillary equipment, several centralized measurements and conveyance requirements may result in very long toolstring. On offshore platforms, rig-up height is limited by the rig-floor. In certain situations, it is necessary to compromise data by removing one or more tools, to accommodate the toolstring in the available rig-up height. Other limiting factors are cranes and pressure control equipment (PCE).

Compared to vertical and slightly deviated wells, the zone of interest in horizontal wells is typically longer. Combined with the slower conveyance speed, especially in down passes, the acquisition program is affected in at least two ways:

- Recording three or four up and down passes would take a long time, and the velocity difference between passes may not be significant. Therefore, in horizontal wells it is common to run a single down and up pass, and, if fortunate, a second set of passes.
- With a single up and down pass it is not possible to calibrate the spinners. Even when running three or four sets of passes, the tools are free to rotate, and the spinner that was immersed in water at a particular depth may be in gas in the following pass. These cannot be used in the same calibration cross-plot.

Therefore, it is common practice to record the calibration passes over a short interval, before the well starts to build angle. This is especially convenient for tractor operations, as in this region tractoring is not necessary, and running on cable only, it is possible to achieve typical cable speeds.

If the calibration passes are recorded with the well shut-in, and over an interval where segregation is observed, then two calibration zones may be used (oil and water in the figure on the right). In this case, a holdup-weighted spinner calibration approach can be used, where the calibration parameters at different depths are calculated based on the fluid mix in which the spinner is immersed.

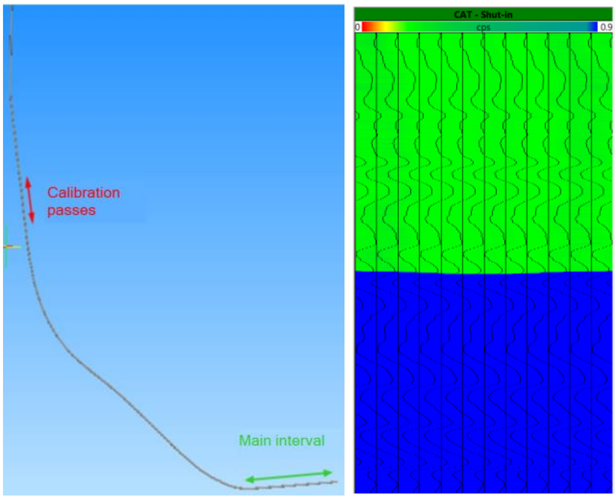

Fig. 6.D.1 – Calibration interval (left) and segregated fluids for spinner calibration (right)

Another point to consider is that horizontal wells typically operate with a lower drawdown when compared to vertical wells. This will be a challenge when planning multirate PL, especially with the purpose of computing the Selective Inflow Performance, as the pressure difference between surveys may be very small.

The conveyance may affect the measurements, especially for coiled tubing in a small ID pipe. Figure 6.B.9 shows a case of swabbing and surging effects, which affect the production profile of the well. In this figure, it can be seen that for the down pass (blue) the deepest inflow is detected nearly one thousand feet above the up pass. This is a consequence of a shear-driven flow, known as Couette-Poiseuille flow, where the fluid reacts not just to the pressure gradient experienced by the well, but also to the moving conveyance. This is exemplified in the following figure, for a situation where the coiled tubing moves to the right, against the fluid moving to the left during run in hole. The green dashed line represents pure Couette flow, while the orange shows the composite behavior. The maximum velocity is less than for the case of no coiled tubing movement, and the pressure increases (Bernoulli). This phenomenon is called 'surging', and the opposite, when the CT moves in the direction of the flow, is called 'swabbing' and leads to a lower pressure.

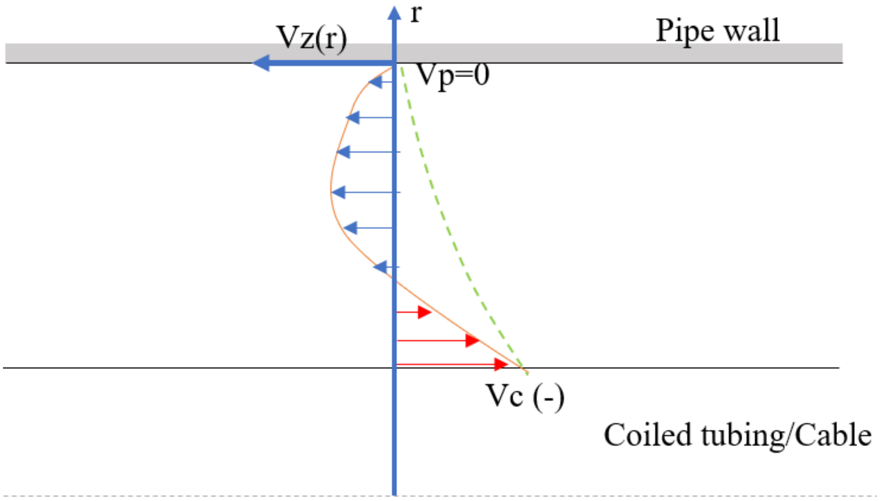

Fig. 6.D.2 – Surging effect due to CT movement

These effects will have a greater impact for low fluid velocities, smaller annular gap and high viscosity.

A different phenomenon is caused by the increased frictional pressure drop along the horizontal section. This will be exacerbated due to the presence of the conveyance method. As can be seen in the equation below, the cross-sectional flow will be reduced, and this will generate an increase in the frictional pressure drop, creating a higher unbalance between heel and toe.

$$\Delta P_F = \frac{2\, f_f\, \rho\, u^2\, L}{g_c\, (D-d)}$$

The difference between the Pwf in normal flowing conditions versus the Pwf when the toolstring and conveyance method are in the well will be the key factors in understanding the validity of the interpreted PLT flow profile.

The bottomhole flowing pressure increases from heel to toe, and due to the annular flow geometry, a selective choking effect for the production coming from the toe of the well is induced. The effect is more pronounced in wells operating with a small drawdown.

Figure 6.D.3 shows a 2.92 in ID tubing logged using a 2 in OD coiled tubing. The top track shows the drawdown, calculated as the difference between the shut-in pressure and flowing pressure (second track).

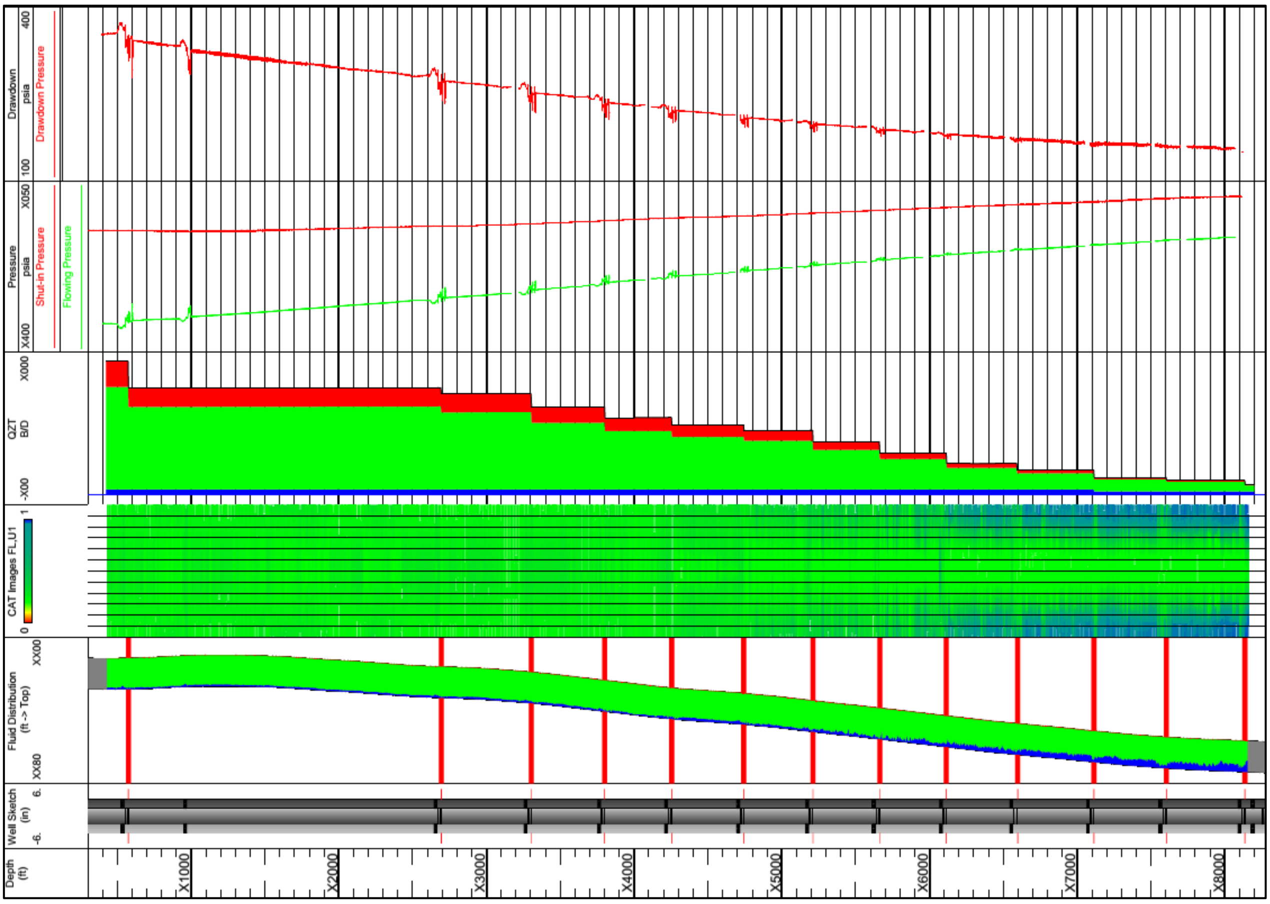

Fig. 6.D.3 – Frictional pressure drop induced by the conveyance (SPE 195506)

At the heel, the drawdown is 350 psi, while at the toe is only 150 psi. Considering a homogenous reservoir and similar completion pressure drop with the same productivity index for all the zones, this pressure imbalance will result in the toe region producing at less than half the rate compared to the heel of the well. Clearly, part of the pressure drop will be present even when the CT is out of the well.

To quantify the pressure increase due to the presence of the coiled tubing it is possible to simulate the pressure log, based on the PL calculated inflows from the different zones. This is shown in the image on the right, where the first track shows the simulated drawdown for tubing flow (CT not present), being only 55 psi different than the drawdown at the toe, compared to 200 psia measured by the PL.

This demonstrates the importance of proper pre-job planning and conveyance selection when designing PL acquisition in horizontal wells.

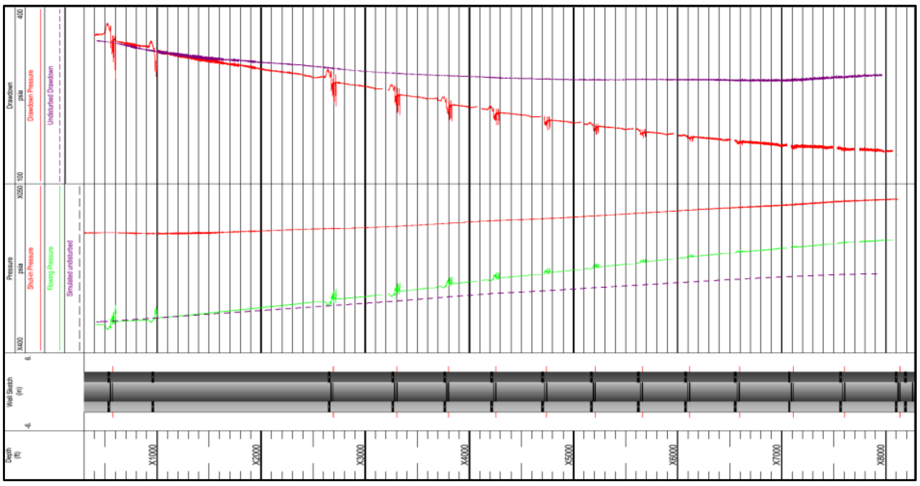

Fig. 6.D.4 – Simulated drawdown and pressure profile without CT (SPE 195506)

6.E MPT Processing

The objective of MPT Processing is to obtain, at every depth, an average value of phase holdups and rates, based on local velocities and holdup measurements. For any MPT tool, the exact position of the probes at a given depth is determined by tool geometry, the local diameter, and the tool bearing which is part of the acquired measurements.

The logged interval is 'spliced' into several cross sections:

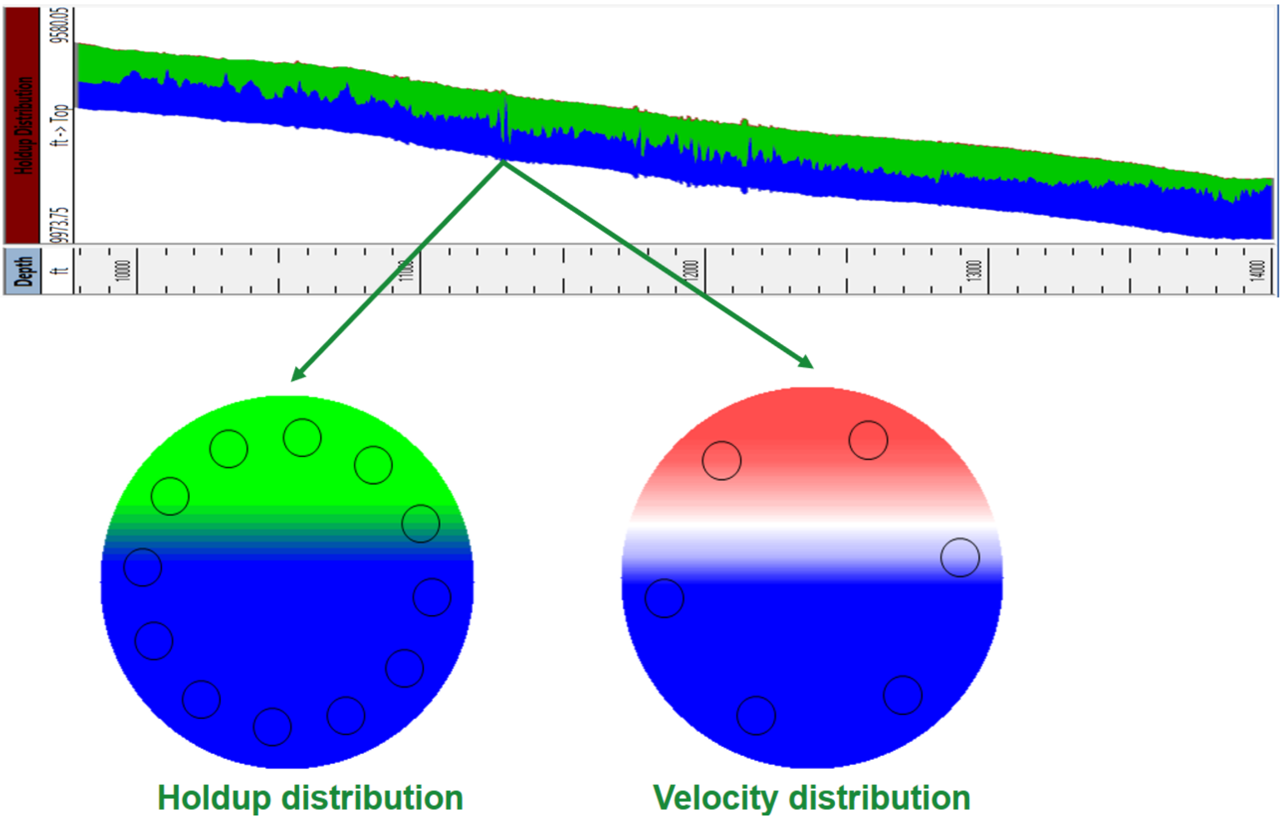

Fig. 6.E.1 – MPT processing - Splicing

For each depth, the measurements are mapped, to move from the discrete values, to a 2D representation. This then serves two purposes:

(1) Integration of the individual properties to arrive at a representative average.

(2) Combination of the local properties to get phase rates and integration.

Imagine for instance that holdups and velocity are determined everywhere. Locally it is assumed that there is no slippage and at every location in the cross-section phase rates are calculated as the local velocity multiplied by the local holdup. By integrating the local phase rates, average phase rates are computed directly, producing a result without the need for slippage models.

Note that multiple tools, even from different vendors, can be combined in MPT processing, to obtain the final averages. It is even possible to include centralized measurements (i.e., capacitance, density) to constrain the mapping.

6.E.1 Mapping models

The objective of mapping is to obtain, at every depth, an expression for the holdups and velocity, as a function of the height in the cross-section. For example, the mapping of a RAT cross-section at certain depth may look like the image below. A water holdup function (Yw(z)) is obtained, and if a physical constraint is imposed, for example that there is no gas, then the RAT would also allow us to obtain an oil holdup function (Yo(z)).

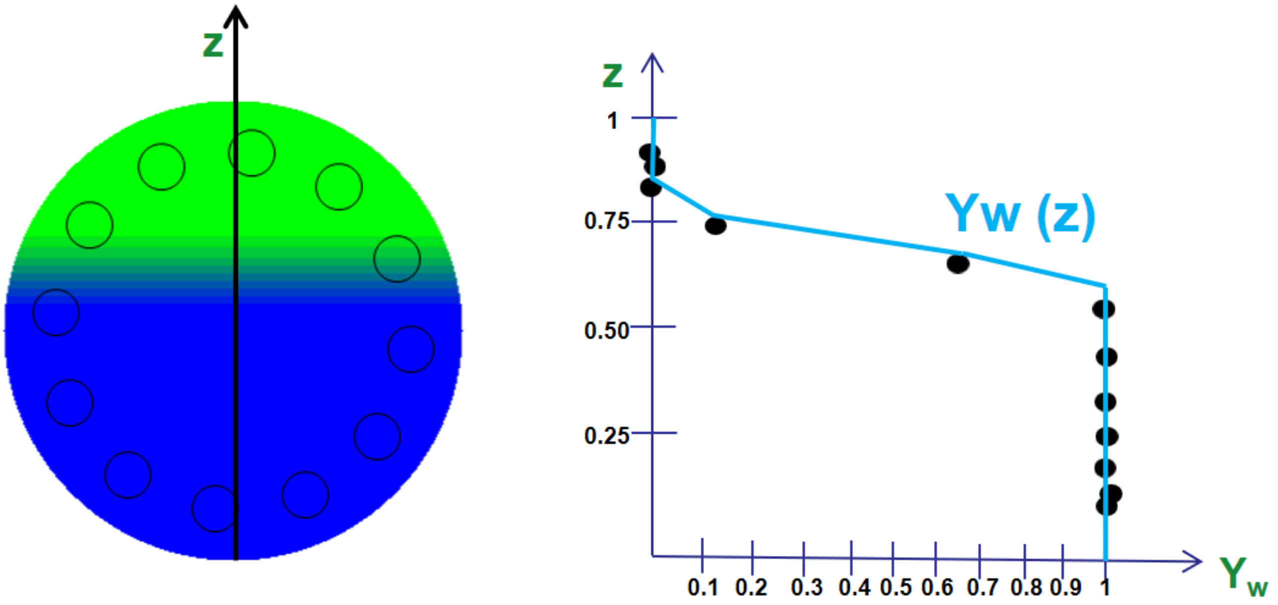

Fig. 6.E.2 – MPT processing - mapping

The different interpolations, or 'mapping' models are reviewed next. Most models assume horizontal stratification. Therefore, 2D mapping results is a 1D interpolation, as there are no lateral changes. However, a real 2D mapping algorithm is also available, that accounts for the areal variations of velocity and holdups.

Note that, at any depth, there is only one oil, gas and water holdup model, regardless of the number of MPT tools used to calculate it. Imagine a well where CAT plus RAT were run. Both tools will provide water holdup values, which may be different due to the measurement principle, incorrect tool calibration, or flow regime influence. To come up with a single water holdup model, a global error function is used based on the residuals calculated on each probe. Even though the MPT processing handles tool redundancy, if large errors are seen between the points and the models (more on this in Section 6.E.3), it is recommended to review the data quality and probe calibration.

6.E.1.a Linear model

The linear model defines the measurement of interest by several variables representing the values of that measurement along the local vertical axis. There are as many variables as there are distinct valid projections of probe readings on this axis. The values are then extended laterally. Without further constraints, this model will perform a linear interpolation through the discrete projected values. The figure below (left) illustrates this for a CAT cross section. The colored 2D map of the water holdup (water = blue, oil = green, gas = red) shows segregation, but at different positions there seems to be layers of water between oil, which is not physically possible. This may be the result of a bad calibration or an arm not fully extended.

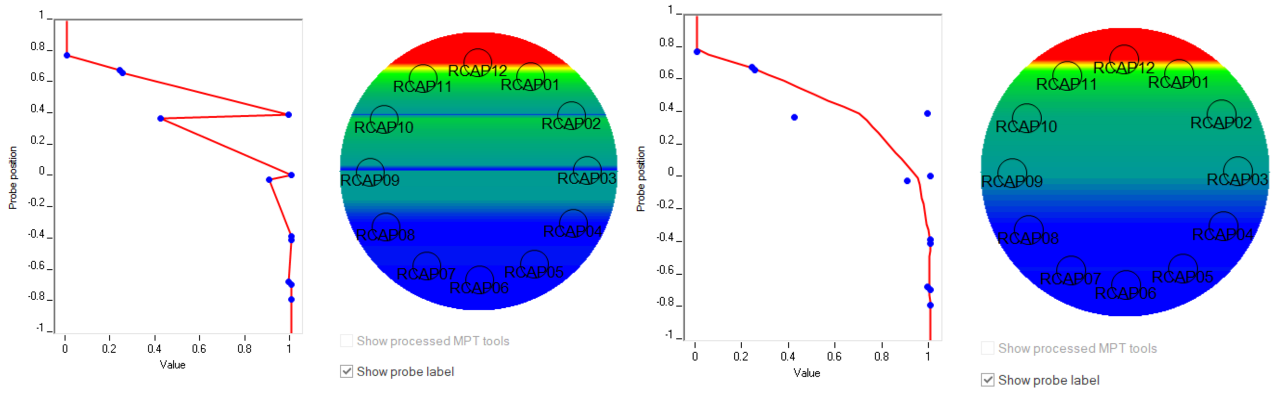

Fig. 6.E.3 – Linear CAT mapping. Without (left) and with (right) segregation constraint

To correct the previous situation, it is possible to alter the linear model using gravity segregation constraints, i.e., imposing that water hold-up decreases from bottom to top, or gas holdup increases from bottom to top. This is shown in the Figure above on the right. A non-linear regression can be used to try to match the values and satisfy the constraints at the same time.

The linear interpolation model can be applied to holdup and velocity data.

6.E.1.b Polynomial model

A polynomial interpolation is offered for the velocity model. By default, the velocity goes to zero at the pipe wall, using both the linear or polynomial. The latter fits the velocity with a grade 3 function and uses a rounding factor close to the pipe wall. The image below shows the difference between linear (left), and polynomial (right) models applied to SAT data:

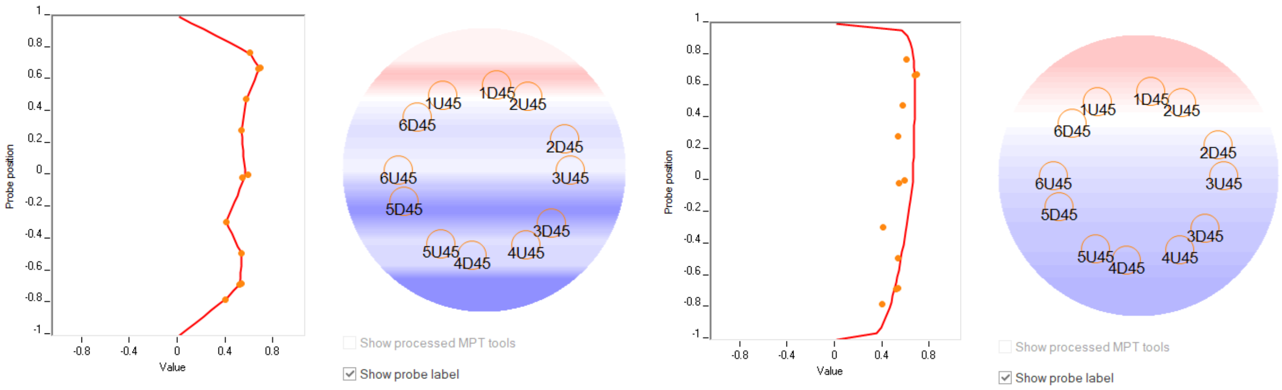

Fig. 6.E.4 – SAT mapping with the linear (left) and polynomial (right) models

This image also shows that it is possible to stack or combine n passes to create an equivalent pass with n-times the number of probes. In this case, two SAT (six minispinners) are combined to form an equivalent twelve measurements cross-section. Before combining passes, it is necessary to check that the tool and well conditions remain constant throughout the survey.

6.E.1.c MapFlo holdup model

This model is restricted to Schlumberger holdup measurements. It can be used with PFCS, DEFT, GHOST, FSI or even combinations. What the model tries to match, like the linear model, is the projection of the measurements on the vertical axis. The MapFlo model is based on two parameters and produces the typical shapes/responses shown below.

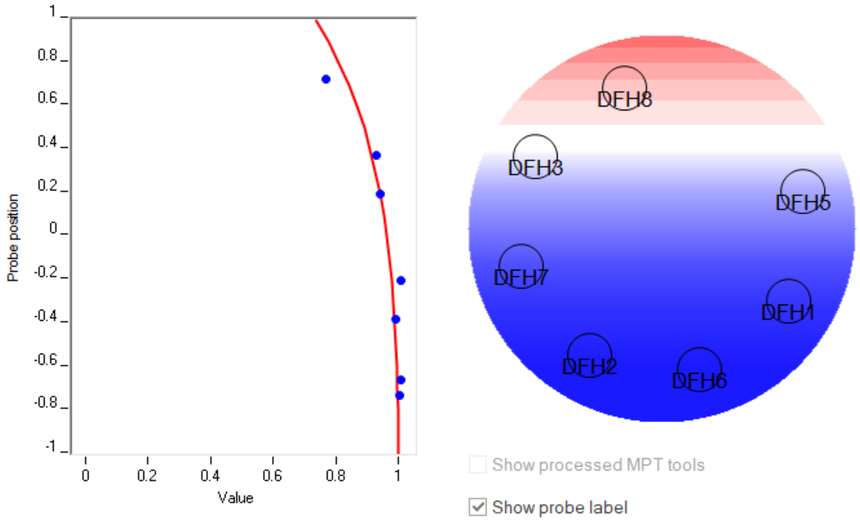

Fig. 6.E.5 – Dual-PFCS mapping with the MapFlo model

This image shows that one probe is missing (30° from the vertical). At the QAQC stage of the data it might be decided to ignore n number of probes during the mapping process.

6.E.1.d Prandtl velocity model

This model can be used for the FSI velocity mapping.

Like MapFlo it is driven by two parameters. The main idea behind this model is to obtain the velocity profile by applying a linear transformation of the holdup profile and then rounding the profile near the pipe walls. More precisely, the velocity profile is obtained with the equation below, regressing on α and β to match the velocity projections.

$$\left[\left(Y_w - Y_g\right) \times \alpha + \beta\right] \times \left(1 - \left|\frac{z}{r}\right|\right)^{1/7}$$

The next Figure shows how the vertical holdup and velocity profiles were obtained on an FSI example with MapFlo and Prandtl combined. The gas holdup is everywhere zero; the water holdup profile is shown in blue (see the Yw scale at the top). The velocity profile is displayed with the yellow curve. The squares represent the discrete measurements (blue=Yw, red=Yg, yellow=V).

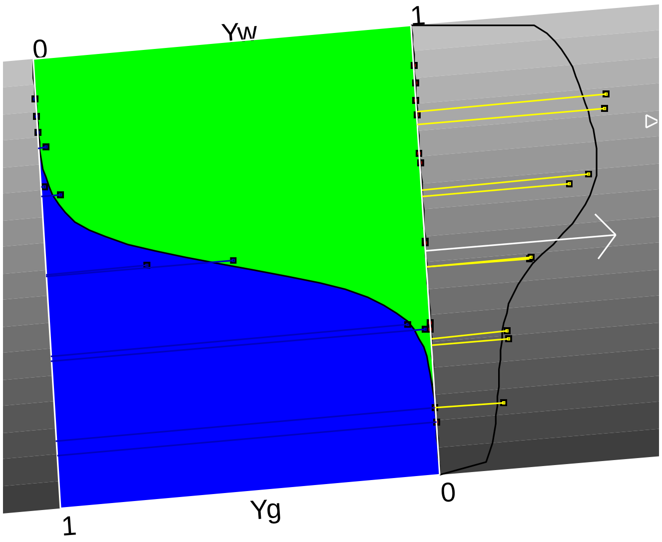

Fig. 6.E.6 – FSI mapping in a deviated well with MapFlo and Prandtl

It should be noted that the Prandtl model rounds the edge of the velocity on the entire circumference and not just at the top and bottom.

A typical 3D velocity profile is shown in the following figure.

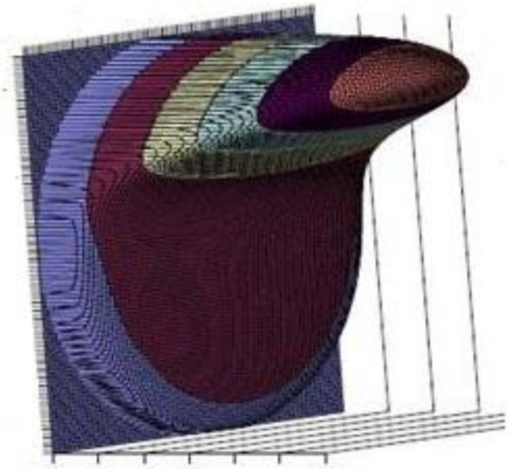

Fig. 6.E.7 – A typical Prandtl Velocity Profile (Courtesy: Schlumberger)

6.E.1.e 2D interpolation model

Instead of assuming local segregation, this approach is based on 2D interpolation algorithms, sometimes used to map petrophysical data: Kriging, linear triangulation, etc. If applicable, central measurements (capacitance, density, spinner) can be used as extra constraints on the model. The image below shows the results of 2D mapping in CAT and SAT data.

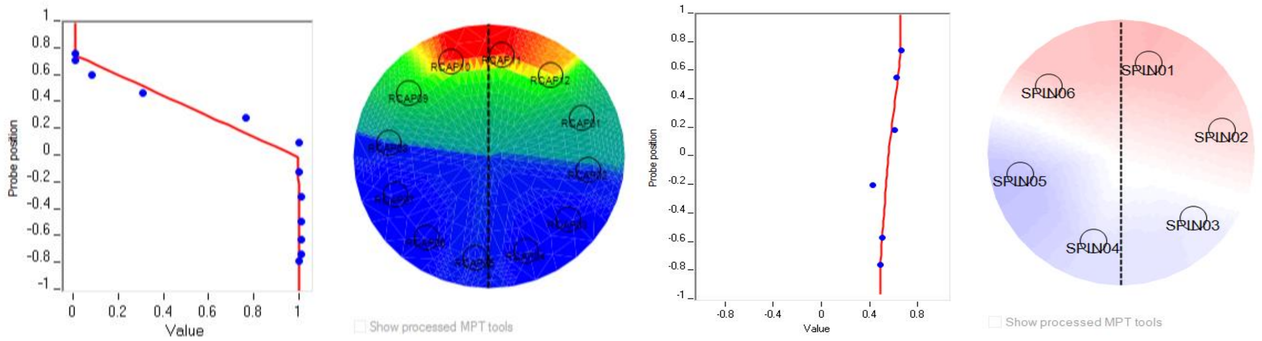

Fig. 6.E.8 – 2D interpolation in CAT (left) and SAT (right) data

6.E.2 Integration

With a holdup and velocity function, the rates can be obtained as:

$$Q_i = V_i * Y_i * A$$

As the holdups and velocities are not constants, but functions of the cross-section vertical axis, numerical integration is used. As explained earlier, with the assumption of no local slippage, the local velocity and holdups are used to obtain phase rates.

$$Q_w = \frac{\int_S Y_w \times V \times dS}{S}\ ;\ Q_o = \frac{\int_S Y_o \times V \times dS}{S};\ Q_g = \frac{\int_S Y_g \times V \times dS}{S}$$

The average holdup values are obtained also via numerical integration over the cross-section at every depth:

$$Y_w = \frac{\int_S Y_w \times dS}{S}\ ;\ Y_g = \frac{\int_S Y_g \times dS}{S};\ Y_o = \frac{\int_S Y_o \times dS}{S};\ V = \frac{\int_S V \times dS}{S}$$

The phase velocities are calculated as a by-product of the numerical integration:

$$v_i = \frac{Q_i}{Y_i}$$

The velocity difference between the different phases is intrinsically calculated by the tools and MPT processing. There is no need to impose an external slippage correlation, as done for conventional PL interpretation.

6.E.3 Interpretation

The interpretation is conducted using the MPT process outputs: holdups, phase rates, total velocity together with any additional tool available. Even though the final answers are in essence already provided (the phase rates are now computed everywhere) the interpretation is still a required step to come up with actual zone contributions and schematic results (QZT, QZI), possibly honouring additional constraints such as sign and surface rates.

Using a loose slip compliance, or the continuous method, is the best choice as it contains a built-in mechanism to by-pass any slippage model honouring that sufficient information is supplied.

Figure 6.E.9 shows the results of a MAPS interpretation in a perforated well. The first three tracks show the oil, water and gas downhole rates, computed during the MPT processing. The interpretation now means defining the rate calculation and inflow zones. For a perforated or selective completion (SSD/ICD) well, this is straightforward (Qcalc zones above and below each perf), but the user may still want to discretize the inflow zones, avoid assigning recirculation as crossflow, and constraining the signs of the inflows. The final QZT and QZI are shown next, and these are the result of the interpreter’s decision. A complete rate track (Q) can be used to identify and discretize the inflows.

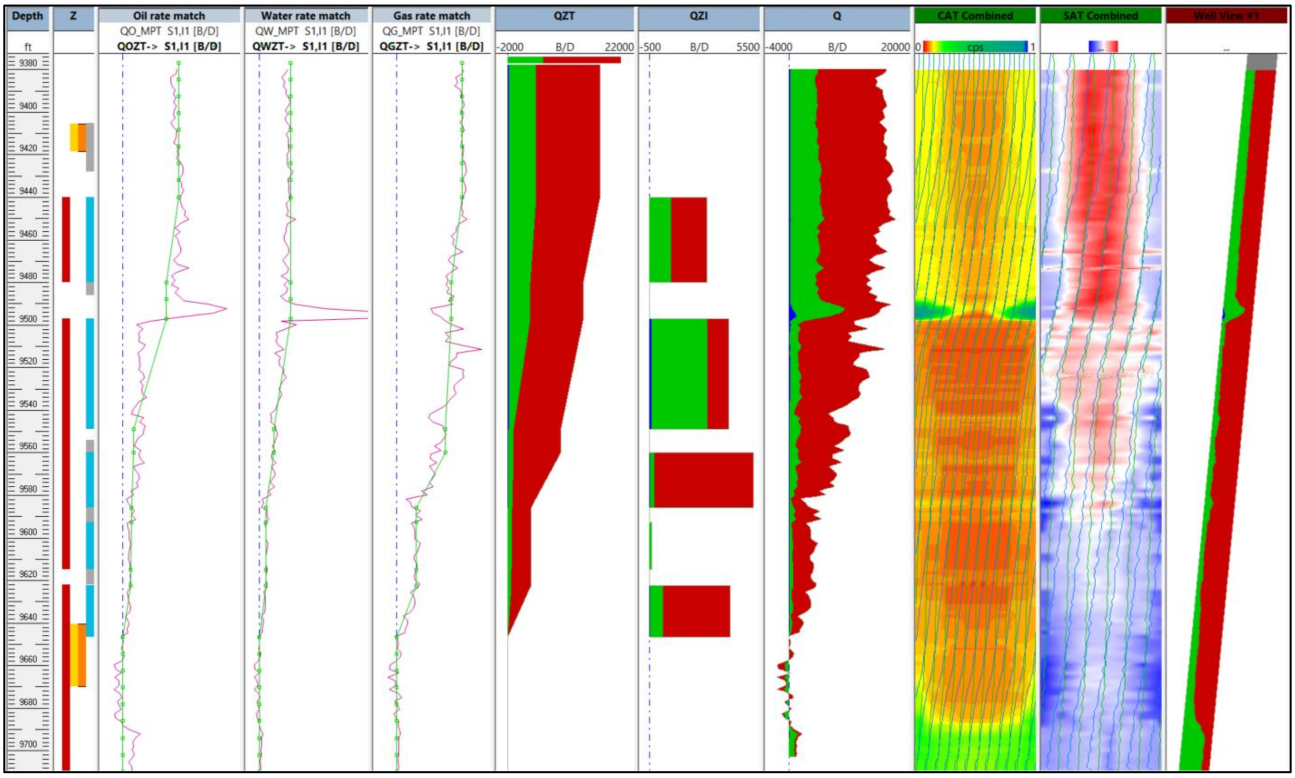

Fig. 6.E.9 – MAPS interpretation

The analyst should look at the holdup and velocity models, as well as the errors calculated for each probe, to understand whether the imposed constraints, models and calibrations are adequate. For example, in the CAT cross-section on the figure below (left) the points in blue are not correctly accounted for by the model. This may be due to difference in fluid distribution between passes, global error minimization when using a second holdup tool, etc.

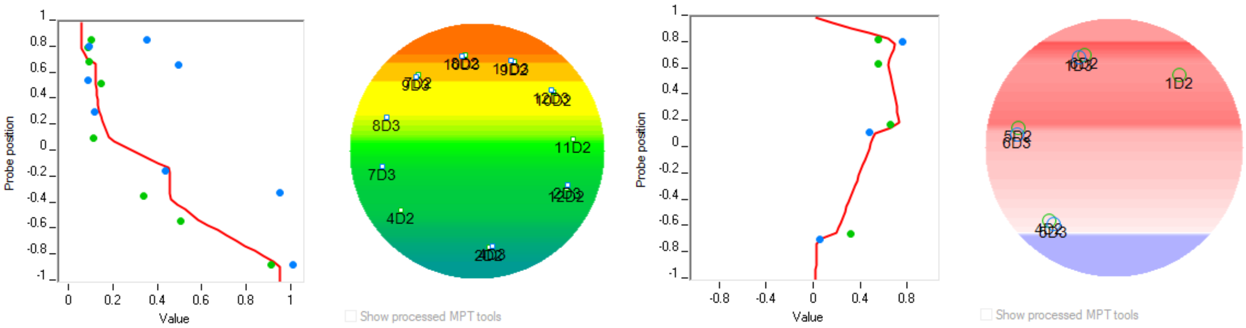

Fig. 6.E.10 – Reconstructed CAT (left) and SAT (right) cross-sections

Note that MPT sensors measure the phase holdups based on a physical principle such as refractive index or resistivity. As a result, the holdups and the downhole rates are not affected by errors in the PVT properties. These will be used to compute the surface rates based on the formation volume factors.

Below is an example for an FSI job in an openhole completion. Defining the rate calculation and inflow zones is at user discretion. It is possible to base the location of the inflow zones from the intervals with rate variation or set zones at an even distance (i.e., 20 m), or base the decision on some geological description.

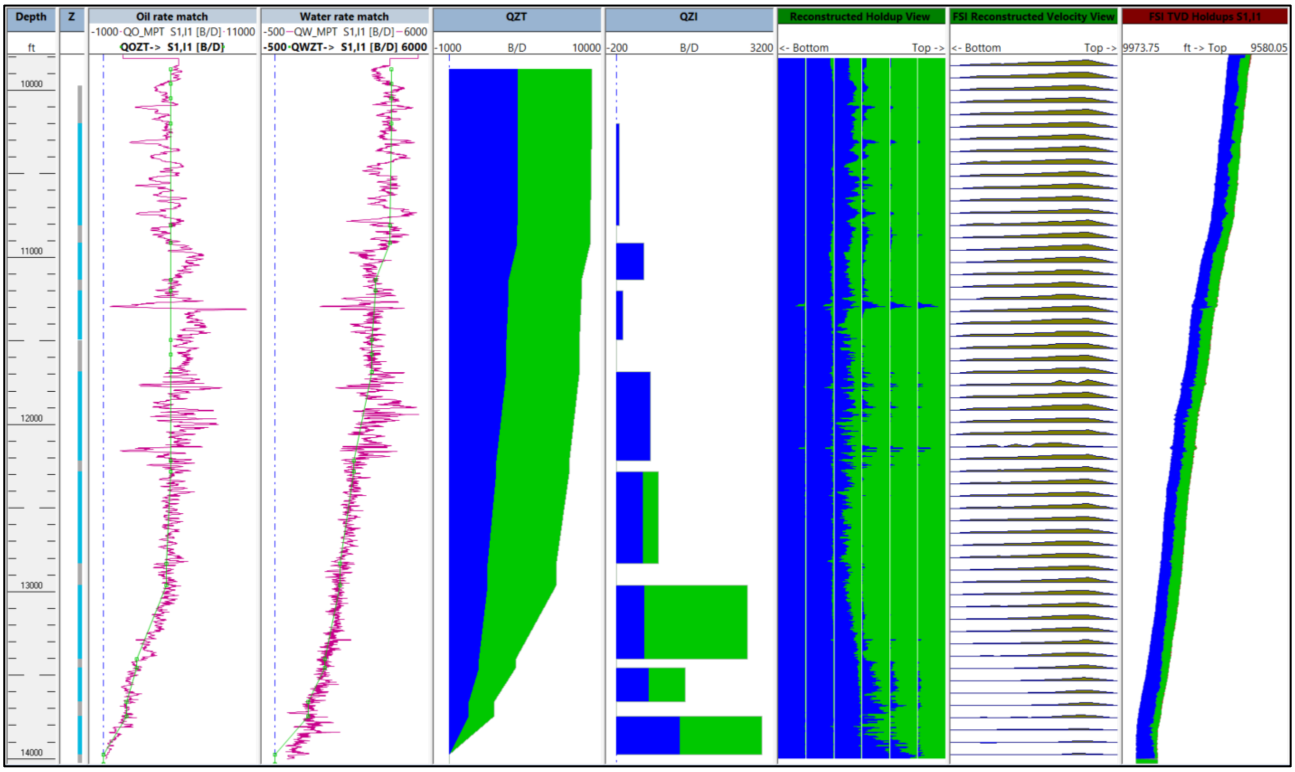

Fig. 6.E.11 – FSI interpretation

7 – Thermal Analysis and Simulation

7.A Introduction

Temperature data is a remarkable source of reservoir and well information throughout the life cycle of the well. There is a wide range of applications for this data including, but not limited to, qualitative indications of flow, completion integrity, assessment of valve operation, quantitative production and injection profiling.

Temperature logging started in the 30’s with methods for temperature-based flow profiling developed shortly after. Latterly, temperature has been recorded as part of production log surveys. Although often considered as a secondary measurement used for PVT calculations and qualitative indications of flow when flowmeter measurements fail, temperature can, with some limitations, prove valuable for quantitative computing of the flow profile. More recently, Distributed Temperature Sensing (DTS) systems based on fibre optics have gained considerable traction as permanent installations as part of the completion, or temporary deployment as part of an intervention. DTS has provided massive, high resolution, data gathering of temperature versus depth at rates up to every 10 seconds.

Similar to permanent downhole pressure gauges (PDG), the ever growing volume of data generated has presented its own challenge. Typically, massive data is required for time stepped qualitative purposes, whilst quantitative interpretation requires relatively very few data points.

This chapter starts by exploring the different applications of temperature data, followed by a summary of the key theoretical concepts on thermodynamics and heat transfer that must be considered to make educated clicks. The different thermal methods offered by KAPPA are also described: for Emeraude, the Energy model, Water Injection Fall-off and different options for forward modeling. For Rubis, the coupled wellbore-reservoir fully transient 3D simulator.

The non-unique nature of the thermal interpretations is emphasised by presenting sensitivity analysis for all available models.

7.B What information can be extracted from Temperature data?

In wells with permanent temperature monitoring installations (DTS, fixed gauges, discrete distributed measurements, etc.) it is possible to extract a variety of information throughout the life of the well. When running temperature acquisition surveys (wireline or slickline) the gauges are typically combined with other sensors (acoustic, calipers, flowmeters, etc.) to facilitate the interpretation. In either case the data that can be extracted includes:

Completion and integrity evaluation

Right from the beginning of the life of the well, permanent installations of fibre optics can help to monitor and extract information about the cementing and stimulations operations. Figure 7.B.1 shows a temperature map during the cementing. The onset of the exothermic curing reaction is clearly seen, together with the top of the cement:

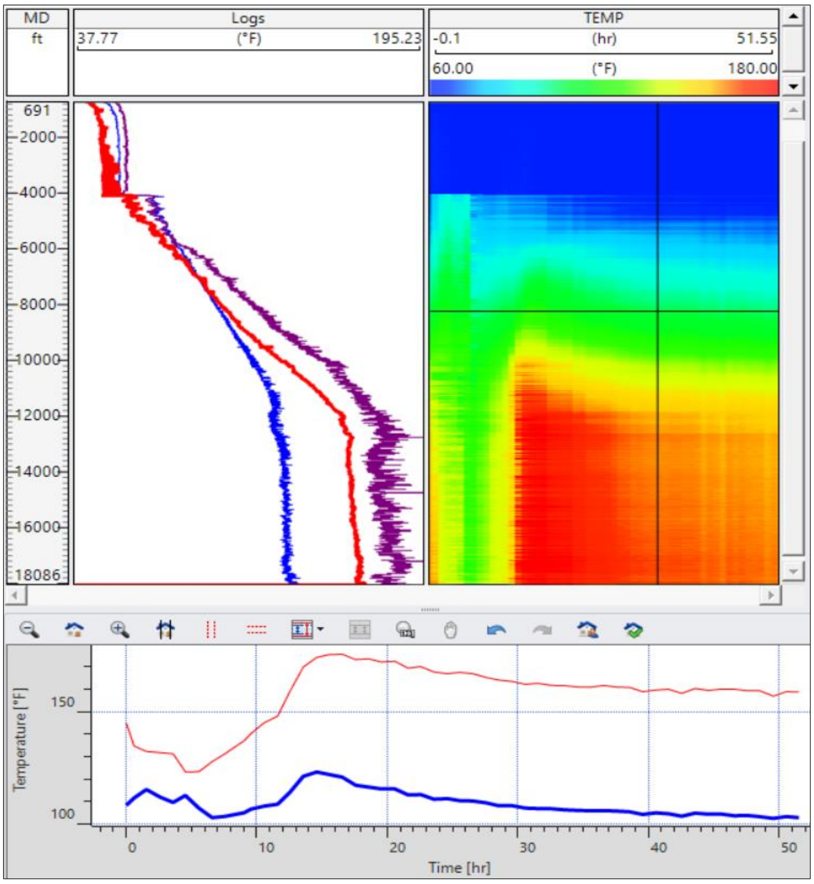

Fig. 7.B.1 – Temperature map during a cementing operation

In hydraulic fracturing operations the water injected typically cools the formation, and this can be observed as local temperature variations around the perforations or sleeves that received water. Also the exothermic reaction as a consequence of minerals dissolution while acidizing can be observed by temperature measurements. This can help to understand the effectiveness and location of the different stimulation treatment.

With the well in production, qualitative information about gas lift valves, packer isolation, cement channelling, producing intervals, leaks, etc. can be extracted. Figure 7.B.2 shows a well that had been closed a number of days. The well was put in production and is clear that the Gas Lift Valve 2 is injecting. The producing interval shows cooling from some perforations, while others do not seem to undergo any change. The operation of the ICVs can also be understood from this picture:

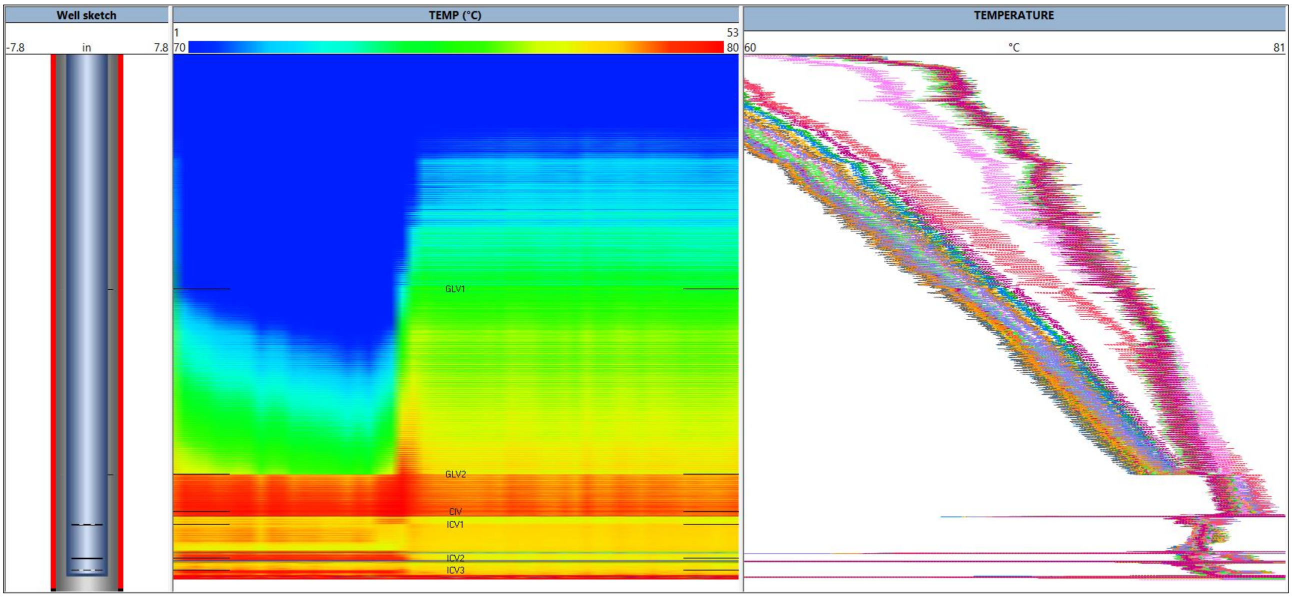

Fig. 7.B.2 – Start-up sequence of a gas-lifted well

Flow profiling

The implementation of the thermal models in Emeraude dates from 2001, where a “Segmented” model (Ramey equation and enthalpy balance) was introduced. Later in 2010 the Energy model was also implemented in Emeraude. Being a PL interpretation software, the early use of these models was in general intended to replace the use of the spinner as main fluid velocity source, when due to the sensor condition (clogged, broken) or the flow regime challenges (recirculation, segregation), the flowmeter measurements did not provide a representative velocity.

Figure 7.B.3 shows a PL acquisition were, below the tubing, the Fullbore spinner indicates downwards moving flow. At the same time, the capacitance and density tools show that this interval is filled with water. What the spinner is actually measuring is the recirculating water, flowing down on the low side of the pipe while the light phase flows upwards on the high side of the pipe. A temperature measurement can be used as a replacement of the spinner in the interval where this indicates downwards flow to quantify the production profile. Other sensors contained in the PL toolstring can be added in the interpretation.

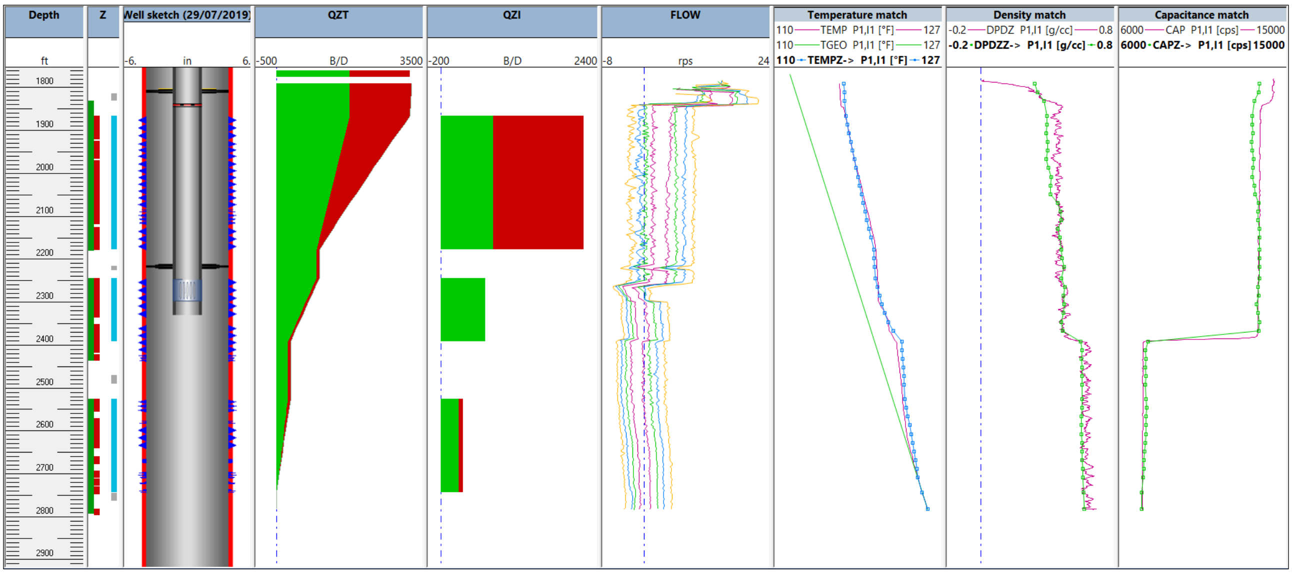

Fig. 7.B.3 – Temperature-based multiphase flow profiling

Water injection profiling

In typical water injection conditions, the water temperature is considerably lower than the formation temperature. While injecting the temperature changes due to the different outflows are in general very small and difficult to be quantified. However, the measured temperature during shut-in conditions after a period of water injection will reflect the volume of injected water that each layer received previously. This can be used for quantifying the injection profile, using a method called Water Injection Fall-off. Figure 7.B.4 shows an injection profile using DTS temperature data only.

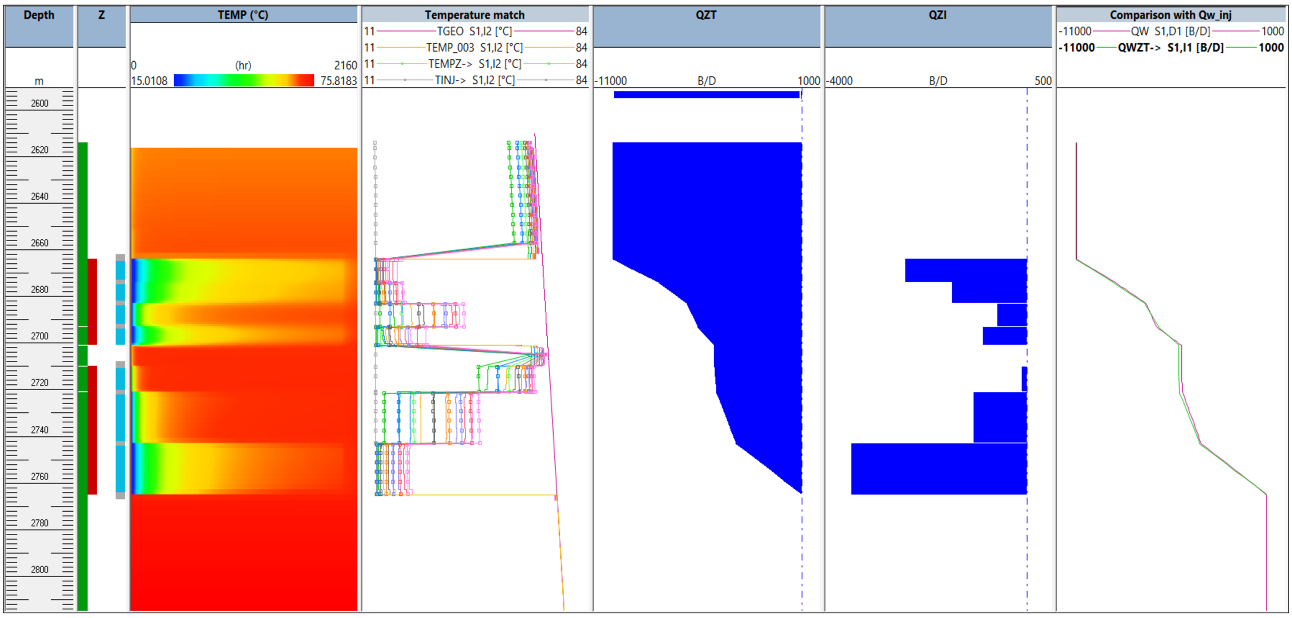

Fig. 7.B.4 – Injection profiling from DTS

Reservoir response

Apart from the single well applications described above, the thermal analysis of a sector of a field might bring interesting insights about different reservoir aspects: interference between wells, connection between producing and injecting wells, high permeability streaks, faults, etc. This type of analysis is on the ground of numerical modelling, where the field model is gridded and the flow and thermal equations are solved for each cell. Rubis incorporates a coupled reservoir-wellbore fully transient, 3D, 3-phase simulator.

Figure 7.B.5 shows the interaction between a producer and injector. The temperature simulations can be displayed as production logs and gauges at any depth (surface, sandface, etc.) facilitating the comparison against measured data. Also the temperature maps are shown in 2D or 3D maps.

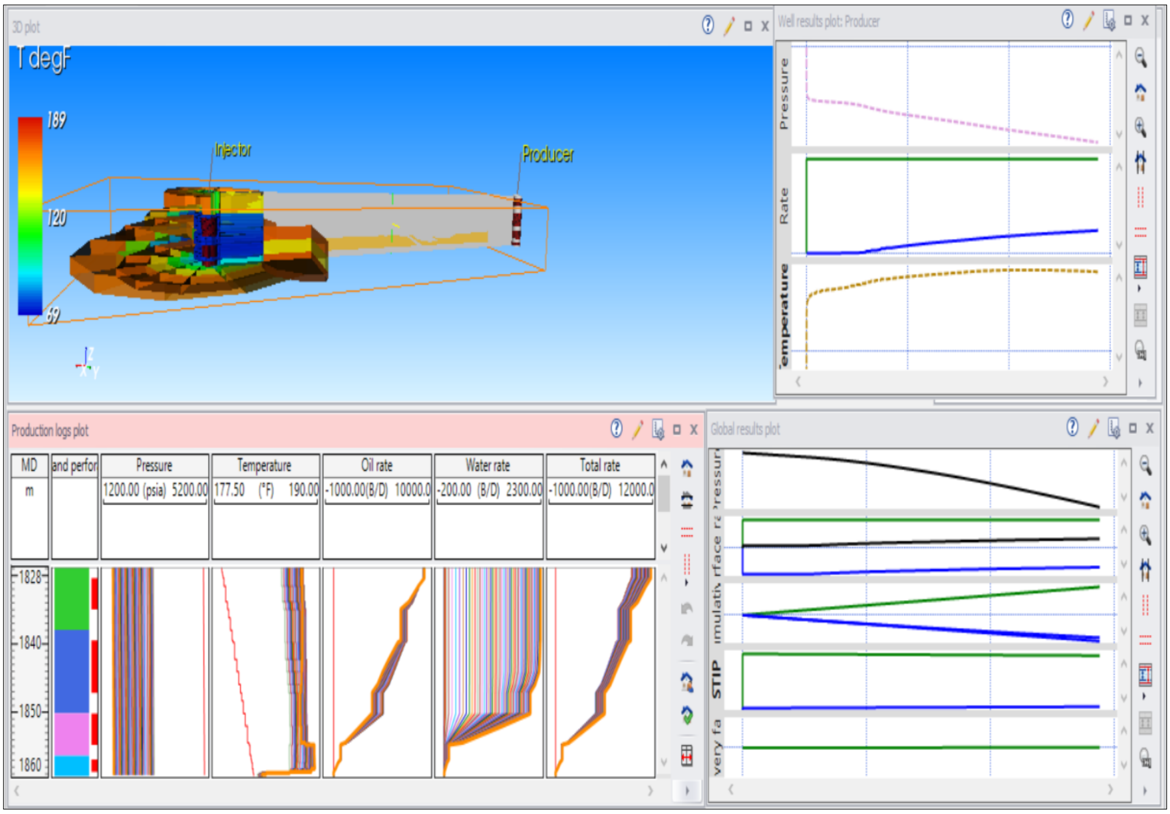

Fig. 7.B.5 – Thermal numerical simulation in Rubis

7.C Temperature Measurements

A brief review of the different technologies on downhole temperature measurements is presented below.

7.C.1 Distributed Temperature Sensing (DTS)

When a monochromatic light interacts with a material like silicon dioxide (SiO_2), the scattered light shows a wavelength shift compared to the incident light. This phenomenon is called Raman Scattering. The molecular vibrations of the SiO_2 lattice structure can gain or lose energy as a result of the interaction with the light's photons. If the material absorbs energy, the backscattered wavelength increases (lower frequency) compared to the incident light. This reflection is called Raman Stokes. On the other hand, if the material loses energy, the wavelength of the backscattered light decreases (higher energy). This is the Raman anti-Stokes peak, and interestingly it has a strong dependency on the temperature of the material. This is the principle of fibre optics temperature measurements.

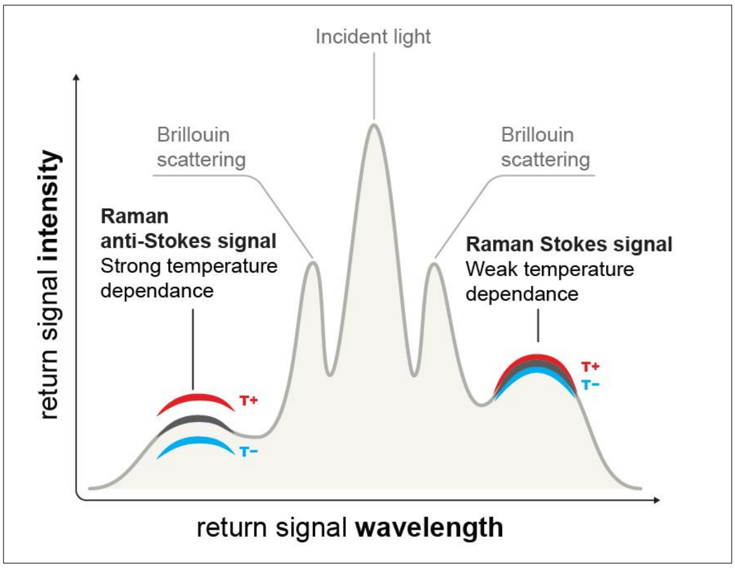

Fig. 7.C.1 – Wavelength spectrum of the backscattered light (Courtesy: AP Sensing)

Distributed Temperature Sensing (DTS) systems couple two main components: a surface opto-electronic interrogator and a fibre optic deployed in the well. The interrogator sends pulses of laser light of short duration (nanoseconds) into the optical fibre. At each depth the photons will interact with the fibre, and the backscattered energy spectrum is analysed at surface. As explained before, the ratio of the Raman Anti-Stokes and Stokes counts is a function of the temperature of the fibre. Assuming that the speed of light through the fibre optic is constant, the location of the backscattered light returning to the surface can be established. This allows obtaining a continuous temperature vs. depth measurements.

The counts received at surface for the different peaks may be small and subject to statistical variation, so a single temperature profile typically results from the computation of multiple laser-fibre interactions. Depending on the acquisition settings, the DTS system can output a temperature trace as few as every couple of seconds or minutes.

The counts per second decrease with depth, reducing the dynamic range between the Stokes and Anti-Stokes counts with the light loss. This can be assessed and corrected by using double ended fibre optics (injecting light through both ends). Otherwise, in single ended fibre optics, a correction factor is applied.

In terms of the metrology of the DTS measurements, the vertical resolution is a function of the length of the pulse, but values down to 0.125 m are reported. Also, a minimum resolution of 0.01 °C is reported, comparable with conventional temperature gauges. To increase the accuracy, temperature is measured independently at the interrogator.

The core glass of the fibre is made of fused silica, typically around 50 µm. This core is surrounded by a glass cladding of lower refractive index than the core, to ensure total reflection and the light staying in the fibre. Multiple optical fibres can be deployed at the same time, and are normally contained in a ruggedized cable (metal or plastic). The picture below shows the different options of fibre optics for downhole applications, contained in a cable and in a rod:

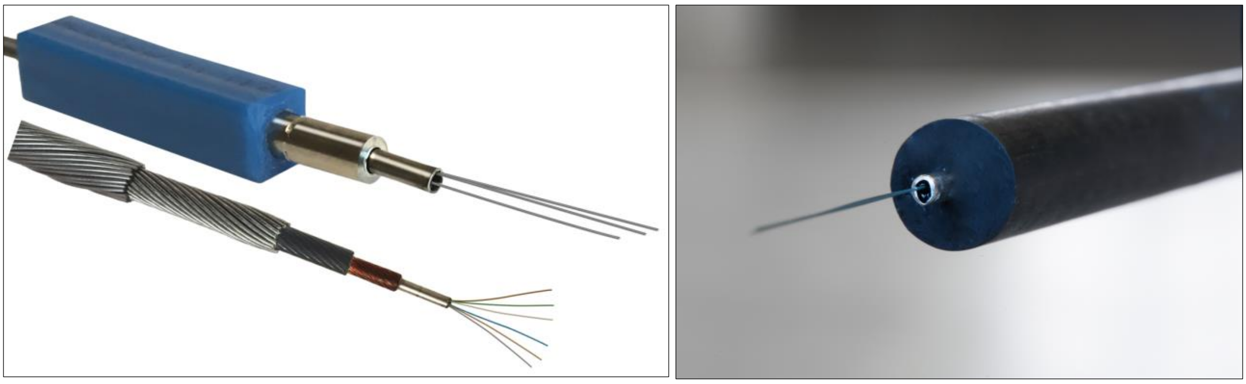

Fig. 7.C.2 – Left Image: Permanent and wireline Fibre Optics (Courtesy: Silixa). Right Image: Carbon rod with fibre optics (Courtesy: Ziebel)

The most typical deployment options are:

- Permanent: strapped on the casing and cemented in place
- Semi-permanent: strapped on the tubing
- Intervention-based: deployed through tubing for a specific acquisition program

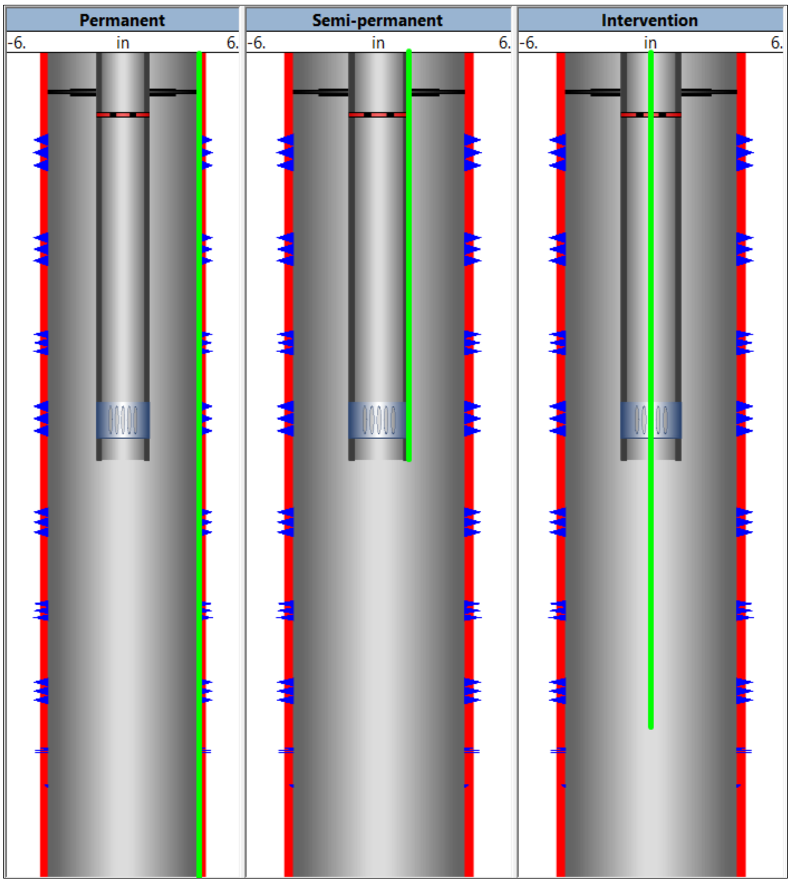

Fig. 7.C.3 – DTS deployment options

Among the advantages of DTS it can be mentioned that there is no need of downhole electronics, that may be prone to degrade with harsh environments. Permanent fibre installations do not require (neither allow) maintenance, but the surface interrogator may be replaced if needed.

7.C.2 Discrete Temperature Sensors

A different technology able to provide a continuous temperature vs. depth profile at different times consist on arrays of discrete temperature sensors. These are clamped onto TCP guns, DST assembly and some completion elements, like sand screens.

The sensors can be very closely spaced, down to 0.2 m, which gives similar vertical resolution than the DTS systems. The sensors require energy, which is provided by batteries. Depending on the duration of the acquisition program, a single battery that lasts up to 30 days may be used, or extended battery packs may be added allowing years of measurements.

The data transmission to surface is wireless, which adds flexibility on the type of completion or tool where this array may be installed.

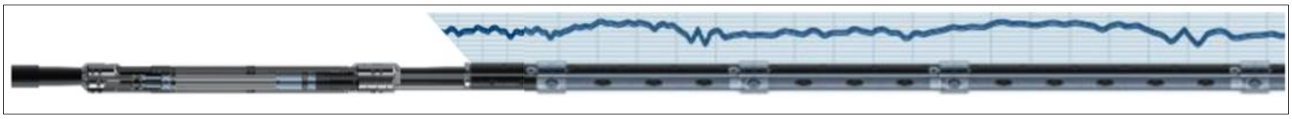

Fig. 7.C.4 – Discrete Temperature Sensors (Courtesy: Metrol – PRO-LOG®)

7.C.3 Temperature gauges

Temperature gauges can be installed at different depths of the well, from surface to typically above the producing interval. These installations are sometimes part of Permanent Downhole Gauges (PDGs), and can provide valuable data especially after water breakthrough or gas production. Moreover, it can be used as targets in thermal PTA or full field simulations.

Temperature gauges are also run as part of PLT acquisitions. Whilst in the past these measurements were meant to provide zonal temperature for PVT calculations and qualitative indications of production/injection and integrity, this chapter will explain how the different thermal models can turn this data into profiles.

The most widely used temperature gauges for PLT applications are platinum resistance thermometers. The resistance of the metals increases pretty much linearly with temperature, and therefore by measuring the voltage of a circuit subject to a constant current, it is possible to obtain a temperature value from a calibrated device.

More recently Micro-Electro-Mechanical Systems (MEMS) started to be used in the industry, featuring monocrystalline sensing elements. These can be packed in small containers of different shapes. The Figure 7.C.5 shows one of these sensors, used for PLT applications.

Fig. 7.C.5 – MEMS Temperature gauge (Courtesy: OpenField)

7.D Theory review

The equations used to model the temperature in the wellbore and the reservoir are based on well-known heat transfer and thermodynamic principles. A revision of the physics involved is presented next.

7.D.1 Heat Conduction

Fourier's Law of heat conduction established that the heat flux (q) is proportional to the temperature gradient along certain material. The constant of proportionality λ is known as the thermal conductivity of the material or fluid. Fourier's law can be expressed as:

$$\vec{q} = -\lambda \nabla T$$

Where the heat flux is a vector quantity and is of opposite sign to the temperature gradient, meaning that heat flows from warmer to cooler areas. This mechanism of heat conduction occurs as a concequence of the energy transfer caused by the molecules movement. In general terms, the thermal conductivity is an anisotropic scalar magnitude and temperature dependent $\lambda = \lambda(x, y, z, T)$. However, for the applications of interest, λ can be considered constant for the range of temperatures and isotropic. For the different materials and fluids found in an oil well, the magnitude of the heat conductivity can vary up to 4 orders of magnitude.

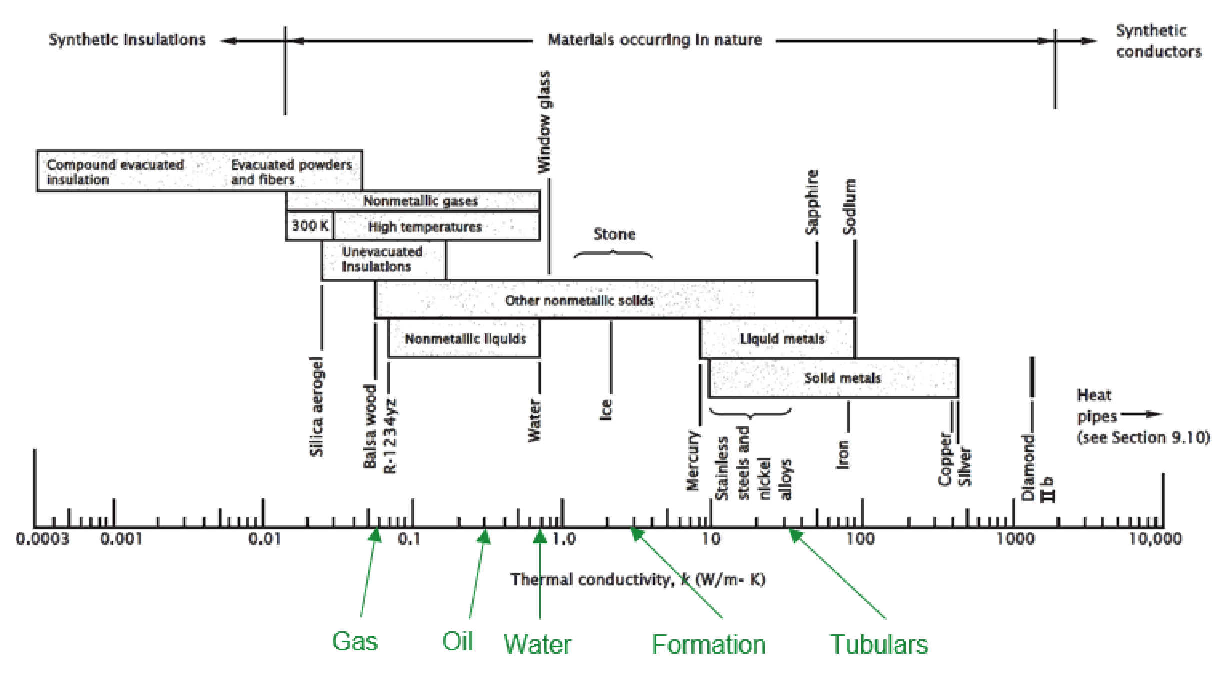

Fig. 7.D.1 – Thermal conductivity for different materials (from Lienhard, 2018)

In producing or injecting wells these different materials are connected in series as shown Figure 7.D.2. A consequence of the large differences between the thermal conductivity of the materials involved is that the casing and tubing will be virtually isothermal and the largest temperature drops will occur in the fluids, since $\frac{dT}{dr} = \frac{q}{\lambda}$. A practical application of this is to fill the casing-tubing annular with nitrogen to minimize the heat losses to avoid flow assurance issues, such as asphaltenes precipitation.

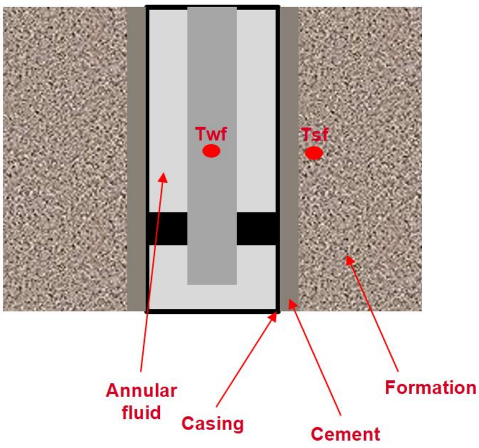

Fig. 7.D.2 – The thermal conductivity of the different components spans over 4 orders of magnitude.

7.D.2 Heat Convection

Convective heat transfer is described by the Newton's law of cooling. The equation indicates that, for a system composed of a body immersed in a fluid at a different temperature, the heat flux is proportional to the temperature difference between the body and the moving fluid. In this case the proportionality constant "h" is called Heat transfer coefficient or sometimes referred as "Film coefficient".

$$\vec{q} = \bar{h}\,(T_{body} - T_{\infty})$$

When the fluid is moving, for example due to a pressure difference or gravity, the heat transfer process is called "Forced convection". However, if the fluid is still, the molecules in contact with the hot body will increase their energy, will start to move faster and its density will decrease. This will create convective currents due to density differences in the fluid column. This is called "Free convection".

The Heat transfer coefficient depends on many factors, including the shape of the body, fluid velocity, temperature difference, thickness of boundary layer, etc.

7.D.3 Radiation

All the bodies emit energy through electromagnetic radiation. Bodies at high temperatures may emit energy in the visible spectrum (fire, the sun, etc.), but the radiation emitted by humans can only be seen with infrared cameras. Compared to conduction and convection, radiation does not require a medium.

Perfect radiators are called "Black Bodies" and they absorb all the energy and reflect none. The Stefan-Boltzmann law for a Black body states that the total energy emitted (integral for all wave lengths) is given by:

$$e(T) = \sigma\,T^4$$

Were σ is the Stefan-Boltzmann constant. This expression implies that the energy emission is independent on the body characteristics and is a strong function of the temperature (fourth power). However, the materials considered in our heat transfer problems are not perfect black bodies. Therefore, an “emittance” coefficient is included in the Stefan-Boltzmann equation to account for real bodies.

In oilfield applications, radiation is the least important heat transfer mechanism for typical temperatures.

7.D.4 Heat Loss Coefficient

It is beyond the scope of this book to derive the thermal diffusivity equation. For cylindrical coordinates, the expression is:

$$\frac{1}{r}\frac{\partial}{\partial r}\left(r\frac{\partial T}{\partial r}\right)+\frac{1}{r^2}\frac{\partial^2 T}{\partial \theta^2}+\frac{\partial^2 T}{\partial z^2}=\frac{1}{\alpha}\frac{\partial T}{\partial t}$$

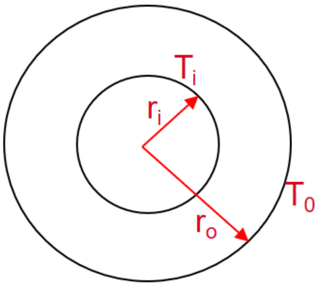

Considering a hollow cylinder (i.e. a pipe) at steady state and where the axial (z) and azimuthal (θ) components are negligible, from the thermal diffusivity equation and the definition of conductive heat transfer (Fourier’s law), it is possible to find that the heat decreases with the radius as:

$$q_{radial}=\frac{\lambda\,\Delta T}{ln\,(\frac{r_o}{r_i})}\,\frac{1}{r}$$

The total heat transfer in the cylinder of length *l* can then be calculated as:

$$Q(W)=\frac{2\pi\,\lambda\,l\,\Delta T}{ln\,(\frac{r_o}{r_i})}$$

This expression resembles other physical processes where a potential (pressure, voltage, concentration, etc.) leads to a flux. Equations of this type are Darcy, Ohm, Fick, etc. As an analogy with Ohm’s law, the thermal resistance can be defined as:

$$R_{t_{cyl}}=\frac{ln\,(\frac{r_o}{r_i})}{2\pi\,\lambda\,l}$$

Starting again from the thermal diffusivity equation in radial coordinates, but replacing the external temperature (T_0) by a convective boundary condition, the total heat transfer can be calculated as follows:

$$Q=\frac{T_i-T_\infty}{\frac{1}{h\,2\,\pi\,r_o\,l}+\frac{ln\,(\frac{r_o}{r_i})}{2\,\pi\,\lambda\,l}}$$

The delta T is now divided by the sum of the convective and conductive thermal resistance. This concept becomes very useful when, apart from having a single cylinder, there are multiple concentric cylinders, as found in wells with tubing, annulus, casing, cement, etc. The Heat transfer coefficient “U” is defined so:

$$Q=U\,A\,\Delta T$$

With the heat transfer coefficient U defined as the sum of all the different completion components, based on their geometry and thermal properties (*i*=inner, *o*=outer):

$$\frac{1}{U}=\frac{r_o\ln({}^{r_o}/_{r_i})}{\lambda_{tub}}+\frac{r_o\ln({}^{r_{ci}}/_{r_o})}{\lambda_{ann}}+\frac{r_o\ln({}^{r_{co}}/_{r_{ci}})}{\lambda_{cas}}+\frac{r_o\ln({}^{r_w}/_{r_{co}})}{\lambda_{cem}}+\frac{r_o}{r_{ci}\,(h_c+h_r)}$$

Where the first four terms are the conductive components of the tubing, annular, casing and cement. The terms h_c and h_r are convective terms accounting for the annulus free convection and the annulus radiation respectively (Hassan and Kabir, 2002). Note that the presence of these corrective terms for the annulus introduces a dependence of *U* on the temperature, increasing the nonlinearity of the system.

For convenience, two other parameters are derived from the Heat transfer coefficient:

- Heat Loss Coefficient: $HLC = U\,2\pi\,r_w$
- Thermal Conductance: $D_{wb} = U\,2\pi\,dL\,r_w$

The required geometrical parameters and thermal properties for each completion element are entered either at the Well intake definition in Rubis or at the interpretation information in Emeraude. Tables with thermal properties for different materials are provided in the software for reference. However, it is important to understand the impact of the thermal and geometrical characteristics of the different components on the Heat transfer (or Heat loss) calculations.

Let’s consider a completion composed by a 7’’ casing (6.184’’ ID) of thermal conductivity of 35 W/m °K, surrounded by cement OD=8.5’’ of 1.3 W/m °K. This base case (BC) leads to a HLC= 41.4 W/m °K. Figure 7.D.3 on the left shows the variation of HLC for changes in either the cement or the casing thermal conductivity. Varying the casing conductivity from 5 to 100 W/m°K does not lead to a significant change in the HLC from the Base case. On the other hand, a change in cement conductivity of between 0.1 to 10 leads to a variation of 200 times of the HLC.

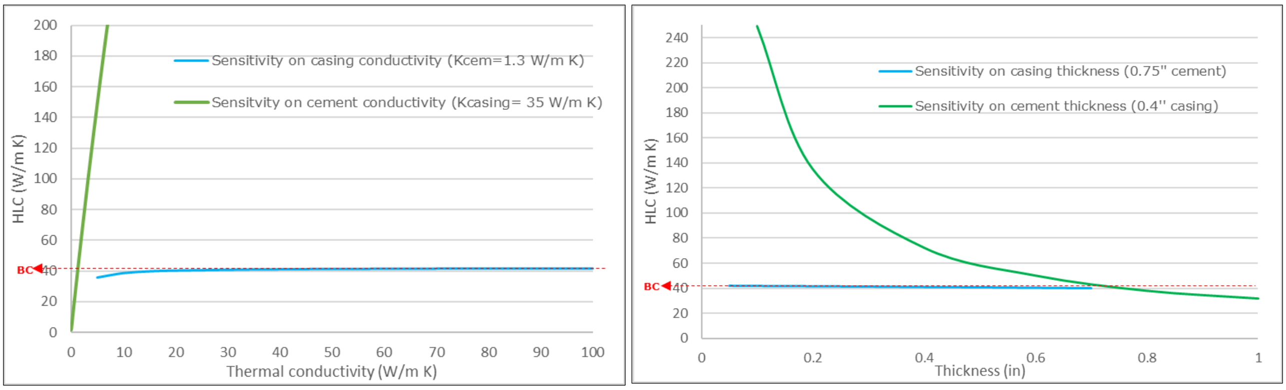

Fig. 7.D.3 – Sensitivities on the HLC estimations.

Similarly, the image on the right shows the variation on HLC for different casing and cement thickness. In this range of normal values, the casing thickness does not have a significant influence on the final HLC. However, an increase in the cement thickness leads to a rapid drop of the HLC.

These sensitivities show that, since the different completion components are connected in series, the influence of the material of lowest thermal conductivity will be preponderant. Errors in the thermal properties of the cement and annular fluids will have a large impact, while the casing and tubing won't have a large effect. A large HLC value favors the heat exchange with the formation, so the fluid between perforations will tend to come back quicker to the geothermal.

7.D.5 Geothermal Gradient

It is estimated that the earth's core temperature is between 5400 to 6000 °C. Clearly the surface of the earth is at a much lower temperature. As a consequence of this temperature gradient, and as shown by the Fourier's law, a net heat flux will exist. This heat flux is not isotropic, and in general is larger in areas where the tectonic plates are in contact, and where seismic or volcanic activity exists.

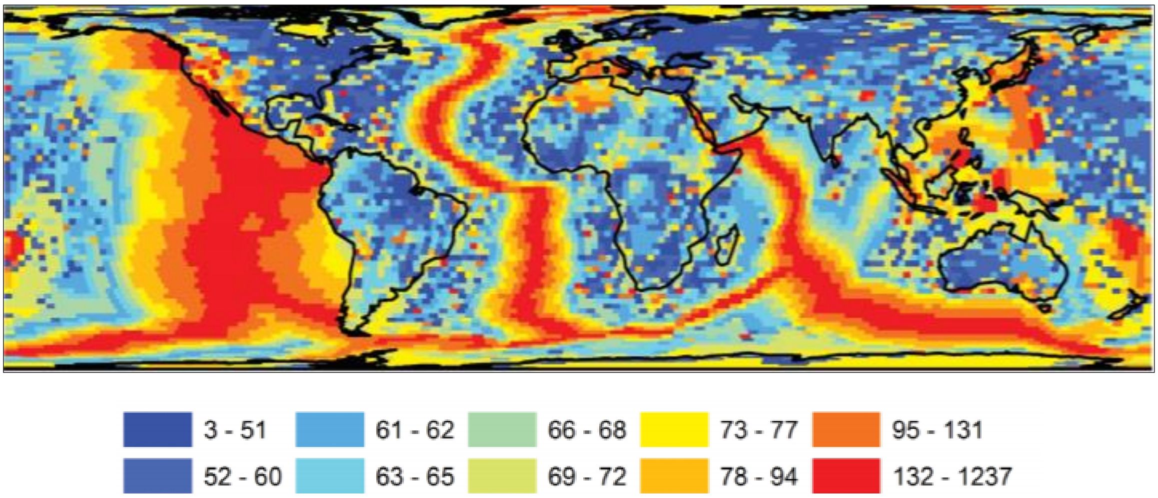

Fig. 7.D.4 – Heat flux map (mW/m2). From Davies (2003)

For a certain location in the earth the heat flux will be constant. When analysing the temperature variation vs. depth, the gradients will be given by $\frac{dT}{dz} = \frac{q}{\lambda}$. The thermal conductivity can be quite different depending on the mineralogy of the formation, with sandstones ~ 2.5 – 4.2 W/m K, shales ~ 1.05 – 1.45 W/m K and Claystone/siltstone ~ 0.8 – 1.25 W/m K. In general, away from the tectonic plates, the temperature increases 10-30 °C per km.

The determination of the geothermal gradient is very important, since the assumption will be that reservoir fluids far from the well are at thermal equilibrium with the formation, and thus at the geothermal temperature at that depth. Establishing the gradient would then consist in measuring an undisturbed formation temperature, during shut-in for example. While this is possible, due to the low thermal conductivity values of the formation, reaching the equilibrium would take a long time and wouldn't be operationally feasible in producing and injecting wells. Also geothermal gradients measured shortly after the well was drilled will be affected by the invasion and circulation of drilling and completion fluids.

The geothermal gradient can sometimes be measured in regions of the well with no fluid movement, like the sump below the bottom producing/injecting interval. Care must be exercised since the temperature in the sump might be affected by fluid movement behind casing or the vertical thermal conductivity due to the fluid production from the deepest perforation. This is shown in Figure 7.D.5, where the PL-derived flow profile shows the deepest perforation, however the temperature track shows temperature variations vs. depth, which could result in non-representative geothermal gradient estimations:

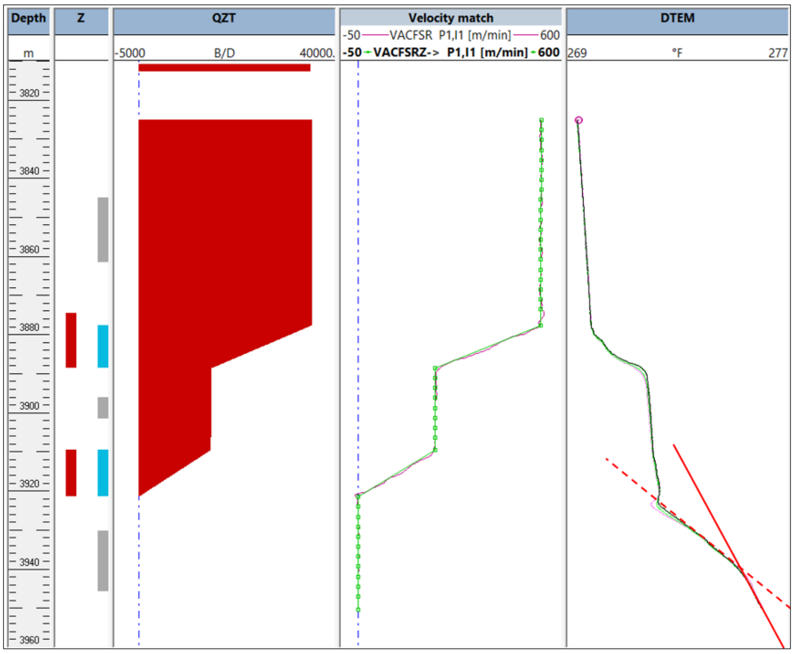

Fig. 7.D.5 – Temperature in the sump varying with depth

In high angle/horizontal wells it may not be possible to establish the geothermal temperature from measurements in the sump or during shut-in. Reference values for the area can be used as a first approach, even though the interpreter may need to treat these values more like a variable rather than a fixed parameter. In deviated wells it is necessary to enter the deviation survey for the gradient to be corrected vs. depth.

7.D.6 Joule-Thomson Effect

In the previous section it was mentioned that far field fluid temperature is equal to the geothermal temperature. However, as the fluid moves towards the well, it undergoes a pressure change (drop for producers) as given by the Darcy law in radial coordinates:

$$p(r) = p_{wf} + \frac{q\,\mu\,B}{k\,h}\ln\left(\frac{r}{r_w} + S\right)$$

The Joule-Thomson effect establishes that the temperature change is proportional to the pressure change, and the proportionality constant is given by the Joule-Thomson coefficient.

$$\Delta T = K_{JT}\,\Delta P$$

Strictly speaking the Joule-Thomson effect describes an isenthalpic process, which is achieved in steady state production conditions. The constant can be obtained from thermodynamic parameters as:

$$K_{JT} = (\frac{dT}{dP})_H = \frac{1}{C_P}\,(T\,\frac{dV}{dT} - V)$$

Where V is the specific volume (inverse density), $\frac{dV}{dT}$ is the thermal expansion and Cp is the specific heat.

Let's consider the production of single phase water. The change in volume for water is negligible in the temperature range that concerns us. Therefore, the expression of the Joule-Thomson coefficient can be reduced to $K_{JT} = \frac{-V}{C_P}$. From $\Delta T = K_{JT}\,\Delta P$ it is clear that as the water approaches the well it decompresses (negative ΔP) and since the K_{JT} is negative, the fluid will experience a warming. This is sometimes referred to as "Viscous heating".

The other extreme is to consider gas, which has a high compressibility and high thermal expansion. For typical downhole pressures the Joule-Thomson coefficient shows a positive sign. As a consequence, as the gas decompresses (negative ΔP), the temperature also drops. However, for high pressures (>7000 psia) there is an inversion point and K_{JT} will be negative, resulting in heating.

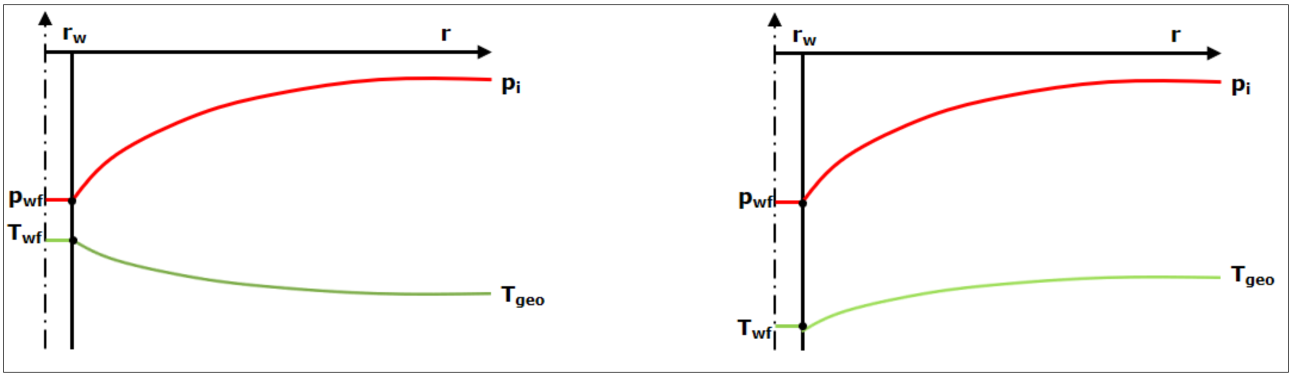

Fig. 7.D.6 – Reservoir Temperature profile predicted by Joule-Thomson for liquids or high pressure gas (left) and gas (right, pressure < 7000 psia)

Typical K_{JT} for water is around -0.0016 °C/psi, while for gas it can be around 0.016 to 0.032 °C/psi. This means that water requires a drawdown 10 times higher than gas to produce a similar ΔT. Oil would also have a negative K_{JT} (leading to heating). The temperature response of a layer producing gas and condensate would depend on the mass of both liquid and gas components, and might end up in cooling or warming.

The ΔP experienced by the fluid on its way to the well shows a sharp change around the wellbore, and it is influenced by the permeability of the formation and damage. From the thermal diffusivity equation, it can be deduced that rapid changes in temperature when shutting-in the well can indicate skin. On the contrary, highly permeable formation or stimulated intervals would show very slow temperature changes.

In thermal interpretation, apart from dealing with the traditional PVT parameters used in PL or PTA interpretation, the definition of certain thermodynamic properties will have an impact on the simulations. Figure 7.D.7 shows the temperature profiles predicted in Emeraude when the produced fluid heat capacity (Cp_g) increases from 0.01 Btu/(lbm.°F) to 5 Btu/(lbm.°F), the zone contributions being unchanged and identical on each zone.

It can be seen that the higher the fluid heat capacity, the lower the cooling effect on the inflow zones as expected by the K_{JT} definition. But also, higher heat capacity means a more efficient convective heat transfer by the fluids coming from deeper depths, and this counterbalance the heat conduction between inflows.

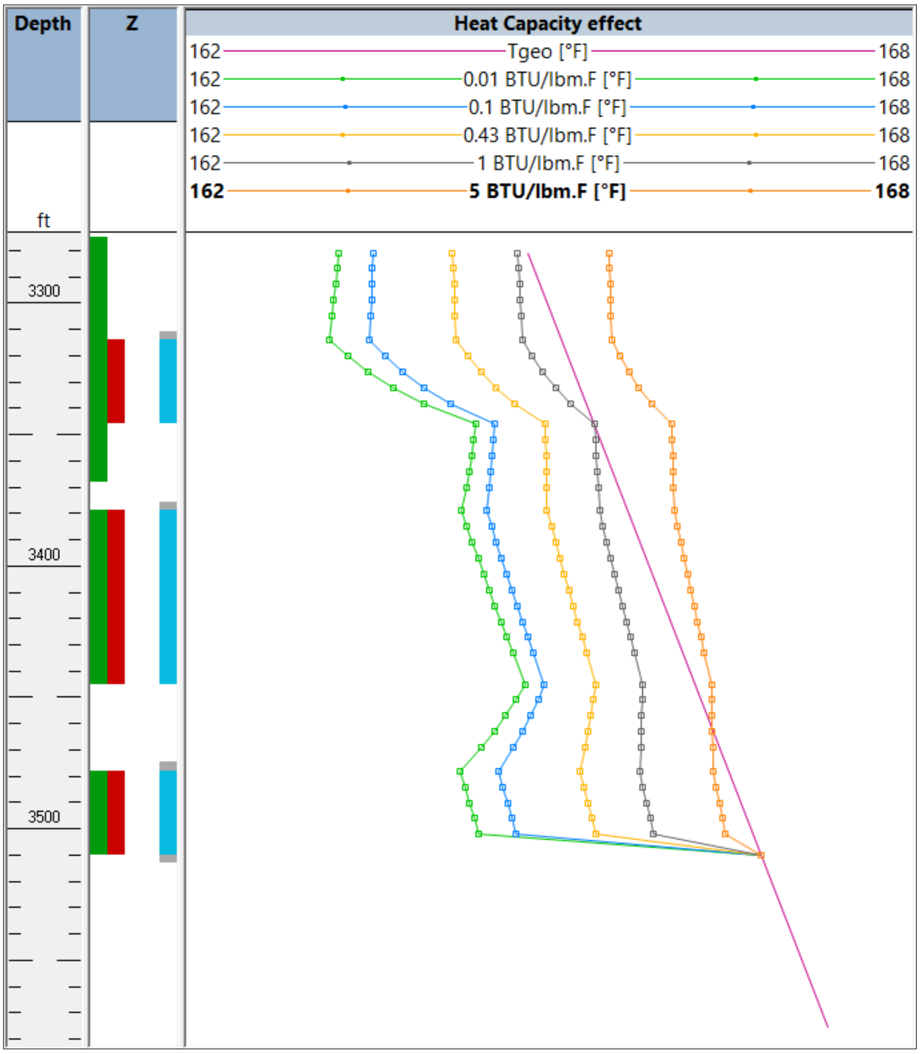

Fig. 7.D.7 – Effect of the fluid heat capacity on the simulated temperature (Gas producer)

7.D.7 Ramey Equation and qualitative analysis

Early models to predict the temperature profile in producing or injecting wells used the work of Ramey (1962) to model the temperature. Ramey's original work dealt mainly with water injectors, and therefore the assumptions are valid for single phase incompressible fluids. Moreover, the inflow/outflow itself is not modelled, and does not account for cooling or warming at the perforation interval.

The Ramey equation shows:

$$T\,(z,t) = T_{ge} - g_G\,z \underset{z}{+} g_G\,A$$

With the term A being a function of the rate (Q), density and heat capacity:

$$A = 1.66\,Q\,\rho_f C_f\,f(t)$$

and the time dependent term:

$$f(t) = -ln\left(\frac{r_{ce}}{2(\lambda t)^2}\right) - 0.29$$

For a producing well, considering no heating or cooling at the inflow point, the fluid will enter at the geothermal temperature. Above that depth the temperature will evolve as predicted by the Ramey equation. When the distance from the inflow "z" is much larger than A, the exponential in the last term of the equation tends to zero. Then the flowing temperature approaches an asymptote parallel to the geothermal, with the offset given by the rate and also time of production. This is shown in Figure 7.D.8 (I).

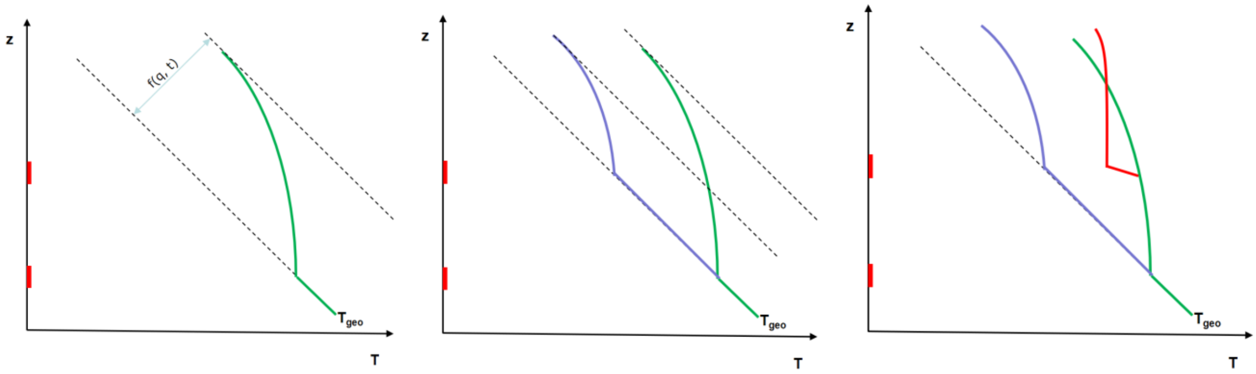

Fig. 7.D.8 – (I) Single inflow at the bottom perforation. (II) Two inflow zones producing independently. (III) Two inflow zones producing comingled.

Consider now the presence of two inflows producing independently of each other (II). From the offset of the temperature profile and the geothermal gradient it is clear that the bottom perforation produces a higher rate than the upper perforation (with all the rest of variables constant).

Finally, considering the commingled production of the two perforations (III), the final response is shown in red. The warmer fluid coming from the bottom perforation is mixed with cooler fluid coming from the upper perforation. This is seen as a temperature drop in the resulting red curve. The offset of the red curve from the geothermal will be given by the sum of the production from both perforations. In real cases, if the perforations are very close together or the rates are very large, it might be impossible to see the stabilization of the measured profile. This limits the applicability of this technique.

The first thermal model implemented in Emeraude was called "Segmented" model and used the Ramey equation plus an enthalpy balance with imposed pressure drops and the different inflows. This model is no longer available in Emeraude since it does not have any advantage compared to the method that will be described next.

7.D.8 Energy and mass balances

At the core of the Rubis thermal engine and Emeraude "Energy" model, equations of Energy and mass balance are solved in the reservoir and the wellbore. The implementation of these balances is different in both modules and will be explained in sections 7.E and 7.G.

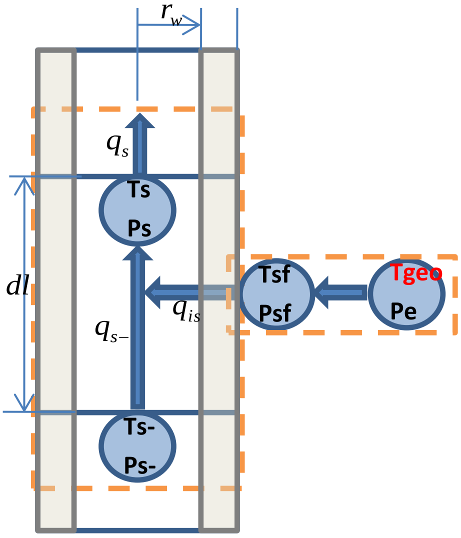

Let's consider a small segment of the wellbore, of length dl, in front of a reservoir zone. The energy coming to the segment minus the energy leaving is equal to the energy accumulation:

$$\frac{dE}{dt} = E_{in} - E_{out}$$

The energy concentration "e" (energy divided by mass) of an infinitesimal volume of fluid is composed by internal energy "u" (thermal movements of molecules), kinetic and potential energy:

$$e = u + \frac{1}{2}v^2 + gdl$$

For a producing well, the energy coming into the segment (E_{in}) can be further expanded into the energy carried by the fluid coming from below in the pipe (q_{s-}), the energy transported by the fluid coming from the reservoir (q_{is}) and the energy transported as heat from the reservoir. Also, incorporating the concept of energy concentration and the expansion work, the energy balance can be expanded as:

$$\frac{dE}{dt} = q_{s-}\,\rho_{s-}\,e_{s-} + q_{is}\,\rho_{is}\,e_{is} - q_s\,\rho_s\,e_s + D\,\Delta T + q_{s-}\,\rho_{s-}\,(\frac{P_{s-}}{\rho_{s-}}) - \ q_s\,\rho_s\,(\frac{P_s}{\rho_s})$$

Grouping the terms of energy coming from below and going to the segment above, and the expansion work (last two terms), the concept of enthalpy is introduced as

$$h = u + \frac{P}{\rho}$$

Putting all together, the energy balance for a segment of the wellbore is defined by:

$$\frac{dE}{dt} = q_{s-}\,\rho_{s-}\,(h_{s-} + \frac{1}{2}(\frac{q_{s-}}{A\,\rho_{s-}})^2 + g\,dl) + q_{is}\,\rho_{is}\,(h_{sf} + \frac{1}{2}(\frac{q_{sf}}{A\,\rho_{sf}})^2 + g\,dl) - q_s\,\rho_s\,(h_s + \frac{1}{2}(\frac{q_s}{A\,\rho_s})^2) + D\,\Delta T$$

The same procedure is done for a small volume of the reservoir. This time it is necessary to consider that the energy accumulation (and thus the temperature change) occurs both in the fluid (contained in the porosity fraction, φ) and the rock fraction (1- φ). Using the concept of material derivative, the energy balance for a reservoir cell can be expressed as:

$$\varphi\rho\,\frac{\partial h}{\partial t} + (1-\varphi)\,\rho_r\,\frac{\partial h_r}{\partial t} + \rho\,v\,\nabla h - \frac{\partial P}{\partial t} = \ \rho g v + \ \nabla(\lambda\,\nabla T)$$

The terms on the left of the equality correspond to the accumulation and convection of enthalpy, while on the right is the energy transferred by the fluid and by heat conduction.

These balances were written for single phase but can be easily extended to multiphase by considering the holdup-weighted sum of the different phases.

For the mass balance, the conservation equation states:

$$\frac{dm}{dt} = m_{in} - m_{out}$$

This equation can be applied both to a small volume of reservoir and to a segment of the well. Clearly, the equations governing the fluid movement in the different media are well known.

7.E Emeraude "Energy" equation - Production and Injection profiling

The implementation of the thermal model in Emeraude is called "Energy" equation. This model consists on a direct simplification of the mass and energy balance equations presented in the previous section. The main assumption is that the flow is steady state, which allows setting the transient terms $\frac{\partial E}{\partial t}$ to zero. Also, in this formulation there is no vertical conduction within the reservoir.

Under steady state conditions, the reservoir is defined by two points:

- An outer point representing the undisturbed conditions at some distance r_e, where the temperature is given by the geothermal T_{geo} and the pressure is the external reservoir pressure P_e
- An inner point representing the sandface temperature and pressure at distance r_w, given by T_{sf} and P_{sf}

Having two nodes in the reservoir introduces the need of an extra equation to relate P_e and P_{sf}. This extra equation is Darcy under steady state conditions, that also allows accounting for the geometrical and mechanical skin terms.

$$\Delta P_{sf-e} = P_e - P_{sf} = \frac{(Q\,\mu)}{2\,\pi\,k_H\,h_T}\left[\frac{h_t}{L_w}\,S + \ln\left(\frac{r_e}{r_w}\right) + S_G\right]$$

The pressure drops are then computed iteratively at the average pressure point and at flowing wellbore temperature.

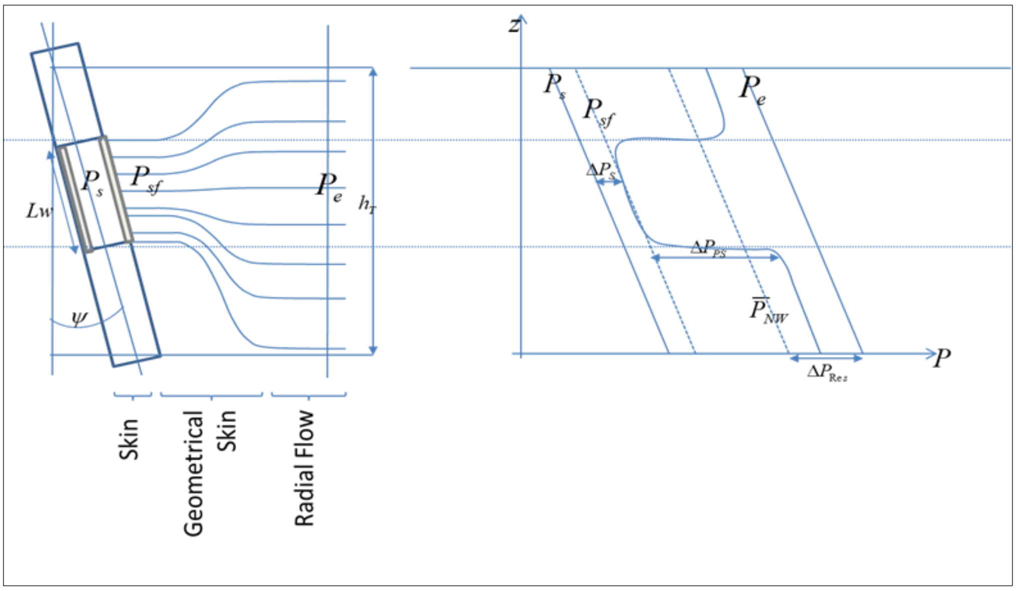

Fig. 7.E.1 – Pressure drop components

The Pseudo-skin, S_G, depends on the well deviation, the anisotropy, the geometry of the perforations and the formation. It is evaluated from Chen et al. (1995), with an anisotropic correction from Pucknell & Clifford (1991).

7.E.1 Resulting formulation of the Energy equation

The energy balances were obtained in the previous section for a generic case. Implementing the steady state assumption and removing the vertical thermal conductivity in the reservoir leads to the following expressions for the energy balance in the wellbore (E1) and reservoir (E2) for different wellbore conditions:

Energy equations for a ***producer***

$$E1 = q_{s-}\,\rho_{s-}\,(h_{s-} + \frac{1}{2}(\frac{q_{s-}}{A\,\rho_{s-}})^2 + g\,dl) + q_{is}\,\rho_{is}\,(h_{sf} + \frac{1}{2}(\frac{q_{is}}{A\,\rho_{sf}})^2 + g\,\frac{dl}{2}) - q_s\,\rho_s\,(h_s + \frac{1}{2}\left(\frac{q_s}{A\,\rho_s}\right)^2) + D_{wb}\,(T_{sf} - \tilde{T}_s) = 0$$

$$E2 = q_{is}\,\rho_{is}\,(h_{sf} + \frac{1}{2}(\frac{q_{sf}}{A\,\rho_{sf}})^2 - h_{res}) + D_{wb}\,(T_{sf} - \tilde{T}_s) + D_{res}\,(T_{sf} - T_{geo}) = 0$$

Energy equations for a ***producer with a thief zone***

$$E1 = q_{s-}\,\rho_{s-}\,(h_{s-} + \frac{1}{2}(\frac{q_{s-}}{A\,\rho_{s-}})^2 + g\,dl) - q_{is}\,\rho_{is}\,(\tilde{h} + \frac{1}{2}(\frac{q_{is}}{A\,\tilde{\rho}})^2 + g\,\frac{dl}{2}) - q_s\,\rho_s\,(h_s + \frac{1}{2}\left(\frac{q_s}{A\,\rho_s}\right)^2) + D_{wb}\,(T_{sf} - \tilde{T}_s) = 0$$

$$E2 = -\,q_{is}\,\rho_{is}\,(\tilde{h} + \frac{1}{2}(\frac{q_{sf}}{A\,\tilde{\rho}})^2 - h_{res}) + D_{wb}\,(T_{sf} - \tilde{T}_s) + D_{res}\,(T_{sf} - T_{geo}) = 0$$

Energy equations for an ***injector***

$$E1 = -\,q_{s-}\,\rho_{s-}\,(h_{s-} + \frac{1}{2}(\frac{q_{s-}}{A\,\rho_{s-}})^2) + q_{is}\,\rho_{is}\left(\tilde{h} + \frac{1}{2}\left(\frac{q_{is}}{A\,\tilde{\rho}}\right)^2 - g\,\frac{dl}{2}\right) + q_s\,\rho_s\,(h_s + \frac{1}{2}\left(\frac{q_s}{A\,\rho_s}\right)^2 + g\,dl) + D_{wb}\,(T_{sf} - \tilde{T}_s) = 0$$

$$E2 = -\,q_{is}\,\rho_{is}\,(\tilde{h} + \frac{1}{2}(\frac{q_{sf}}{A\,\tilde{\rho}})^2 - h_{geo}) + D_{wb}\,(T_{sf} - \tilde{T}_s) + D_{res}\,(T_{sf} - T_{geo}) = 0$$

The resulting set of equations is solved simultaneously for the couple of unknown (T_s, T_{sf}), which is performed by an iterative method until convergence is achieved. For a producer, the temperature is updated starting from the lowest producing segment and going up the well to the top reservoir. For an injector, it is updated from the injection point going down the well.

These equations require the knowledge of the pressure and PVT properties. In Emeraude the pressure profile can be either an input (measured pressure) or simulated using a reference pressure (external reservoir, sandface, surface) and the corresponding equations to calculate the hydrostatic and frictional components in single or multiphase situations.

7.E.2 Summarized interpretation workflow

The temperature data to be used for qualitative purposes may come from different sources as explained in Section 7.C. If the interpretation is based on temperature only, the workflow will be almost identical, apart from the data loading and editing stages.

DTS data is loaded either in a single .las file containing multiple traces, or multiple .las files with a single trace per file, .csv files, etc. The traces may be time-referenced or not. The files may contain thousands of traces and not all of them might be of interest. Therefore, the data is “explored” to pick the traces at different times and these are used for the interpretation purposes. Figure 7.E.2 shows the “Explore” option of Emeraude, where it is possible to pick data at any time to display it vs. depth, and also at any depth to display it vs. time.

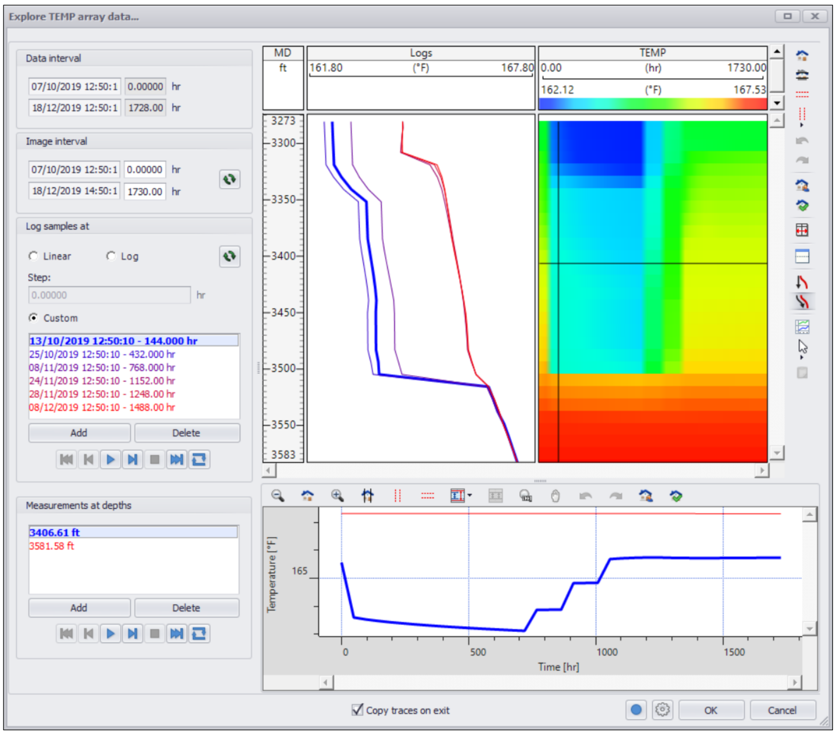

Explore TEMP array data...

Data interval

07/10/2019 12:50:1 0.00000 hr

18/12/2019 12:50:1 1728.00 hr

Image interval

07/10/2019 12:50:1 0.00000 hr

18/12/2019 14:50:1 1730.00 hr

Log samples at

○ Linear ○ Log

Step: 0.00000 hr

● Custom

13/10/2019 12:50:10 - 144.000 hr

25/10/2019 12:50:10 - 432.000 hr

08/11/2019 12:50:10 - 768.000 hr

24/11/2019 12:50:10 - 1152.00 hr

28/11/2019 12:50:10 - 1248.00 hr

08/12/2019 12:50:10 - 1488.00 hr

Measurements at depths

3406.61 ft

3581.58 ft

☑ Copy traces on exit

Fig. 7.E.2 – Emeraude "Explore"
Temperature traces of interest are selected for analysis

Once the traces of interest are exported, it is possible to save the rest of the DTS data as an image, which reduces considerably the size of the file and allows using the data for qualitative purposes.

The thermal interpretation is created. In Emeraude, the "Continuous" method (see PL chapter) is used, since the integral temperature response must be considered: the temperature at certain depth is a function of the temperature profile below (producer), or above (injector). From the traces extracted from the DTS array, it is necessary to define what trace is going to be analysed. This "reference channel" has to be selected bearing in mind the hypothesis of the Energy method, mainly the steady state assumption. Surface rates can be used as a reference of the trace condition.

The completion dimensions and thermal properties need to be entered for calculating the Heat loss coefficient. Emeraude includes a table with different materials and their thermal properties. It was mentioned in Section 7.D.4 that the material with smaller thermal conductivity dominates the magnitude of the HLC. Sensitivities will be presented in the next section. Figure 7.E.3 shows a completion with a tubing down to 3200 ft. The completion dimensions and thermal properties can be defined in segments, to account for the different variations. However, if the temperature-derived flow profile is limited to the producing interval (bottom of the well) then it is not relevant to detail every single change in diameter occurring above this region. Figure 7.E.3 also shows that the free annular convection option is checked. This induces a nonlinear calculation, since the heat transfer coefficient is a function of the temperature.

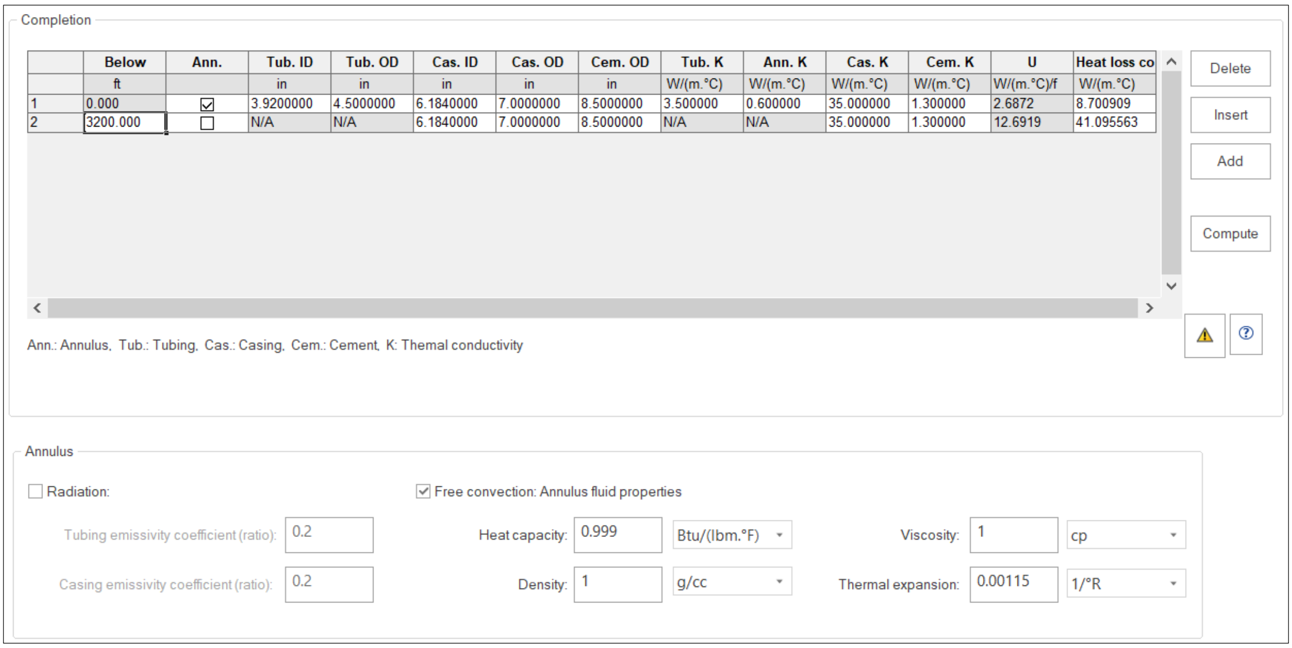

Completion

	Below	Ann.	Tub. ID	Tub. OD	Cas. ID	Cas. OD	Cem. OD	Tub. K	Ann. K	Cas. K	Cem. K	U	Heat loss co
	ft		in	in	in	in	in	W/(m.°C)	W/(m.°C)	W/(m.°C)	W/(m.°C)	W/(m.°C)/f	W/(m.°C)
1	0.000	☑	3.9200000	4.5000000	6.1840000	7.0000000	8.5000000	3.500000	0.600000	35.000000	1.300000	2.6872	8.700909
2	3200.000	☐	N/A	N/A	6.1840000	7.0000000	8.5000000	N/A	N/A	35.000000	1.300000	12.6919	41.095563

Ann.: Annulus, Tub.: Tubing, Cas.: Casing, Cem.: Cement, K: Themal conductivity

Annulus

☐ Radiation:

Tubing emissivity coefficient (ratio): 0.2

Casing emissivity coefficient (ratio): 0.2

☑ Free convection: Annulus fluid properties

Heat capacity: 0.999 Btu/(lbm.°F)

Density: 1 g/cc

Viscosity: 1 cp

Thermal expansion: 0.00115 1/°R

Fig. 7.E.3 – HLC calculation

The next step is to define the geothermal gradient. There are three options:

- Based on a reference depth and temperature, plus the gradient (slope)
- Based on an input curve: either a theoretical geothermal gradient or one of the traces (i.e. a stabilised temperature trace after a long shut-in)
- Based on a line fit in a region of thermal equilibrium. For example, in Figure 7.E.4 it can be assumed that the sump represents the geothermal gradient, and regress on the measured temperature (red curve, right track) to obtain the geothermal temperature (green curve, right track):

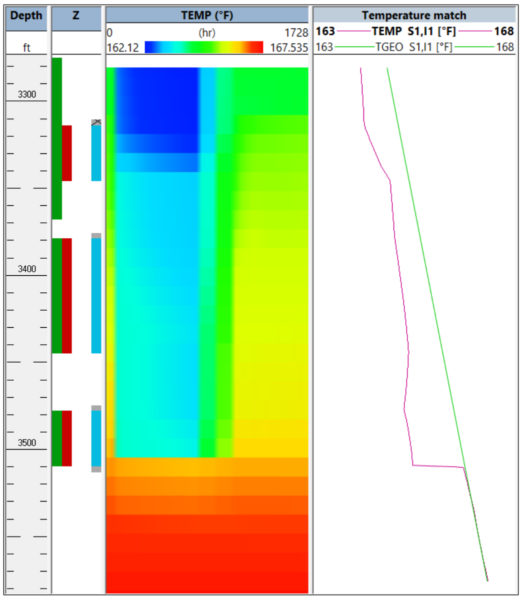

Fig. 7.E.4 – Geothermal gradient estimation from regression in the sump

As mentioned previously, the wellbore pressure is a necessary input. In case the user does not enter a pressure curve, then the pressure must be simulated. The image below indicates that reservoir pressure at maximum depth is equal to 2714 psia.

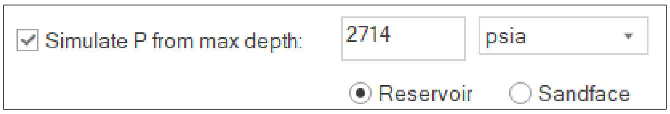

☑ Simulate P from max depth: 2714 psia

● Reservoir ○ Sandface

It is also necessary to enter the rock thermal conductivity, which in general will dominate the heat transfer to the formation since its thermal conductivity is very small. A transient correction is available (see Section 7.E.4).

Reservoir parameters, including external reservoir radius, permeability and skin are necessary since the pressure drop in the reservoir (from external pressure to sandface) is computed using the Darcy equation. The inflow length to reservoir length thickness will be used for the mechanical skin calculation.

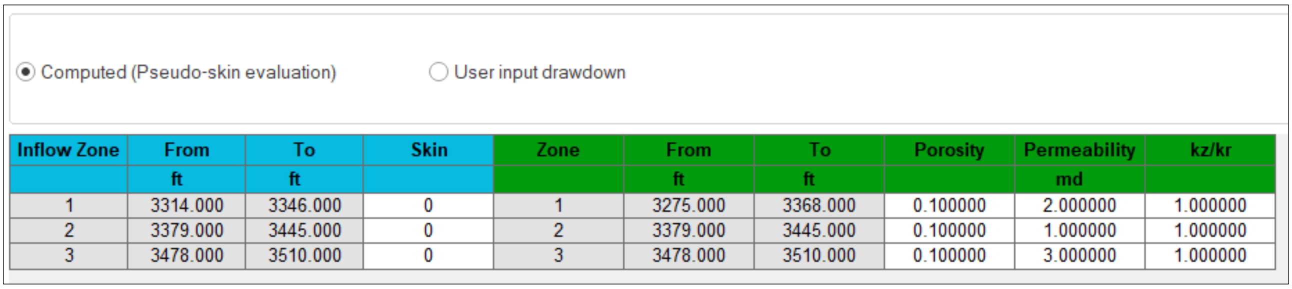

● Computed (Pseudo-skin evaluation) ○ User input drawdown

Inflow Zone	From	To	Skin	Zone	From	To	Porosity	Permeability	kz/kr
	ft	ft			ft	ft		md	
1	3314.000	3346.000	0	1	3275.000	3368.000	0.100000	2.000000	1.000000
2	3379.000	3445.000	0	2	3379.000	3445.000	0.100000	1.000000	1.000000
3	3478.000	3510.000	0	3	3478.000	3510.000	0.100000	3.000000	1.000000

Fig. 7.E.5 – Petrophysical parameters

Having described the completion, reservoir and fluids properties, it is possible to run the regression on the temperature curve. When using temperature measurements only, the location of the rate calculation zones is irrelevant. From the Contributions tab, the contributions for the different zones are shown. The seeds value for the inflow rates of the different zones (1 to 3 in the Figure 7.E.6) were all equal. When clicking on Global Improve the regression is launched, with the objective being to minimize the error between the measured and simulated temperature along the input temperature curve:

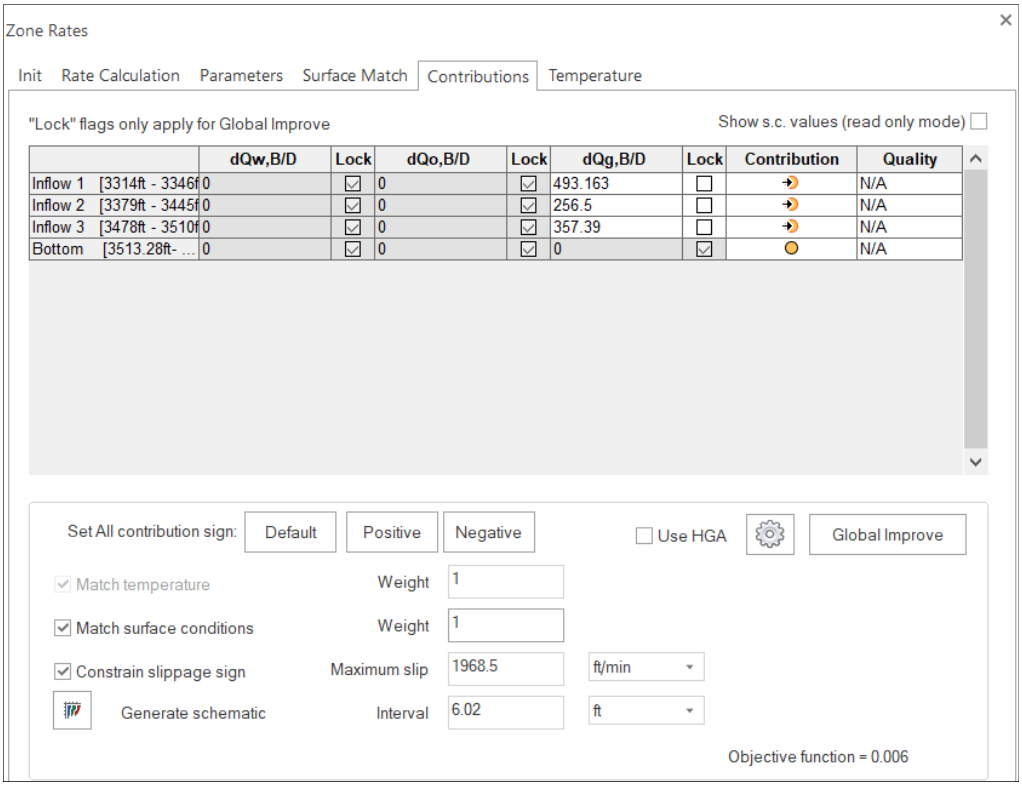

"Lock" flags only apply for Global Improve

Show s.c. values (read only mode) ☐

	dQw,B/D	Lock	dQo,B/D	Lock	dQg,B/D	Lock	Contribution	Quality
Inflow 1 [3314ft - 3346f	0	☑	0	☑	493.163	☐	→	N/A
Inflow 2 [3379ft - 3445f	0	☑	0	☑	256.5	☐	→	N/A
Inflow 3 [3478ft - 3510f	0	☑	0	☑	357.39	☐	→	N/A
Bottom [3513.28ft- ...	0	☑	0	☑	0	☑	●	N/A

Set All contribution sign:

☐ Use HGA

☑ Match temperature Weight 1

☑ Match surface conditions Weight 1

☑ Constrain slippage sign Maximum slip 1968.5 ft/min

Generate schematic Interval 6.02 ft

Objective function = 0.006

Fig. 7.E.6 – Inflow rates and Global regression

The regression also allows for extra constraints: in this case the "Match surface conditions" box is checked. However, there may be other curves or stations entered as part of the interpretation reference channels (passes or stations).

Figure 7.E.7 shows the typical outputs of a temperature-based interpretation. The "Temperature match" track shows in red the input temperature curve, in green the geothermal gradient and in blue the simulated temperature. The QZT and QZI plots correspond to the cumulative flow profile and the contributions plot. Finally, the last track (Pres_KZ) shows the simulated pressure.

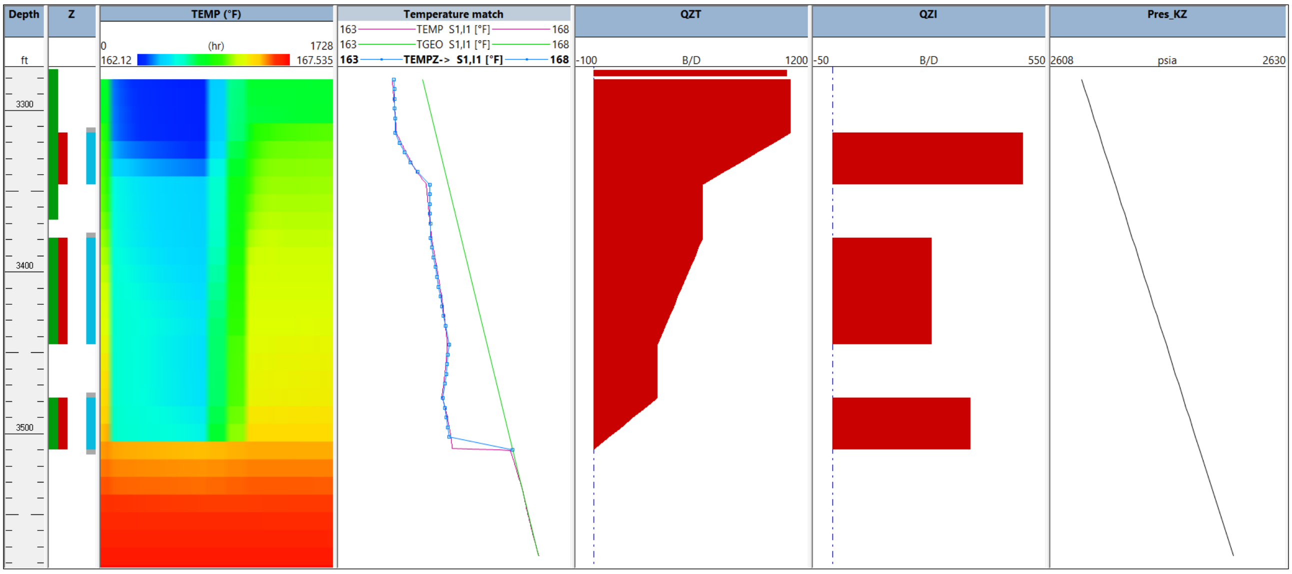

Fig. 7.E.7 – Resulting profile and simulated measurements

In a signals and systems theory context, this type of interpretation constitutes an inverse problem. The first iteration starts from a seed value of contribution per layer (assuming an even production). These layer rates are convolved with the system description, which includes all the thermal properties, completion details, user's decisions on the presence/absence of radiation and convection, the selection of the correlations, etc. The output of this operation is a temperature profile. In the first iteration the simulated temperature is likely to be off compared to the measured (reference) temperature. This difference constitutes the error, which can have weight if other constraints are used in the regression. The input is updated and a new iteration is run, until the convergence criteria is reached (i.e. the error E is minimized):

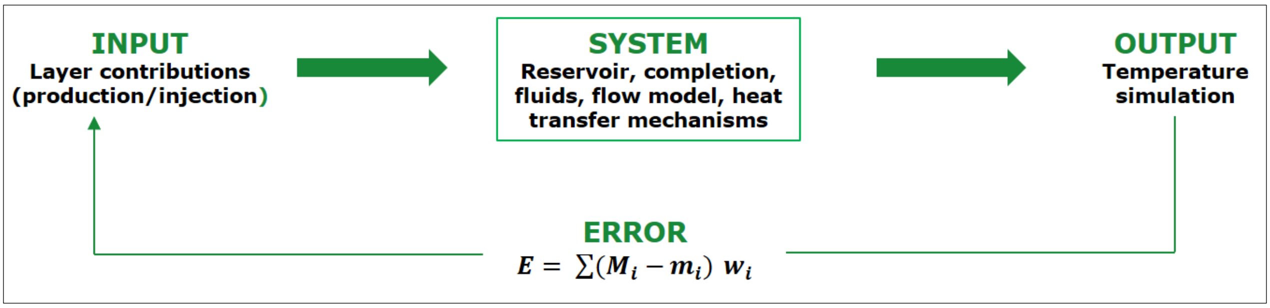

$$E = \sum (M_i - m_i)\, w_i$$

Fig. 7.E.8 – Diagram of the inverse problem for flow profiling

The profile obtained for a certain temperature is "a solution" of the error minimization process. The user must bear in mind the impact of the different inputs, and how these can affect the simulated profile. Compared to PL-based flow profiling, Temperature-based profiles require a larger number of numerical inputs, some of which can be constrained to small ranges, while others can be quite unknown. This is the subject of the next section.

7.E.3 Sensitivity to input parameters

Starting from the contributions obtained in the previous example, let's analyze how the simulated temperature would be affected by rock thermal conductivity (between 0.1 and 30 W/m K), Reservoir Radius (between 1 and 1E6 ft) and HLC (between 0.1 and 1000 W/m K). Figure 7.E.9 shows the original temperature match in the first track and the sensitivity to the parameters in the other tracks:

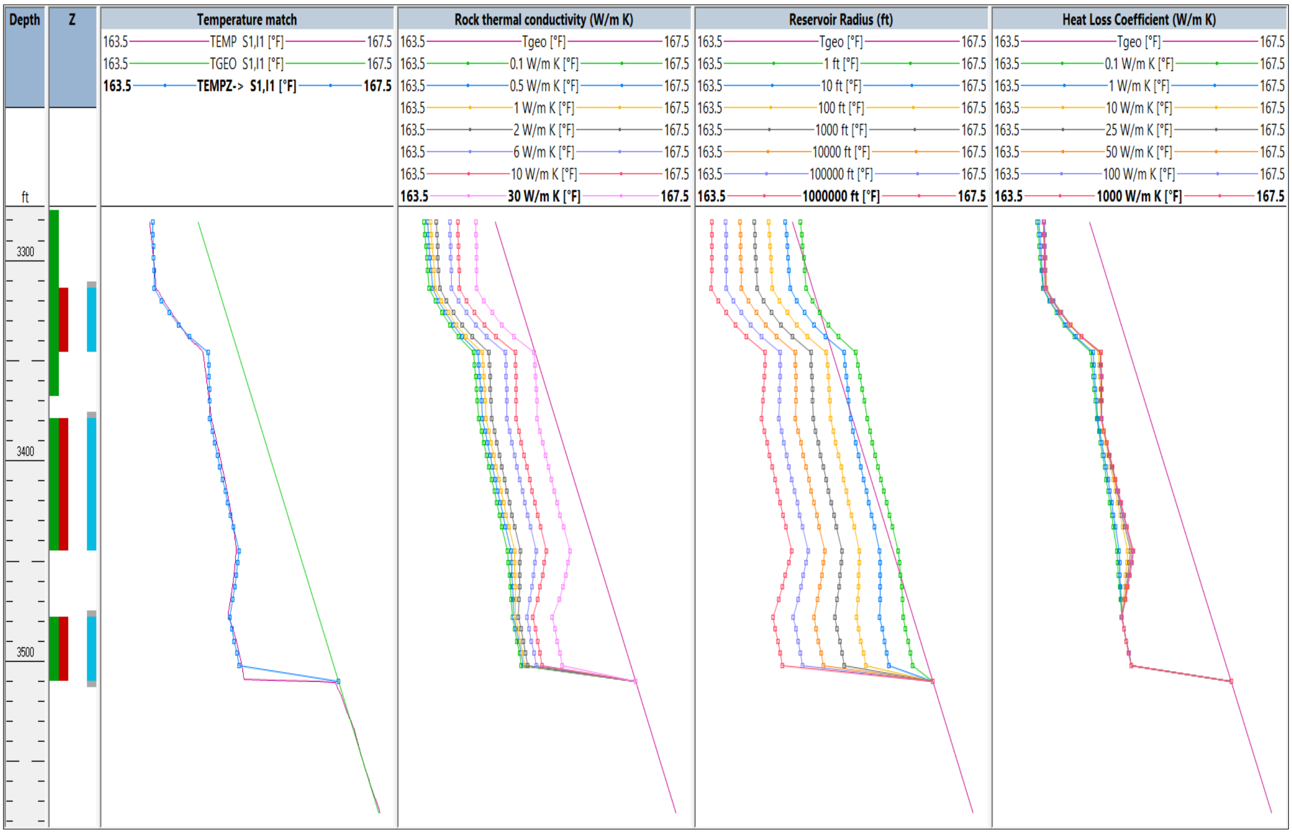

Fig. 7.E.9 – Sensitivities to reservoir thermal conductivity, external radius and HLC

- **Reservoir Thermal conductivity (λ_{res}):** Starting from the geothermal below the lowest inflow, a cooling can be seen over this inflow: it corresponds to an important pressure drop across the reservoir. One can notice that the higher the reservoir thermal conductivity, the smaller the cooling. Then, between the bottom inflow and the middle one, the temperature predicted by the Energy Model tends to the geothermal value, and this tendency increases with λ_{res}. As the reservoir thermal conductivity increases, the temperature in the well homogenizes faster and tends towards the geothermal value.

- **Reservoir Radius (r_e):** Increasing the reservoir radius means that the geothermal profile is reached further away from the wellbore: for a given set of parameters, the bigger the reservoir radius, the lower the temperature homogenization due to conduction.
- **Heat Loss Coefficient (HLC):** The factors affecting the HLC value were discussed previously. As the HLC increases, the temperature homogenizes slightly faster and tends towards the sandface temperature. However, this change is barely noticed for this range of HLC values, since this effect is strongly limited by the small reservoir thermal conductivity (λ_{res}). The HLC effect would be more pronounced for larger λ_{res} or smaller values of production time, for which the sandface temperature profile would be closer to the geothermal one.

The PVT properties of the fluid will also impact the final solution. Previously it was demonstrated that the gas heat capacity plays an important role in the Joule-Thomson coefficient, and also on the capacity of the fluid to transfer heat through convection. The Joule-Thomson coefficient is also a function of the thermal expansion, which is calculated through PVT correlations. Figure 7.E.10 shows that the four different Z factor correlations available in Emeraude lead to none-unique results. The track on the right demonstrates that the effect of the thermal conductivity of the gas, in a range of logical values, has a smaller effect.

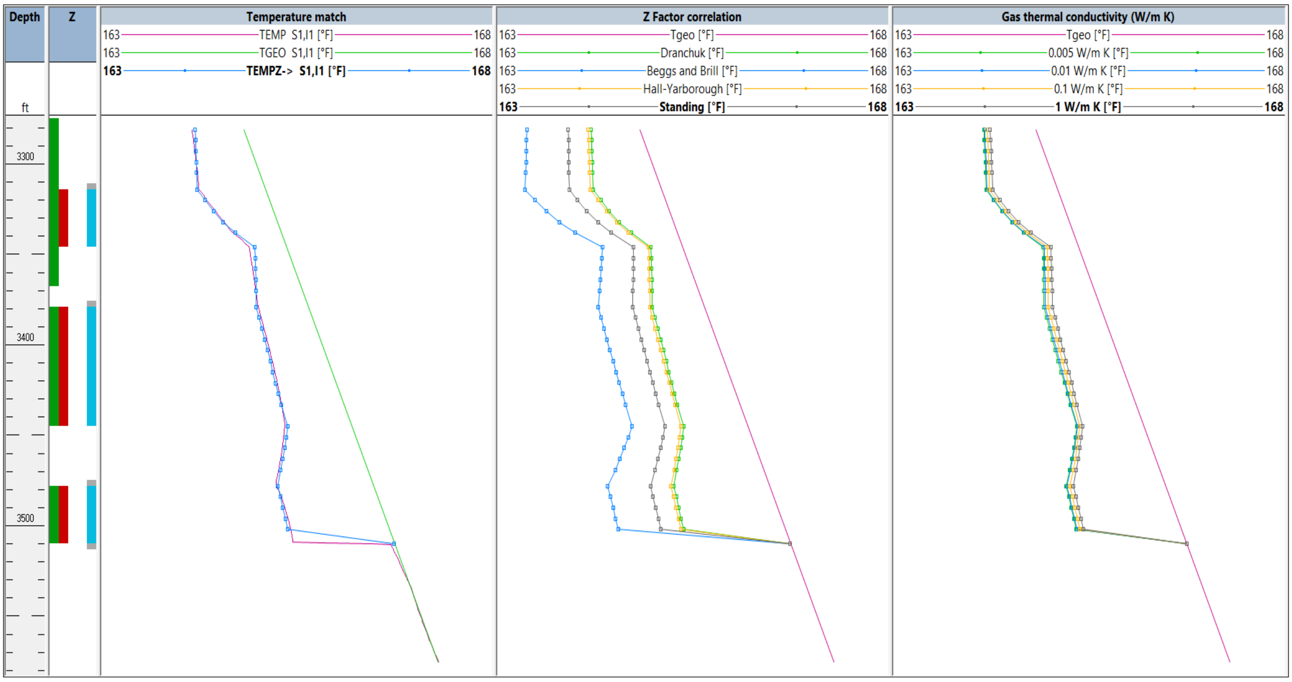

Fig. 7.E.10 – Sensitivities to the fluid properties

These sensitivities were meant to raise the awareness level on the impact of the different inputs, rather than discouraging the user on performing a temperature analysis. Since this type of analysis is an inverse problem solving, the validity of the resulting profile depends on the reliable characterization of all the parameters involved. Uncertainty in the input parameters will automatically translate into uncertainty in the answer. Given the large number of parameters, even single phase interpretation can turn out to be completely undefined and lead to random results. Clearly, hoping to solve in multiphase if only the temperature is supplied is totally unrealistic.

7.E.4 Time dependency

If the well has been shut-in for a long period, it would be fair to assume that the sandface temperature would be close to the geothermal temperature. Then, when putting the well in production, not only the temperature inside the wellbore will drop, but also the temperature in the reservoir, as explained in the Joule-Thomson section. Therefore, the magnitude of the heat flux due to conduction will also drop, because the sandface temperature will be closer to the wellbore temperature.

This phenomenon introduces a time dependency, which in principle is not compatible with the steady-state formulation of the Energy model in Emeraude. A transient correction on the conductive heat transfer was incorporated, which allows to account for the production time. The transient is modeled throughout a scaling of the reservoir thermal conductivity so that at early time the solution corresponds to the steady state solution obtained from a large reservoir thermal conductivity (sand face temperature close to the geothermal) and as time increases the solution tends toward the steady state solution obtained from the entered reservoir thermal conductivity:

$$\lambda^{*}_{res,trans} = \lambda_{res,0}\, max(1, \frac{ln\left(\frac{r_e}{r_w}\right)}{f(t)})$$

Figure 7.E.11 shows the temperature profile for different times of production, based on the layer rates obtained before. For short times, heat transfer is maximum and then the temperature tends to be closer to the geothermal gradient. This effect is reduced with the increase in production time:

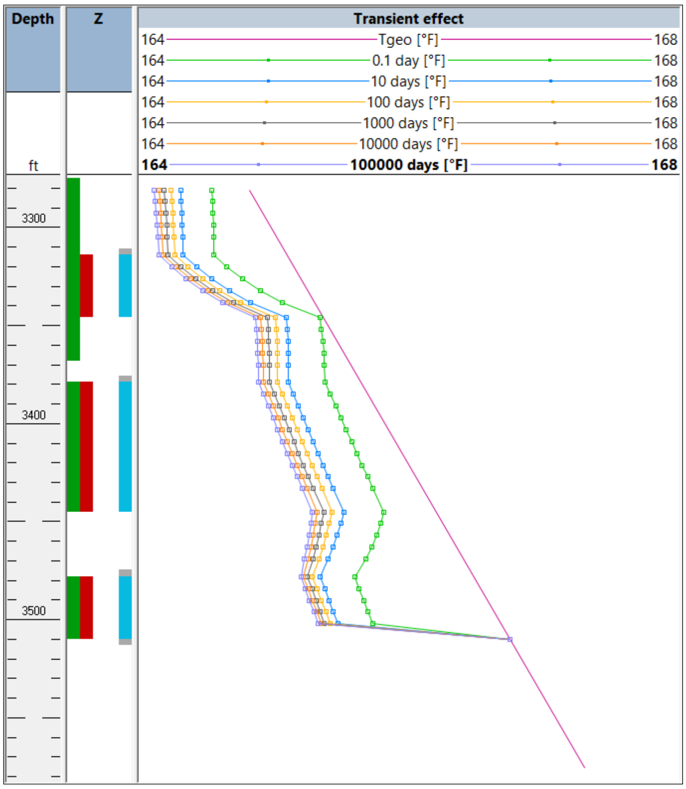

Fig. 7.E.11 – Sensitivity to the production time

7.E.5 Annular convection

The Energy Model allows considering annular free convection when evaluating heat transfer. This is often negligible, however it may have a significant impact on the solution when the annular fluid is particularly sensitive to the thermal gradient existing across and along the well (typically, when invaded with gas).

The following plot shows the multiphase field case described by Hassan & Kabir (SPE 22948). The red dots correspond to the measurements, the blue curve to the Energy Model without considering the annular free convection, and the green curve to the Energy Model while considering annular free convection.

Fig. 7.E.12 – Annular convection

This shows the importance of the annular free convection and it also provides a good assessment of the Energy Model in multiphase flow.

7.E.6 Multiphase profiling

Having analysed the sensitivities to the input parameters in single phase, it is easy to understand that the inverse problem in multiphase can only get worse. There is general agreement that the inverse problem is undefined in multiphase if the only available measurement is temperature.

The figure below provides an illustration where 2 completely different production profiles, one with 4% Water cut and the other with 55% Wcut, produce the same temperature profile:

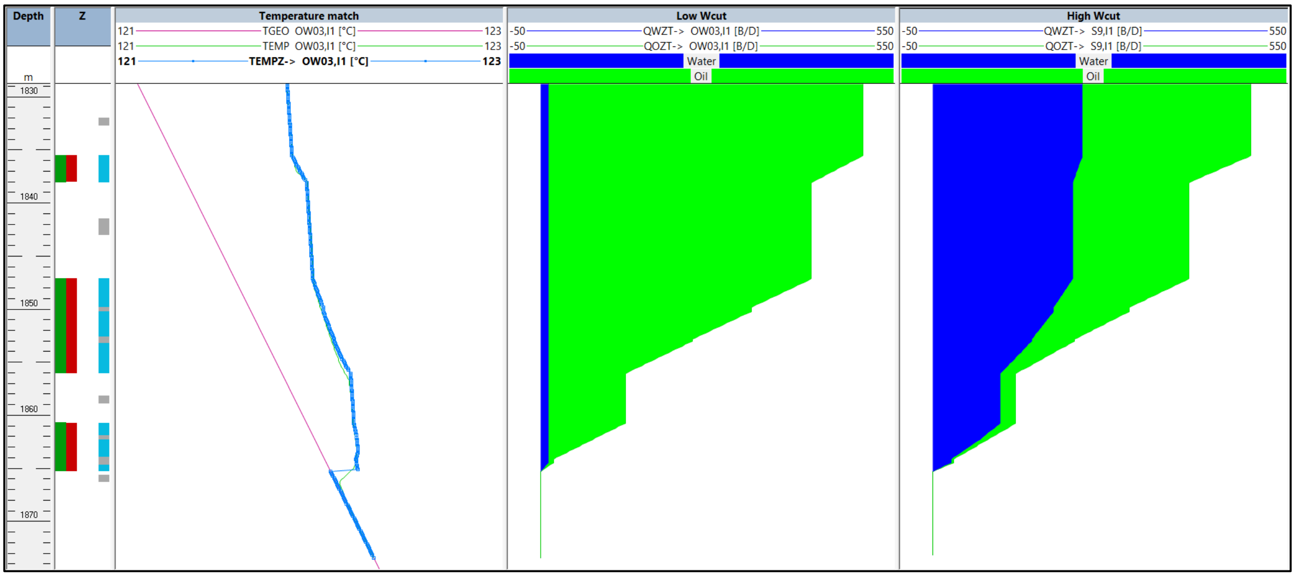

Fig. 7.E.13 – Completely different flow profiles lead to the same temperature response

Whilst in this case the interpreter can use the surface measurements to assess the validity of the different profiles, in other situations it might be impossible to choose one solution over another.

In multiphase situations it is necesseray to incorporate one or multiple holdup measurements (density, capacitance, holdup tools, DAS) or direct downhole rates. This way it will be possible to extend the balance equations to multiphase, using real measurement. Figure 7.E.14 shows a multiphase flow profile obtained from the temperature measurement plus density and capacitance. The spinner was disregarded since it shows recirculation in the casing area and wouldn’t reflect the production behind the tubing above the packer.

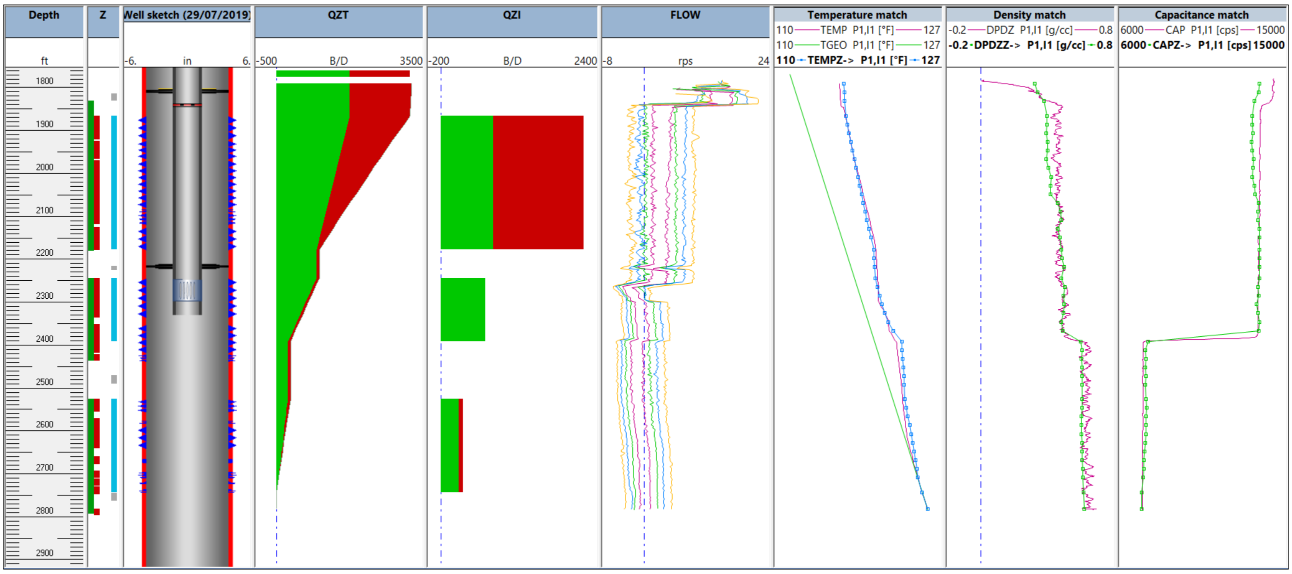

Fig. 7.E.14 – Multiphase profile from temperature, density and capacitance

The user can modify the weights given to the different measurements locally (in the rate calculation zones), since the representativeness of the holdup/velocity measurements will vary with the well deviation and flow conditions.

7.E.7 Horizontal wells

In liquid producers where the viscous heating is small, then the inflow fluid temperature will be equal to the geothermal temperature. In vertical wells, if the perforations are not too close together, then it should be possible to identify (and maybe quantify) the inflows from the different perforation, as seen in Section 7.D.7.

In horizontal wells with no TVD difference one should expect no geothermal temperature difference between the different inflow points. Therefore, unless there is considerable cooling or warming, the identification and quantification of the different inflows might be severely limited. Unfortunately, one of the characteristics of the horizontal wells is that the drawdown is smaller than vertical wells, which necessary leads to a smaller Joule-Thomson ΔT. Figure 7.E.15 shows a PL-derived flow profile, with a total cumulative downhole rate of 9000 B/D (not small) and a TVD variation from heel to toe of 40 ft. Temperature variation in this range is 0.4 °F, which is slightly larger than the resolution of the temperature measurements.

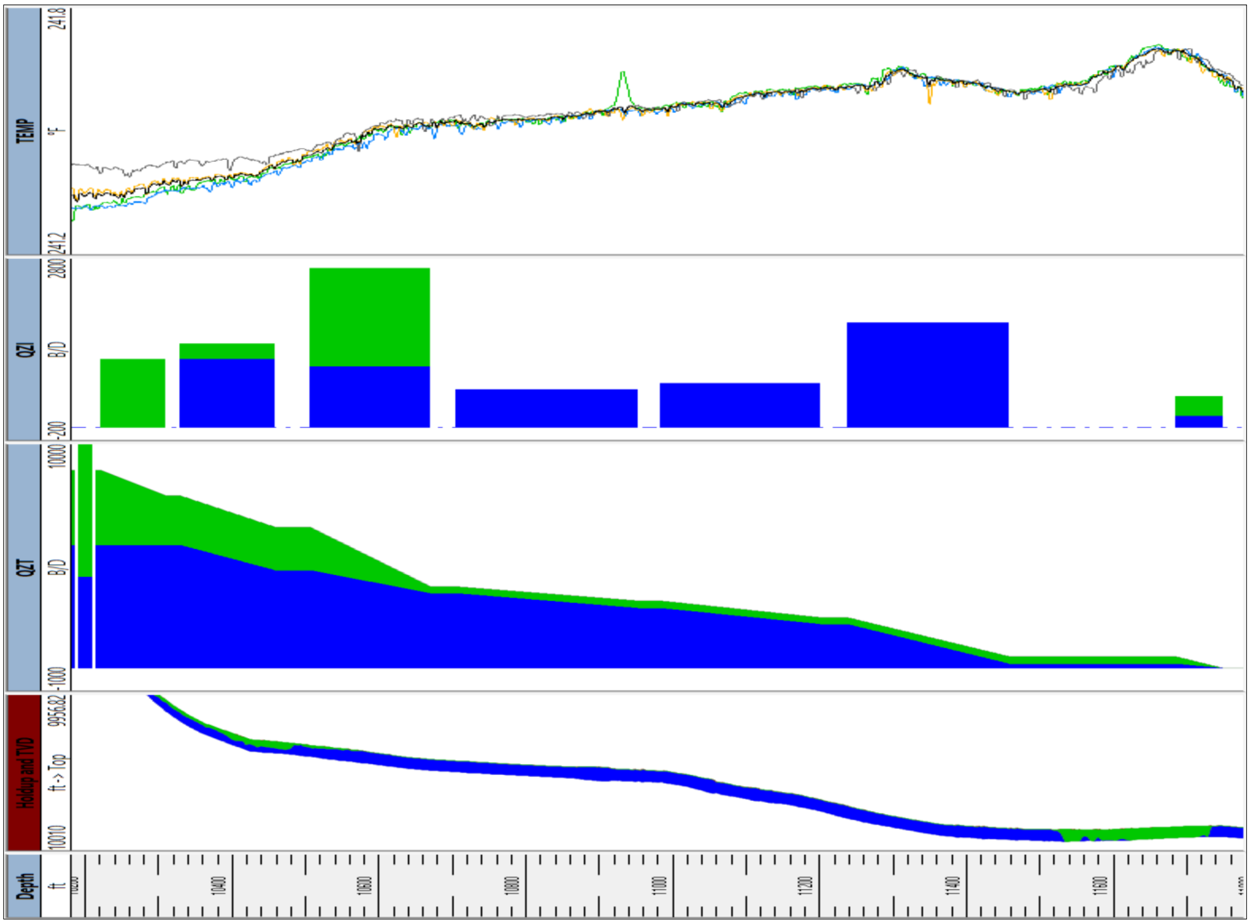

Fig. 7.E.15 – Temperature response of a horizontal Oil-water producer

When the temperature range is so small, the impact of the uncertainty of the inputs is even larger. Whilst the Energy model in Emeraude will still be available for any well deviation, it is up to the interpreter to understand the limitations of the measurements and the response to the different fluids.

In gas producers the Joule-Thomson constant will be 10 times larger than in liquids (and with positive sign), so for the same drawdown, gas producers will show a larger temperature response than in liquids. However, it should be remembered that the drawdown in long wells can be very small. Trying to quantify the production from every single perforation of a horizontal multifrac gas producer is in general completely unrealistic. In situations like this it is more convenient to lump the contributions of multiple perforations (or clusters) into a single zone.

7.E.8 Summary and limitations

As a conclusion, the Energy model allows going into great details in the definition of the fluid, completion and reservoir, for which it requires a number of input parameters, where the uncertainty on them is translated directly to the result. This thermal model allows accounting for the following energy transfer mechanisms:

- Enthalpy/convection
- Kinetic Energy
- Potential Energy
- Thermal Conduction (radial) in the well and reservoir

The required input parameters are:

- Geothermal temperature
- External reservoir pressure and radius
- Thermal conductivity of the completion and reservoir
- Permeability, skin, reservoir/perforation thickness

In terms of the limitations, analysing the hypothesis of the energy balance, it is clear that the far field temperature is the geothermal temperature. It can be concluded that the Energy model works for geothermal fluid entries. However, if certain inflow produces fluid which external temperature is not the geothermal, the model has no means to know what temperature it is. The model does not work for **Non-geothermal fluid entries:**

- Injector – Producer connection
- Tgeo disturbed by drilling operations
- Exothermic reactions (acid jobs)
- Annular fluid movement (tubing leak)
- Cement channeling

Some other limitations that have been discussed in this section are:

- In the absence of an external holdup measurement input, the method remains single phase
- In Horizontal liquid producers with no Tgeo difference, it is normally not possible to quantify the inflow profile
- In injection conditions, there is normally very little heat exchange between the fluid and completion/formation. Normally not possible to quantify the injection profile.
- Vertical thermal conductivity is simulated

7.F Water Injection Fall-off – Emeraude

Recalling from the section on Joule-Thomson effect, the water has a negative coefficient, which in an injection case would lead to a small increase in temperature at the outflow depth. However, in most real life cases, the injection temperature is significantly lower than the formation temperature. Therefore, the temperature profile will be strongly influenced by the convective heat transfer of the colder water being injected to the reservoir. For example, Figure 7.F.1 shows a PL-derived injection profile, with a total injection rate around 60000 BWPD. Even though some relatively small layers take up to 30000 B/D, the temperature measured by the 3 passes (track on the right) shows no response in front of the perforations. Only two things can be extracted from the temperature in this case: the surface injection temperature is changing (increasing) as the PL acquisition progresses (first pass in black, third pass in blue). The other thing is that below the bottom perforation there is no fluid movement, and the temperature will tend to be at equilibrium with the formation. Therefore, the bottom of the logs shows the temperature going back to the geothermal.

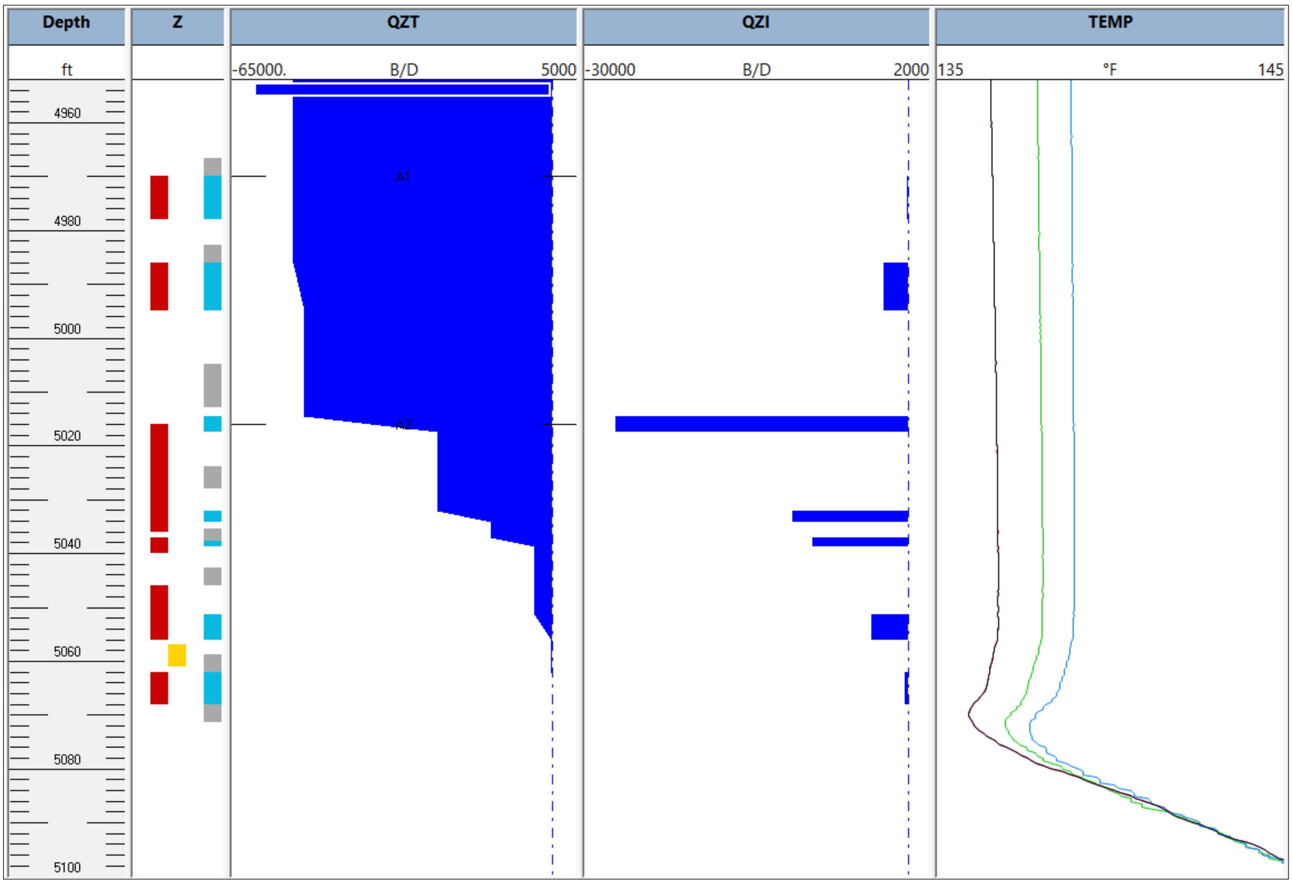

Fig. 7.F.1 – Temperature response while injecting

Temperature measurements while injecting can therefore provide very little information about the perforations injecting. It can only be used as a guide to understand what is the deepest outflow in the well, since below this depth the temperature will go back to the geothermal.

Fortunately, more information can be extracted from temperature with the injection well at shut-in conditions. As the water enters in the reservoir (while injecting) it will form a bank around the well, and heat will flow from the hotter reservoir to the cooler water. For layers that inject very little water, the reservoir will be very efficient at transferring heat since the gradients are very large. However, for layers that took large volumes of water, the cooler water bank will be larger and the heat transfer will be slower. When the well is finally closed, heat transfer will occur essentially by conduction (assuming no fluid movement). The temperature gradient between the reservoir and the wellbore will be larger in intervals that took zero (overburden) or little water. These zones will warm back quicker towards the geothermal temperature. This is the principle of the Warmback analysis.

This explanation referred to colder water and warmer reservoir. However, the model is not limited to that. If the injection water is warmer than the geothermal temperature (shallow injectors), then the model will predict the cool down of the fluid. That is why, the model is called "Water Injection Fall-off" and does not make reference to the evolution of the temperature during the test.

Thermal modelling of fall-off tests following water injection can be used for injectivity profiling in multilayered reservoirs, multiple perforation intervals or even a single long perforated interval or open-hole section. A semi-analytical model has been proposed in SPE 97023 (Pimenov et al., 2005) for horizontal wells using distributed temperature measurement along the wellbore. In Emeraude, this model has been modified and extended for other well configurations and also varying rock properties.

The basis of this model is a solution for the transient heat conduction problem in cylindrical coordinates as described by Carslaw and Jaeger (1959). Assuming conduction only in the radial direction, the temperature as a function of the elapsed time from the beginning of the shut-in can be calculated based on:

$$\frac{T_f - T(x,\tau_{sh})}{T_f - T(x,\tau_{in})} = \frac{1}{2\,\tau_{sh}}\int_0^\infty \exp(-\frac{\xi^2}{2\,\tau_{sh}})\,\xi\,\psi(\xi,v,\tau_{in})\,d\xi$$

This equation contains a number of dimensional parameters which are detailed in the above-mentioned publication. However, as a summary it can be seen that the temperature at any depth, function of the elapsed shut-in time ($T(x,\tau_{sh})$), is calculated as a function of the mass rate injected to each perforation, which is actually what we are looking for, the injection profile. $\psi(\xi,v,\tau_{in})$ describes the radial temperature distribution at the end of the injection. Therefore, the injection time (τ_{in}) is also an input variable.

Compared to the Energy model, this is an approximation of a transient solution. If multiple temperature traces are recorded during the shut-in, then an injection profile can be established for each trace. Emeraude allows regressing on multiple traces at the same time, to reduce the uncertainty and account for possible quality issues of each individual trace. This method is also an inverse problem, where it is necessary to describe the system (reservoir properties) to obtain the Input (layered injection rates) based on the Output (Temperature profile).

The two main assumptions of the model were mentioned above: there is no vertical heat conduction, both across the formation and completion. In reality the temperature profile will be smoother than the one predicted by the model.

7.F.1 Summarized interpretation workflow

Temperature data can come from different sources, and the loading and quality check may vary as explained in the previous section. Figure 7.F.2 shows the Explore option of Emeraude, where a DTS array image can be looked in detail, traces at different times can be extracted for analysis and profiles vs. time are displayed. In this case, the DTS acquisition encompasses the injection period (colder temperature trace) and nearly one month of shut-in. Temperature warms back and tends to be closer to the geothermal, but the warmback rate is not even for the different zones. This is clearly seen when displaying the data vs. time at different depths, shown at the bottom of the image.

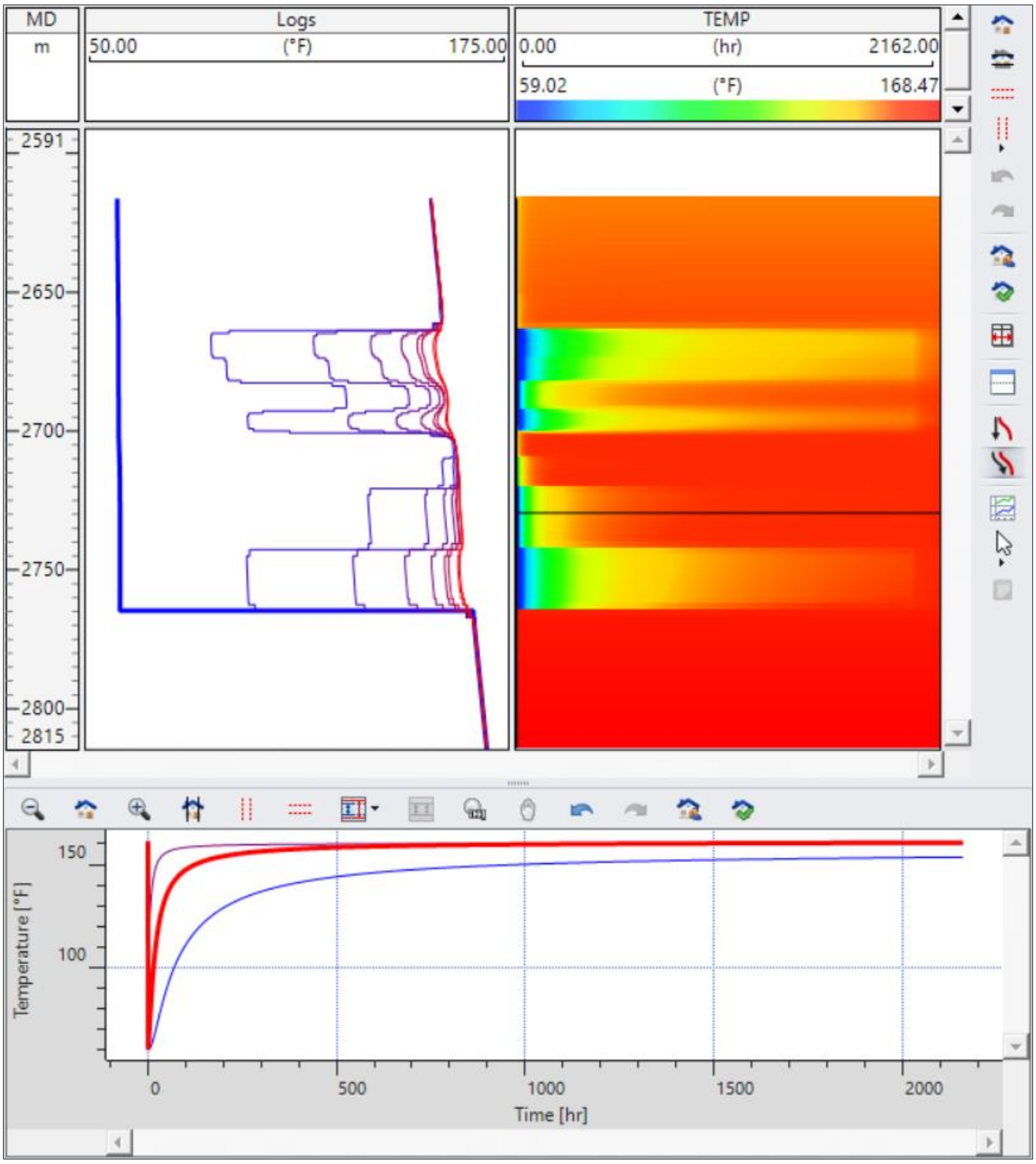

Fig. 7.F.2 – Temperature traces while injecting and warming back

Multiple traces are exported for analysis. Compared to the Energy model, all the traces can be used for a single analysis.

The traces are time referenced, which is needed for the model to calculate the elapsed time between the beginning of the shut-in and the measurement time. In case that the source of the temperature data is a pass recorded during an intervention (i.e. PLT, P&T survey), then the passes have to be referenced. It is also necessary to enter the duration of the injection period and the rate. For a long and more complex injection history these inputs are not so straightforward, and may require the use of an equivalent injection time/rate. This topic will be expanded in the following section.

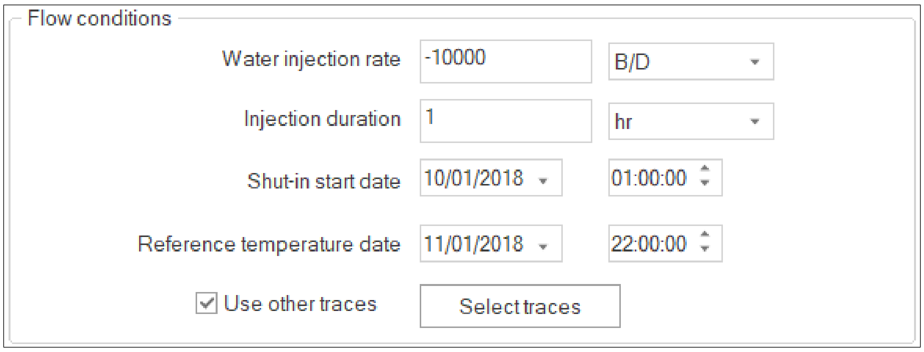

Flow conditions

Water injection rate: -10000 B/D

Injection duration: 1 hr

Shut-in start date: 10/01/2018 01:00:00

Reference temperature date: 11/01/2018 22:00:00

☑ Use other traces

In case of not having loaded a pressure measurement, this can be calculated based on surface or downhole (reservoir top) input parameters. Note that if surface conditions are entered, the Heat Loss coefficient needs to be defined from surface.

Finally, the number of thermal properties needed for this model is smaller than the Energy model. The wellbore is not accounted for by the use of the HLC (again, unless the pressure is calculated from wellhead). Reservoir heat conductivity and heat capacity are the two properties required.

Figure 7.F.3 shows the resulting injection profile and simulated curves from the Water Injection Fall-off model. The Temperature match track shows one simulated curve per trace. The global error minimization uses all the traces at the same time. Also, this track shows the simulated water injection temperature, which can be compared to the measured temperature. Finally, the track on the right shows the simulated pressure. Similar to the Energy model, it is possible to add external constraints to the Global regression, such as downhole measurements or surface rates.

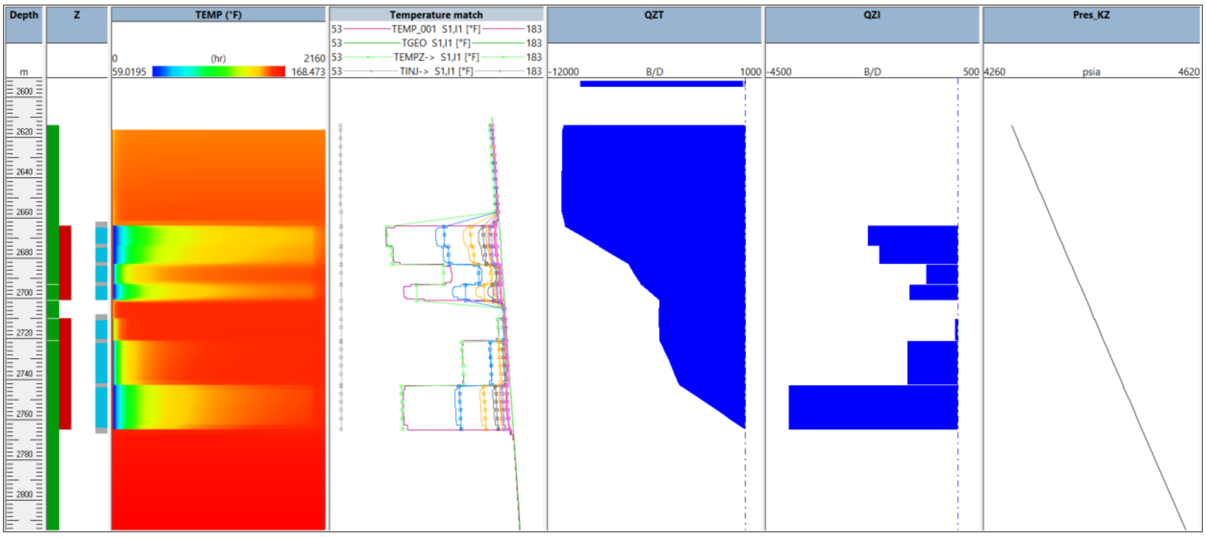

Fig. 7.F.3 – Resulting profile and simulated curves

7.F.2 Sensitivities to the input parameters

From an operational point of view, a key aspect is for how long the well should be closed for the temperature to show a significant and quantifiable response. We don't want the shut-in to be too short and the wellbore temperature to still be very close to the original injection profile. On the other hand, we don't want to stop the injection of the well for a period longer than needed. This is controlled by the rate of heat conduction, which as we have seen before is a function of the radial temperature gradient. The temperature gradient in the near wellbore region depends on the injection history (rates, duration, time) and thermal conductivity.

The sensitivities to the injection parameters are presented below. The second and third tracks show the wellbore temperature after 48 hs of shut-in as a function of the injection duration and water injection rate. These two parameters control the volume of water injected to the different layers, which in turn leads to a lower sandface temperature (in this case the water temperature is ~100 °F lower than the geothermal). In summary, the larger the injection times and/or rates, the smaller the difference between sandface and wellbore temperature, and thus the slower the warmback. If the warmback is too small, then the temperature measurement may not be used for quantitative purposes.

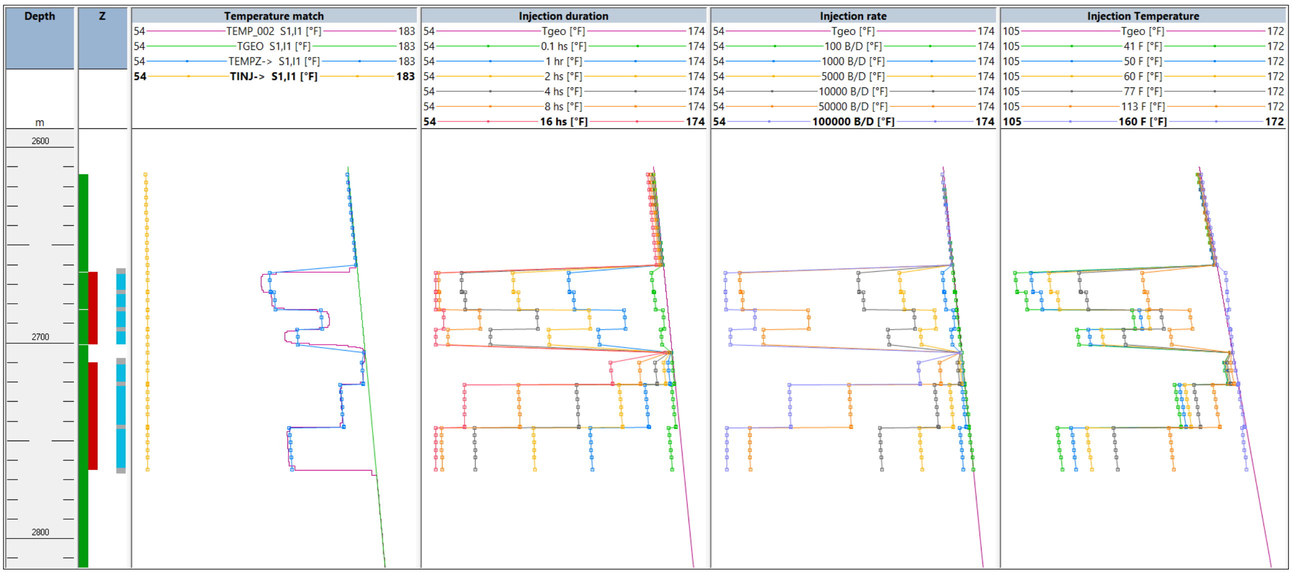

Fig. 7.F.4 – Sensitivities to injection parameters

The last track of Figure 7.F.4 shows the effect of changing the water injection temperature from 40 to 160 °F. The larger the difference between the injection and geothermal temperature, the larger will be the temperature disturbance in the wellbore. Note that as the injection temperature increase, the temperature variations between the injecting and non-injecting zones start to decrease. Eventually if the injection temperature becomes too close to the geothermal, the warmback would not be observed. This has implications in shallow water injectors, whose Tgeo can be around 25-30 °C, and the injection temperature coming from the water plant would be around the same temperature. In some cases, it has been decided to heat up the water and observe the cool down during the shut-in. Note that for the injection temperature at 160 °F, which is the same as the geothermal, there is an increase in temperature at the top perforation. As explained in the section about Joule-Thomson, water temperature will increase as it decompresses (negative K_{JT}) on its way from the wellbore to the formation. Whilst at lower injection temperatures, convection dominates the heat exchange, at temperatures close to the geothermal, the model predicts the warming at the perforation level.

The tracks 2 and 3 of Figure 7.F.5 show the sensitivity of the shut-in temperature (after 48 hrs of shut-in) and the injection temperature to a variation in reservoir thermal conductivity from 0.1 W/m K (a bit too low for reservoir rocks) to 8 W/m K (more than double the maximum theoretical values). The shut-in temperature after 48 hrs remains very close to the injection temperature when the thermal conductivity is small. The larger the thermal conductivity, the quicker will be the return of the wellbore temperature to the geothermal. For the injected water temperature, it can be seen that large thermal conductivities would lead to a quicker heat transfer and the water getting warmer due to the formation temperature. However, for normal reservoir rocks thermal conductivities (less than 3 W/m K) the effect is negligible (less than 0.5 °F in the simulation below). Finally, the heat capacity of the reservoir rock does not have a significant role on the shut-in temperature evolution.

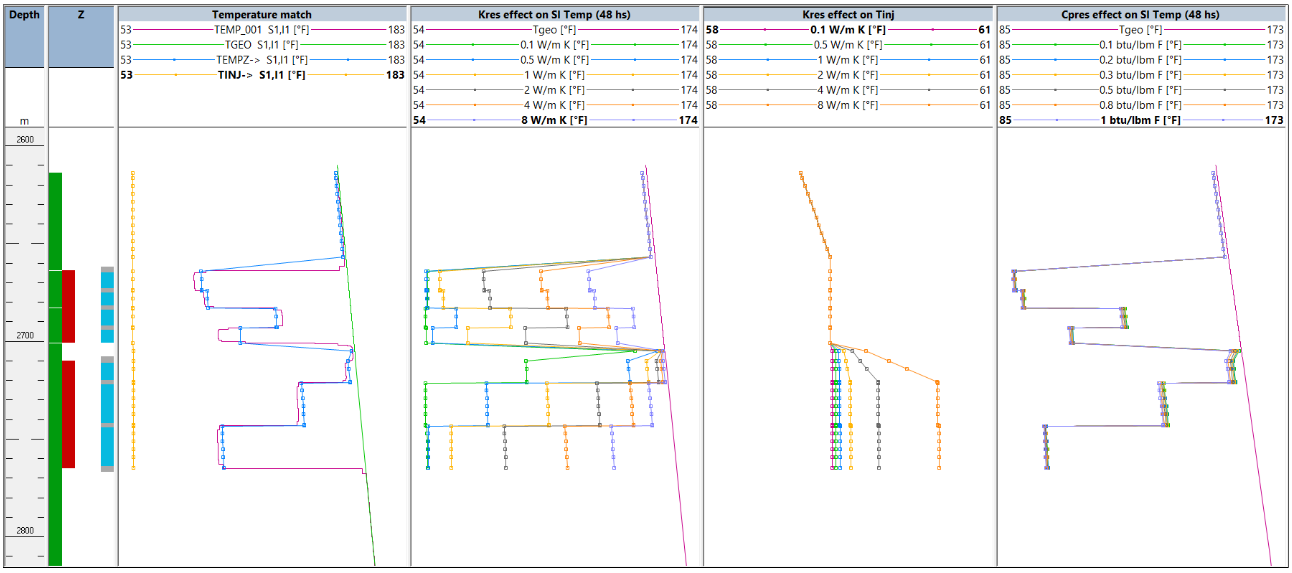

Fig. 7.F.5 – Sensitivities to thermal conductivity and heat capacity

7.G Numerical Simulation – Rubis

In Rubis thermal, the mass and energy balance equations are solved numerically for each reservoir cell and wellbore segment, which leads to a multiphase, transient, fully coupled wellbore-reservoir thermal simulator. Here are some characteristics:

- Single phase and multiphase compositional formulations
- Black Oil and compositional EOS PVT
- Full 3D resolution (no assumption of symmetry with respect to well axis)
- 3D Voronoi grid, with near-well refinement
- Finite volume formulation, fully implicit in pressure and temperature
- Heterogeneous media (permeability and thermal properties such as conductivity and specific heat capacity are not necessarily uniform).
- Multiwell
- Segmented well model(s) coupled to the reservoir, using a fully implicit formulation

Simulated temperatures and pressures can be output as a function of time at any input depth of the well (similar to a gauge), or as a function of depth along the well at specified times (similar to well logs). In the reservoir, pressure and temperature fields can also be output at user-specified time intervals.

7.G.1 Formulation

Notations

For a single phase case, the primary unknowns at any location of the reservoir are the pressure P and the temperature T. In a multiphase case, the additional unknowns of the problem are, for each phase p and each component k, the phase saturation S_p, and the phase composition C_p^k.

The main PVT coefficients are, for each phase p: the viscosity μ_p, the density ρ_p, the massic fluid enthalpy h_p, and the thermal conductivity λ_p. At any simulation time, and any location of the reservoir, these can be evaluated as functions of (P, T and C_p^k) the PVT module.

We also introduce the following rock properties: porosity φ, rock density ρ_r and rock thermal conductivity λ_r. The input distribution of these rock properties can be heterogeneous. The porosity depends on pressure, in order to account for the rock compressibility or unconsolidation, however its dependence on temperature is ignored.

Conservation equations and numerical discretization

In the reservoir, the kinetic energy of the fluid can be neglected, as well as the mechanical energy. Using these assumptions, a few derivations beyond the scope of this Chapter lead from the first principle equation for the conservation of total energy to a simplified volumetric expression of the energy conservation. For a single phase, the following system of continuous conservation equations is obtained:

$$\frac{\partial}{\partial t}(\varphi\rho)+\nabla\cdot\left(\rho\cdot\vec{v}\right)=0$$

(mass conservation)

$$\varphi\rho\frac{\partial h}{\partial t}+(1-\Phi)\rho_r\frac{\partial h_r}{\partial t}+\rho\vec{v}\cdot\nabla h-\rho\vec{g}\vec{v}-\frac{\partial P}{\partial t}-\nabla\left(\lambda^*\nabla T\right)=0$$

(energy conservation)

Where $\vec{v}$ is the fluid velocity, h_r is the rock enthalpy and λ^* is the bulk thermal conductivity of the saturated medium, as detailed further below.

Rubis follows a finite-volume, fully implicit discretization approach. The mass conservation equation is integrated over a cell i of volume V_i, as detailed in given in the Chapter dedicated to numerical simulation in the DDA book [14]. If we note J_i, W_i and B_i the sets of reservoir cells, wells and reservoir bounds connected to the considered cell i, we obtain for each cell i, at the end of a time step $n+1$:

$$V_i \frac{\varphi_i^{n+1}\rho_i^{n+1} - \varphi_i^n \rho_i^n}{\Delta t} + \sum_{j \in J_i, W_i, B_i} q_{ij}^{n+1} = 0$$

In the above equation, q_{ij} is the mass flux between the cell i and a neigbour cell, bound or well segment j. In the compositional context, this equation becomes:

$$\frac{V_i}{\Delta t} \cdot \sum_p \left[\left(\varphi_i^{n+1} S_{p,i}^{n+1} \rho_{p,i}^{n+1} C_{p,i}^{k,n+1}\right) - \left(\varphi_i^n S_{p,i}^n \rho_{p,i}^n C_{p,i}^{k,n}\right)\right] + \sum_{j \in J_i, W_i, B_i} \left(\sum_p q_{pij}^{k,n+1}\right) = 0$$

Similarly, the equation for the conservation of energy is integrated over the cell volumes. We obtain for each cell i, at the end of a time step $n+1$:

$$\frac{V_i}{\Delta t}\left(\varphi_i^{n+1}\rho_i^{n+1}h_i^{n+1} - \varphi_i^n \rho_i^n h_i^n\right) + V_i\left(1-\varphi_i\right)\rho_{ri} \frac{h_{ri}^{n+1} - h_{ri}^n}{\Delta t}$$
$$- V_i \frac{P_i^{n+1} - P_i^n}{\Delta t} + \sum_{j \in J_i, W_i, B_i} \left(h_{ij} + g\Delta z_{ij}\right) q_{ij} + \sum_{j \in J_i, W_i, B_i} q_{ij}^T = 0$$

In the above equation, Δz_{ij} is the difference of altitude between the upstream cell and the downstream cell - arising from the potential energy term.

In order to estimate the convective flux of energy between the cell i and one of its neighbors j (cell, well or boundary), the mixed enthalpy function h_{ij} is evaluated via the PVT module using the upstream values, i.e. $h_{ij} = h(P_i, T_i)$ if i is the upstream cell, otherwise $h_{ij} = h(P_j, T_j)$. We will see in paragraph 7.G.4 that this scheme can have some important consequences on the transient thermal simulation results and on the best choice for the simulation grid.

In the compositional context, this equation becomes:

$$\frac{V_i}{\Delta t} \cdot \sum_p \left(\varphi_i^{n+1} S_{p,i}^{n+1} \rho_{p,i}^{n+1} h_{p,i}^{n+1} - \varphi_i^n S_{p,i}^n \rho_{p,i}^n h_{p,i}^n\right) + V_i\left(1-\varphi_i\right)\rho_{ri} \frac{h_{r,i}^{n+1} - h_{r,i}^n}{\Delta t} - V_i \frac{P_i^{n+1} - P_i^n}{\Delta t}$$
$$+ \sum_{j \in J_i, W_i, B_i} \sum_p \left(\left(h_{p,ij} + g\Delta z_{ij}\right) \cdot \sum_k q_{p,ij}^{k,n+1}\right) + \sum_{j \in J_i, W_i, B_i} D_{ij} \cdot \Delta T_{ij} = 0$$

Where h_p is the mass enthalpy of phase p.

This discretization over all the cells leads to a (potentially large) single system of coupled equations (for each cell: one mass conservation equation per independent component + one energy conservation), solved simultaneously by the non-linear solver (fully implicit coupling) at every simulation time step.

Enthalpy calculations

As previously mentioned, the massic fluid enthalpy h_p is obtained at any location via the PVT module, knowing the local values of (P, T and C_p^k)

In the EOS PVT context, for the hydrocarbon phases, the user inputs the heat capacity coefficients of single components, $Cp_{i,1}$, as well as the component's reference enthalpy H_{0i} at temperature T_{ref}. The single component molar enthalpy is then derived from:

$$H_i^* = H_{0i} + \sum_{l=1}^{hk} \frac{Cp_{i,l-1}}{l} \cdot (T - T_{ref})^l \quad ,$$

from which we get the molar enthalpy of phase p:

$$H_p = \sum_{i=1}^{Nk} H_i^* \cdot x_i + H_p^{EOS} - P \cdot \sum_{i=1}^{Nk} x_i \cdot c_i$$

Where $x_i$are the molar compositions, the last right hand side term corresponds to the volume shift correction, and where:

$$H_p^{EOS} = R \cdot T \cdot (Z-1) + \frac{T \cdot \frac{\partial a}{\partial T} - a}{2\sqrt{2} \cdot b} \cdot \ln\left(\frac{Z + (1+\sqrt{2}) \cdot B}{Z + (1-\sqrt{2}) \cdot B} \right)$$

Finally, we get the massic enthalpy via: $h_p = \frac{1}{M_p} \cdot H_p$

For all the other contexts (ex: black oil multiphase thermal, single phase thermal…), the enthalpy is simply derived from successive integrations, based on the input PVT correlations or tables for the density and compressibility, as explained below.

From the density function $\rho(P,T)$, accessible with the PVT module, the coefficient of thermal expansion of the fluid can be derived, for any values of P and T, with $\beta_T = -\frac{1}{\rho}\frac{\partial \rho}{\partial T}$. The massic specific heat capacity of the fluid (assumed constant at reference pressure *P0*) is a user input: c_f. In the Rubis interface, this reference pressure is assumed to be P0 = 1atm. These coefficients β_T and c_f are related to the enthalpy derivatives $\frac{\partial h}{\partial P} = \frac{1-\beta_T T}{\rho}$ and $\left(\frac{\partial h}{\partial T}\right)_{P=P_0} = c_f$. The enthalpy *h(P,T)* is then obtained using the following integration:

$$h(P,T) = h(P_0,T_0) + c_f (T - T_0) + \int_{P_0}^{P} \frac{1 + \frac{1}{\rho}\frac{\partial \rho}{\partial T}}{\rho} dP$$

This integration ensures the coherence of the PVT, i.e. $\frac{\partial h}{\partial P}$ is constrained by $\frac{\partial \rho}{\partial T}$. The Joule-Thomson coefficient, as well as the coefficient of isothermal compressibility $\chi = \frac{1}{\rho}\frac{\partial \rho}{\partial P}$, are not assumed to be constant during the simulation.

Rock Properties

The thermal conductivity, λ_r, the massic specific heat capacity, c_r, and the density of the rock are inputs from the user and are assumed to be constant and known. Since the rock density is constant, the coefficient of thermal expansion of the rock is equal to zero, so we have $\frac{\partial h_r}{\partial T} = c_r$ and $\frac{\partial h_r}{\partial P} = \frac{1}{\rho_r}$. The rock enthalpy is then obtained from:

$$h_r(P,T) = h_r(P_0,T_0) + \frac{(P-P_0)}{\rho_r} + \frac{(T-T_0)}{c_r}$$

NB - Arbitrary reference enthalpy values $h(P_0,T_0)$ and $h_r(P_0,T_0)$ appear in these integrations. These values have no consequence on the final result, since only enthalpy differences or derivatives will actually impact the global system.

Conduction

The conductive thermal flux of energy q_{ij}^T between cell *i* and a neighbour cell, well segment or bound *j* is given by: $q_{ij}^T = D_{ij}\,(T_i - T_j)$

Where D_{ij} is an analog for conduction to the "transmissibility" concept used to express the massic flux as a function of the pressure gradient (see numerical chapter in the DDA book [14]). D_{ij} depends only on the geometry of the cells (constant values) and on the bulk conductivity λ_i^* and λ_j^* of each connected cell. In the single-phase context, the following averaging model is chosen to express for the bulk thermal conductivity of the medium: $\lambda^* = \lambda_{fluid}^{\varphi} \cdot \lambda_r^{1-\varphi}$,

where the fluid thermal conductivity λ_{fluid}, input from the user, is assumed to be constant and known. Hence we see that D_{ij} is constant in the single-phase context. In the multiphase context, however, this assumption is no longer valid, and the model from Boris and Prat (1995) is followed:

$$\lambda^* = \lambda_{fluid}^{\varphi} \cdot \lambda_r^{1-\varphi} = \lambda_r^{1-\varphi} \prod_p \lambda_p^{(\varphi \cdot S_p)},$$

where phase thermal conductivities λ_f are user-inputs, assumed to be independent of *(P,T).*

Reservoir boundary conditions

As described in the Chapter on numerical simulation in the DDA book [14], three types of fluid flow conditions can be assigned to the reservoir lateral, bottom and top bounds for the mass equation: no flow, constant pressure or aquifer. Whatever boundary condition is chosen for the mass, Rubis assumes that the temperature of the boundary remains constant during the simulation – except for the specific case of the numerical aquifer, which is described further below.

The convection term between a cell *i* and a bound *b* is: $q_{ib}(h_{ib}+g\Delta z_{ib})$, where h_{ib} is evaluated upstream, i.e. the enthalpy of the fluid will be evaluated at the bound's values *(Tb, Pb)* when the flow comes from the boundary into the reservoir. When no-flow conditions prevail, this contribution by convection is of course equal to zero. In the potential energy term, $\Delta z_{ib}$is the relative altitude of the boundary with respect to the considered cell *i*.

When the reservoir boundary is no-flow, constant pressure or an analytical aquifer, the temperature is assumed to be constant inside the aquifer and along the aquifer/ reservoir limit. The conduction term from the boundary is then given by: $D_{ib}\,(T_i-T_b)$, where T_b is the constant bound temperature, T_i is the varying temperature of the connected reservoir cell, and the conductance D_{ib} is evaluated using the global conducvitiy λ_i^* of this cell (described above) - i.e. there is no need to input a conductivity for the aquifer.

When the reservoir boundary is a numerical aquifer, the constant temperature condition is not assigned to the aquifer/ reservoir limit, but to the outer boundaries of the aquifer itself. The conductivity and thermal capacity values inside the aquifer are assumed to be equal to those in the zone of the reservoir connected by the aquifer. As a consequence, the temperature is not necessarily constant inside the aquifer, nor at the boundary between the reservoir and the numerical aquifer.

Overburden, gaps and dead zones

In Rubis, it is possible to define "Dead" zones, where the 3D cells are simply deactivated and disappear from the system. These zones act both as perfect thermal insulator and absolute barrier to flow. At the boundary between a dead and an active zone, the flux of energy is hence null, and the temperature is not assumed to be constant.

It is also possible to define the geometry of any layer independently of its neighbors. In particular, it is possible to introduce a geometrical "gap" between two reservoir layers, as shown on Fig 7.G.1. Such gaps act as a pure thermal isolation.

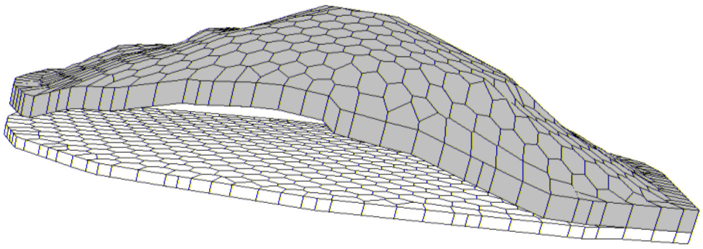

Fig. 7.G.1 – Two reservoir layers separated by a gap

In the example corresponding to the Fig 7.G.1, the bottom and the top sides of the reservoir will have constant temperature conditions, while the faces of cells pointing toward the gap will have "no thermal flux" conditions. As a consequence, these gaps are exactly equivalent to "dead" zones.

Because of these assumptions, it is recommended to avoid using dead zones or geometrical gaps in the thermal context. Instead, a standard property set can be used, with a net to gross value assigned to zero in this set. The corresponding zone will then act as an absolute barrier to flow with null porosity, but its thermal properties (rock conductivity and *Cp* values) will still be defined and accounted for. Hence, the temperature will not be uniform or constant in this zone. This is particularly useful in order to model the thermal effects of non-reservoir interlayers (Fig 7.G.2), or in order to include effect of the over/underburden in the simulation.

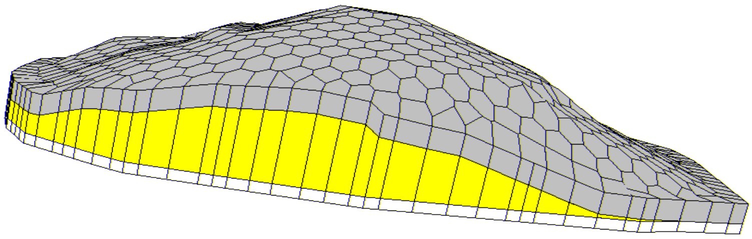

Fig. 7.G.2 – Non-reservoir interval layer explicitly included in the model

Treatment of faults and fractures

Three kinds of faults can be defined in Rubis, which influence the flow along/across the fault: leaky, finite conductivity and infinite conductivity faults. Fractures (well hydraulic fractures or DFN) can be finite conductivity or infinite conductivity.

Leaky faults are simple transmissibility multipliers between all the reservoir cells separated by the fault. As a consequence, there is no flow occurring along these fault planes, and they only influence the convection fluxes, with no impact on thermal conduction.

On the contrary, flow occurs along the direction of finite or infinite conductivity and faults (or fractures), and thin 3D cells are associated to this type of faults (or fractures), with related pressure and temperature values. In Rubis, no thermal properties can be input for the faults and fractures, and several assumptions are made by the simulator for the associated thermal conductivity connections:

For the connection between reservoir and fault (or fracture) cells, the thermal conduction across the fault is assumed to be infinite. In other words, the fault has no effect on the conductivity in this direction.

In the direction of a conductive fault (or fracture), the conduction effects are assumed to be small compared to convection effects. As a consequence, the thermal conductivity was neglected between two fault (or fracture) cells.

Dual porosity

No rigorous treatment of the double porosity has yet been implemented in Rubis for the thermal context. In particular, the matrix-fissure thermal connections are missing.

7.G.2 Wellbore coupling

Within the reservoir interval definition, the wellbore trajectory is divided into various segments *s*, honoring the perforated intervals and the intersections of the wellbore trajectory with the reservoir grid. The numerical well model implemented in Rubis assumes that all the phases travel at the same speed along the wellbore. As a consequence, global compositions instead of phase compositions are used, and the mass conservation equation for component *k* in a given segment *s* reduces to:

$$\frac{V_s}{\Delta t}\cdot\left[\left(\rho_s C_s^k\right)^n-\left(\rho_s C_s^k\right)^{n-1}\right]+q_{(s-1)s}^k-q_{s(s+1)}^k+\sum_i q_{is}^k=0 \quad ,$$

where C_s^k is the global composition and ρ_s is the global density in segment *s*.

Let's now consider the energy conservation equation into the wellbore. In order to simplify the model, the following assumptions will be made:

- The longitudinal conductivity exchange along the wellbore is negligible compared with other terms (especially longitudinal convection)
- The kinetic and potential energy change in the expansion term are negligible during a simulation time step
- The kinetic energy between cell *i* and segment s is negligible (kinetic energy is neglected in the reservoir part, as seen above.

The energy equation becomes:

$$\frac{V_s}{\Delta t}\cdot\left[\sum_p\left(\rho_{ps}^{n-1}h_{ps}^{n-1}-\rho_{ps}^{n}h_{ps}^{n}\right)-\left(P_s^{n-1}-P_s^{n}\right)\right]+\sum_p q_{p,(s-1)s}\cdot\left(h_{p(s-1)s}+ec_{p(s-1)s}+ep_{(s-1)s}\right)$$
$$-\sum_p q_{p,s(s+1)}\cdot\left(h_{ps(s+1)}+ec_{ps(s+1)}+ep_{s(s+1)}\right)+\sum_i\left[\sum_p q_{p,is}\cdot\left(h_{pis}+ep_{is}\right)+D_{is}\cdot\left(T_i-T_s\right)\right]=0$$

Compared to the Emeraude formulation, we see that the transient terms $\frac{\partial E}{\partial t}$ are kept (first left hand side block). We also see that the potential energy, kinetic energy and convective fluxes appear in the segment terms (no conduction between segments). The reservoir contribution involves convective fluxes, conduction and potential energy (kinetic energy neglected).

The conductive flux between the reservoir cell containing the well segment and the segment itself is obtained via a "composite" conductance D_{is} derived internally. This conductance, which depends on the geometry of the cell, combines the rock+fluid effective conductivity λ^* (previously defined) and the well Heat Transfer Coefficient defined earlier in this chapter.

As in the reservoir, the phase massic fluid enthalpy in any segment is evaluated via the PVT module, $h_{ps}(P_s,T_s,C_{ps}^k)$.

When using the thermal engine in Rubis, it is necessary to define the well intake. The pressure drops and rates between the segments are then related based on classical correlations accounting for slippage, frictions, etc. In the Rubis interface, the well intake definition also allows to define the completion geometry and the thermal parameters used to compute the Heat Loss Coefficient.

This discretization over all the segments leads to a system of coupled equations (for each segment: one mass conservation equation + one energy conservation, plus the constraint equations for each well). This system and the reservoir system described above are combined and solved simultaneously by the non-linear solver (fully implicit well-reservoir coupling) at every simulation time step.

7.G.3 Non-geothermal fluid entry

The Energy model in Emeraude is limited to single well simulations, and the assumption is that the far field temperature is equal to the geothermal temperature at that depth. For more complex situations, such as non-geothermal fluid entries or the influence of another well, then it is necessary to build and run a numerical model.

Let’s consider the situation of a producing well, where shortly after water breakthrough from an injector well, a temperature drop is observed at the perforation level (through DTS, PLT or downhole gauge). Understanding the nature of the water breakthrough can be helpful to learn more about the flow pattern from the injector to the producer. Are they connected via a fault or fracture? Or is there a high permeability streak? This knowledge can have an impact on the production strategy and the way the waterflooding patterns are arranged.

Figure 7.G.3 shows a cross section of the saturations (top) and temperature (bottom) maps, between the injector and producing wells. This simulation assumes that one of the layers (the one that shows the breakthrough) has a higher permeability than the other layers. From the saturations map is clear that that the water breakthrough has occurred, as the water saturation goes above the irreducible. The temperature map, on the other hand, shows that the “thermal front” is confined to the region close to the injector. The cold injection water exchanges heat with the formation as it moves away from the wellbore. When the permeability is large, the fluid diffusion will be much faster than the thermal diffusion. Eventually, the cold front may reach the producer but will definitely take more time and would not explain the temperature drop observed at the producer.

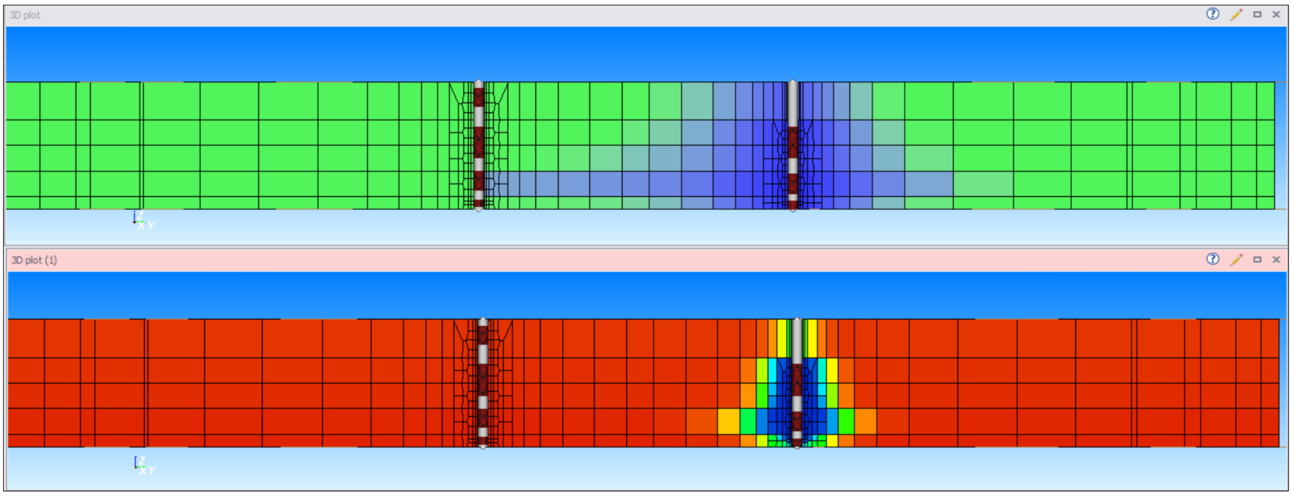

Fig. 7.G.3 – Saturation and temperature cross sections

If the high permeability streak is replaced by a fracture between the producer and injector, the water breakthrough would occur pretty much at the same time, so it would not be possible to note the difference if looking at the surface rates only. Figure 7.G.3 shows the simulation results for this scenario. It is clear that when there is a fracture connection between wells, the cold temperature front propagation is much faster. The results can be displayed in the form of temperature gauges and production logs. This facilitates the comparison of the simulations with the different possible sources of temperature measurements.

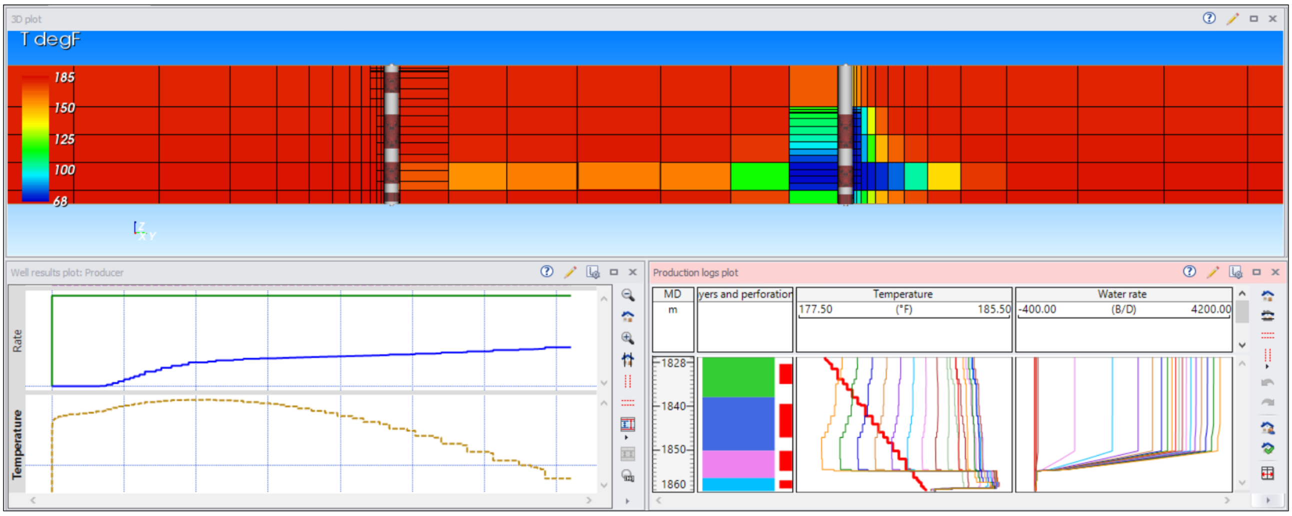

Fig. 7.G.4 – Simulation results – fracture connection

This type of what-if scenarios can be conducted relatively quickly in Rubis, keeping the complexity of the problem, including transient conditions, 3D, multiphase, etc.

7.G.4 Transient temperature logs

By fully coupling the segmented wellbore model to a complex reservoir system, the thermal numerical model is able to accurately capture the transient effects occurring in the vicinity of the wellbore.

Let us consider a vertical well perforated in two reservoir units, consisting of several layers with varying permeability and porosity (Fig 7.G.5). We simulate the injection of a cold fluid (15°C) at constant rate for one hour, followed by a long shut-in.

During the injection period, via convection, the cold temperature front associated to the injection fluid propagates further in the more permeable layers, while in the layers of low permeability the temperature remains closer to the initial, geothermal value (Fig 7.G.6). Crossflow and thermal conduction across the communicating layers are rigorously captured.

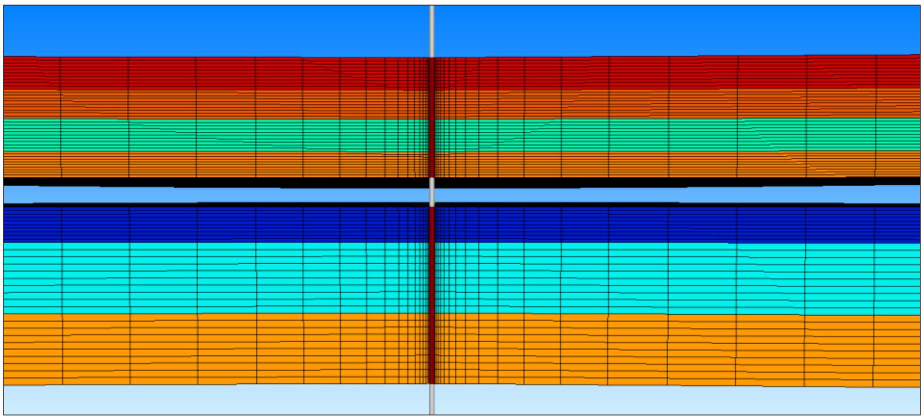

Fig. 7.G.5 – Vertical cross section and reservoir layers

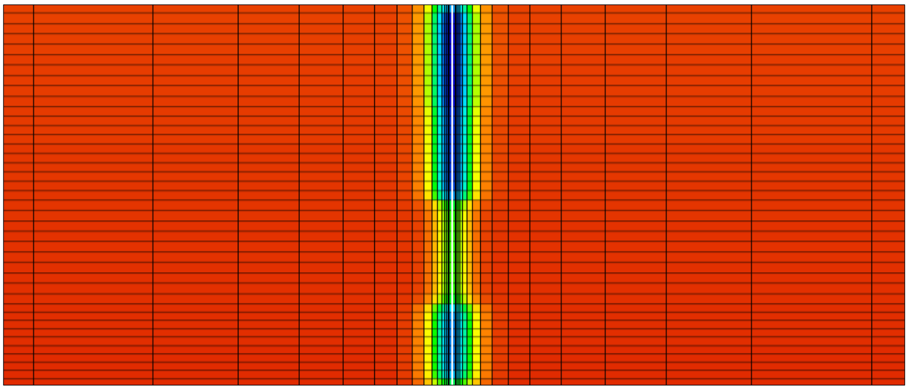

Fig. 7.G.6 – Temperature field after injection (1 hour) in the top unit

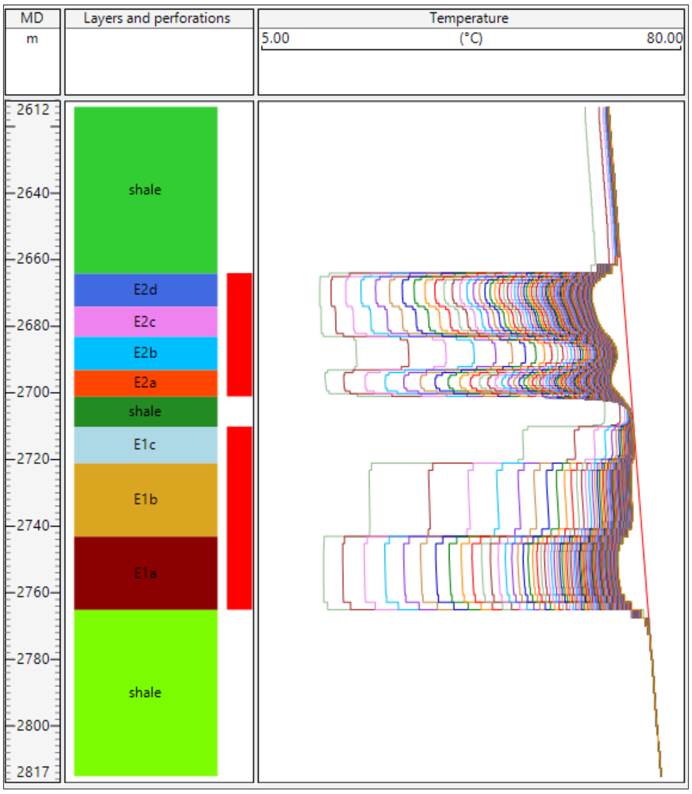

Fig. 7.G.7 – Temperature logs during shut-in

During the shut-in period, thermal conduction becomes the principal mechanism, through which each layer will slowly warm back to the geothermal value. The warm back speed depends on the depth of penetration of the cold injection fluid in this layer – hence on its permeability. The corresponding evolution of the well temperature logs during warm back can be simulated, which gives access to the permeability distribution of the intercepted layers (Fig 7.G.7). Here again, any crossflow and heat exchange occurring between the layers during the re-equilibrating process is captured by the simulator.

7.G.5 Gridding and transient thermal effects

The Numerical Simulation Chapter of the DDA book [14], shows that the grid resolution around wells can be easily modified in Rubis, with transmissibility and well index values being automatically adjusted via numerical near-well upscaling procedures. This approach is quite robust for non-thermal single-phase flow, even when very large coarsening factors and/or heterogeneity are considered. In the thermal context, however, the near-well temperature can remain transient for very long periods of time, and the simulation results become very sensitive to the near-well grid resolution. As a consequence, a significantly higher grid refinement is usually required in the thermal context.

This problem can be illustrated with a vertical producer located at the centre of a single layer, circular oil reservoir. This well is fully perforating the layer and produces at constant rate q_0. The lateral boundaries have constant pressure conditions, while no-flow conditions prevail at top and bottom boundaries. The model is simulated for various grid refinement levels. In the isothermal context, all the grid-dependent pressure transient effects are concentrated during the first hour of simulation, and the resulting well pressure history is shown to be fairly independent on the upscaling level. But when the same model is simulated in the thermal context, the transient temperature evolution at the well is shown to be very dependent to the grid size (see Fig 7.G.8). The time scale of the influence of near-well refinement, which was limited to about one hour in the isothermal case, becomes much larger. In this example, the simulated pressure remains insensitive to the grid refinement level. However, for some cases (ex: strong dependence of the viscosity to temperature), the error on temperature can also impacts the simulated pressure evolution.

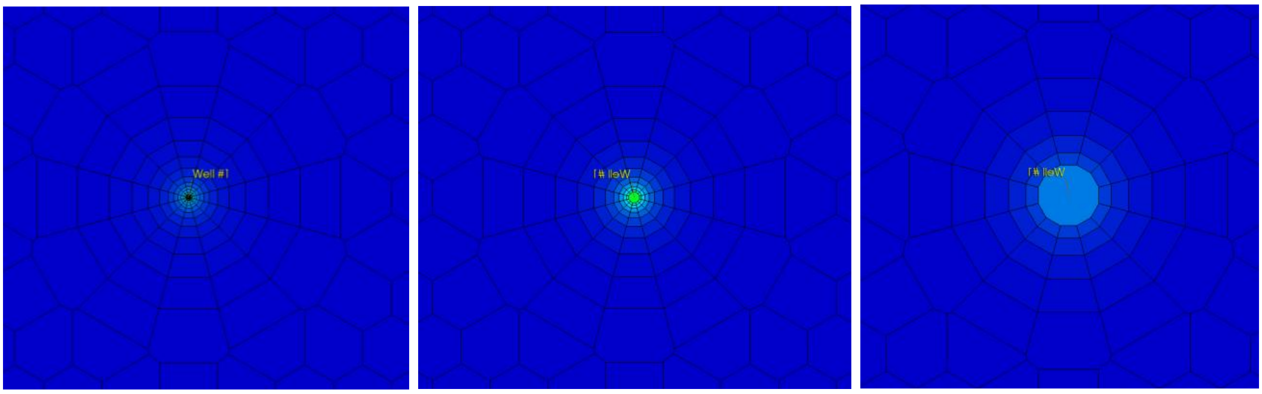

Fig. 7.G.8 – Temperature field around a producing vertical well for fine, intermediate and coarse simulation grids.

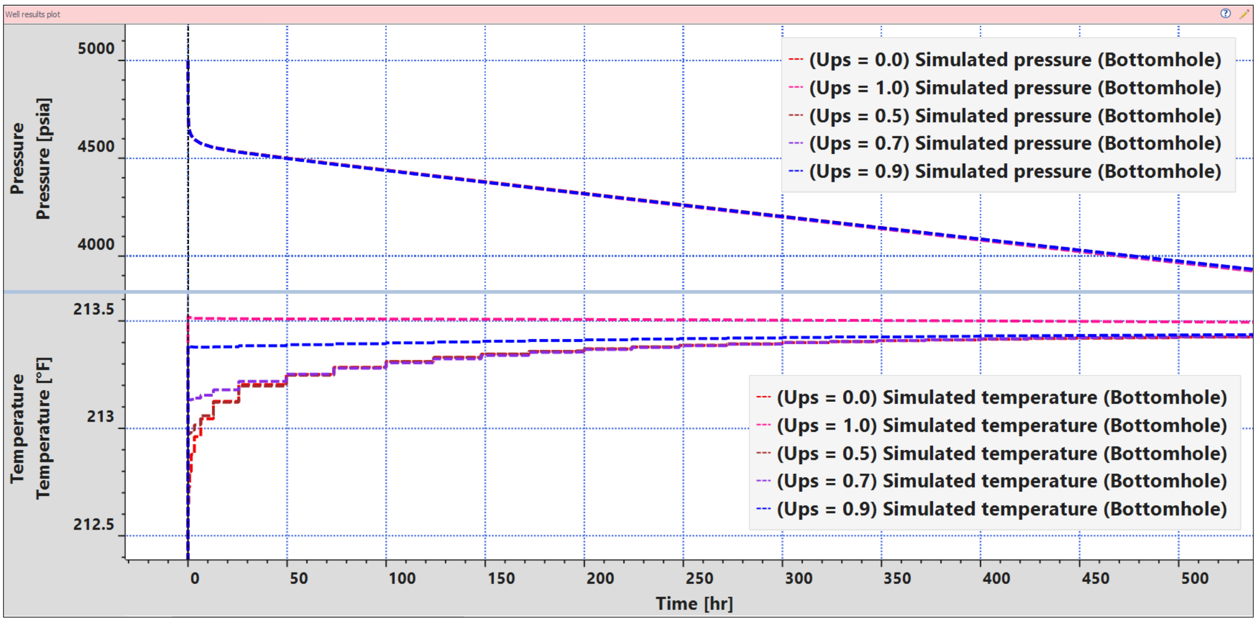

Fig. 7.G.9 – Simulated bottomhole pressure and temperature vs time for various upscaling levels in thermal case.

This dependence to the grid resolution is primarily influenced by the connections between well cells and reservoir cells. For these connections, as described previously, the convection term involves $q_{iw} h_{iw}$, where q_{iw} is the mass flux between the well cell and the wellbore, and h_{iw} is evaluated using the upstream value, which means for a producer: $h_{iw} = h_i$. When the enthalpy gradient is steep in the vicinity of the wellbore, we see (Fig 7.G.10) that a low resolution can lead to a discretization error on the value of the enthalpy flowing to the well - with the above described consequences on temperature estimations.

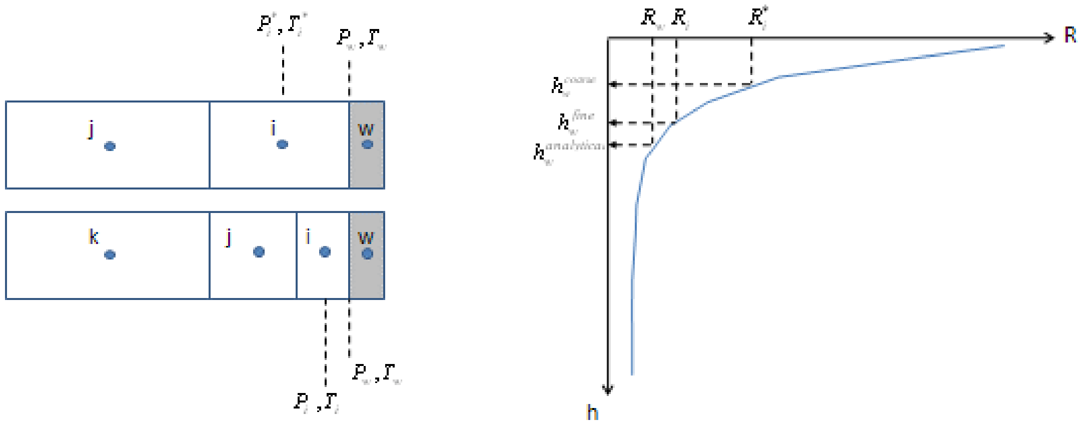

Fig. 7.G.10 – Enthalpy at well for two well cell radii, compared to the analytical value

7.G.6 Thermal Proxy model

When simulating thermal models, a 2D single well proxy thermal transient model may be generated.

Consider a multilayer reservoir and a generic well trajectory:

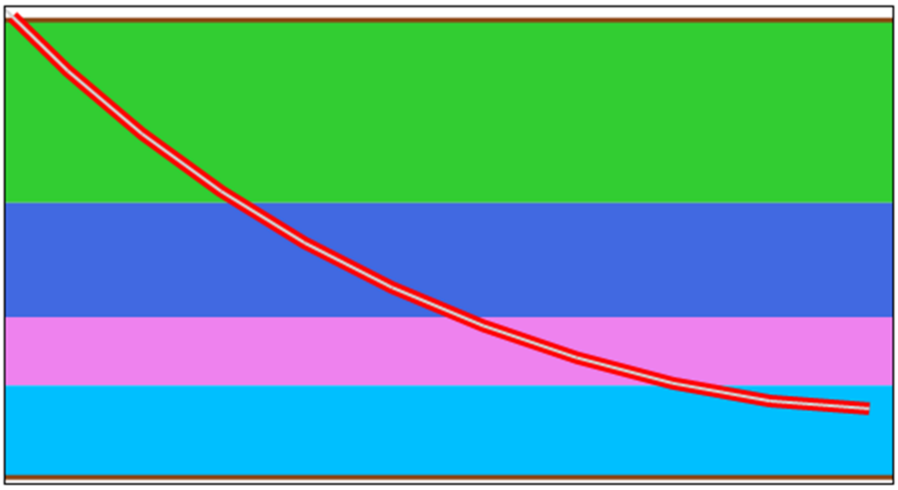

Fig. 7.G.11 – Complex well trajectory in cross section

The rigorous approach for the numerical modelling of this configuration is to build a complex 3D grid honouring the geometry of the horizons. The perforated well trajectory is discretized into segments honouring the perforations and horizons, and intercepting the 3D reservoir grid. This leads to a complex 3D system to solve, which leads to CPU intensive simulations when the problem is thermal.

If we are only interested in short-term, transient behavior in the vicinity of the well, a simplified approach can be used – here call ‘thermal proxy’.

From the full 3D grid and the segmented well geometry, the local petrophysical and thermal properties for each segment are recorded. Well segments are then transformed to a 2D proxy grid, with fully cylindrical cells around each segment, assuming radial flow towards the well segment in a given proxy grid layer, and linear flow between proxy grid layers:

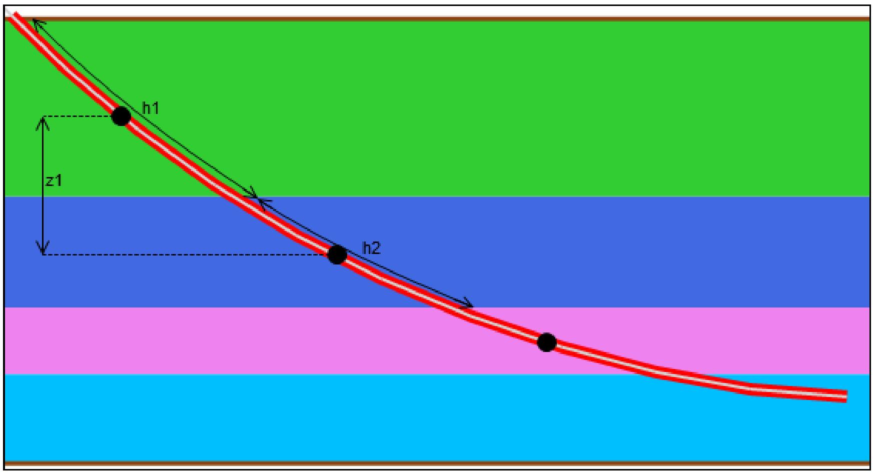

Fig. 7.G.12 – 3D segmented well trajectory

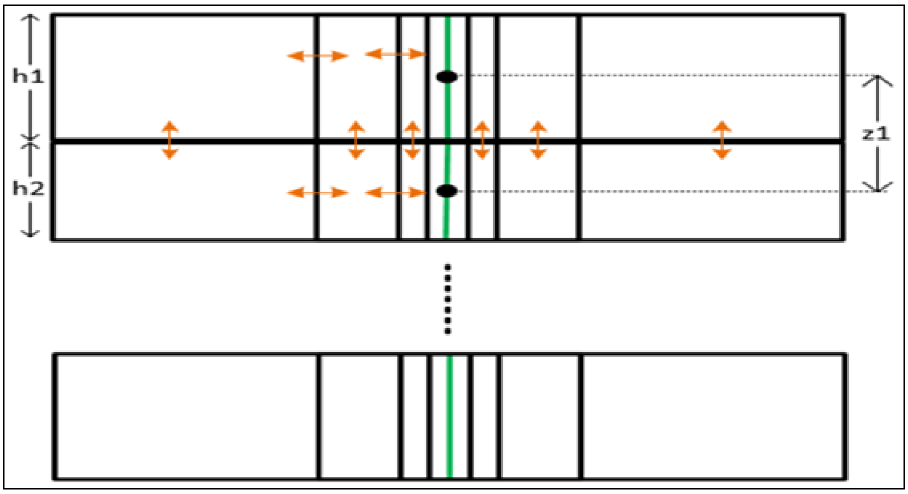

Fig. 7.G.13 – Well segments in 2D proxy grid

From the top, this corresponds to a series of cylinders centered on the well :

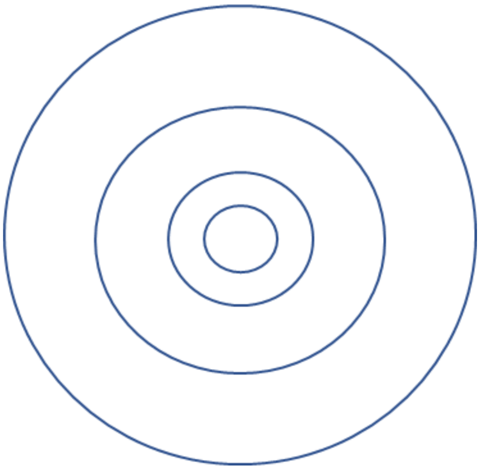

Fig. 7.G.14 –2D proxy grid view from top

The petrophysical properties and the thickness are constant in each layer, and equal to their actual value at the corresponding wellbore location.

Due to the symmetry of the proxy and the radial flow assumption in each proxy grid layer, the model is suitable only for early time well behavior, when the influence of the layers geometry and heterogeneity away from the perforations is negligible.

Since the true Δz is honored when constructing the simplified grid, model initialization (and assignment of correct properties i.e. pressures, saturations) is correctly mapped on to the simplified simulation grid.

7.H Forward Temperature simulation – Emeraude

In Forward simulation mode, the inputs are the layer rates (production or injection) plus the system description (Reservoir, wellbore, fluids, etc.). Using the Energy Equation and WIFO models, then it is possible to simulate the temperature response for any arbitrary production or injection profile.

Unless PL results are available, the layer rates are unknown. Therefore, this mode is useful for pre-job planning purposes, what-if scenarios or to understand what the impact of the uncertainty of different input parameters. All the sensitivities presented above for the Energy Equation and WIFO models can be obtained by conducting Forward simulations.

Emeraude presents two Forward simulation models which are based on the Energy equation, but the specific formulation is different to account for the particular wellbore flowing conditions. The Steam injection and Leak simulation methods are presented next.

7.H.1 Steam Injection

The main objective of steam injection is to maximise the amount of heat transfer between the steam and oil in the formation. The heat contained by the water is largely a function of its temperature. However, in this case since water exists in liquid and vapour form, the evaporation enthalpy or "latent heat" of the vapour will play a key role. Hot liquid water reaching the formation will transfer less energy than vapour at the same temperature.

As the hot vapour is injected from surface, heat exchange will occur, leading to a temperature drop and part of the vapour condensing to liquid water. At any depth of the well, the Steam quality is defined by the mass of steam divided by the total mass of injected water:

$$\chi = \frac{m_{vapour}}{m_{vapour} + m_{liquid}}$$

The objective of the steam injection design is then to maximise the steam quality reaching the perforations. This can be modelled in Emeraude, and sensitivities on the completion design and injection conditions can be carried out.

In this situation, liquid and vapour will coexist, and the system has only one degree of freedom, meaning that temperature and pressure are not independent. At equilibrium, in order to fully determine the state of the fluid it is necessary to know the pressure or temperature, plus the enthalpy (can be the entropy or specific volume too).

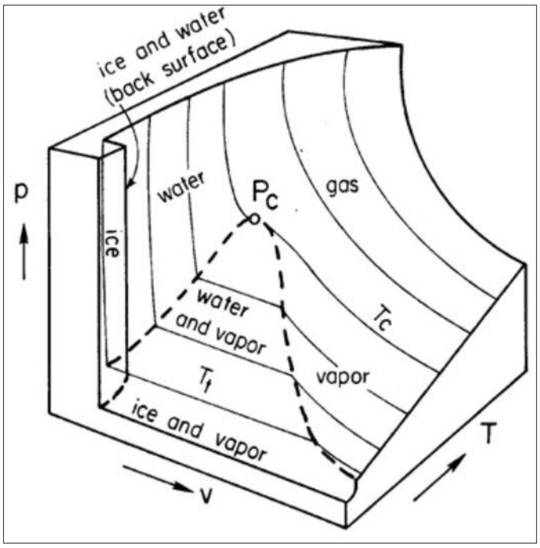

Fig. 7.H.1 – Water phase diagram – From Godson (1973)

In order to calculate the Enthalpy profile, it is necessary to define the surface injection conditions (rate, pressure and temperature) plus a tubing (or casing) pressure profile. Since liquid and vapour will travel at different velocities, multiphase flow correlations are used to compute the pressure profile.

Starting from the surface conditions, it is possible to apply the Energy equation to integrate downwards in order to obtain the temperature and the Steam quality profiles. The rate of injected water per layer is one of the inputs of the model, and this needs to be obtained by other means (i.e. reservoir simulation).

The results of a steam injection simulation are shown in Figure 7.H.2. The QZT and QZI tracks show the vapour fraction in red and liquid in blue. Steam quality drops from around 0.7 at surface to zero above the bottom perforation. This means that only hot water is injected at the bottom perforation.

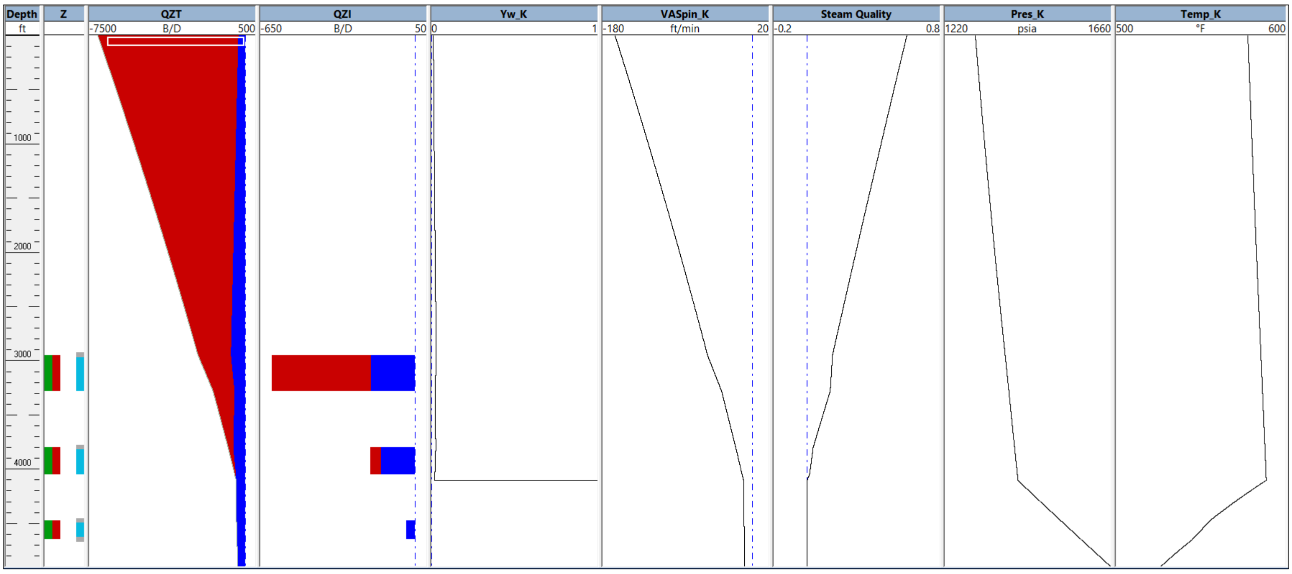

Fig. 7.H.2 – Steam injection simulation

From this base case it is possible to perform some sensitivities. When an annular is present, the fluid filling it will have a large impact. Liquid water has a large thermal conductivity compared to gases, which leads to a larger heat loss coefficient, facilitating the heat exchange. Also, based on the available surface injection facilities, the injection pressure and quality can be increased to maximise the steam quality at the perforation level.

7.H.2 Leak detection

Increased annular pressure detected at surface is likely to be an indication of tubing to casing leak. This may be a result of tubing corrosion, problem with valves, expansion joints, etc. Sustained annular pressure is an integrity concern, and the leak position has to be determined as soon as possible.

In general, leak rates are low and normally missed by conventional spinners. More specific cased hole logging tools can be run, such as Multifinger calipers, acoustic energy (noise) and temperature measurements. It is important to understand, before running the tools, what is the expected temperature response to different leak rates. This can be done in Emeraude. It has to be remembered that this simulation is exclusively for a tubing leak in a situation where water is injected through tubing and circulated back via annular.

The leak simulation is a specific formulation derived from the Energy Equation model. The temperature profile along the tubing and annulus are simulated. Also, the interest is now in small localized features, the thermal conductivity in the axial condition is also accounted for. The diagram below shows the energy balance for a segment of the well. The arrows in red show conduction, both in the vertical (tubing, annular, casing) and in the horizontal direction. Forced convection in the tubing and annular are also taken into account (blue arrows):

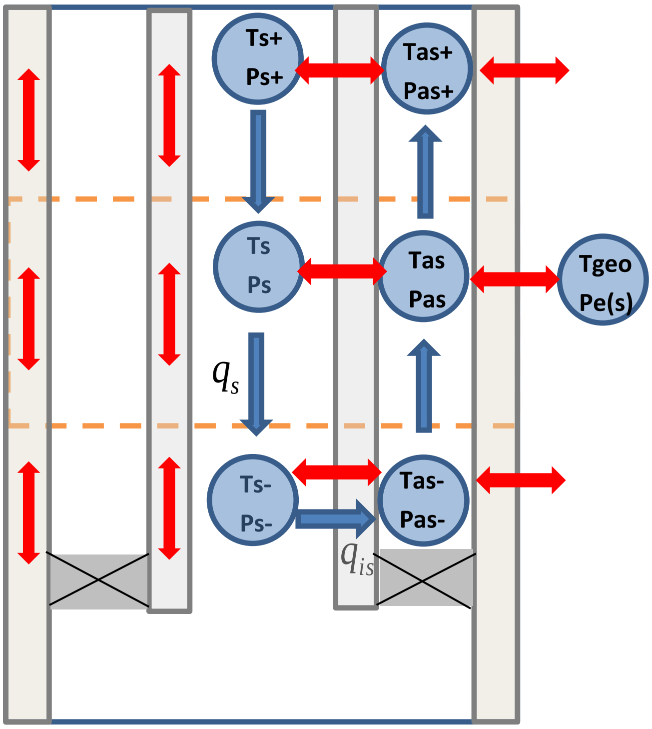

Fig. 7.H.3 – Energy balance for leak simulation

Figure 7.H.4 shows a noise log indicating the possible depth of the tubing to annulus communication. The leak design option can be used, based on the injection conditions (rate, pressure, temperature) and the same heat transfer parameters used in the Energy model. The Temperature match track shows the simulation of the annular (blue) and tubing (green) temperature for a set of injection parameters. In this situation, both show an increase compared to the geothermal gradient.

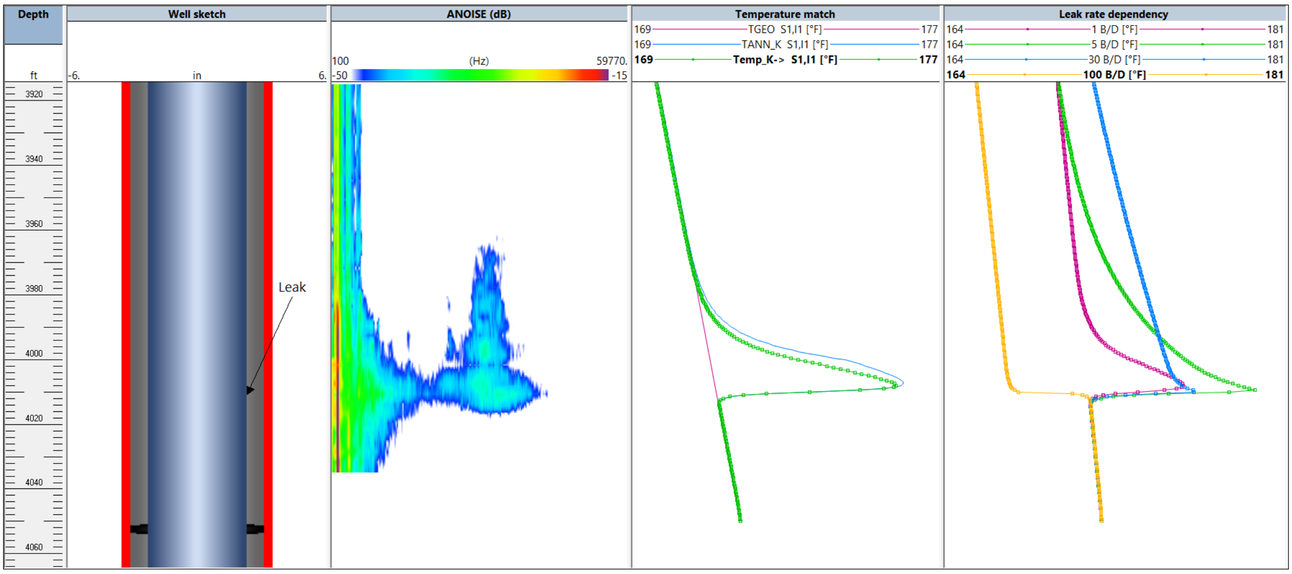

Fig. 7.H.4 – Leak simulation results and rate sensitivities

The last track shows a sensitivity of the temperature measured in the tubing for different leak rates. Similar to what is observed in traditional injection cases, when the injected water is colder than the downhole temperature, two mechanisms will be in play. The throttling effect through the leak (larger for increased delta P) leads to a localised increase in temperature. On the other hand, the convection of the colder water from surface leads to a decrease in temperature. Therefore, in the above picture, for rates of 1, 5 and 30 B/D, a temperature increase is observed. On the other hand, for 100 B/D the temperature decreases at the leak point. Clearly, the resulting temperature response is given by a balance of both mechanisms.

This type of simulation can help to set the expectations bar on the temperature response and optimise the surface injection conditions. Shallow leaks or warm injected water can lead to small delta T. In these cases, it will be possible to play with the Delta P at the leak, which in turn is given by the annular pressure (and therefore the bleeding rate).

8 – MFC Interpretation and Applications

8.A Introduction

Multifinger Calipers (MFC) were introduced in the 1950s and still remain one of the most popular measurements for casing and tubing monitoring. Despite the advances in electronics, materials, and mechanical design, the working principles remain the same.

Multifinger Calipers are downhole inspection tools that measure the internal radius of the pipe through several fingers. A continuous log of the pipe's internal diameter quantifies the metal loss due to corrosion or erosion caused by the downhole environment. As the pipe loses metal and the wall thickness decreases, the mechanical properties required to withstand the internal and external pressures and stresses can be compromised. Reduction of the internal diameter may be caused by the deposition of salts, carbonates, hydrates, etc. This can impact the well productivity due to increased pressure losses. For extreme cases of deposition, it may not be possible to pass the restriction, limiting future well intervention activities. Severe earth stresses can cause deformation, which complicates the well entry operations, and represents an integrity risk.

MFC can be used to diagnose the following conditions, among others:

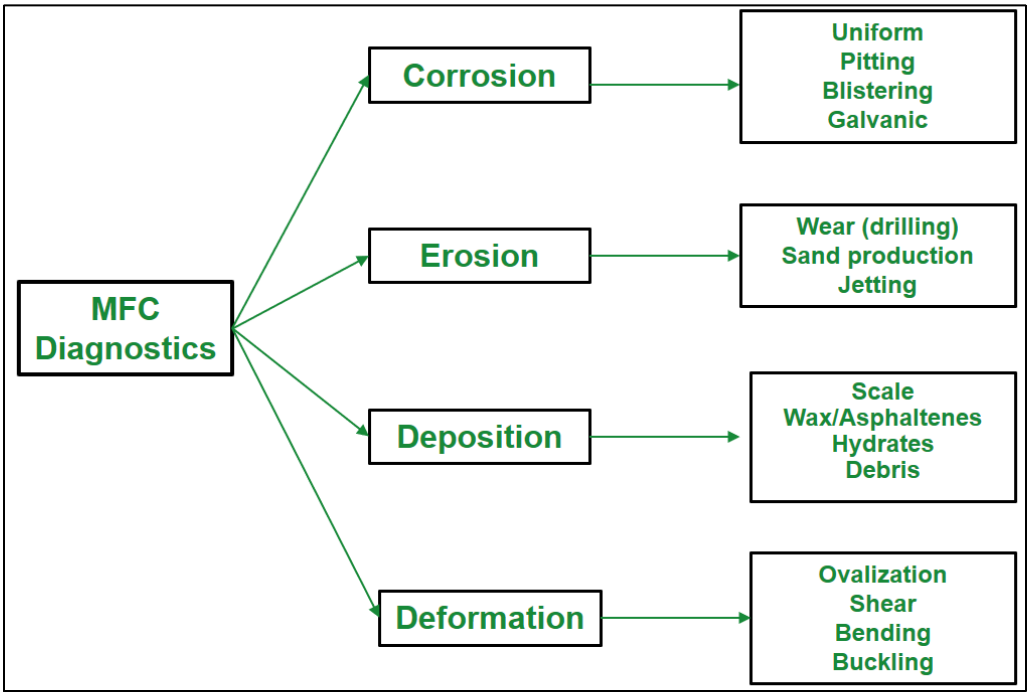

Fig. 8.A.1 – MFC Applications

This Chapter provides an introduction to the main applications for Multifinger Caliper Interpretation. A number of Frequently Asked Questions (FAQs) on common topics are answered in the different sections. Section 8.G offers a brief introduction to pipe integrity evaluation through ultrasonic pulse-echo tools.

8.B MFC Tools

Multifinger Caliper tools contain an array of arms or 'fingers', which independently measure the radius from the centre of the tool, to the pipe wall. After processing, these radii values provide a map of the internal pipe condition, to quantify penetration, deposition, deformation, etc.

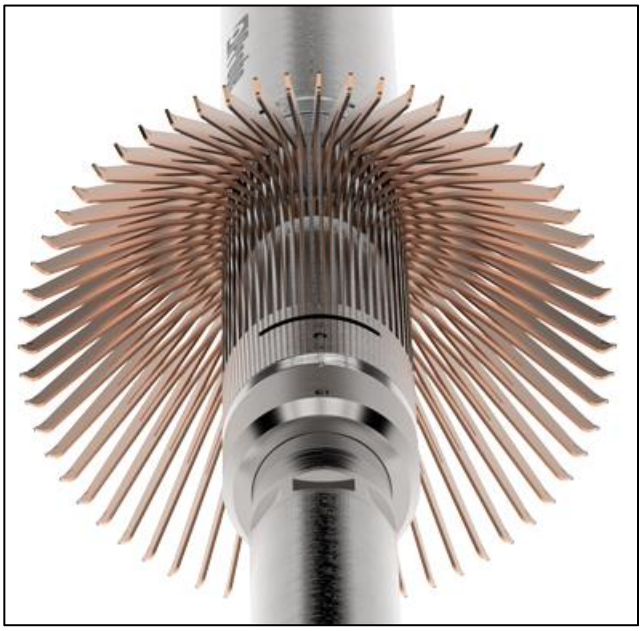

Fig. 8.B.1 – 60 finger Caliper (Courtesy: Probe - ProMAC^{TM})

MFC tools come with a different number of fingers to suit various pipe sizes. The most typical configurations are listed below:

Fingers	Tool OD (in)	Maximum measurable Pipe ID (in)
24	1 11/16	4.5 (7″ extended fingers)
40	2 ¾	7 (10″ extended fingers)
60	3.9 - 4	10 (13 - 14″ extended fingers)

An extended finger can be fitted to increase the maximum finger opening. Other MFC tools not listed in the previous table come with 56 and 80 fingers.

The quoted fingers radial resolution is around 0.001 – 0.004 in, for standard fingers (not extended). The radial accuracy is about +/- 0.02 – 0.04 in. These metrology characteristics make the tool very sensitive to ID changes. For example, for a 7 in, 29 lb/ft (nominal pipe thickness of 0.408 in), it is possible to quantify penetration variations of ~0.6%.

These tools are designed to measure only during up passes. To achieve a good vertical resolution, the standard logging speeds are ~ 30 ft/min (10 m/min). The vertical resolution is a function of the data transmission (telemetry rate), but at the typical logging speeds, it is common to have 100 samples per foot for this type of measurement. Compared to Production Logging, where the typical output is at 2 samples per foot and where only a particular range of the well is logged, the MFC data file size is generally much larger.

While running in the hole, the fingers are closed. Only when reaching the target depth, are these opened using a motor, which drives a lead screw, providing the linear motion to open and close the fingers. This can be done both in real time (wireline operations) and through memory commands.

For achieving this level of radial accuracy and resolution, proper tool centralization is critical. In Section 8.C, the effect of the tool eccentricity on the measurements is presented. Strong mechanical centralizers must be set above and below the MFC.

The MFC deployment includes setting a knuckle joint, with the objective of decoupling the toolstring from the momentum and torque created by the conveyance method and possible weight bars. Also, swivel joints can help to avoid excessive tool rotation.

Modern MFC tools include a relative bearing measurement used to orient the fingers, which positions the features found during the survey. Apart from the MFC, depth control measurements (CCL, GR) are included. Also, depending on the objectives of the survey, temperature, pressure, spinner, and noise sensors can complement the MFC toolstring.

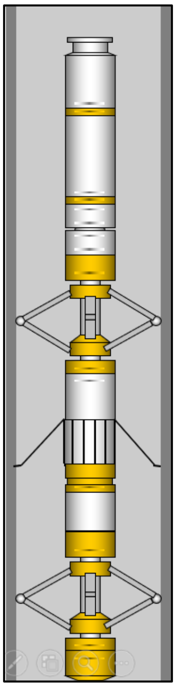

Fig. 8.B.2 – MFC toolstring schematic

FAQ 1: What is the circumferential resolution of the MFC measurements?

The rest of this section details the main characteristics of the fingers. But at this stage, it is necessary to know that the finger tip width in contact with the pipe is about 0.063 in (1.6 mm). Therefore, for an *n* fingers caliper, that the surveyed perimeter of the pipe is *n*0.063 in.*

The nominal internal perimeter of the pipe is π*ID. For example, for a 7 in, 29 lb/ft pipe (6.184 in), the nominal pipe perimeter is 19.42 in.

So what percentage of the pipe will be covered? Considering a 40 fingers caliper, then the percentage is:

$$\%Covered = \frac{0.063 * 40}{\pi * 6.184} * 100 \cong 13\%$$

This calculation gives an idea of how much may be missed between fingers. In general, this will not impact the detection of deformation, homogeneous deposition/metal loss, or ovalization, but a small hole or isolated pitting may not be detected.

In general:

$$\%Covered = \frac{finger\ tip\ width * number\ of\ fingers}{\pi * nominal\ ID} * 100$$

8.B.1 MFC fingers

Once at the bottom log depth, the fingers open and (hopefully) make contact with the inner pipe wall. Each finger assembly is independent and contains a number of elements, as shown in Figure 8.B.3:

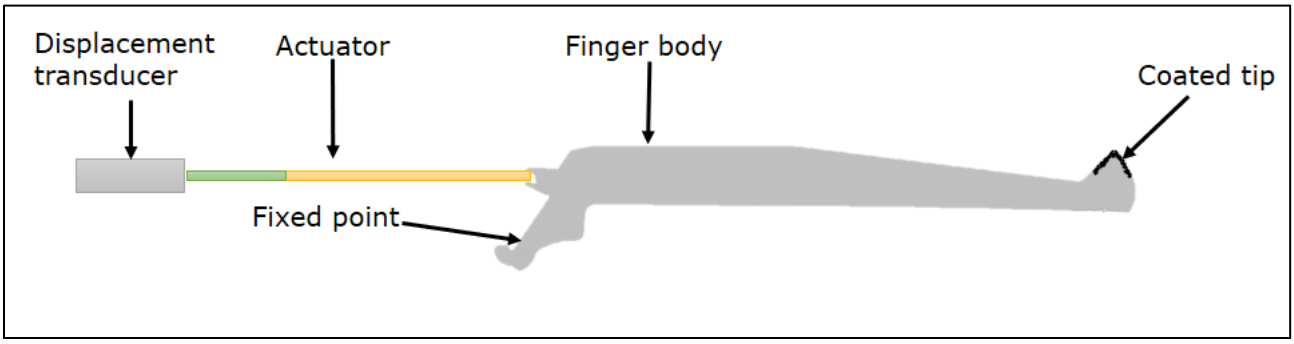

Fig. 8.B.3 – Finger assembly

- Finger body: Made of bendable material (low Young modulus) that can withstand fatigue, for example, Beryllium copper. Depending on the design, the finger body may contain a spring that pushes the finger open. The fingers exert a contact force (~ 1lbf) on the pipe.
- The tip of the finger scratches the internal surface of the pipe for thousands of feet and is coated with a hard, abrasive material, such as tungsten carbide. The fingers are re-coted after a certain number of feet of logging (i.e., 40-60k ft).
- The fixed point or pivot: This part is inside the tool housing (not visible when the tool is assembled). The fixed point does not allow lateral or vertical movement, only angular rotation.
- Actuator: A magnetic actuator rod is connected to the finger. As the finger opens and closes, the actuator moves horizontally.
- Displacement transducer: Typically uses LVDT (Linear Variable Displacement Transducer) or DVRT (Differential Variable Reluctance Transducer). Both types of transducers contain coils that produce an inductance change as the actuator moves in and out. This electrical response is associated with the displacement of the rod, controlled by the finger opening.

Figure 8.B.4 shows the measurement’s principle. In response to a pipe ID variation, the finger opens or closes at a certain angle. This angular displacement is related to the transducer's electrical response, as the actuator moves in and out of the coils.

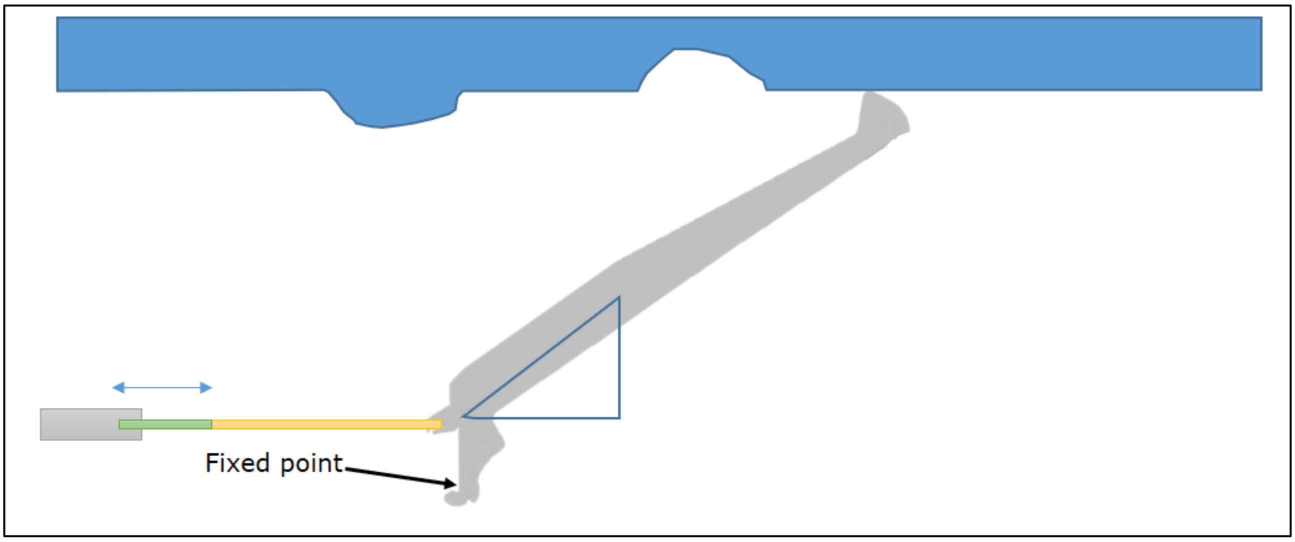

Fig. 8.B.4 – Finger movement

8.B.2 Fingers surface calibration

Relating the transducer's electrical signal to the finger's radius requires a surface calibration procedure. As explained previously, the actuator position is a function of the angular movement of the finger. But also the temperature will play an important role, as materials suffer from expansion, the electrical response changes, etc. Tool manufacturers and service companies follow different guidelines to conduct these calibrations.

The first calibration type is conducted at room temperature and consists of running the MFC tool through a number of calibrated rings. The sensor's electrical response is measured and plotted vs. ring size. In general, a pre and post job calibration should be performed, and these should include the pipe sizes to be logged during the job.

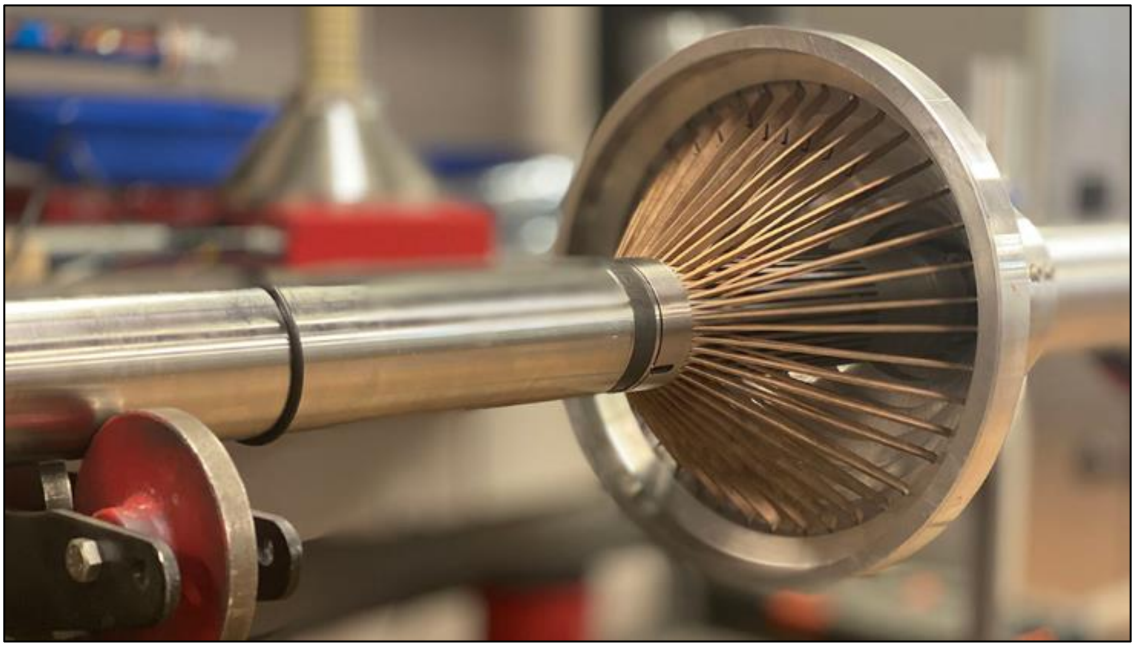

Fig. 8.B.5 – Fingers surface calibration (Courtesy: Probe)

The second calibration type is known as 'Temperature compensation'. The tool is put inside an industrial oven and is subjected to temperature variations, typically increasing steps. There may be a number (i.e., 8) of rings of different diameters. This type of calibration is not performed as often as the first type.

The results of these calibrations are several files that are loaded into the acquisition system to convert the electrical response into a radius value. The plots below show the typical shape of these calibrations.

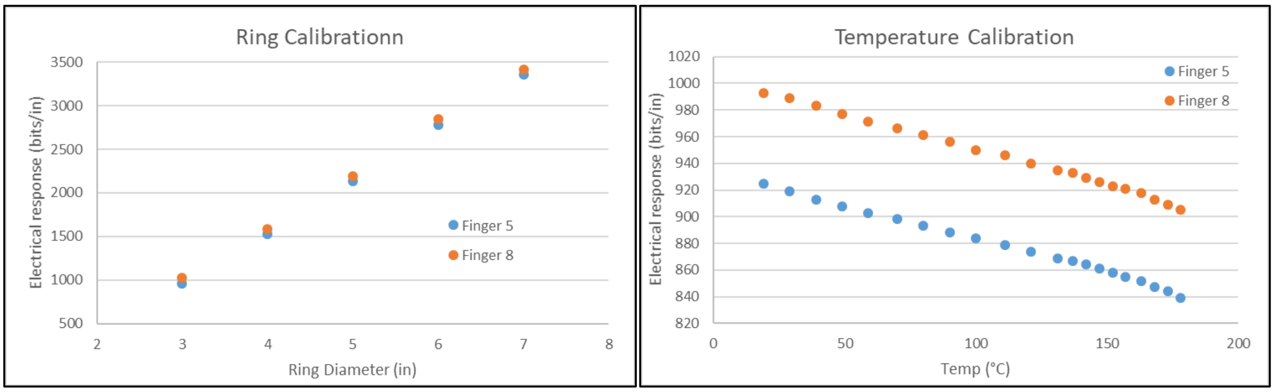

Fig. 8.B.6 – Fingers ring calibration at room temperature (left) and temperature compensation at constant ring size (right)

8.C MFC Processing

This section details the processing steps to go from raw MFC data to the stage where meaningful statistics can be extracted. The starting point for the MFC processing is, in general, a file containing one radius value for each finger, without any other processing applied by the acquisition system, apart from the calibration and temperature compensation.

As with any log, telemetry or electronic noise may be present, which in many cases may be solved by applying an adequate filter. Also, malfunctioning fingers should be removed, and their value can be replaced by a statistic or average value from neighbouring fingers.

MFC tools contain an even number of fingers, and sometimes the acquisition system allows the export of the computed diameters based on the sum of opposite fingers. For reasons explained next, it is recommended to always start from raw fingers radii values.

8.C.1 Centralization

Figure 8.B.2 shows the schematic of an MFC tool, perfectly concentric with the pipe. Even though the tool is run with centralizers and knuckle joints, eccentricity cannot be avoided. MFC are, in general, heavier than production logging sensors. Also, MFC are sometimes run in tandem with other heavy modules, like cement tools. Even for low deviations (i.e., 5°), the toolstring is displaced from the centre, as shown in Figure 8.C.1.

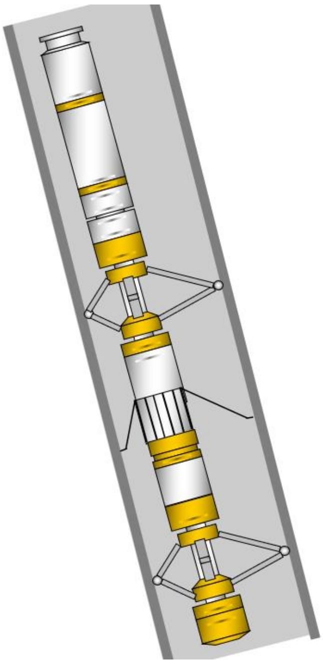

Fig. 8.C.1 – MFC toolstring schematic

A cross-sectional image of the ideal centralized case (Figure 8.B.2) and eccentric MFC (Figure 8.C.1) are shown in Figure 8.C.2, for a 16 finger MFC, with finger 1 pointing up (0°) and 9 fingers pointing down (180°). The radius measured by each finger is displayed as perfectly centralized(blue) and eccentric (black).

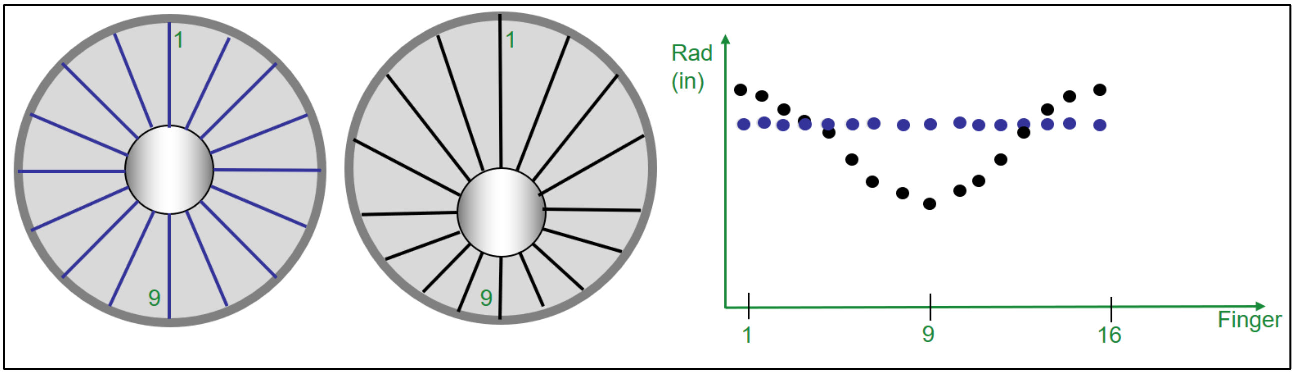

Fig. 8.C.2 – MFC toolstring schematic

In the case of a perfectly centralized MFC, the measured radii can be used directly to obtain the diameters and statistics (penetration, reduction, etc.). For a pipe in perfect condition, the radii measured by all fingers should be the same.

For the eccentric pipe, gravity pushes the MFC down. Finger 1 is now opened more than finger 9, and the radii distribution resembles a sinusoid. These radii readings cannot be used directly to compute the statistics.

Different automatic tracks generated by Emeraude can be used for identifying eccentricity and assess the need for centralization. The image below shows a 10000 ft long pipe, with deviation going from 0° to 75°.

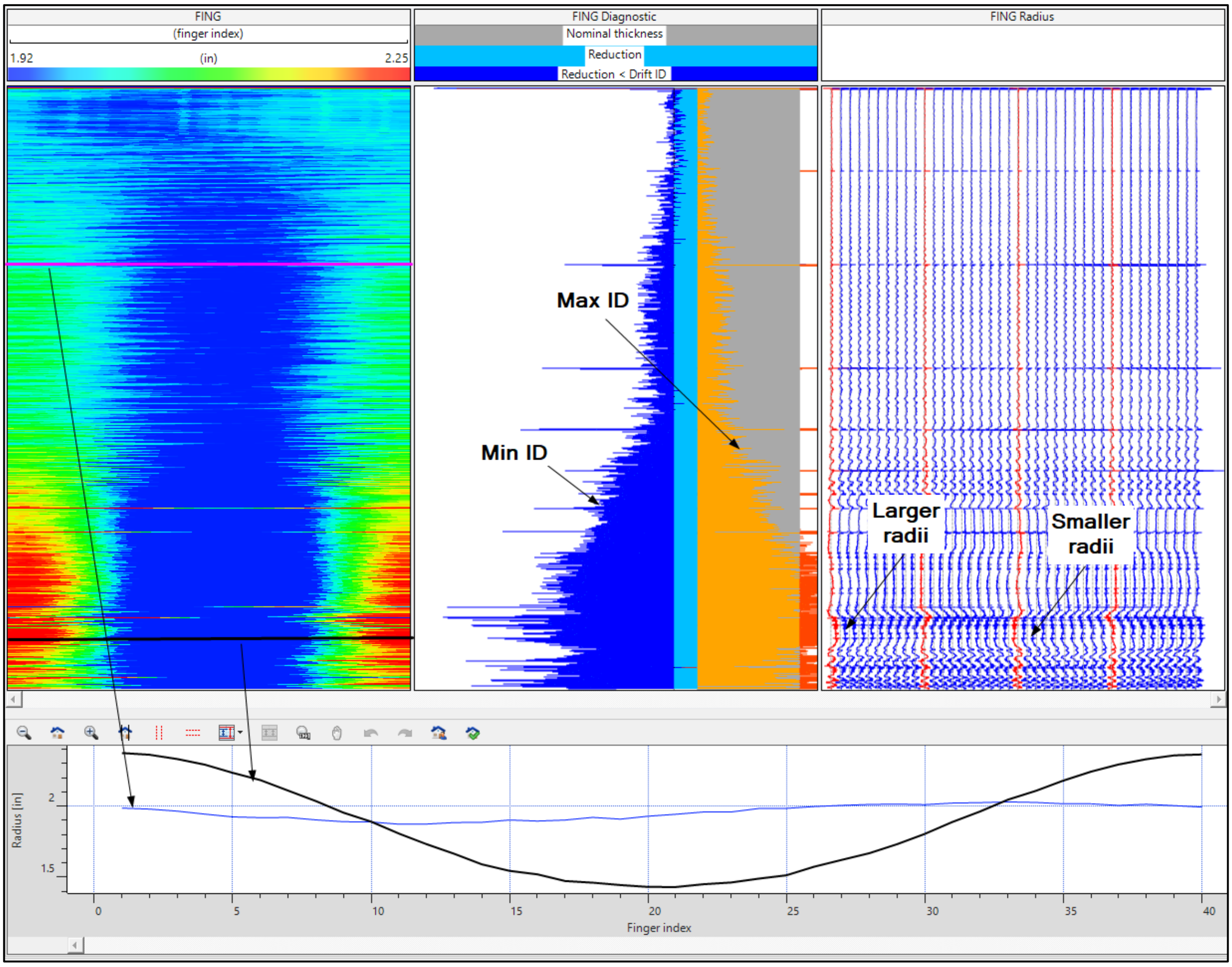

Fig. 8.C.3 – Diagnostic plots for eccentricity

- The MFC image corrected for bearings show that the radii measurements on the low side of the pipe (centre of the image) are smaller than on the high side of the pipe. This radius difference becomes more pronounced with depth as the deviation increases.
- The MFC Diagnostic plot shows large differences between Maximum and Minimum ID, and this difference increases with deviation.
- The Radius track shows that some of the fingers measure higher than the nominal radius, while others measure below nominal.
- The Radius vs. finger view shows the radii distribution for two different depths, the shallower depth (blue) and at a deeper depth (black). The sinusoidal shape is present in both cases, even though at a deeper depth, the amplitude is higher due to the larger contrast between Min and Max Radii.

The cross-section image presented in Figure 8.C.4 shows the nominal pipe geometry (black) and the MFC measurements (red). The circular pipe is detected by the tool, but is displaced with respect to the nominal pipe.

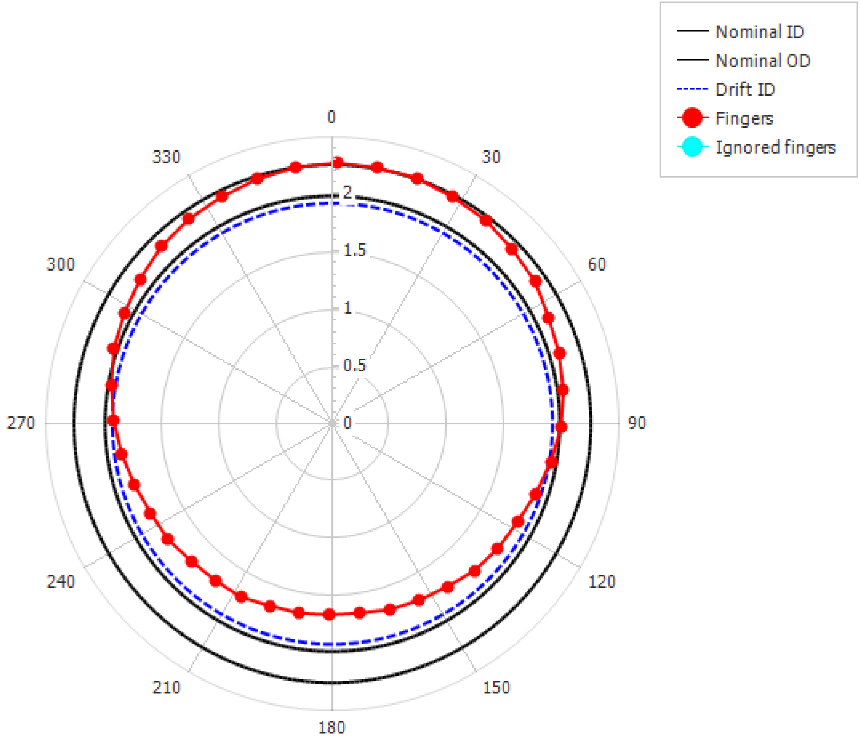

Fig. 8.C.4 – Eccentric cross-section

All these diagnostic plots help to understand the need of centralization.

The fingers measurements are given in cylindrical coordinates: radius, angle, and depth. The radius measurements are located on a Cartesian coordinate system for every depth, using sine and cosine relationships. The image below shows a circular pipe in perfect internal condition.

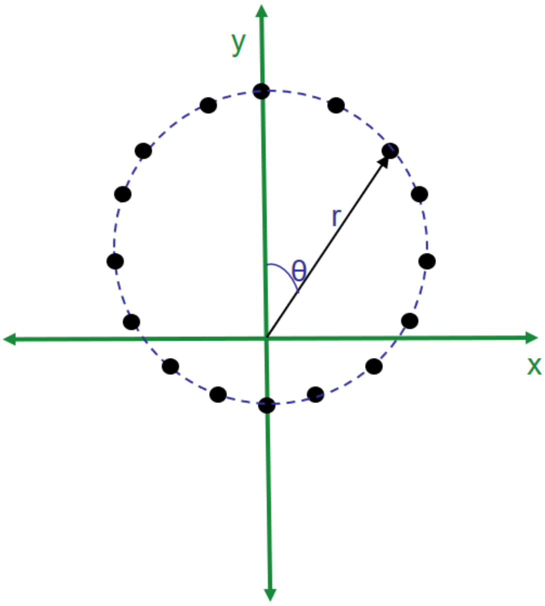

Fig. 8.C.5 – Radii measurements in a Cartesian plane

The first part of the centralization consists of fitting a shape to the measured points. The simplest approach is to use the equation of an eccentric circle:

$$R^2 = (x - x_c)^2 + (y - y_c)^2$$

Where x_c and y_c are the coordinates of the actual centre of the pipe.

However, due to the stresses in the formation or induced by the manufacturing process, the pipe may be ovalized. In this case, an ellipse shape would better fit the measured points. The equation of the eccentric ellipse is:

$$1 = \frac{(x - x_c)^2}{a^2} + \frac{(y - y_c)^2}{b^2}$$

Where *a* and *b* are the semi-minor and semi-major axis of the ellipse, the actual equation used in Emeraude takes into account the ellipse orientation, as in the formula presented above, the axes are orthogonal with *x* and *y*. Note that when *a*=*b*=*r*, the equation is again that of the eccentric circle. As the ellipse equation is a more generic solution, it is used by default in Emeraude unless the analyst explicitly chooses a circular fitting.

The second part of the centralization is basically a transformation of coordinates. Once the actual centre of the pipe is determined, the radius and angle of each finger is recomputed, using the Euclidian distance approach:

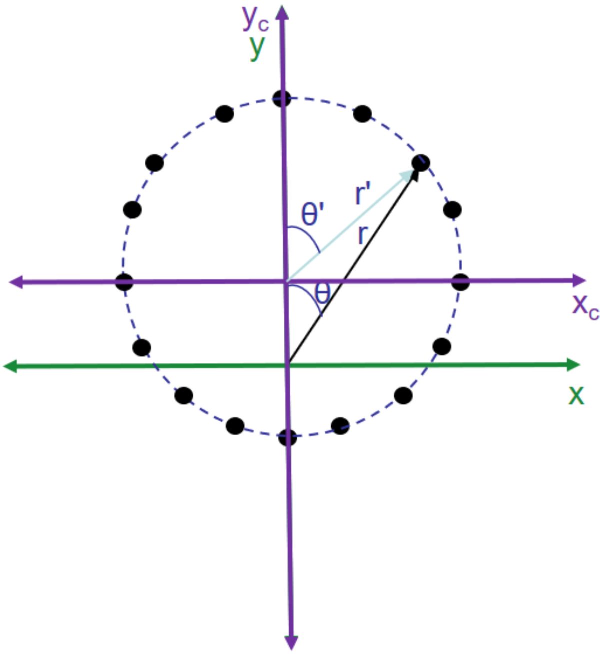

Fig. 8.C.6 – Recomputed radii after centralization.

So far, the centralization description has considered a pipe with a perfect internal condition. In reality, the caliper is likely to find a number of penetrating or depositional features, altering the shape of the pipe. Let’s imagine that the drilling bit left a grove that is sensed by 2 fingers (yellow), as shown in Figure 8.C.7. The computed center of the pipe would be shifted if the non-linear regression includes the fingers that ‘feel’ the grove and are not part of the perfect circle or ellipse. By excluding these two outliers, the centre of the ‘unaffected’ part of the pipe is computed.

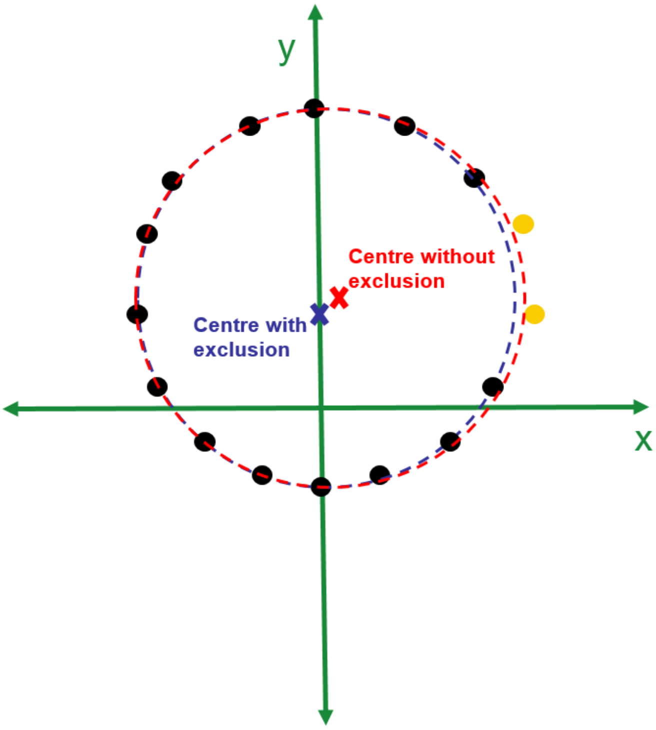

Fig. 8.C.7 – Fingers exclusion.

Emeraude offers a number of exclusion options, based on the distance between the finger's measurement and the fitted shape. The analyst may decide to exclude *n* fingers that maximize the distance above (Maximum), below (Minimum), or both (Absolute) compared to the fitted ellipse or circle. Another option is to base the exclusion criteria based on the percentage variation of the radius of consecutive fingers.

Once the centralization is applied using certain exclusion criteria, the cross-section image displays the excluded fingers (blue), as shown in Figure 8.C.8. For example, three of the excluded points correspond to a penetrating feature, and it is correct to remove them from the fitting. However, there is one isolated measurement that was removed based on the exclusion criteria (in this case, maximum absolute distance), which should not be removed. In this case, there are still 36 valid finger values for the fitting. However, as with any non-linear regression, the unnecessary removal of valid data reduces the statistical validity of the fitting. The analyst must navigate through the raw dataset, understand the nature and distribution of the penetrating and depositional features, and apply the centralization accordingly. Different exclusion criteria can be applied throughout the log.

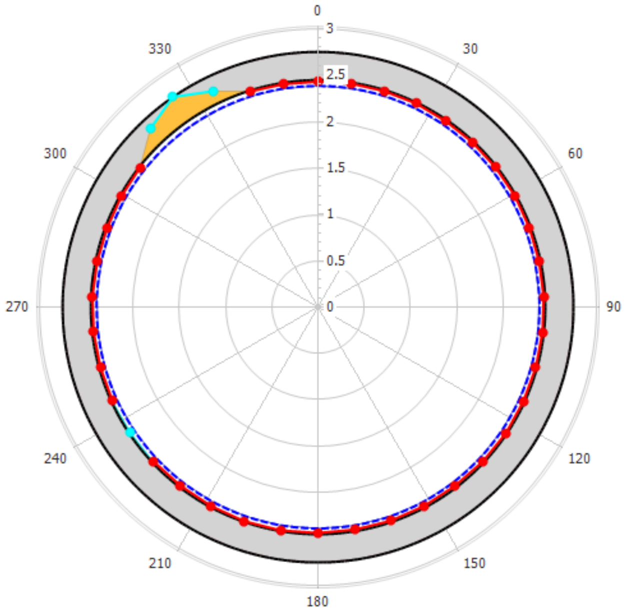

Fig. 8.C.8 – Excluded fingers in the Cross-section image

Once the centralization is completed, the Eccentricity will be calculated, as the difference between the centre of the pipe and the centre of the MFC tool. Also, the regression residual expressed as chi-square (1-R^2) is displayed.

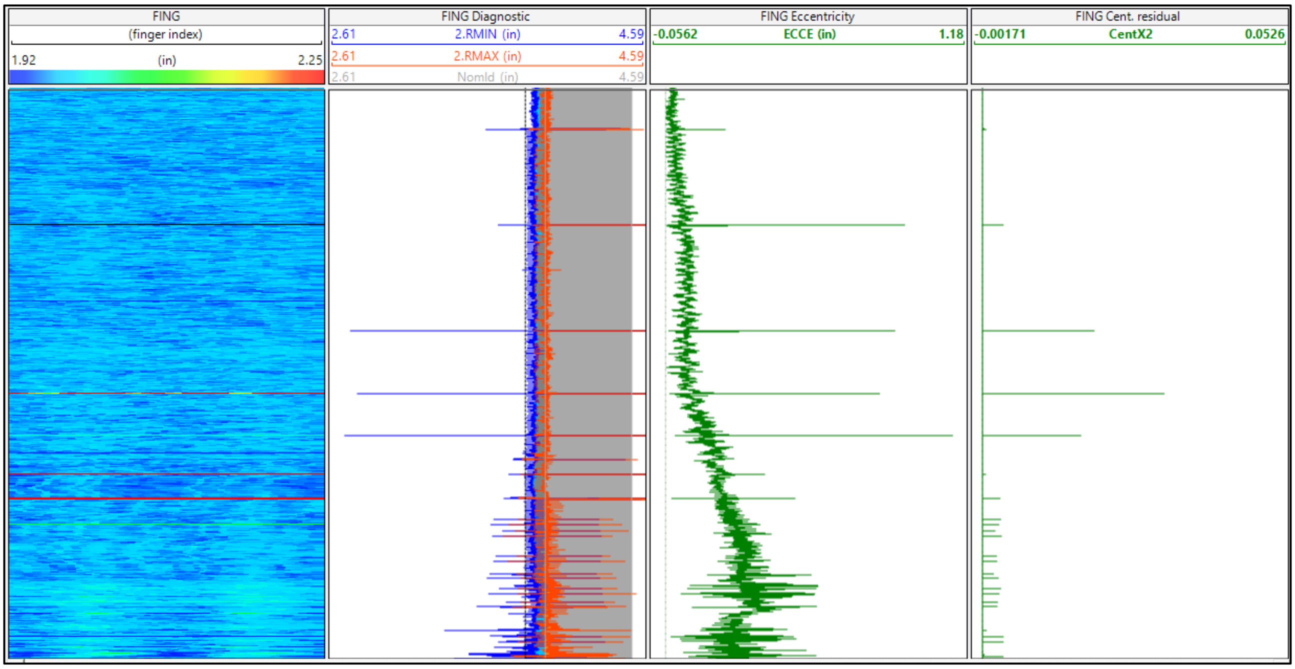

Fig. 8.C.9 – Centralization results

Spikes on the residual indicate that the fit is less satisfactory in certain intervals. For example, the log shown in Figure 8.C.9 was centralized using an ellipse fit, excluding the 4 fingers with a larger absolute difference. The spikes that are seen in the residual (also in the eccentricity) correspond to valves, SSDs and side pocket mandrels. Figure 8.C.10 shows one of the SPMs, where 8 fingers sense the increased diameter. When fitting these elements, by only excluding the 4 fingers of larger absolute distance, Emeraude uses the ellipse (purple) in the image below (left). The 4 excluded fingers are indeed the correct ones (blue), but not the only ones that should have been removed from the fitting. A local centralization excluding 8 fingers is shown on the right, and with this exclusion criteria, the SPM body can be fitted by a perfect circle:

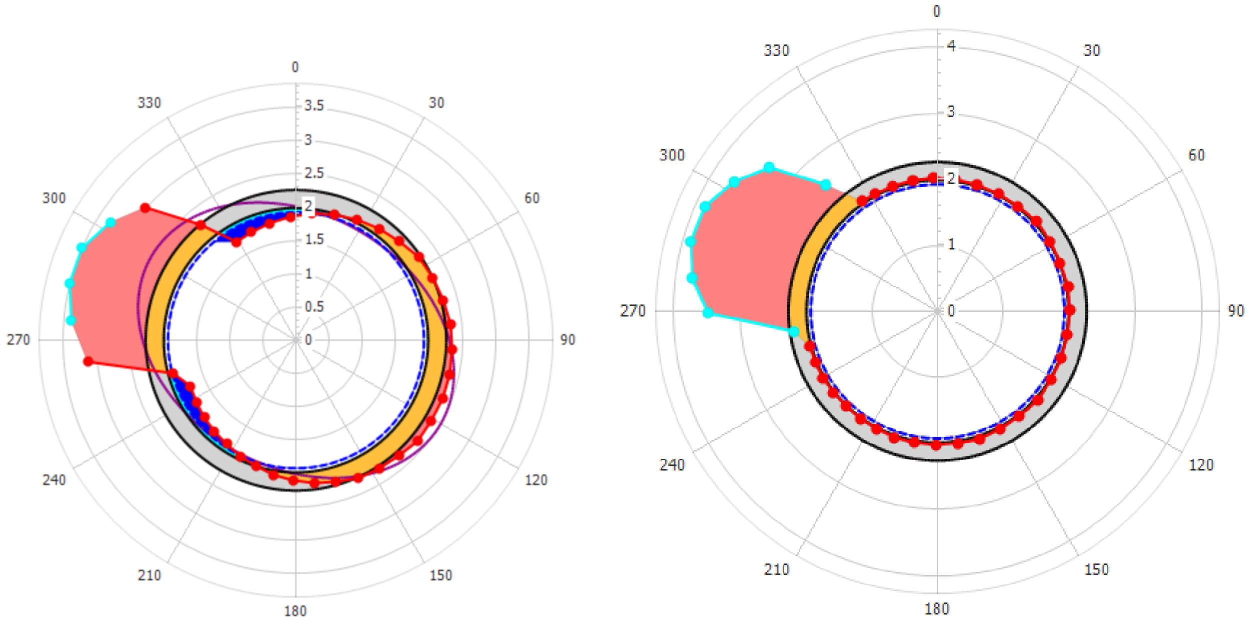

Fig. 8.C.10 – Excluded fingers in the Cross-section image

These types of completion elements do not represent the nominal pipe joints; however, this example demonstrates the importance of understanding the settings of the centralization.

FAQ 2: What is the maximum eccentricity that your centralization algorithm can handle?

This question comes from the heritage of older centralization algorithms, which used a 1D fitting (i.e., sinusoidal). As can be concluded from the explanation above, as long as the fingers measurements are accurately located on a Cartesian coordinate system, then there are no restrictions on the level of eccentricity from the algorithm point of view.

So the question should be, does the eccentricity affect the accuracy or resolution of the fingers measurements?

And the answer is yes. The finger's resolution is based on the actuator's displacement quantification, which is driven by the angular movement of the finger. For an eccentric MFC, the fingers on the side of the short radius measurements will experience a much smaller angular movement, meaning that the actuator displacement will also be smaller. This is the same cause why extended fingers reduce the radial resolution compared to the standard finger in a pipe where both fingers types are suitable.

FAQ 3: Can centralization 'deform' the pipe shape?

This question is typically asked based on the fact that the fitting uses an ellipse or a circular fitting.

The answer is that the centralization does not deform the fingers measurements. The fitting provides the centre of the ideal shape, and then the fingers radii are recomputed using the actual MFC measurements. Therefore, the shape will not be modified: if the pipe is ovalized or there are penetrating/depositional features, these will be there before and after the centralization. However, as shown in Figure 8.C.10, a wrong estimation of the geometrical centre by the fitting results in a translation of the fingers measurements. This will have consequences, as the computed maximum and minimum radius measurements will be affected, which propagates to the calculations of penetration, reduction, etc. The shape of the pipe is not modified, just displaced.

In situations like shown in Figure 8.C.11, where the cross-section is reduced due to the presence of gas hydrates, the ellipse fitting does the best job it can through error minimization, shown by the purple oval. The centre of the pipe cannot be determined anyway, as the fingers are not touching the pipe wall. In situations like this, the analyst must understand that the measurements after centralization can be displaced, and care should be exercised when reporting the statistics (max/min ID, penetration, reduction, etc.)

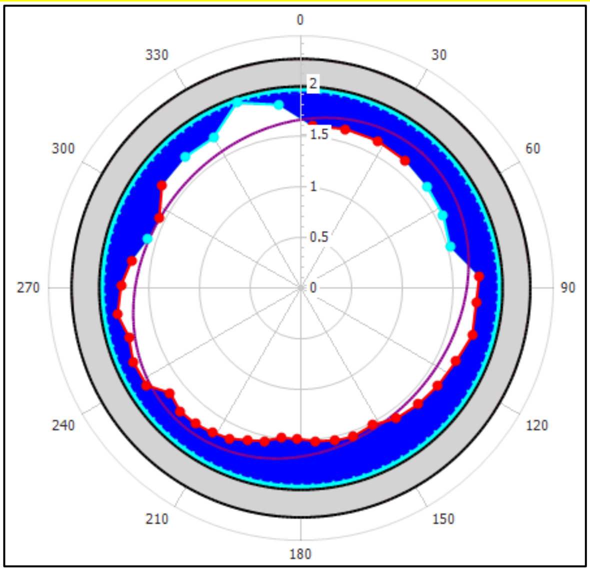

Fig. 8.C.11 – Centralization in the presence of gas hydrates

A special case, however, is when the pipe is actually deformed (bent, buckled, etc.). Blindly applying centralization can have severe consequences, as explained in section 8.F.

8.C.2 Re-Calibration

The word ‘Calibration’ was previously used for the operation of transforming the finger’s electrical response to a radius value. This is achieved by a number of surface calibrations, both isothermal and using a number of temperature steps.

‘Re-calibration’ is applied if the computed radius values using the surface calibrations are no longer representative of the internal pipe radius. This can occur due to a number of reasons:

- Finger tip wear: The dimensions of the fingers may have changed compared to the surface calibration, as the finger tip scratches the inner surface of the pipe.
- The electrical properties of the circuit (especially the inductance) may not be the same as it was originally. This can cause some drift on the measurements.
- Invalid calibration: The calibration file may not correspond to the specific survey, it may be out of range, etc.

Suppose one of these situations is present in the full acquisition or part of the log. In that case, there will be a consistent positive or negative error in the measurement of the affected finger.

Suppose all fingers show an error in the same direction and magnitude (i.e., a positive offset of 0.05 in). In that case, it will be challenging to differentiate the error with respect to an actual metal loss or deposition. Fortunately, in most cases, the need for re-calibration can be assessed by looking at the MFC image, MFC radius, and by extracting the radius measurements at different depths:

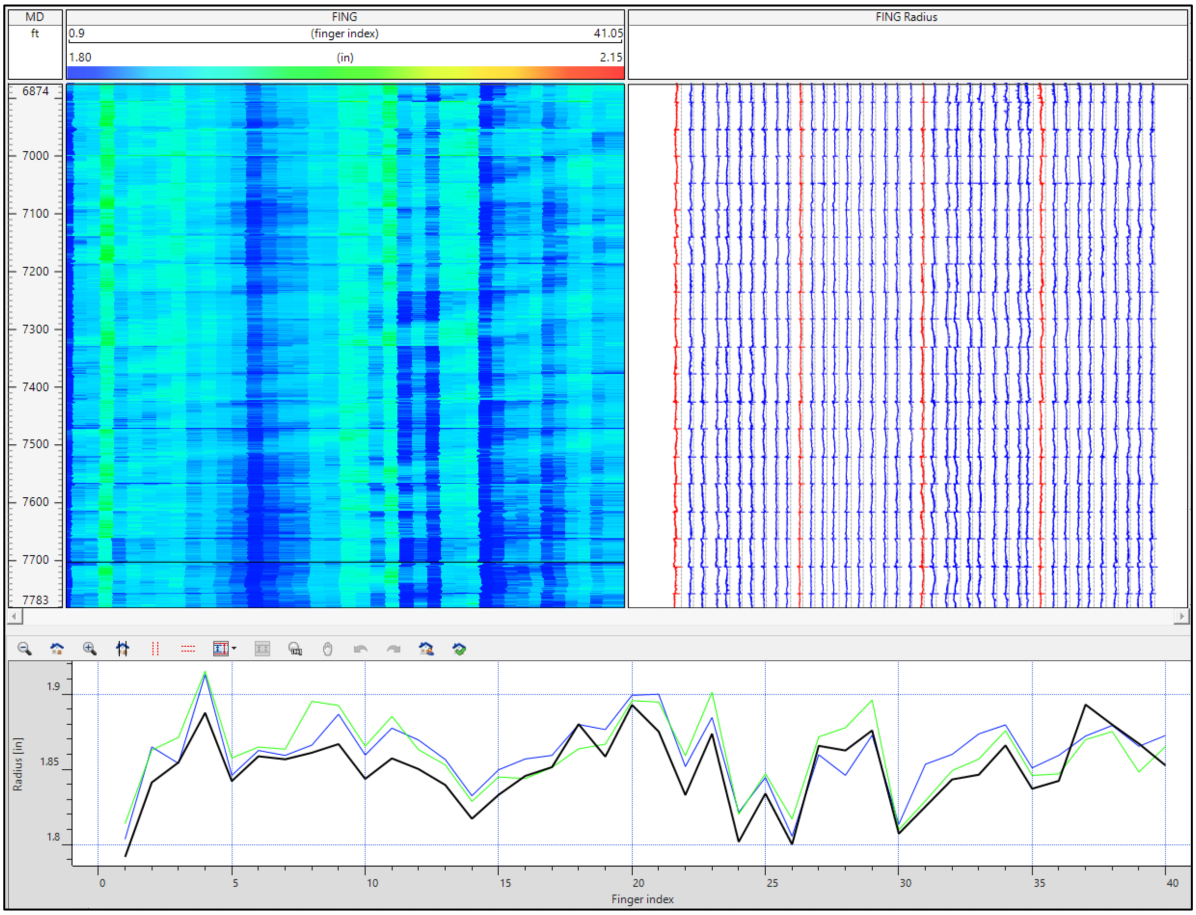

Fig. 8.C.12 – Assessing the need of re-calibration

- The MFC image uncorrected for bearing shows a striped behavior, present across several pipe joints.
- The MFC Radius track shows an offset between the nominal ID (dashed lines) and the finger's measurement. This offset is of a different magnitude for the various fingers.
- The radius measurements at different depths show a repeatable behavior, with some fingers always measuring higher or lower than the mean.

Once the MFC data is loaded into Emeraude, it is no longer an option to apply a re-calibration in the same fashion as the original calibration. This is because the actual pipe radius is unknown, and it is not constant due to the penetration and deposition features. An alternative approach is used, which consists on calculating the average radius value for all the fingers over a certain re-calibration interval. These averages are then compared against:

- Mean or median of all the fingers over the same interval
- Known ID (nominal) over the same interval.

The difference between the average finger radius (RADi) and the overall MFC radius as obtained by one of these two methods is used to compute the individual fingers shifts. These shifts are different for each finger, and will be applied for all the data over the selected range:

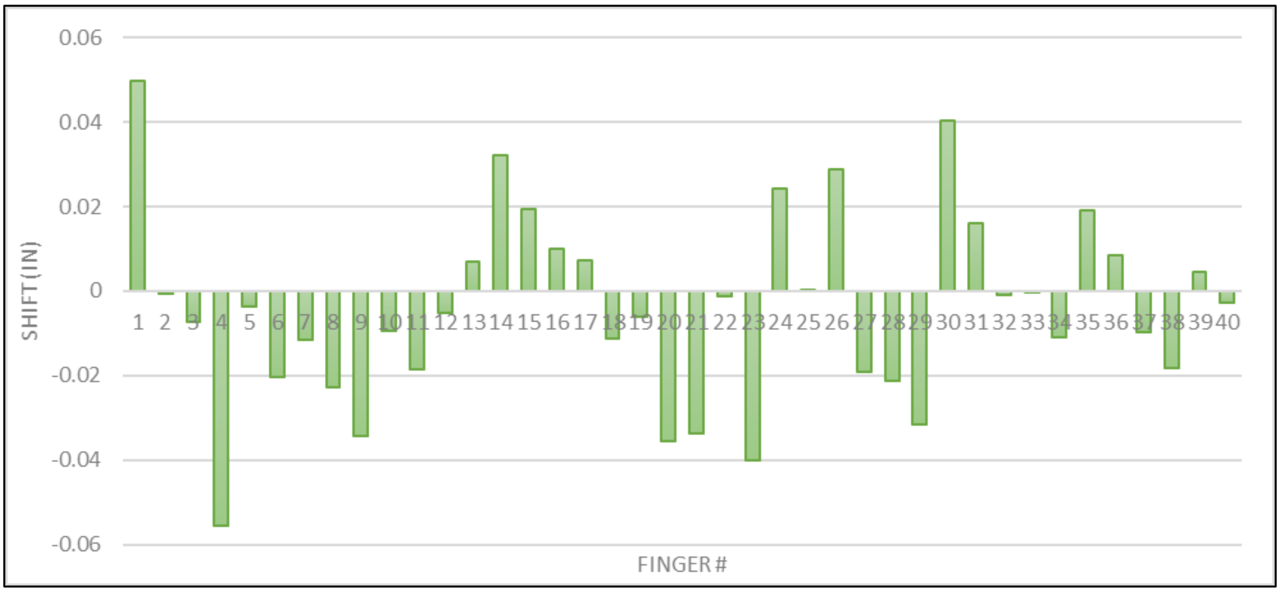

Fig. 8.C.13 – Calculated shift per finger

To apply the first approach, where a statistical value (median or mean) is considered, it is necessary to ensure that the re-calibration interval includes only pipes of the same size (OD, weight). The selected interval should not include areas of severe damage or deposition, which can lead to non-representative statistics.

The second approach, which uses a known ID, should only be applied when there is confidence that the tubulars have the same ID as the informed nominal. When the pipe has suffered metal loss or deposition, this is no longer true. However, even for new pipes in good condition, there is a 12.5% thickness tolerance. Valves, nipples, and other special completion elements have stricter dimensional tolerances than the casing, and are preferred for using the 'known ID' re-calibration method.

A single re-calibration zone may be enough if the surveyed pipe size is constant and there is no evidence of drift. Otherwise, different re-calibration zones are needed to apply zonal shifts.

Figure 8.C.14 shows the same depth range as Figure 8.C.12, but in this case, the interval marked in red has been re-calibrated. The radius is more homogeneous, there is evidence of spiralling (manufacturing-induced small ovalization), and the extracted fingers in black (inside re-calibrated interval) show much lower variance than the green and red curves (outside the interval). Before re-calibration, the real pipe features were masked by the erroneous fingers in the initial radii. In this case, it would be necessary to recalibrate the whole depth range.

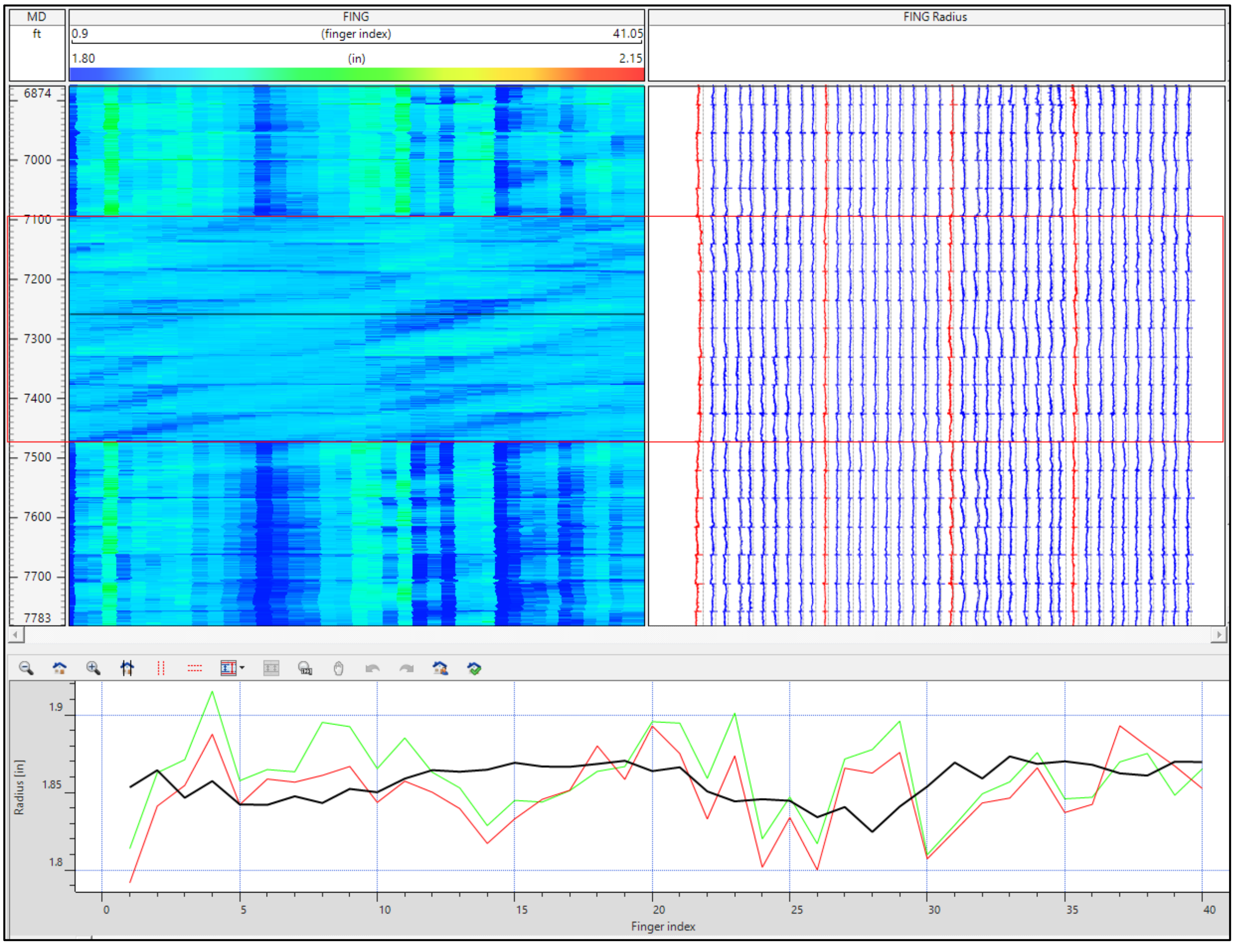

Fig. 8.C.14 – Calculated shift per finger

FAQ 4: Re-calibration after Centralization. Is the data ready?

It is necessary to perform a centralization before re-calibrating the fingers. In case the user does not explicitly run the centralization before, when the re-calibration is launched, a default centralization will be automatically applied by Emeraude (not persisted).

So the question is, after centralization and re-calibration, is the data ready for obtaining representative statistics of the pipe joints?

The original centralization included data that was later modified by the applied re-calibration shifts. The original data may have contained outliers that were excluded from the centralization. These were artefacts due to improper fingers calibration and not real pipe characteristics.

By looking at the pre-recalibration data on Figure 8.C.12, it can be seen that Fingers 1, 24, 26, and 30 consistently measure lower values, which are confirmed by the shift magnitudes displayed in Figure 8.C.13. When the centralization is applied to this data, the excluded fingers are exactly those mentioned before:

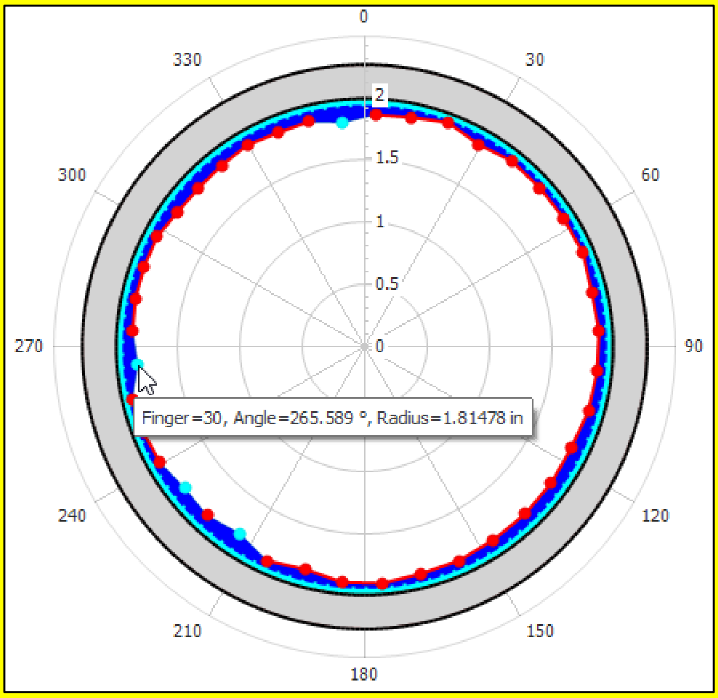

Fig. 8.C.15 – Original (pre-recalibration) centralization

When the re-calibration shifts are applied, the shape of the data will change. The fingers that were originally taken as outliers will not necessarily be off from the centralization shape after re-calibration.

In conclusion, if a re-calibration was applied after the centralization, a new (second) centralization may be necessary, especially when the magnitude of the shifts was significant.

8.C.3 Joints Identification

Different types of threaded connections can be found in the surveyed tubulars. ‘Integral connections’ refer to joints connected without an intermediate tubular. These can be ‘upset’ or ‘non-upset’ (flush), whether the pipe end has an increased wall thickness or not. Coupled connections connect two casing joints through an externally threaded short tubular.

Regardless of the connection type, when reporting the diameters and statistics of the surveyed pipe, it is necessary to remove the influence of the connections. Figure 8.C.16 shows two different connection types. If the statistics were to include the connections, the one on the left would show as an increased penetration, while the one on the right would be a peak on the reduction:

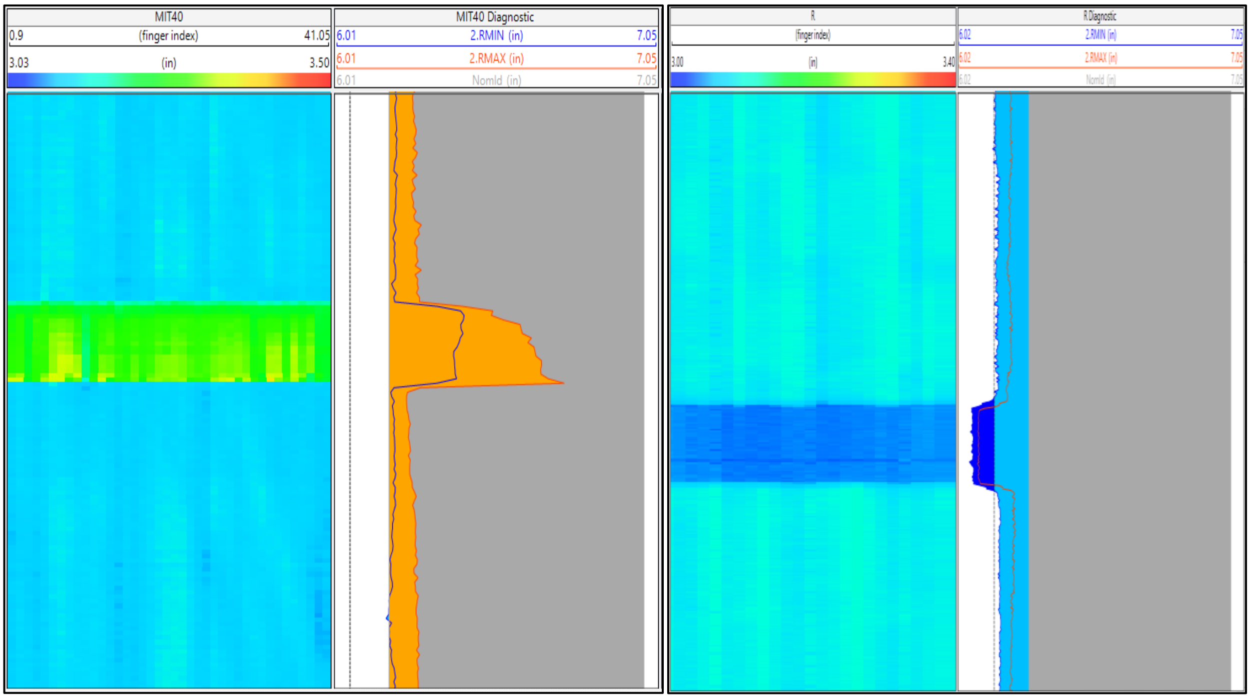

Fig. 8.C.16 – Different connection types

In the previous figure, the connections can easily be identified through the penetration or metal loss tracks. Alternatively, a CCL can be used to locate the connections. In Emeraude, this is done manually or interactively by defining a threshold value on one of these tracks.

The identified tubing or casing connection should include the fraction of the pipe body affected by the connection. As shown in Figure 8.C.17, for an upset connection, the internal diameter is smaller above and below the connection. This part is not representative of the main pipe body. In Emeraude, an offset between the position where the threshold intersects the reference curve and the beginning of the joint can be established:

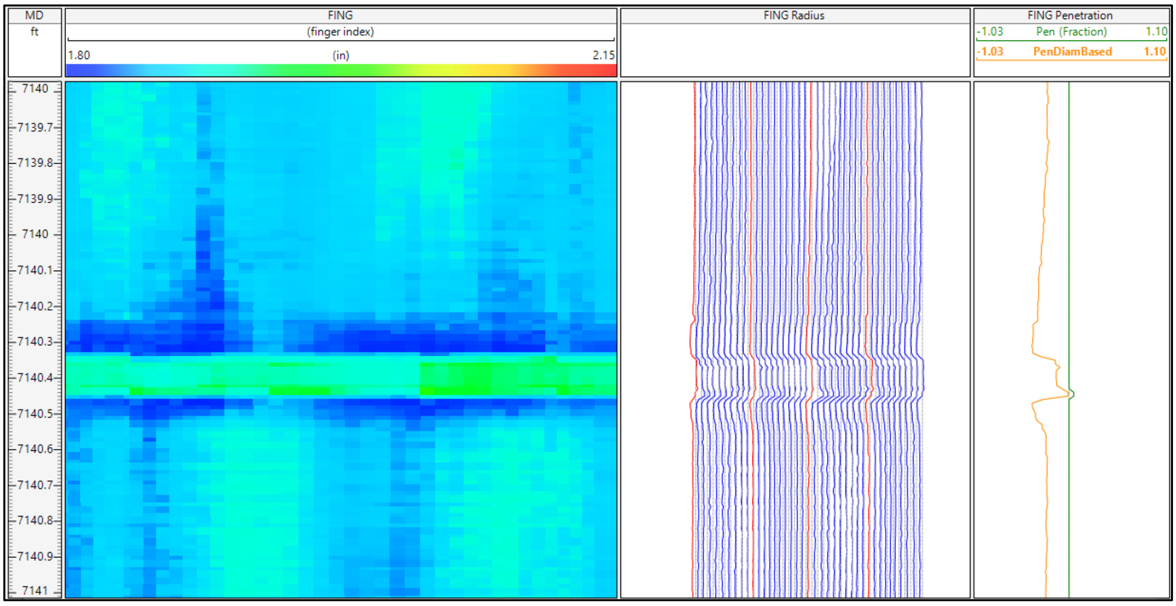

Fig. 8.C.17 – Affected pipe around the connection

8.D MFC Results

After processing the MFC data, pipe statistics are computed for all depths. These are presented versus depth as logs and tabulated for every identified joint.

As the MFC fingers measures radius, the primary statistics for all depths are the Maximum and Minimum Radius (RADMAX and RADMIN), the average radius (RADAVG), the median (RADMED) and the standard deviation of the radii measurements.

Results are also displayed as diameters. The opposite fingers' radii are summed up to compute *n/2* diameters (where *n* is the number of fingers). The same statistics mentioned above for the radii are computed for the diameters. However, it will be demonstrated that the maximum and minimum ID calculated as the sum of opposite fingers (IDMAX and IDMIN) may not be appropriate to compute statistics to describe the actual condition of the pipe:

8.D.1 Penetration and maximum ID

At all depths, the maximum finger radius is determined (*RADMAX*). The penetration represents the pipe's maximum internal metal loss relative to the pipe thickness, as:

$$Penetration = (2 * RADMAX - IDNOM)/(ODNOM - IDNOM)$$

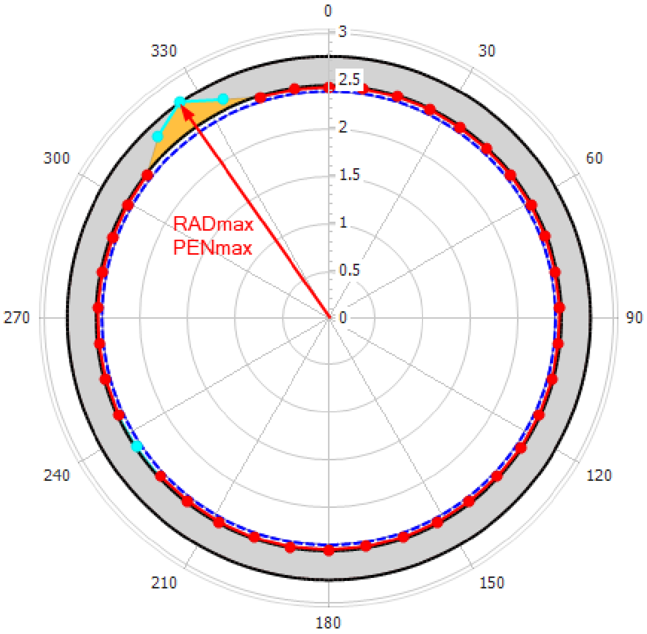

*Fig. 8.D.1 – Maximum ID (2*RADMAX) and Penetration*

FAQ 5: Double radius or sum of opposite fingers?

The penetration equation is typically presented as a function of diameters (IDNOM, ODNOM), but instead of showing directly IDMAX it uses '2*RADMAX'. Why is that?

Imagine that the finger showing maximum penetration in Figure 8.D.1 (at around 325°) is exactly a fully penetrating feature (RAD= OD/2). The opposite arm (145 deg), does not sense any penetration (RAD= ID/2). If opposite fingers diameter was used, the penetration would be 0.5 (50%). This is counter-intuitive, since a full wall penetration feature is present.

Therefore, for IDMAX and IDMIN, 2*RADMAX and 2*RADMIN is used in the MFC Diagnostic track, in the Joints table and to calculate the penetration and reduction.

8.D.2 Metal Loss

Similar to the Penetration, the metal loss is a representation of how much the radius goes above nominal ID. However, the metal loss considers all the fingers (compared to the one of RADMAX used for penetration), giving a cross-sectional average indication of the wall thickness reduction.

$$MLOSS = \frac{1}{n}\frac{\sum_{i=1}^{n}(4 * RAD_i^{\,2} - ID^2)}{(OD^2 - ID^2)}$$

As seen in the image below, the influence of localized pitting in the metal loss is not as severe as in the penetration, as an average of all fingers is used. Metal loss may be misleading when there are ‘as manufactured’ joint variation, as observed between joints 58 to 60.

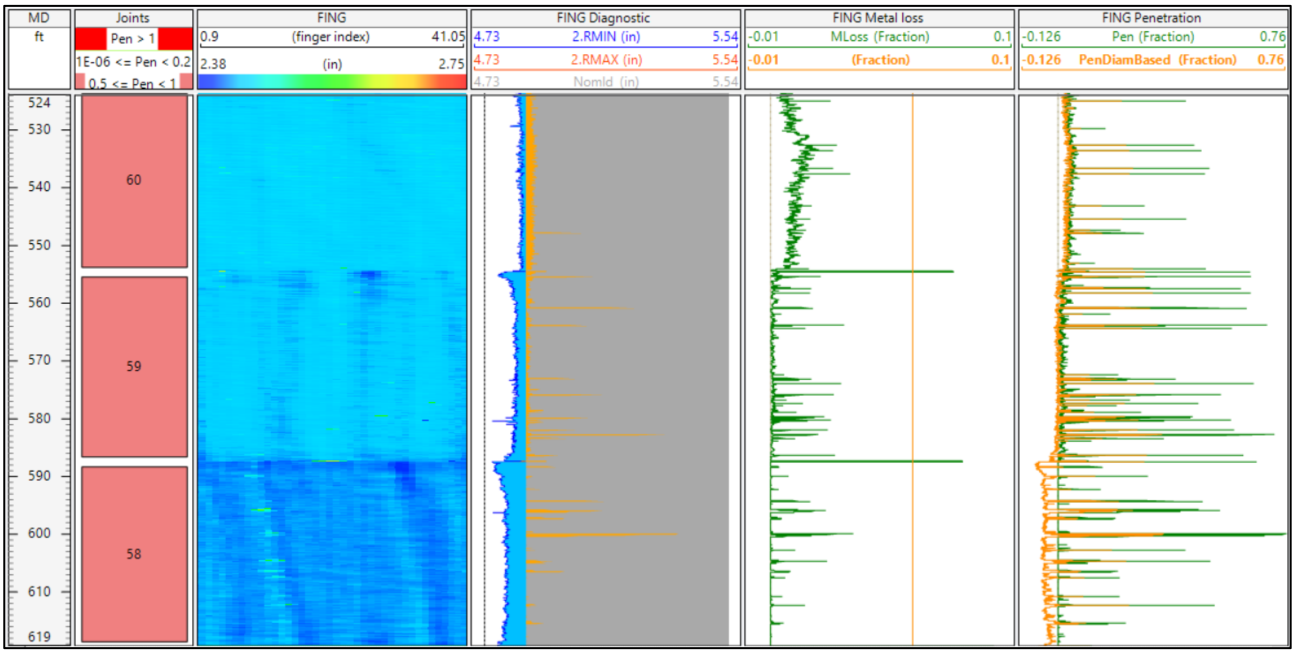

Fig. 8.D.2 – Metal Loss and Penetration

This statistic is sometimes used to determine the remnant mechanical properties of the pipes, since these properties are a stronger function of the generalized metal loss than isolated pitting.

8.D.3 Reduction and minimum ID

At any depth, the minimum ID is determined based on 2*RADMIN (for the reasons explained above).

The minimum radius is used to calculate the reduction value as:

$$Reduction = \frac{\frac{ID}{2} - MINRAD}{\frac{ID}{2}}$$

A reduction of one (not possible as the minimum measured radius is limited by the tool OD) means that the maximum diameter of a circular object going through it is equal to pipe ID/2.

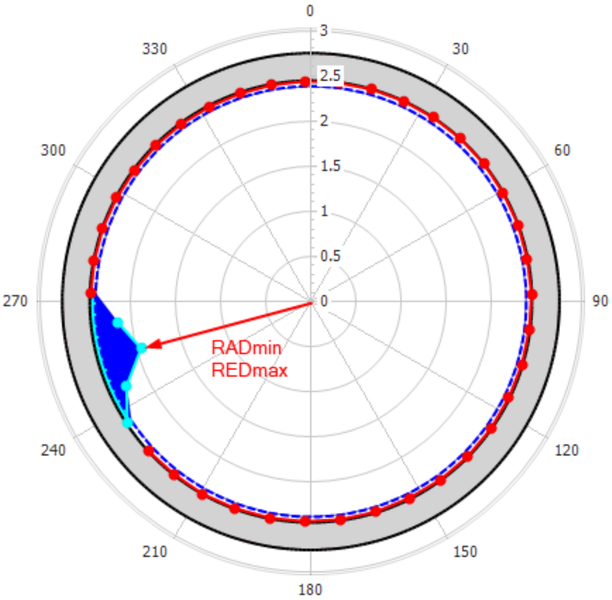

Fig. 8.D.3 – Minimum ID and Reduction

8.D.4 Ovalization

Pipe ovality refers to the distortion of the cross-section of the tubular from its normal, circular shape. This is a key statistic for plug or packer setting, as the presence of ovalization affects the sealing capacity of the packing elements. Various standards and completion manufacturers define maximum allowable ovalization for plug and packer setting.

The ovalization is calculated as:

$$Oval = \frac{(IDMAX - IDMIN)}{IDAVG}$$

In this case, the opposite fingers IDMAX and IDMIN are used. If these values were equal, ovality would be zero.

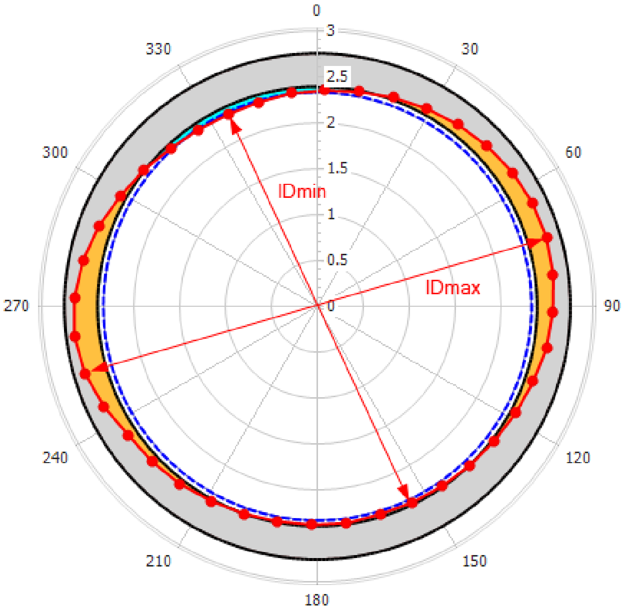

Fig. 8.D.4 – Ovalization

Note that pipe ovality definition is not the same for the different available standards and recommended practices. Make sure you know which equations they use.

FAQ 6: What is the nominal pipe ID?

Most of the casing and tubing are manufactured according to API 5CT (ISO 11960) standard. Due to the manufacturing process, it is difficult to measure the internal pipe diameter with high accuracy. Therefore, this standard establishes tolerances on the outer pipe diameter (easier to measure than the ID), as follows:

- For pipe less than 4.5'', the tolerance is +/- 0.79 mm (+/- 0.031 in)
- For pipes equal or larger than 4.5'', the tolerance is + 1% to -0.5% OD

The internal diameter is estimated based on the pipe weight and material density, allowing to calculate the pipe thickness and the ID. Moreover, the pipe mass has an associated tolerance (i.e. 6.5% to -3.5% for single lengths).

For these reasons, API 5CT establishes the well know 12.5% permissible under-tolerance on the pipe thickness. This is sometimes known as the 'API penetration tolerance'.

This uncertainty impacts on the accuracy of different statistics, such as the penetration, metal loss. As will be explained in section 8.E, this uncertainty also impacts the calculations of the pipe's mechanical properties.

Stringent well integrity monitoring typically includes a baseline MFC run, during or right after well completion. This provides a valid 'nominal' ID of the pipe, that can be used in time-lapse MFC to accurately estimate the evolution of the pipe thickness.

The default option for statistics calculation is the nominal ID, as shown in the pipe catalogues. When there is evidence of 'as manufactured' smaller pipe thickness, some analysts account for the 12.5% of thickness reduction by manually modifying the ID. Other option is to use a statistical value, for example, when localized pitting is present, it is possible to use the average or median joint ID as the nominal ID.

Make sure you understand how the error on the nominal ID propagates into the different results and choose the right approach.

8.D.5 Status of completion elements

The statistics presented in this section are, in general, used to describe the condition of the tubing, casing and pup joints. As shown in Figure 8.C.10, when completion elements are surveyed, they show abnormal penetration or reduction values. These are typically excluded from the final summary table. However, important information about the status of various elements can be extracted by visual inspection of the MFC images and statistics.

For example, Sliding Sleeves (SSDs) can be shifted open or closed through wireline or coiled tubing intervention, to avoid unwanted fluids or improve the reservoir sweep. Verifying the current status of the SSD is greatly facilitated by comparing the MFC measurements to the open and close fingerprints. An SSD in open (left) and closed (right) positions are shown in Figure 8.D.5.

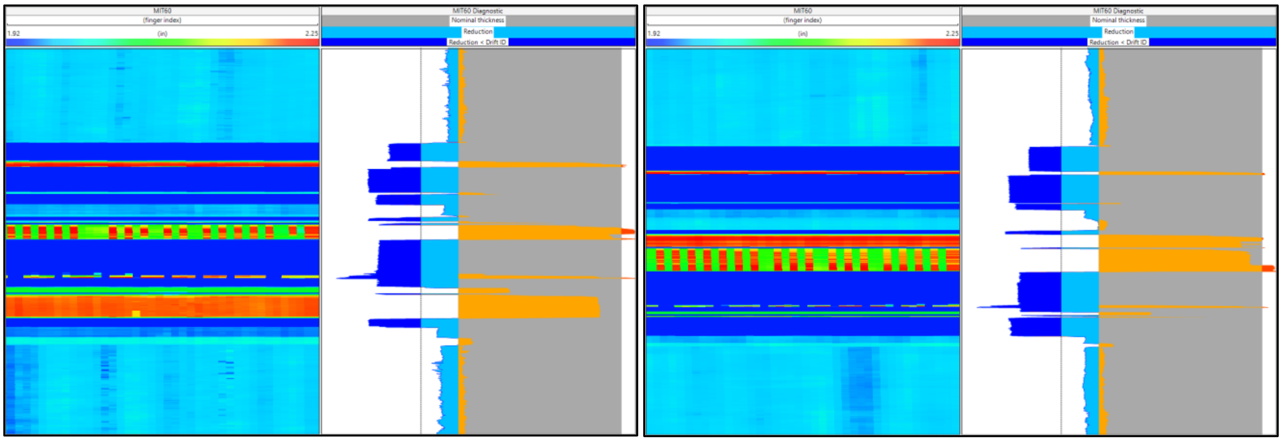

Fig. 8.D.5 – SSD status. Left: Open – Right: Closed

It is useful to keep snapshots of the MFC image and diagnostic tracks of different completion elements. This helps to quickly diagnose the status of these elements, look for problems (partially open/closed, deposition, deformed, etc.). The fingerprints can be recorded both in-situ (downhole measurements) or through yard logging. The latter allows better control of the operation and the condition of the element (inverted, full/partially open, etc.).

8.E Mechanical properties calculation

This section is an introduction to the calculation of the remnant pipe mechanical properties based on Multitier Caliper results. This analysis helps to understand if the surveyed pipe is still fit for service and if it can withstand a well operation that includes pressurizing the pipe or annulus (killing the well, cementing, hydraulic stimulation, venting, etc.).

By no means this is an exhaustive treatment, and the equations presented below should be applied with extreme care, given the number of assumptions used to derive them. The American Petroleum Institute Standard API TR 5C3 (*Calculating Performance Properties of Pipe Used as Casing or Tubing*) details the equations and their hypothesis. This section briefly shows how the MFC-calculated pipe dimensions of the surveyed pipe can be used to update the mechanical properties.

8.E.1 Theory background

In mechanics of materials, pipes are treated as 'thin-walled pressure vessels'. The second part of this definition refers to the fact that these structures are capable of holding internal pressure. The concept of thin wall implies that, given the small thickness/diameter ratio, the distribution of the normal stresses on a cut is essentially uniform through the thickness of the shell. This leads to a planar stress condition on the outer pipe surface, formed by a longitudinal stress (σ_z) and a tangential or 'hoop' stress (σ_θ).

Considering a pipe subject only to internal pressure, a free body diagram can be used to obtain the magnitude of the hoop stresses. The following equation is known as Barlow's Formula. If the tension reaches a critical value, the pipe will 'burst'.

$$\sigma_\theta = \frac{Pd}{2\,t}$$

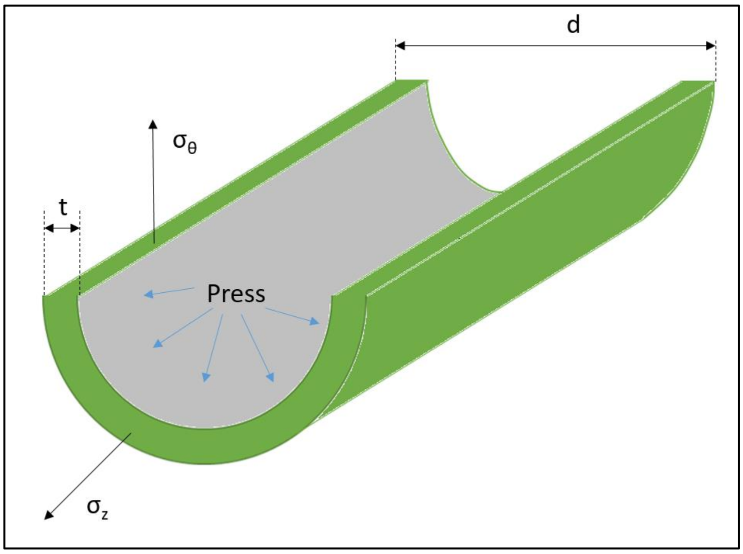

Fig. 8.E.1 – Stresses on a pipe subject to internal pressure

If a pipe is subject to an axial load *F* (i.e. hanged tubing supporting its own weight or compressional force while running the casing) the experienced longitudinal stress will be equal to:

$$\sigma_z = \frac{4\,F}{\pi\,(OD^2 - ID^2)}$$

Through this formula it is possible to calculate the maximum load for tensile failure, when the stress reaches, for example, the yield stress (more on this below). This formula can also be applied for compressive axial loads; however, pipes may undergo compressive axial buckling before reaching compressive failure.

Finally, a pipe subject to a high external pressure can 'collapse'. As shown later, API presents different equations for collapse pressure, depending on the thickness to OD ratio. At this point it is important to mention that some of the collapse equations can be derived analytically from the Lamé equation for thick wall pressure vessels. Compared to the Barlow's formula, in thick wall pipes the hoop stress varies along the shell (maximum on the inside) and there is a net radial stress component. The hoop stress obtained from the Lamé equation at the internal radius can be expressed as:

$$\sigma_\theta = \left[\frac{d_o^2 + d_i^2}{d_o^2 - d_i^2}\right] P_i - \left[\frac{2\,d_o^2}{d_o^2 - d_i^2}\right] P_o$$

These equations were derived for perfectly circular pipes. However, experimental data and finite element simulations show that the collapse pressure significantly decreases with pipe ovality.

The concepts and equations of four failure modes existing in pipes have been presented: Burst, Collapse, Compression and Tension. In general, pipes are subject to other loads, including buckling, torsion, etc., which are beyond the scope of this material. Bi-axial and Tri-axial stress models are commonly used by well design engineers, where the different stress components are combined using the Distortion Energy Theory, known as Von Misses equation.

This section uses API definitions, where failure occurs when one of the uniaxial stress states reaches a critical stress of the material, called Yield Strength.

FAQ 7: What is the strength of the pipe?

API 5CT specifies the technical delivery conditions for steel pipes. The steel grades are labelled by a code like K55, L80, P110, etc. The prefix letter designation has no special meaning. The number following the letter corresponds to the Specified Minimum Yield Strength (SMYS) of the pipe in Ksi (thousands of psi). For example, the steel grade L80 has a SMYS of 80000 psi.

As an industry practice, it is established that casing and tubing strings are limited to the elastic stress-strain regime. Therefore, the API Standard considers the Yield Strength as the critical stress for failure (typically with a safety coefficient).

The actual material strength (Ultimate tensile strength – UTC) is greater than the Yield strength. However, for design purposes the elastic regime is considered, which means that after unloading, the material length's goes back to original (zero strain).

8.E.2 API Definitions

The API TR 5C3 Standard presents the formulas used to calculate the remnant mechanical properties of the pipe. This section focuses on the Burst and Collapse pressures using the uniaxial approach, as opposed to the complete triaxial calculation. Estimating other stress components require more inputs from the cement, completion string, temperature effects, etc., that are not accounted for in this analysis.

It cannot be stressed enough that these formulas have to be treated with caution. Catastrophic failures due to burst or collapse may involve human lives, environmental and legal consequences.

It is also important to understand that the API standard does not mention at any point the words Multifinger Caliper or Magnetic/ultrasonic thickness. This means that there are no references to old pipes. The next section discusses some considerations when using MFC to obtain inputs for these equations.

8.E.2.a Burst Pressure

Based on Barrow’s formula, using the yield strength as maximum allowed. It considers the 12.5% tolerance on the pipe thickness (API 5CT) through a 0.875 factor:

$$P = 0.875\ (\frac{2\,Y_p\,t}{D})$$

8.E.2.b Collapse Pressure

The collapse pressure calculation includes four regions, depending of the t/D ratio. The regions are called: Yield collapse, Plastic collapse, Transition collapse and Elastic collapse. The formulas for the Yield and Elastic collapse can be theoretically derived (Lamé). The formula of Plastic collapse is empirical, while the Transition formula accounts for the cases between elastic and plastic collapse pressures.

- Yield Collapse: The necessary external pressure for the hoop stresses (Lamé) to reach the Yield stress (so not necessarily a true collapse):

  $$P_{Y_P} = 2\,Y_P \left[\frac{({}^{D}/_{t}) - 1}{({}^{D}/_{t})^2}\right]$$

  This formula is applicable to D/t values up to the intersection with the plastic collapse formula, given by:

  $$(D/t)_{YP} = \frac{\sqrt{(A-2)^2 + 8\,(B + \frac{C}{Y_P})} + (A-2)}{2\,(B + \frac{C}{Y_P})}$$

- Plastic collapse: Experimentally-derived equation which predicts the necessary external pressure to cause plastic collapse (permanent deformation):

  $$P_P = \ Y_P\left[\frac{A}{D/t} - B\right] - C$$

  This equation is applicable for D/t from $(D/t)_{YP}$ to the transition with D/t transition:

  $$(D/t)_{PT} = \frac{Y_P\,(A-F)}{C + \ Y_P(B-G)}$$

- Transition collapse: In the transition zone between plastic and elastic, the necessary pressure to cause collapse can be calculated as:

  $$P_T = \ Y_P\left[\frac{F}{D/t} - G\right]$$

  This equation is applicable for D/t from $(D/t)_{PT}$ to the transition with D/t transition:

  $$(D/t)_{TE} = \frac{2 + B/A}{3B/A}$$

- Elastic collapse: In this region is predicted that the pipe will lose its elastic stability under the action of an external pressure. Note that the formula below, which is theoretically derived, is not a function of the pipe yield strength, as this collapse type is dependent on the elastic modulus and geometry only.

$$P_E = \frac{46.95\ 10^6}{\left(\frac{D}{t}\right)(D/t-1)^2}$$

Applicable for D/t >= $(D/t)_{TE}$

The constants for different API pipes are presented in the table below:

Steel Grade	D/t Range			Plastic Collapse Pressure Factors			Elastoplastic Collapse Pressure Factors	
	$(D/t)_{YP}$	$(D/t)_{PE}$	$(D/t)_{TE}$	A	B	C	F	G
H40	16.4	27.01	42.64	2.95	0.0465	754	2.063	0.0325
J/K55	14.81	25.01	37.21	2.991	0.0541	1206	1.989	0.036
J/K60	14.44	24.42	35.73	3.005	0.0566	1356	1.983	0.0373
L/N80	13.38	22.47	31.02	3.071	0.0667	1955	1.998	0.0434
C90	13.01	21.69	29.18	3.106	0.0718	2254	2.017	0.0466
C/T95	12.85	21.33	28.36	3.124	0.0743	2404	2.029	0.0482
P110	12.44	20.41	26.22	3.181	0.0819	2852	2.066	0.0532
Q125	12.11	19.63	24.46	3.239	0.0895	3301	2.106	0.0582
A140	11.84	18.97	22.98	3.297	0.0971	3751	2.146	0.0632
A150	11.67	18.57	22.11	3.336	0.1021	4053	2.174	0.0666

8.E.3 Remnant mechanical properties

A well that was designed to withstand certain level of pressures and mechanical loads many years ago, when the casing and tubing joints were new, may not support these currently or in the future, after the pipe has suffered corrosion or erosion. This becomes critical when planning workovers, side-tracks, P&A, refracking, etc.

The formulas presented in the previous section are functions of the pipe thickness. Even before running the completion there is uncertainty due to the API tolerance, which leads to the use of safety factors. Once the completion is in place, the only way to obtain the wall thickness is by running downhole measurements.

Pipe thickness can be calculated as $t = \frac{(OD-ID)}{2}$

When using MFC as the primary source of pipe thickness, the following points must be taken into account:

8.E.3.a Outer pipe diameter

Corrosion on the outer pipe diameter may decrease the pipe thickness, not accounted by the MFC measurement. In the absence of a pipe thickness measurement (i.e. magnetic), the analyst makes a big assumption on the outer pipe diameter. Setting the OD equal to the nominal pipe OD may not always be representative for cases where the external pipe wall is in contact with the reservoir fluids (i.e. non cemented intervals), tubing with liquid-filled annular, etc.

As mentioned in FAQ 6, API 5CT establishes a tolerance on the external pipe diameter, which impacts the thickness calculation, especially for small thickness pipes.

8.E.3.b Initial internal diameter

The issue of using nominal internal diameter as reference value for the metal loss and reduction statistics becomes evident when analysing the implications on the mechanical properties calculation. The dimensional tolerance specified by API, allows certain room for ID variation change. 'As manufactured' joint variations are shown in Figure 8.E.2. Joints 12 and 13 fall below nominal ID, but still remain above drift ID. This is not deposition, as it would not be restricted to these two joints, and deposits are never as homogenous as in this image. These pipes show zero metal loss, but this was calculated using nominal ID as reference.

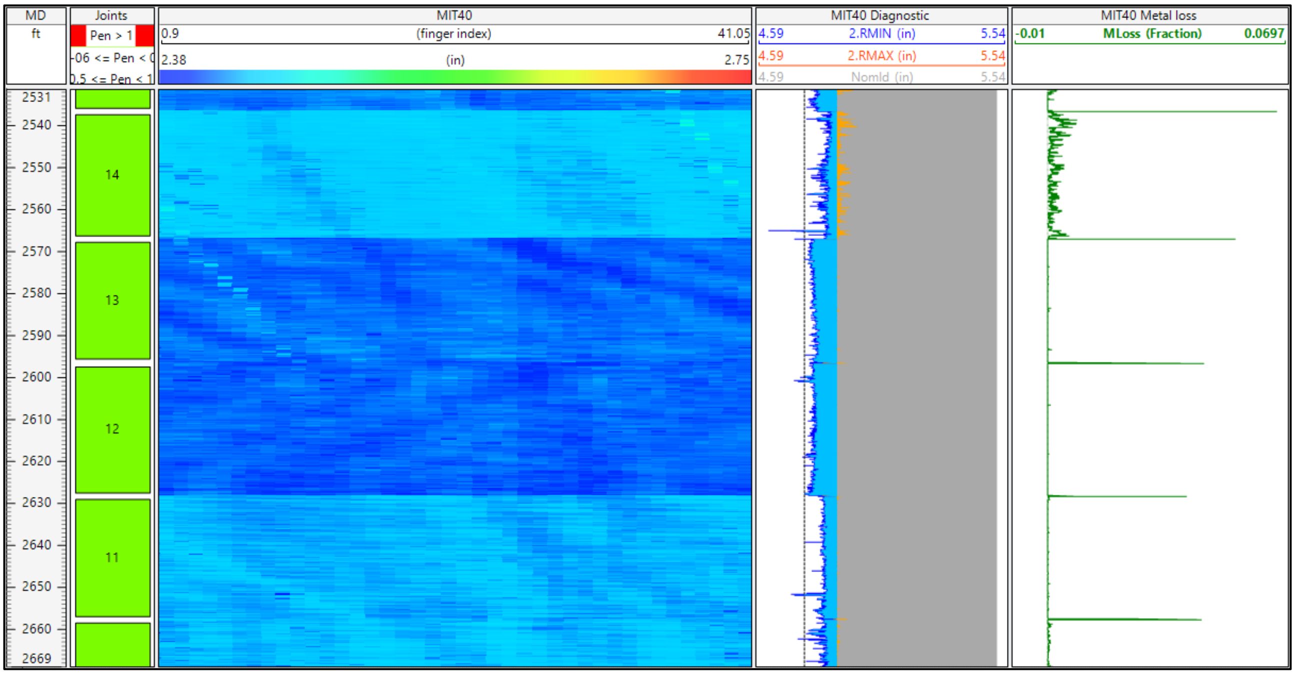

Fig. 8.E.2 – As manufactured joint variations

This image also shows the benefits of running a baseline MFC, right after running the completion or early in the life of the well.

8.E.3.c Current Internal diameter

From the MFC analysis, a number of diameters are computed, such as ID average, ID mean, ID max, ID min. What diameter should be used to compute the pipe thickness? Again, there is no reference to this on the API standard.

Consider the following cases:

- **Isolated pitting**: A number of isolated, not-fully penetrating pits are showed in the image below, reaching penetration values up to 70%. Using the maximum ID to calculate the pipe thickness would imply a reduction of the burst pressure of 70% compared to the pipe with nominal ID. However, the mean ID is not significantly different than the nominal ID, resulting in an overall low metal loss (average 1%).

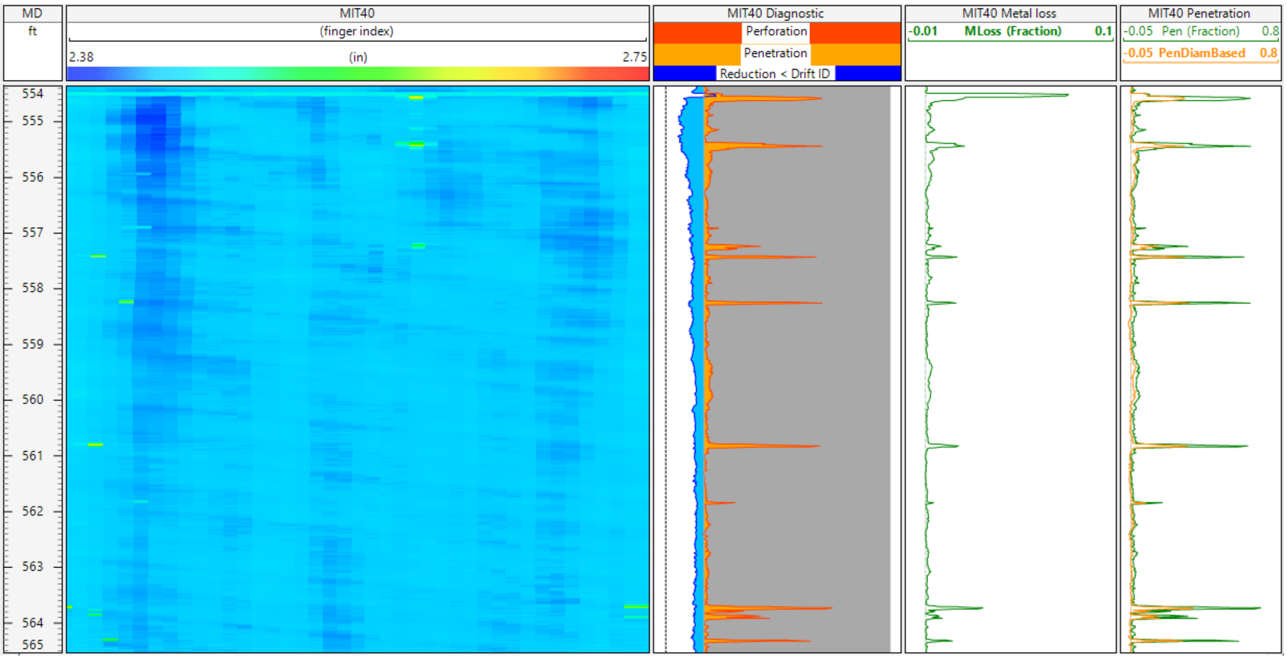

Fig. 8.E.3 – Isolated pitting

This is an interdisciplinary decision, and requires understanding the mechanism of corrosion and its morphology. In this case, high CO_2 concentrations allow to anticipate sweet corrosion, with isolated pitting as characteristic morphology. Field experience suggests that the failure mechanism from CO_2 corrosion in tubing is leakage to the annular, rather than an overall loss on the mechanical properties that may lead to early burst.

Recommended practices (i.e. DNV-RP-F101 'Corroded pipelines') introduce the definition of Single Defect and Interacting Defect. In single defects, the failure pressure is independent from other defects. However, when there is interaction, the failure pressure will be lower. Whether the defect is isolated or not is based on the circumferential ($\emptyset$) and axial (s) spacing between adjacent defects:

$$\emptyset > 360\sqrt{\frac{t}{D}}$$

$$s > 2\sqrt{Dt}$$

In this case, the presence of the isolated pitting does not affect the overall pressure-bearing capacity of the pipe, and the mean ID can be used to estimate the current diameter.

- **Homogeneous metal loss:** When uniform corrosion is present, the metal loss value is similar to the penetration. Figure 8.E.4 shows a case of circumferentially-homogeneous metal loss, which would have an impact on the remnant mechanical properties of the pipe.

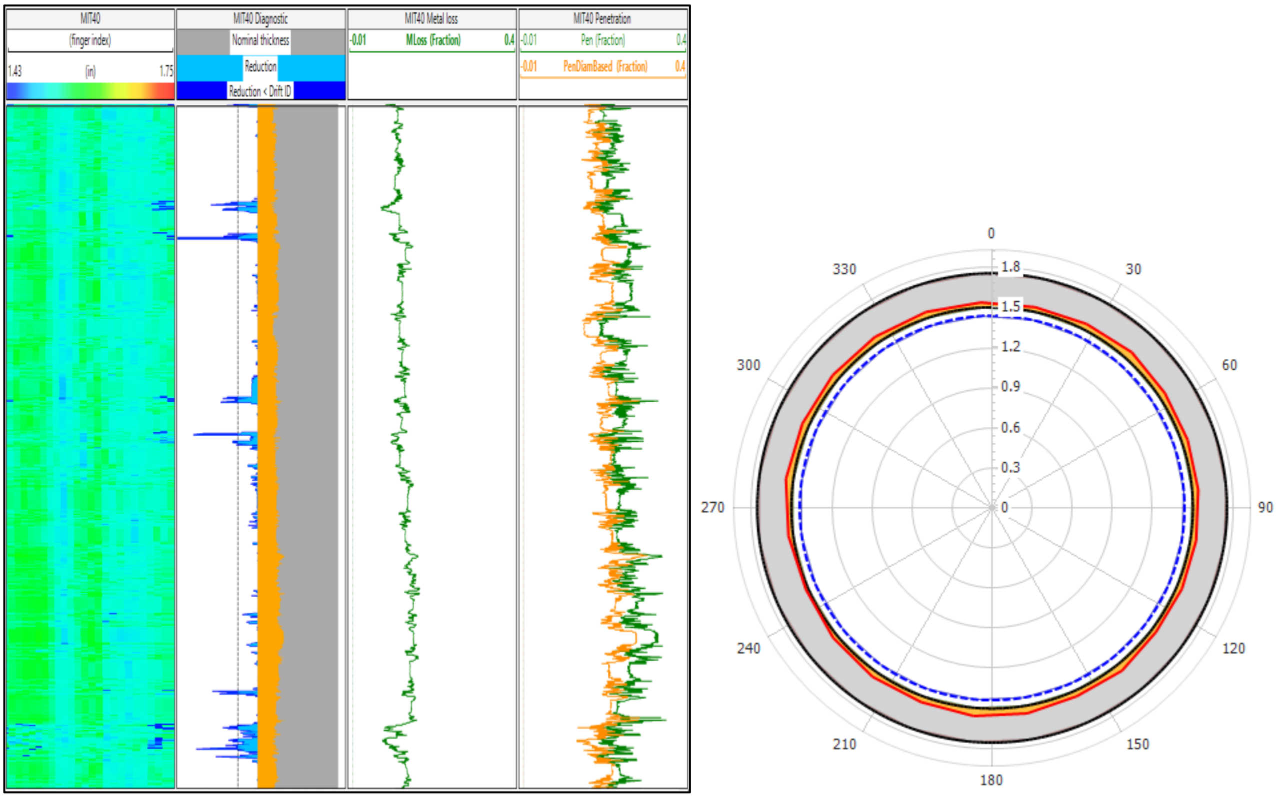

Fig. 8.E.4 – Uniform corrosion

These two examples demonstrate the different choices of internal diameter that may need to be used, and are by no means recommendations on future decisions on the calculation of mechanical properties.

Some companies define their guidelines directly in terms of maximum allowable metal loss or pipe wear, instead of a diameter. Assuming homogenous corrosion, the API Burst pressure prediction is inversely proportional to the metal loss, as shown in the image below:

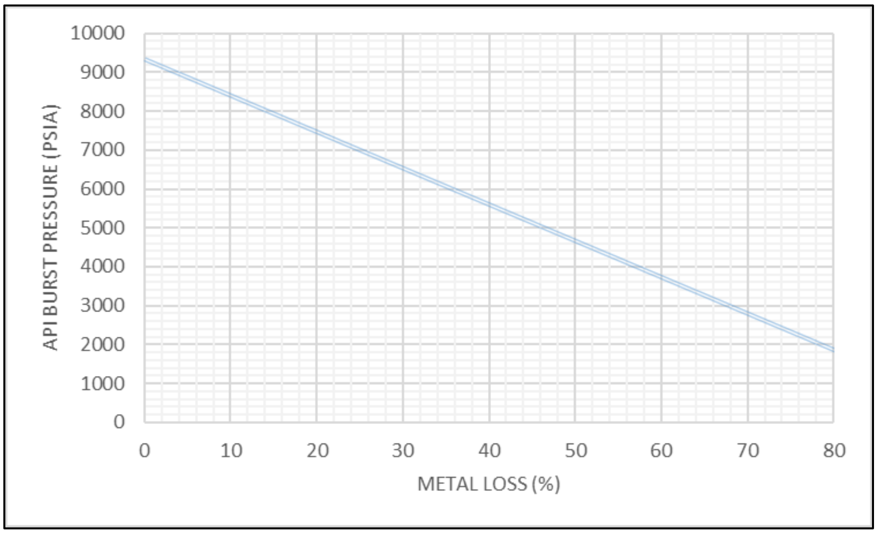

Fig. 8.E.5 – Burst Pressure as a function of Metal loss for a 7 in (29 lb/ft) L80 casing

8.F Pipe deformation

At this point in the Chapter, the reader should have a fairly good idea on how to obtain a number of pipe statics from a raw MFC dataset, and how these impact on the mechanical properties of the pipe.

Consider the case where the pipe is deformed by stresses in the formation or the loads during the well completion. 'Deformed pipe' refers to a loss on the circularity (i.e. ovalization) or a modification of the original pipe trajectory (lateral displacement). These cases would not raise any flag in the statistical results covered in the previous section (apart from the ovalization). The analyst must understand the images and curves help to diagnose deformation.

Severe cases of pipe deformation lead to well access problems. Ovalization can cause issues like leaking packers or plugs, leaks on casing hangers, and eventually it may not be possible to run a bottomhole assembly through this interval. Also, due to pipe tortuosity, it may not possible to re-enter the well, creating numerous problems for the design of remedial workovers, stimulation, and ultimately P&A.

8.F.1 Stresses in the earth's crust

Consider a small cube of formation, buried at certain depth in the earth's crust. This cube is subject to a complex stress condition, represented by the stress tensor. In general, this is a 9-component tensor, but due to equilibrium symmetry, the shear stresses S_{ij} are equal to S_{ji}. Still, there are 6 independent components, which would be quite complex to characterize. Fortunately, by applying a tensor transformation, the cube is oriented in a way that the only components of the stress tensor are the principal components, as shown in the image below:

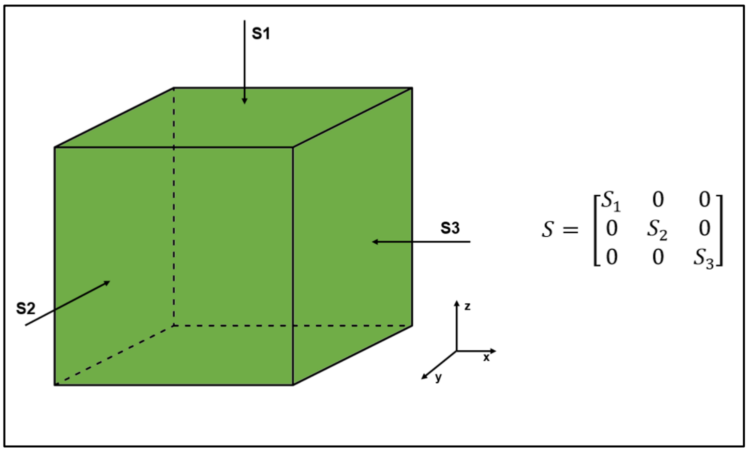

$$S = \begin{bmatrix} S_1 & 0 & 0 \\ 0 & S_2 & 0 \\ 0 & 0 & S_3 \end{bmatrix}$$

Fig. 8.F.1 – Principal stresses in the formation

In most cases, the principal stress directions are aligned with the vertical and horizontal axis (x, y and z). These stresses are called:

- S_V (S1 in the cube): this is the vertical, or overburden stress. The cube supports the weight of the formation above, and therefore is a compressive stress.
- The horizontal stresses (S2 and S3 in the cube above). If a compressive load is applied to a cube of certain material, it will compress vertically and expand laterally, as predicted by its Poisson coefficient (ν). A cube of formation cannot expand freely as its neighboring cubes are also subject to compressive stresses from the overburden. Therefore, the cube feels a horizontal stress of at least:

$$S_{2-3} = S_V \left(\frac{\nu}{1-\nu}\right)$$

This calculation of the horizontal stress is an absolute minimum, as in reality the tectonic stresses will impose a larger magnitude of the horizontal components. In general, the horizontal stresses are called:

- S_{Hmax}: Maximum horizontal principal stress
- S_{hmin}: Minimum horizontal principal stress

The S_{hmin} can be estimated through minifrac, as the fracture will propagate perpendicular to the direction of the minimum value of the 3 principal stresses.

Due to the poroelastic behavior of the rock, the effective stresses felt by the rock are also related to the formation (or pore) pressure, which counteracts the effect of the principal stresses. The effective stresses are calculated as:

$$S_{i_{eff}} = S_i - \alpha\, P_P$$

Where P_p is the formation (pore) pressure and α is the Biot coefficient.

Due to poroelastic behavior, the stresses in the formation can change throughout the well's life. As the reservoir depletes, the vertical and horizontal stresses vary. This is very clear in high compressibility rocks that exhibit subsidence. In commingled reservoirs, differential depletion may lead to vertical variations on the effective horizontal stresses.

In formations where there is a large horizontal stresses contrast, ovalization can occur. A cross section of a cased well is shown in Figure 8.D.4, with S_{Hmax} acting in the direction of the IDmin arrow. Once the casing is effectively cemented in place, the stresses are transmitted from the borehole to the formation.

Finally, tectonic movements, typically along faults or bedding planes, can occur. This leads to shear deformation of the casing along the fault plane. This may occur suddenly at some stage of the well's life.

8.F.2 Identifying deformation from MFC data

The MFC image, diagnostic plots and statistics of processed MFC data (after centralization) of deformed pipes do not show any sign that something may be wrong. This has caused problems in the past, when the whole dataset was centralized blindly (or automatically by the acquisition system) and the interpreter missed the hints on the raw data and the calculated eccentricity.

The next explanation considers a case of planar shear, but this is later extended to other types of deformation. Figure 8.F.2 shows the raw MFC image, diagnostic plot, Eccentricity, schematic on the MFC going through the deformed interval and cross sections.

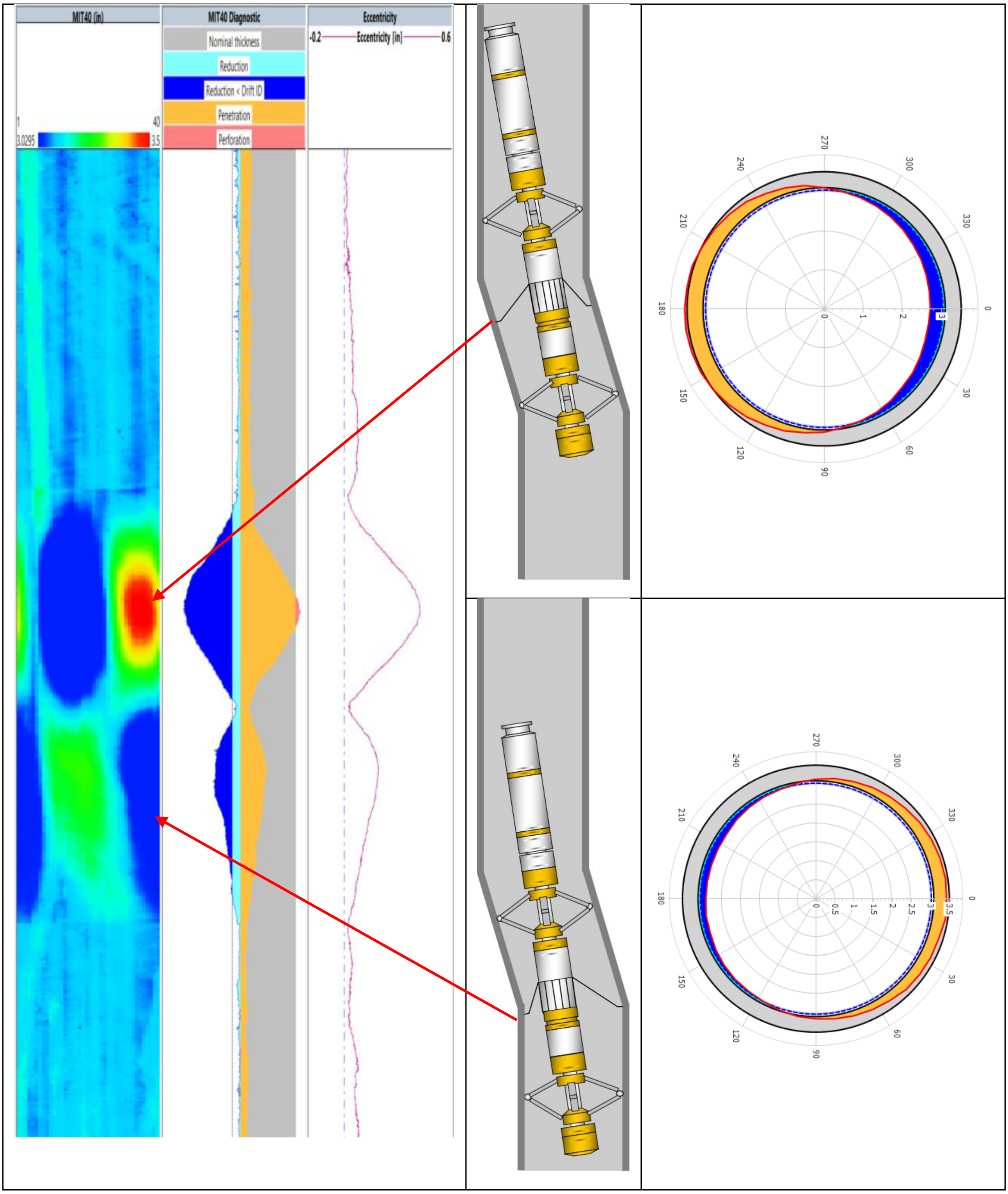

Fig. 8.F.2 – Shear deformation and MFC behavior

MFC tools are always run with centralizers above and below. It is assumed that the centralizer body is in the middle of the pipe (no eccentricity), and that the MFC tool is rigid. The MFC measurement as the tools moves from bottom to top are described below:

1. Before the top centralizer reaches the deformed interval, the MFC has a 'baseline' eccentricity value, function of the deviation, tool weight, etc.
2. As the top centralizer enters in the deformed region (lower bend), it remains centred in the cross-section, and the MFC starts to experience an increased eccentricity as the tool

centre moves to the side (closer to the bend). The eccentricity reaches a maximum when the fingers are at the exactly at the lower bend.

3. When both centralizers, and consequently the MFC, are in the deformed section, the tool is parallel to the deformed well trajectory. The eccentricity goes back to the baseline value.
4. As the top centralizer reaches the end of the deformed interval (upper bend), the eccentricity increases again, but compared to the bottom bend, the eccentricity direction is opposite for a case of planar deformation. Maximum eccentricity is reached when the MFC is exactly at the bend depth.
5. As the tool continues moving up, the eccentricity decreases until the bottom centralizer leaves the deformation (upper bend). Above, the eccentricity returns to its baseline.

From this analysis is clear that the measured distance between the eccentricity peaks corresponds to the deformed length. Using the magnitude and direction of the eccentricity, and with the knowing the toolstring dimensions, the trajectory changes can be estimated in 3D. This helps to understand the severity of the deformation, and assess whether it will be possible to re-enter the well with certain tool or pipe diameter.

Figure 8.F.3 below shows the same interval after centralization. Apart from the high eccentricity value, the image and statistics do not provide any sign that this interval of the well may be deformed. This stresses the need for a thorough QAQC of the raw data, before jumping into the MFC processing options.

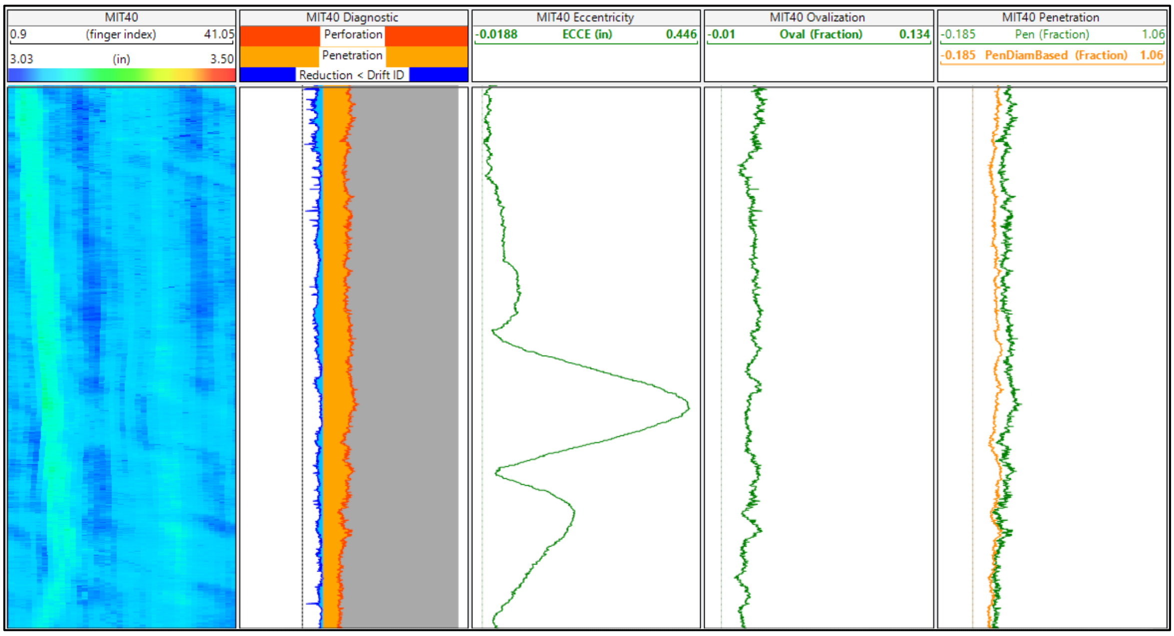

Fig. 8.F.3 – Centralized deformed interval

8.F.3 Other types of deformation

Apart from ovalization and shear, there are other deformation mechanisms that can be diagnosed through MFC. For shear, two peaks are detected in the eccentricity curve (with opposite eccentricity direction) meaning that the pipe moves laterally (in X, Y or both axis). The cases presented next include more than one lateral displacement, leading to more eccentricity peaks. The same explanation presented above can be extrapolated to the following scenarios:

8.F.3.a Bending

Compared to a shear deformation, adding an extra peak on the eccentricity with opposite direction, leads to a 'bend', shown in Figure 8.F.4. This failure type can represent a serious well access problem when the bend occurs over a short distance, as the tortuosity increases. This image also shows the radius track, which is a must for diagnosing any type of deformation, due to the very characteristic shape and clear indications of eccentricity change in both magnitude and direction.

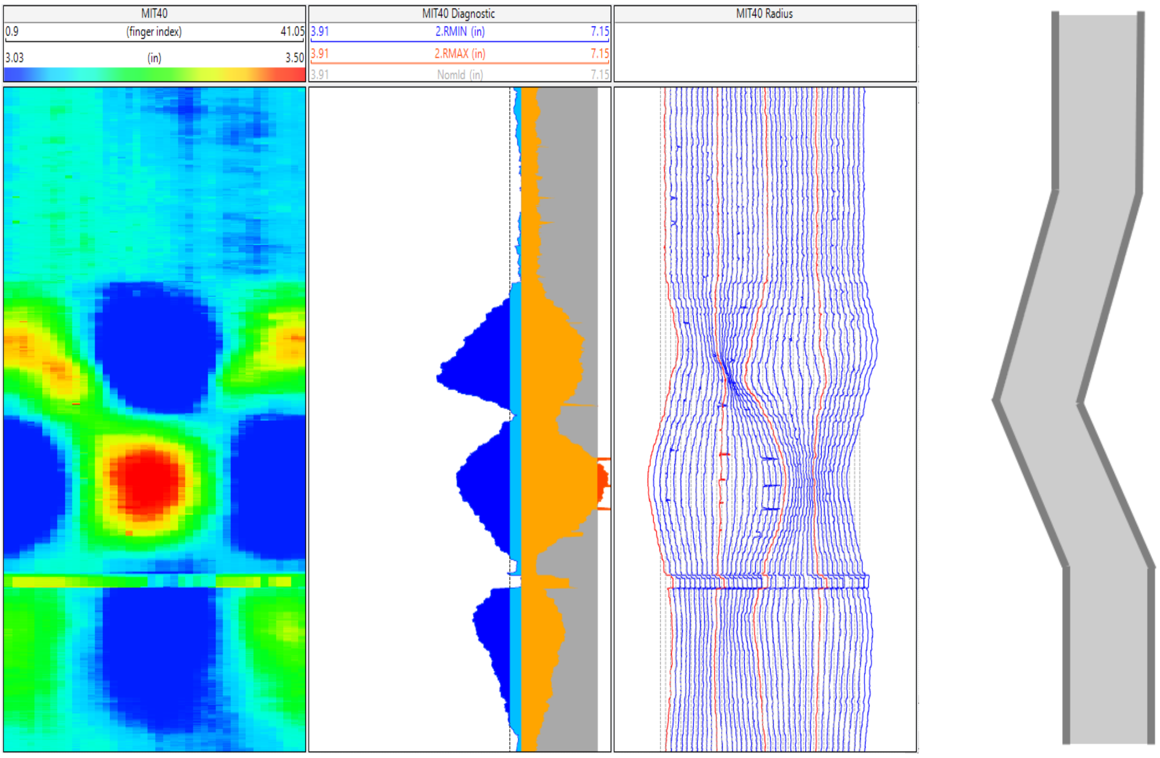

Fig. 8.F.4 – Bend on a casing

8.F.3.b Buckling

Axial loads in the pipe may be induced by the weight of the different completion components, thermal expansion, pressure loads, etc. When these loads are high enough, the casing or tubing can deform and adopt a deformed configuration inside the borehole or the pipe which contains it. This new configuration can be S-shaped (typical in coiled tubing operations) or helical.

Figure 8.F.5 shows a typical case of helical buckling. The eccentricity track shows 6 peaks, meaning that there are 5 intervals where the pipe changes trajectory due to deformation. However, compared to previous cases, the eccentricity direction does not change 180 degrees between peaks, but progressively rotates clockwise (from bottom to top). The radius track is again a key QC plot for assessing deformation.

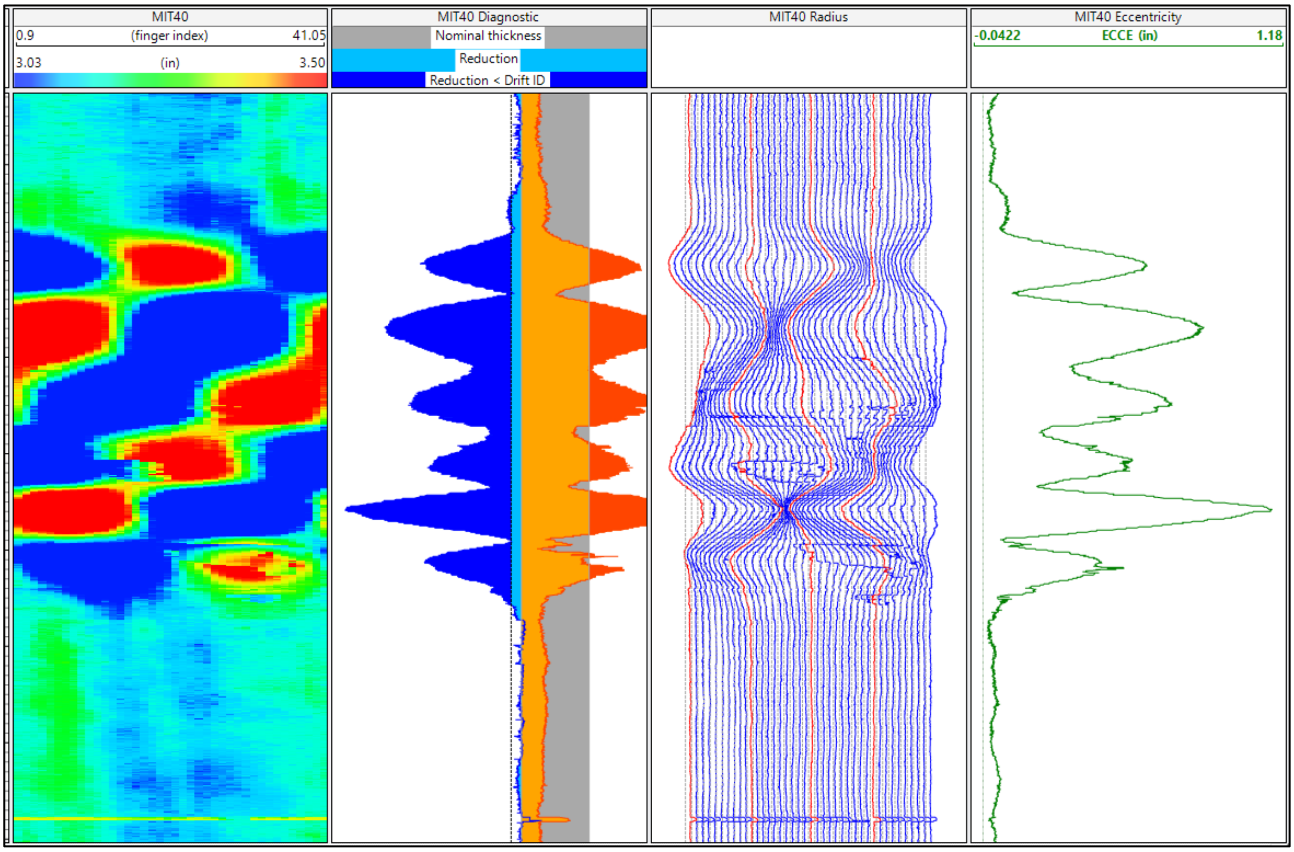

Fig. 8.F.5 – Helical buckling

Due to its shape, the buckled pipe shape is known as 'corkscrew'. The 3D image presented in Figure 8.F.6 helps to understand the variations of the eccentricity direction along the deformed interval.

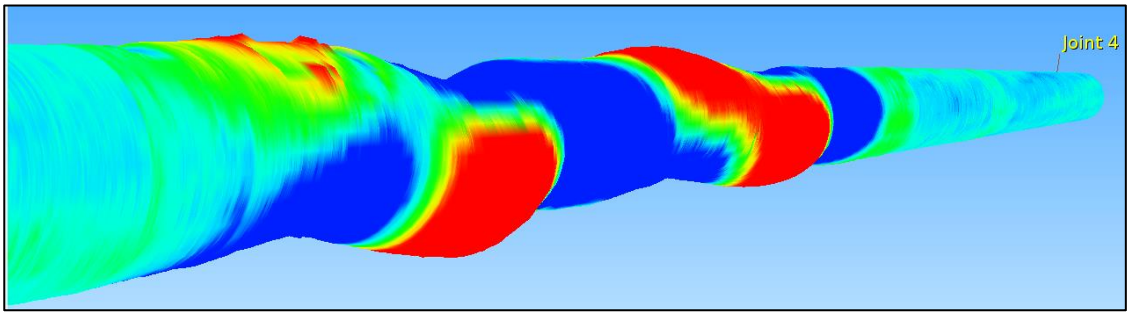

Fig. 8.F.6 – 3D image of a buckled pipe

Locating the deformation and understanding the severity of the tortuosity are key aspects for the design of future well interventions. An extreme deformation may impede accessing the well, with severe consequences on its production performance, and conditioning the Plug and Abandonment strategy.

8.G Ultrasonic tools

Another technology for determining the internal pipe radius uses the transit time of an ultrasonic pulse, emitted by a rotating head as it sweeps the internal circumference. This family of tools, generically known as Pulse-Echo or Acoustic Televiewers, is also used for other applications, including open hole (borehole) images, pipe thickness and cement evaluation. This Chapter focuses on the determination of the internal radius and its processing. Chapter 10 demonstrates the applications for cement evaluation purposes.

The typical field deliverables include the calculated pipe internal radius and derived statistics, based on the processing of the transit time. Like MFCs, these tools suffer from eccentricity, and centralization is necessary for obtaining a representative radius map. The implications of a poor or an automatic centralization were explained in the previous sections, and these are equally applicable to ultrasonic tools. The objective of this section is to describe the steps to go from the raw to processed ultrasonic data. This helps to QC the field product, and recompute the internal radius if necessary.

8.G.1 Measurement principle

Ultrasonic tools use a rotating sub, which turns several times per second (5-8 RPS). While rotating, high frequency ultrasonic pulses (> 150 kHz) are emitted. The same transducer that generates the pulse measures the return of the acoustic waves after these interacted with the fluid, pipe and cement, formation.

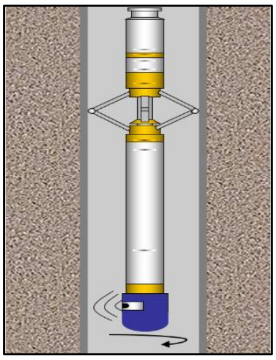

Fig. 8.G.1 – Schematic of ultrasonic tool

The ultrasonic pulse travels through the borehole fluid (mud, water, oil, etc.) at certain velocity. When it reaches the first interface (pipe), part of the energy is reflected, and part is transmitted through the pipe wall, where it will travel at a different velocity. The amount of energy reflected and transmitted is a function of the material’s acoustic impedance (Z), given by the density multiplied by the velocity. The acoustic impedance has units of Rayleigh, typically abbreviated MRayl. For planar waves, the Reflection (R) and Transmission (T) coefficients, are given by:

$$R = \frac{(Z_2 - Z_1)}{(Z_2 + Z_1)} \qquad \mathrm{T} = \frac{2\,Z_2}{(Z_2 + Z_1)}$$

The first reflection at the pipe wall that contains the information about the distance from the transducer to the pipe. However, the fraction of the acoustic wave transmitted through the pipe wall, soon finds another interface. This is either the cement or the fluid that remained between the pipe and the formation. Therefore, more transmissions and reflections occur, with the soundwave bouncing back and forth between the pipe ID and OD.

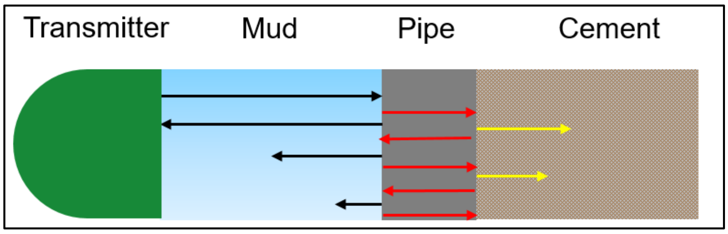

Fig. 8.G.2 – Acoustic interactions with the different materials

The subsequent arrivals at the transducer contain information about the pipe thickness and the cement impedance. This analysis is done in the frequency domain. However, as mentioned previously, this Chapter focuses on the determination of the internal radius, done in the time domain through the transit time of the first return.

The tool is configured to emit a number of pulses per rotation (18, 46, 72, etc.). For each pulse, the tool records the complete returning waveform. As shown in Figure 8.G.3, for each angle or 'azimuth' a VDL plot is presented, from where is possible to analyze the waveform at any depth. The transit time from the pulse firing to the return of the pipe bounce, is presented for one depth below the VDL. Repeating this process for all depths and all the angles results in a transit time map.

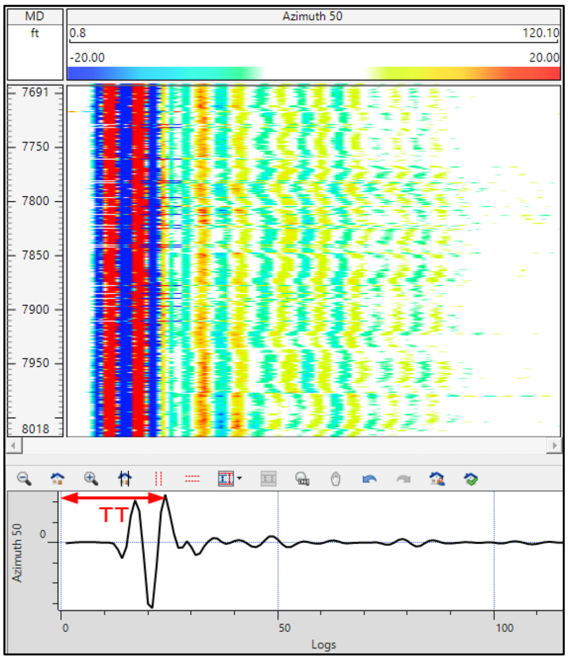

Fig. 8.G.3 – Waveform VDL for one angle

8.G.2 Internal radius from transit time

The calculated transit time for the entire pipe circumference is presented as an array image in Figure 8.G.4. The transit time measurements at two depths reveal the presence of eccentricity, given by the sinusoidal distribution of the measurements versus the azimuth. However, before considering the centralization, first it is necessary to move from time to length units.

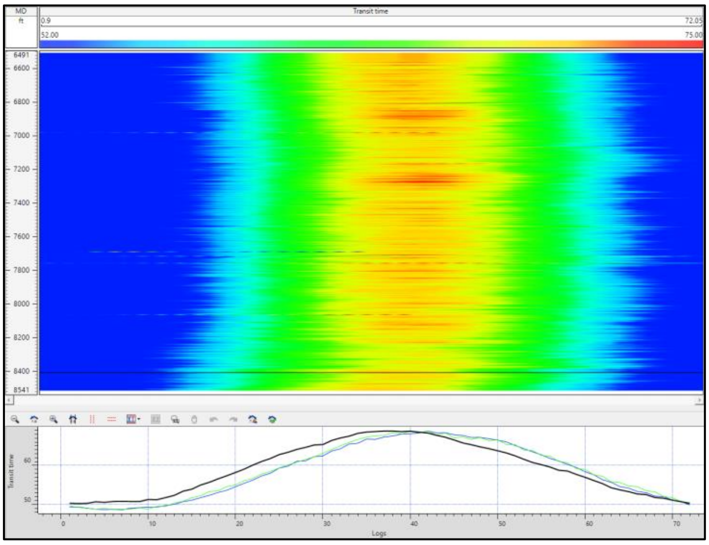

Fig. 8.G.4 – Transit time map in microseconds

The acoustic velocity and impedance of the borehole fluid vary with depth, pressure and temperature. Since various outputs of the ultrasonic tools rely on the acoustic velocity, it would not be accurate enough to use correlations to compute the downhole values. Instead, in-situ fluid properties measurements of impedance and density are recorded by the tool. At different depths, the properties of the fluid between the transduced and a target plate, located inside the tool sub, are measured.

After measuring the fluid velocity (FV), also expressed as 'fluid slowness' (inverse velocity), the internal radius is calculated as:

$$IR_{TT} = \frac{TT}{2} * FV + Offset$$

The offset accounts for the fact that the transducer is not exactly at r=0 in the tool, but it is at certain distance from the tool centre. This depends on the sub type, as there are various sizes depending on the pipe ID to be measured. In Emeraude, the internal radius can be computed from the transit time using the '*ab'* option.

In Figure 8.G.5, the transit time is shown next to the Internal radius images and the MFC diagnostic plot. The next step is centralization, and should be conducted with the considerations explained in Section 8.C.

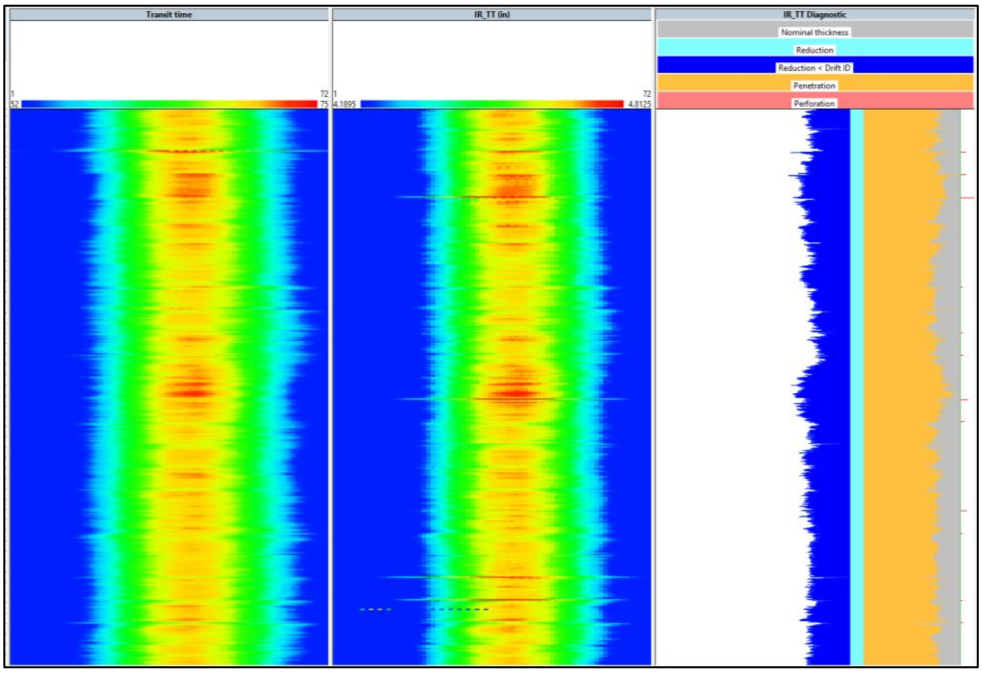

Fig. 8.G.5 – Transit time, Internal radius and Diagnostic track.

8.G.3 Final results

After centralizing the transit time-derived internal radius data, the statistics per joint are computed and the final results are presented. It should not be necessary to apply any other editing, unless there is telemetry or electronic noise. The results are shown Figure 8.G.6. With the knowledge that this log was run as part of a cement evaluation job during the well construction phase, a measured internal similar to the nominal, or at least within tolerance, is expected. As seen in Figure 8.G.6, the penetration is larger than 20% in most joints (yellow color coding).

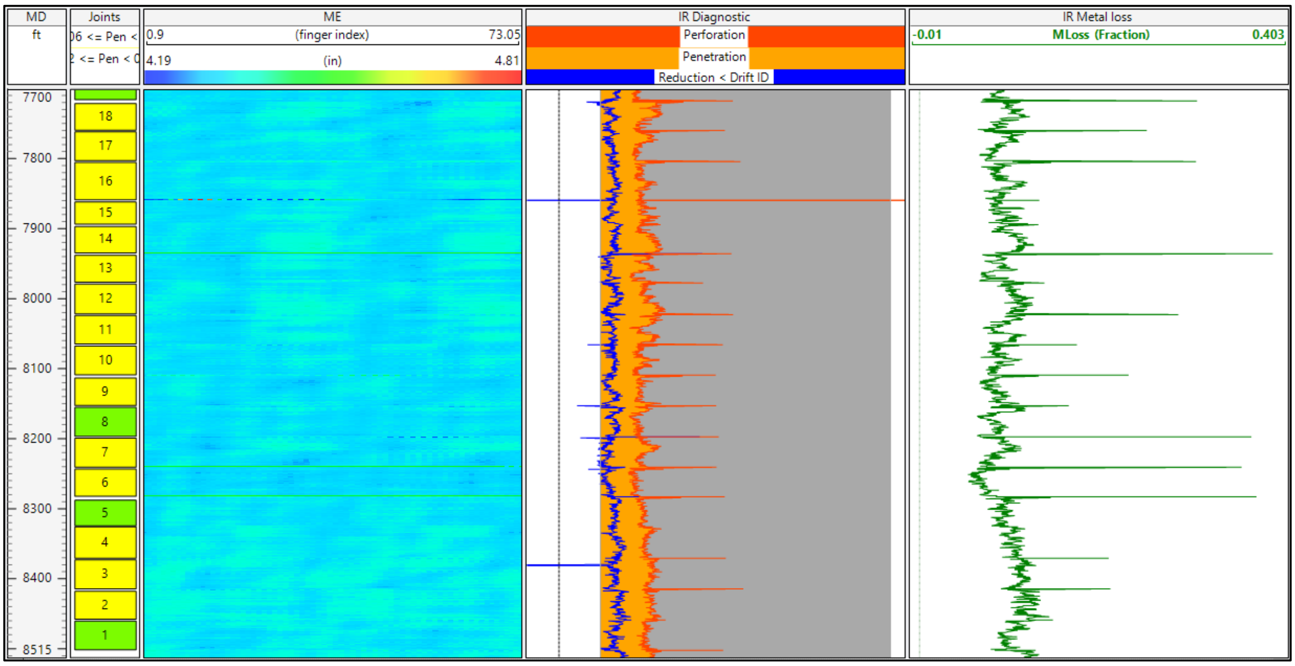

Fig. 8.G.6 – Final results from Ultrasonic radius measurement

An error on the internal radius calculation from transit time can be caused by the following, apart from tool failure:

- Transit time errors: can be related to the gating and should be fixed by re-setting the gates on the acquisition system
- Offset: If the radii values were calculated using a wrong tool geometry definition, then these will show a consistent larger or smaller value than the actual pipe
- Fluid velocity: The value used for computation may not be representative due to wrong measurements or different downhole conditions (pressure, temperature, density)

The first step is to identify the source of the discrepancy. If this is due to wrong fluid velocity, it is possible to apply the Recalibrate option in Emeraude, where a known ID can be used to compare the radius computations and, if necessary, apply shifts to the different radius computations.

9 – Passive Acoustic Logging

9.A Introduction

Intuitively, if we want to spy on the neighbors next door, we make silence and put the ear on the wall. We do not emit any type of pulse, wave or energy, but simply listen. This is the principle of *Passive Acoustic Logging*, where a listening device similar to a microphone records the different sounds downhole.

The sounds or noises are generated mainly as turbulent dissipation in response to fluid flow. The flow may occur behind the pipe, and with these tools, we can obtain information about flow through the cement or in the formation, locations where conventional flowmeters cannot. As large turbulence dissipation will be generated at the leaks and perforations these tools can allow us to locate fluid entries. Flow inside the pipe, including liquids, gas and solids (i.e. sand) will also generate a characteristic sound, which can be used to quantitatively or qualitatively describe the wellbore conditions. To understand the sound and identify its source, it is best to analyze the spectral frequency response.

These types of logs are not new. Enright (1955) proposed the use of listening devices for locating leaks. Since then, both the sensors and the signal processing techniques have greatly evolved. These types of sensors are known as Noise, Spectral Noise or Acoustic Energy logging tools, and are the focus of this Chapter (Section 9.B). Towards the end (Section 9.E), two other passive techniques will be presented: fiber optics DAS and acoustic sand detectors.

Section 9.C will explore the theory on how the noise is generated, how it propagates and our ability to quantify the rates from it. In Section 9.D we will review the main application of Passive acoustic logging techniques when run standalone and combined with other downhole sensors.

9.B Noise logging tools

The methodology proposed by Enright in 1955 used the peak noise (total energy) to determine the depth of the leak. In fact, for many years the logging engineer would use earphones to listen to the well to extract conclusions about the well integrity.

In 1973 McKinley presented the results of early spectral noise logging tools. Instead of looking at the total acoustic energy, the sound amplitude over a frequency range was reported. This allowed the engineer to characterize the noise based on its frequency structure, and hopefully associate it with certain type of fluid flow in the wellbore or behind pipe. The spectral noise logging tools will be detailed in the next section.

9.B.1 Tool description

The acoustic signal is measured using a highly sensitive 'hydrophone' (a microphone designed to record underwater). A Piezoelectric ceramic acts as an electroacoustic transducer, converting the acoustic energy into electrical energy. As the transducer is hit by an acoustic pressure wave, it will deform (compress) and due to direct piezoelectric effects, a voltage will be generated. This voltage will be transformed into quantifiable sound information as it will be later explained. A block diagram of the system is presented below:

Fig. 9.B.1 – Noise logging tool – main components

The architecture of the noise logging tools available in the market depends mainly on the number of hydrophones. Figure 9.B.2 shows two tools developed by Archer: Point, with one hydrophone, and VIVID with two. The length of the tool typically increases with the number of hydrophones, starting from around 50 cm (19'') for one sensor, 74.5 cm (30'') for the VIVID with two sensors, and more than 2 m (6.5 ft) for tools containing a radial array of sensors (8, 16, 38). Other tool providers include temperature, battery, and memory in the same module, leading to a larger length. The typical tool diameter is 1.69 in.

Fig. 9.B.2 – Point® (top) and VIVID® (bottom) (Courtesy: Archer)

The hydrophones are contained in a cavity of the tool housing. Depending on the tool model and provider, the cavity may be filled with a hydraulic fluid (oil), or the sensor may be integrated into the tool housing by the use of O-rings.

Tools that contain multiple hydrophones can have frequency-dependent equalization. The gain of the signal is adjusted to detect both, the low and high amplitude noise. A poor equalization may lead to a saturated signal if very loud sounds are detected. With two sensors, it is possible to adjust the gain of one of them for the low and other for the high frequency region, as the frequency structure is quite different across the spectrum.

All the noise logging tools available in the market can work in memory mode, and some of them allow telemetry for Surface Read Out (wireline).

9.B.2 Operation

To achieve the objectives of the operation, Noise tools are not run alone. As with any other logging operation, depth control measurements such as Gamma Ray or CCL are included. A high sensitivity temperature measurement is a typical companion of noise tools, especially for locating leaks, flow behind pipe or flow profile quantification. One or more spinners may also be added, which helps to correlate the noise amplitude with the rate of the fluid inflow/outflow.

Figure 9.B.3 presents a typical noise logging toolstring for leak detection purposes. In this case, two Sondex NTO tools were included (more on this later in this section). There are 2 spinners (Continuous and inline), pressure, temperature and capacitance. Note that in this case, probably due to the well deviation, three centralizers are present. For conventional noise tools (excluding arrays), centralization is not critical for the measurement quality but may be important for the conveyance. With or without centralizers, the metal-to-metal scratch caused by the conveyance and tool movement inside the pipe will cause a loud noise that will affect the analysis.

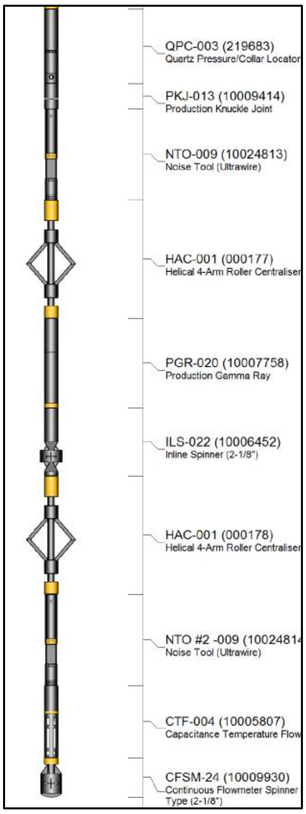

Fig. 9.B.3 – Noise logging toolstring (Courtesy: READ Cased Hole)

The noise generated by the tool and cable movement is known as 'road noise' and will govern how the noise logging surveys are recorded. Figure 9.B.4 shows (top to bottom) the normalized acoustic energy, depth, cable speeds and spectrogram versus time. Without going into details of the meaning of the energy and spectrogram (to be presented in Section 9.B.3) it is clear that in the stationary data (zero cable speed and no variation of depth) the energy is much lower and the frequency structure is also different than in the regions where the tool is moving. Therefore, noise logging operations consist of several stationary data recordings, as during these periods we can hear more clearly the sounds generated by the fluid flow.

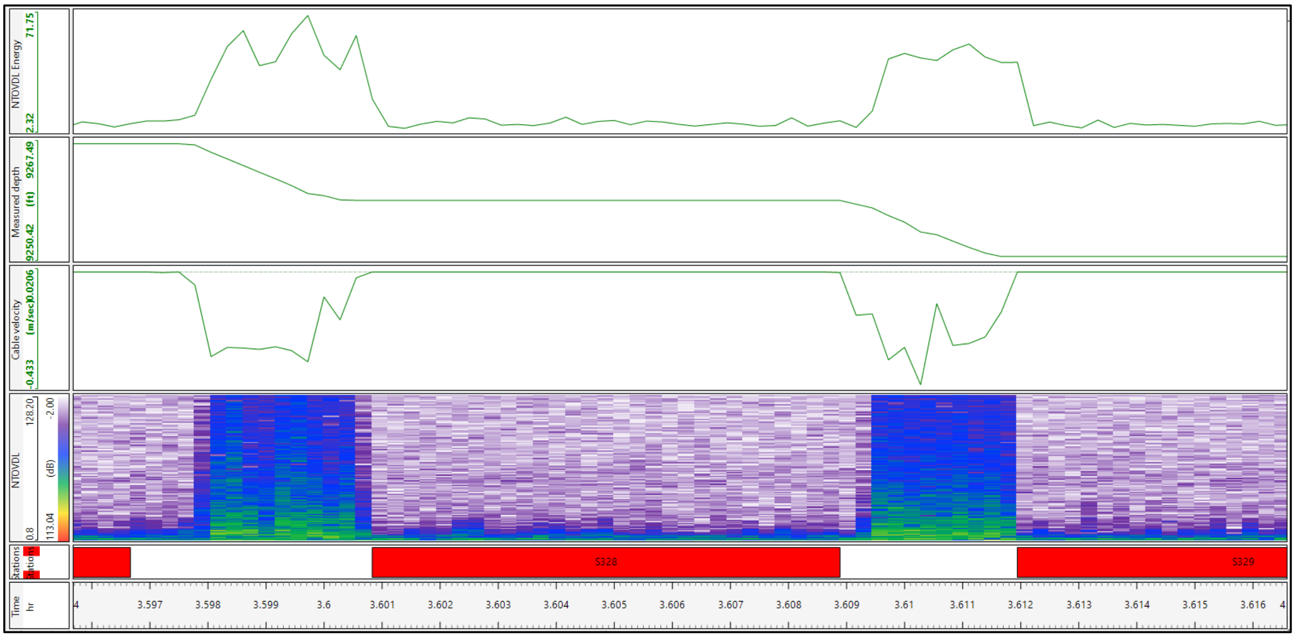

Fig. 9.B.4 – Noise recording with moving tool and during stations

Note that different tool providers have worked on sensor technology and filtering techniques to circumvent the need for stations and record the whole job as a continuous pass. At the time of writing (2021) stationary noise recordings over the whole interval or a region of interest remains the basis of noise acquisition.

In Section 9.B.4 we will see how to go from the stations to the versus depth noise log. The length of the stations is typically between 15 seconds and 2 minutes. However, we may record longer stations at specific depths, especially when modifying the operational conditions of the well (starting production/injecting, bleeding the annular, etc.).

The next question is how many stations should we record. And this has to do with the objectives of the operations. Let's imagine that sustained annular pressure was detected in the B annulus and the production packer is 4000 meters deep. In general, we will not go for 1-meter spacing stations for 4000 meters, as the operation would take very long and we will get lots of spurious data. In other cases, we have a hint of where the issue may be, and therefore the measurement range will be constrained.

It is common, and especially helpful in real time operations, to start with a continuous down pass from the surface to target depth. Apart from using it for correlation purposes, the temperature can help us to locate zones of interest and define the depths for stations. Noise stations will typically be recorded during the up pass. However, note that since the measurements are stationary, it is irrelevant if the stations are acquired during the up or down pass. Initially, or in regions of the well of no particular interest, the stations are recorded with a larger spacing (10 meters – 30 ft). In intervals of interest, the stations may be recorded with very fine spacing (1 meter or less). A schematic of the operation is presented next.

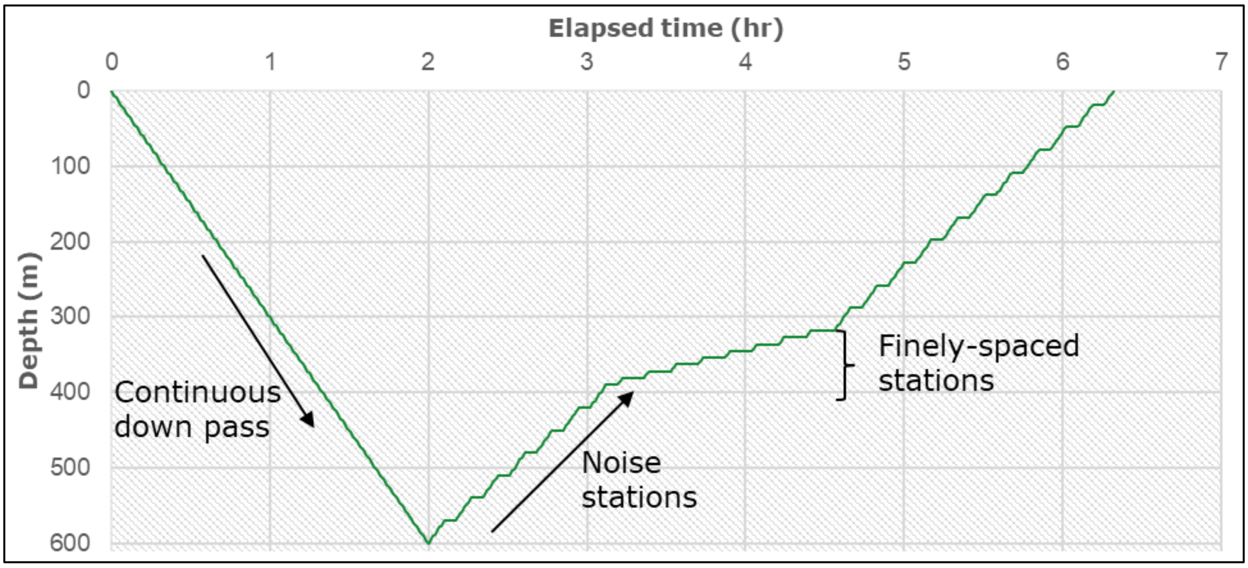

Fig. 9.B.5 – Schematic Noise logging acquisition program

The continuous temperature recording during the down pass may be used for quantitative interpretation. If a pressure measurement is run, a continuous pass can be used to obtain the pseudo-density to understand the fluid distribution in the well.

Coming back to the toolstring diagram presented in Figure 9.B.3, it can be seen that adding a second noise tool in the toolstring can help reduce the number of station stops, especially in the region of interest, where the spacing between stations is smaller.

FAQ 1: Should we record the noise log in flowing or shut-in conditions?

It is key to remember that the noises that we are trying to hear are generated by turbulence dissipation caused by the flow of the different phases downhole. Therefore, we need the Delta P to create the quantifiable fluid flow, and for this, the well has to be flowing. The most effective way to create the noise may not necessarily be by just putting the well in production. It may involve bleeding the annulus to create a delta P between tubing and casing, injecting through the annulus and producing through the tubing. If we suspect of flow behind pipe, the drawdown has to be of enough magnitude to activate the channeling. In summary, we need the fluids to be moving in the way they maximize the noise we are trying to find.

It would be of additional value to record stations during shut-in conditions, as they can serve as a baseline when there is no fluid movement. But this should be considered as a secondary objective.

Finally, if the toolstring includes spinners (as Figure 9.B.3) then the acquisition program should include passes at different cable speeds. This way we would be able to obtain the fluid velocity and correlate the different noise events to fluid inflows/outflows.

9.B.3 Sound processing

Sounds are pressure waves traveling through a certain fluid (liquid or gas). In 1877 Thomas Edison invented the phonograph, which allowed for the first time to record the pressure waves onto a physical medium and later play them back as sounds. With the phonograph, the pressure waves would cause a disk to vibrate, and a needle would indent a tinfoil, which would allow to record the sound. Sound pressure waves, or *Waveforms*, look like this:

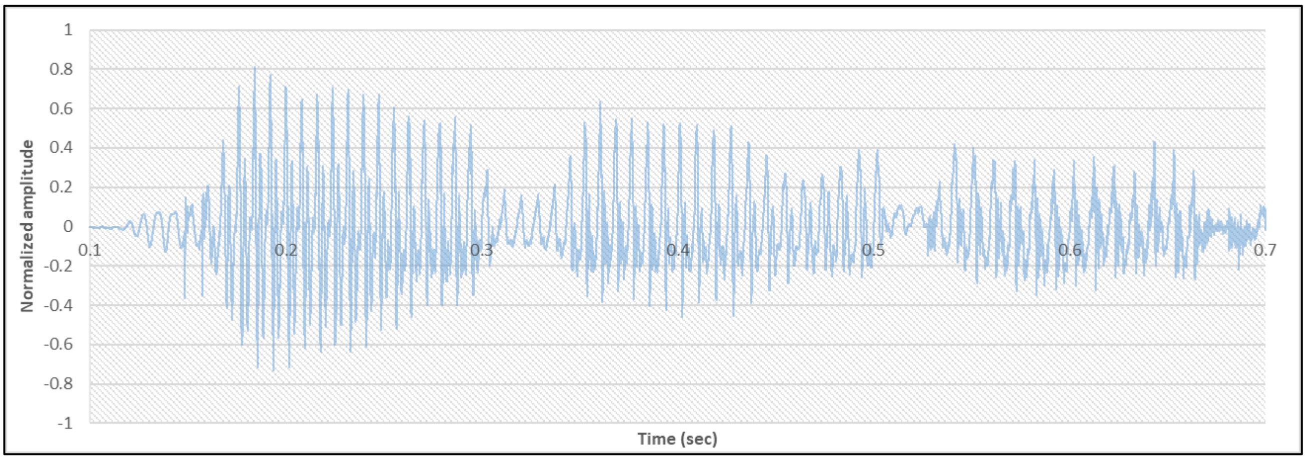

Fig. 9.B.6 – Sound Waveform

The vertical axis of the waveform may reflect the principle of the measurement technique, like millivolts for the sound detected by ceramic piezoelectric transducers. However, it is very common to display the normalized measurement or the decibels.

Sound measurements like the phonograph or a cassette are *Analog*, and they represent the shape of the waveform directly. For the type of processing we want to perform, we will need to move to the digital world.

9.B.3.a Analog to digital

Digital sound recording samples the waveform at evenly-spaced time points, representing each sample as a precise number. Compared to the analogue counterpart, the digital recording does not degrade with time, and several processes can be applied. As mentioned previously, it is possible to apply a gain to certain frequencies, and also to remove spurious data by use of filters.

The quality of the digital audio recording, and our ability to hear the noises of different nature in the well, depends mainly on two factors: the sample rate and the ‘bit depth’ (or sample format).

The sample rate (Hz) is a value of the number of samples capture per second. The higher the sample rate, the higher the audio frequencies that can be represented.

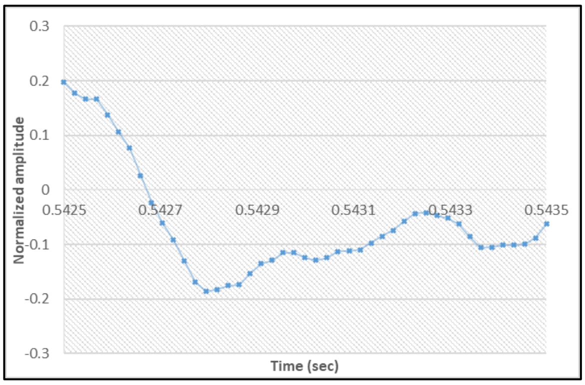

Fig. 9.B.7 – Digital waveform representation

FAQ 2: What determines the frequency range that a tool can measure?

Provided that the sample rate is more than double than the highest audio frequency that we want to capture, the waveform can be reconstructed exactly from the digital sample. This was defined by Nyquist in the *Sampling theorem*. The *Nyquist frequency* establishes that there is an upper limit for the frequencies we can represent, and this is given by half the sampling rate. Frequencies above this limit cannot be correctly represented by the digital sample and would cause a kind of distortion called aliasing. Filtering techniques (called anti-aliasing filters) are required to avoid distortion of the signal caused by high frequencies.

To give a common example, human speech is intelligible even when frequencies above 4000 Hz are eliminated. Telephones transmit frequencies between 200 Hz and 4000 Hz. Therefore, the sampling rate of telephones is 8000 Hz, which is sometimes known as *speech quality.*

To summarize, the measurable frequency range is given by the sampling rate. This is handled from the analogue-digital converter of the tool and is limited by the electronics and its firmware.

The 'bit depth' is the number of bits used to represent each sample. The larger the number, the more precise the representation of the sample. But this also allows us to increase the 'dynamic range', which is the difference in volume between the loudest and softest sounds to be represented. The dynamic range of noise logging tools is measured in decibels (dB).

The Sound Pressure Level (SPL) is a function of the average sound pressure (P_{avg}) and a reference pressure (P_{ref}) of typically 20 μPa.

$$SPL\ (dB) = 20 \log(\frac{P_{avg}}{P_{ref}})$$

The physical response of the piezoelectric transducer to a sound wave is the voltage. To go from mV to dB, a calibration value (or hydrophone sensitivity) is used. This has units of $\frac{mV}{Pa}$. This response exposes the need for a linear transducer response across the measured frequency.

Typical maximum frequency measured by noise tools available in the market are: 12.8 kHz, 60 kHz, 128 kHz, 656 kHz. The most typical dynamic range is 90-110 dB.

Increasing the sampling rate and the number of bits would increase the quality of the sound representation. But at the same time, the size of the data would dramatically increase, complicating its storage and transmission to surface. We will see next that most tools do not store or transmit the full waveform to surface.

9.B.3.b Sound spectrum

Apart from the bandwidth limitations to transmit the data to surface, as mentioned previously, modern noise logging interpretation is based on the frequency structure of the recorded sound. Therefore, we need to move from the time domain of the waveform to the frequency domain. This is done downhole by the tool.

A Fast Fourier Transform (FFT) is the typical algorithm used to decompose a sequence of time values into components of different frequencies. The time signal (waveform) is x[n], where *x* is the amplitude (in mV, dB, etc.) of the waveform at time (or sample) *n*. Through the Fourier transform we move to the frequency domain, x[k], where *x* is till the amplitude but now expressed for each frequency component, *k.* An example for a cement VDL signal is shown in Figure 9.B.8:

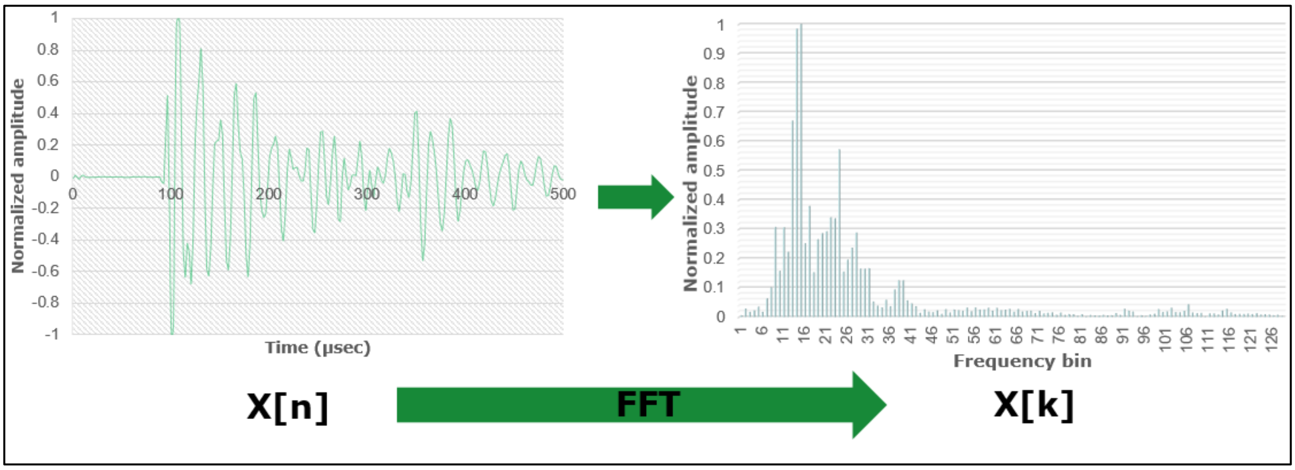

Fig. 9.B.8 – From time domain to frequency domain through FFT

For sound processing, we take a certain time window (i.e. 1 sec). The size of the FFT window will determine how much frequency detail you see. A larger FFT window size gives more frequency resolution, but at the same time it decreases the temporal resolution. For most downhole applications we do not expect sudden changes of the nature of the noise, and therefore many tools compute 1 or 2 FFT per second. However, some tools incorporate a special processing with more than 200 FFT per second, to capture short-lived events like sand detection.

Noise logging tools will output the noise amplitude (dB or mV) for a number of frequency bins. Knowing the range of each bin, we can plot the amplitude as a function of the actual frequency. For example, NTO output is 128 frequency bins of 100 Hz each. Therefore, the tool range is 100 Hz to 12.8 kHz, and we can tell the amplitude for certain frequency.

With the sound signal in the frequency domain, we will compute two values to characterize the sound:

- Sound energy: the energy of a spectrum is calculated as:

$$Energy = \sum_{k=0}^{N-1} |X[k]|^2$$

  To avoid facing units' issues (as the amplitude is not always in the same unit), in Emeraude we present the *Normalized Energy*, with respect to the maximum energy.

- Spectral centroid: This is the center of mass of a spectral distribution and is a typical way to characterize the *pitch* of a sound:

$$Centroid = \frac{\sum_{k=0}^{N-1} k * X[k]}{\sum_{k=0}^{N-1} X[k]}$$

Figure 9.B.9 shows the amplitude (in dB) for 128 frequency bins. With this plot it is difficult to extract qualitative information, and we will see next how the spectrum is best represented.

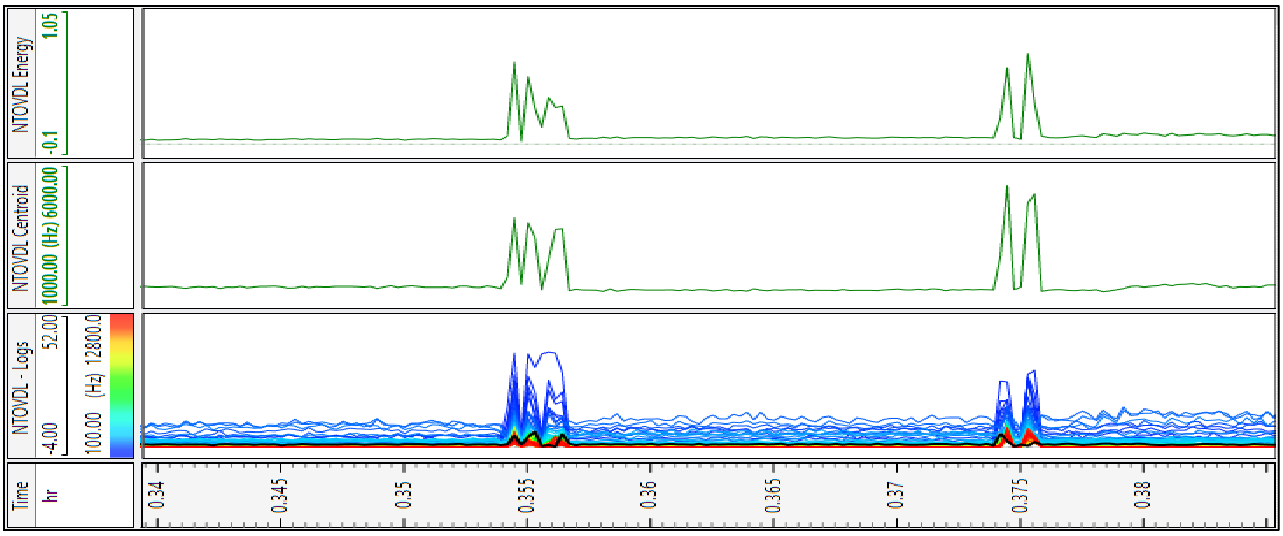

Fig. 9.B.9 – Amplitude for 128 frequency bins (bottom), Centroid (middle) and Energy (top)

9.B.3.c The spectrogram

The data presented in Figure 9.B.9 is 3D: Amplitude vs. frequency vs. time (or depth). The most typical way to display this is by using a 2D map, with frequency vs. time (or depth) and the amplitude for each frequency represented by a color. This is called a *spectrogram*, and takes a series of FFTs amplitudes and overlaps them to illustrate how the spectrum (frequency domain) changes with time.

The spectrogram presented in Figure 9.B.10 shows 256 frequency band, with the frequency band #1 on the left margin and the #256 on the right margin. The color scale is adjusted to highlight the noises of interest. Low amplitude or background noise is shown in white, while the maximum amplitude is shown in red. Right to the spectrogram, the amplitude for specific frequency bands is displayed: 73-blue, 145, green, 228 red:

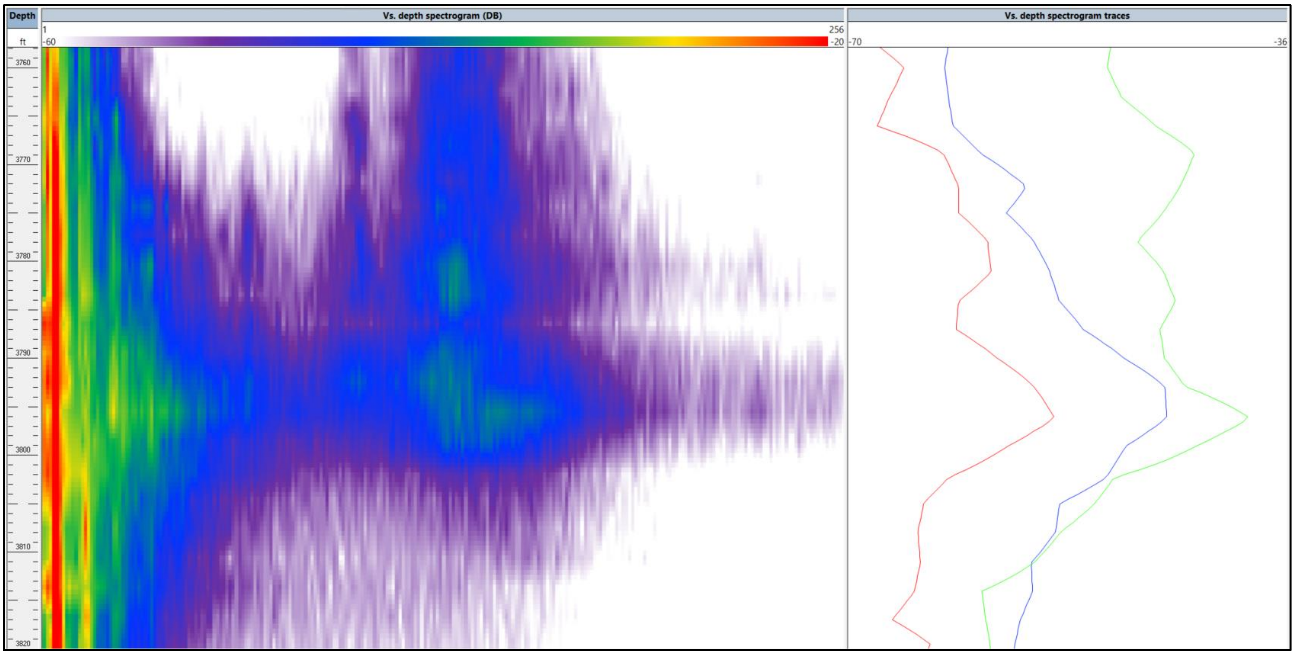

Fig. 9.B.10 – Vs. depth spectrogram and amplitude for selected frequencies

9.B.4 Noise logging processing summary

Noise logging processing refers to the steps to go from the noise tool output to the final versus depth spectrogram. The interpretation of the spectrogram will be discussed in the next sections.

The tool output from a noise logging job is, in general, a long time-driven file, which contains the recording of the whole job, including stationary periods and moving tool. The amplitude for each frequency bin is present, as well as high pass filters at various frequency cut-offs. Other sensors run with the noise tool can also be loaded.

Upon loading, Emeraude will plot the noise array as a vs. time spectrogram. As we are interested mainly in the stationary periods, the stations identification is automatically launched. For this, the cable speed and depth measurements are used. As many noise acquisitions are memory jobs, the noise array and the cable data may be in different files, and synchronization between them may be needed. A time shift can be applied directly from the Noise Explore (Emeraude window where the processing is conducted).

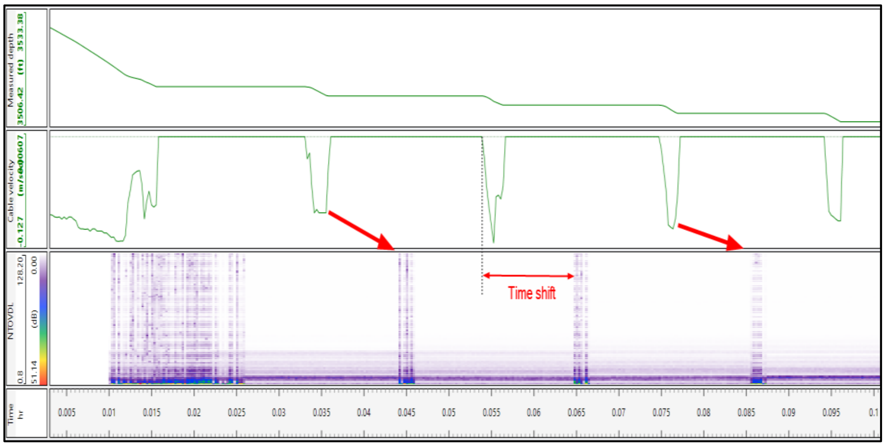

Fig. 9.B.11 – Offset between noise and cable data

With the data synchronized, the stations are automatically identified and presented in a specific track (in red in the figure below). Note that there may be spurious cable speed values that may 'break' a station. A threshold in cable speed or depth variation may be added, to avoid a stationary period to be split.

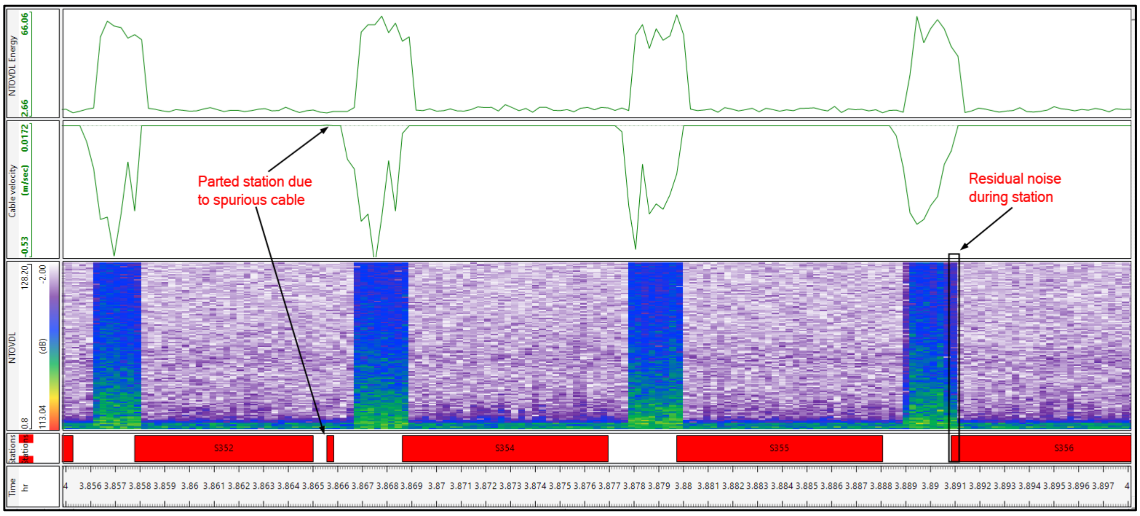

Fig. 9.B.12 – Stations identification

The versus depth spectrogram will be created by compiling the spectrum data of each station. It is possible to choose between an instantaneous value (i.e. the spectrum after 10 seconds of recording), or an average or median value over the station range. When using a statistical value, avoid the first and last few seconds of the recording, in case there is residual noise from the tool movement, as shown in Figure 9.B.12.

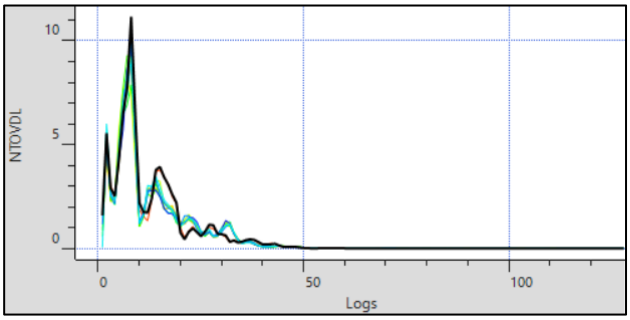

Fig. 9.B.13 – Spectra recorded within a station

We finish the processing when we arrive at the versus depth spectrogram, extract different amplitudes (Figure 9.B.10) and display the spectra at different depths. The energy and spectrum centroid is calculated automatically for the versus depth and versus time data. So what do we do with this data? We will try to answer that in the next two sections.

9.C Noise data interpretation

9.C.1 What creates the sound?

The waveform behavior demonstrates that sounds are pressure waves traveling through certain media, with a characteristic amplitude and frequency that are of interest for noise logging interpretation. The generation of these pressure waves requires an excitation and vibration of certain structures (i.e. vibrating vocal folds, the release of stress in a string, etc.). When the structure vibrates, small-scale pressure fluctuations will propagate at the speed of sound of the medium. This is called 'sound radiation' and can occur through rock or pipes vibrations.

Another sound generation mechanism is the flow-induced vibrations. In turbulent flow, vortices or eddies create local fluctuations in velocity and pressure, which can be sensed as sound. Turbulence is an instability generated by shear, the stronger the shear the stronger the turbulence. Therefore, turbulence can be generated by friction forces (flow through conduits, flow past bodies) or by the flow of layers of fluids with different velocities (multiphase flow). The presence of large velocity gradients in the vicinity of an obstacle (perforation, leak, pore throats) is one of the main sources of noise in downhole applications.

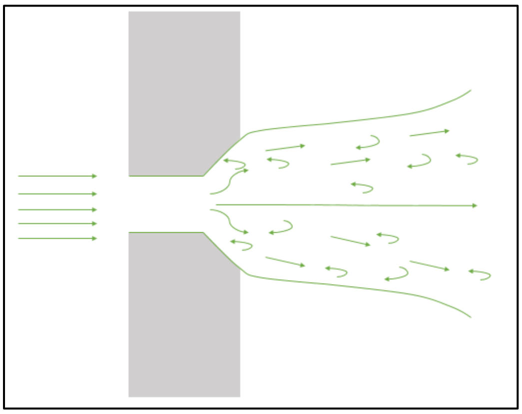

Fig. 9.C.1 – Vorticity and sound generation

Any source of noise has a characteristic sound power (W), which is a property of the source only. The concept of power (Energy/time) can be associated with energy dissipation ($\frac{dE}{dt}$). A simplified way to understand the source of the power of the sound would be by multiplying the different components of the fluid energy (Bernoulli) by the rate:

$$\left(P+\frac{1}{2}\rho\, v^2+\rho g h\right) * Q = power$$

Higher rates and higher pressure gradients will contribute to a larger power. Note that sound production represents only a very small fraction of the energy in the flow, making the prediction of sound generation very difficult. This is particularly dramatic in free space and low subsonic speeds.

The pressure gradient and rate not only affect the total rate. The turbulence theory predicts that the spectrum frequency peak is related to the kinematic viscosity (ν) and the characteristic scale of turbulence by:

$$f_{max} \sim \frac{\nu}{l^2}$$

This was demonstrated experimentally by McKinley (1973), who showed that increasing the pressure gradient shifts the peak to higher frequencies. This is caused by a smaller scale of turbulence (eddies).

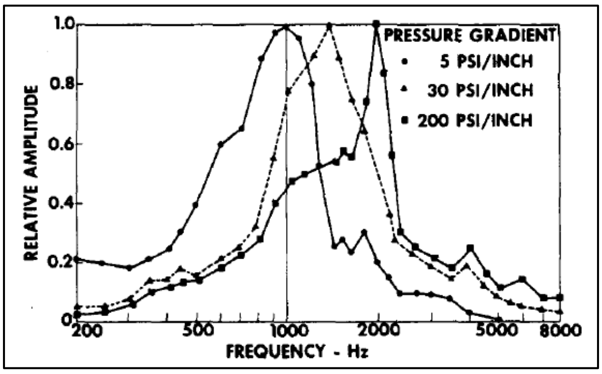

Fig. 9.C.2 – Water leak for various pressure gradients (McKinley – SPE3999)

In summary, sound is a consequence of turbulence, and can be generated because of flow in pipes, flow through leaks/perforation, flow through cement channels, flow through reservoir matrix, natural fissures, etc. For the flow in the reservoir, due to the logarithmic pressure drawdown behavior, most of the noise will be generated in the near wellbore region where the gradients are steeper.

9.C.1.a From the source to the receiver

The sound pressure level that the transducer will feel is a function of the distance to the source, the medium (including PVT and velocity), what is in the middle, etc. Small sound sources can be modeled as point sources if their dimensions are small compared to the distance with the receiver. If the wave propagates spherically, the intensity (sound power per unit area) can be calculated as:

$$I = \frac{W}{4\,\pi\,r^2}$$

The intensity can also be expressed as $I = \frac{p^2}{\rho C}$. Combining the above equation (that shows that the intensity is inversely proportional to the square of the distance) with the sound pressure level (SPL) definition, will demonstrate that the attenuation is 6 dB as the distance doubles. This imposes limits on the 'radius of investigation' of the noise tools, especially for the reservoir sounds.

For the sound to reach the noise tool, it has to go through different media, where depending on the impedance, a fraction of the wave will be transmitted and part will be reflected. To further complicate things, the transmission through 'walls' will be a function of the frequency. The transmission loss (TL) through a limp wall of mass *m,* is a function of the impedance (Z_0) and the sound frequency (*f*):

$$TL = 10\log\left[1 + (\frac{\pi f m}{Z_0})^2\right]$$

Low frequencies are transmitted more effectively through walls. People living in flats will know that when a neighbor watches TV they hear more of the low (bass) frequencies. These frequencies can create resonance/vibration in walls and this helps propagate sound waves.

There are two more things to consider: the sound attenuation due to distance from the source to the receiver, and the frequency dependency of the sound transmission.

9.C.2 Quantitative interpretation

Predicting the noise characteristics (amplitude and dominant frequency) from flow through certain control volume is a discipline called 'Aeroacoustics'. The field was pioneered by Lighthill (1952), trying to predict the noise radiated by jets. The flow was modeled by means of the Navier-Stokes equations, rearranged into the form of a linear wave equation with a quadrople-type source term. Since this problem involves modeling turbulence, these equations are solved through numerical methods. First, the geometry and flow conditions are defined and modelled through computational fluid dynamics (CFD). Then, through the aeroacoustics analogies, it predicts the noise frequency and amplitude. Later, further numerical modeling is required to predict the sound propagation.

Hopefully this introduction gives a sense of the complexity of solving the direct problem. It should not be difficult to understand that the inverse problem, this is predicting the flow rate from noise amplitude and frequency, is out of scope for most practical cases. The accurate description of the flow geometry of the cases that we are trying to diagnose through noise logs (channeling, leaks, flow in porous media) is nearly impossible, and this will cascade through the rest of the interpretation. With a noise log only we do not know the shape, distance and pressure drop characteristics of a channel in the cement, natural fracture, etc.

FAQ 3: Is 1+1=2 always?

Not for sound perception and the decibel scale. Let's imagine that you are listening to loud music (i.e. 80 dB) and someone tries to tell you something as loud as they can (another 80 dB). Intuitively we know that you do not perceive a sound pressure level of twice the music loudness (160 dB). This is because we need to sum source powers and not decibels.

$$SPL_{1+2} = SPL_1 + SPL_2 = 20\log(\frac{P_1 + P_2}{P_{ref}})$$

Thus, 80 dB+80 dB= 83 dB.

How is this relevant to noise logging? The immediate consequence is that if we have a number of noise sources, for example 2 leaks 5 meters away, the sound in between them will be dominated by the loudest event. 80 dB + 75 dB = 81.2 dB

Also the noise amplitude is not 'cumulative' as we see with a conventional flowmeter spinner. The noise will not necessarily increase from bottom to top for a producing well, and therefore obtaining the flow rate from the acoustic amplitude and frequency is not doable.

Whilst the cumulative noise profile is not typically used for flow profiling, going back to the source of noise based on turbulence it is possible to see that the relative amplitudes or normalized energy can be used qualitatively for predicting inflow rates. As noise power is proportional to pressure times rate, if the pressure drops are similar (which require similar perforation characteristics, cement and formation) then the normalized energy should indicate the inflow rate. This can be used in scenarios where the loudest noise (at least in the producing interval) is the different inflow, and when the sources are sufficiently apart to be resolvable.

In summary, the accepted approach nowadays (2021) is to use the noise tool as a qualitative tool. In some cases, for example, a leak in the tubing, it will be enough for us to determine the depth of the maximum energy peak to be reasonably certain that the leak is there. However, when possible, the measured frequency spectrum should be compared to the 'footprint' of different flow events, typically obtained by flowloop testing. The normalized energy as qualitative inflow rate indication can also be used (Section 9.D.3) with caution.

Section 9.E.1 will briefly introduce the concept of speed of sound calculation, which is currently used with DAS data for flowmetering purposes.

9.C.3 Flowloop testing

So far this section has dealt with the complexity of sound generation, propagation and characterization. The noise reaching the hydrophones will be different in frequency structure and amplitude compared to the one radiating from the source. A common question that may arise is whether the tool will be able to detect the noise generated under certain conditions. Flowloop testing can be the answer to this.

Figure 9.C.3 shows the results from Archer's VIVID, while the water flows through an induced microannulus in rate stages from 620 ml/min to zero. Down to a rate 150 ml/min (1.35 bbl/d), the tool detects the water movement. At the bottom, the noise response when the pump is stopped can be seen. For the same microannulus, a gas flow rate down to 3.5 l/min at a differential pressure of 50 psi was detected by this tool.

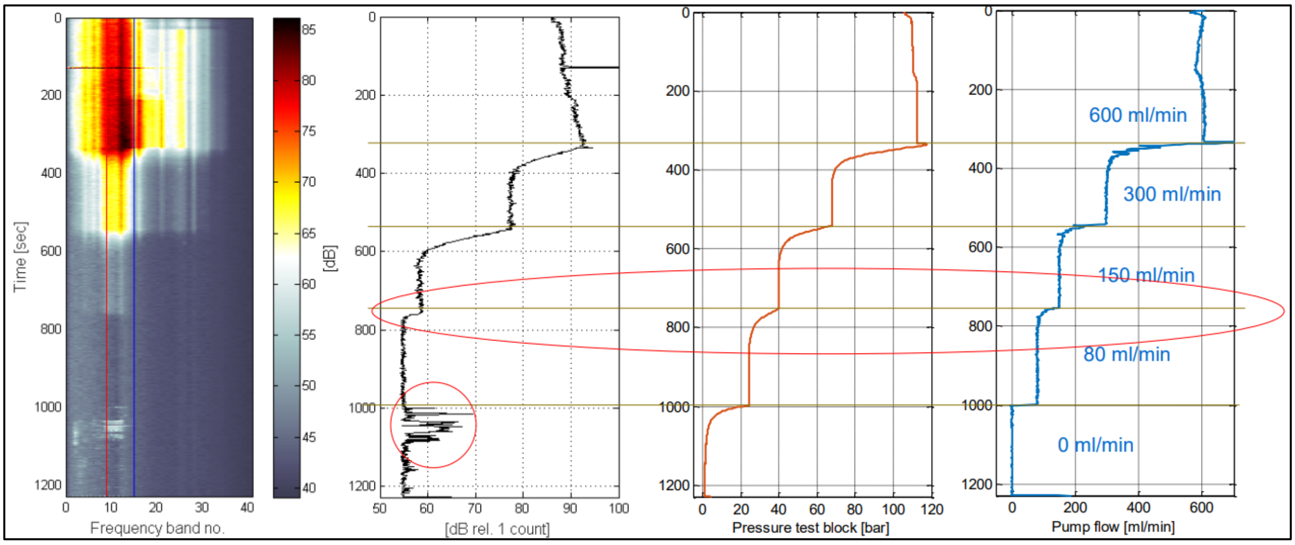

Fig. 9.C.3 – Microannulus flowloop testing (Courtesy: Archer)

Note that these results are exclusive for this tool and were performed under controlled flow loop testing conditions. Hence, the reader should not generalize these conclusions to other tools or flow scenarios.

Various papers, including the work by McKinley, include the spectral response for flow in pipes and through leaks under a variety of conditions: different differential pressure, single/multiphase, etc.

9.D Applications

Several common applications are presented in this section. It will be evident from the images that to arrive at more robust conclusions, it is best to include open and cased hole logs into the analysis.

9.D.1 Leak detection

Multiple logs can be run to determine the presence of a leak: Temperature, multifinger caliper, spinner, electro-magnetic and noise logs. The ability of a given tool to detect the leak is influenced by different factors, including leak rate, leak size, measurement resolution, etc. For noise logging to detect the leak there must be active flow through it, to create the necessary turbulence that leads to the sound radiation. Achieving this condition may include bleeding the annular, setting a plug on a nipple and injecting, etc.

Figure 9.D.1 shows the presence of a leak around 690 ft. The multifinger caliper shows a fully penetrating feature, while temperature reveals a warming (characteristic of small leaks with large delta P). The noise spectrogram clearly shows that the maximum amplitude is located at the same depth as the other measurements. The frequency spans over the full range (from 1 to 12.8 kHz). The large frequency spectrum agrees with the possibility of a small leak size, which can lead to a smaller turbulence scale and therefore higher characteristic frequency.

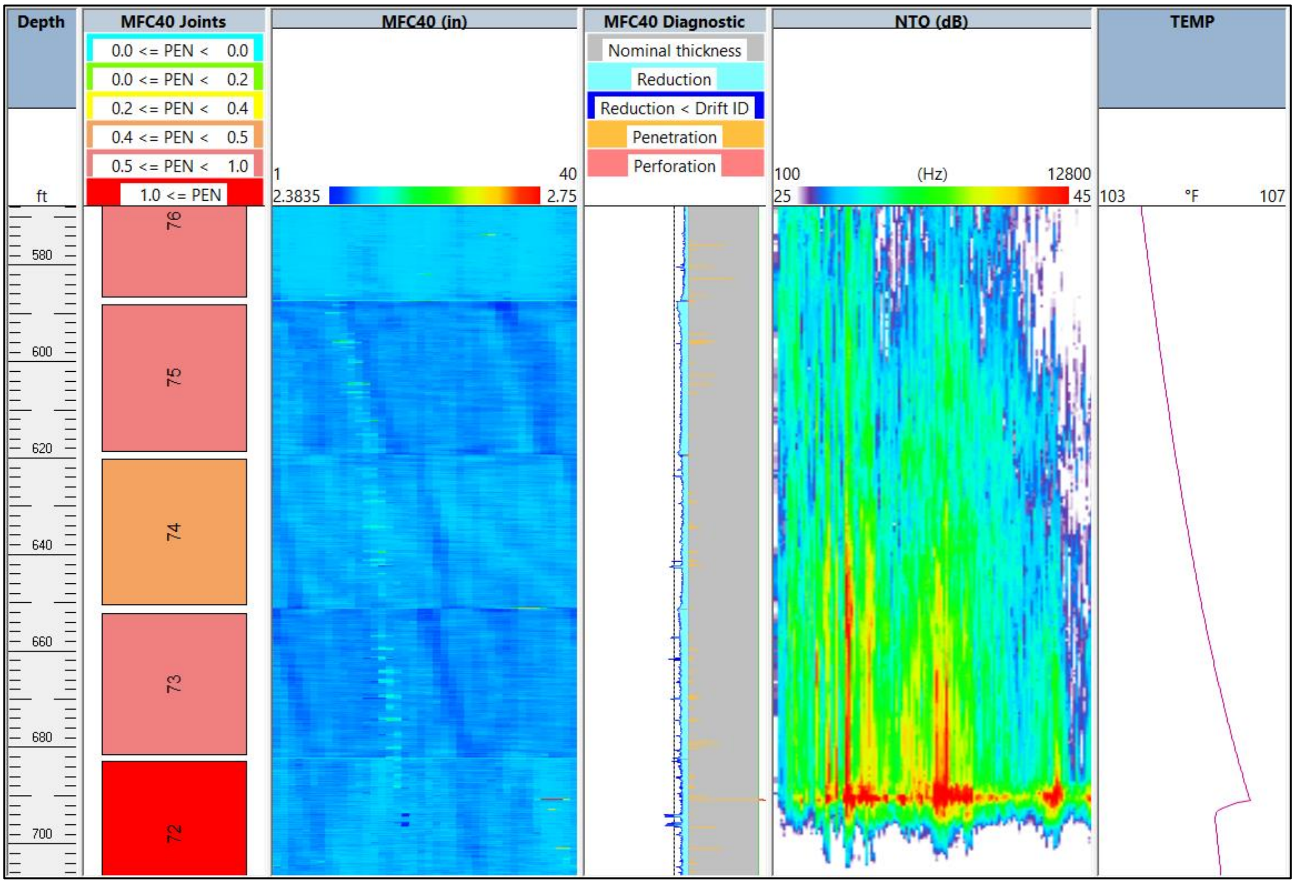

Fig. 9.D.1 – Leak detected through noise logs, MFC and temperature

In this situation, no further analysis is required to conclude with a large level of certainty that the leak is there.

In some cases, noise logs and temperature can prove to be the only ways to determine the presence of a leak. For example, small holes below the circumferential resolution of the MFC, leak rates smaller than the spinner resolution, leaks through connections, completion elements (i.e. side pocket mandrel), etc.

9.D.2 Flow behind pipe

This is an application where noise tools have a real advantage, as other sensors cannot see behind the first barrier. This ability is shared with temperature logs, and the results are more conclusive when run together. One of the earliest field examples was published by McKinley and is shown in Figure 9.D.2. The well was completed with a 5.5 in casing and 2 7/8 in tubing and targeted an oil reservoir at depths deeper than displayed in the logs. At a shallower depth, the well goes through three non-produced gas bearing sands, labeled 1, 2 and 3. A 20 °F cooling is detected above sand 2, which agrees with the major noise peak. Two other minor noise peaks are detected at the depths of Sands 1 and 3. This allows us to conclude that gas is flowing through the cement, from a high pressure sand (2) to the layers above and below.

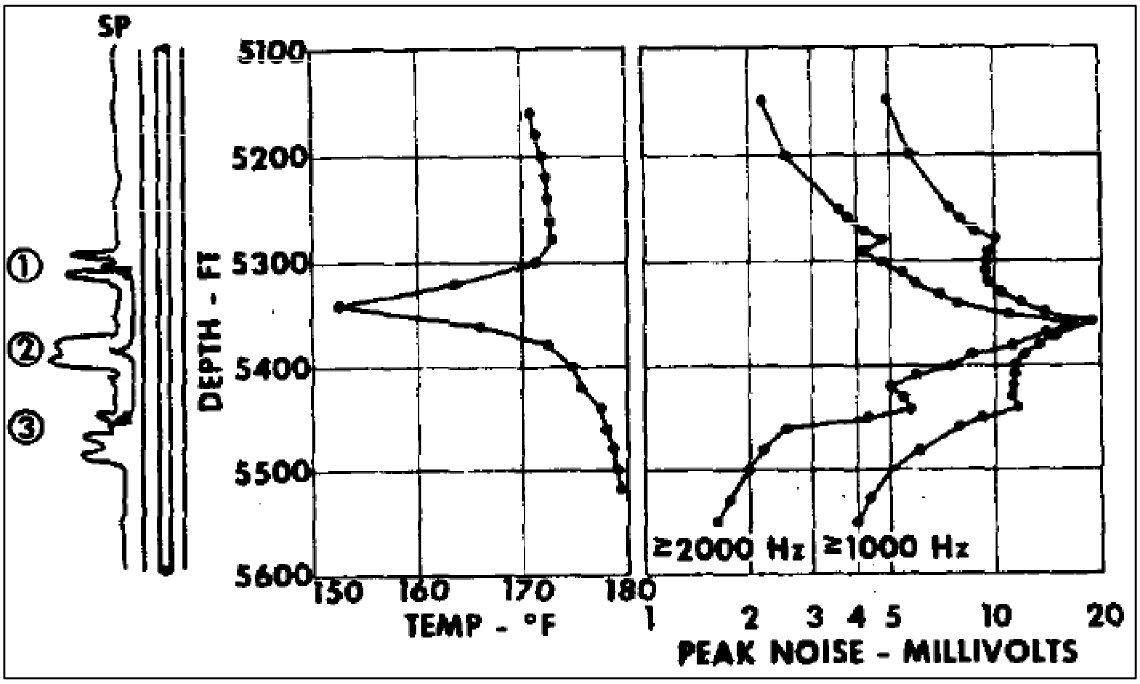

Fig. 9.D.2 – Leak detected through noise logs, MFC and temperature (McKinley – SPE3999)

The diagnosis of flow through cement channels is also enhanced when integrating the noise data with cement logs, as shown in Figure 9.D.3. A PLT interpretation indicates that the most perforated interval contributes to the total production ('OIL RATE PLT' track). However, the noise spectrogram shows that the only active reservoir is the one close to the bottom perforation. In this interval, frequencies higher than 5 kHz are present. Above this interval, only low frequency noise (peak at 1 kHz) is detected, which can be associated with wellbore flow. The cement CBL (AMP), VDL and cement maps allow you to conclude that the cement placement along the perforated interval is not optimal. High CBL (~40 mV) and VDL casing arrivals are seen at multiple depths.

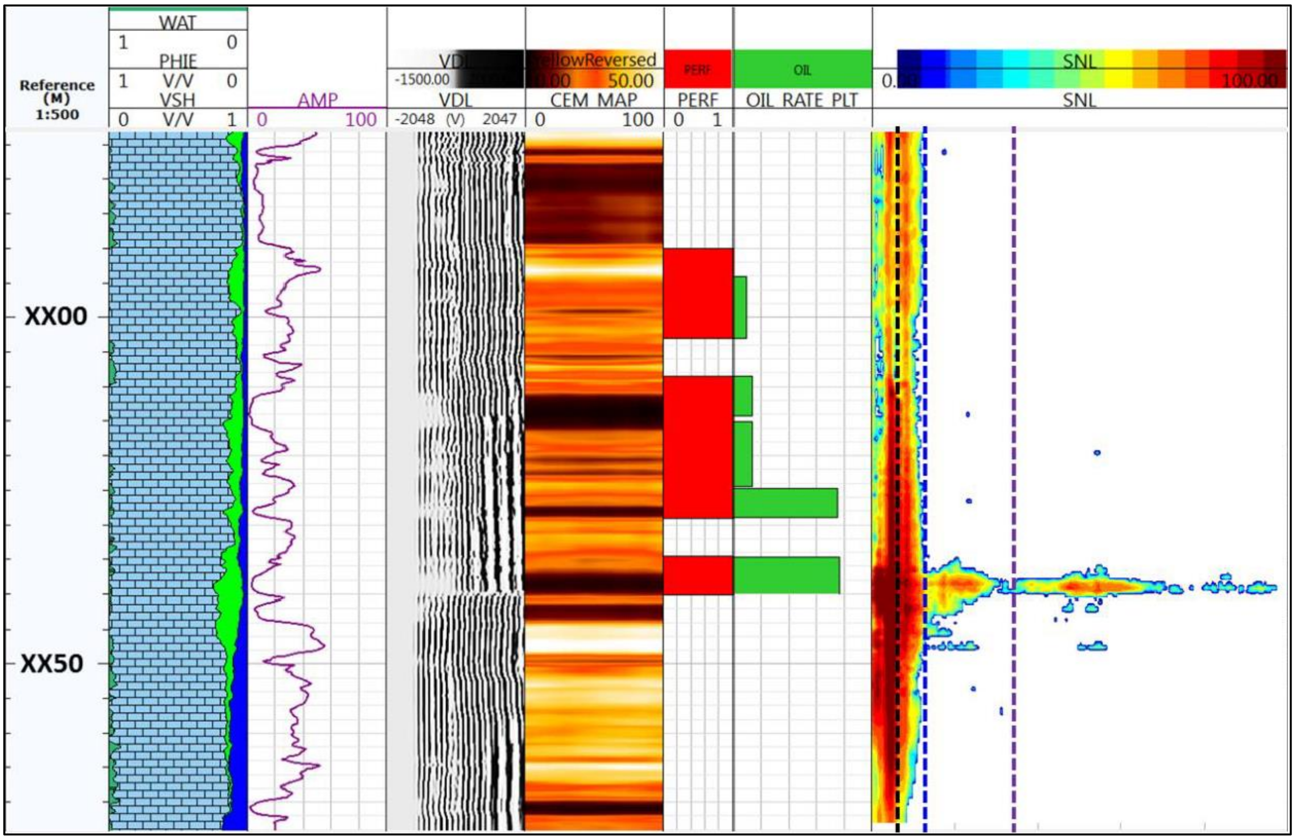

Fig. 9.D.3 – Image from 'Quantitative Spectral Analysis of Noise Log Measurements for Enhanced Dynamic Characterization of Complex Reservoirs' – Cicione, Galli, Pirrone and Raimondi – ENI S.p.A (presented at OMC-2017)

Putting it all together conclude that the bottom reservoir is responsible for the production of the total oil rate. Part of the oil is produced directly by the bottom perforation, while the rest flows up through cement channels and is produced by the other perforations.

Another flow behind pipe scenario consists of flow through leaky packers. A classical completion design for long horizontal wells producing from heterogeneous formations (i.e. fractured carbonates, vuggy porosity) consists of isolating the segments of the reservoir by using swellable packers and producing through sliding sleeves. If a PLT reveals that one zone is producing excessive water or the production is uneven, then it is possible to shift one SSD and delay the unwanted production of that interval. This is true only if the swellable packers provide the necessary isolation between zones.

Figure 9.D.4 shows an opened SSD at the top of the log with clear indications of production. A PLT revealed that this zone is producing water, which was not expected for this interval of the well. The noise log shows high amplitude noise across the packer, which indicates the existence of flow between the packer and the formation. Therefore, the production from the bottom zone, which SSD was closed due to excessive water, will be produced by the top SSD. The reduced annular section leads to high fluid velocity, which in turn generates a large noise amplitude as previously explained.

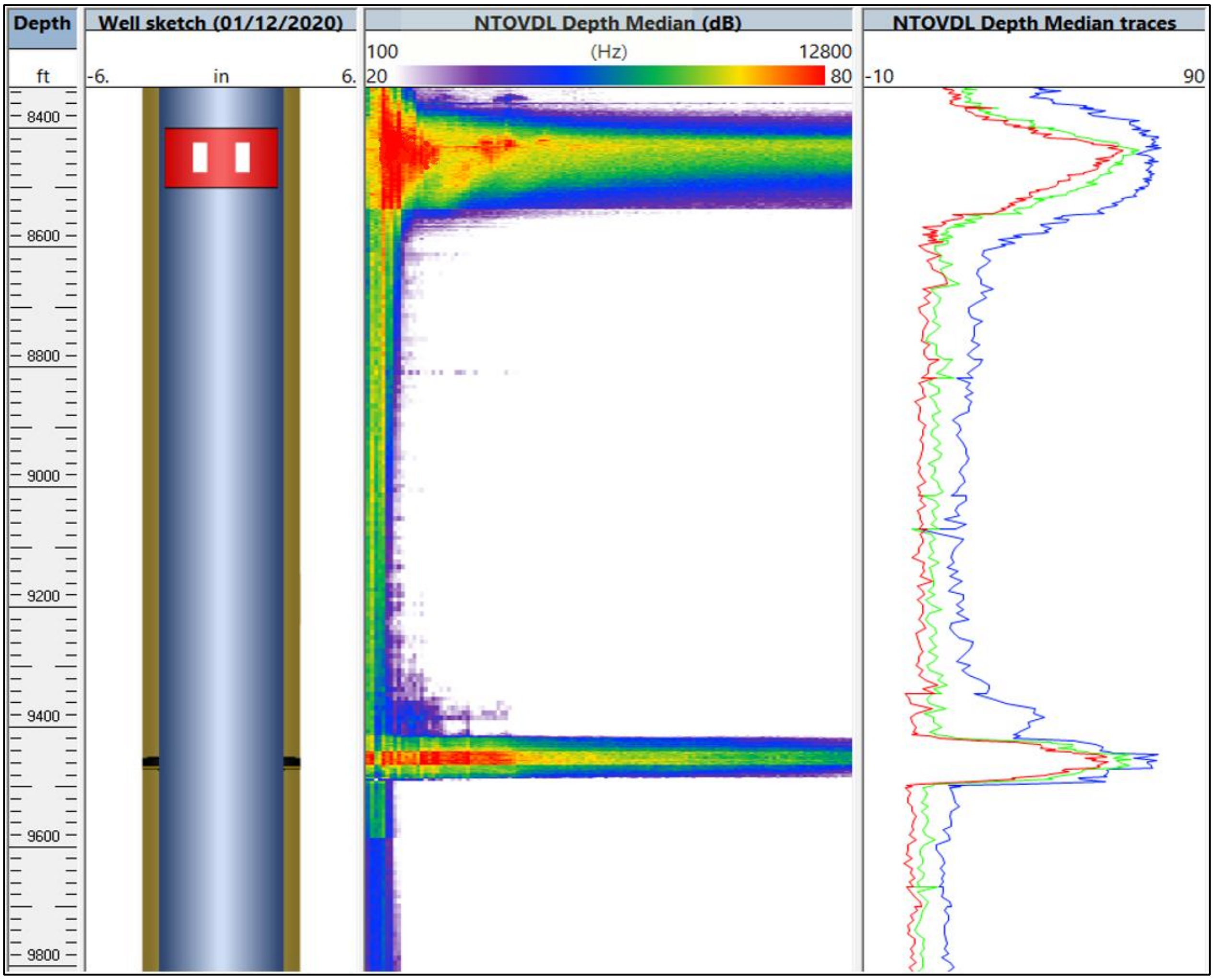

Fig. 9.D.4 – Flow through leaky swell packers

The three flow behind pipe cases that we have seen so far can not only have negative consequences on the well productivity, but also integrity concerns. Each part of the well is built to establish pressure isolation for any pressure of flow that the well will see during further drilling, completion, intervention, production and even during the well abandonment. Failure of one of these barriers may result in an integrity incident.

Figure 9.D.5 shows a schematic of multiple flow behind pipe mechanisms: cement channeling, leaky packers, sustained annular pressure, etc. Let’s imagine that sustained B annular pressure (behind the production casing) is detected. With tubing in place, direct access to the casing for MFC inspection would require a work over. However, noise logs can act as a through-barrier detection tool, provided that the noise amplitude at the leak is enough, and does not get too attenuated, to reach the receiver. Again, a through barrier diagnostic would typically require injection and annular bleeding.

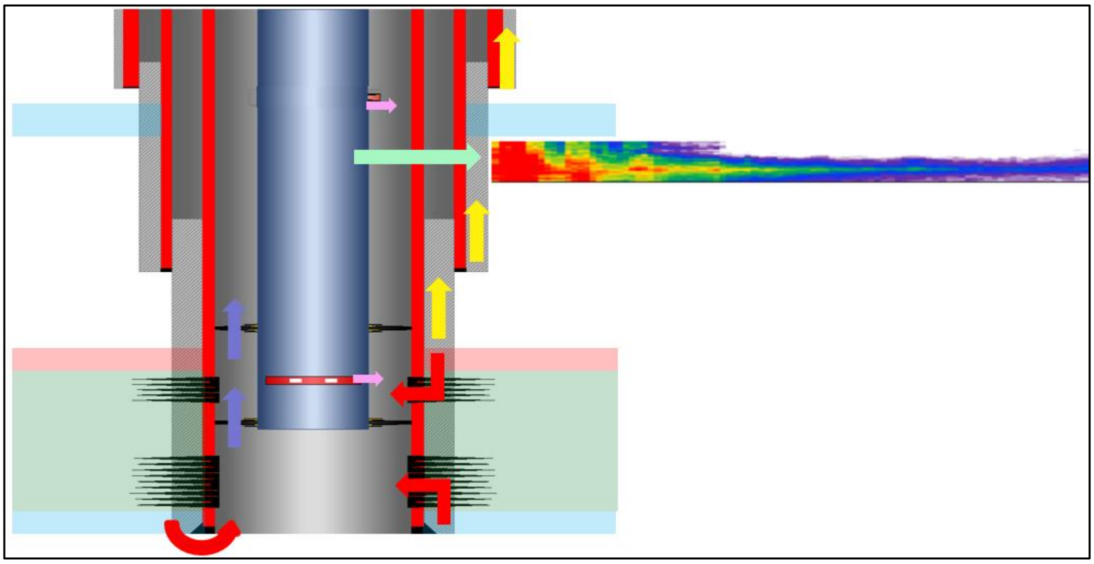

Fig. 9.D.5 – Schematic cases of flow behind pipe and multibarrier noise detection

9.D.3 Reservoir characterization

The noise data presented in Figure 9.D.3, not only shows cement channeling due to poor annular cement but also provides valuable reservoir information. First, further investigation on the causes of the lack of activity from the reservoir above the bottom one is required, as if these are put in production it could add more barrels of production. Therefore, understanding if the perforations are establishing hydraulic communication from the reservoir and whether a stimulation treatment would help, are part of the analysis that should be conducted. Secondly, the perforated interval is 36 m, producing interval (from PLT) is 30 m and thickness with reservoir activity is only 10 m. From a pressure transient analysis, we can obtain the total permeability-thickness product (KH), and therefore having an accurate reservoir thickness estimate is key to understand the permeability.

Another case from the same publication is presented in Figure 9.D.6. In this case, the cement logs (CBL-VDL-Impedance) show several bands of good isolation, and flow behind pipe is not expected. The noise log helps to refine the estimation of the producing thickness, which leads to a better understanding of the reservoir structure and a more accurate calculation of the commingled permeability.

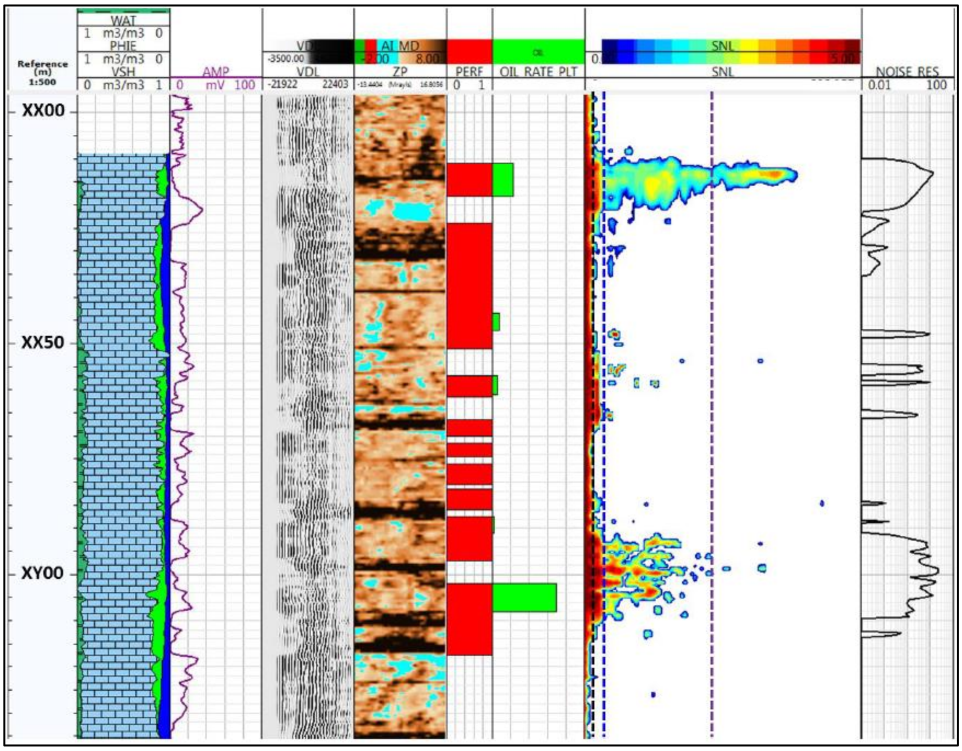

Fig. 9.D.6 – Image from 'Quantitative Spectral Analysis of Noise Log Measurements for Enhanced Dynamic Characterization of Complex Reservoirs' – Cicione, Galli, Pirrone and Raimondi – ENI S.p.A (presented at OMC 2017)

Apart from dealing with the total noise amplitude or energy, it is important to look at the frequency structure of the different contributions. The vertical dashed lines in the noise track correspond to the 1 (black), 2 (blue) and 10 (purple) kHz frequency cut-offs. The top perforation experiences high amplitude noise both, below and above 10 kHz, while the bottom perforation the frequency remains between 2 and 10 kHz.

As discussed in Section 9.C, the characteristic frequency depends on the scale of the turbulence (*l*), which in short has to do with the size of the conduits and obstacles that the flow encounters. In the borehole, the frequency peak is typically low (1 kHz), through leaks is slightly larger (see Figure 9.C.2) and in the reservoir, as the flow goes through pore-throats, the dominant frequency is shifted to larger values. Some publications suggest that flow through fractures and macropores would generate a peak at between 2 and 5/10 kHz, while matrix flow is in general higher than 10 kHz. The tighter the formation, the larger the frequency.

From this analysis it would be possible to conclude that the noise detected at the level of the bottom perforation is fracture-dominated, while for the upper perforation it would be possible to identify matrix flow (also seen in Figure 9.D.3). The authors of this study have integrated NMR, special core analysis and noise data to validate their conclusions.

Another reservoir application consists of estimating the relative contributions from different intervals, utilizing the normalized spectrum energy. In the case shown in Figure 9.D.7, the authors use a minimum frequency of 3.5 kHz to compute the total energy and focus on the reservoir contributions. The contribution percentages (first track from the right) are calculated based on the ratio of the peak energy to the total energy (second track from the right). Note that since the energy peaks correspond to reservoir response, the contributions are allocated directly to reservoir intervals, and not to the sliding sleeves shown in the well schematic.

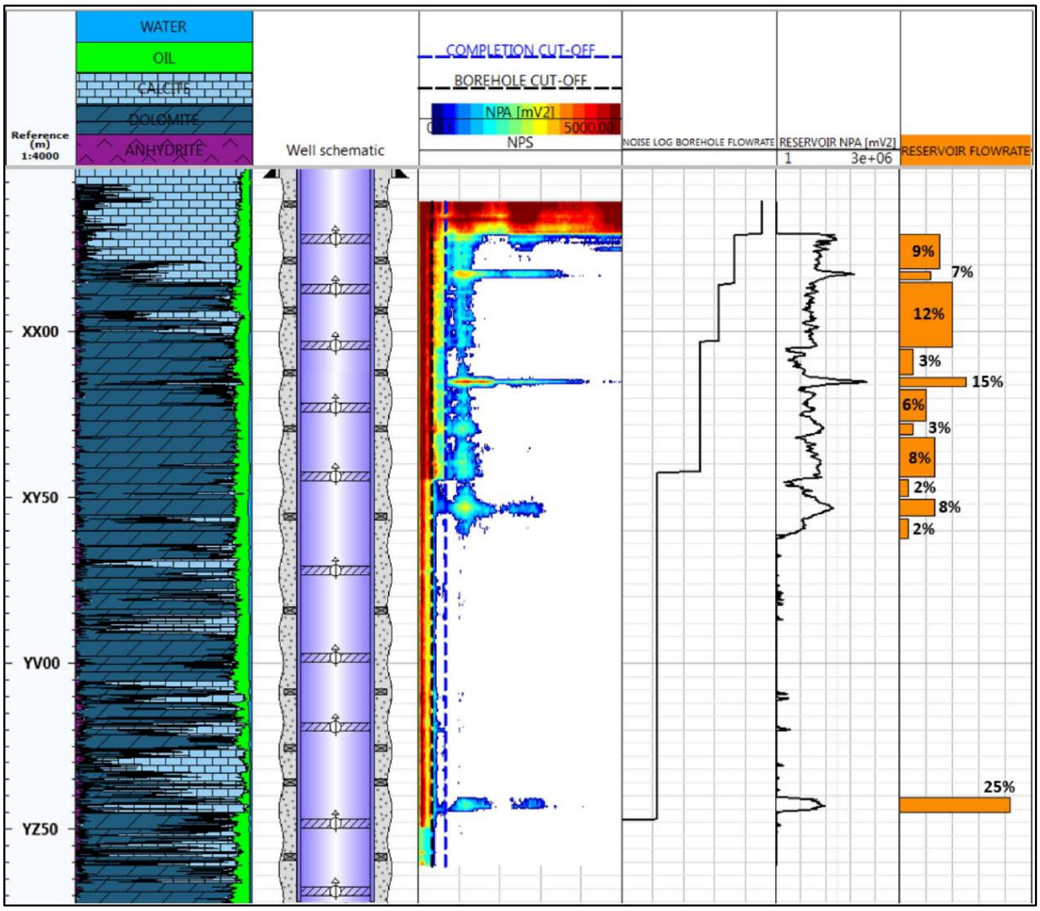

Fig. 9.D.7 – Image from 'Advanced Spectral Modeling of Noise Log Data: The Key for a Comprehensive Downhole Dynamic Characterization' – Rocco, Pirrone, Galli, Moriggi - SPE-193318-MS (presented at ADIPEC 2018)

In the cited publication in the figure above, the authors show a strong agreement with a PLT-based flow profile. As discussed in Section 9.C.2, this will be true for cases where the pressure gradients experienced by the different intervals are similar. The presence of very different lithology across the logged interval will be a challenge for this method. The presence of leaks or channels should be identified as these may not be significant to the total production but still can be of large amplitude.

9.D.4 Sand detection

Sand production is a common integrity and production concern in unconsolidated formations, but also can occur as a consequence of depletion (rock cohesion), excessive drawdown, and tends to be exacerbated when the water cut starts to increase. The acoustic response to sand production can be divided into two components:

- The direct impact of the sand on the detector or the pipe
- The characteristic sound of the fluid transporting the sand, with certain amplitude and frequency as it enters the pipe through a perforation, sand screen, etc.

As the fluid noise increases, and especially with low sand production rate, it can mask the sand impacts.

As mentioned in Section 9.C.3, a larger number of FFT per second increases the temporal resolution of the measured noise. Apart from looking at the averages calculated for a certain time window, the quantification of the transient spikes will be of importance for sand detection. This would allow to focus on the impacts and decrease (or remove) the noise generated by the fluid flow.

An example of sand production is presented in Figure 9.D.8. The well was completed with sliding sleeves and sand screens. A plug had been set on the nipple at the bottom of the tubing to test the integrity. While depressurizing the tubing fluid starts to flow and a well-defined leak in the tubing can be detected (Figure 9.D.8-left). Looking at the same dataset, but focusing on the transient spikes, the signature is completely different. It is not possible to perceive the presence of the tubing, but at the bottom of the log, we see the sand movement (hundreds of kHz region) behind the screens.

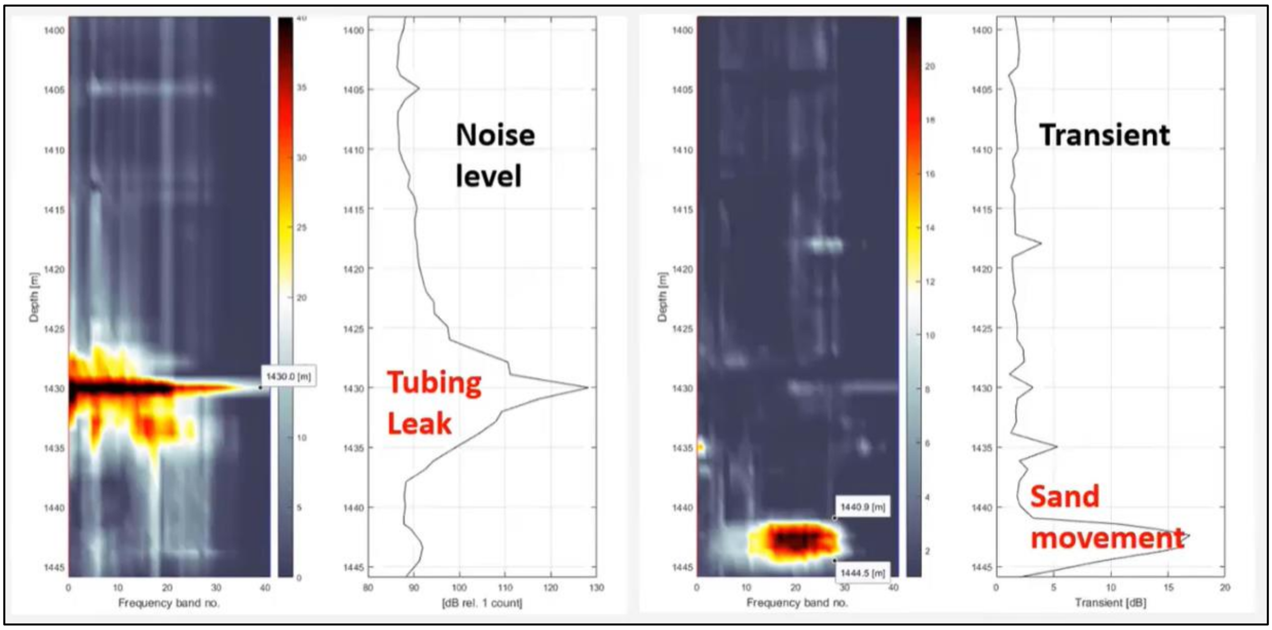

Fig. 9.D.8 – Sand detection behind tubing (Courtesy: Archer – VIVID^{TM})

9.E Other passive acoustic measurements

This section offers a brief introduction to sand detection probes and distributed acoustic sensing technologies.

9.E.1 Sand detection probes

As mentioned in Section 9.D.4, the impact of sand and other solids with a downhole tool or a pipe generates a sudden spike in the acoustic response. Through noise logging tools quantify this spike using an increased temporal resolution.

An alternative way to detect sand movement is to place a sensor that acts as an impact counter in the path of the flow. Figure 9.E.1 shows the tip of a sand detection probe by OpenField. In this case, the probe diameter is 1.6mm and can be incorporated as part of the FAST Production Logging tool.

A piezoelectric transducer sampled at high frequency detects voltage spikes, which allows you to quantify the counts per second. The current grain size limitation is 0.1 mm.

Note that as the measurement principle relies on direct impacts, in horizontal wells where the sand moves on the low side of the pipe, it may be necessary to add multiple detectors to increase the coverage and have a sensor on the low side despite the tool rotation.

Fig. 9.E.1 – Sand detection probe (Courtesy: OpenField Technology)

9.E.2 Distributed acoustic sensing (DAS)

The 'Thermal Analysis and Simulation' chapter provides an introduction to Distributed Temperature Sensing (DTS), where a laser pulse fired from a surface optoelectronic interrogator interacts with the structure of fiber optics. From the backscattered energy spectrum, the Raman Anti-Stokes and Stokes counts are used calculating the temperature as a function of the depth.

The same fiber optics can be used for Distributed Acoustic Sensing (DAS), to measure acoustic amplitude, phase and frequency along a fiber (images of fiber optics are shown in the Thermal chapter). The surface DAS interrogator (different than the one used for DTS) sends coherent laser pulses of very stable, narrow-band wavelengths, along the fiber. This technology is typically known as "Coherent Time-Optical Domain Refractometer" (C-OTDR). As the silica glass is not perfect, inside the fiber there are variations on the refractive index. When we pass a train of photons through the core of the fiber there will be Rayleigh scattering (same frequency as the incident light), and some of the light will travel back to the interrogator. Similar to DTS, the optical travel time (or time of flight) is used to map the depth of the returning light.

The pressure waves that generate the acoustic response along the well produce strain (microscopic compression or elongation) in the fiber, which causes variations in the backscattered pattern, mainly in the amplitude and phase difference.

DAS technology is currently used for a variety of downhole monitoring applications, including leak detection, hydraulic fracturing monitoring, interwell interference, seismic survey, and flow profiling.

The interrogator is fired typically 10000 per second but may reach higher frequencies (up to 15 kHz) in shorter fibers. The raw data collected by the DAS interrogator is a 3D array of acoustic power (dB) versus time and depth. Making an analogy with noise logs, it is like having thousands of sensors recording the waveform during a period of time. The size of the recorded data is huge, and in normal monitoring operations can lead to Gigabytes of data per second, and terabytes in the lapse of a day. One of the main challenges of DAS data is how to manage these volumes. Also, except for high noise events, minimum conclusions can be extracted from the raw data. Typical post processing includes moving to the frequency domain through Fast Fourier Transform and Frequency band extractions. Specific post-processing can be performed on DAS data to quantify the fluid velocity, as explained next.

9.E.2.a Speed of sound technique

The mechanisms of sound generation through flow-induced vibrations were reviewed in Section 9.B. In the case of pipe flow, the acoustic fluctuations may be of very low frequency and amplitude, thus difficult to detect by DAS. However, for other inflow types (perforations, ICDs, leaks), as the acoustic amplitude and frequency increase, there are better chances to quantify the noise. From the depth where the noise is generated, the acoustic wave can travel with the flow (c_u) or against the flow (c_d). These waves will lead to strain in the DAS, and this is processed as explained above. And as the DAS measures these fluctuations continuously along the well, the speed of sound can be calculated based on the time of flight.

Having acoustic data in the time domain and the frequency domain allows us to analyze the sound in the frequency-wavenumber (*f-k*) domain. This type of analysis is known as 2D FFT, and at every depth, obtain a plot like the one shown in Figure 9.E.2.

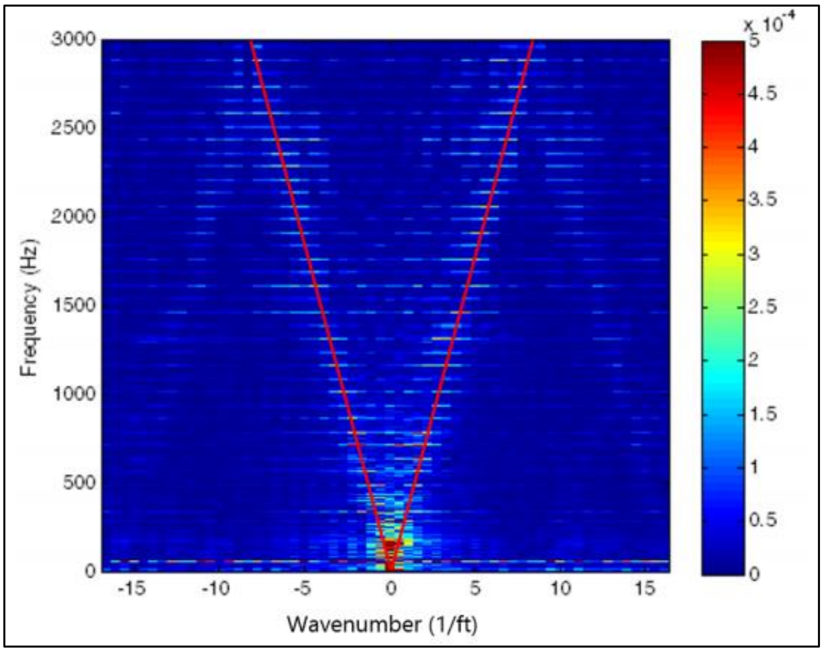

Fig. 9.E.2 – Frequency-wavenumber plot
(SPE 170679 - Abukhamsin & Horne, 2014)

The propagation speed of a wave, which in this case corresponds to the speed of sound, is calculated as the wavelength (λ) times the frequency (f). From the frequency-wavenumber plot obtain the upgoing and downgoing speeds of sound through this particular medium, as the slopes emanating from the origin of the f-k plot, since:

$$c_m = \lambda f = \frac{2\,\pi\,f}{k} = \frac{f}{\bar{v}}$$

Where k is the angular wavenumber and $\bar{v}$ is the wavenumber.

If the f-k analysis is repeated at multiple depths, we would end up with 2 continuous plots of the speed of sound versus depth, as shown in Figure 9.E.3. Finally, it is possible to compute the fluid velocity (and phase rate if we know the pipe diameter) based on the Doppler effect principle and the way a frequency is perceived by a static observation point, in the cases of the acoustic wave moving towards or away from the observer. The mixture velocity can be calculated as:

$$v_m = \frac{1}{2}(c_u - c_d)$$

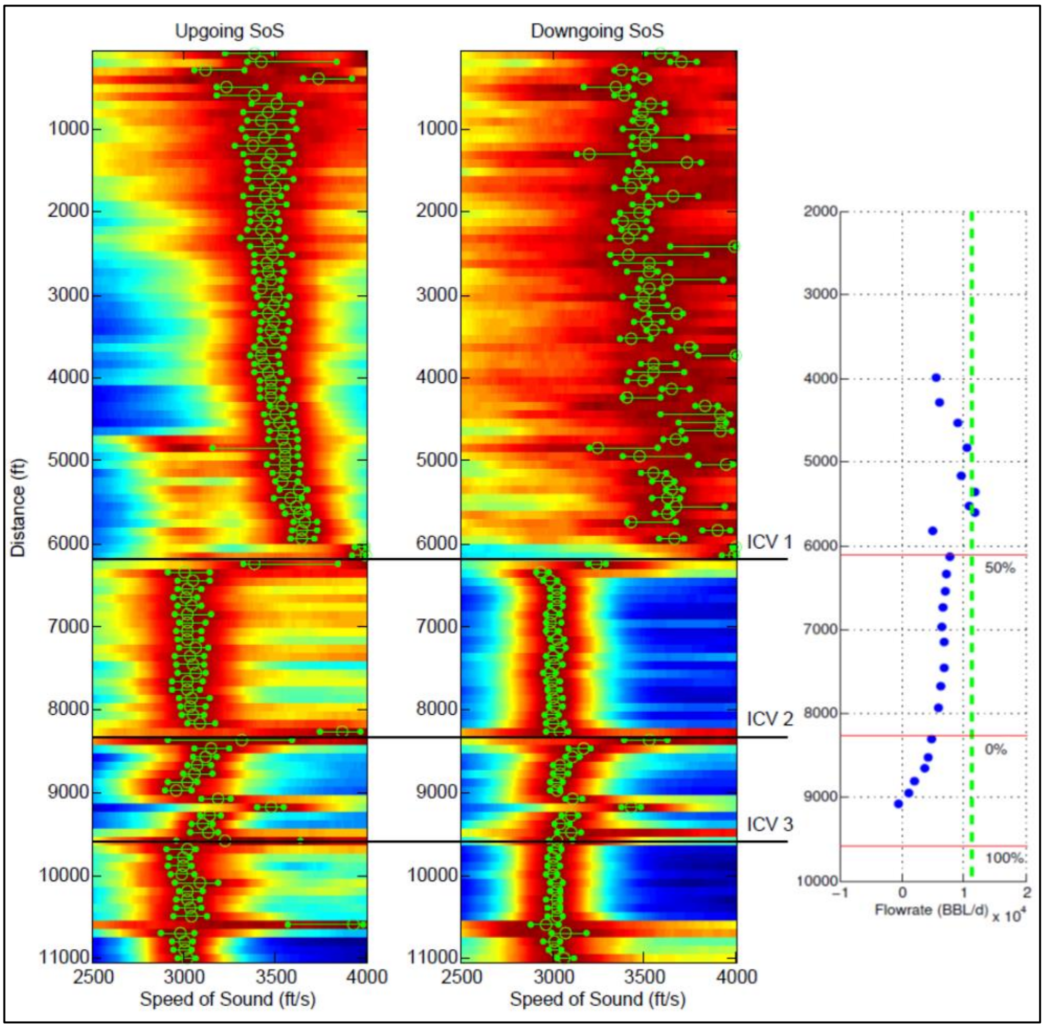

Fig. 9.E.3 – Speed of sound and flow rate calculation
(SPE 170679 - Abukhamsin & Horne, 2014)

The log on the right of Figure 9.E.3 shows the computed flow rate for a single-phase oil produced, based on the procedure explained before. It also shows the use of fluid mixing models to obtain the holdups in a multiphase situation.

10 – Cement Evaluation

10.A Introduction

Primary cementing is a key operation during well construction, consisting of placing cement in the annulus between the casing and the formation. After curing, a successful cement placement should provide:

1. Zonal isolation: If the well intersects reservoirs with different fluids (gas, oil, water), or these are at different pressures, then zonal isolation is vital for production control. This is also applicable for intermediate casings, as they may be in contact with overpressured zones, lost circulation zones, etc.
2. Casing protection: Avoids the external casing surface to contact formation fluids, which may be corrosive. Also, cement may reduce plastic deformation by certain formations.
3. Borehole support: The formation may cave in, especially in unconsolidated formations.
4. Casing tension support: The cement in place will provide axial support for the cemented casing and other strings that may be run (i.e., liner).
5. Environmental protection: Especially for the surface casing, the cement protects surface freshwater formations.

Failure of the primary cement isolation can cause many problems, going from the production of undesired fluids, accelerated corrosion, mechanical failure of the completion, contamination of shallow water formations, etc. In some cases, it would be possible to perform a secondary cementing, or a squeeze, to try to repair one of these undesired situations.

When running a cement evaluation log, the final user (operator) typically tries to understand if there is hydraulic isolation along the measured interval. And if not, would it be possible to perform a secondary cement job?

This chapter presents the principle of the two most common cement evaluation techniques: Sonic tools (CBL, VDL, and segmented receivers) presented in Section 10.B, and Ultrasonic tools (rotating head and pad tools) in Section 10.C. Finally, Section 10.D shows the tool response for several common scenarios. This final section also demonstrates the use of flags to determine zones of different degrees of isolation.

This introduction should be considered as a warning on the relevance of the evaluation of cement logs and the possible severe consequences of misinterpretation. One of the most catastrophic environmental disasters recently suffered by the industry (the Gulf of Mexico, 2010) was caused by lack of annular isolation, even though a cement log was not run afterward. The reader should always refer to local and company regulations and standards. It is crucial to remember that none of these techniques measure the hydraulic seal directly. Instead, this is determined by analysing acoustic signals after interacting with different media and having received a number of processing and conditioning steps at the logging unit. The log's quality is influenced by the degree of the cement curing, centralization of the tool, calibration, and other parameters discussed in the chapter.

Note that this Chapter will focus on conventional sonic tools to evaluate the annular fill. In other chapters, we will review the use of passive acoustic (noise logs) and temperature measurements to evaluate the possibility of fluid movement behind pipe due to lack of cement or channeling.

10.B Sonic tools

Sonic tools are active acoustic logging tools, which emit pulses of acoustic energy in the sonic range, typically between 15 and 30 kHz. Different configurations are available in the market, some of them incorporating multiple receivers. This topic starts from the conventional CBL-VDL.

The earliest version of the Cement Bond Log (CBL) tool goes back to 1960 (SPE-1512), where the authors noted that "the amplitude of a sound signal after it has traveled in a firmly cemented pipe is only a fraction of that recorded by the same device in free pipe." This is a short but powerful summary of the technique.

The first versions of the CBL tool had only one receiver. Quickly the benefits of adding a second receiver were realized, and the tool architecture and dimensions became the standard.

The CBL tool contains an omni-directional piezoelectric transmitter crystal, which generates an acoustic pulse in response to an electric excitation (typically ~20 kHz). The pulse propagates through the different media and travels at a characteristic velocity.

Two piezoelectric receiver crystals are present:

- At 3 ft: from where we will obtain the CBL amplitude (or E1) and transit time. Note that in the conventional CBL tool, this receiver is also omnidirectional, but in Section 10.B.3, it will be shown that this can be segmented and therefore is azimuthal
- At 5 ft: from where we will obtain the VDL

As shown in Figure 10.B.2, the tool housing contains slotted sleeves, which prevent the direct transmission of the sound from the transmitter to the receiver.

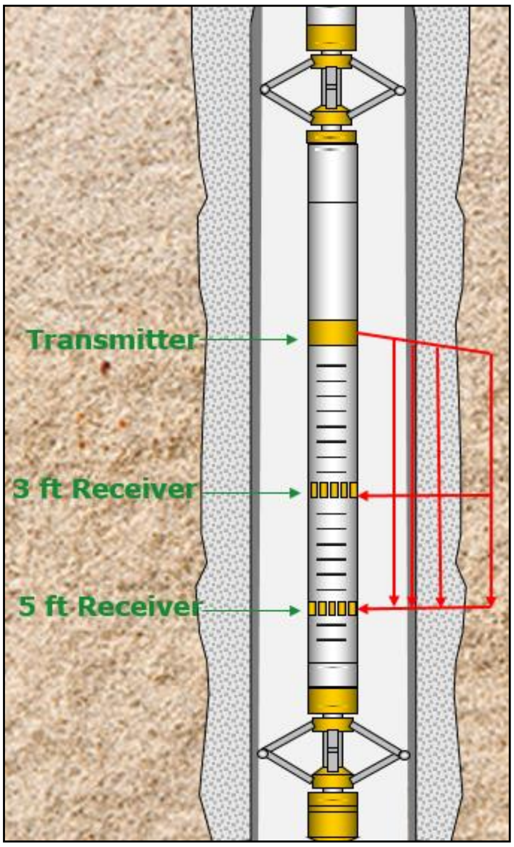

Fig. 10.B.1 – Schematic CBL tool

Fig. 10.B.2 – Slotted sleeves on CBL housing (Courtesy: Probe RADii)

Cement tools must be run centralized, as we will see later. The tool OD is larger than other cased hole tools (i.e., 2 ¾'', 3 1/7'') but there are "slim" tools of 1 11/16''. Different providers offer both surface readout and memory mode. As with any other Cased Hole Log, gamma-ray and CCL are necessary for depth control purposes.

Pre-job workshop calibration of sonic tools is recommended. The centralized tool is put in a free pipe (not bonded) of known ID, and the 3 ft receiver amplitude is measured (more on this in Section 10.B.2). The measured amplitude is compared to a reference value, and a gain may be applied.

The signal measured at the receivers takes different paths to reach its destination. Initially, from the transmitter, it radiates in all directions as compressional waves and starts traveling through the fluid. When the wave hits the casing ID, part will be refracted according to Snell's law:

$$\frac{V_1}{\sin \alpha_1} = \frac{V_2}{\sin \alpha_2}$$

At a specific angle of incidence (critical angle), the acoustic wave is refracted parallel to the casing, as a pressure pulse called "Lamb" wave.

The part of the wave transmitted will propagate to the cement and finally to the formation. Figure 10.B.3 shows the waveform response to the individual travel paths and the composite signal that would be measured at the receivers. The composite shows that the first arrival corresponds to the casing. Typically, and excepting fast formations, the formation comes next (although the acoustic velocity may be higher than the casing, the path is longer). From the composite, it is generally difficult to identify the cement arrivals overwhelmed by the formation. Finally, the slower propagation of the waves corresponds to the ones through the borehole fluid.

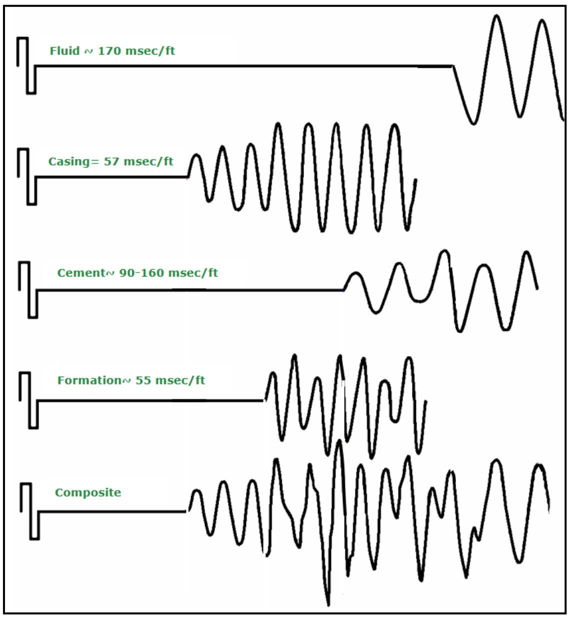

Fig. 10.B.3 – Waveform response through different media

The sonic signal arriving at both receivers are conditioned and digitalized. These waveforms are generally stored in memory or transmitted to surface. Two different processes are conducted for the 3 ft and 5 ft receiver, as explained in the next two sections.

10.B.1 CBL

The arriving waveform at the 3 ft receiver, at any depth, looks like the one shown in Figure 10.B.4. We now understand that the first part corresponds to the casing arrivals. The attenuation of these arrivals is primarily due to the shear coupling of the material behind casing, which is higher in a good bonding condition. This is because the cement has a higher impedance (5-7 MRayls) than the fluids (1.5 – 3 Mrayls). The transmission coefficient at an interface between two materials is given by:

$$T = \frac{2\,Z_2}{(Z_2 + Z_1)}$$

One of the materials (Z_1) is the casing steel, with an impedance of 46 Mrayl. It is simple to prove that the cement behind casing leads to a transmission coefficient 3 times higher than typical drilling fluids or cement slurries. Therefore, good annular cement allows the acoustic energy to dissipate into the formation, contributing to the decrease in amplitude of the signal traveling through the casing leading to attenuation. A value is required to quantify this attenuation.

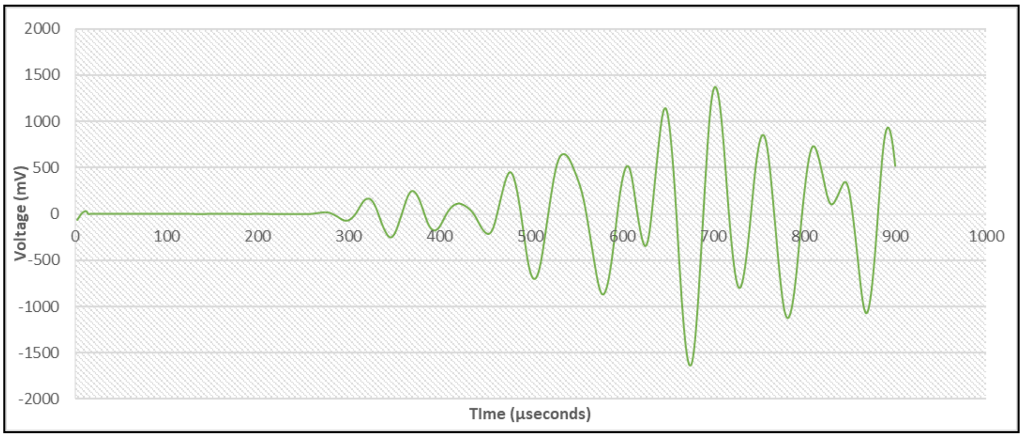

Fig. 10.B.4 – Waveform at 3ft receiver

The amplitude of the first positive peak (known as E1 peak) is called the CBL, 3 ft Amplitude or E1 amplitude. It is measured in mV and it provides an indication of the level of bonding between the pipe and cement. A free pipe scenario results in the largest possible CBL amplitude (no shear support), and a fully bonded pipe with good quality cement leads to the minimum CBL amplitude.

Another parameter extracted from the 3 ft receiver is the "Transit time", with units of microseconds (µsec). This is the time it takes the signal to travel from the transmitter to the E1 arrival.

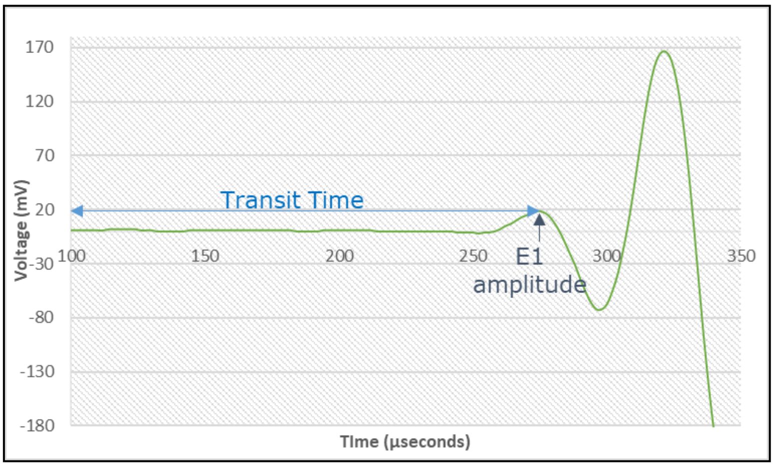

Fig. 10.B.5 – CBL and Transit Time definition

If the sound speed in the borehole fluid and casing is known, then the transit time from the transmitter to the receiver can be easily calculated as $(Pipe\ ID - Tool\ OD) * v_{fl} + 3ft * v_{casing}$. Charts of expected transit times are available for tools and pipes of different sizes. Note that for this equation to be valid, the tool must be centralized in the pipe. If the tool is eccentric, then the E1 arrival will reach the receiver earlier. This can be used as a QC parameter for identifying eccentricity.

To quantify the amplitude of E1 and the transit time, "gates" are set in the logging acquisition system. These can be time gates (i.e., 170 – 370 µsec), or can also be triggered when the waveform reaches a minimum amplitude value (i.e., 5 mV). This is a crucial step that can affect the validity of the log. As can be deducted from the transit time equation, a time gating will be valid for a constant pipe size and no (or very small) eccentricity. A necessary quality check is required to verify if E1 falls in the predefined gates at a certain depth. If not, it is possible to reset the gates and extract the CBL amplitude, provided that the waveforms are still available. If an amplitude gate is used, and the E1 amplitude is smaller than this, the CBL will wrongly show the amplitude of the following peak (called E3) at that depth. This situation is called 'cycle skip'.

The analysis of the waveforms measured at the 3 ft receiver leads to a continuous vs. depth CBL and TT log as shown in Figure 10.B.6 for a 9 5/8'' pipe. At the top of the log, the amplitude is around 53 mV which corresponds to free pipe. Below 8640 ft, the amplitude starts to decrease and reaches a minimum of around 5 mV at 8790 ft. Later it will be shown how to interpret this data qualitatively, but for now, it can be established that the top of cement (TOC) is around 8640 ft, and below this depth, the bonding may go from poor to good. The CCL is also displayed to demonstrate that the presence of connections affects the measurements.

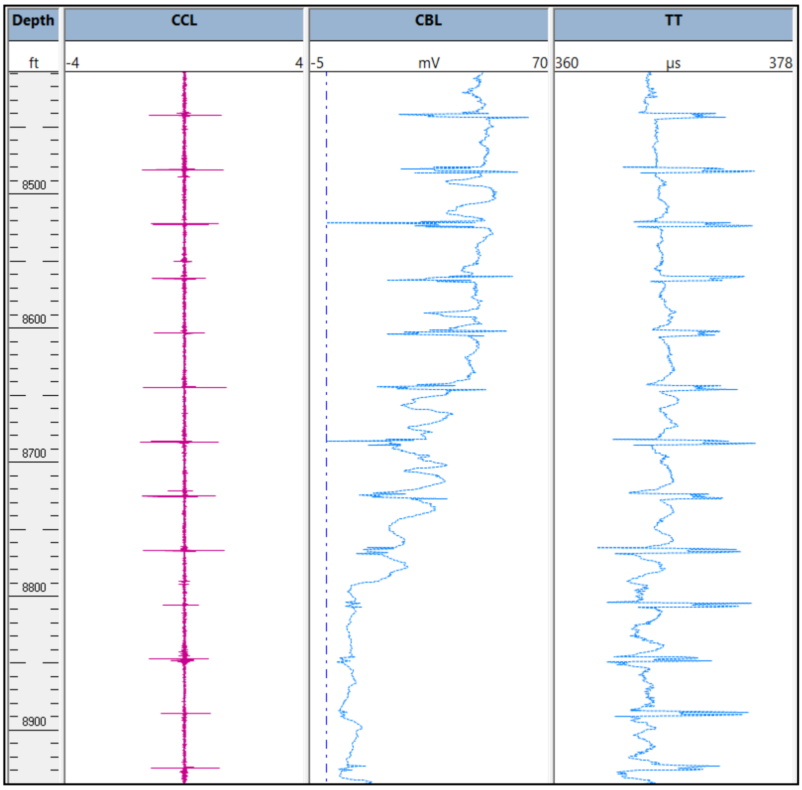

Fig. 10.B.6 – CBL and Transit Time definition

When possible, during the cement logging operation, it is recommended to log a free pipe interval and compare this value to the expected amplitude and transit time for the pipe-tool combination. This will indicate if the tool is properly calibrated, the level of eccentricity, and gating.

10.B.1.a Attenuation and Bond Index

The attenuation is a value that relates the amplitude damping over a certain distance, which in this case of interest is 3 ft (transmitter to receiver). It has units of dB/ft (or dB/m) and can be calculated as:

$$Attenuation\ (z) = \frac{20}{d}\log(\frac{CBL(z)}{A_0})$$

Where *d* is 3 ft and A_0 is the amplitude signal at the transmitter, which is typically approximated as the free pipe amplitude. Attenuation is commonly used instead of amplitude, as the latter is influenced by casing size, fluid type, transducer resolution, etc.

For certain casing sizes and tool types, the CBL attenuation depends on two factors: the surface area of the pipe with actual bonding, and the quality of the cement, expressed as the Cement compressional strength. The conventional CBL has no azimuthal capabilities and cannot distinguish between these two factors.

If the pipe circumferential coverage is 100%, then the CBL amplitude can be related to the cement compressive strength. Service companies may offer nomograms, as shown in Figure 10.B.7, which are tool-dependent and are obtained with the tool immersed in certain fluid types (typically freshwater).

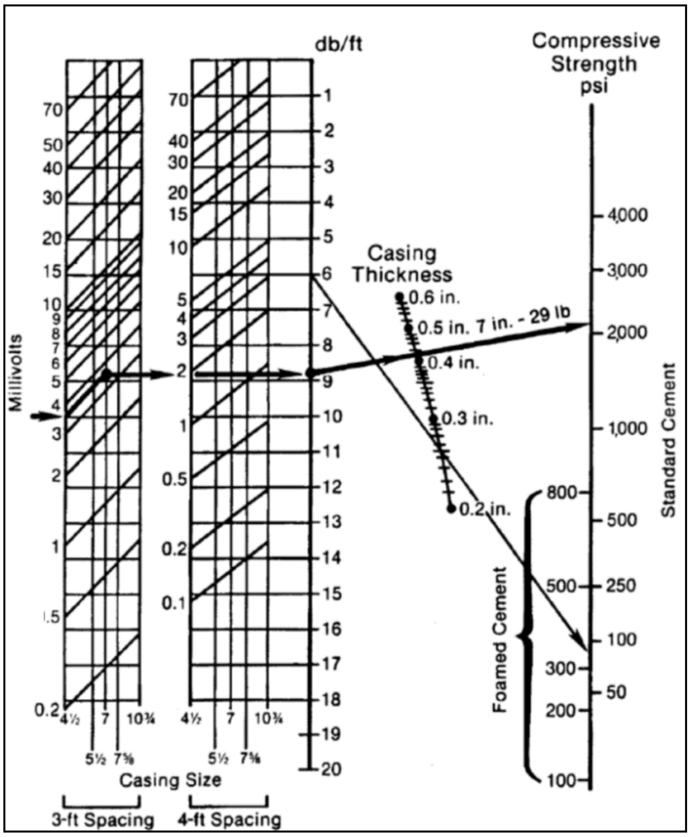

Fig. 10.B.7 – CBL nomogram (Courtesy: Schlumberger)

FAQ 1: How are attenuation and compressive strength related?

Pardue et al. derived the following expression for the attenuation of a steel plate acoustically coupled to material of different properties and infinite thickness:

$$Attenuation\ [dB/ft] = \frac{52.2\left(\frac{\rho_{cement}}{\rho_{steel}}\right)\frac{1}{t}}{\left[\left(\frac{V_{plate}}{V_p}\right)^2 - 1\right]^{-0.5} + \left[\left(\frac{V_{plate}}{V_s}\right)^2 - 1\right]^{0.5}}$$

Where V_p and V_s are the compressional and shear wave velocities in the cement, V_{plate} is the Lamb wave velocity in the steel, and *t* is the casing thickness.

The cement's compressional strength is a function of its shear modulus, and the shear wave velocity is also a function of the shear modulus (see FAQ 2). Therefore, attenuation and compressional strength are related via shear wave velocity. Attenuation also increases with cement density.

The nomograms offered by the different tool providers experimentally show this relationship. Cement mechanical properties were tested under controlled conditions, and the acoustic response for different casing sizes was also measured. Combining the two separate tests forms the type of charts presented in Figure 10.B.7.

Pardue also shows that for cement sheath thickness larger than 0.75'', the attenuation does not increase further, noting that above this thickness, the cement can be considered 'infinite'.

The other factor affecting the cement attenuation is the circumferential coverage. Assuming that the compressive strength is homogenous around the pipe, then the CBL amplitude can be related with the percentage of the bonded pipe, through the concept of Bond Index:

$$Bond\ Index\ (z) = \frac{Attenuation\ (z)}{Attenuation\ well\ bonded} = \frac{log\ (\frac{CBL\ (z)}{free\ pipe})}{log\ (\frac{100\%}{free\ pipe})}$$

A Bond Index of 1 corresponds to a casing with 100% of circumferential coverage, with a cement of a CBL value as entered for the *100%* input of the above equation. Historically, it was considered that a value of 0.8 provides reasonable assurance of isolation if it extends over a certain length. This implied that the cement isolation could not be perfect everywhere, with 20% of the circumference (72°) not bonded, as the channels will not necessarily be connected over the interval suggested for each pipe.

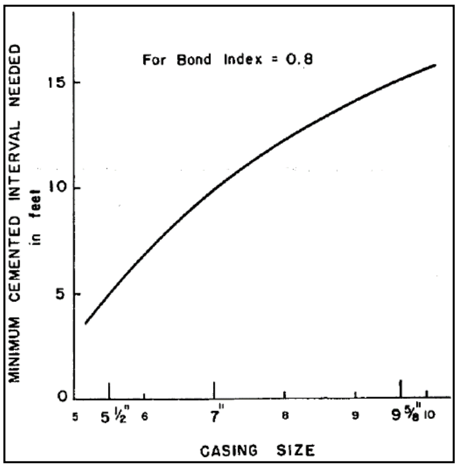

Fig. 10.B.8 – Cemented interval for different casing sizes

Note that even though this criterion has been widely applied in the industry, it does not necessarily meet local regulations or standards. For example, NORSOK D-010 establishes that to use the annular cement as part of the barrier for a permanent P&A, a minimum length of 100 m is required.

The tool manufacturers typically provide tables of free pipe amplitude, transit time, and bonded amplitude, for different casing sizes. As shown below, the free pipe amplitude decreases with the pipe OD, as the signal is more attenuated by the borehole fluid as it travels from and to the tool. Also, the transit time decreases with the pipe weight due to a smaller acoustic path. The bonded amplitude is inversely proportional to the casing thickness, as predicted by Pardue’s derivation of the attenuation.

OD (in)	Free Pipe Amplitude (mV)	Weight (lb/ft)	Transit time (µsec)	Bonded Amplitude (mV)
5	77	15	203	1.0
		18	201	2.4
		21	199	4.0
9 5/8	51.3	43.5	277	2.55
		47	276	3.0
		53	274	4.5

These tables and derived nomograms are tool-dependent and were obtained for certain borehole fluid and cement types. They must be used with caution.

10.B.1.b Limitations

The CBL amplitude and the bond index are used extensively in the industry. Unfortunately, these two values are often abused, and wells that are supposed to be properly isolated end up suffering from annular pressure. Before deciding based on a CBL, ensure:

- The CBL is measured correctly: Verify the tool gating and the surface/downhole calibration (free pipe amplitude). Look for cycle skip as an increase in transit time.
- The tool is centralized: The CBL amplitude drops with the level of eccentricity. For example, a 0.5″ eccentricity leads to a 70% drop in the amplitude. This can have severe consequences when computing the BI or choosing intervals with different degrees of bonding. This is exacerbated if the eccentricity varies with depth, as can occur if the deviation is not constant along the logged interval.

As opposed to MFC interpretations, there are no corrections for tool eccentricity in this type of measurement.

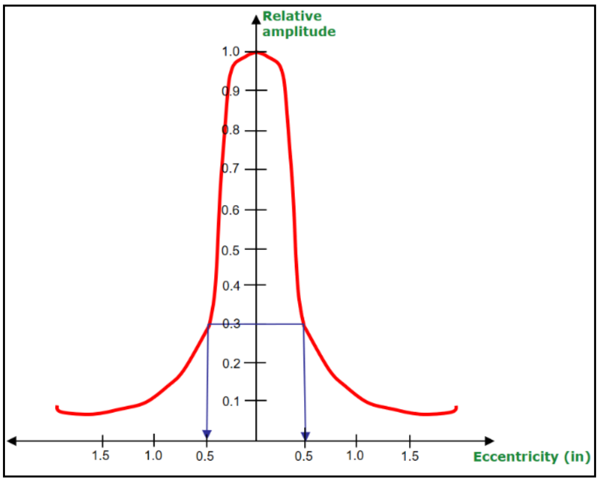

Fig. 10.B.9 – Tool eccentricity and amplitude

For conventional CBL tools, the only indication of eccentricity will be a reduction in the transit time.

- The compressive strength does not change along the measured interval: The attenuation is related to the cement compressive strength. Suppose throughout the log there are changes in cement quality (i.e., lead and tail cement), contamination, varying temperature effects, etc. In that case, the CBL amplitude cannot be used directly to compare different zones. Moreover, the concept of Bond Index assumes that the only variable is the circumferential coverage, which is not true for scenarios where the compressive strength varies with depth.
- There is no microannulus: A small separation between the pipe and cement may occur due to contraction of the casing. The microannulus may be filled with gas or liquid, and either will alter the transmission coefficient, making the acoustic energy not able to dissipate to the formation. Microannulus will appear as a free pipe but there may be relatively good isolation. If microannulus is suspected, the log may be run with the pipe under pressure. (see Section 10.D.5)
- The log does not include fast formations: It is assumed that the first arrival of the waveform corresponds to the casing, as shown in Figure 10.B.3. If the sounds through the formation are higher than in the casing, then the formation arrivals will be detected first. Formations faster than steel include Dolomite (43.5 msec/ft) and Limestone (47.5 msec/ft). This will lead to a variable transit time and amplitude. (see Section 10.D.7)
- To calculate the bond index, it is necessary to estimate the maximum attenuation given by the CBL amplitude of a section 100% bonded. The common approach is to use the minimum measured amplitude over the interval. This does not guarantee that this section will be 100% bonded. Relatively low amplitude of 6 mV may be the case of a good cement of 3 mV, which has small channels.

It is not always possible to find a section of the well with good bond, and in that case, it might be necessary to use charts. These were developed under controlled lab conditions that may not replicate the real scenario found downhole.

- Time since the cement job: The compressional strength of the cement increases with the curing time, and typically (for non-contaminated slurries), it reaches 90% of the maximum in around 72 hrs. Therefore, standards and local regulations recommend a minimum curing time before running the cement log. This recommendation is not always followed, as it may increase the rig time. Running a log while the cement is curing will result in poorer measured properties than the final cured cement.

10.B.2 VDL

At the 5 ft receiver, the acoustic waveform is digitalized and recorded. While in the 3 ft receiver, only the portion between certain time gate is used (hopefully the E1 arrival), the 5 ft waveform is displayed, and no further processing is applied. This leads to a 3D array of data: amplitude vs. time vs. depth. We would face some issues trying to display this on paper. Therefore, the waveform arrivals at the 5 ft receiver are shown in the well-known, Variable Density Log, or VDL. Typically, only the data between 200 and 1200 µsec from the pulse firing is displayed. Figure 10.B.10 shows a typical VDL from and 2 waveform extractions. A white-to-black color scale (grayscale) is used, and the standard is to display only the positive part of the waveform. White corresponds to zero or negative, and the darker the color, the higher the amplitude.

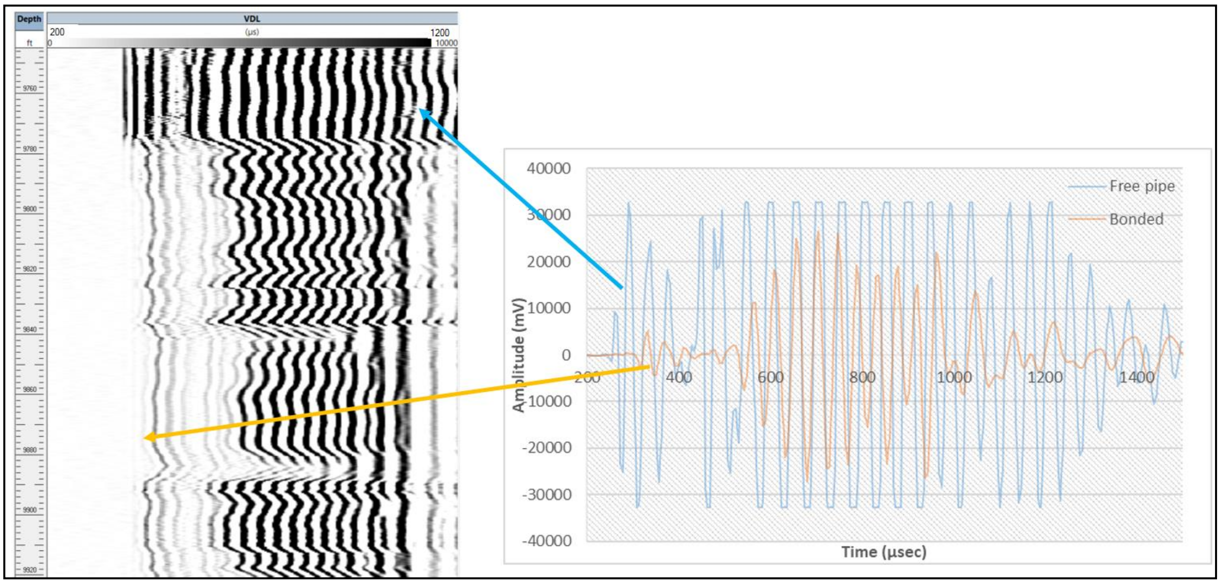

Fig. 10.B.10 – VDL plot

The VDL shown in Figure 10.B.10 includes a free-pipe interval at the top of the log (above 9775 m). This section is characterized by practically parallel black and white lines. The waveform extraction at this depth (blue) shows high amplitude waveforms that exhibit periodicity and reach the measurements' dynamic range. In this interval, due to the lack of annular cement, which leads to very little transmission of acoustic energy to the formation, the sound waves travel down to the receiver through the pipe wall, with the maximum ringing.

Below this, there is good bonding. With this color scale, the first two arrivals that correspond to the casing are not seen. However, the casing arrivals are still there and at the same time, as can be seen in the orange waveform. The first part of the waveform is very attenuated as the pipe is not able to vibrate freely. After a certain period, the formation arrivals are detected, characterized by the zigzag arrivals. Finally, the mud arrivals are detected.

FAQ 2: Why the formation arrivals show a zigzag pattern?

The time for the wave to arrive at the receiver is determined by the path distance and the acoustic velocity. The part of the acoustic burst that has traveled through the formation has propagated as compressional and shear waves, with velocities given by:

$$v_c = \sqrt{\frac{Y}{\rho}} \; v_s = \sqrt{\frac{\mu}{\rho}}$$

Where Y is the Young modulus, μ is the shear modulus, and ρ is the density.

This dependency with the formation properties has been widely exploited in open hole logging, initially relating the compressional velocity (or slowness) with the porosity. Later, it uses these measurements to characterize lithology and mechanical properties.

The formation arrivals show a zigzag pattern as the acoustic velocity is not constant due to the changing properties and lithology. The acoustic path may change with more or less cement, creeping formations, caves, etc.

In general: the VDL plot will allow us to see the arrivals from:

- Casing: Strong casing arrivals are bad news as they indicate low levels of bonding. These arrivals will be received at:

$$TT_{casing} = V_f * csgID + V_{csg} * 5ft$$

- Formation: Not going to be clearly seen in regions of free pipe. Note that the CBL and the VDL may indicate relatively good pipe to cement bonding, but no evidence of formation arrivals in the VDL. Therefore, the formation arrivals tell us about the cement to formation bonding. These arrivals will be received at:

$$TT_{formation} = V_f * csgID + V_{csg} * (csgOD - csgID) + V_{formation} * 5ft$$

The formation arrivals may be quicker than the casing if $V_{formation} > V_{csg}$, which occurs in fast formations.

- Borehole fluid: The last to be detected due to the slow acoustic propagation velocity:

$$TT_{casing} = V_{fluid} * 5ft$$

Section 10.D will go deeper into the interpretation of this log and combine it with other measurements. So far, it can be concluded that:

- The CBL provides information of the CASING-TO-CEMENT BOND through its amplitude, BI, or attenuation, with the limitations numbered before.
- The VDL also provides this information, although it is difficult to quantify from an image. The unique information that this log provides is the determination of formation arrivals. The VDL offers information of the CEMENT-TO-FORMATION BOND.

10.B.3 Segmented receivers

A big limitation of the conventional CBL-VDL is the lack of azimuthal capability. A high CBL amplitude may not distinguish between a contaminated cement with lower compressional strength or the presence of voids (or channels) behind the casing.

To solve this issue, radial bond tools were developed. Their architecture is similar to conventional CBL-VDL tools, with one piezoelectric transmitter emitting bursts of ~20 kHz sound waves. The difference lies in their 3 ft receiver, which consists of a radial piezoelectric crystal assembly instead of a single element, with 6 or 8 transducers. The signal received by each radial transducer is digitalized, which allows computing the oriented amplitude and transit time. The 5 ft receiver is not azimuthal and records the VDL waveform. Other tools incorporate an extra 2 ft radial receiver, apart from the 3 and 5 ft omnidirectional.

These tools' benefits become evident in the image below for a 7 in casing (expected free pipe amplitude of ~60 mV). The first track shows the CBL amplitude calculated as an average of the 8 sectors, shown in the second track. The average CBL amplitude away from the connections is between 8 and 20 mV, and the VDL is not conclusive. If there was only the CBL-VDL it would be difficult to properly diagnose what this amplitude is showing.

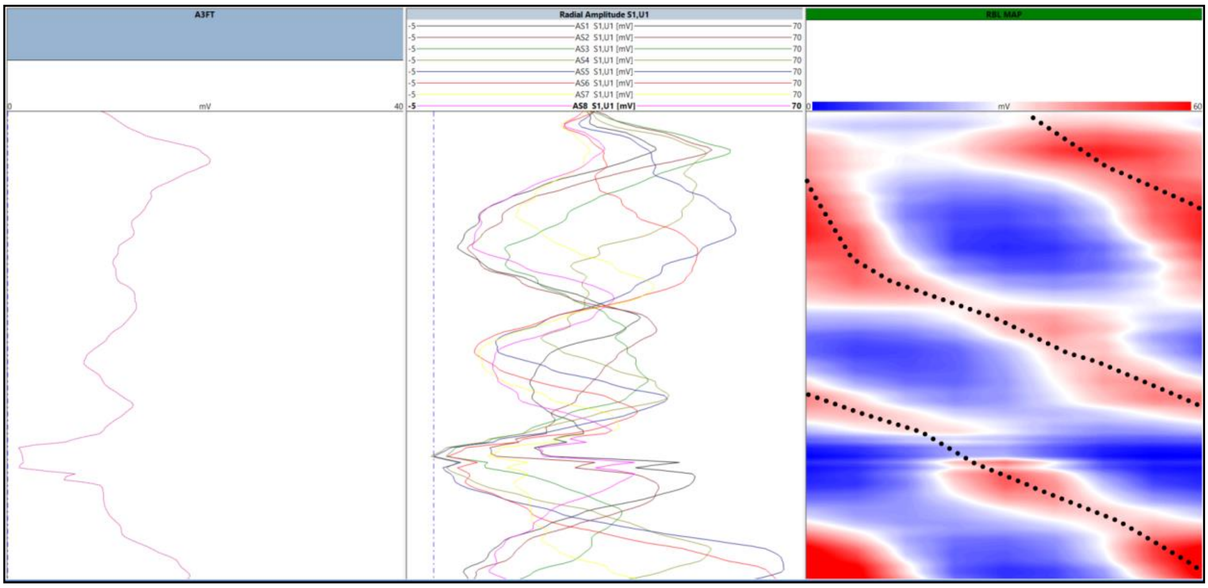

Fig. 10.B.11 – Average and radial response of sonic tools

The third track shows the cement amplitude map where it is possible to see connected intervals of poor bonding (in red). Over this log, the whole cross-sectional amplitude only becomes small at the connection, which is an artifact. It can be concluded that there is around 50 m of connected channels of no cement behind casing marked in black dotted lines. At every depth, the channel is detected by at least 1 sector, corresponding to a 45 degrees opening. The spiraling is due to tool rotation as the tool is pulled out of the hole. If the same image is displayed accounting for relative bearing at any depth, it would be possible to see the amplitude distribution displayed in Figure 10.B.12, with the minimum at the top and the maximum at the bottom of the cross section. We will see next to why this happens.

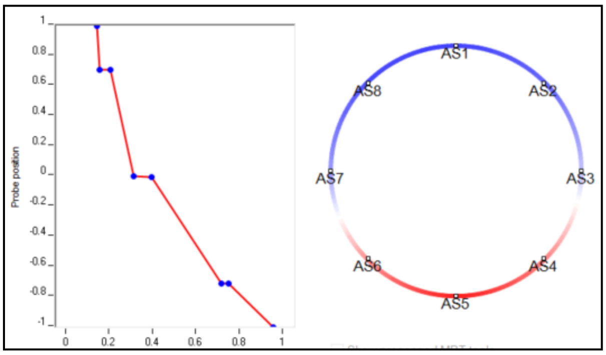

Fig. 10.B.12 – Cross-section of the sectors amplitude

FAQ 3: What causes channeling?

When a well is cemented, the objective is to completely fill the annular space between the pipe and the formation with a cement of certain compressional strength. This is not always achieved, and parts of the annular section are not filled with cement, which leads to voids or channels through where the fluids can flow over long distances behind the casing, responding to a pressure gradient. Note that it is accepted that cement channels may exist over short periods, and provided that there is at least a small channel-free interval between two zones, they will be hydraulically isolated.

A typical cause of cement channeling in deviated wells is due to the reduced standoff of the pipe with respect to the formation, as the casing tends to lie on the low side of the hole. The cement filling will occur preferentially on the high side of the cross section, where the cement can access more easily. Publications show that the highest incidence of channels occurs in the 30° to 60° region of well deviation. Centralizers can be used to achieve a better annular filling.

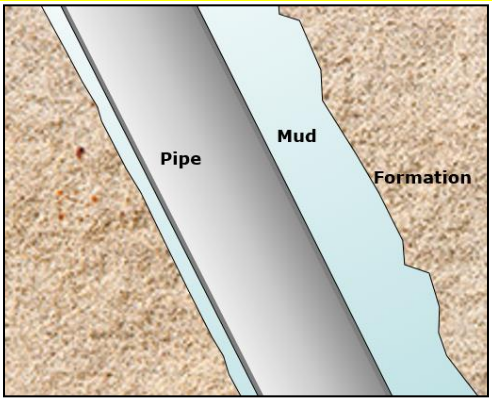

Fig. 10.B.13 – Eccentric casing and uneven annular filling

Other causes include gas migration into the annulus as the cement starts to cure, pipe rotation and reciprocation, inability to displace mud from around the pipe, etc. These factors will create channels with different morphology, some of them in contact with the pipe, others in contact with the formation, some looking like a high porosity material. The channels that are not in direct contact with the pipe will prove challenging to detect unless they are very large.

Another important feature of the radial tools is the segmented transit time that allows to diagnose tool eccentricity, which is detrimental to the measurement quality. A perfectly centralized tool would lead to equal transit times in all sectors. As the eccentricity increases, the transit time of the sector closest to the pipe decreases, and the one in the opposite direction will increase. This analysis can be aided with the use of the relative bearing to understand where the different sectors are located. Recall Figure 10.B.9 and the dramatic effect of the eccentricity on the amplitude. This analysis can help indicate whether a low amplitude in one sector has a good bond or is an artifact due to eccentricity.

Fig. 10.B.14 – Tool eccentricity effect on transit time

10.C Ultrasonic tools

As the name suggests, ultrasonic tools operate at higher frequencies than sonic tools, typically in the order of 200-700 kHz. These tools are sometimes called Pulse-Echo or acoustic televiewer. They can be used for pipe integrity and acoustic borehole images, apart from the topic that will be focused on next, cement evaluation. Ultrasonic tools provide an effective acoustic impedance of the annular material behind the casing with large azimuthal resolution. This section will show how the impedance is measured and its value in terms of cement (and hopefully isolation) quality.

10.C.1 Tool description

Modern ultrasonic tools contain a single piezoelectric transducer that provides 360° coverage by means of a rotating head or rotating mirror that collimates the acoustic beam. The transducer acts as both transmitter and receiver. For each measurement azimuth, the transducer fires an ultrasonic pulse by applying a voltage pulse across the piezoelectric ceramic. The transducer goes into receiver mode, recording the returning waveform after multiple interactions as described below.

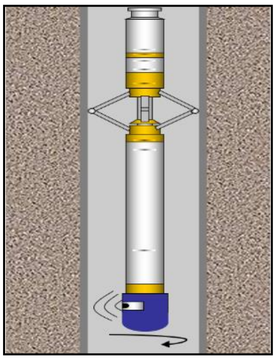

Fig. 10.C.1 – Rotating head ultrasonic tools

Fig. 10.C.2 – CAST-XR Ultrasonic tool with rotating head (Courtesy: Halliburton)

The firing-listening cycle is repeated many times per revolution, providing an azimuthal resolution which, allows to create array images or maps of the various modes of measurement. Early models of the rotating head tool typically fired around 18 times per revolution. Later they went up to 36 and 72 times. With the latter, it is possible to get an angular resolution of 5 degrees. The head typically rotates around 6-8 times per second. In the case of tools with a rotating mirror, up to 12 revolutions per second have been reported.

Different sizes of rotating subs are available, depending on the ID of the casing to be measured. The sub OD ranges between 3” and 9’’.

For reasons that will be explained later in Section 10.C.2, the calculation of the cement impedance requires knowledge of the borehole fluid acoustic impedance at downhole pressure and temperature. This is done in situ by pointing the transducer to the inside of the tool, where the signal is reflected off a target plate at a known distance. The fluid properties are measured at stations along the well or sometimes continuously during the down pass. This will create a log of impedance and fluid velocity versus depth.

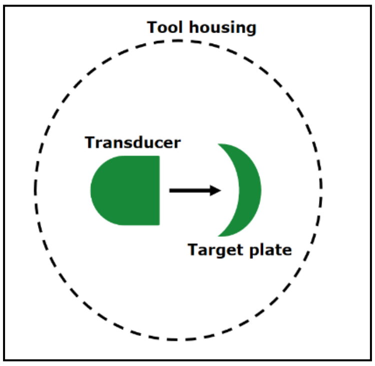

Fig. 10.C.3 – Fluids property measurement

The waveform received at each azimuth is digitalized and presented versus depth. Figure 10.C.4 shows the waveform at one azimuth out of 72 measured directions. This means that there will be another 71 of these plots. The waveform is displayed as a typical VDL plot, and the amplitude versus time can be displayed at any depth. The tool includes a relative bearing or a 3-axis accelerometers, so the measurement can be oriented.

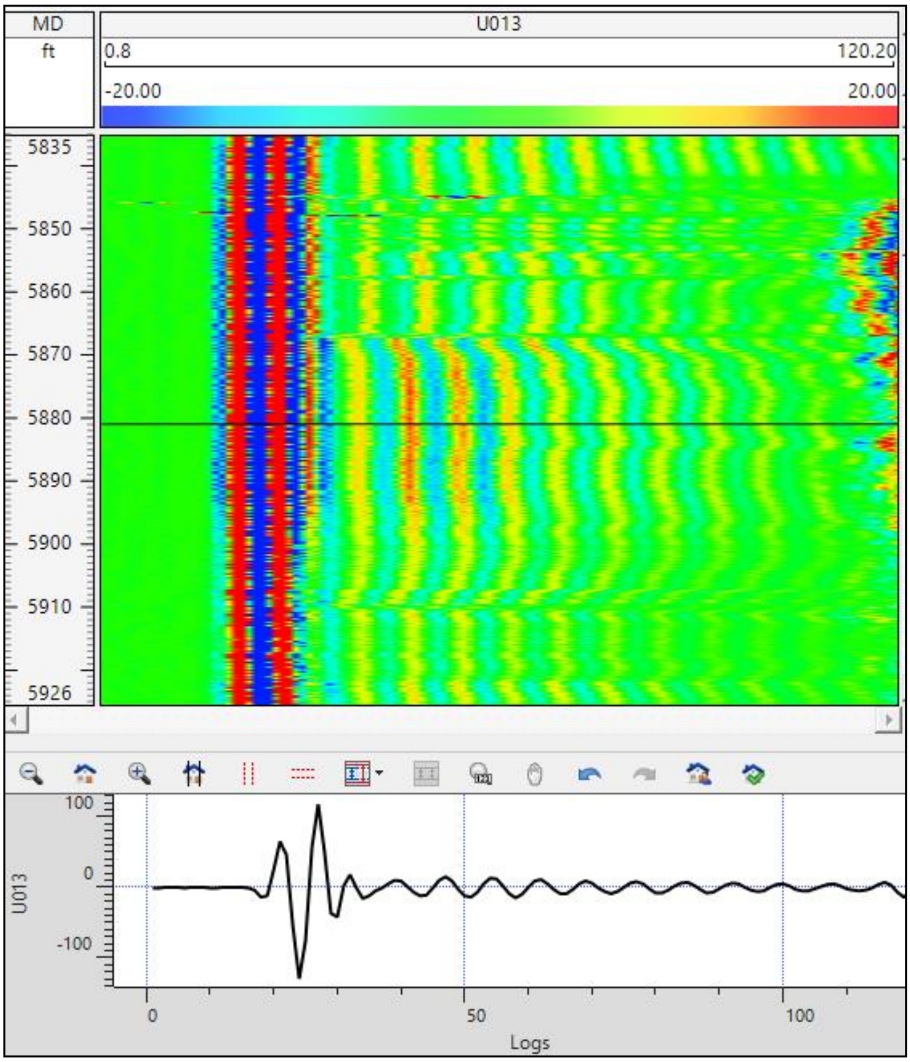

Fig. 10.C.4 – Waveform arrivals at 1 azimuth (out of 72)

10.C.2 Ultrasonic propagation

The shape of the waveform arrivals reveals information about the casing integrity and cement and is generated due to several interactions summarized in the image below:

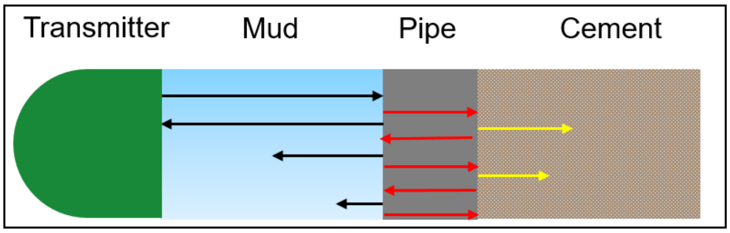

Fig. 10.C.5 – Acoustic interactions with the different materials

At every interface between two different media, part of the acoustic signal is transmitted, and part is reflected, given by the acoustic impedance of each material. The transmission (T) and reflection (R) coefficients are calculated as:

$$R = \frac{(Z_2 - Z_1)}{(Z_2 + Z_1)} \qquad T = \frac{2\,Z_2}{(Z_2 + Z_1)}$$

Acoustic impedance is calculated as the product of the density times the sound velocity in the media. The units are called Rayleigh (1 Rayl = 1 gr * m^{-2} * sec^{-1}) are typically referred to in Mega Rayleigh, or simply Mrayl. Some relevant values are shown below:

Media	Density (g/cc)	Velocity (m/sec)	Acoustic Impedance (Mrayl)
Casing (steel)	7.8	5900	46
Water	1	1500	1.5
Air	0.0013-0.13	330	0.004 – 0.04
Drilling mud	1 – 2	1300 - 1800	1.5 – 3
Class G Cement	1.9	2700 – 3700	5 – 7
Light Cement	1.4	2200 - 2600	3.1 – 3.6

So let’s now analyze the different interactions shown in Figure 10.C.5:

- **First interface: Borehole fluid – Pipe**

Using the acoustic impedance values from the table above, we can see that most of the wave will be reflected. For water, R is 94% and for mud is a minimum of 90%. The main parameter obtained from this interface is the transit time, which is a direct indication of the distance between the transmitter and the pipe. This is treated in the MFC chapter, as it can be used as a source of radius like a mechanical multifinger caliper.

- **Second interface: Pipe – Annular material**

The fraction of acoustic energy that made it to the pipe undergoes transmissions and reflections with the media behind the casing which hopefully is cement, but may be liquid or gas. The pipe 'resonates', (vibrates at a certain characteristic frequency), depending on the material, shape, etc. The casing will not resonate forever in response to a short ultrasonic pulse, as it is damped by the material surrounding the pipe (inner and outer). The ratio of the initial energy of a resonator to the energy dissipated in each cycle is given by a dimensionless parameter called Quality Factor, or Q Factor. A higher Q Factor means that the system resonates strongly, while a low Q factor implies the opposite. If the acoustic properties of the borehole fluid (measured by the tool) are known, then the measured dampening can be related to the impedance of the annular fill. This is shown schematically in Figure 10.C.6, for two cases: water is both inside the casing and the annular (green), and water is inside the casing and cement in the annular (red).

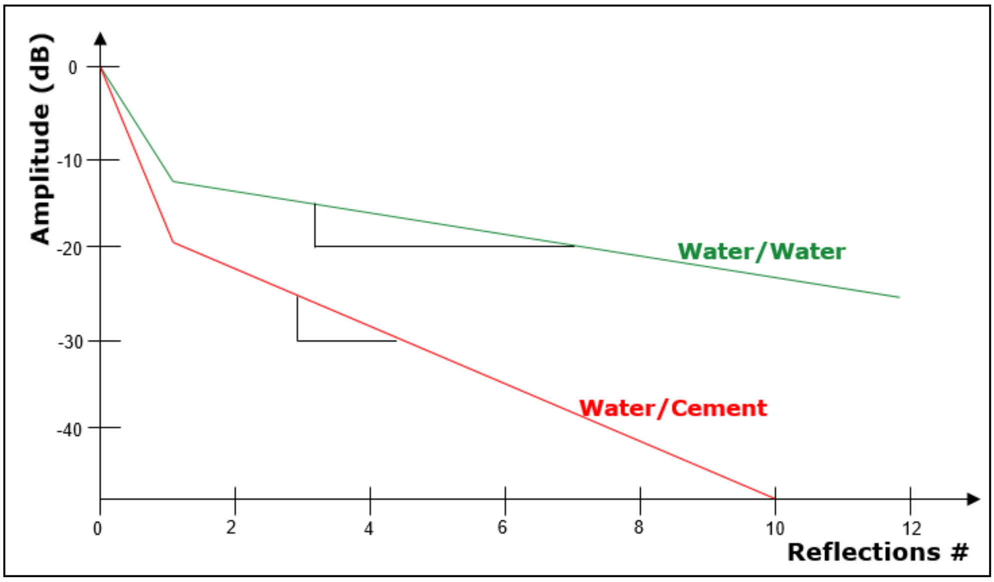

Fig. 10.C.6 – Amplitude vs number of reflections at casing/annular interface

The decay rate is sensitive to the material in the annular. The calculation of the impedance from the waveform is beyond the scope of this Chapter. In summary it consists of taking the data to the frequency domain through Fast Fourier Transform, and applying an inversion process that leverages the decay of the mode resonance and relates it with the acoustic impedance, using a 1D compressional wave (plane wave) model. The acoustic impedance of the mud is required, and errors tend to be amplified during the inversion.

In short, at every azimuth, the tool will provide a value of the acoustic impedance of the annular material. The pipe thickness is also calculated from the resonant frequency.

- **Third interface: Annular material – Formation**

The amplitude of the signal reaching the formation is very low, especially in the presence of cement. Formation reflections are detected at the receiver, but in practical cases, these are not used for quantitative purposes. In general, it is not possible to evaluate the cement to formation bond as done with the VDL. Formation interference will cause 'Galaxy patterns', explained in Section 10.D.7.

Figure 10.C.7 summarizes the interactions and data extracted from the multiple ultrasonic interactions:

- Pipe radius: from transit time to the first arrival
- Pipe surface rugosity: from the amplitude of the first arrival
- Pipe thickness: from resonance frequency
- Cement impedance: from decay in the signal

Fig. 10.C.7 – Summary of ultrasonic interactions

All these results are azimuthal and output as array datasets (measurements vs. angle vs. depth). As shown in the image below, there are radius, thickness, and impedance maps. Statistical values are obtained for each map and displayed as logs: minimum, maximum, and average.

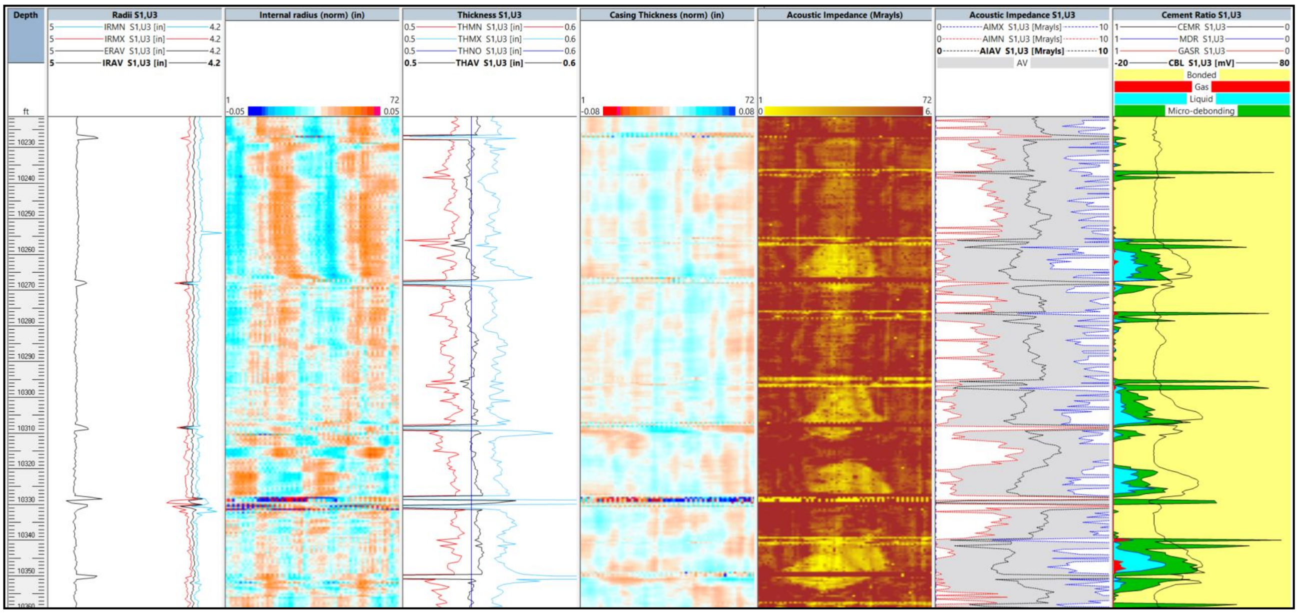

Fig. 10.C.8 – Presentation of ultrasonic logs

The next section will deal with the analysis of the impedance data to determine the characteristics of the annular material.

10.C.3 Impedance analysis

The impedance of common materials was presented in the table in Section 10.C.2. This table shows that values lower than 0.3 Mrayl indicate gas, between 1.5 and 3 Mrayls indicate liquid, and the impedance of set Class G cement is between 5 and 7 Mrayls. This suggests setting impedance thresholds differentiates between the different materials. Some tools output a cement ratio map, which presents for every depth the ratio of gas, liquid, and cement readings, as a function of the total number of azimuths, as shown in the last track of Figure 10.C.8. For example, if 60 azimuths out of 72 measured values higher than the cement threshold, then the cement ratio would be 83%. Recalling the definition of bond index, both refer to the same, providing the cement quality is good.

Schlumberger ultrasonic tools include an algorithm that classifies patches of low impedance cement as 'micro-debonded' cement. This is based on comparing the acoustic impedance at a certain depth and azimuth, with the values along the same depth, azimuth, and diagonals. If the standard deviation is larger than a certain threshold, then the local value is deemed locally debonded.

The impedance of light cements (3.1-3.6 Mrayls) is very similar to mud, leading to a low contrast between the two. This is a limitation of these type of tools, and a new methodology called Flexural attenuation has been developed to overcome this problem.

It is important to remember that the cement property obtained through ultrasonic tools is the impedance and not the compressive strength. Going back to light cements, they may have similar compressive strength to Class G cement, however, its impedance is much smaller. When analysing a light cement using a 7 Mrayls impedance as the benchmark, it may be observed that there is no cement behind pipe and wrongly recommend remedial cementing.

The analyst should know beforehand the expected cement impedance to be found in the well for both the lead and tail. This is given by the cement type and is a function of the curing time. It is convenient to know the maximum theoretical top of the cement (again for both lead and tail) based on cement volumes pumped.

10.C.4 Pad tools

This type of segmented tools typically comprises six or eight pads in contact with the casing through spring-loaded centralizers. Each pad includes a piezoelectric transmitter and receiver, with approximately 1 ft separation. As the pads are in contact with the casing, these tools are practically insensitive to borehole fluids effects as the signal does not propagate through this media. This is advantageous when logging in heavy muds (high signal attenuation) or gas-cut fluids (very low impedance). The typical maximum casing size is 16'', but the tool may also be extended to 24''. Compared to other tools in the market, provided that the pads are still in contact with the casing, the measurements are not affected by eccentricity. Due to the transmitter and receiver's short spacing, the tool is not affected by fast formations.

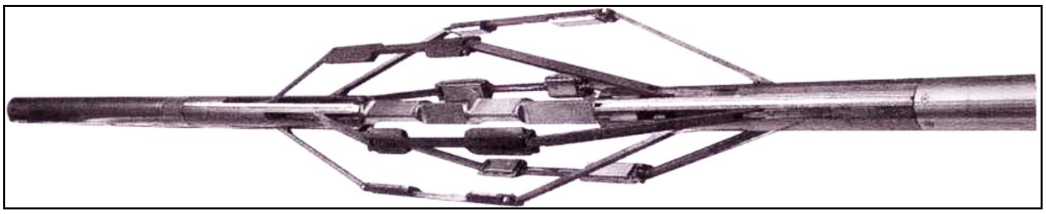

Fig. 10.C.9 – SBT (Courtesy: Baker Hughes)

For every receiver, the tool outputs an attenuation rate (dB/ft). The transmitters are fired in sequence, in such a way that the signal propagates through the casing and becomes the first arrival to the adjacent received. A schematic of this arrangement is shown in Figure 10.C.10. The attenuation reported for each pad is an average of the different transmitter-receiver interactions.

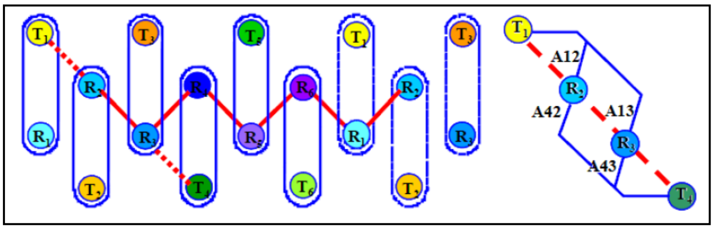

Fig. 10.C.10 – SBT pads configuration

It is common practice to run these tools in tandem with conventional CBL-VDL. A typical log is shown in Figure 10.C.11, which includes the attenuation rate for each pad, attenuation map, and VDL. There is an interval with large attenuation in all pads at the top of the log, no casing arrivals, and wavy formation signal in the VDL, which characterizes a good cement. There is free pipe segment characterized by minimum attenuation and strong casing arrivals in the VDL.

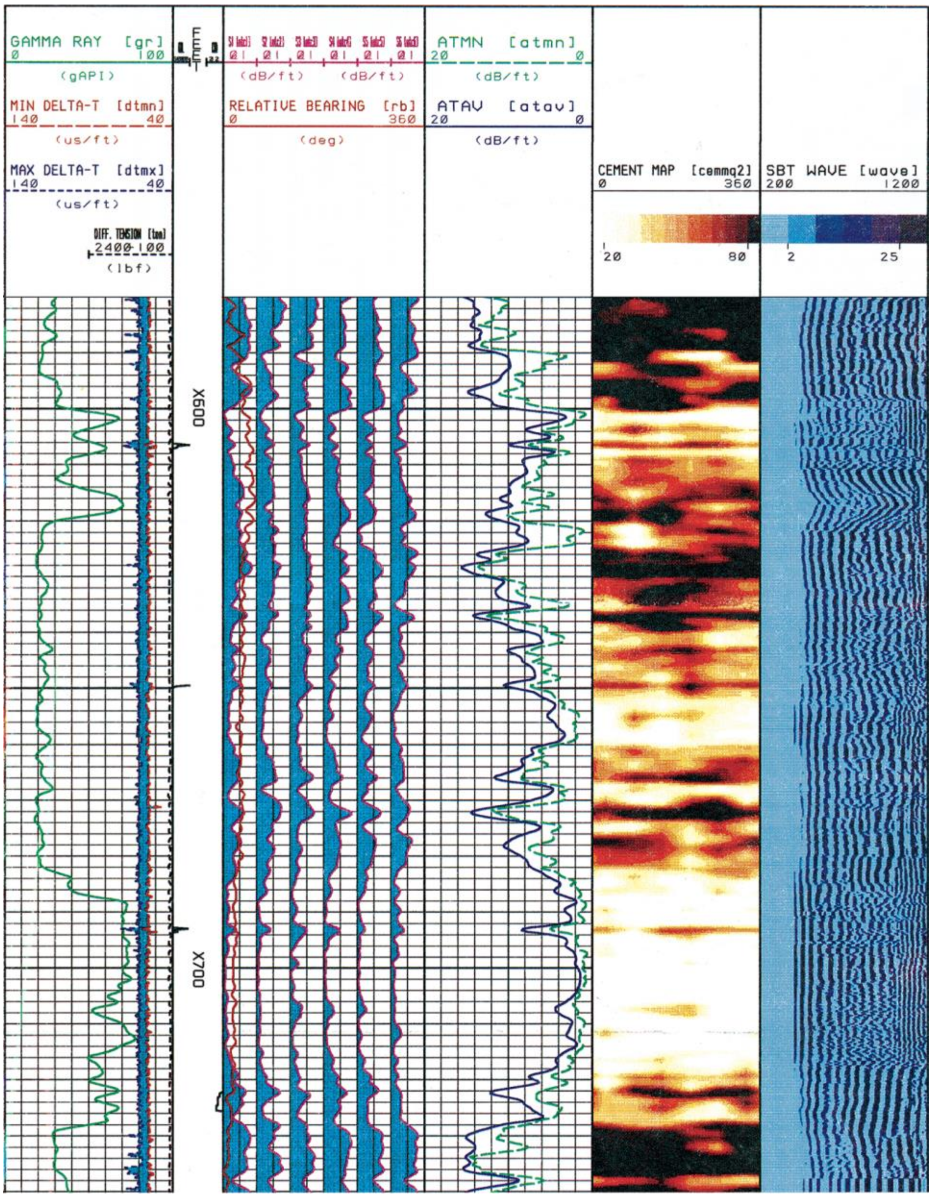

Fig. 10.C.11 – SBT log presentation (Courtesy: Baker Hughes)

10.D Interpretation

The interpretation of common scenarios is presented in sections 10.D.1 to 10.D.7. These are based on qualitative and quantitative considerations. Section 10.D.8 demonstrates the use of flags to establish the isolation potential based on all the available logs and user thresholds.

10.D.1 Bad cement

Figure 10.D.2 shows an interval where no hydraulic isolation is expected. The casing size is 9 5/8'' (53.5 lb/ft) with an expected free pipe amplitude of 51.3 mV. A cement Class G (1.9 GTTTZ) was used, with 5.6 Mrayls of expected acoustic impedance. The horizontal red dashed line divides the log into two regions with different levels of bad cement. The upper part is behaving like free pipe, while the lower part shows characteristics of slightly better cement, yet not enough to achieve isolation.

A summary of the measurements displayed in Figure 10.D.2 is presented below:

- **CBL:** Goes from the expected free pipe amplitude at the top of the log to a minimum of 28 mV (excluding connections), meaning that the casing still rings loudly. At this stage, it would not be possible to obtain a BI as the value for good bonding is unknown.
- **VDL:** Below the red line, formation arrivals are seen continuously, while above this line, it is sometimes difficult to detect them. Comparing the waveform above (blue) and below (black) the red line (Figure 10.D.2), there is more attenuation in the bottom part of the log.

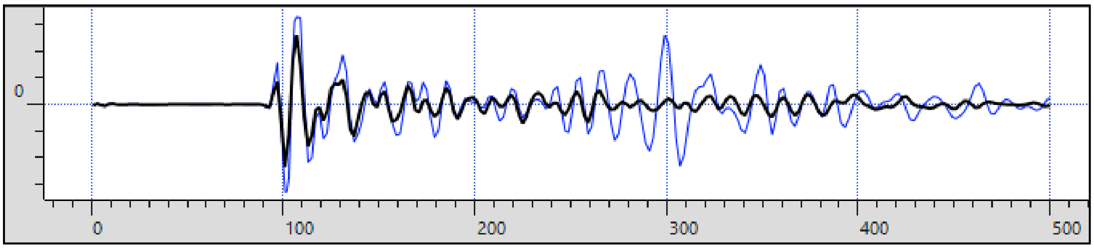

- **Impedance:** This measurement helps to understand the CBL-VDL. In the upper part of the log, the liquid is the continuous media detected in the annular, with some patches of cement of moderate impedance (around 4.5 Mrayls). Below the red line, the amount of cement increases, in some regions up to 50% (see cement ratio map), and the impedance reaches an average of 5.6 Mrayls. It is easy to see how the fluids would percolate through the annular volume that is not filled by cement.

The cement ratio, calculated from the acoustic impedance values larger than the water threshold, is in good agreement with the CBL, as shown in the crossplot on the right. In cases where the log spans over intervals with different coverage, this type of crossplot is useful to obtain the expected CBL endpoints for the BI calculation.

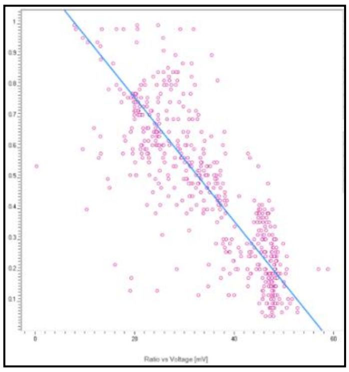

Fig. 10.D.1 – Cement Ratio vs. CBL crossplot

In conclusion, this interval has no potential for isolation. As in this case, it is necessary to subdivide the logs into smaller intervals and be specific about the quality, presence, or absence of cement. Saying that the 'cement bond is poor', or 'patchy but existent', is different than saying that 'there is free pipe' (like shown in Figure 10.B.10). In the latter, a cement squeeze may be attempted.

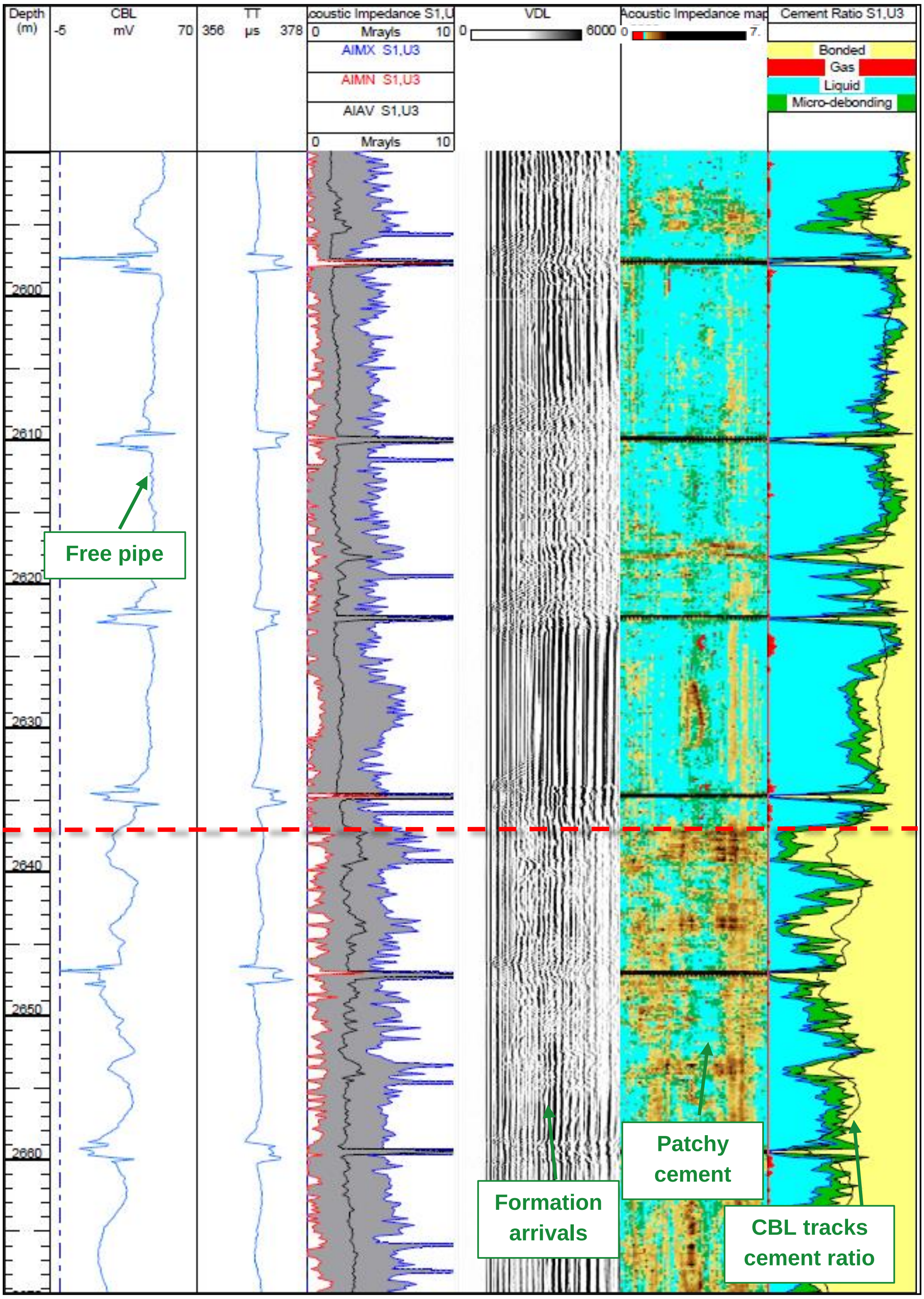

Fig. 10.D.2 – Presentation of ultrasonic logs (Courtesy: Equinor)

Figure 10.D.3 shows a case where an interval with poor cement properties correlates with a GR decrease. It is important to incorporate petrophysics information to identify zones that can lead to increased losses, damage, or swelling, for future development plans of the field.

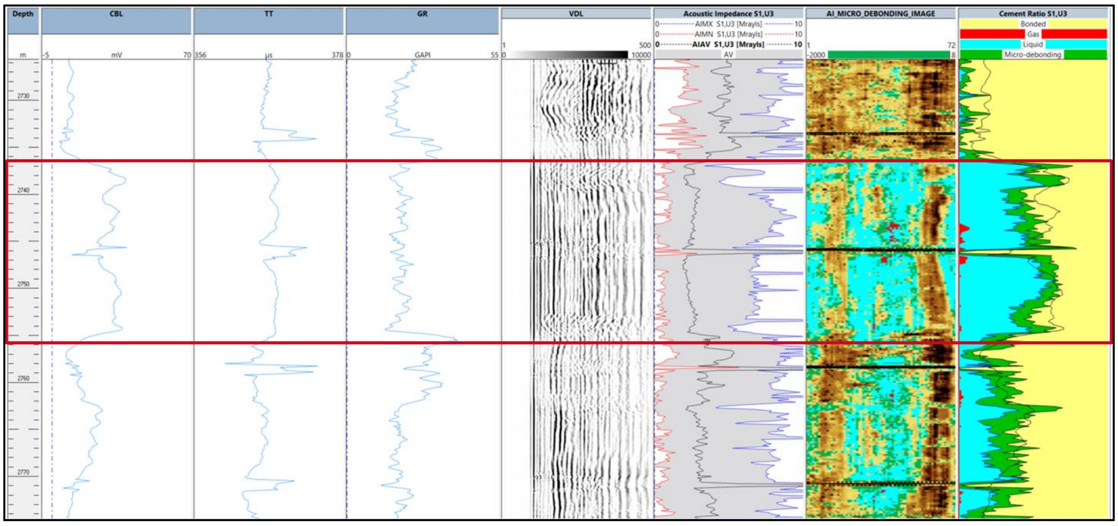

Fig. 10.D.3 – Correlation with geological features (Courtesy: Equinor)

10.D.2 Good cement

Figure 10.D.4 shows a well logged with a segmented sonic tool, which presents good cement in the upper part (above 3425 ft). Below this depth, the log shows characteristics of free pipe, the typical 'train tracks' for casing arrivals, and chevron patterns in the connections are observed in the VDL. In the good cement interval, the train tracks completely disappear (with the appropriate scale), the CBL amplitude drops to less than 2 mV, and there is a very small separation between the minimum and maximum values. The cement map shows homogeneous amplitude, ruling out the presence of detectable channeling. Isolation is expected for this interval.

An ultrasonic tool would show circumferentially homogeneous values of the impedance of expected magnitude (a function of the cement type).

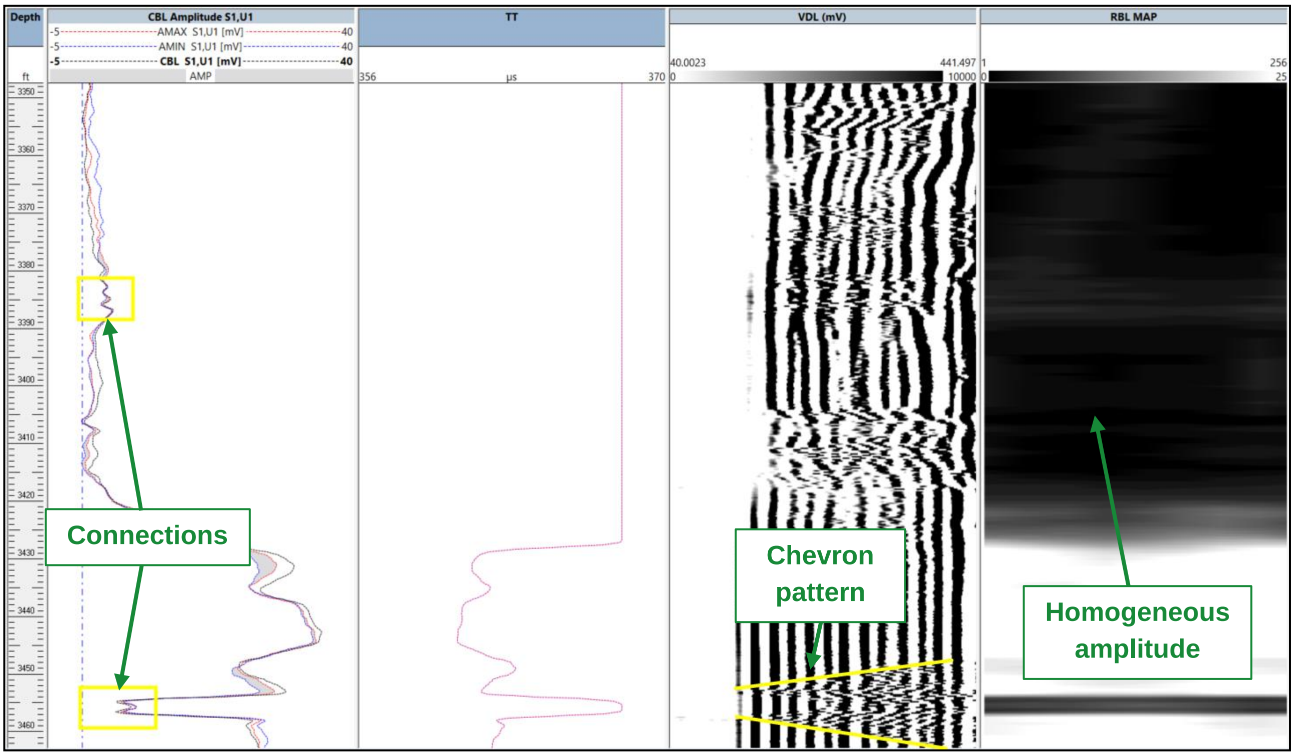

Connections

Chevron pattern

Homogeneous amplitude

Fig. 10.D.4 – Good cement

10.D.3 Channeling

Channeling is a difficult condition to evaluate if the only available log is a conventional CBL-VDL. An azimuthal tool (segmented sonic or ultrasonic) is needed to understand whether the CBL amplitude is high due to poor cement or lack of circumferential coverage.

In this case, the ultrasonic image shows a low side fluid channel that extends for at least 4 casing joints. The maximum impedance reaches the value for good cement (7 Mrayls in this case), indicating the quality is expected to be good on that part of the circumference. The fraction of the circumference without good cement may be enough for conducting undesired fluids to travel behind the casing, under certain pressure differential between zones.

The VDL response is a combination of the bonded and unbonded sections. There are formation arrivals (crooked lines), but at the same time we get casing arrivals from the unbonded casing which can ring loudly. The latter will also lead to an intermediate CBL amplitude.

With radial tools, look for the maps as shown in Figure 10.B.11. It is useful to orient the image using the relative bearing to check for consistency in the location of the channel.

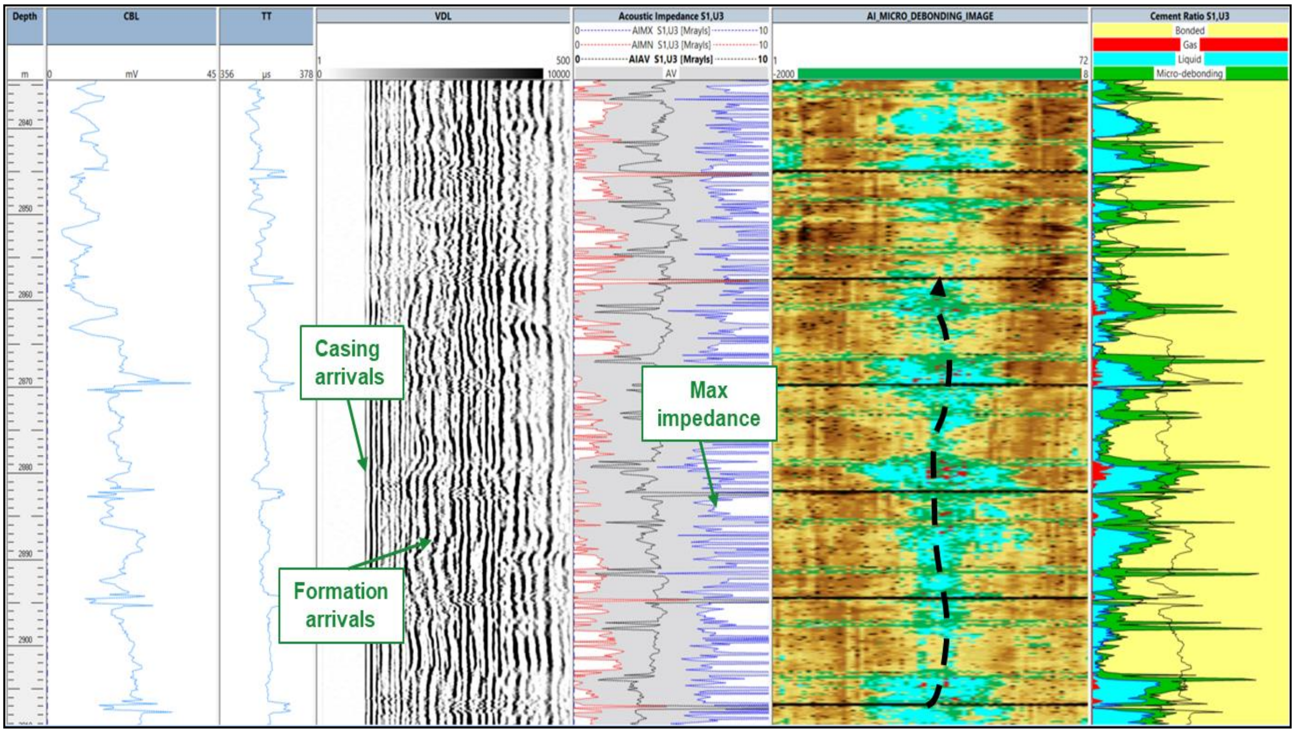

Fig. 10.D.5 – Low side channeling (Courtesy: Equinor)

10.D.4 Isolated liquid pockets

Figure 10.D.6 shows a section of the well with overall good bonding but with a number of isolated liquid-filled pockets on the low side of the hole, as seen in the impedance image. Note that outside the pockets, the CBL reads an average of 4 mV, and the VDL does not detect casing arrivals. There are sudden amplitude spikes and VDL straight lines throughout these pockets.

In terms of overall isolation potential, assess whether these pockets are connected and form a continuous channel. In this case, isolation is expected between the liquid pockets, as indicated by the CBL and impedance values. Note that the impedance in the low side of the hole is smaller yet remains around 5.5 Mrayls. This is caused by the pipe being eccentric towards the low side of the hole.

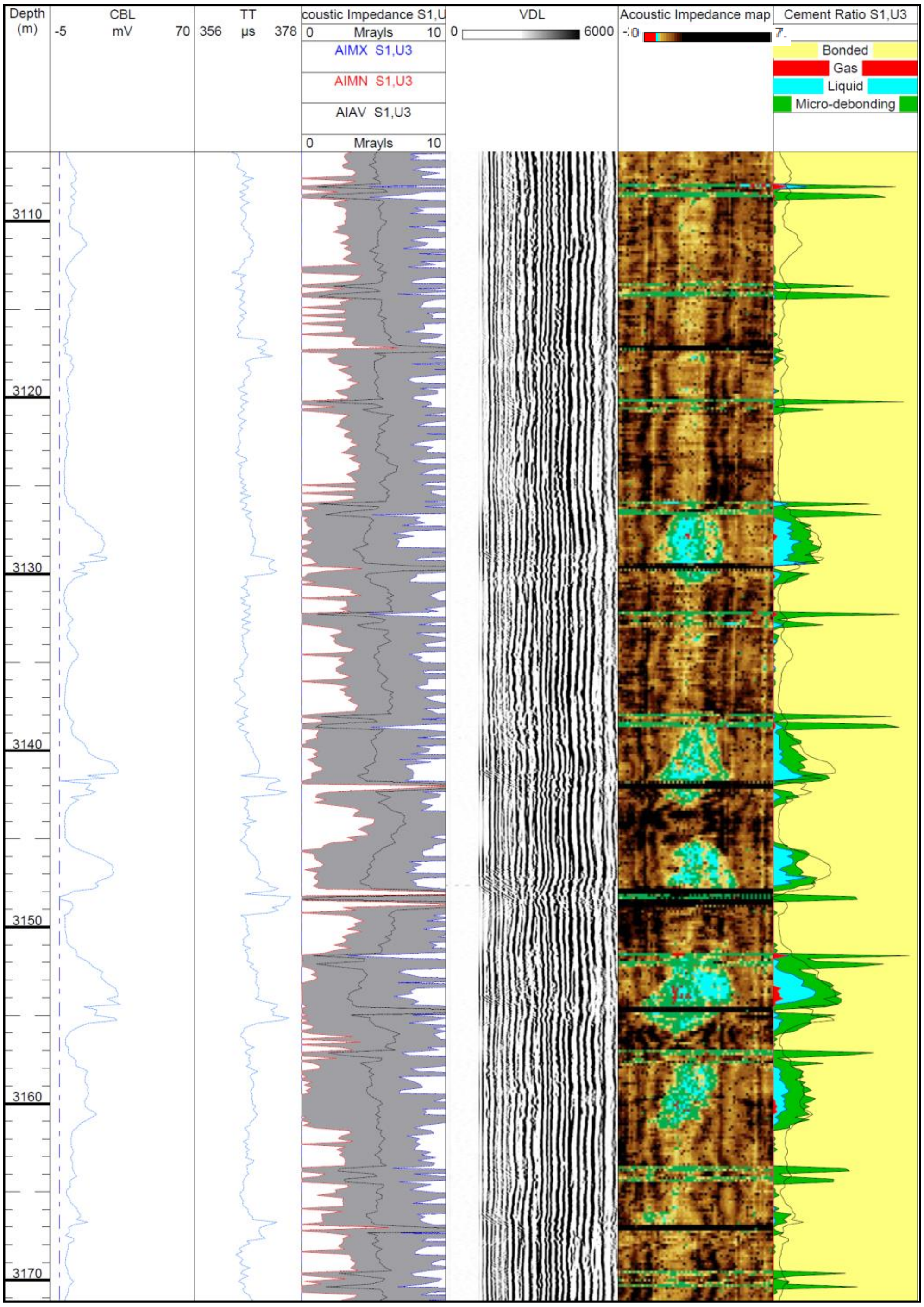

Fig. 10.D.6 – Low side isolated liquid pockets (Courtesy: Equinor)

10.D.5 Microannulus

Temperature and pressure changes may lead to significant expansion or contraction. In some cases, a small gap between the casing and the cement may exist, around hundreds of microns. This is referred to as microannulus and may be filled by liquids or gas. Different authors suggest that with common liquid-filled microannulus, there is still good isolation. The cement log may be run with the casing under pressure in an attempt to close the gap and eliminate undesired effects. If the microannulus is filled by gas and/or in the presence of large pressure gradients, then it can increase the risk of fluid movement behind casing.

Figure 10.D.7 shows a liquid-filled, also known as 'wet', microannulus. In this case, the CBL signal undergoes partial attenuation (depending on the microannulus gap). The amplitude is larger than good bonded intervals but smaller than free pipe as it cannot vibrate freely (unless the microannulus is very large). The VDL is affected in a similar way, with strong casing arrivals and showing formation arrivals. The ultrasonic measurements are not severely affected by small liquid-filled microannulus (up to 100 µm), as the gap is a small fraction of the acoustic wavelength. The measured acoustic impedance will be smaller than for good cement.

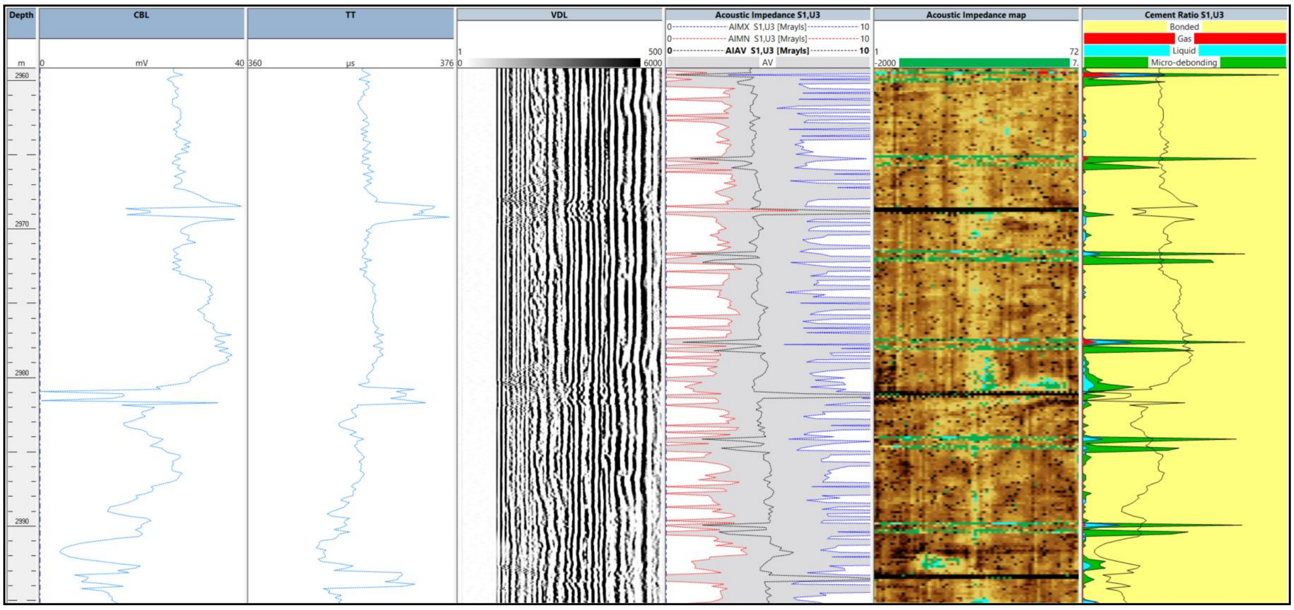

Fig. 10.D.7 – Wet microannulus (Courtesy: Equinor)

On the other hand, a gas-filled or 'dry' microannulus will severely affect the ultrasonic logs. Due to poor acoustic coupling, the impedance will indicate gas, but the CBL will not be affected by small microannulus. Therefore, the combination of sonic and ultrasonic tools helps to identify the presence and type of microannulus.

10.D.6 Fast formations

In Section 10.B it was shown that the first arrivals received at the 3 ft and 5 ft transducers correspond to the casing. This is not true for fast formation, with acoustic velocity larger than the casing. Typical cases are dolomites and limestones.

Figure 10.D.8 shows a case of fast formation detected through a segmented tool. The first arrivals observed in the VDL correspond to the formation. These are wavy and occur earlier than for a free pipe condition. The transit time for the 3 ft receiver will be shorter. The CBL will not give information about the casing to cement bond, as the E1 arrival is now a formation arrival. The CBL may read higher or lower but should not be used for evaluation purposes.

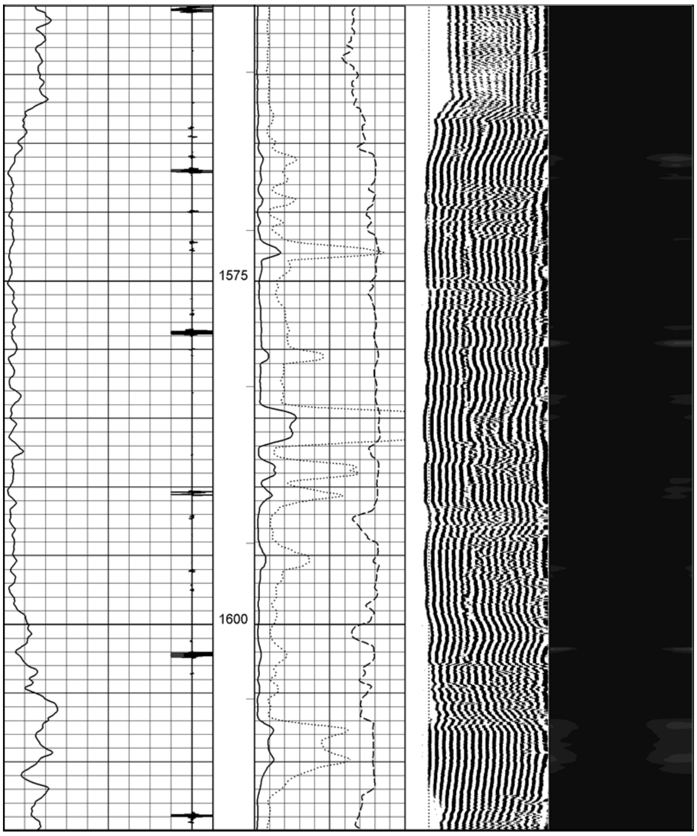

Fig. 10.D.8 – Fast formation (Courtesy: Voltage Wireline)

10.D.7 Galaxy patterns

When the casing is close to the borehole, ultrasonic tools may show formation/casing reflections which create a characteristic footprint, known as galaxy patterns. These are created in the narrowest part of the annular, which corresponds to the low side in deviated wells. Due to constructive and destructive interference, the apparent impedance is reduced or increased, resulting in fringes, as shown in Figure 10.D.9.

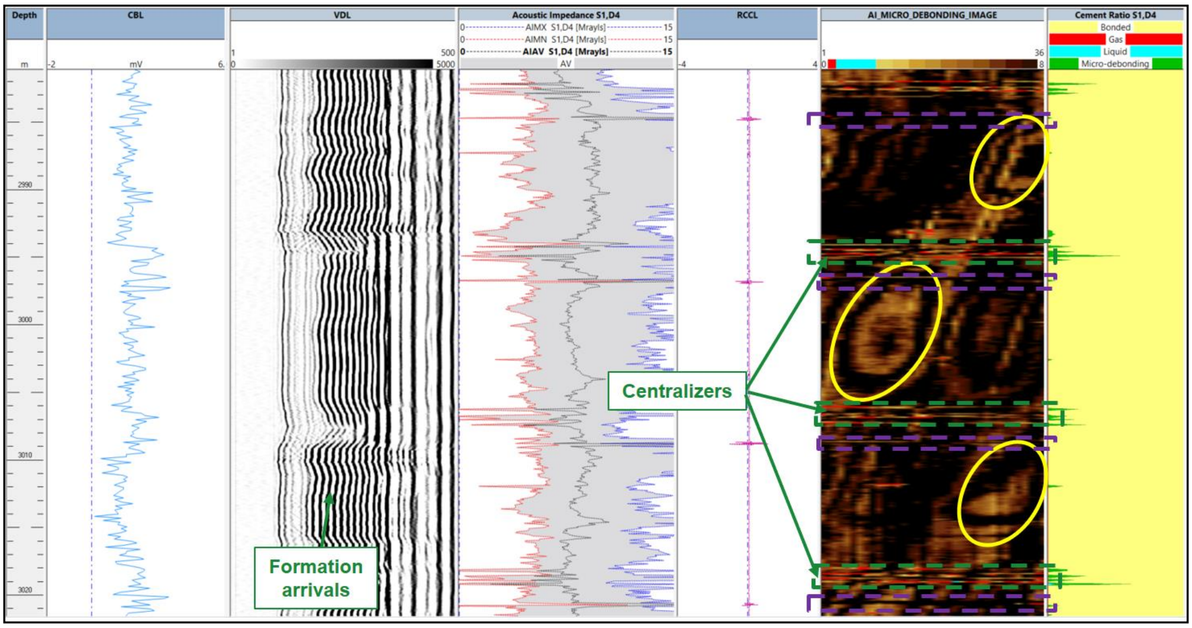

Fig. 10.D.9 – Galaxy patterns (Courtesy: Equinor)

In this image, there are external casing centralizers (marked in green). It is clear that the galaxy patterns occur half way between centralizers, where the casing sets to the formation. In this case, the impedance is very high, both in the fringes and between, meaning that there is likely zonal isolation. VDL reveals formation arrivals and attenuated casing, which is also a good sign.

10.D.8 Zones and flags

In the introduction in Section 10.A it was stated that the main question that we are trying to answer is: do we have hydraulic isolation? It is time to put all the logs together and answer whether isolation is expected.

The concepts of Bond Index and minimum length with certain coverage (as a function of the pipe size) were introduced in Section 10.B. This method is based on the CBL amplitude only and allows channels to exist and extend over a certain length. As the Bond I is a function of CBL amplitudes only, it is affected by the casing to cement bonding only and not by the cement to formation bond. Even if the channels are detected in a small segment of the casing, if these are connected, then isolation between zones may no longer exist.

Similarly, for ultrasonic tools, the acoustic impedance of intervals can be established with good cement, where the casing to cement isolation is expected. As these tools are azimuthal, channels may be found by visual inspection of the log.

As the amount of information available depends on the tools run and data quality, the workflow to establish zonal isolation is flexible and depends on user numerical input and visual inspection. The typical steps are given below:

1. **Evaluate the casing to cement bond:** Use the CBL amplitude or the acoustic impedance. For example, in Figure 10.D.10, the CBL is used as the primary measurement. Two CBL amplitudes are manually input by the user: *Good cement* and *Acceptable cement*. Amplitudes below the good cement are colored in blue, between good, and acceptable are brown, and above acceptable are red.

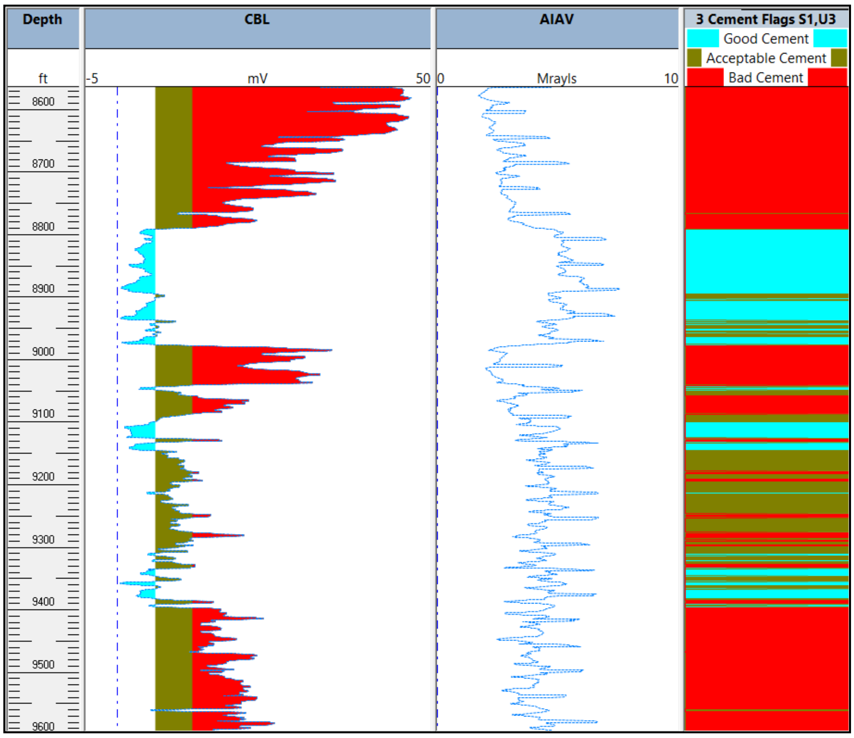

Fig. 10.D.10 – CBL/Impedance cement flags

The track on the right shows these cement flags with the corresponding color coding. The analyst may prefer to use 5 flags instead, named: Good Cement, Acceptable Cement, Poor Cement, Bad Cement, and Free pipe. For this, 4 input CBL amplitudes are required.

This analysis could be done with the impedance as well. Note that in both cases, the presence of the connections affects the readings, which may lead to spurious localized good/bad bonding. Median filters are helpful to remove these effects.

2. **Evaluate the cement to formation bond:** This is typically done by visually locating formation arrivals in the VDL. In Emeraude this is done by interactively defining custom zones (Figure 10.D.11-left). Poor bond to formation may be assumed if the VDL does not exhibit strong formation arrivals or is not present.

3. **Evaluate the presence of channels:** This is done by inspecting the amplitude map of segmented receivers or the acoustic impedance. Figure 10.D.11-right uses the acoustic impedance, and 3 zones where channeling is possible are identified, based on continuous intervals of low impedance. The upper part of the log is an interval with no isolation, but it is unnecessary to set a channeling flag if the amplitude of the CBL is in the Bad cement region.

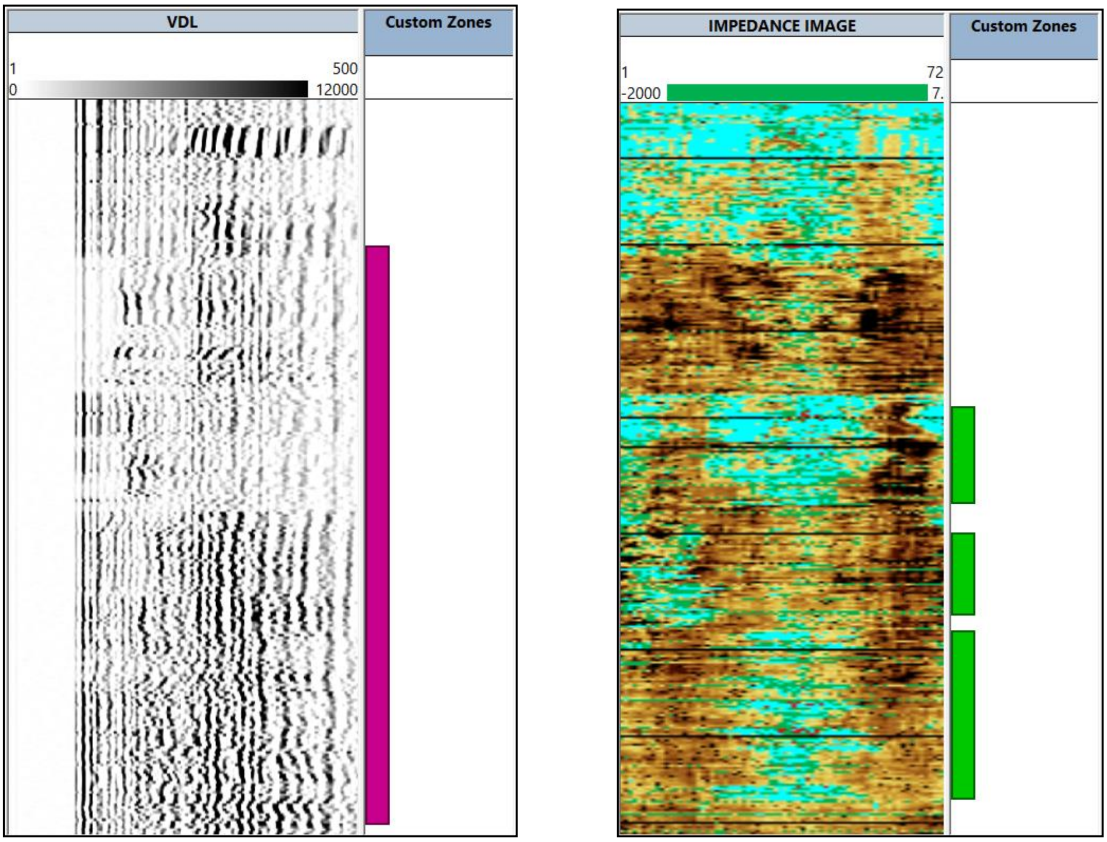

Fig. 10.D.11 – Formation arrivals zone

4. **Combining all flags:**

This analysis concludes with a traffic light system based on the three isolation criteria established previously: casing-cement bond, cement-formation bond, and channeling. Passing all the isolation criteria means that there is good casing bond, formation arrivals were detected, and no channeling was identified. A partial pass would correspond to the case of an acceptable bond but still detecting formation arrivals and no channels. The presence of any of the channeling, no formation bond, or bad cement flags is enough for failing the overall criteria:

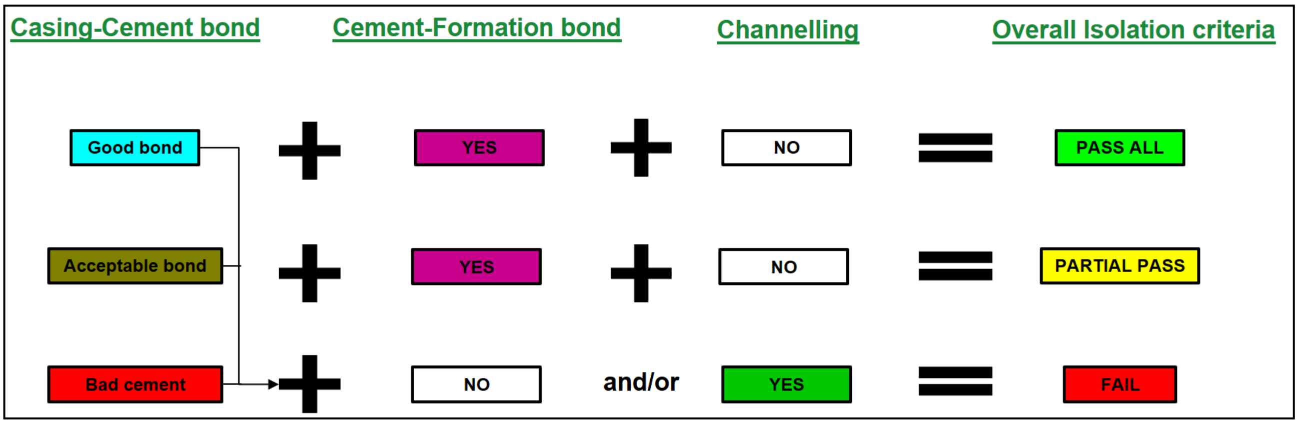

Fig. 10.D.12 – Overall isolation criteria

Failing the cement criteria means that the zone has no cement at all (free pipe), or that the presence of the cement is not enough to avoid channeling or crossflow. Partial pass, on the other hand, means that the cement bond is weaker than expected for a good cement, not enough curing time, microannulus, etc.

The final product of the analysis will be a plot with a track displaying the overall isolation analysis, which shows the potential for isolation in 3 simple colors. This is presented in Figure 10.D.13.

After this analysis, it is necessary to incorporate petrophysical and reservoir data to understand where the flow units of interest are and to check if the intervals without isolation may cause production issues due to fluid movement to surface or other perforations. For example, suppose there is a high pressure zone at the bottom of the log, in the region of no isolation. In that case, it is very unlikely that fluid from this unit will make it to the top of the log, as there are several feet of continuous annular interval with expected isolation. However, if a perforation was present in the zone of bad cement at the bottom, then this zone may produce fluids from the reservoir at that depth and intervals below/above due to crossflow.

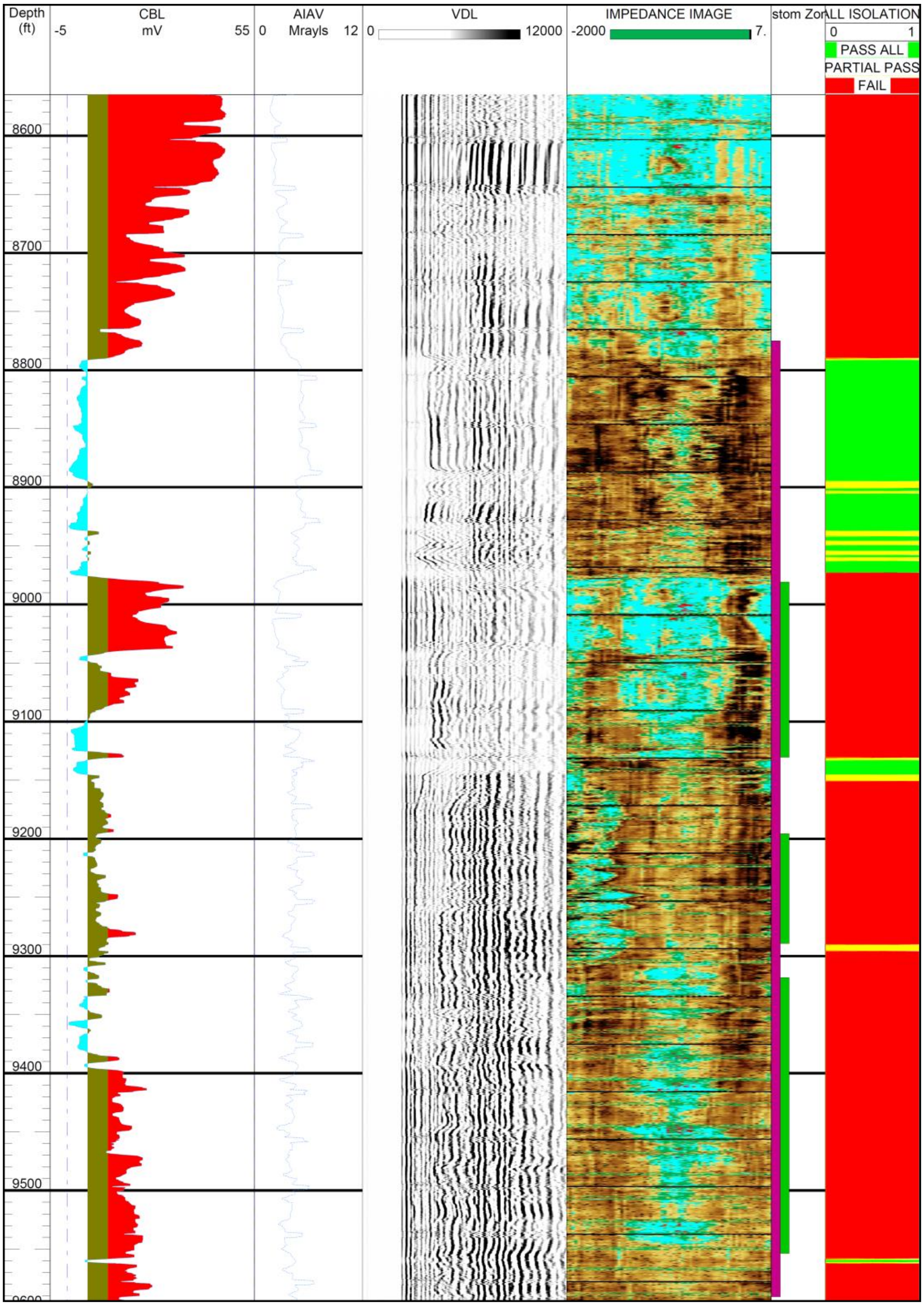

Fig. 10.D.13 – Overall isolation criteria (Courtesy: Equinor)

Final Note:

Multiple images shown in Section 10.D are courtesy of Equinor and the Volve Field partners. The author, on behalf of KAPPA, wishes to thank them for making this data available for public use.

The interpretation, conclusions, comments, or data adaptation made in this document are based on the author's criteria and do not reflect the operator's actual analysis.

T&Cs: https://www.equinor.com/en/how-and-why/digitalisation-in-our-dna/volve-field-data-village-download.html

11 – Pulsed Neutron Logging

11.A Introduction

Formation saturations are one of the building blocks for reservoir description. These are used, together with porosity and reservoir volume, to estimate the hydrocarbon in place. This is one of the main factors to determine whether a development project will be profitable or not. After the well is completed, the conductive casing prevents the use of typical open-hole resistivity logs for water saturation measurement. Pulsed neutron logging, or simply PNL tools, provide a way to monitor and evaluate the water saturation, reservoir contacts, detect by-passed reserves, identify and quantify gas saturation, etc. PNL are also run in wells with an incomplete set of open hole logs.

Pulsed neutron tools emit neutrons that interact with the matter and generate Gamma rays. The analysis of this radiation as a function of time and energy is exploited by the various PNL techniques. Section 11.B describes the modern PNL tools, including their detectors and generators. The neutron interactions with the formation, completion, and fluids are the topic of Section 11.C.

One way to estimate the water saturation through PNL is called Capture or Sigma mode, which requires high formation salinity. The principle and interpretation techniques are presented in Section 11.D. The other PNL mode to estimate the oil and water saturations is known as Carbon/Oxygen (C/O) logging. At the time of writing (2021), this method is not supported in the current Emeraude version (5.40), and therefore only a brief introduction is provided in Section 11.E.

Finally, PNL tools can be used for flow profiling. Oxygen activation or Water Flow logs is a technique that allows to measure the water velocity. This can be an input of multiphase production logging interpretation. Oxygen activation mode is covered in Section 11.F.

11.B Pulsed Neutron Tools

The first Pulsed Neutron Logging (PNL) tool dates back to 1964. Developed by Lane Wells and named 'Well Neutron Lifetime Log', this tool contained one neutron generator and one detector and only worked in Sigma mode. Schlumberger followed in 1968 with the first model of the Thermal Decay Time (TDT-K) tool, still with one detector. Shortly after, in 1972, the benefits of adding an extra detector were realized, and the first model of the TDT-K dual detector was introduced. The evolution of PNL tools continued by reducing the tool OD, as the initial 3 5/8-inch tools proved limited in small-size completions. Currently, many PNL tools are 'slim', measuring 1 11/16-inches. Other improvements consisted of improved and additional detectors with a higher number of time gates, etc. The tools also became shorter and compatible with other CHL.

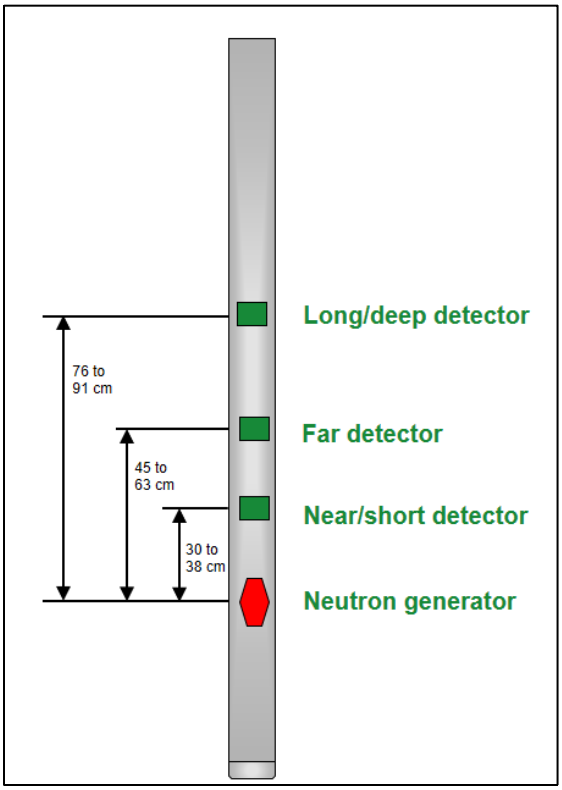

Fig. 11.B.1 – PNL tool schematic

A schematic of a PNL tool is presented in Figure 11.B.1. The neutrons source consists of an electrical accelerator tube, also known as Minitron. The neutrons are only generated if the tool is energized, avoiding HSE issues of the chemical sources. As the generators have several safety mechanisms in place, the neutrons are only generated when reaching a certain depth (controlled by the pressure). PNL tools contain 2 or 3 detectors.

The schematic shows a tool with 3 detectors, which is the case of the most modern models (RPM, PNX, RAS). The detectors can be of two types: Gamma ray or Neutron. Gamma ray detectors allow for spectroscopy (necessary for C/O logging), while neutron detectors are limited to Sigma mode (and water flow logs). This Chapter focuses on the Gamma ray detectors tools. The distance between the generator and detectors impacts the Gamma ray counts. Typical industry detectors spacing is indicated in the schematic.

Due to the high energy requirements, many PNL tools in the market work only on wireline. However, currently some tools also work on memory and battery. The tool length ranges between 4.6 to 10 meters, with an OD between 1.69 and 2.215 inches. Also, most of the tools in the market work on a single mode, but recent models offer simultaneous Sigma and C/O logging.

11.B.1 Neutron generators

Neutrons are heavy particles without electrical charge and have a proton like mass. Due to their mass, high energy, and lack of charge, these particles are highly penetrating, and interact with the completion, formation, and fluids in several ways, as explained in Section 11.C.

Neutrons are almost never emitted spontaneously and are created as a result of nuclear fission or particle bombardment. The neutron generators included in PNL tools work as small particle accelerators, where deuterium (1 proton + 1 neutron) collides with tritium (1 proton + 2 neutrons) to generate high energy neutrons and Helium.

The deuterium is accelerated by applying a large potential difference (~ 2kV), hitting a tritium-impregnated target. The resulting reaction emits around 100 million neutrons per second, with an energy around 14.1 Mega Electron Volts (MeV), with the neutrons moving at 17% of the speed of light. The depth of investigation is between 7.5 and 14 inches larger than chemical sources (2-5 inches). As the name of the tool suggests, the neutrons are not generated continuously but in pulses, controlled by the application of the potential. This is also a difference compared to chemical sources, with a steady particle output

Neutron generators can be as small as 15 centimetres. They require maintenance and replacement after hours of operation.

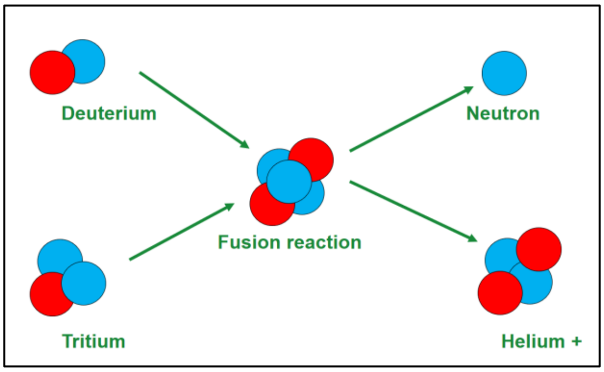

Fig. 11.B.2 – Neutron generation reaction

11.B.2 Gamma ray detectors

As will become clear in the next section, the PNL tool emits neutrons, but the quantitative results are extracted from the generated Gamma rays as a result of the neutron-matter interactions.

Gamma ray detectors were introduced in Chapter 2, in the context of depth correlation and radioactive scale detection. The measurement principle for PNL applications is the same, and the image presented in Section 2.D.3 is repeated below for convenience.

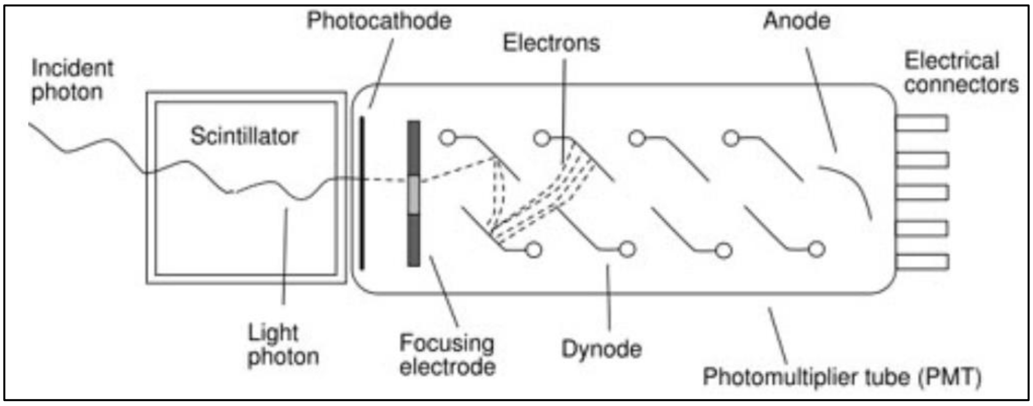

Fig. 11.B.3 – GR detection and quantification
(Courtesy: Stanford Scintillator Materials group)

Gamma ray detectors used in PNL measures counts in two domains: versus time and versus energy.

Apart from the NaI crystals presented previously, modern PNL tools also use other scintillation crystals, including $LaBr_3$, $LaCl_3$, GSO, YAP, etc. This is because their spectral performance, better than NaI, is critical for the C/O ratio technique, where the counts at different energy windows are measured. The photomultiplication process is similar to the one described previously.

Apart from the spectral analysis, in Sigma mode the detectors measure the total counts per second. For this, multiple time gates are set after the firing of the neutrons, and the Gamma ray counts are measured. The next section will show that the rate of Gamma ray decay is the key parameter for Sigma logging. Early tools measured the counts in 2, 8, or 16 fixed gates, while current tools use hundreds of gates. Figure 11.B.4 shows the Gamma ray counts (color) versus depth and time, for one of the detectors, in a period including two neutron firings. This type of plot is commonly available for the Near and Far detectors.

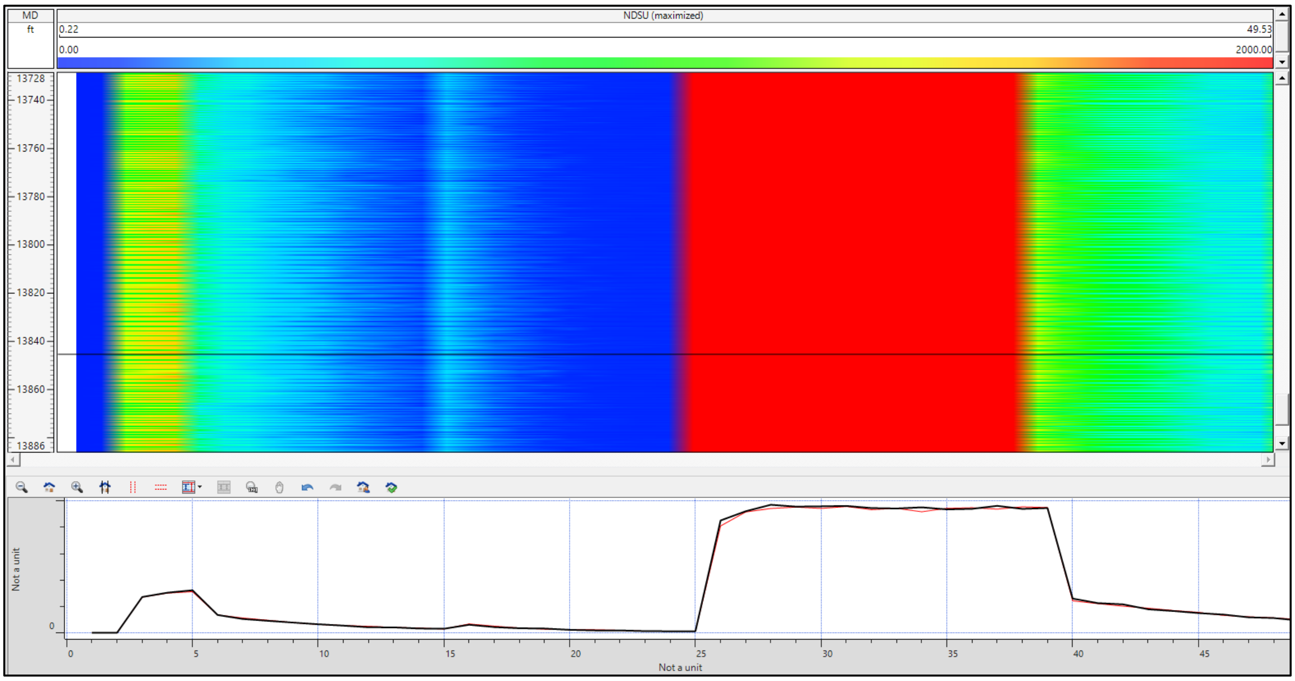

Fig. 11.B.4 – GR counts from a Near detector of a Schlumberger RST tool

Modern tools incorporate a third detector (known as long or deep), which is less affected by neutrons diffusion and has a higher gas sensitivity. Gas saturation calculations offered by many tools typically use this third sensor.

11.B.3 Logging operations

The different PNL acquisition modes rely on Gamma ray detection, which is highly statistical and benefit from long acquisition time, given by slow passes. For Sigma logging, the maximum recommended cable speed is between 5 and 9 meters per minute, and in general, a main and a repeat pass are recorded. The statistical nature is exacerbated in C/O logging, and the recommended pass velocity is slower, 2-3 m/min. When possible, 3 or more passes are recorded, from which an average can be calculated.

Formation saturation logging is generally recorded with the well shut-in. However, at the perforation levels in high permeability zones, fluids in the wellbore may invade the formation (near wellbore), resulting in disturbed saturation measurements. If the depth interval of interest includes the perforated interval, PNL passes with the well flowing may be considered.

The presence of radioactive scale depositions in the pipe impacts the data quality, as a larger Gamma ray count is expected in the intervals with deposition. This affects both the Sigma and C/O mode.

The PNL is typically run together with pressure, temperature, CCL. Fluid identification tools (i.e., capacitance, density) are helpful, as the wellbore fluid affects the neutrons' diffusion.

11.C Neutron Interactions

The high-energy neutrons emitted by the tool interact with nuclei in two ways: scattering and capture. The type of interaction depends on the energy of the neutron and the nucleus itself. Figure 11.C.1 shows the energy of a neutron emitted by a source (14.1 MeV) as it undergoes a number of interactions with other particles. Depending on their energy, neutrons are classified as Fast, Intermediate, Epithermal, and Thermal.

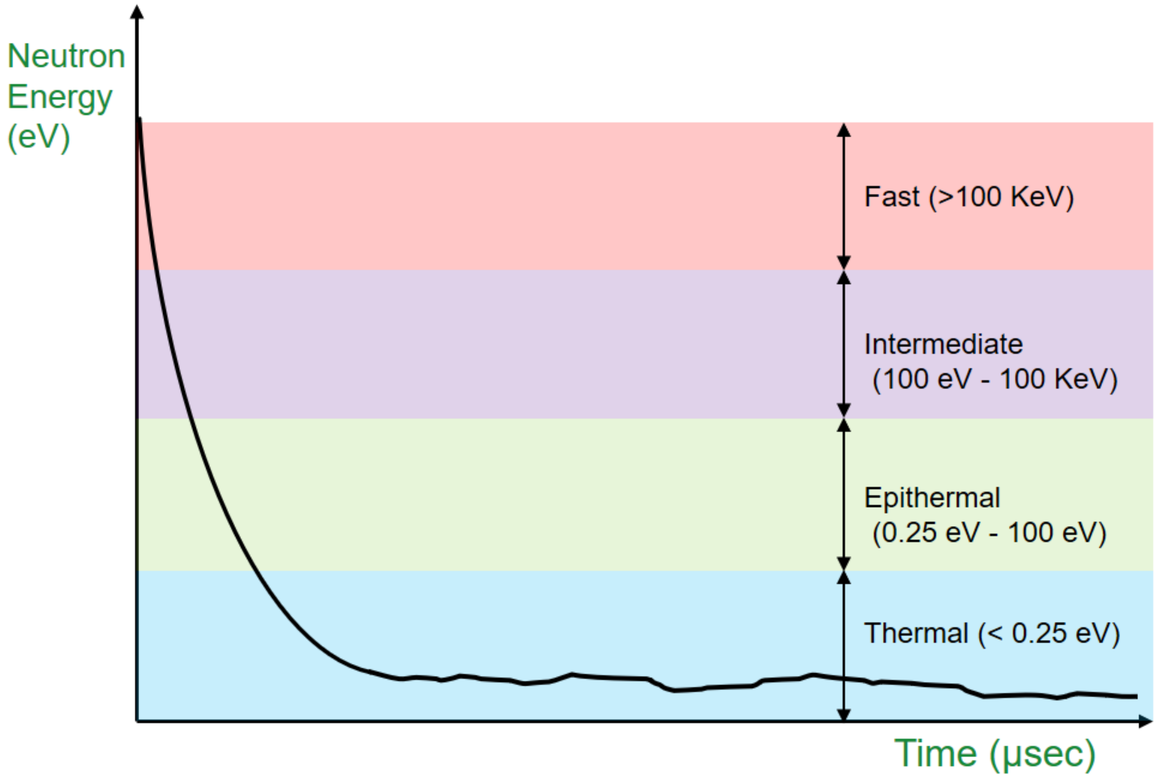

Fig. 11.C.1 – GR energy versus time

Within the first tens of microseconds, the high energy (Fast) neutrons scatter inelastically with various formation and completion elements, for example, Carbon (present in the hydrocarbons, carbonates, etc.) and Oxygen (present in water), among others. During **Inelastic** interactions, there is a transfer of kinetic and internal energy. The nuclei impacted by the neutrons are disturbed, adopting an excited energy state. To return to its normal level, the nucleus gives off a Gamma ray, whose energy structure is characteristic of the emitting element. Analyzing the energy spectrum, it is possible to determine the internal structure of the nuclei present in the formation. As shown in Figure 11.C.2, Carbon has a characteristic peak at 4.43 MeV, and Oxygen's main peak is located at 6.13 MeV. This is the principle of Carbon/Oxygen (C/O) logging.

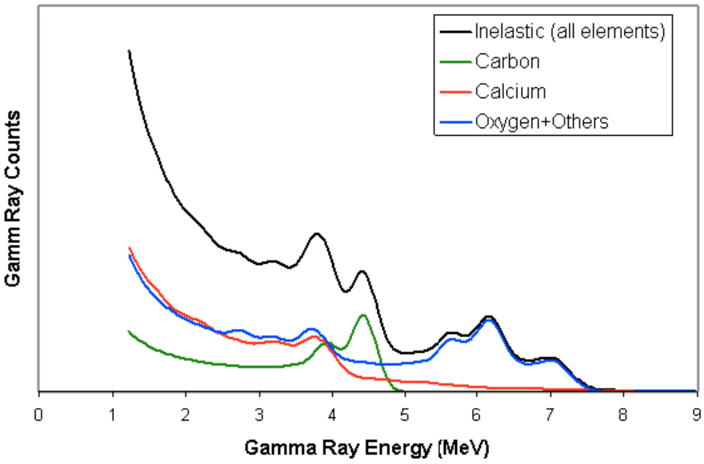

Fig. 11.C.2 – Inelastic GR energy spectrum - Li, Fusheng and X. Han. "Monte Carlo Numerical Models for Nuclear Logging Applications." (2012)

Elastic scattering occurs for all the neutron energies and is characterized by kinetic energy transfer only (no Gamma rays emitted). With each collision, the neutron loses energy, and slows down. The maximum kinetic energy loss occurs when the neutron hits a particle of the same weight: the hydrogen nucleus. This principle is exploited in the open hole neutron porosity measurement, based on the hydrogen index. The reduction of the neutron energy, or 'thermalization', is proportional to the porosity.

Eventually, after thousands of microseconds, the neutrons are slowed down and reach a 'thermal' energy state. In this condition, the probability of the neutron being absorbed by a nucleus increases. This process is called **Capture**, and after the nucleus absorbs the neutron, it goes back to its original energy state by releasing Gamma rays. The various elements have different probabilities to capture a thermal neutron. The probability of a specific reaction to occur is called 'cross-section', and for capture is called 'capture cross-section', or simply Sigma. This is the principle of the Capture or Sigma logging mode. The Sigma of different minerals and reservoir fluids are presented in Figure 11.C.3, in mass-normalized absorption cross-section, with units of 'capture units', c.u.

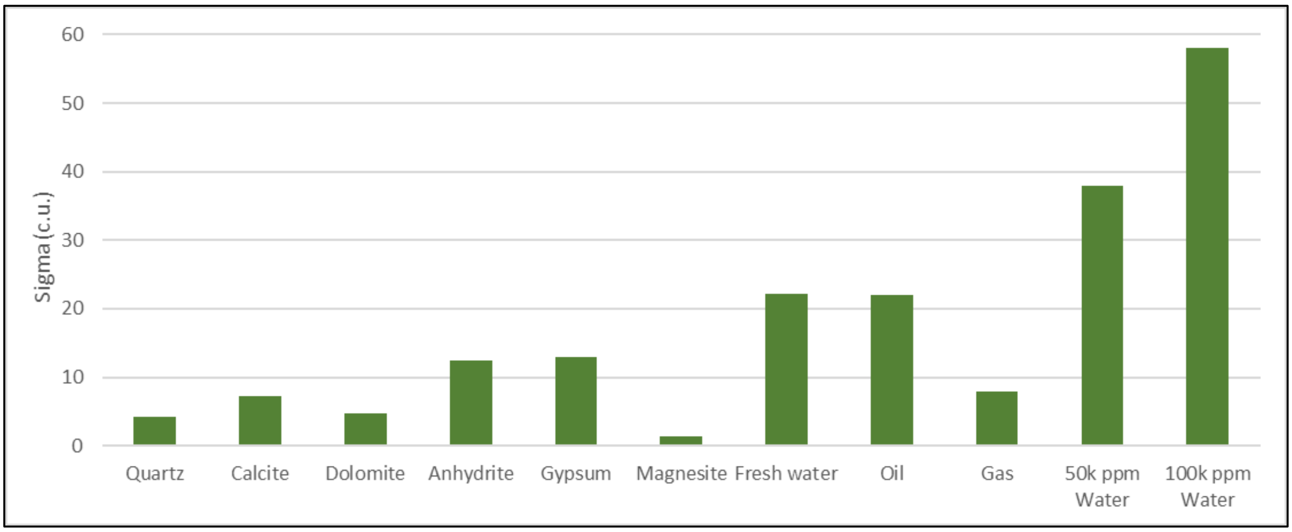

Fig. 11.C.3 – Sigma for different materials

The large tendency of chlorine present in salty water to absorb neutrons determines the formation water saturation. Boron, present in small proportions in some shales, has a Sigma of 760 c.u. This material is used in the control rods of nuclear reactors due to its large tendency to absorb neutrons.

In summary, the three types of neutron interactions are Inelastic scattering, Elastic scattering and Capture. Inelastic takes place with Fast neutrons, and is the basis of the C/O logging. It requires a Gamma ray spectroscopy measurement to associate the GR energy with the emitting element. Elastic scattering occurs for all the neutron energy states and constitutes the main mechanism for neutron slow down. Elastic scattering is used in neutron porosity logging. Capture occurs when the neutrons have very low energy, called 'thermal'. The higher capture tendency of the chlorine present in the salt allows the water saturation quantification based on Capture mode.

11.D Capture mode

Capture logging, also known as Sigma, is a technique to determine the water saturation behind casing when the formation water has enough salinity, resulting in a clear Sigma contrast with the hydrocarbons. This section explains how the Sigma is computed and how this is used to estimate the water saturation.

11.D.1 Measurement

As shown in Figure 11.B.4, the Gamma ray detectors record the counts versus time in a number of fixed time gates. After the pulse of high energy neutrons has been emitted, the Gamma ray counts decay, as shown schematically in Figure 11.D.1. The rate of decay is used to obtain the formation Sigma.

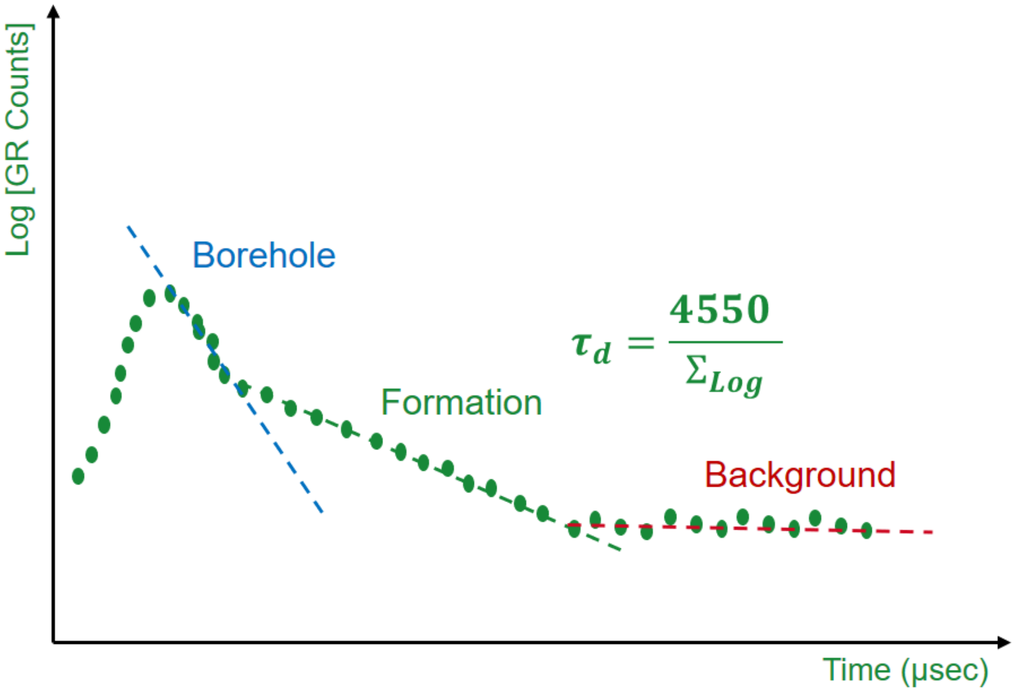

Fig. 11.D.1 – Gamma ray decay and Sigma calculation

The early time behavior is characterized by a fast decay, dominated mainly by the borehole and the casing. This is not representative of the formation and consequently is fitted with a separate regression.

The exponential decay observed during the mid-time behavior responds to the formation characteristics. A rapid decay of the Gamma ray population is observed for a large water saturation of enough salinity, corresponding to a high Sigma fluid, as the neutrons are quickly captured. On the other hand, a slow decay indicates that the neutrons are not being captured, indicating that the Sigma is low. This dependency of the decay of the Gamma ray population explains why the tools were originally named “Thermal decay time”. The formation Sigma (Σ_{log}) is obtained by applying a linear fit to the mid-time Gamma ray decay (τ_d) and applying the following equation:

$$\Sigma_{log} = \frac{4550}{\tau_d}$$

The end time behavior is dominated by the natural formation radiation and the activation caused by the neutron generator. Background corrections are applied, as this manifests as extra counts, which impacts the measured Sigma.

Going back to the calculation for the formation Sigma (Σ_{log}), in its core, it is a linear regression of the mid-time Gamma ray decay. The settings of the regression, gating, etc., are key tool parameters, as these impact the final Sigma value and consequently, propagate to the saturation calculation. This is critical when comparing two or more Sigma logs at different times (time-lapse analysis), as the Sigma calculation may differ between tools. As mentioned in Section 11.B, early tools measured the Gamma ray counts in 2, 6, or 16 fixed gates, compared to the hundreds of gates of modern tools. This will have an impact on the Sigma calculation due to the higher statistical reliability. Another point to consider is the data range used for the regression. Early tools performed a single regression over the entire range (avoiding the first peak). Later, the 'dual component fit' was implemented, differentiating between borehole and formation decay, as shown in Figure 11.D.1. Modern tools still offer the Sigma calculation based on both methods to allow the comparison between time-lapse logs.

Neutron capture is not the only mechanism that explains the Gamma ray decay used to calculate the formation Sigma. Neutrons also diffuse away through the borehole, formation, and completion, and this mechanism is more severe when the matter has a low capture cross-section. This is seen in gas-filled boreholes. Due to the lower tendency to capture neutrons, the Gamma ray population decays quicker, which can be wrongly interpreted as a higher formation Sigma. The formation Sigma received by the final user contains diffusion corrections, which depend on the tool provider. Some corrections are based on empirical databases, others use Monte Carlo simulations, and others apply mechanistic approaches (Boltzmann transport equation), etc.

The block diagram presented in Figure 11.D.2 summarizes the main steps from raw Gamma ray counts to the final formation Sigma. Note that the process is parallel for both, Near and Far detectors, and the final Sigma contains a weighted-average of both detectors. Whilst the Near detector is the best statistically, it is also more affected by downhole conditions.

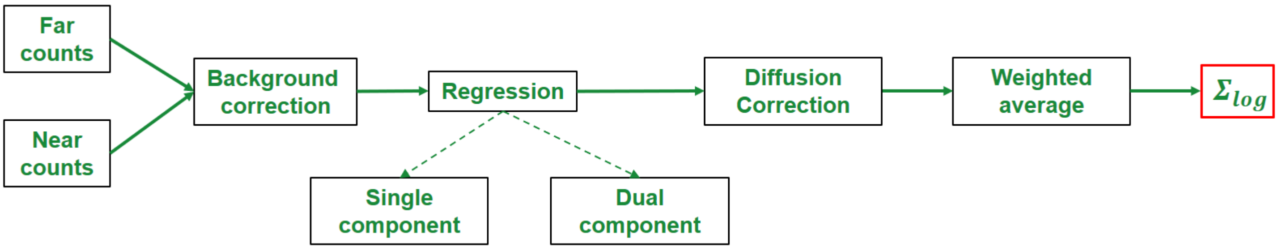

Fig. 11.D.2 – Sigma computation

The methodology applied in the various processing steps is different for the various tools. Moreover, the different scintillation crystals show a different response (counts) as they are hit by the same Gamma ray. This effect is minimized by the fact that Sigma is calculated as the slope of the decay and not the counts itself. Also, the separation between source and detector varies between the different tool models. All these factors lead to differences in the reported Sigma by the different tools, affecting the saturation calculation and is especially relevant in time-lapse analysis. It is common to see some tool outputs name 'Sigma-TDT like' or 'Sigma-RST like', where the results are adjusted to replicate what other tool models would measure.

The interpretation of Sigma to compute the water saturation will be presented in the next section. Figure 11.D.3 shows the Gamma ray counts for the Near and Far detectors, as images on the last two tracks (right). Apart from computing Sigma (track 1), PNL tools typically compute the total capture and inelastic counts for each detector, expressed as ratios (track 2 and 3, respectively). These are used as qualitative indicators of borehole fluids and also used for gas identification. In the presence of gas, the neutron's slowdown takes longer, leading to larger GR counts in the Far detector. The borehole Sigma (or borehole decay) based on the early capture cross-section is reported to understand borehole fluid changes, as these impact diffusion corrections. A thermal decay porosity is generated based on the ratio of near-to-far capture count rates and a proprietary algorithm that considers borehole size, fluids, etc.

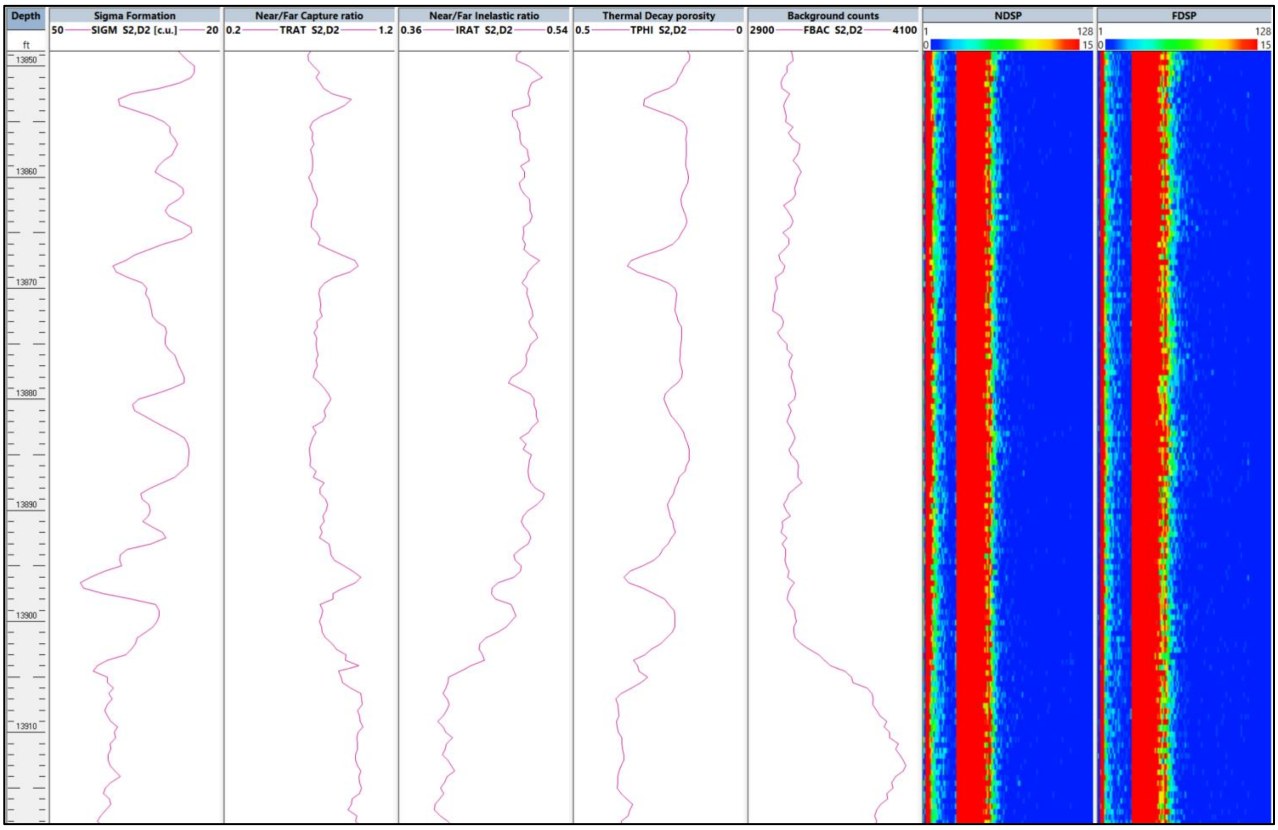

Fig. 11.D.3 – PNL Sigma outputs

As shown on the near and far detector images, a dual-burst sequence is used in most modern tools. The first burst is shorter, and it also is the first measurement window. As explained previously, the early decay is primarily given by the borehole fluids. The second burst and its measurement window are longer, and from here the Sigma used for water saturation estimation is computed.

11.D.2 Interpretation

The water saturation calculation in Capture mode relies on the principle that the measured Sigma responds as a volume-weighted average of the fluids and formation of individual Sigma values. Consider a burst of neutrons interacting with a microscopic formation sample, as shown in Figure 11.D.3. The porous media is filled with water (blue) and oil (green).

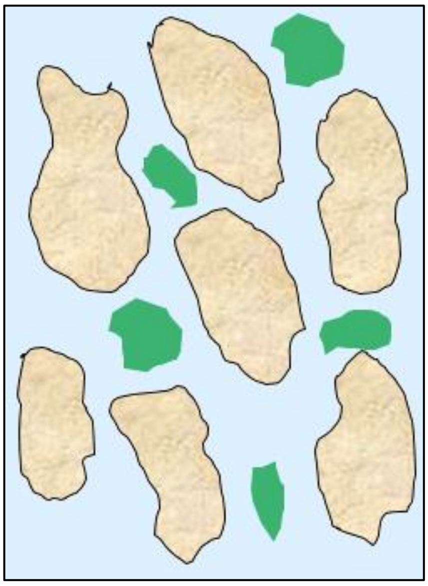

Fig. 11.D.4 – Bulk formation volume

In equations, the volume-average response of the measured Sigma can be expressed as:

$$\Sigma_{log} = \Sigma_{matrix} * (1-\varphi) + \Sigma_{fluid} * \varphi$$

Where Σ_{matrix} represents the formation Sigma and φ the effective porosity. However, the porous media is occupied by both water and oil. Expanding:

$$\Sigma_{log} = \Sigma_{matrix} * (1-\varphi) + \Sigma_{water} * \varphi * S_w + \Sigma_{HC} * \varphi * (1-S_w)$$

Where Σ_{water} is a function of the water salinity, Σ_{HC} depends on the fluid composition and downhole conditions. S_w is the water saturation, and its estimation is the objective of the PNL Capture log. This equation assumes that the formation is composed by the matrix only. Later will be shown how it can be adapted to shaly formations.

11.D.2.a Correlations and mineral composition

The previous equation shows that the water saturation (S_w) can be calculated analytically based on a Sigma log, a porosity log, and the individual Sigma values of the different components in the equation (matrix, water, and hydrocarbon). After checking the quality of the input logs, the interpretation consists of selecting the most representative Sigma values for the different components.

The hydrocarbon Sigma can be determined by correlations. For example, Clavier proposed the following expressions for liquid hydrocarbon Sigma (Σ_{HC}), as a function of the oil density at standard conditions (ρ_{do}), solution GOR (R_s), formation volume factor (B_o) and gas specific gravity (γ_g):

$$\Sigma_{HC} = \frac{\rho_{do}}{B_o} * (53.5 - 32\rho_{do}) + \frac{R_s}{1000} * \frac{\gamma_g}{B_o} * (13.5 - 3.4\,\gamma_g)$$

This equation shows that for a gas gravity of 0.7 and Rs smaller than 800 cf/bbl, the hydrocarbons Sigma ranges between 20.5 and 22.5 c.u. for API gravities between 20 and 60.

For water, correlations relate the Sigma value with the salinity. Pure water (0 ppm) presents a Sigma of 22.2 c.u., which is in the same range as the liquid hydrocarbon. This establishes a limitation on the use of Capture logs in low salinity formations, and in general, a minimum salinity of 40000 ppm is recommended to get a good contrast between the different fluids.

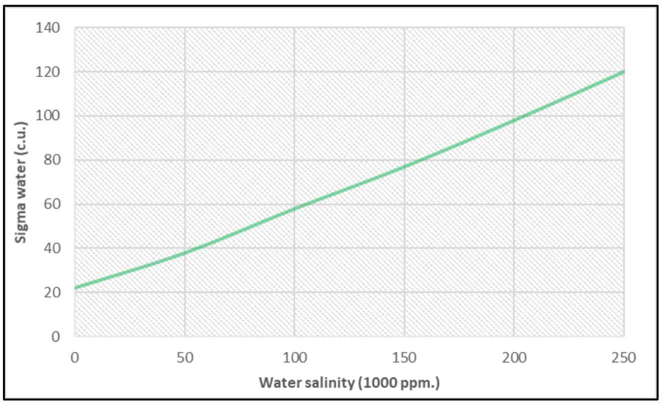

Fig. 11.D.5 – Sigma Water versus salinity at 75 °F

Similarly, Clavier proposed an equation for the gas Sigma (Σ_g), as a function of the methane Sigma ($\Sigma_{methane}$) and the specific gravity (γ_g):

$$\Sigma_g = \Sigma_{methane} * (0.23 + 1.4\,\gamma_g)$$

For matrix Sigma, it is possible to use values reported in the literature based on the lithology of the formation. Figure 11.C.4 provides the values for various minerals, from which the formation Sigma can be estimated based on a complete petrophysical description. However, the analytical determination of the matrix Sigma may prove difficult due to unaccounted lithology variations.

11.D.2.b Cross-plots

The end point Sigma values can be obtained or verified by using cross-plots. The most typical one is Sigma versus effective porosity. Three end points can be established:

- For 0% porosity, the Sigma value is equal to that of the matrix
- For 100% porosity and 0% water saturation, the Sigma value is equal to that of the hydrocarbon
- For 100% porosity and 100% water saturation, the Sigma value is equal to that of the water

As shown in Figure 11.D.6 (left), and based on the Sigma equation previously presented for clean formations, theoretically, it would be enough to provide 2 points at different porosities along the 0% and 100% water saturation lines, to accurately determine the three end points.

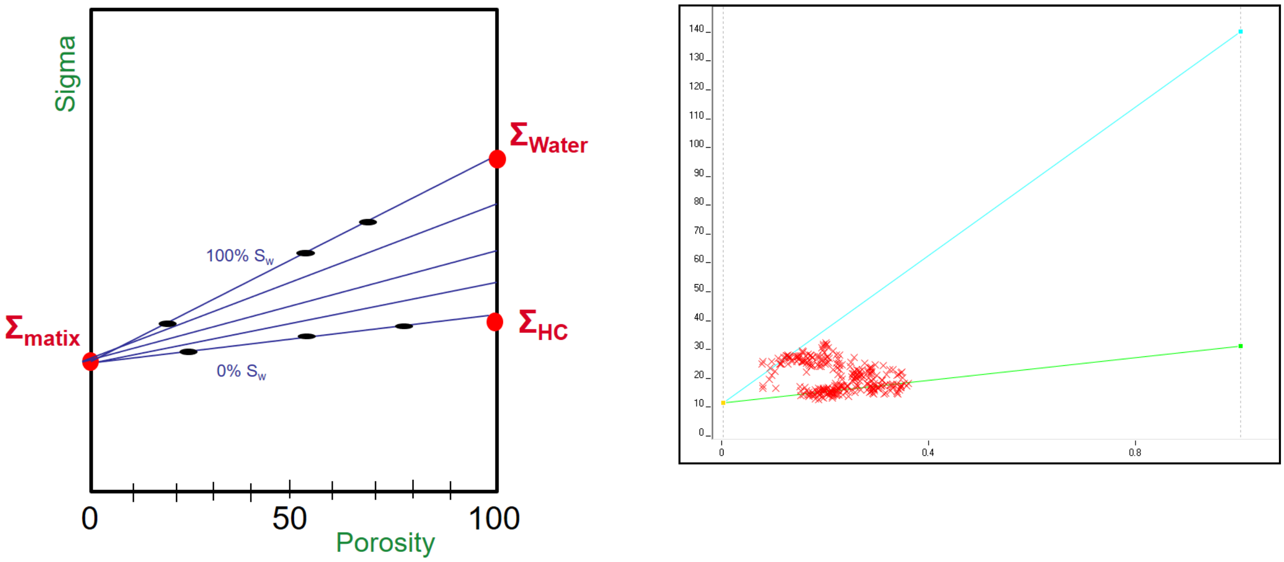

Fig. 11.D.6 – Schematic (left) and real (right) Sigma-Porosity Cross-plot

In practice, the cross-plot looks like the one presented in Figure 11.D.6 (right). Since the matrix Sigma depends on the lithology, the cross-plot must be created using a depth range with no lithology variations and over the same interval where the saturation calculation will be performed. The data range should ideally include a wide porosity range and water saturations between 0 and 100% to fit a straight line from the matrix to the water and hydrocarbons. The final parameters selection is a combination of cross-plot, correlation values, and the analyst's knowledge of the tool and formation.

In this cross-plot the effect of low salinity water is very clear, as the two end points for 100% porosity would get very close and eventually overlap, amplifying the errors, and ultimately preventing the use of this measurement for qualitative or quantitative evaluation. This cross-plot shows that for very low formation porosity, all the points are located close to the matrix end point, leading to higher uncertainty when linearly extrapolating these to 100% porosity.

In fields where Pulsed Neutron monitoring is planned, it is common to run a baseline Sigma log immediately after completing the well. In this situation, the water saturation is known from open hole logs, and the baseline pulsed neutron log can be used for refining the estimate of the end points. Starting from the previously-presented equation:

$$\Sigma_{log} = \Sigma_{matrix} * (1 - \varphi) + \Sigma_{water} * \varphi * S_w + \Sigma_{HC} * \varphi * (1 - S_w)$$

Instead of using Sigma and porosity, the Sigma equivalent and porosity equivalent concepts are introduced, since the water saturation is known:

$$\Sigma_{eq} = \frac{\Sigma_{log} - \Sigma_{HC} * \varphi * (1 - S_w)}{1 - \varphi\ (1 - S_w)} \qquad \varphi_{eq} = \frac{S_w * \varphi}{1 - \varphi * (1 - S_w)}$$

The equation can be re-written as:

$$\Sigma_{eq} = \Sigma_{matrix} * \left(1 - \varphi_{eq}\right) + \Sigma_{water} * \varphi_{eq}$$

By plotting Sigma equivalent versus porosity equivalent, a straight line connects the matrix and formation Sigma values. This plot was constructed assuming that the water saturation log provided is valid at the time of the PNL log. This is not true if the logged range experienced changes in saturations due to depletion, flooding, contact movement, etc. It may be possible to use an old saturation log to estimate the end points in non-producing intervals, for example.

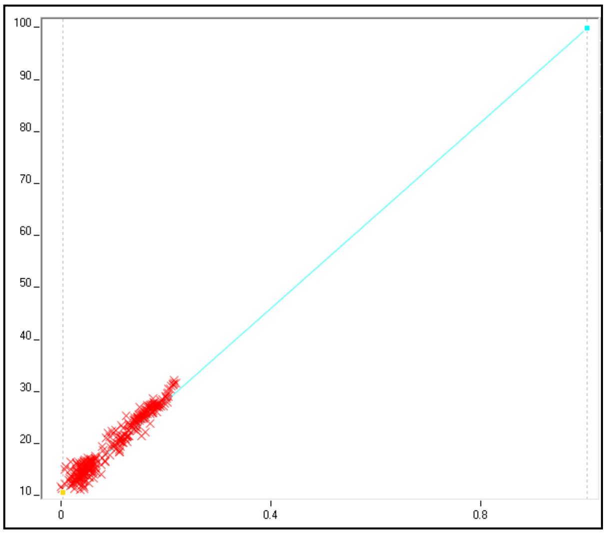

Fig. 11.D.7 – Sigma equivalent versus porosity equivalent

Similarly, when the water saturation is known, the Sigma matrix can be calculated from:

$$\Sigma_{matrix} = \frac{\Sigma_{log} - V_{sh} * \Sigma_{shale} - \varphi * (S_w * \Sigma_w + (1 - S_w) * \Sigma_{hc})}{V_{sh}}$$

This equation incorporates the shale volume (V_{sh}) and Sigma Shale (Σ_{shale}), which will be detailed in the next section.

This can be plotted as a function of the matrix volume, given by:

$$V_{matrix} = 1 - V_{sh} - \varphi$$

The Σ_{matrix} - V_{matrix} crossplot shows a trend of data points funneling towards the value of Sigma matrix as the V_{matrix} approaches 1. At this value, both the porosity and V_{sh} are zero, and the measured Sigma would be given entirely by the matrix mineralogy. An example of this cross-plot is shown in Figure 11.D.8, where the Sigma matrix averages 9.6 c.u. as the volume of matrix tends to 1.

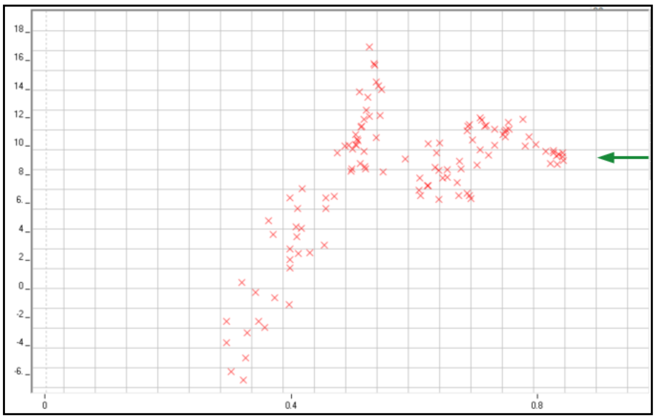

Fig. 11.D.8 – Sigma matrix versus matrix volume Cross-plot

In summary, the different cross-plots presented in this section are available tools for the analyst to define the most representative Sigma end points for the different components: hydrocarbon, water, and matrix. The data displayed in the cross-plots must be from zones with no changing properties, mainly lithology, and salinity. All the cross-plots require the measured Sigma and effective porosity. Note that in some cases, especially in old wells with an incomplete set of open hole logs, the PNL porosity may be the only source of porosity available. This porosity can be converted to an effective porosity by subtracting the effect of the shale (more on this in the next section):

$$\varphi_{eff} = \varphi_N - V_{sh} * \varphi_{sh}$$

11.D.2.c Shaly formations

The previous analysis considered the reservoir Sigma to be equal to the matrix Sigma, which occurs in clean formations. For shaly formations, the volume-weighted Sigma response incorporates an extra term:

$$\Sigma_{log} = \Sigma_{matrix} * (1 - \varphi - V_{sh}) + \Sigma_{shale} * V_{sh} + \Sigma_{water} * \varphi * S_w + \Sigma_{HC} * \varphi * (1 - S_w)$$

For shaly formations two new parameters are required: V_{sh}, obtained from petrophysical interpretation, and Σ_{shale} which needs to be established by the PNL analyst. The latter is, in general, one of the main uncertainties of the Sigma interpretation. Shale Sigma is normally in the range of 35 to 55 c.u., larger than conventional matrix formations. Boron and other absorbers are responsible for the large Sigma shale.

The simplest way to compute the shale volume is to normalize the Gamma ray response between clean formation (GR_{clean}) and 100% shale intervals (GR_{sh}):

$$V_{sh} = \frac{GR_{log} - GR_{clean}}{GR_{sh} - GR_{clean}}$$

Note that the Gamma ray end points selection may be affected by the presence of non-shale high GR formations. Various empirical correlations (Stieber, Larionov, Clavier) are applicable for specific rock types or take into account regional considerations.

Cross-plot techniques are still applicable but require some adaptations. The effect of the shale is to increase both the capture cross-section and the apparent formation porosity of the neutron porosity log. In the vertical axis, instead of using Sigma, a Sigma corrected for shaliness (Σ_{cor}) is used:

$$\Sigma_{cor} = \Sigma_{log} - V_{sh} * (\Sigma_{shale} - \Sigma_{matrix})$$

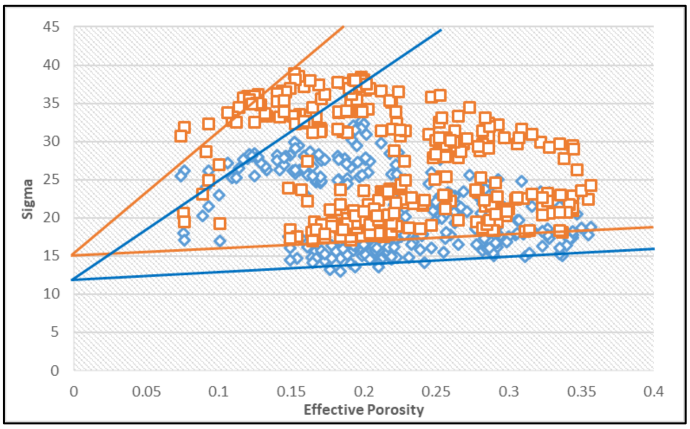

Fig. 11.D.9 – Corrected (blue) and uncorrected (orange) Sigma cross-plot

Figure 11.D.9 shows the data plotted with (blue) and without (orange) the shale correction. Note that this correction also applies to the other cross-plots presented in the previous section.

11.D.2.d Dual Water model

A proven sophistication of the Single Water shaly reservoir model considers that the particles of clay minerals are surrounded by bound water. Bound water consists of water molecules tied to the surface of the clay particles by electrostatic forces. These forces easily overcome drag forces, such as created by pressure differentials during the production stage of the reservoir. The bound water will not be produced and therefore poses no threat to the production engineers. But because of its salinity, the bound water will affect logging measurements (amongst which PNL logs). Hence, it is important to differentiate the bound water from the connate, free water, which is a difficult task owing to the different properties of the two types of water. The need to cope with this situation has entailed the development of the so-called Dual Water model and the adaptation of PNL logging to the requirements of this model.

The total porosity (φ_t) is defined as the sum of the effective porosity (φ) and the bound water volume (V_{wb}) as $\varphi_t = \varphi + V_{wb}$.

The effect of the bound water is seen in two other properties:

- The shale volume is now$V_{sh} = V_{wb} + V_k$, where V_k is the volume of dry clay minerals
- The total water saturation is composed by the free and bounded water saturations, as per $S_{wt} = S_{wf} + S_{wb}$

S_{wb} is determined by petrophysical analysis using S_{wb} indicators, pretty much in the same way V_{sh} is determined by shale indicators in the Single Water model. The difference is the presence of two types of water in the formation is taken into the formulation of the derivation of S_{wb} from the corresponding measurements. In particular, the Gamma ray allows the determination of S_{wb} using the formula:

$$S_{wb} = \left(\frac{GR_{log} - GR_{clean}}{GR_{sh} - GR_{clean}}\right)^M$$

Because of the similarity between the S_{wb} and V_{sh} derivations from the Gamma ray, a typical first approximation consists of using $S_{wb} = V_{sh}$. It should be noted that making this assumption is equivalent to assuming that the proportions of dry clay and bound water in the shales are the same as the proportions of total solids (dry clay + matrix) and total liquids in the bulk volume. In other words, the porosity of the shales would equal the porosity of the formation.

In theory, this has no reason for being true, but nevertheless, the tradition persists. A more rigorous solution for PNL logging consists of using a S_{wb} computation previously performed on the set of open hole logs by using a suitable Dual Water shaly reservoir model.

To estimate the water saturation using the Dual Water model, the response equation of PNL logs simplifies when the porosity and saturation are taken as φ_t and S_{wt}, not as φ and S_w. Using the previous definitions, and considering that:

$$S_w = \frac{V_{wf}}{\varphi} = \frac{S_{wt} - S_{wb}}{1 - S_{wb}} \qquad \varphi = \varphi_t * (1 - S_{wb})$$

The volume-weighted Sigma response can be expressed as follows:

$$\Sigma_{log} = \Sigma_{matrix} + \varphi_t * \left[(\Sigma_{HC} - \Sigma_{matrix}) + S_{wt} * \left(\Sigma_{wf} - \Sigma_{HC}\right) - S_{wb} * \left(\Sigma_{wf} - \Sigma_{wb}\right)\right]$$

Compared to the Single Water shaly model, the shale volume is not an input of the dual-water model, which relies on the accurate determination of the bound water saturation (S_{wb}). The free water saturation determination requires representative inputs of the volumes and Sigma values of all the parameters shown in the previous equation.

11.D.2.e Water saturation calculation

Regardless of the selected mode (clean, shaly single water, or dual water), PNL Sigma interpretation consists of providing the most representative Sigma values and volumes of the different components. Effective porosity and V_{sh} are log inputs, and the rest are zonal constants. Once this is done, the water saturation is computed by solving for S_w the Sigma response equation for the corresponding model, as presented previously.

Figure 11.D.10 shows the results from a Sigma interpretation. From left to right, the Gamma ray is displayed in the first track. Next, the perforations (red) and the PNL zones (blue), which are the intervals where the data displayed in the cross-plots is selected. As mentioned previously, the analyst needs to ensure there are not changes in lithology or water salinity within the zone. The measured Sigma log is displayed next, and finally the calculated water saturation (SWCalc) is computed. A typical way to display the results is to use a Bulk Volume analysis, where the volume percentage of the different components is displayed with filled areas.

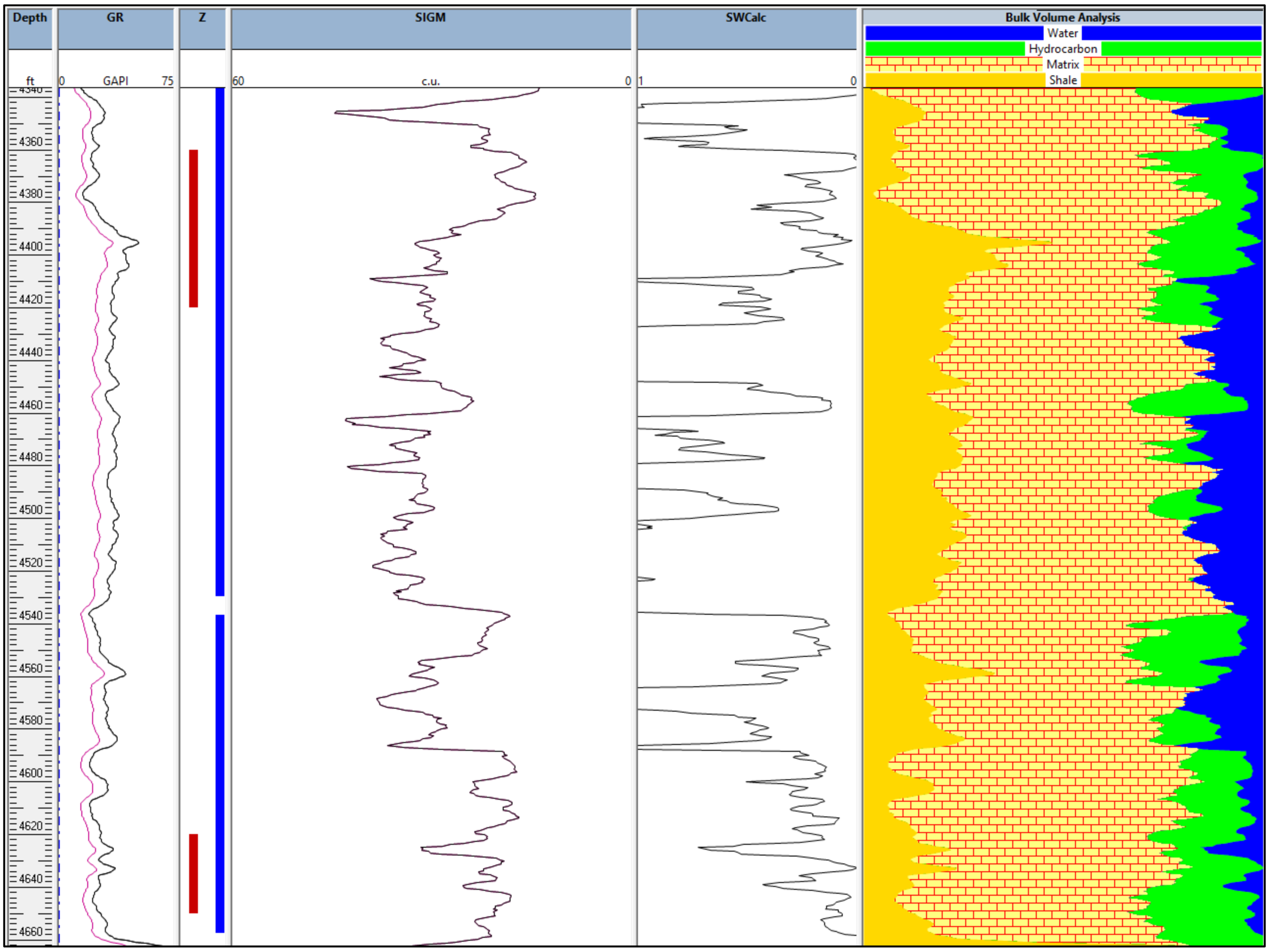

Fig. 11.D.10 – PNL Sigma results

The uncertainty of the input parameters on the water saturation estimation propagates in a volume-weighted average fashion. In general, the hydrocarbon saturation is the component with minimal impact on the calculation, as its value is reasonably constrained. Sigma water can be calculated from correlations that are a function of the salinity, provided that the produced water (from where the salinity is measured) is the same as the formation water. Figure 11.D.11 shows the sensitivity to 10% increase and decrease in the water Sigma, resulting in an approximate 10% decrease and increase on the water saturation calculation.

The smaller the porosity, the larger the matrix volume, leading to a larger impact on variations on the Sigma matrix. For an increase and decrease of 5 c.u., the water saturation calculation changes by more than half and more than double the original water saturation.

As mentioned previously, shale Sigma is a difficult value typically to quantify. The larger the shale volume, the greater the impact on the Sigma shale uncertainty.

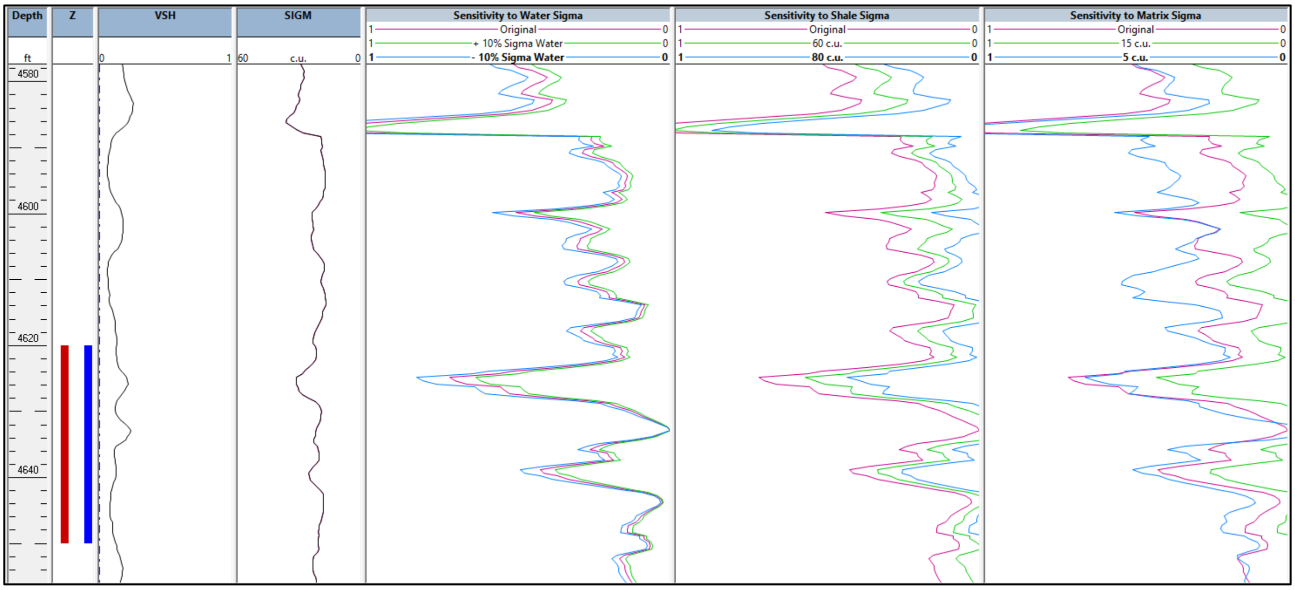

Fig. 11.D.11 – Uncertainty in the water saturation calculation

It is important to remember that water saturation has a direct impact on the hydrocarbon in place calculation. A 1% difference may result in millions of barrels of oil more or less in the company inventory. Selecting the most representative Sigma values and input logs is a multidisciplinary effort, and all the available reservoir, geology, and petrophysical data should be incorporated.

11.D.2.f Time-lapse

PNL logs are often run at repeated time intervals ('time-lapse') to check for hydrocarbon depletion and encroachment of water. The use of time-lapse PNL logs has the advantage that many of the parameters needed to derive the water saturation keep an assumed constant value. Such are Sigma matrix, hydrocarbon, and water. The latter is true only if there are no salinity changes, which would be caused, for example, by injection water.

When the above conditions are met, and assuming that the effective porosity remains constant, the change in saturation in a reservoir can be directly inferred from the change in Sigma values between old and new runs, as follows:

$$\Delta S_w = \frac{\Sigma_{new} - \Sigma_{old}}{\varphi * (\Sigma_{water} - \Sigma_{HC})}$$

To apply this equation, all the variables apart from saturation must remain constant. Variations in porosity (i.e., compaction), hydrocarbon (i.e., free gas in the reservoir), water salinity, etc., would invalidate the assumptions to use the equation.

Changes in saturation are best visualized by calculating the Bulk Volume of Water (BVW) for each run of the PNL log and by plotting BVW1, BVW2, & BVWn on the same track representing the total pore space. BVW is defined as the product of the porosity by the water saturation:

$$BVW_n = \varphi * S_{wn}$$

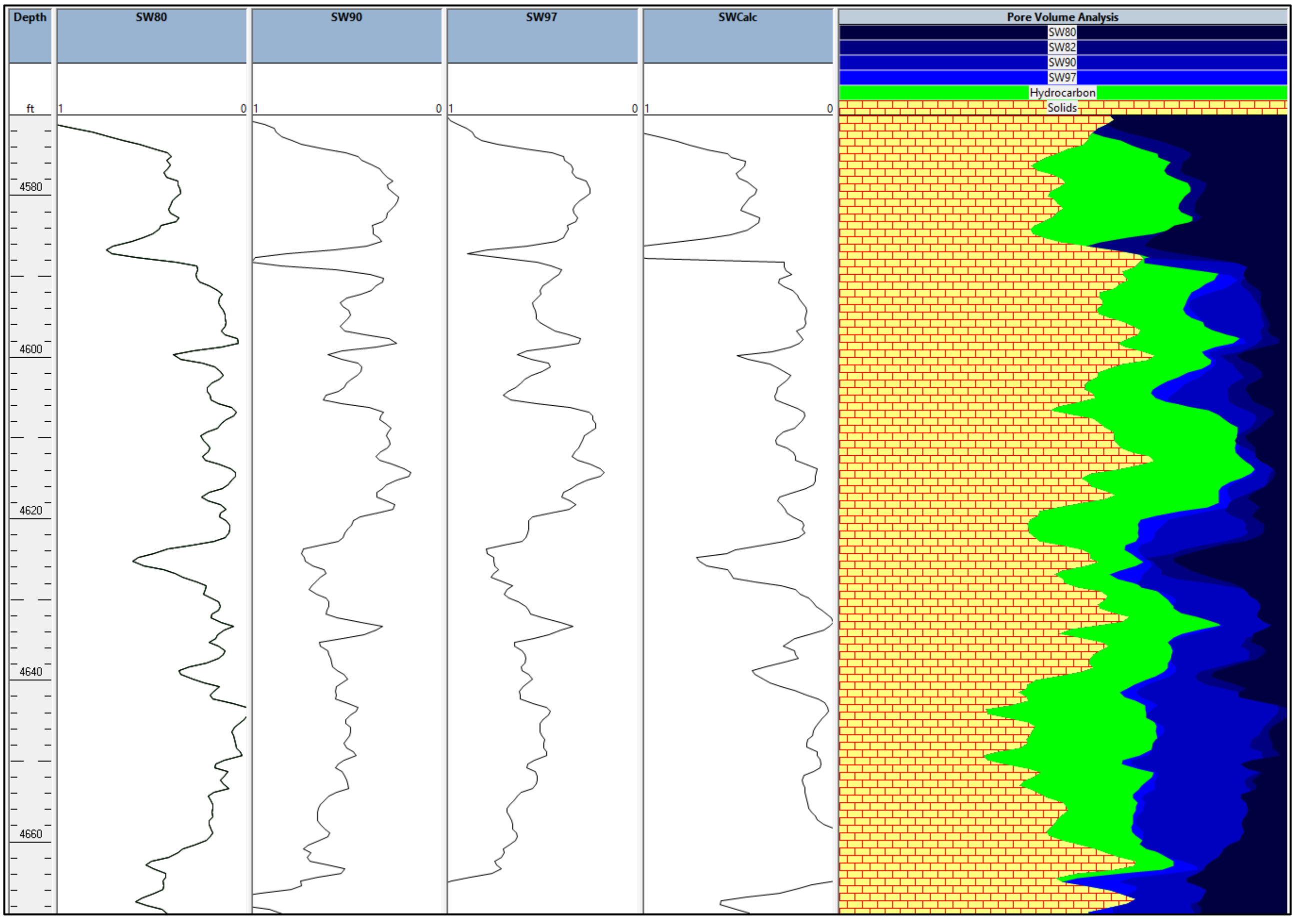

Fig. 11.D.12 – Uncertainty in the water saturation calculation

The Pore Volume Analysis (PVA) presents the stacked successive BVW curves with color-coding (each shade of blue representing a Sigma log), allowing visualization of the extent to which hydrocarbons in the reservoir are gradually replaced by water. The time-lapse technique also applies to operations like Log-Inject-Log and Acid Effect.

In the Log-Inject-Log technique, two Sigma logs are run, the first after injecting fresh water, and the second after injecting salty water. If the salinity of the injected water is known, the Sigma water (fresh and salty) can be calculated, and the water saturation is estimated as:

$$\Delta S_w = \frac{\Sigma_2 - \Sigma_1}{\varphi * (\Sigma_{wsalt} - \Sigma_{fresh})}$$

Where Σ_1 and Σ_2 are the logs after the fresh and salty water injection.

This method is not applied very often due to the complexity of the operation.

In the Acid Effect technique, the target objective is rather the change in porosity resulting, for example, from the dissolution of fines by the acid.

11.D.2.g Gas detection and quantification

At reservoir conditions, gas presents a Sigma value between 0 and 15 c.u. Its detection and quantification are possible using the previously presented models. Also, the capture and inelastic counts of the near and far detectors have been used for qualitative gas detection purposes for decades.

Due to its lower density, the neutron's slowdown time is longer in the presence of gas. Consequently, the inelastic counts of the far detector increase, while the near detector counts decrease. Something similar occurs with the total capture counts.

This phenomenon is currently exploited by different tool providers to quantify the gas saturation based on the different ratios. Figure 11.D.13 shows a time-lapse calculation in a CO_2-EOR well. The PNL tool used in this study contains 3 detectors, facilitating the gas detection as the increase in GR counts is larger (relative to the near detector) as the distance from the source increases. The gas saturation quantification, shown in tracks (d) and (e), was obtained using a proprietary algorithm, based on the ratio of short to long capture counts (RATO13 in track (b)) and the measured Sigma in track (c).

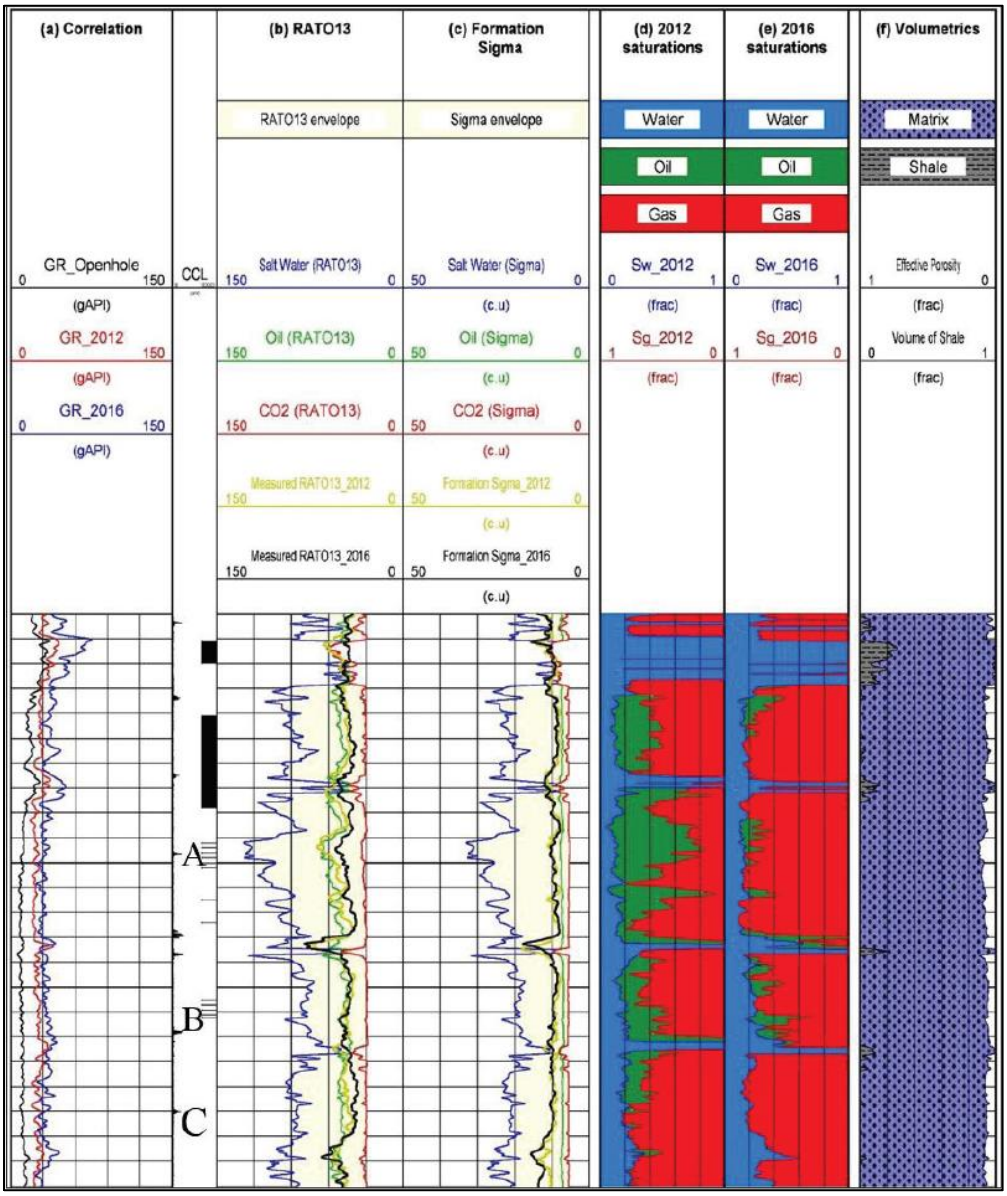

Fig. 11.D.13 – Gas quantification using capture ratio and Sigma – "Developing best practices for evaluation fluid saturations with pulsed neutron capture logging across multiple active CO_2-EOR fields". A. Conner, D. Chase, et al.

11.E Carbon/Oxygen inelastic mode

As discussed in Section 11.C, early neutron interactions with the formation are dominated by inelastic collisions. Here, the element hit by the neutron will become temporarily excited and will eventually go back to its natural energy state by giving off a characteristic Gamma ray of a certain energy. These interactions occur with multiple elements in the formation and completion, and a composite Gamma ray spectrum, as shown in black in Figure 11.E.1, is measured. From this spectrum, two particular peaks, the one of Carbon (4.43 MeV) and the one of Oxygen (6.13 MeV), are of interest for saturation calculations. Instead of looking directly at counts, which depend on the tool geometry, type of detector, and source characteristics, the output is expressed as a ratio of the Carbon to Oxygen counts. The carbon/oxygen, or simply 'C/O' logging technique, determines the oil and water saturation, regardless of the salinity of the formation water, as this does not affect the amount of oxygen. Compared to Capture mode, where the total Gamma ray counts are measured versus time, C/O logging is a GR spectroscopy technique. The depth of investigation is very shallow, between 5 and 7 inches.

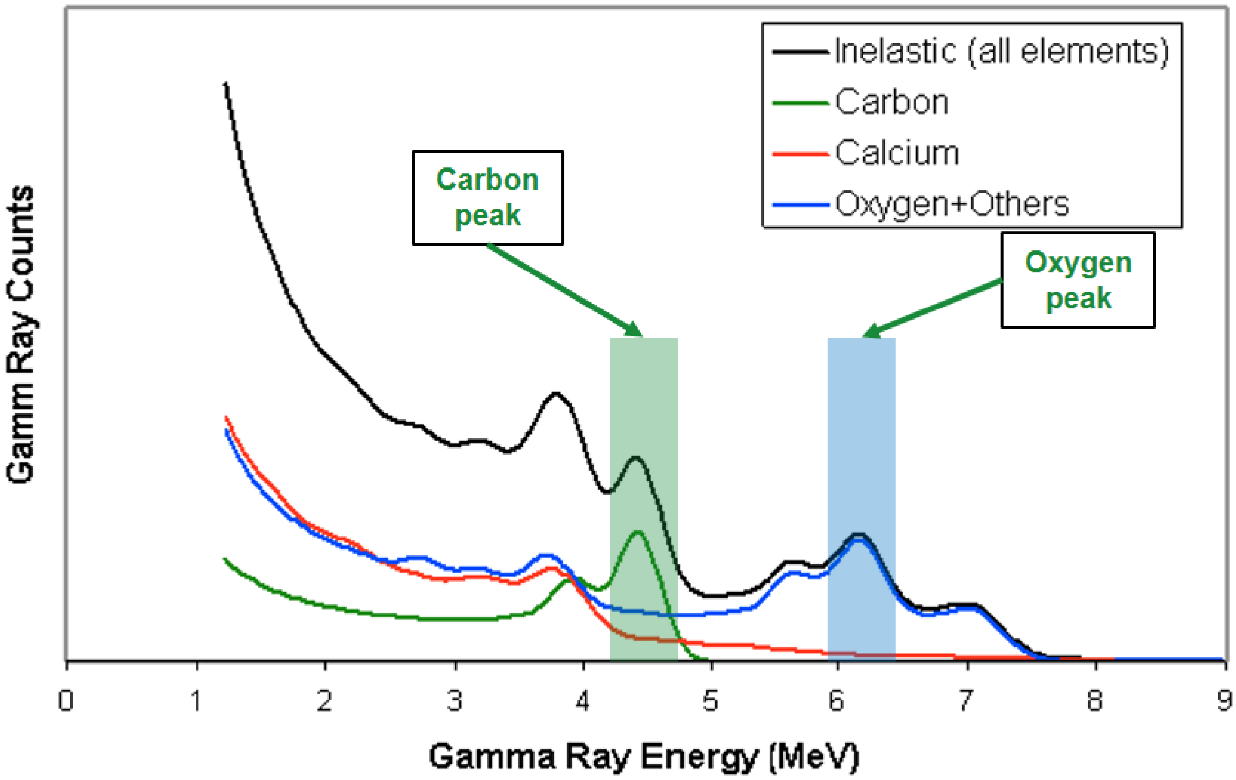

Fig. 11.E.1 – Inelastic Gamma ray spectrum

This technique allows to compute the oil and water saturation, due to the large contrast in Carbon and Oxygen densities. However, these two elements are not only present in the formation fluids. Limestone ($CaCO_3$), oil in the borehole, steel casing, cement, etc., contain different concentrations of Carbon, resulting in a different C/O ratio. Also, the C/O ratio is a function of the porosity. At 0% porosity, the C/O of the formation would be measured, which is different for $CaCO_3$ or SiO_2. This dependency with the porosity led to cross-plots of C/O versus porosity, also known as 'fan charts'. There are as many fan charts as combinations between formation lithology, borehole size, borehole fluid, presence/absence of cement, etc., exists. For example, Figure 11.E.2 shows four fan charts in a 6-inch open hole well. On the left, the C/O for limestone and sandstones in an oil-filled borehole are shown. Due to the change in the formation composition, the C/O ratio is higher for the carbon-rich limestone. Similar to the

Sigma-porosity cross-plot, the two curves joining 0% with 100% porosity represent the 0% and 100% oil saturation conditions (blue and green, respectively). The dashed lines represent the 25, 50, and 75% oil saturations in the limestone.

Figure 11.E.2 (right), the C/O response to the same limestone and sandstone formations are now presented for a water-filled borehole. The carbon counts decrease due to the absence of oil.

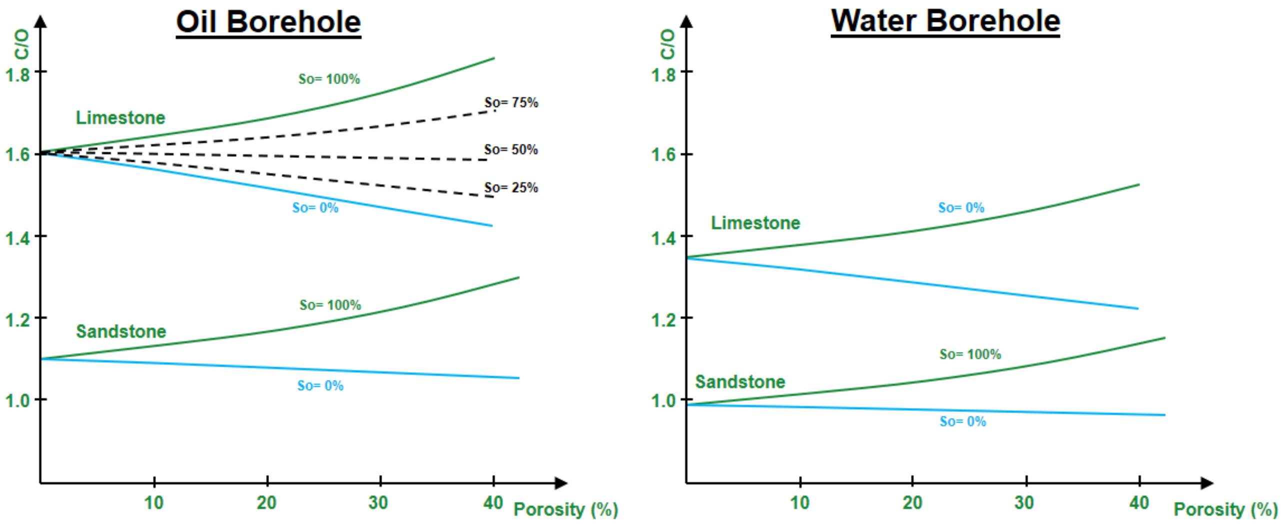

Fig. 11.E.2 – Fan charts for Limestone and Sandstone in oil (left) and water (right) boreholes

These are just 4 charts, but the number of possible combinations is huge. The C/O interpretation requires a detailed formation petrophysical analysis and extra information such as caliper, holdups, porosity, etc.

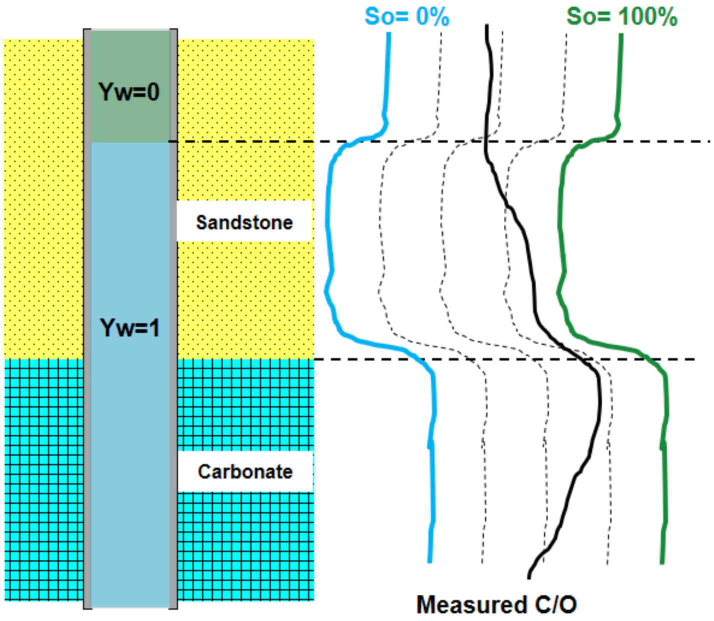

If a representative fan chart is defined at every depth of the log, then the oil saturation can be calculated directly, as schematically shown in Figure 11.E.3. In this case, the log goes through a carbonate and sandstone formation, and also a water-oil contact is detected inside the pipe. These factors affect the 0 and 100% C/O end points. This schematic is for a constant porosity, as the separation of the end points remains constant. But typically, the separation will also change as the porosity varies with depth.

Fig. 11.E.3 – Saturation calculation from C/O

Modern interpretation approaches include the use of elemental yields, which compute the concentrations of the elements to match the measured energy spectra. This is done through proprietary algorithms and are sometimes difficult to validate by third parties.

11.F Oxygen activation mode

Oxygen activation mode is used to monitor and quantify the water movement inside the pipe and behind the casing. This method is known as the Water Flow Log.

The 14 MeV neutron burst irradiates the surrounding water, which contains oxygen. The neutron-oxygen interaction can be described as an exchange or 'n,p' reaction, which generate ^{16}N. This isotope decays, with a half-life of 7.13 seconds, producing Gamma rays of 6.13 MeV:

$$^{16}O + n \Rightarrow p + {}^{16}N^* \Rightarrow {}^{16}O^* \Rightarrow {}^{16}O + \gamma$$

The 'activated' oxygen travels at the water velocity, either inside or behind the casing. At the different detectors, a Gamma ray cloud will be observed. Since the distance between the source and the detectors is known, the water velocity may be estimated by dividing the distance by the time of the peak, since the firing of the neutron:

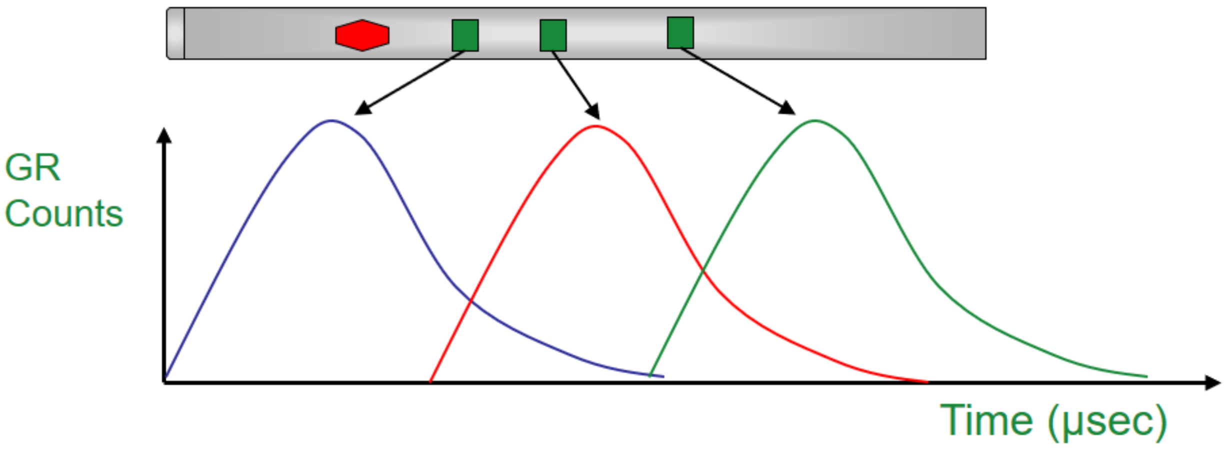

Fig. 11.F.1 – Schematic of oxygen activation logs

In oxygen activation mode, the PNL detectors work on spectral mode, focusing on the energy peaks of the produced Gamma rays. The measurement is recorded in stations, typically composed by multiple neutron firings, to obtain several readings, from where an average response is obtained. It is necessary to subtract the background Gamma ray counts to obtain a clean signal. Radioactive scale depositions may overwhelm the 'useful' Gamma ray signal, making the extraction of a representative water velocity impossible.

In this PNL mode, the tool configuration is important. The detectors must be downstream from the generator, which requires a clear understanding of the well's flow and is problematic. For PNL tools with two GR detectors, it is common to add a third detector to improve the statistical validity of the measurements. This third detector can also help to detect the decaying Gamma rays in high velocity wells. The 7.13 seconds half-life of the ^{16}N isotope imposes limitations on the maximum and minimum fluid velocity. For high velocity wells (> 150 m/min) the Gamma ray decay may occur once the water has passed the second detector. On the other hand, low velocity wells, specially deviated multiphase with recirculation, the decay may occur before the first detector, or the GR readings may not show a clear peak to select. Note that the water flow may occur inside or behind the pipe, making this tool a good candidate to check for channeling and other integrity issues.

Figure 11.F.2 shows an oil injector, with four perforations located above the expected water-oil contact. Water, however, is produced by the bottom perforation, as indicated by the spinner and density measurement. The VDL shows clear train tracks below the bottom perforation, corresponding to casing arrivals. This is an indication that the annular cement is not good. Moreover, the temperature departs from the geothermal gradient below the bottom perforation, indicating fluid movement. Based on the lack of spinner deflection below the bottom perforation, it is expected that the fluid, in this case water, flows behind the pipe.

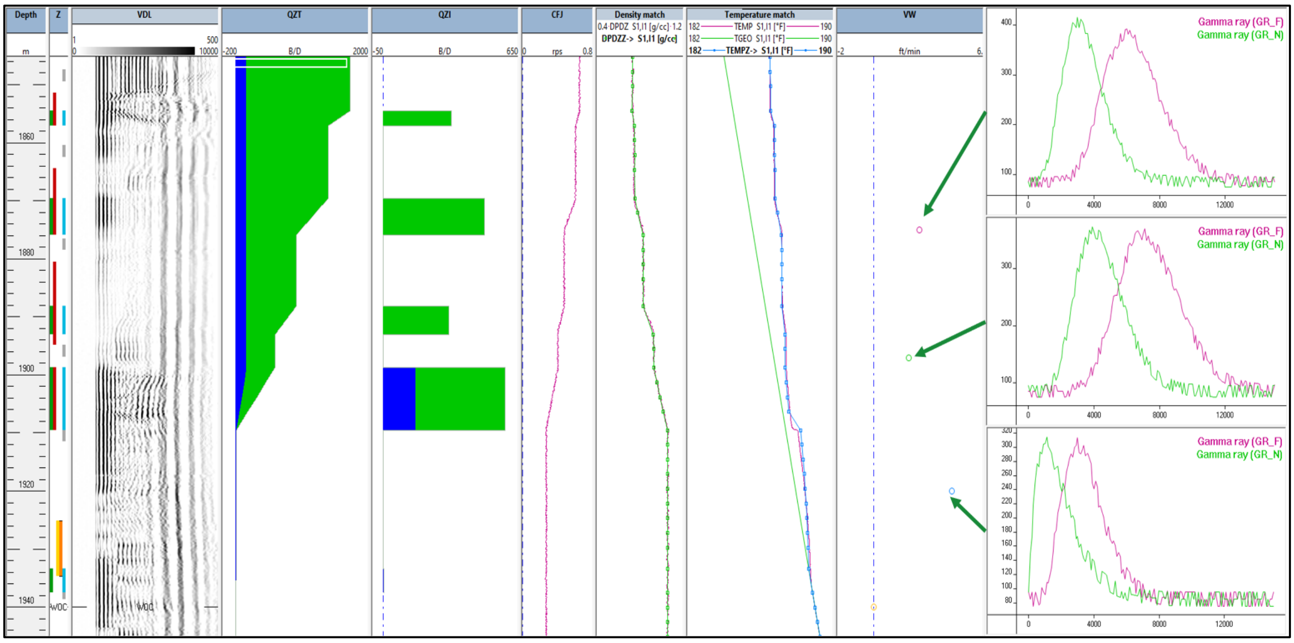

Fig. 11.F.2 – Water velocity measurement inside and behind pipe

An oxygen activation log was run, and the results are presented as Water velocity stations in the last track on the right. Next to this are the near (green) and far (red) Gamma ray counts (cps) versus time (msec). Below the bottom perforation, where the water flows behind pipe, the Gamma ray counts occur very early, showing higher water velocity than the other stations. This is likely due to the small size of the channels, compared to the pipe ID above the bottom perforation. Also, the Gamma rays counts from below the bottom perforation are lower, as these are produced behind casing, which attenuates the measurements.

In Emeraude, the water velocity from an oxygen activation log can be used as an input of a single or multiphase PL interpretation, assuming that the water flows through the pipe ID.

12 – Appendices

12.A Selective Inflow Performance

In multilayered reservoirs, monitoring the layers' pressure and productivity index, is key for production optimization and future drilling plans. When multiple reservoirs are produced commingled, differential layer depletion may occur, leading to cross-flow and sub-optimal well production. It is possible to measure the individual layer pressures with Formation Testers, but this can only be done during the drilling stage. Once cased, to test the various layers individually, it would be necessary to isolate them, using plug and packers, in an operation that would be very expensive, as a rig is required.

Stewart (SPE-10209) proposed the use of Production Logging to compute the layer's Inflow Performance Relationship (IPR), in a technique called Selective Inflow Performance, or SIP. The well is flowed at several different stabilized surface rates and for each rate, a production log is run across the entire producing interval to record simultaneous profiles of downhole flow rates and flowing pressure.

Figure 12.A.1 shows a typical multirate acquisition sequence, necessary for performing an SIP analysis. The up and down red arrows correspond to the Production logging passes. These are recorded once the rates and pressures are considered stable. The horizontal black arrows correspond to the stabilization periods. For SIP analysis, it is not necessary to record the pressure stabilization, even though it is helpful to assess the well's stability. However, multirate PL acquisitions are sometimes run as part of multilayer transient analysis, where stationary pressure measurements are necessary.

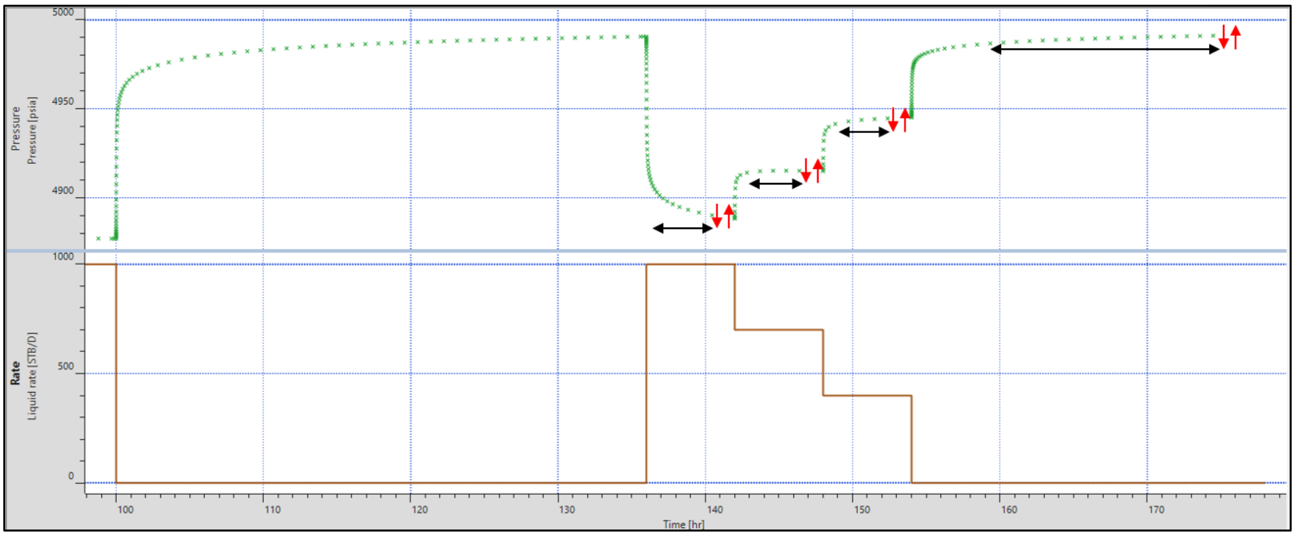

Fig. 12.A.1 – Multirate PL acquisition.

Consider the multirate PL acquisition presented in Figure 12.A.2. In this gas well, three flowing surveys and one final shut-in were recorded. From left to right, this image shows the maximum rate, 2/3, 1/3 and shut-in. Even during the 1/3 flowing condition, cross-flow is observed, with the upper layer producing, and the bottom layer acting as a thief zone. During the shut-in, the cross-flow rate increases even more, due to the decrease of the bottomhole pressure. The presence of cross-flow indicates that the reservoir units are hydraulically isolated.

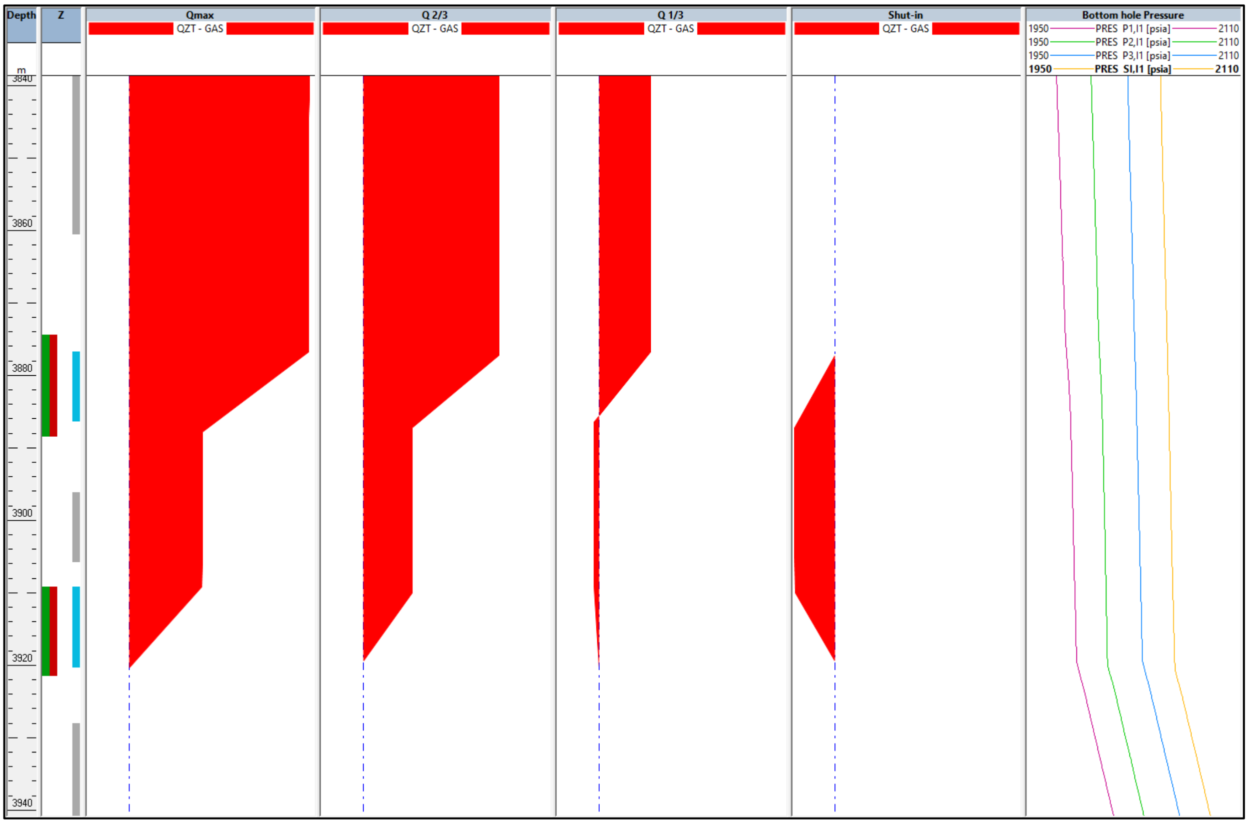

Fig. 12.A.2 – Multirate PL acquisition

Each PL survey is interpreted as explained in Chapters 3 to 6. As a result, for each survey, a couple [rate, pressure] is obtained for the various reservoir zone. These are the axes variables of a conventional IPR plot. The PL-measured in-situ rates can be converted to surface conditions using PVT data.

For the pressure, the interpretation reference channel is interpolated at the top of the zone. For the rate, the value used in the SIP is the contribution. It is calculated for a given reservoir zone as the difference between the values interpolated on the schematic at the top and the bottom of that zone.

Figure 12.A.3 shows the SIP plot, based on the logs and pressure presented in Figure 2. The IPR for each layer was obtained by regressing over the four [rate, pressure] from each survey. The upper layer is shown in purple, and the bottom in green.

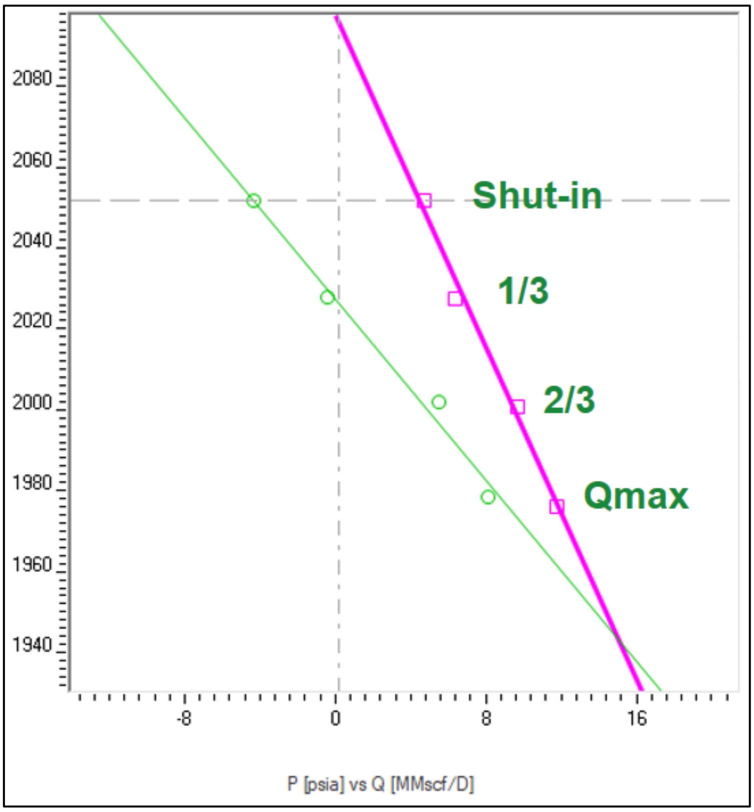

Fig. 12.A.3 – SIP analysis for a 2-layers well with four PL surveys

This analysis provides very valuable information about the two layers. As expected from the PL profiles, the upper layer (purple) is at a higher pressure. On the other hand, the productivity index (inverse of the slope) of the lower layer (green) is higher. This combination of lower reservoir pressure for the highest productivity layer is expected, as this layers are preferentially produced at early stages of the life of the well, resulting in a quicker pressure drop.

This analysis also shows that there is a bottomhole flowing pressure range where cross-flow exists, however this would not be noted from surface. The black line Figure 12.A.4 shows the composite well behavior, this is, the total rate (sum of all layers) and the pressure at the top of the uppermost layer. This replicates the typical commingled IPR that can be measured from surface with traditional multirate testing (flow-after-flow, isochronal, etc.). In the area highlighted by the red triangle, the composite line indicates that the well is producing. However, at this pressure range, the upper layer produces, while the bottom layer takes part of the production. To avoid cross-flow, the maximum bottom hole flowing pressure this well should be produced at is then at the bottom of the triangle, where the bottom layer goes from thief to producing.

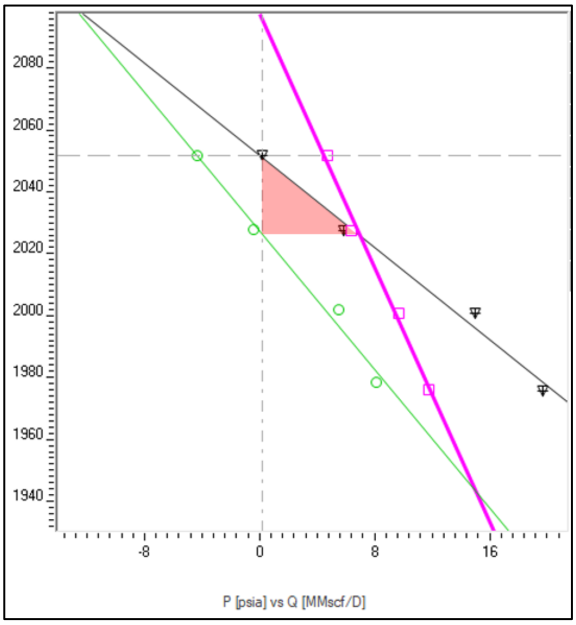

Fig. 12.A.4 – Bottomhole flowing pressure range where cross-flow exists

In summary, after interpreting the various Production Logging surveys, the SIP method consists in fitting the [rate, pressure] points with an IPR model. In Figures 3 and 4, a straight line was used, which is not theoretically correct for gas wells. Three IPR models available in Emeraude are presented next.

Figure 12.A.5 shows two important aspects of the SIP analysis:

1. It can be applied to injector wells. This helps to differentiate between over-pressurized layers and low injectivity (i.e. due to damage, clay swelling).
2. As shown in the Zones track (first on the left), the reservoir zones in green may include multiple perforations.

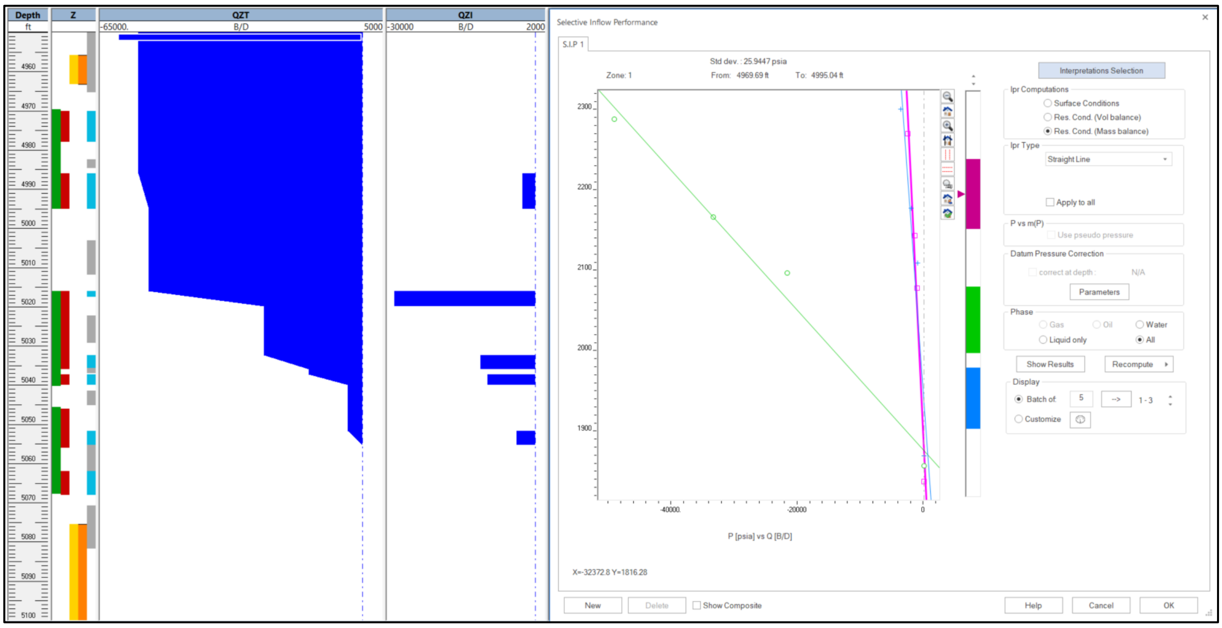

Std dev. : 25.9447 psia
Zone: 1 From: 4969.69 ft To: 4995.04 ft

Ipr Computations
○ Surface Conditions
○ Res. Cond. (Vol balance)
● Res. Cond. (Mass balance)

Ipr Type: Straight Line
☐ Apply to all

P vs m(P)
☐ Use pseudo pressure

Datum Pressure Correction
☐ correct at depth : N/A

Phase
○ Gas ○ Oil ○ Water
○ Liquid only ● All

Display
● Batch of: 5 --> 1 - 3
○ Customize

X=-32372.8 Y=1816.28

☐ Show Composite

Fig. 12.A.5 – SIP analysis in an injector well

In the previous analysis, the middle reservoir takes 88% of the total water. This can be caused either by a low reservoir pressure, or better formation and completion properties. Through the SIP analysis it can be concluded that the middle reservoir (green line) has a better injectivity than the other layers. Therefore, just by increasing the injection pressure, the flooding of the top or bottom layer will not be improved. Stimulation treatments need to be considered.

12.A.1 IPR Types

Straight line: Darcy

The pseudo-steady state Darcy equation in cylindrical coordinates, for a fully-penetrating well, allows to compute the production rate (*q*), based on:

$$q = \frac{k\,h}{141.2\,B\,\mu}\,\frac{(\bar{p} - p_{wf})}{(\ln\frac{r_e}{r_w} + S)}$$

Where *k* is the permeability, *h* the net formation drained thickness, *B* the formation volume factor, *μ* the fluid viscosity, r_e the drainage radius, r_w the wellbore radius, *S* is the skin, $\bar{p}$ is the average pressure and p_{wf} is the bottomhole flowing pressure.

The lumped terms on the right-hand side of the equation, apart from the pressure difference, is called the Productivity Index (PI). The previous equation can be re-written as:

$$q = PI * (\bar{p} - p_{wf})$$

Plotting Pwf versus q gives a Straight line, where the slope is 1/PI and the Y-axis intercept is $\bar{p}$.

This option requires at least two valid data points, meaning two surveys. One can be flowing, the other shut-in. As with any regression technique, more points lead to a better statistical validity.

L.I.T.: a & b

The Laminar Inertial Turbulent (LIT) equation is deduced from the Forchheimer or Houpeurt equation. As the name suggest, it incorporates the turbulence effects, typically seen in high-rate gas wells.

This IPR can be expressed as:

$$\bar{p}^2 - p_{wf}^2 = aq + bq^2$$

Where *a* is the Darcy term, and *b* is the turbulence flow term. The use of the pressures-squared is a traditional way to linearize the diffusivity equation, but is only applicable for low pressures, where the product $\mu_{g}*z$ is constant. A more general solution consists of using pseudo-pressures:

$$m(\overline{p}) - m(p_{wf}) = aq + bq^2$$

The terms *a* and *b* are given by the Jones equation. *a* has a similar meaning as the PI, including the Darcy flow, Skin, viscosity. *b* is a rate dependent-skin, and includes the turbulence coefficient.

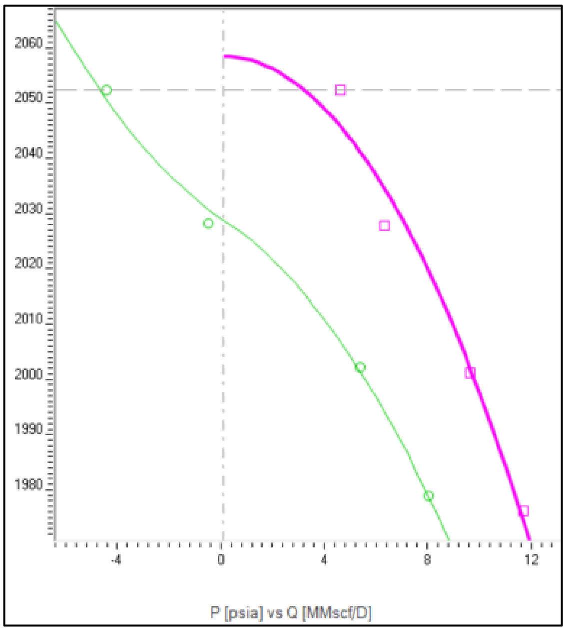

Figure 12.A.6 shows the use of the LIT IPR to the data previously presented. Note that the IPR model affects the estimate of the average pressure calculation. If a layer contains positive and negative rate points (like the green curve), the associated error on the average pressure is lower than for layer with only positive rates (due to extrapolation).

As regression is used, some points may not fit the proposed model. The analyst has to review the PL interpretations and evaluate the applicability of the model to the particular well.

Fig. 12.A.6 – LIT IPR

Fetkovich: C & n

The empirical equation was originally presented by Rawlins and Schellhard for gas, and later extended for oil wells by Fetkovich.

$$q = C * (\bar{p}^2 - p_{wf}^2)^n$$

Using pseudo-pressures:

$$q = C * (m(\overline{p}) - m(p_{wf}))^n$$

C is the performance coefficient, and *n* is the turbulence exponent (0.5 for fully turbulent and 1 for laminar).

12.A.2 Other Considerations

Pseudo-pressures

The equations used in the IPR analysis assume constant fluid characteristics (compressibility, viscosity, formation volume factor). In gas this is seldom the case, and as previously shown, pressure-squared is used as an approximation, but with limited applicability. The most general approach is to use the real gas potential or pseudo pressure m(p).

$$m(p) = \int_{p_0}^{p} \frac{p * dp}{\mu * z}$$

Where p is the pressure and p_0 is taken as the atmospheric pressure. The calculation of z(p,t) and μ(p,t) uses the pressure and temperature reference channels of the considered interpretation and the associated PVT module.

Datum Correction

The pressure used in the SIP analysis is the one directly measured by the PL toolstring. However, simply due to the depth difference between layers, the bottomhole pressure will be different. To evaluate depletion, highlight the cross-flow, reference the measurements to a bottomhole gauge, etc., it is recommended to apply the datum correction. The wellbore fluid column, typically obtained from a shut-in pass (p_{ref}), is used to shift the pressure points to the selected depth:

$$\Delta p_{IPR} = P_{ref}(datum\ depth) - P_{ref}(IPR\ depth)$$

Limitations

The IPR theory only applies to single phase flow, as there are no relative permeabilities involved. However, in practice the SIP method is applied in multiphase wells. Provided that the well is stable, the calculated average layer pressures should be valid. The productivity index or performance coefficients can still be used as qualitative indicators, but relating them to the reservoir properties (permeability, skin, etc.) is not recommended.

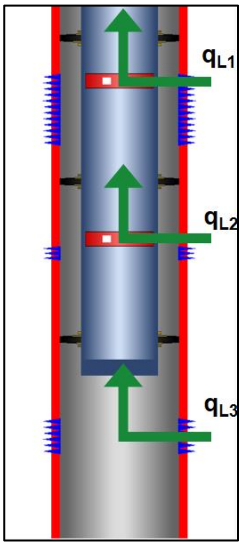

When comparing the SIP results with the theoretical IPR behavior, the analyst must remember that the PL measurements are performed inside the wellbore, and therefore are affected by the completion characteristics. For example, in Figure 12.A.7, the two upper inflow zones are located inside the tubing. The produced fluid has to go through the perforations and then through the SSDs, to finally reach the tubing. This completion configuration is different than what is seen at the bottom perforation, where the pressure drop for the fluid to enter to the position where the toolstring is located is lower, due to the absence of the tubing and SSD. Variations in the completion along the log must be taken into account before comparing productivities of the various logged intervals.

Fig. 12.A.7 – Effect of the completion on the inflow performance

The IPR equations were derived for pseudo-steady state. This condition exists when the pressure disturbance has reached the boundaries, and the shape of the pressure profile stabilizes and moves downwards as the reservoir depletes. In this condition, a relationship between the production and pressure difference $(\bar{p} - p_{wf})$ can be established, as predicted by the equations presented previously.

The stabilization periods of the multirate PL acquisition must be planned based on the reservoir characteristics. Low permeability formations take longer to stabilize, and may remain in transient for weeks or months. In practice, most of the time PSS is not reached before acquiring the downhole data. Therefore, the well is considered stable when the pressure changes are small enough to be ignored.

Figure 12.A.8 shows the typical transient IPR behavior, where the productivity index decreases with time, until pseudo-steady state is reached. Note that in the case of SIP, since the IPRs are calculated by regression, the transient effect may also affect the pressure layer calculation due to extrapolation errors.

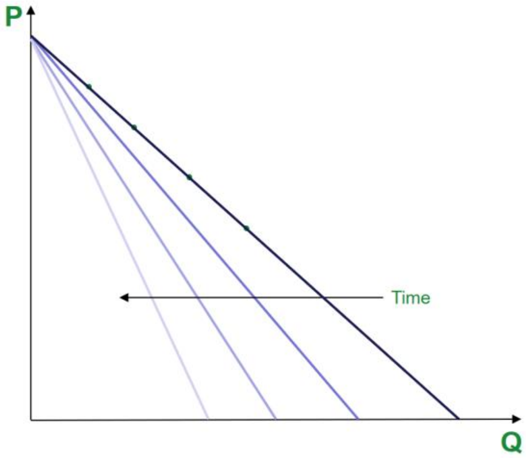

Fig. 12.A.8 – Transient IPR behavior

12.B APERM

A traditional way to estimate the reservoir permeability from open hole logs consists of applying a transformation to the porosity log. Core data is used to obtain a relationship between permeability and porosity, and this is applied to the open hole porosity log, resulting in a permeability log. The effective reservoir permeability, however can be dramatically different from the matrix permeability in the presence of vuggy porosity or fractured reservoirs. This is especially relevant in carbonate reservoirs, as the primary source of flow capacity are fractures. The commingled effective permeability can be estimated through conventional Pressure Transient Analysis. However, for heterogeneous reservoirs with vertical properties variation, the commingled behavior may not be representative of the different flow units.

The effective permeability can be calculated from production log inflows. This method, presented in SPE-102894, was first applied in Tengiz field, producing from a giant carbonate reservoir. The use of this permeability as input to a reservoir model, constitutes an inherent match to fluid flow. Models prepared with this input depict the correct amount of production by layer, resulting in much less time required to obtain a history match, with fewer adjustments.

While the technique is applicable to sandstone and carbonate reservoirs, it is most needed in carbonates due to the presence of "excess permeability" zones, typically due to fractures and vuggy porosity. These intervals can be difficult to identify, and accurate prediction of permeability from static petrophysical well logs is not possible.

The APERM method uses Darcy pseudo-steady state equation to solve for the permeability-thickness (*kh*) product of each inflow zone:

$$k\,h = \frac{q * 141.2\,B\,\mu}{(\bar{p} - p_{wf})}\left(\ln\frac{r_e}{r_w} - 0.75 + S\right)$$

These parameters were presented in the Appendix 1, for the Darcy IPR.

The sources of the inputs are:

- q is the contribution (QZI) obtained from a PL interpretation. This can be single-phase or a fluid mixture. Note that the Darcy equation is valid for single-phase flow (no relative permeabilities)
- B is taken as 1, as the inflow rates are calculated at downhole conditions
- μ is obtained from PVT. If a liquid mixture is considered, the oil viscosity is used, leading to an oil effective permeability calculation. If gas is considered, Darcy equation in terms of pseudo-pressure is used.
- p_{wf} is measured by the PL toolstring
- $\bar{p}$ may come from a Selective Inflow Performance analysis, requiring a multirate PL acquisition. Otherwise, a manual $\bar{p}$ input is required.
- r_e and r_w are user inputs. Being inside a natural logarithm, $\frac{r_e}{r_w}$ is around 9 for typical drainage radius (~3000 ft).
- The layer skin S is probably the main parameter affecting the permeability calculation. It may come from a pressure transient analysis, but this value is likely to be a commingled response. Determining the most representative skin value usually involves a close examination of the completion and stimulation history, plus checking for other factors which may have created wellbore damage.

Figure 12.B.1 shows the permeability thickness product as a function of the skin, for a fixed productivity index (PI) in 3 different layers. Layer 1 shows the lowest PI, and an uncertainty of 1 unit in the skin is reflected as a 2 mD*ft *kh* variation. On the other hand, Layer 3 presenting the highest PI, shows that an uncertainty of 1 unit in the skin leads to a variation of 9 md*ft.

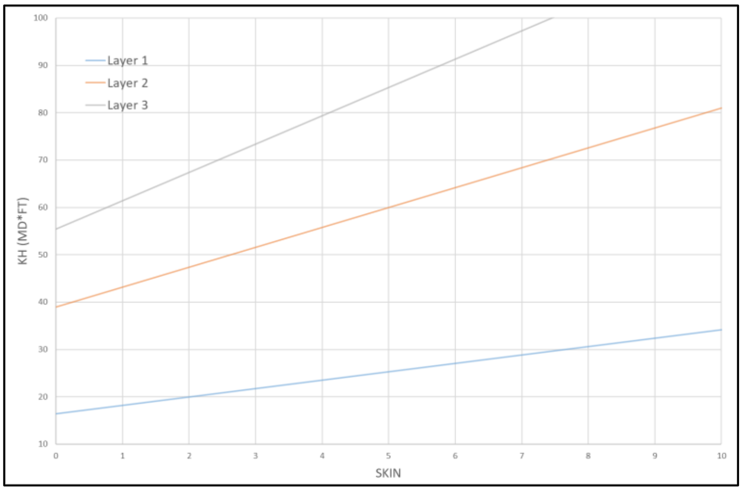

Fig. 12.B.1 – Multirate PL acquisition

12.B.1 Calculation

With a valid PL interpretation and representative inputs required by the Darcy equation, the PL-derived permeability can be calculated. Figure 12.B.2 shows the results of the analysis. The track 'APERM Transform k' shows the open hole permeability in red, and PL-calculated permeability in blue. Commonly, a well test total KH product (kh_{WT}) is used as a normalization parameter for the individual layers APERM calculation. The normalized KH ($k\,h_{PL\_NORM\_i}$) is calculated as:

$$k\,h_{PL\_NORM\_i} = \frac{k\,h_{PL\_i}}{\sum h_i} * \frac{kh_{WT}}{k\,h_{PL_{cum}}}$$

The layer inflows and cumulative profile are calculated solving the Darcy equation, based on the inputs and results of the APERM analysis. As shown in 'APERM QOZI/QOZT comparison' track, these calculations are compared with the PL interpretation results. Discrepancies between measured and predicted flowrates may indicate non-producing perforations or errors in the permeability calculations.

The APERM BOOST track shows the multiplier required to match the transform permeability with normalized permeability-thickness products. BOOST$_i$ values lower than one correspond to apparent permeability being lower than transform. The likely causes are overoptimistic permeability transform and/or underestimated skin. BOOST$_i$ values higher than one correspond to excess permeability (apparent permeability is higher than transform). The likely causes are vuggy porosity, natural fractures and/or overestimated skin.

$$BOOST_i = \frac{k\,h_{PL\_NORM\_I}}{\sum k_{transform\_j} * h_i}$$

The Final track in Figure 12.B.2 shows the cumulative permeability-thickness product. The two logs displayed are the modified transform permeability (KH_APERM) and the normalized permeability from PL. The difference suggests that one or more perforated intervals are not contributing to flow.

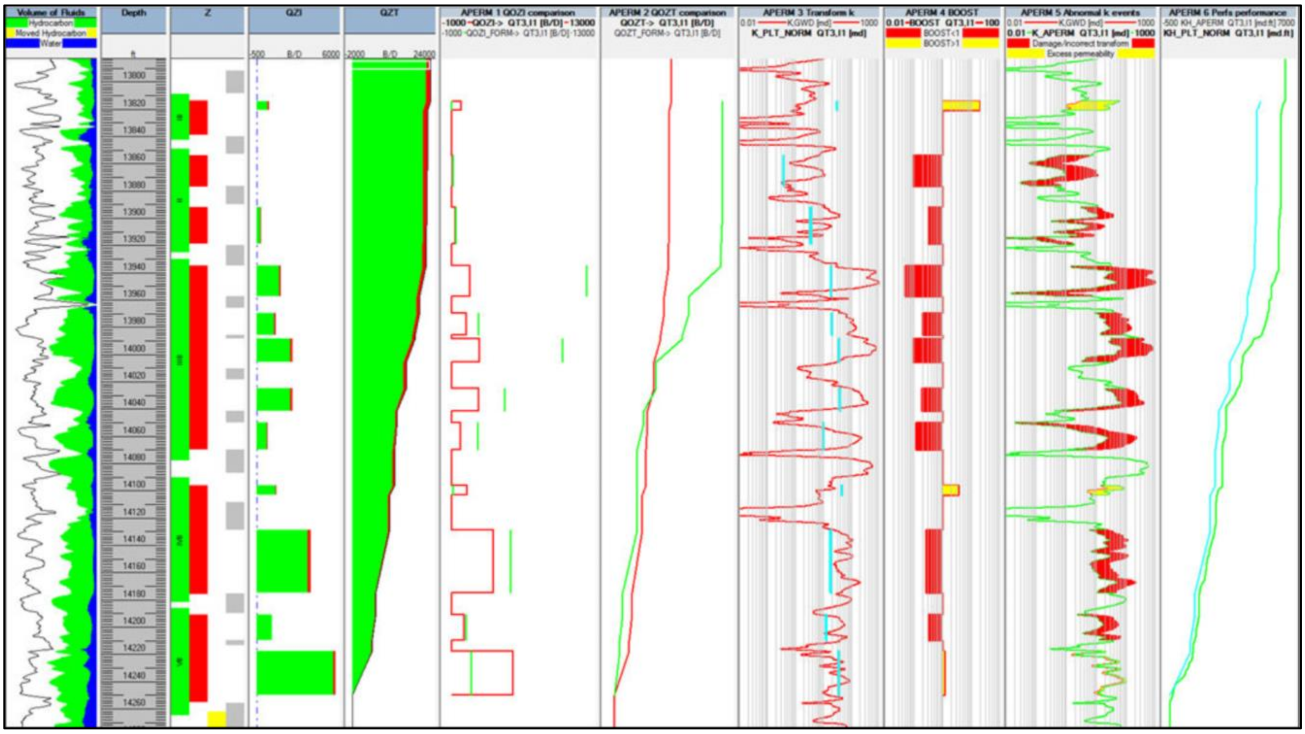

Fig. 12.B.2 – APERM Results

13 – References

General references

Houze, O., Viturat, D., Fjaere, O. "Dynamic Data Analysis", v5.40, KAPPA, 2021.

Ellis, D., Singer, J. "Well Logging for Earth Scientists", 2nd Edition, Springer, 2008.

Serra, O. "Fundamentals of Well-Log Interpretation", Elsevier, 1984.

Whittaker, C. "Fundamentals of Production Logging". Schlumberger, 2013.

Smolen, J. "Cased Hole Logging and Production Log Evaluation", PenWell, 1996.

Hill A.D. "Production Logging – Theoretical and Interpretive Elements", SPE Monograph Vol.14, 1990.

Chapter 1: Why CHL?

NORSOK Standard D-010, Rev 3, 2004. "Well Integrity in Drilling and Well Operations"

Davies, R., Almond, S., Ward, R., Jackson, R., Adams, C., Worrall, F., Herringshaw, L.G., Gluyas, J.G., Whitehead, M.A. "Oil and Gas Wells and their Integrity: Implications for Shale and Unconventional Resource Exploitation", Marine and Petroleum Geology 56 (2014), 239-254.

Bourgoyne, A., Scott, S., Manowski, W. "A Review of Sustained Casing Pressure Occurring on the OCS", Louisiana State University report, 2000.

Kinik, K. "Risk of Well Integrity Failure due to Sustained Casing Pressure", MSc Thesis, Louisiana State University, 2012.

Aichinger, F., Dao, N.H., Brillaud, L., Nobbs, B., Delapierre, A., Pinault, C., Rossi, X. "Systematic Field Validation of New Casing Wear Qualification Process", SPE-193386-MS, 2016.

Chapter 2: Acquisition and Operations

NORSOK Standard D-SR-008, Rev 1, 1996. "System Requirements - Wireline Equipment"

International Coiled Tubing Association (ICOTA), "An introduction to Coiled Tubing: History, Applications and Benefits", 2005.

Chapter 3: Flowmeters and Single-phase Profiling

Abbassi, L., Tavarnier, E., Donzier, E., Gysen, A., Gysen, M., Chen, C.K., Zied, A., Cedillo, G. "Efficiency Improvements in Production Profiling Using Ultracompact Flow Array Sensing Technology", Petrophysics 59 (2018), No. 4, 457-488.

Chapter 4: Fluid Identification Tools

Zett, A., Webster, M., Noordermeer, A., Hockley, M., Lockyer, G., Browne, H., Donkin, C. “New Sensor Development Helps Optimise Production Logging Data Acquisition in Horizontal Wells”, SPWLA 52nd Annual Logging Symposium, 2011.

George, A.K., Singh, R.N. “Correlation of Refractive Index and Density of Crude Oil and Liquid Hydrocarbon”, International Journal of Chemical, Environmental & Biological Sciences (2015), Vol 3, Issue 5.

Chapter 5: Multiphase Flow and Profiling

Brennen, C.E., “Fundamentals of Multiphase Flows”, Cambridge University Press, 2005.

Duns H., and Ros N., "Vertical Flow of Gas and Liquid Mixtures in Wells", Proceedings of the Sixth World Petroleum Congress, Frankfurt (1963), Vol. 10, p 694.

Beggs H., Brill J., "A Study of Two-Phase Flow in Inclined Pipes", JPT (May 1973), 607-617.

Taitel Y., Barnea D., Dukler A. E., "Modelling Flow Pattern Transitions for Steady Upward Gas-Liquid Flow in Vertical Tubes", AIChe J. (1980) Vol. 26, No.3 pp. 345-354.

Hassan, A.R., Kabir. C.S. "A Simplified Model for Oil-Water Flow in Vertical and Deviated Wellbores", SPE-49163, 1998.

Nicolas, Y., and Witterholt E.J.: "Measurements of Multiphase Fluid Flow", SPE 4023, 1972.

Choquette, Vertical two-phase flow systems and interpretation of the flowmeter and the gradiomanometer production logs, MSc Thesis, Stanford University, 1975.

Whittaker, A.C., Lenn, C.P. “Improving Management and Allocation of Gas Production in Maturing Reservoirs: A Multi-Phase Spinner Response Model for the 21st Century”, SPE-93135, 2005.

Chapter 6: High Deviation and Horizontal PL

Theron, B.E., Unwin, T. “Stratified Flow Model and Interpretation in Horizontal Wells”, SPE-36560, 1998.

Kotlar, N. “30 Years of Horizontal Production Logging. What are we Really Measuring”, SPE-195506-MS, 2019.

Chapter 7: Thermal Analysis and Simulation

Lienhard, J.H. “A Heat Transfer Textbook”, Phlogiston Press, Fourth edition, 2018.

Carlslaw, H.S., Jaeger, J.C. “Conduction of Heat in Solids”, Clarendon Press, 1959.

Maubeuge, F., Didek, M., Beardsell. M.B., Arquis, E., Bertrand, O., Caltagirone, J.P. “MOTHER: A Model for Interpreting Thermometrics”, SPE-28588, 1994.

Pimenov, V., Brown, G, Tertychnyi, V., Shandrygin, A, Popov, Y. “Injectivity Profiling in Horizontal Wells Through Distributed Temperature Monitoring”, SPE-97023, 2005.

Chapter 8: Multifinger Caliper Interpretation and Applications

Sawaryn, S.J., Pattillo, P.D., Brown, C., Schoepf, V. "Assessing Casing Wear in the Absence of a Baseline Caliper Log", SPE 173143-PA, 2015.

Billingham, M.A., King, B., Murray, A. "Maximising the Life of Corroding Tubing by Combining Accurate Multi-Finger Caliper Data with Corrosion Modelling", SPE 159484, 2012.

API Bulletin 5C3, Sixth Edition, 1994, "Bulletin on Formulas and Calculations for Casing, Tubing, Drill Pipe, and Line Pipe Properties".

Atakishiyev, F., Alkhasov, E., Schoepft, V., Zett, A. "The Role of Internal Diameter Tolerances in Interpreting Casing Inspection Logs", SPE-188981-MS, 2017.

Chapter 9: Passive Acoustic Logging

McKinley, R.M., Bower, F.M., Rumble, R.C., "The Structure and Interpretation of Noise From Flow Behind Cemented Casing", Journal of Petroleum Technology (1973), 329-338.

Lighthill, M.J. "On Sound Generated Aerodynamically. I. General Theory", Proceedings of the Royal Society, A211:564-587, 1952.

Cicione, S., Galli, G., Pirrone, M., Raimondi Cominesi, N. "Quantitative Spectral Analysis of Noise Log Measurements for Enhanced Dynamic Characterization of Complex reservoirs", presented at the 13th Offshore Mediterranean Conference and Exhibition in Ravenna, Italy, 2017.

Rocco, F., Pirrone, M., Galli, G., Moriggi, S. "Advanced Spectral Modeling of Noise Log Data: The Key for a Comprehensive Downhole Dynamic Characterization", SPE-193318-MS, 2018.

Abukhamsin, A. Y. "Inflow Profiling and Production Optimization in Smart Wells Using Distributed Acoustic and Temperature Measurements", PhD Thesis, Stanford University, 2017.

Chapter 10: Cement Evaluation

Pardue, G.H., Morris, R.L., Gollwitzer, L.H., Moran, J.H. "Cement Bond Log – A Study of Cement and Casing Variables", SPE-453, 1962.

Wang, H., Tao, G., Shang, X. "Understanding Acoustic Methods for Cement Bond Logging", The Journal of the Acoustical Society of America, Vol 139, Issue 5, May 2016, 2407-2416.

Chapter 11: Pulsed Neutron Logging

Clavier, C., Hoyler, W., Meunier, D., "Quantitative Interpretation of Thermal Neutron Decay Time Logs: Part I. Fundamentals and Techniques", SPE-2658, 1971.

Conner, A., Chace, D., Abou-Saleh, J., Kim, Y., McNeil, C., Gerst, J., Kelley, M., Place, M., Pardini, R., Gupta, N. "Developing Best Practices for Evaluating Fluid Saturations with Pulsed Neutron Capture Logging Across Multiple Active CO2-EOR Fields", 13th International Conference on Greenhouse Gas Control Technologies, 2016.

TABLE OF CONTENTS